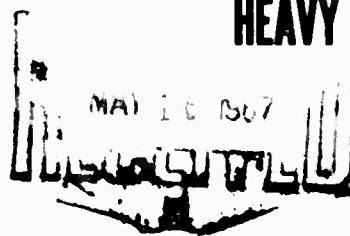


AD

AD 651416

USAAVLABS TECHNICAL REPORT 66-56

PARAMETRIC ANALYSIS AND PRELIMINARY DESIGN OF A SHAFT-DRIVEN ROTOR SYSTEM FOR A HEAVY LIFT HELICOPTER



By

Walter J. Dutton

February 1967

U. S. ARMY AVIATION MATERIEL LABORATORIES
FORT EUSTIS, VIRGINIA

CONTRACT DA 44-177-AMC-275(T)
SIKORSKY AIRCRAFT
DIVISION OF UNITED AIRCRAFT CORPORATION
STRATFORD, CONNECTICUT

Distribution of this
document is unlimited



ARCHIVE COPY

Disclaimers

The findings in this report are not to be construed as an official Department of the Army position unless so designated by other authorized documents.

When Government drawings, specifications, or other data are used for any purpose other than in connection with a definitely related Government procurement operation, the United States Government thereby incurs no responsibility nor any obligation whatsoever; and the fact that the Government may have formulated, furnished, or in any way supplied the said drawings, specifications, or other data is not to be regarded by implication or otherwise as in any manner licensing the holder or any other person or corporation, or conveying any rights or permission, to manufacture, use, or sell any patented invention that may in any way be related thereto.

Trade names cited in this report do not constitute an official endorsement or approval of the use of such commercial hardware or software.

Disposition Instructions

Destroy this report when no longer needed. Do not return it to originator.

ACCESSION NO.	
CFSTI	WHITE SECTION <input type="checkbox"/>
DDC	DIFF SECTION <input checked="" type="checkbox"/>
UNANNOUCED	<input type="checkbox"/>
JUSTIFICATION	
BY	
DISTRIBUTION/AVAILABILITY CODES	
DIST.	AVAIL. and/or SPECIAL
1	



DEPARTMENT OF THE ARMY
U. S. ARMY AVIATION MATERIEL LABORATORIES
FORT EUSTIS, VIRGINIA 23604

This report has been reviewed by the U. S. Army Aviation Materiel Laboratories, and basic technical data presented herein are considered to be sound. However, assumptions dependent upon design philosophy and/or engineering judgment are those of the contractor and do not necessarily reflect the views of the U. S. Army Aviation Materiel Laboratories.

This report is published for the dissemination of information and the stimulation of ideas.

Task ID131001D157
Contract DA 44-177-AMC-275(T)
USAAVLABS Technical Report 66-56
February 1967

PARAMETRIC ANALYSIS AND PRELIMINARY DESIGN
OF A
SHAFT-DRIVEN ROTOR SYSTEM
FOR A

HEAVY LIFT HELICOPTER
Sikorsky Engineering Report 50444

By
Walter J. Dutton

Prepared By
Sikorsky Aircraft
Division of United Aircraft Corporation
Stratford, Connecticut

for
U. S. ARMY AVIATION MATERIEL LABORATORIES
FORT EUSTIS, VIRGINIA

Distribution of this
document is unlimited

ABSTRACT

- The primary objective of this program was to select and design a shaft-driven lifting rotor system for a heavy lift helicopter. The selection included a complete parametric analysis of the aircraft, based on three defined missions: lifting a 20-ton payload 20 nautical miles, lifting a 12-ton payload 100 nautical miles, and ferrying. Several aircraft configurations were studied, and a single rotor crane arrangement was selected. Included in the study were selection of engines and parametric sizing of all major aircraft component systems.

- The aircraft defined in this study has a takeoff gross weight for the 20-ton mission of approximately 79,000 pounds, and uses a single lifting rotor 91.6 feet in diameter. Ferry range exceeds 2400 nautical miles.

While differing in detail from any existing hardware, the rotor system design follows directly from present practice. Methods of analysis and allowable stresses used in this study are the same as those used in existing models. Analyses of aircraft stability and control characteristics and rotor system stability for the selected configuration have been performed, and the methods and results reported herein. For all of the properties studied, both the aircraft and the rotor system have been shown to meet or exceed the requirements of applicable specifications and/or accepted practice.

FOREWORD

This report covers the parametric analysis and preliminary design and structural analysis of a shaft-driven lifting rotor system for a heavy lift helicopter. Sikorsky Aircraft, a Division of United Aircraft Corporation, performed this study under contract for the Department of the Army. Principal investigators were D. S. Jenney and J. R. Olson in performance; D. E. Cooper and R. A. Monteleone in handling qualities; W. F. Paul, R. G. Carlson, and B. R. Traphan in dynamics; W. F. Schlenk and M. L. Marquis in weights; J. A. Longobardi and N. J. Francis in rotor blade design; and L. Vacca and G. A. Smith in rotor head design. The engineering team was headed by W. J. Dutton, Supervisor of the Experimental Blade Group. The study was administered for the U. S. Army Aviation Materiel Laboratories, Fort Eustis, Virginia, by Mr. J. Yeates, Group Leader, Aeromechanics Group, and Mr. W. E. Nettles, Project Engineer.

CONTENTS

	<u>Page</u>
ABSTRACT	iii
FOREWORD	v
LIST OF ILLUSTRATIONS	ix
LIST OF TABLES	xxvi
LIST OF SYMBOLS	xxx
SUMMARY	1
DESIGN REQUIREMENTS	1
AIRCRAFT CONFIGURATION	2
PERFORMANCE	5
BLADE DESIGN	7
ROTOR HEAD DESIGN	7
AIRCRAFT STABILITY AND CONTROL	8
WEIGHT BREAKDOWN	9
PARAMETRIC ANALYSIS	15
CONCLUSIONS	15
DESIGN CRITERIA	18
BASIC DESIGN INFORMATION	20
PARAMETRIC WEIGHT RELATIONSHIPS	31
ROTOR PERFORMANCE METHODS	51
ENGINE SELECTION	53
ROTOR PARAMETRIC METHODOLOGY	60
PARAMETRIC RESULTS	79
EVALUATION OF OPTIMIZED CONFIGURATIONS	91
STABILITY AND CONTROL CHARACTERISTICS	105
DYNAMIC CHARACTERISTICS	108
ROTOR BLADE ANALYSIS	108
AIRCRAFT VIBRATION	112
AIRFRAME VIBRATION CHARACTERISTICS	112
RELIABILITY	123
FINAL CONFIGURATION SELECTION	129
DESIGN PERTURBATIONS	130
WEIGHT/SIZE GROWTH FACTORS	137
MISSION PERFORMANCE FOR DRAG	137

	<u>Page</u>
PRELIMINARY DESIGN AND STRUCTURAL ANALYSIS	145
BLADE DESIGN	145
ROTOR HEAD DESIGN	160
ALTERNATE BLADE AND ROTOR HEAD DESIGNS	178
ARTICULATED ROTOR BLADE STRUCTURAL ANALYSIS	204
ROTOR BLADE LOADS	224
ROTOR BLADE RESULTANT AIRLOADS, SHEARS AND MOMENTS	226
ROTOR BLADE STRUCTURAL ANALYSIS	303
ROTOR HEAD STRUCTURAL ANALYSIS	346
METHODS OF STRUCTURAL DESIGN ANALYSIS	351
CALCULATION OF DESIGN LOADS	359
STATIC STRESS ANALYSIS	375
 AIRCRAFT AEROELASTIC AND FLUTTER ANALYSES AND DYNAMIC STABILITY	 462
CONCLUSIONS	462
HLH AEROELASTIC ANALYSIS	463
CLASSICAL FLUTTER ANALYSIS	479
STALL FLUTTER ANALYSIS	480
TORSIONAL DIVERGENCE	482
PITCH LAG INSTABILITY	484
GROUND RESONANCE	486
HLH GUST RESPONSE	489
AIRCRAFT AERODYNAMIC STABILITY AND CONTROL	494
DESIGN TECHNIQUES AND PHILOSOPHY	496
AUTOMATIC FLIGHT CONTROL SYSTEM	547
COMPLIANCE WITH MIL-H-8501-A	553
 REFERENCES	 570
 DISTRIBUTION	 576
 APPENDIX	 578
MAIN ROTOR BLADE DESIGN STUDY RESULTS	578
ROTOR LOADS FOR DYNAMIC ANALYSIS	588

ILLUSTRATIONS

<u>Figure</u>		<u>Page</u>
1	HLH Payload Versus Mission Radius	6
2	Single and Tandem Rotor Configurations	19
3	Slipstream Impingement on Airframe	22
4	Hovering Induced Power Correction Due to Overlap	24
5	Tail Rotor Sizing Data (Diameter)	27
6	Tail Rotor Sizing Data (Blade Area)	27
7	Horizontal Tail Sizing, Single Rotor	28
8	Main Rotor Blade Weight	32
9	Rotor Group Weight	34
10	Variation of Centrifugal Force with Aspect Ratio	36
11	Tail Rotor Weight	38
12	Stabilizer Weight	39
13	Total Body Weight	42
14	Fuselage Wetted Area	43
15	Alighting Gear Weight	44
16	Flight Controls Weight	45
17	Drive System Weight	47
18	Fixed Equipment Weight	48
19	Hover Performance Correlation	52
20	Single Rotor Engine Selection	54
21	Tandem Rotor Engine Selection	54

ILLUSTRATIONS (cont'd.)

<u>Figure</u>		<u>Page</u>
22	Estimated Minimum Performance of T64/S4A Engine Under Static Conditions	56
23	Estimated Minimum Performance of T64/S4A Engine at Sea Level	57
24	Estimated Minimum Performance of T64/S4A Engine at 5,000-Foot Altitude	58
25	Estimated Minimum Performance of T64/S4A Engine at 10,000-Foot Altitude	59
26	Rotor System Parametrics, Flow Chart	61
27	Preliminary Airfoil Selection, Twist Effect	63
28	Preliminary Airfoil Selection, Tip Speed Effect	64
29	Preliminary Airfoil Selection, Airfoil Effect	65
30	Payload Versus Rotor Radius, Single Rotor	73
31	Payload Versus Rotor Radius, Tandem Rotor	74
32	Takeoff Gross Weight Versus Rotor Radius, Single Rotor	75
33	Takeoff Gross Weight Versus Rotor Radius, Tandem Rotor	76
34	Gross Weight Versus Rotor Radius, Single Rotor	77
35	Gross Weight Versus Rotor Radius, Tandem Rotor	78
36	Final Perturbations, Twist Effect	83
37	Final Perturbations, Tip Speed Effect	84
38	Final Perturbations, Airfoil Effect	85
39	General Arrangement, Single Rotor, 12-20 Ton Skycrane®	87

ILLUSTRATIONS (cont'd.)

<u>Figure</u>		<u>Page</u>
40	General Arrangement, Tandem Rotor, 12-20-Ton Skycrane®	89
41	Hover Ceiling Versus Gross Weight, Single Rotor	95
42	Hover Ceiling Versus Gross Weight, Tandem Rotor	96
43	Forward Flight Characteristics, Single Rotor Basic Fuselage Configuration	97
44	Forward Flight Characteristics, Single Rotor External Load Configuration	98
45	Forward Flight Characteristics, Tandem Rotor Basic Fuselage Configuration	99
46	Forward Flight Characteristics, Tandem Rotor External Load Configuration	100
47	Best Rate of Climb Versus Gross Weight	101
48	Speed at Onset of Stall	102
49	Ferry Range Versus Takeoff Gross Weight	103
50	Blade Natural Frequency, Flapwise Bending	110
51	Blade Natural Frequency, Edgewise Bending	111
52	Dynamic Analysis Models	113
53	Fuselage Dynamic Analysis, Tandem Rotor	114
54	Fuselage Dynamic Analysis, Single Rotor	115
55	Vertical Bending Mode Frequencies	116
56	1/rev Response Due to Out-of -Track Moment	117
57	N/rev Response, Highest Cockpit Vibration	118
58	N/rev Response, Lowest Cockpit Vibration	119

ILLUSTRATIONS (cont'd)

<u>Figure</u>	<u>Page</u>
59 Typical Response Between Coupled Modes	122
60 Typical Response Between Uncoupled Modes	122
61 Rotor Drive and Control System, Single Rotor	126
62 Rotor Drive and Control System, Tandem Rotor	127
63 Rotor Drive and Control System, Redundant Tandem Rotor	128
64 Forward Speed Versus Gross Weight	131
65 Specific Range Versus Gross Weight	132
66 Payload Versus Mission Radius, 12-Ton Mission	133
67 Payload Versus Mission Radius, 20-Ton Mission	134
68 Dynamic System Schematic, Single Rotor, 12-20-Ton Skycrane [®]	141
69 Flex-Rotor TM Blade, 12-20-Ton Skycrane [®]	143
70 Spar Section	145
71 Fairing	146
72 Blade Tip Assembly	147
73 Cuff-Spar Attachment	148
74 Counterweight	149
75 Flex-Rotor TM Pressurized Blade, 12-20-Ton Skycrane [®]	151
76 Point Mass Displaced In and Out of Plane of Rotation	155
77 Full Span Monocoque Blade Structure	155
78 Bim [®] Indicator	158
79 Rotor System	161

ILLUSTRATIONS (cont'd)

<u>Figure</u>		<u>Page</u>
80	Flex-Rotor _{TM} Head, Plan View, 12-20-Ton Skycrane [®]	163
81	Flex-Rotor _{TM} Head, Elevation View, 12-20-Ton Skycrane [®]	165
82	Integral Hub-Shaft Main Gearbox	167
83	Hub Arm	168
84	Flapping Hinge	168
85	Spindle	169
86	Sleeve	169
87	Typical Diaphragm Seal Installation	171
88	Control System, Mid Pitch, Flex-Rotor _{TM} Head, 12-20-Ton Skycrane [®]	173
89	Control System, High Pitch, Flex-Rotor _{TM} Head, 12-20-Ton Skycrane [®]	175
90	Alternate Blade Design	179
91	Built-Up Spar Configuration	181
92	Alternate Hub Assembly, Flex-Rotor _{TM} Head, 12-20-Ton Skycrane [®]	185
93	Number of Blades and Blade Aspect Ratio Versus Total Rotor System Weight	191
94	Ground Resonance, Tricycle Landing Gear, HLH Alternate Rotor Design	192
95	Comparison of Tricycle and Quadracycle Landing Gear	194
96	Pre-Cone Angle Versus Stress	195
97	Stiffness Distribution, Hingeless Blade I	198
98	Flapwise Stress Distribution, Hingeless Blade I	199

ILLUSTRATIONS (cont'd)

<u>Figure</u>		<u>Page</u>
99	Edgewise Stress Distribution, Hingeless Blade I	200
100	Stiffness Distribution, Hingeless Blade II	201
101	Flapwise Stress Distribution, Hingeless Blade II	202
102	Edgewise Stress Distribution, Hingeless Blade II	203
103	Rotor Blade, General Arrangement	206
104	Blade Weight Distribution	207
105	Spar Area Distribution	208
106	Spar Thickness Distribution	209
107	Spar Flapwise Moment of Inertia Distribution	210
108	Spar Edgewise Moment of Inertia Distribution	211
109	Spar Flapwise Section Modulus Distribution	212
110	Spar Edgewise Section Modulus Distribution	213
111	Spar Sectional Center-of-Gravity Variation	214
112	Spar Shear Flow Determination	215
113	Typical Shear Flow Distribution	217
114	Spar Shear Center Variation	218
115	Spar Section Loaded in Torsion	219
116	Shear on Spar Element (Reference Figure 115)	219
117	Distribution of Enclosed Area Within Mean Line of Spar Wall	222
118	Spar Torsional Stiffness Distribution	223
119	Airload Distribution, Condition 1a	230

ILLUSTRATIONS (cont'd)

<u>Figure</u>		<u>Page</u>
120	Flapwise Shear and Moment Distribution, Condition 1a	231
121	Edgewise Shear and Moment Distribution, Condition 1a	232
122	Airload Distribution, Condition 1b	234
123	Flapwise Shear and Moment Distribution, Condition 1b	235
124	Edgewise Shear and Moment Distribution, Condition 1b	236
125	Airload Distribution, Condition 1c	238
126	Flapwise Shear and Moment Distribution, Condition 1c	239
127	Edgewise Shear and Moment Distribution, Condition 1c	240
128	Flapwise and Edgewise Airload Distribution, Condition 2a	242
129	Flapwise Shear and Moment Distribution, Condition 2a	243
130	Edgewise Shear and Moment Distribution, Condition 2a	244
131	Flapwise and Edgewise Airload Distribution, Condition 2b	246
132	Flapwise Shear and Moment Distribution, Condition 2b	247
133	Edgewise Shear and Moment Distribution, Condition 2b	248
134	Flapwise and Edgewise Airload Distribution, Condition 2c	250
135	Flapwise Shear and Moment Distribution, Condition 2c	251
136	Edgewise Shear and Moment Distribution, Condition 2c	252
137	Flapwise Airload Distribution, Condition 3a	254
138	Flapwise Shear and Moment Envelope, Condition 3a	255
139	Edgewise Airload Distribution, Condition 3a	256
140	Edgewise Shear and Moment Envelope, Condition 3a	257

ILLUSTRATIONS (cont'd)

<u>Figure</u>		<u>Page</u>
141	Flapwise Airload Distribution, Condition 3b	259
142	Flapwise Shear and Moment Envelope, Condition 3b	260
143	Edgewise Airload Distribution, Condition 3b	261 •
144	Edgewise Shear and Moment Envelope, Condition 3b	262
145	Flapwise Airload Distribution, Condition 3c	264 •
146	Flapwise Shear and Moment Envelope, Condition 3c	265
147	Edgewise Airload Distribution, Condition 3b	266
148	Edgewise Shear and Moment Distribution, Condition 3c	267
149	Flapwise Airload Distribution, Condition 4a	270
150	Flapwise Shear and Moment Envelope, Condition 4a	271
151	Edgewise Airload Distribution, Condition 4a	272
152	Edgewise Shear and Moment Envelope, Condition 4a	273
153	Compressibility Increment, Condition 4a	274
154	Flapwise Airload Distribution, Condition 4b	276
155	Flapwise Shear and Moment Envelope, Condition 4b	277
156	Edgewise Airload Distribution, Condition 4b	278
157	Edgewise Shear and Moment Envelope, Condition 4b	279 •
158	Flapwise Airload Distribution, Condition 4c	281
159	Flapwise Shear and Moment Envelope, Condition 4c	282 •
160	Edgewise Airload Distribution, Condition 4c	283
161	Edgewise Shear and Moment Envelope, Condition 4c	284

ILLUSTRATIONS (cont'd)

<u>Figure</u>	<u>Page</u>
162 Flapwise Airload Distribution, Condition 5a	286
163 Flapwise Shear and Moment Envelope, Condition 5a	287
164 Edgewise Airload Distribution, Condition 5a	288
165 Edgewise Shear and Moment Envelope, Condition 5a	289
166 Compressibility Increment, Condition 5a	291
167 Flapwise Airload Distribution, Condition 5b	293
168 Flapwise Shear and Moment Envelope, Condition 5b	294
169 Edgewise Airload Distribution, Condition 5b	295
170 Edgewise Shear and Moment Envelope, Condition 5b	296
171 Flapwise Airload Distribution, Condition 5c	298
172 Flapwise Shear and Moment Envelope, Condition 5c	299
173 Edgewise Airload Distribution, Condition 5c	300
174 Edgewise Shear and Moment Envelope, Condition 5c	301
175 Shear and Bending Moment Due to Weight, Condition 6	302
176 Sign Convention for Blade Motion	304
177 Equivalent Cuff Area Resisting Bending	306
178 Centrifugal Tension	308
179 Flapwise and Edgewise Shear Vector	310
180 Bolt Loading Distribution	311
181 Blade Root End Assembly	313
182 Cuff-to-Spar Attachment Bolt Pattern	314

ILLUSTRATIONS (cont'd)

<u>Figure</u>		<u>Page</u>
183	Inboard Bolt Loading	315
184	Outboard Bolt Loading	316
185	Spar-Cuff Sections with Maximum Stress	320
186	Eccentric Moment of Blade Mass About the Elastic Axis	325
187	Spar Loading	326
188	Form Factors for "D" Section Extrusion	328
189	Maximum Vibratory, Back Corner Stress Versus Cycles to Crack Initiation	335
190	Blade Planform	338
191	Spar Sidewall Element	339
192	Chordwise Force Distribution, Secondary Bending Analysis, $x = .244$	341
193	Chordwise Force Distribution, Secondary Bending Analysis, $x = .86$	342
194	Chordwise Loading Analogy	343
195	Moment, Slope, and Deflection Due To Secondary Spar Bending, $x = .224$	344
196	Moment, Slope, and Deflection Due To Secondary Spar Bending, $x = .86$	345
197	General Standard S-N Curve	347
198	Nondimensionalized S-N Curve	347
199	Typical Component S-N Curve	348
200	Standard S-N Curve Applied to Loading Spectrum	348
201	Rotor Head Fatigue Design Loads	349

ILLUSTRATIONS (cont'd)

<u>Figure</u>		<u>Page</u>
202	General Lug Configuration	354
203	Fatigue Size Effect	355
204	Allowable Endurance Limit	356
205	Soderberg Diagrams	358
206	Blade Shear Distribution Under Starting Condition	359
207	Blade Flapping Angles	363
208	Flapping Angle Versus Structural Replacement Time, Titanium without Chafing	364
209	Flapping Angle Versus Structural Replacement Time, Steel without Chafing	365
210	Flapping Angle Versus Structural Replacement Time, Steel and Titanium with Chafing	366
211	Swashplate Assembly Loading	372
212	Stationary Swashplate Servo Loading	374
213	Sleeve with Integral Control Arm	377
214	Spindle	381
215	Flapping Hinge	388
216	Hub Arm	391
217	Effective Lug	392
218	Effective Lug with Efficiency Factor	393
219	Bell Crank, Outboard	407
220	Primary Control Rod	413
221	Transfer Link	417

ILLUSTRATIONS (cont'd)

<u>Figure</u>		<u>Page</u>
222	Adjustable Control Rod	420
223	Rotating Swashplate	423
224	Vertical Shear Loading Geometry, Section A-A, Rotating Swashplate	426
225	Shear on Critical Ring Cross Section, Rotating Swashplate	427
226	Bending Moments on Critical Ring Cross Section, Rotating Swashplate	428
227	Stationary Swashplate	430
228	Flapping Hinge Fatigue Loading	435
229	Hub Arm	443
230	Alternate Hub Detail	451
231	Radial Load Distribution in Stiffening Ring	453
232	Shear Load Distribution on Lower Ring Plate	454
233	Compressive Load Distribution Between Stiffening Ring and Corresponding Ring Plate	454
234	Stress in Stiffening Ring	457
235	Natural Frequency, Flapwise Bending	465
236	Natural Frequency, Edgewise Bending	466
237	Flapwise Natural Frequencies and Mode Shapes	467
238	Edgewise Natural Frequencies and Mode Shapes	468
239	Flapwise Moment, Condition 3, Dynamic Analysis	469
240	Flapwise Moment, Condition 2, Dynamic Analysis	470
241	Flapwise Moment, Condition 1, Dynamic Analysis	471

ILLUSTRATIONS (cont'd)

<u>Figure</u>		<u>Page</u>
242	Maximum Flapwise Steady Stress, Dynamic Analysis	472
243	Maximum Flapwise Vibratory Stress, Dynamic Analysis	473
• 244	Flapwise Moment, Dynamic Analysis	474
245	Cyclic Pitch Versus Azimuth Position, Dynamic Analysis	475
' 246	Mach Number Versus Azimuth Position, Dynamic Analysis	476
247	Angle of Attack Versus Azimuth Position, Dynamic Analysis	477
248	Flapping Angles Versus Azimuth Position, Dynamic Analysis	478
249	Classical Flutter, Dynamic Analysis	481
250	Stall Flutter, Dynamic Analysis	483
251	Torsional Divergence	485
252	HLH Pitch Coupling, Blade Angle Versus Lag Angle for Various Cone Angles	487
253	Pitch-Lag Instability	488
254	HLH Ground Resonance	490
255	Gust Response Analysis - Flapping Angle	492
256	Gust Response Analysis - Transient Stress Magnification	493
257	Lift/q Versus Angle of Attack, CH-54A	497
258	Drag/q Versus Angle of Attack, CH-54A	498
' 259	Pitch Moment/q Versus Angle of Attack, CH-54A	499
260	Side Force/q Versus Yaw Angle, CH-54A	500
261	Yaw Moment/q Versus Yaw Angle, CH-54A	501

ILLUSTRATIONS (cont'd)

<u>Figure</u>	<u>Page</u>
262 HLH Lift/q Versus Angle of Attack	502
263 HLH Pitch Moment/q Versus Angle of Attack	503
264 HLH Side Force/q Versus Yaw Angle	504
265 HLH Comparison of Pitch Attitude and Cyclic Required for Various Shaft Tilts, Offsets and CG Locations	505
266 HLH Comparison of Longitudinal Trim Characteristics for Various Shaft and Tail Incidences Versus CG in Level Flight	506
267 HLH Comparison of Roll Attitude and Cyclic Required for Various Lateral Shaft Tilts and CG Locations	508
268 HLH Lateral Trim Versus Lateral CG Position in Hover	509
269 Lateral Trim Versus Lateral CG Position in Hover, CH-54A	510
270 HLH Longitudinal Trim Characteristics	511
271 HLH Longitudinal Trim Characteristics	512
272 HLH Longitudinal Trim Characteristics	513
273 HLH Longitudinal Trim Characteristics	514
274 HLH Longitudinal Trim Characteristics	515
275 HLH Longitudinal Trim Characteristics	517
276 HLH Lateral Trim Characteristics	516
277 HLH Lateral Trim Characteristics	518
278 HLH Lateral Trim Characteristics	519
279 Longitudinal Trim Characteristics, CH-54A	520
280 Longitudinal Trim Characteristics, CH-54A	521

ILLUSTRATIONS (cont'd)

<u>Figure</u>		<u>Page</u>
281	Lateral Trim Characteristics, Zero Sideslip, CH-54A	522
282	HLH Longitudinal Static Stability	523
283	HLH Longitudinal Static Stability	524
284	CH-54A AFCS Transfer Functions	526
285	Longitudinal Characteristics, HLH Root Locus Survey, Hover	527
286	Longitudinal Characteristics, HLH Root Locus Survey, 60 Knots	528
287	Longitudinal Characteristics, HLH Root Locus Survey, 110 Knots	529
288	Lateral - Directional Characteristics, HLH Root Locus Survey	530
289	Longitudinal Characteristics, CH-54A Root Locus, AFCS Off	531
290	Longitudinal Characteristics, CH-54A Root Locus, AFCS On	532
291	Lateral - Directional Characteristics, CH-54A Root Locus	533
292	HLH Longitudinal Time History for Pull and Return in Hover	534
293	HLH Longitudinal Time History for Pull and Hold in Hover	535
294	HLH Longitudinal Time History for Pull and Return at 60 Knots	536
295	HLH Longitudinal Time History for Pull and Hold at 60 Knots	537
296	HLH Longitudinal Time History for Pull and Return at 110 Knots	538

ILLUSTRATIONS (cont'd)

<u>Figure</u>		<u>Page</u>
297	HLH Longitudinal Time History for Pull and Hold at 110 Knots	539
298	HLH Lateral Time History for Pull and Return at 110 Knots	540
299	HLH Lateral Time History for Pull and Hold at 110 Knots	541
300	HLH Longitudinal Trim Versus CG Position in Hover	542
301	Comparison of Damping/Inertia	544
302	Comparison of Control Power/Inertia	545
303	Comparison of Amplitude Ratio and Frequency for HLH and CH-54A in Fore and Aft Translation	546
304	Pitch and Roll Switching	549
305	Pitch Channel Block Diagram	550
306	Roll Channel Block Diagram	551
307	Yaw/Altitude Switching	552
308	Yaw Channel Block Diagram	554
309	Altitude Block Diagram	555
310	HLH Lateral Trim Characteristics Versus Sideslip	560
311	Lateral Trim Characteristics Versus Sideslip, CH-54A	561
312	HLH Outboard Blade Section	579
313	HLH Spar Half-Sections	580
314	HLH Spar Half-Sections	581
315	Main Rotor Blade Spar Area	582
316	Main Rotor Blade Flapwise Moment of Inertia	583

ILLUSTRATIONS (cont'd)

<u>Figure</u>		<u>Page</u>
317	Main Rotor Blade Edgewise Moment of Inertia	584
318	Main Rotor Blade Weight Distribution	585
319	Blade Weight Versus Design Tip Speed	586
320	Main Rotor Blade Moment Envelope	587

TABLES

<u>Table</u>		<u>Page</u>
I	Mission Requirements	1
II	HLH Parameters - Characteristics	3
III	HLH Parameters - Weight	4
IV	HLH Parameters - Performance, Propulsion	5
V	Characteristics of Single and Tandem Rotors	15
VI	Mission Requirements	18
VII	Component Drag	20
VIII	Net Vertical Drag, Percent Rotor Thrust	22
IX	Summary of Basic Design Data	30
X	Fixed Weight Components	50
XI	Engine Performance Data	53
XII	Parametric Variables	67
XIII	Helicopter Weight Breakdown, Single Rotor, R = 40 Feet	69
XIV	Helicopter Weight Breakdown, Single Rotor, R = 50 Feet	70
XV	Helicopter Weight Breakdown, Single Rotor, R = 60 Feet	71
XVI	Helicopter Weight Breakdown, Tandem, Three- Bladed Rotors	72
XVII	Design Parameters for Selected Rotors	79
XVIII	Mission Fuel Breakdown	81
XIX	Weight Breakdown	82

TABLE (cont'd.)

<u>Table</u>		<u>Page</u>
XX	Summary of Physical Characteristics	91
XXI	Tail Rotor and Induced Power Increment	93
XXII	Design Mission Performance	94
XXIII	Stability Characteristics	108
XXIV	First-Mode Frequencies at Normal Rotor Speed for Several Main Rotor Blades	109
XXV	Influence of Speed on Mission Performance	135
XXVI	Influence of Transmission Power Rating on Weight and Rotor Size	136
XXVII	Summary of Growth Factors, Single and Tandem Rotors	137
XXVIII	Summary of Mission Trade-Offs	138
XXIX	Growth Estimation Using Higher Drag Values	138
XXX	Summary of Margins of Safety for Main Rotor Blade Components	205
XXXI	Blade Conditions Investigated	226
XXXII	Summary of Basic Design Constants for all Conditions	228
XXXIII	Condition 1a, Hover, 20-Ton Mission, Basic Design Parameters	229
XXXIV	Condition 1b, Hover, 12-Ton Mission, Basic Design Parameters	233
XXXV	Condition 1c, Hover, Ferry Mission, Basic Design Parameters	237
XXXVI	Condition 2a, Vertical Takeoff, 20-Ton Mission, Basic Design Parameters	241

TABLE (cont'd.)

<u>Table</u>		<u>Page</u>
XXXVII	Condition 2b, Vertical Takeoff, 12-Ton Mission, Basic Design Parameters	245
XXXVIII	Condition 2c, Vertical Takeoff, Ferry Mission, Basic Design Parameters	249
XXXIX	Condition 3a, Cruise, 20-Ton Mission, Basic Design Parameters	253
XXXX	Condition 3b, Cruise, 12-Ton Mission, Basic Design Parameters	258
XXXXI	Condition 3c, Cruise, Ferry Mission, Basic Design Parameters	263
XXXXII	Condition 4a, Symmetrical Dive and Pullout, 20-Ton Mission, Basic Design Parameters	268
XXXXIII	Compressibility Increment, Condition 4a	269
XXXXIV	Condition 4b, Symmetrical Dive and Pullout, 12-Ton Mission, Basic Design Parameters	275
XXXXV	Condition 4c, Symmetrical Dive and Pullout, Ferry Mission, Basic Design Parameters	280
XXXXVI	Condition 5a, Autorotative Dive and Pullout, 20-Ton Mission, Basic Design Parameters	285
XXXXVII	Compressibility Increment, Condition 5a	290
XXXXVIII	Condition 5b, Autorotative Dive and Pullout, 12-Ton Mission, Basic Design Parameters	292
XLIX	Condition 5c, Autorotative Dive and Pullout, Ferry Mission, Basic Design Parameters	297
L	Summary of Loads, Moments, and Stresses for Condition 4a	329
LI	Summary of Loads, Moments, and Stresses for Condition 5a	331

TABLE (cont'd)

<u>Table</u>		<u>Page</u>
LII	Fatigue Analysis of Spar	334
LIII	Preliminary Main Rotor Flapping Spectra	350
• LIV	Preliminary Main Rotor Power Spectra	351
LV	Material Properties	352
• LVI	Material Mean Endurance Limit Stress	353
LVII	Standard Endurance Limits for Lugs with Chafing	354
LVIII	Probability Factors for 99.99 Percent Reliability	356
LIX	Blade Coning Angle Iteration	363
LX	Design Fatigue Load Summary	376
LXI	Comparison of HLH and CH-54A Major Properties	494
LXII	Control Forces and Gradients	567
LXIII	Comparison of HLH and CH-54A Hover Characteristics	568

SYMBOLS

a	Slope of Lift Curve
a_f	Angle of Attack, deg
a_{ls}	Longitudinal Flapping, deg
A	Area, in ²
A_{ls}	Lateral Cyclic, deg
A_o	Velocity of Sound, ft/sec
A_k	Enclosed Area of Blade Element to the Moment Center on Blade Cross Section, in ²
A_{trb}	Tail Rotor Blade Area (bRC), ft ²
A_w	Fuselage Wetted Area, ft ²
$AR = R/C$	Blade Aspect Ratio
AFCS	Automatic Flight Control System
b	Blade, Number of Blades
$bc/\pi R$	Solidity
b_s	Blade Semi-Chord, in
B_{ls}	Longitudinal Cyclic, deg
c	Distance in Mc/l
C	Chord, in
C_l	Horizontal Tail Drag Coefficient
C_d	Drag Coefficient
C_T	Thrust Coefficient
C_{LT}	Tail Lift Coefficient = $\text{Lift} / \frac{1}{2} \rho V^2 S_t$
C_L	Lift Coefficient

CP	Control Power
D	Damping, ft-lb/rad/sec
DA	Disk Area, ft ²
deg	Degree
DGW	Design Gross Weight, lb
D _v	Vertical Drag, lb
e	Rotor Head Offset, in
ε ₀	Reference Elastic Axis Offset, in
e _z	Distance From Moment Center to Shear Center on Blade Cross Section, in
ext	External
E	Modulus of Elasticity, in ⁴
E' _m	Mean Endurance Limit
f	Drag, ft ²
°F	Degrees Fahrenheit
F _c	Centrifugal Force, lb
(F _c) _o	Centrifugal Force at Flapping Hinge, lb
F _{cap}	Fuel Capacity, gal
f _{br}	Bearing Stress, lb/in ²
f _c	Centrifugal Tensile Stress, lb/in ²
f _s	Shear Unit Stress, lb/in ²
ft	Feet
ft ²	Square Feet
ft/sec	Feet Per Second

f_{edge}	Edgewise Bending Stress, lb/in ²
f_{flap}	Flapwise Bending Stress, lb/in ²
f_t	Tensile Stress, lb/in ²
F_{bry}	Bearing Yield Stress, lb/in ²
F_{bru}	Ultimate Bearing Stress, lb/in ²
F_{tu}	Ultimate Tensile Stress, lb/in ²
F_{su}	Ultimate Shear Stress, lb/in ²
FS	Fuselage Station, in
FSCG	Fuselage Station Center of Gravity, in
g	Gravity
G	Torsion Modulus of Rigidity, lb/in ²
gal	Gallons
GW	Gross Weight, lb
hr	Hour
HP	Horsepower
i_g	Longitudinal Shaft Incidence, deg
i_t	Horizontal Tail Incidence, deg
I_m	Mass Moment of Inertia, slug-ft ²
I_r	Roll Mass Moment of Inertia, slug-ft ²
I_x	Equivalent Aircraft Inertia About x Axis, slug-ft ²
I_y	Equivalent Aircraft Inertia About y Axis, slug-ft ²
I_z	Equivalent Aircraft Inertia About z Axis, slug-ft ²
I_R	Rotor Inertia, slug-ft ²

IFR	Instrument Flight Rules
IGE	In-Ground Effect
I_{ZZ}	Yawing Moment of Inertia, slug-ft ²
J	Polar Moment of Inertia, in ⁴
K	Concentration Factor
kn	Knots
K_{β}	Pitch-Flapping Coupling
K_{ξ}	Pitch-Lag Coupling
K_h	Total Lateral Spring Rate
K_{θ}	Total Roll Spring Rate
lb	Pounds
lb/ft ²	Pounds Per Square Foot
LER	Leading Edge Radius, in
LF	Load Factor
min	Minutes
M	Bending Moment, in-lb
MF	Machining Factor
MN	Mach Number
MS	Margin of Safety
MRHP	Main Rotor Horsepower
M_{edge}	Edgewise Bending Moment, in-lb
M_{flap}	Flapwise Bending Moment, in-lb
M_T	Torsional Moment, in-lb
M_{ecc}	Eccentric Moment About Blade Elastic Axis Due to F_C , in-lb

M_d	Damping Moment, in-lb
M_p	Pitching Moment, in-lb
$(M_p)_v$	Vibratory Pitching Moment, in-lb
naut mi	Nautical Miles
N	Revolutions
NACA	National Advisory Committee for Aeronautics
NRP	Normal Rated Power
OEI	One Engine Inoperative
OGE	Out of Ground Effect
P	Resultant Bolt Loads $(P_x^2 + P_y^2)^{\frac{1}{2}}$, lb
P_I	Induce Power
P_{br}	Bearing Load, lb
P_d	Damper Reaction Load, lb
P_{fc}	Centrifugal Bolt Load, lb
$P_{m(edge)x}$	Edgewise Moment Bolt Load in x Direction, lb
$P_{m(edge)y}$	Edgewise Moment Bolt Load in y Direction, lb
$P_{m(flap)}$	Bolt Load Due to Shear from Flapwise Moment, lb
P_{mt}	Bolt Load Due to Shear from Torsional Moment, lb
$P_{s(edge)}$	Bolt Load Due to Shear from Edgewise Moment, lb
P_x	Total Bolt Load in x Direction, lb
P_y	Total Bolt Load in y Direction, lb
PF	Probability Factor
P_n	Swashplate Loads (n = 1 through 6), lb

P_S	Control Rod Steady Load, lb
P_V	Control Rod Vibratory Load, lb
q	Dynamic Pressure, lb/ft
q'	Shear Flow, lb/in
r	Some Point on Blade Radius
rpm	Revolutions Per Minute
R	Rotor Blade Radius
R_1	Tensile Bolt Load Stress Ratio
R_2	Flapwise Bolt Load Stress Ratio
R_3	Edgewise Bolt Load Stress Ratio
R_t	$R_1 + R_2 + R_3$
R_S	Shear Bolt Load Stress Ratio
R_{MR}	Main Rotor Radius
RAI	Relative Autorotative Index
ROC	Rate of Climb
s_t	Tail Area, ft ²
S	Fuselage Area, ft ²
S_a	Stabilizer Area, ft ²
S_{edge}	Edgewise Shear, lb
S_{flap}	Flapwise Shear, lb
S_R	Resultant of Flapwise and Edgewise Shear, lb
SCF	Stress Concentration Factor

SFC	Specific Fuel Consumption, lb/HP-hr
SEF	Size Effect Factor
SL	Sea Level
SLS	Sea Level Standard
STOL	Short Takeoff and Landing
t	Blade Thickness, in
t/c	Blade Thickness to Chord Ratio
T	Thrust, lb
TOGW	Takeoff Gross Weight, lb
V	Speed, kn
V_I	Induced Velocity, ft/sec
V_c	Chordwise Shear Force, lb
$(V_c)_s$	Steady Chordwise Shear Force, lb
$(V_c)_v$	Vibratory Chordwise Shear Force, lb
(V_n)	Normal Shear Force, lb
$(V_n)_s$	Steady Normal Shear Force, lb
V_t	Tip Speed, ft/sec
VFR	Visual Flight Rules
V_Z	Shear Load on Blade, lb
W_{alg}	Alighting Gear Weight, lb
W_b	Blade Weight, lb
W_{bg}	Total Body Group Weight, lb
W_{ds}	Drive System Weight, lb

W_{fc}	Flight Control Group Weight, lb
W_{fe}	Fixed Equipment Weight, lb
W_{fs}	Fuel System Weight, lb
W_{rg}	Total Main Rotor Group Weight, lb
W_s	Stabilizer Weight, lb
W_{tr}	Tail Rotor Weight, lb
WL	Water Line, in
WLCG	Water Line Center of Gravity, in
$x = r/R$	Ratio of Point on Blade to Blade Radius, in
Z	Section Modulus, in ³
β_f	Flapping Angle = $a_0 - a_1 \cos\psi - b_1 \sin\psi - a_2 \cos 2\psi - b_2 \sin 2\psi$
β_0, β_s	Steady-State Coning Angle, deg
β_v	Vibratory Flapping Angle, deg
β'	Fuselage Sideslip Angle, deg
γ_θ	First Torsional Mode Shape
δ_a	Axial Stress, lb/in ²
δ_b	Bending Stress, lb/in ²
δ_{en}	Working Endurance Limit, lb/in ²
$(\delta_{en})_m$	Mean Endurance Limit, lb/in ²
δ_s	Steady Stress, lb/in ²
δ_{ty}	Tensile Yield Stress, lb/in ²
δ_{tu}	Ultimate Tensile Stress, lb/in ²
δ_v	Vibratory Stress, lb/in ²

θ_f	Fuselage Pitch Attitude, deg
θ_o	Steady-State Pitch Angle, deg
θ_t	Tail Rotor Pitch, deg
μ	Advance Ratio, $\frac{V}{\Omega R}$
ρ	Density, slug/ft ³
σ	Solidity, $bC/\pi R$
τ_a	Axial Shear Stress, lb/in ²
τ_b	Bending Shear Stress, lb/in ²
τ_s	Shear Stress, lb/in ²
τ_{su}	Ultimate Shear Stress, lb/in ²
ϕ_f	Fuselage Roll Attitude, deg
ψ_a	Yaw Angle, deg
ψ	Azimuth Position, deg
ω_p	Roll and Lateral Rigid Body Natural Frequency
ω_a	First Blade Torsional Natural Frequency
Ω	Angular Velocity, rad/sec
%	Percent

SUMMARY

DESIGN REQUIREMENTS

Based on service experience with many models of Army helicopters, including the CH-54A, initial design requirements were established to provide a practical helicopter, utilizing proven design features to facilitate application to many military logistics operations.

To load and unload large cargoes quickly and easily, leading to rapid turn-around and high productivity, and to allow the greatest variety of load geometry, external cargo carrying was deemed necessary. To permit loading in advance of takeoff and autorotative landings with a load, a clear load space 12 feet high under the fuselage was required. A wide-spread landing gear was required to straddle large loads, and to maintain stability on uneven terrain. The pilot's compartment was required to provide an aft-facing pilot's station, from which the aircraft can be flown and the winch system operated for accurate load placement.

TABLE I
MISSION REQUIREMENTS

	Transport	Heavy Lift
Payload (outbound only)	12 tons	20 tons
Radius	100 naut mi	20 naut mi
V cruise	12-ton payload, 110 kn	20-ton payload, 95 kn
V cruise	No payload, 130 kn	No payload, 130 kn
Hovering time	3-min takeoff 2-min mid-point	5-min takeoff 10 min @ destination (with payload)
Reserve fuel	10% of initial fuel	10% of initial fuel
Hover capability	6,000 ft, 95° F(OGE)	SL, 59° F (OGE)
Cruise altitude	SLS atmosphere	SLS atmosphere
Fuel allowance for start, warm-up, and takeoff	MIL-C-5011A	MIL-C-5011A
<u>Ferry</u>		
Ferry range	1500 naut mi (no payload-STOL takeoff)	
Reserve fuel	10% of initial fuel	
Fuel allowance for start, warm-up, and takeoff	MIL-C-5011A	
Minimum design load factor	2.0g	

All major components were required to be designed for replacement or repair "on condition", with design characteristics to permit at least 1200 hours between overhauls and 3600 hours' retirement. This necessitates self-inspecting devices, such as chip detection systems for transmission system components and automatic blade structural inspection devices. Maintenance requirements were to be minimized, leading to the selection of automatic oil lubrication of rotor system components. And above all other requirements, stability and handling qualities were to be as good as, or better than, existing aircraft, allowing absolutely no compromise which would sacrifice control characteristics for size.

The design missions were rigidly adhered to. Initial investigations showed that the maximum cost effectiveness could be obtained by designing exactly to the missions, and that an oversize aircraft would be as unsatisfactory a design solution as an undersize aircraft. A description of the design missions is shown in Table I.

AIRCRAFT CONFIGURATION

The principal parameters of the selected configuration are grouped in the following tables. Dimensions, basic design performance parameters, and general arrangement data are tabulated as characteristics in Table II. A breakdown of the weight empty and the three mission gross weights is given in Table III. The propulsion and performance characteristics are summarized in Table IV. The general arrangement of the aircraft is shown in Figure 39.

TABLE II
HLH PARAMETERS - CHARACTERISTICS

Rotor diameter, ft	91.6
Blade chord, ft	2.58
No. of blades per rotor	6
Blade aspect ratio (R/C)	17.7
Rotor solidity ($bC/\pi R$)	.108
Blade airfoil section	NACA 0012
Blade twist (negative),deg	8
Flapping hinge offset, percent radius	8
Rotor tip speed (ΩR),ft/sec	700
Max mean blade lift coefficient, approx	.7
C_T/σ (6000 ft, 95° F, 12-ton mission)	.110
Disk loading, 20-ton mission, lb/ft ²	12.4
Fuselage length, ft	103.6
Fuselage width, ft	7.0
Fuselage depth (average),ft	5.6
Overlap, percent diameter	-
Configuration	Crane
Max load length, ft	no aft limit
Max load width, ft	22.5
Max load height, ft (on-ground loading)	12.9
Drag, ft ² : No external load	83.8
Ferry	93.8
Outbound, transport mission	133.8
Outbound, heavy lift mission	133.8
Payload external	50.0
Vertical drag (with ext load),percent thrust	3.81
Vertical drag (without ext load),percent thrust	3.56
Internal fuel tankage, gal	970
Tail rotor diameter, ft	22.67
Max tail rotor C_T/σ	.15

TABLE III
HLH PARAMETERS - WEIGHT

<u>EMPTY WEIGHT (lb)</u>		
Rotor group		7, 115
Tail group		1, 330
Body group		5, 190
Alighting gear group		3, 275
Flight controls group		2, 360
Propulsion group		9, 675
Horizontal stabilizer		213
Fuel system		408
Fixed equipment		<u>3, 555</u>
Total weight empty		33, 121
<u>GROSS WEIGHT (lb)</u>		
20-ton mission:	Empty weight	33, 121
	Crew (3)	600
	Fuel	3, 250
	Oil and trapped fluids	100
	Cargo	40, 000
	Winch	<u>2, 000</u>
	Total	79, 071
12-ton mission:	Empty weight	33, 121
	Crew (3)	600
	Fuel	6, 300
	Oil and trapped fluids	100
	Cargo	24, 000
	Winch	<u>2, 000</u>
	Total	66, 121
1500-naut-mi-ferry:	Empty weight	33, 121
	Crew (3)	600
	Fuel	36, 202
	Oil and trapped fluids	100
	Aux tankage	<u>2, 300</u>
	Total	<u>72, 323</u>

TABLE IV
HILL PARAMETERS - PERFORMANCE, PROPULSION

PERFORMANCE

Velocity (SLS, with ext load) kn:	
Cruise, 20-ton payload	95
Cruise, 12-ton payload	128
Max, 20-ton payload	105
Max, 12-ton payload	138
Average, ferry mission	100
Max, ferry mission	126
Max ferry range, naut mi	2,080
Takeoff weight, load factor 2.0 g, lb	98,400
Arbitrary altitude limit, ft	10,000

PROPULSION

Engine type	T64/S4A
No. of engines	4
Available power (SLS),HP	13,740
Available mil power (6000 ft, 95°F),HP	10,600
Transmission 3600 hour rating, HP	11,980
Drive system mechanical efficiency, percent	96.3

PERFORMANCE

The 12- and 20-ton missions have been used to size the helicopter. Hovering capability out of ground effect at 6000-foot-altitude, 95-degree Fahrenheit day conditions is that required to perform the 12-ton, 100-nautical-mile radius mission. Hovering capability out of ground effect under sea level standard day conditions is that required to perform the 20-ton, 20-nautical-mile radius mission.

Actual combinations of payload and mission radius that can be flown by the aircraft depend largely on the conditions under which the aircraft must be hovered. Various combinations are shown in Figure 1, from which it will be noted that limiting the mission hovering requirement to hovering in ground effect at sea level standard day conditions allows a payload of nearly 26 tons to be carried. The envelopes show the effect of load geometry, in terms of parasite drag area.

Cruise speeds at sea level standard day conditions are 95 knots for the 20-ton mission and 134 knots for the 12-ton mission. Cruising flight can

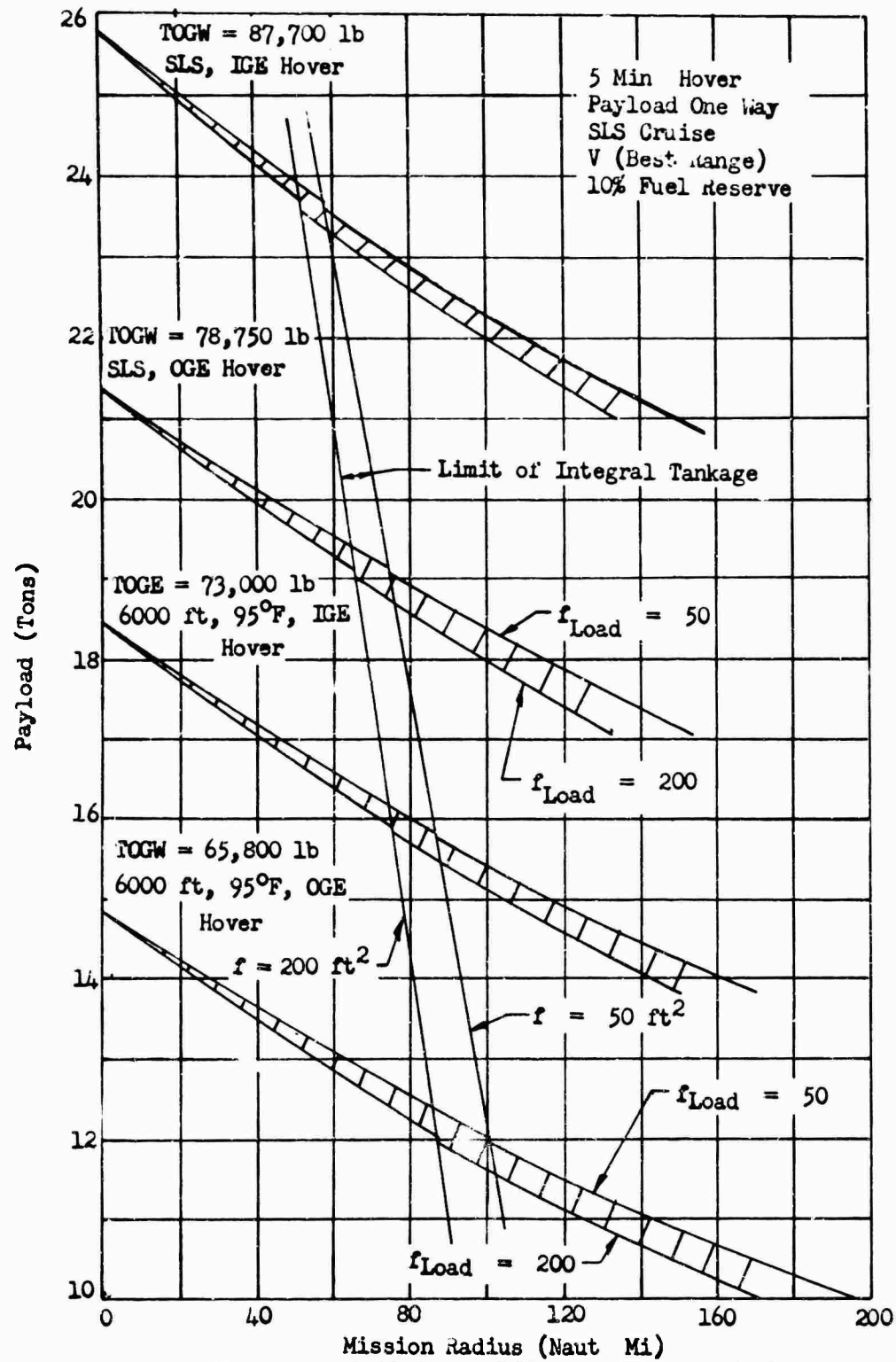


Figure 1 HLH Payload Versus Mission Radius

be maintained with 2 engines inoperative, without exceeding normal rated power of the remaining 2 engines. For 4-engine operation at 20-ton mission gross weight, the best rate of climb is approximately 2350 feet per minute. Climb rates at lower gross weights are correspondingly higher.

The ferry requirement does not dictate any of the design features of the aircraft, since the vehicle configured for the 12- and 20-ton missions is capable of a ferry range exceeding the stipulated requirement of 1500 nautical miles, while retaining vertical takeoff capability. By using 2-engine cruise for the latter part of the flight and using a streamlined ferry tank, a range in excess of 2400 nautical miles is obtained.

BLADE DESIGN

The blade is essentially all metal, consisting chiefly of an aluminum alloy spar, a titanium alloy root end attachment fitting, and trailing edge fairings made from aluminum alloy sheet. The spar, a "D" shaped extrusion machined on its outer contour, forms the blade leading edge, and contains non-structural counterweights in its "nose" portion. The root end fitting is bolted to the spar, to transfer blade loads to the rotor head. The trailing edge fairings form a discontinuous, and therefore non-structural, trailing edge. To fair the tip to a clear aerodynamic shape, a sheet metal tip cap, extending over the full chord, is attached at the blade's outboard end.

To provide constant monitoring of the blade's structural integrity, the spar is sealed and pressurized. A pressure loss indicator located at the inboard end provides for an easy, reliable structural inspection before each flight.

The rotor blade has been analyzed for both cruise and maneuver conditions. All components have positive margins of safety, and calculated fatigue lives far exceed the required 3600 hours. Because of its excellent structural characteristics, the continual automatic monitoring of its integrity, and the extensive service background with blades of similar construction, the blade can be used indefinitely. Overhaul is not required at any stated interval. Repair or retirement should be only as required by the blade's actual condition.

ROTOR HEAD DESIGN

The rotor head retains the rotor blades to the main rotor shaft, while permitting the blades to move freely and align themselves with the resultant of the dynamic and aerodynamic forces imposed upon them. Each blade is attached to a cylindrical sleeve which surrounds the feathering

hinge bearings. Motion about this hinge is controlled by the rotor control mechanism, which transmits control inputs from the non-rotating system, through a swashplate, to the rotor head.

The inner member of the feathering hinge is retained through a system of two perpendicular hinges, roughly analogous to a universal joint, to the rotor hub. All of the blade hinges are equipped with oil-lubricated, rolling element bearings. The flapping hinges are offset from the rotor centerline by a radial distance of 36 inches, providing attitude control of the aircraft with a variety of center-of-gravity positions. The hub consists of 6 conical members, bolted to the shaft.

The major components which react blade loads are machined from titanium alloy forgings, while the swashplate assembly and other major rotor control system components are of forged aluminum alloy. Like the blade, the rotor head has been analyzed structurally for both maneuver and cruise conditions, with positive margins of safety throughout.

AIRCRAFT STABILITY AND CONTROL

The stability and control characteristics of the HLH were analytically investigated. Wind tunnel data for the similarly configured CH-54A were used extensively in the estimation of HLH fuselage aerodynamics. The geometric solution for the HLH rotor system underwent further aerodynamic analyses in conjunction with the assumed fuselage. Trim solutions were obtained and used to determine optimum tail and shaft incidence. Stability derivatives were calculated for the final configuration and used for the dynamic stability investigation. Root locus techniques were used to show the dynamic characteristics of the basic airframe in six degrees of freedom, and representative solutions with Automatic Flight Control System (AFCS) added were also obtained. The requirements of MIL-H-8501-A (Reference 4) were discussed paragraph by paragraph. For Visual Flight Rules (VFR), the basic airframe meets all important stability requirements without AFCS. The addition of AFCS yielded a solution for all the VFR requirements and, although not discussed in detail, would also satisfy the Instrument Flight Rules (IFR) section of the specification. Point-by-point comparison of the HLH to the production CH-54A shows the similarities and differences expected for the HLH. The investigation of size effects showed that handling qualities of the HLH are equal or in some cases better than those of the CH-54A. In particular, such relative improvements as the 80-square-foot horizontal tail yielded considerably less nose-down attitude at high forward speeds. The 3-foot rotor offset, coupled with a 2-degree shaft incidence, allows CG variation of ± 2 feet in any direction. The lateral shaft incidence allows level roll attitudes with a minimum of sideslip throughout the speed range. The aft-facing pilot of the CH-54A is again considered for the HLH.

WEIGHT BREAKDOWN

A summary weight breakdown in accordance with MIL-STD-451, Part 1, is shown on the following pages.

MIL-STD-451, Part I

NAME _____

DATE _____

PAGE _____

MODEL HLH

REPORT _____

SUMMARY WEIGHT STATEMENT
ROTORCRAFT ONLY
ESTIMATED

CONTRACT DA 44-177-AMC-275(T)
ROTORCRAFT, GOVERNMENT NUMBER _____
ROTORCRAFT, CONTRACTOR NUMBER _____
MANUFACTURED BY _____

		MAIN	AUXILIARY
ENGINE	MANUFACTURED BY	G.E.	
	MODEL	T64/S4A	
	NUMBER	4	
PROPELLER	MANUFACTURED BY		
	MODEL		
	NUMBER		

MIL-STD-451 PART 1

NAME

DATE

ROTORCRAFT
SUMMARY WEIGHT STATEMENT
WEIGHT EMPTY

PAGE
MODEL HIN
REPORT

1							
2	ROTOR GROUP						7,115
3	BLADE ASSEMBLY					3,299	
4	HUB					776	
5	HINGE AND BLADE RETENTION					2,340	
6		FLAPPING			904		
7		LEAD LAG			536		
8		PITCH			500		
9		FOLDING					
10	WING GROUP						
11	WING PANELS-BASIC STRUCTURE						
12	CENTER SECTION-BASIC STRUCTURE						
13	INTERMEDIATE PANEL-BASIC STRUCTURE						
14	OUTER PANEL-BASIC STRUCTURE-INCL TIPS					LBS	
15	SECONDARY STRUCT-INCL FOLD MECH					LBS	
16	AILERONS-INCL BALANCE WTS					LBS	
17	FLAPS						
18	-TRAILING EDGE						
19	-LEADING EDGE						
20	SLATS						
21	SPOILERS						
22							
23	TAIL GROUP						1,543
24	TAIL ROTOR					1,330	
25	-BLADES						
26	-HUB						
27	STABILIZER-BASIC STRUCTURE					213	
28	FINS-BASIC STRUCTURE-INCL DORSAL					LBS	
29	SECONDARY STRUCTURE -STABILIZER AND FINS						
30	ELEVATOR - INCL BALANCE WEIGHT					LBS	
31	RUDDER - INCL BALANCE WEIGHT					LBS	
32							
33	BODY GROUP						5,190
34	FUSELAGE OR HULL - BASIC STRUCTURE						
35	BOOMS - BASIC STRUCTURE						
36	SECONDARY STRUCTURE - FUSELAGE OR HULL						
37	- BOOMS						
38	- DOORS, PANELS & MISC						
39							
40							
41	ALIGNING GEAR - LAND TYPE						3,275
42	LOCATION	ROLLING	STRUCT	CONTROLS			
43		ASSEMBLY					
44							
45							
46							
47							
48							
49							
50	ALIGNING GEAR GROUP - WATER TYPE						
51	LOCATION	FLOATS	STRUCT	CONTROLS			
52							
53							
54							
55							
56							
57							

*WHEELS, BRAKES, TIRES, TUBES AND AIR

MIL-STD-451 PART 1

NAME

DATE

ROTORCRAFT
SUMMARY WEIGHT STATEMENT
WEIGHT EMPTY

PAGE

MODEL 11H

REPORT

1									
2	FLIGHT CONTROLS GROUP								2,360
3	COCKPIT CONTROLS							1,707	
4	AUTOMATIC STABILIZATION								
5	SYSTEM CONTROLS - ROTOR	NON ROTATING						272	
6		ROTATING						381	
7	- FIXED WING								
8									
9									
10	ENGINE SECTION OR MAGELLE GROUP								770
11	INBOARD								
12	CENTER								
13	OUTBOARD								
14	DOORS, PANELS AND MISC								
15									
16	PROPULSION GROUP								
17		X	AUXILIARY	X	X	MAIN	X		27,523
18	ENGINE INSTALLATION								
19	ENGINE (4)							2,52	
20	TIP BURNERS								
21	LOAD COMPRESSOR								
22	REDUCTION GEAR BOX, ETC								
23	ACCESSORY GEAR BOXES AND DRIVES								
24	SUPERCHARGER-FOR TURBOS								
25	AIR INDUCTION SYSTEM							60	
26	EXHAUST SYSTEM							60	
27	COOLING SYSTEM								
28	LUBRICATING SYSTEM							110	
29	TANKS								
30	BACKING BD, TANK SUP & PADDING								
31	COOLING INSTALLATION								
32	PLUMBING, ETC								
33	FUEL SYSTEM							108	
34	TANKS - UNPROTECTED								
35	- PROTECTED								
36	BACKING BD, TANK SUP & PADDING								
37	PLUMBING, ETC								
38	WATER INJECTION SYSTEM								
39	ENGINE CONTROLS							50	
40	STARTING SYSTEM							130	
41	PROPELLER INSTALLATION								
42	DRIVE SYSTEM							6,823	
43	GEAR BOXES								
44	LUBE SYSTEM								
45	CLUTCH AND MISC								
46	TRANSMISSION DRIVE								
47	ROTOR SHAFT								
48	JET DRIVE								
49									
50									
51									
52	AUXILIARY POWER PLANT GROUP								160
53									
54									
55									
56									
57									

MIL-STD-451 PART I

NAME

DATE

ROTORCRAFT
SUMMARY WEIGHT STATEMENT
WEIGHT EMPTY

PAGE

MODEL HLR

REPORT

1						
2						
3						
4	INSTRUMENT AND NAVIGATIONAL EQUIPMENT GROUP					277
5	INSTRUMENTS					
6	NAVIGATIONAL EQUIPMENT					
7						
8						
9	HYDRAULIC AND PNEUMATIC GROUP					276
10	HYDRAULIC					
11	PNEUMATIC					
12						
13						
14	ELECTRICAL GROUP					610
15	AC SYSTEM					
16	DC SYSTEM					
17						
18						
19	ELECTRONICS GROUP					290
20	EQUIPMENT					
21	INSTALLATION					
22						
23						
24	ARMAMENT GROUP - INCL GUNFIRE PROTECTION				LBS	
25						
26	FURNISHINGS AND EQUIPMENT GROUP					318
27	ACCOMMODATIONS FOR PERSONNEL					
28	MISCELLANEOUS EQUIPMENT	X INCL			LBS BALLASTX	
29	FURNISHINGS					
30	EMERGENCY EQUIPMENT					
31						
32						
33						
34	AIR CONDITIONING AND ANTI-ICING EQUIPMENT					253
35	AIR CONDITIONING					
36	ANTI-ICING					
37						
38						
39	PHOTOGRAPHIC GROUP					
40	EQUIPMENT					
41	INSTALLATION					
42						
43	AUXILIARY GEAR GROUP					171
44	AIRCRAFT HANDLING GEAR					
45	LOAD HANDLING GEAR					
46	ATO GEAR					
47						
48						
49						
50						
51						
52						
53						
54	MANUFACTURING VARIATION					
55						
56						
57	TOTAL-WEIGHT EMPTY - PAGES 2, 3 AND 4					33,121

MIL-STD-451 PART I

NAME

SUMMARY WEIGHT STATEMENT

PAGE

MODEL 12H

DATE

REPORT

1	LOAD CONDITION	12 TON-100-NAUTICAL MILE	20 TON-20NAUTICAL MILE
2		RADUS MISSION	RADUS MISSION
3	CREW - NO.	600	600
4	PASSENGERS - NO.		
5	FUEL	LOCATION	TYPE
6	UNUSABLE		30
7	INTERNAL	6,300	3,250
8			
9			
10			
11	EXTERNAL		
12			
13			
14			
15	BOMB BAY		
16			
17			
18			
19	OIL		
20	UNUSABLE	20	20
21	ENGINE	50	50
22			
23			
24			
25	BAGGAGE		
26	CARGO	24,000	18,000
27			
28	ARMAMENT		
29	GUNS - LOCATION	TYPE**	QUANTITY CALIBER
30			
31			
32			
33			
34	AMM		
35			
36			
37			
38	BOMB INSTL*		
39	BOMBS		
40			
41	TORPEDO INSTL*		
42	TORPEDGES		
43			
44	ROCKET INSTL*		
45	ROCKETS		
46			
47	EQUIPMENT - PYROTECHNICS		
48	- PHOTOGRAPHIC		
49			
50	- OXYGEN		
51			
52	- MISCELLANEOUS		
53	WINCH SYSTEM	2,000	2,000
54			
55	USEFUL LOAD	33,000	15,950
56			
57	GROSS WEIGHTS - PAGES 2-5	66,121	79,071

* IF NOT SPECIFIED AS WEIGHT EMPTY

**FIXED, FLEXIBLE, ETC.

PARAMETRIC ANALYSIS

CONCLUSIONS

The rotor system parametric analysis for the 12-to 20-ton Army crane helicopter has yielded the following results and conclusions:

1. The following table lists the important characteristics of the single and tandem rotor configurations derived in this analysis.

TABLE V
CHARACTERISTICS OF SINGLE AND TANDEM ROTORS

	Single Rotor	Tandem Rotor
GW, 12-ton mission, lb	65,800	67,300
GW, 20-ton mission, lb	78,750	80,050
Weight empty, lb	32,800	33,880
Rotor diameter, ft	91.6	70.6
Number of blades per rotor	6	3
Rotor solidity	.108	.102
Blade aspect ratio	17.7	9.4
Disk loading, 20-ton mission GW, lb/ft ²	12.4	12.0
C_T/σ , 6000-ft, 95°F, 12-ton mission GW	.110	.110
Transmission limit power, HP	11,980	11,860

Both configurations are powered by four T64/S4A engines rated at 2,650 HP for 6000 feet, 95 degrees Fahrenheit, with transmissions rated at that power necessary for sea level standard day OGE hover at the 20-ton mission weight. The weights for the two solutions are similar, the single rotor configuration being slightly less. Off-design performance and stability and control characteristics of the two configurations are similar. The single rotor design has superior vibration characteristics and has a very low risk of catastrophic component failure.

2. The 6000-foot, 95-degree Fahrenheit hover requirement for the 12-ton, 100-nautical-mile radius mission is the critical design condition for establishment of engine power and rotor diameter. Rotor blade area is that required to avoid blade stall at the required 95-knot outbound cruise speed with the 20-ton-payload mission.
3. Optimum installed power consists of four T64/S4A engines rated at 2,650 HP each at 6000 feet, 95 degrees Fahrenheit. Higher installed power would yield slightly lower gross weights at the expense of

increased disk loading and fuel consumption. Flat rating of installed power by limiting the transmission to the power required for sea level standard hover at the 20-ton mission weight reduces gross weight by about 3400 pounds and the rotor diameter by 8 feet compared to that required if the transmission were configured to absorb full SLS power available.

4. The following trends were established for the rotor system variables investigated in the parametric study:

Rotor diameter should be the minimum required to meet the critical 6000-foot, 95-degree Fahrenheit hover requirement.

Greater number of blades improves aerodynamic efficiency and yields a slight rotor system weight advantage; however, avoidance of high blade aspect ratios (>20), which increase the rotor-fuselage clearance required to allow for static blade droop, limits the practical number of blades for the single rotor configuration to six.

Blade area resulting in a maximum C_T/σ of .115 is allowable; however, the 95-knot 20-ton mission cruise requirement dictates a greater total blade area to prevent retreating blade stall. The result is a maximum allowable C_T/σ of .110 for both the single and tandem rotor configurations at 6000 feet, 95 degrees Fahrenheit, 12-ton gross weight. Increased blade area would raise stall-limited cruise speed, but at a cost of about 340 pounds gross weight per knot and a diameter increase of .8 foot per knot.

A tip speed of 700 feet per second provides the best compromise between good rotor hovering performance, characteristics of low tip speed and low blade stresses in cruise, characteristic of high tip speed.

A blade twist of -8 degrees yields suitably high rotor aerodynamic efficiency without excessive blade vibratory stresses in cruise.

A 0012 blade section provides good low-speed performance and is sufficiently thin to prevent excessive blade stresses due to compressibility at the cruise speeds required. This selection is in contrast to current practice for higher-speed helicopters which must utilize thickness ratios as low as 10 percent to alleviate compressibility problems.

For the 5-foot CG range used in the parametric study, an 8-percent radius flapping hinge offset for the single rotor configuration provides necessary pitch trim control. For smaller design CG ranges, smaller offsets can be used. Lateral CG travel and control power are accommodated in the tandem with 1.5-percent radius offset.

5. In the tandem rotor configuration, the rotors are overlapped 33 percent of diameter, as is currently being done in production tandem machines. More overlap would result in interference between the blades of the front rotor and the rear rotor pylon, while less overlap would lengthen the fuselage and increase empty weight. The number of blades is then limited to three per rotor to prevent blade interference due to in-plane hunting motion, in-plane deflections, and changes of rotor phasing resulting from interconnecting shaft windup. The limit on number of blades, in turn, requires the use of low aspect ratios to obtain satisfactory rotor solidity. These blade aspect ratios are less than those used in current practice and introduce weight and aerodynamic uncertainties which reduce the confidence level in hardware achievability of the parametrically derived solution. If a minimum allowable blade aspect ratio were established (12, for instance) for which blade weight and cruise performance could be established to a high degree of confidence, the parametric optimization would result in a larger diameter, somewhat heavier tandem configuration.
6. The parametric solutions for both the single and tandem rotor configurations are highly sensitive to the body group weight. As a result, care must be exercised to provide satisfactory fuselage dynamic characteristics and stiffness-length distribution. The 2.5g flight load factor requirement has little impact on body group weight.
7. The 1,500-nautical-mile ferry range requirement imposes no restriction on the helicopter design for the selected engines. Approximately 2,100- and 1,900-nautical-mile range, for the single and tandem versions respectively, is available at a 2g load factor takeoff gross weight, and 2,300 nautical miles is attainable with minor modifications to reduce drag and empty weight and by judicious engine shutdown.
8. For the large single rotor helicopters required for the Army heavy lift missions, further weight savings over those shown herein are believed to be possible in the areas of the tail rotor and body groups. Multi-tail rotor configurations ("V" tail, for instance) may be lighter than a single large tail rotor and may also offer other advantages such as improved longitudinal stability and pitch control. Possible use of a "soft" fuselage to avoid the structural weight needed to

provide stiffness to assure higher than 1/rev fuselage natural frequency response also merits further investigation for the large crane-type fuselages required.

DESIGN CRITERIA

In order to evaluate properly the effects of rotor parametric variation, the basic heavy lift operational features of the helicopter must be held constant. Thus the basic mission capability, load handling features, and cargo geometry envelope are standardized.

Mission requirements are defined by the Army as follows:

TABLE VI
MISSION REQUIREMENTS

	12-Ton Payload	20-Ton Payload	Ferry
OGE hover at takeoff	6,000 ft, 95° F	SLS	Not required
Mission radius	100 naut mi	20 naut mi	--
Range	--	--	1500 naut mi
Cruise speed outbound	110 kn	95 kn	Optimum
Cruise speed inbound (no payload)	130 kn	130 kn	--
Cruise altitude	SLS	SLS	Optimum
Hover time at takeoff	3 min	5 min	None
Hover time at midpoint	2 min	10 min	None

All missions require 10-percent fuel reserve, 5-percent SFC increase, and 2 minutes at normal rated power for warm-up and takeoff (MIL-C-5011A).

To facilitate rapid cargo loading and unloading, improve operational flexibility, and maximize payload for a given gross weight, the external loading, crane-type fuselage is used. Ground straddling of the load is then possible, and rearward-facing pilot visibility during cargo handling is a feature. Anticipated use of special-purpose detachable pods provides internal loading capability without sacrificing the weight necessary to carry around a permanently large fuselage. Bulky external loads can be snugged up to the crane airframe, imposing no penalty on STOL capability, reducing the parasite drag of the load, and permitting full ground-effect utilization in hover. In addition, safe and rapid landings can be made with bulky loads attached in the event of any malfunction.

A fuselage clearance of 13 feet provides for on-ground loading and unloading of the Army inventory of heavy vehicles and weapons. The fuselage

and landing gear are designed to allow a load measuring 40 feet long by 15 feet wide (representative of Army floating bridge equipment) to be snugged up to the fuselage. Landing gear and tail groups are configured to allow "drive under" loading. Structural provisions are provided for both single and four point load suspension. A longitudinal CG travel of ± 2.5 feet for up to the full 20-ton design payload is provided, based on a survey of that needed to handle the Army's inventory of heavy equipment.

For the tandem rotor configuration, three-bladed rotors overlapped 33 percent of diameter are assumed, consistent with current practice. More overlap results in interference between the blades of the front rotor and the rear rotor pylon, while less overlap increases fuselage length and empty weight. The number of blades is limited to three per rotor to prevent blade mechanical interference due to in-plane hunting motion, in-plane blade deflection, and changes in rotor phasing due to interconnecting shaft windup.

Fuselage vibration will be minimized by assuring that the first vertical bending mode natural frequency of the single rotor fuselage both with and without an external load attached exceeds 110 percent of 1/rev. The first mode of the tandem fuselage for both vertical bending and torsion will be above 1/rev. Hover and cruise rotor rpm's will be held constant to reduce fuselage vibrational excitation.

In order to improve operational maintainability and aircraft availability, it is assumed that no removable or adjustable aerodynamic fairings will be used except for special cases such as extended ferry range where the drag cleanup potential outweighs the need for mechanical simplicity.

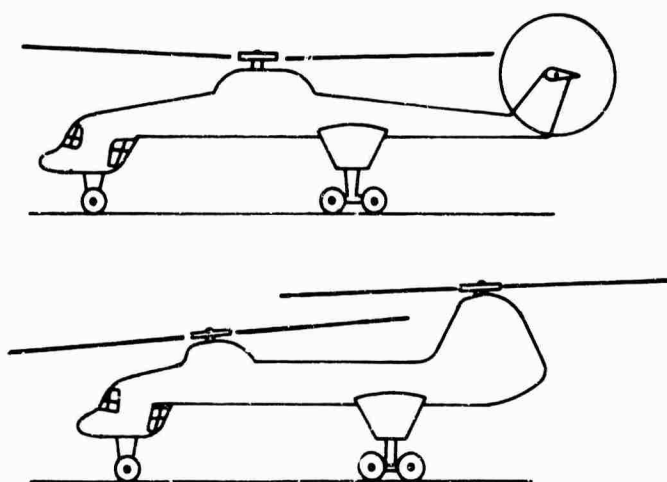


Figure 2 Single and Tandem Rotor Configurations

Engine installation will be arranged to take advantage of engine/transmission studies already completed. The sketches of Figure 2 illustrate the general arrangement of the two configurations.

BASIC DESIGN INFORMATION

This section deals with the design information necessary to convert isolated rotor system performance into overall helicopter capability. Included are parasite and vertical drag, drive system efficiency and accessory power, mutual rotor aerodynamic interference and asymmetrical loading (tandem), tail rotor/horizontal tail sizing, and flapping hinge offset determination.

Parasite Drag

The basic heavy lift missions, by virtue of their relatively short range and low speed requirements, do not demand a high level of aerodynamic cleanliness. However, ferry range capability is a consideration, and thus drag has been minimized as much as possible without sacrificing weight or operational flexibility. The crane-type fuselage with an external load offers substantial drag savings over the cabin-type with an external load, since the load can be snugged up behind the cockpit, presenting far less frontal area.

TABLE VII
COMPONENT DRAG

Item	Drag, f,ft ²	
	Single Rotor	Tandem Rotor
Fuselage (including cockpit)	19.9	23.1
Rotor pylons	3.7	5.4
Engine nacelles	6.0	4.1
Main rotor head (s)	19.5	21.9
Tail rotor head	3.9	-
Main landing gear	14.1	14.1
Nose landing gear	5.3	5.3
Horizontal tail ($C_1 = .5$)	1.2	-
Antennae, lights, etc	2.5	2.5
Momentum cooling losses (130 kn)	3.7	3.7
Miscellaneous leakage (5%)	4.0	4.0
Total	83.8	84.1
Typical external load	50.0	50.0
Total with external load	133.8	134.1

Component drag was estimated using published, semiempirical data (Reference 24) and Sikorsky Aircraft test data where applicable. Preliminary three-view sketches of both the single and tandem rotor configurations were used to establish component geometry. Table VII summarizes the component drag breakdown for each configuration.

Although the component breakdown differs, the total drags of the single and tandem configurations are the same: $f = 134$ square feet and 84 square feet with and without load, respectively. The tandem has higher fuselage drag and pylon drag (support of two rotors rather than one), while the single rotor configuration has slightly higher engine nacelle drag (grouped together rather than in separated pairs) and combined rotor head drag. The single rotor helicopter also has a horizontal tail which is lacking in the tandem.

Rotor head drag represents about 25 percent of the total airframe drag, and is based on analysis of the detailed design configured for the 12-to 20-ton crane of the 1962 study (Reference 28). Sikorsky Aircraft has conducted wind tunnel tests of various rotor head configurations, including full-scale investigation of the SH-3A head. These tests have resulted in the establishment of a rotor head drag coefficient, based on a projected frontal area of 1.35 for non-automatic blade folding rotor heads. This coefficient, applied to the 1962 crane design, produces a rotor head drag of 23.1 square feet. It has also been established that rotor head size, and resulting drag, is a characteristic function of total blade area. Non-dimensionalizing on this basis (blade area), the 1962 rotor head drag coefficient is .0275. This coefficient is applied to determine the drag values quoted in Table VII.

Identical drag penalties are assumed for both the single and tandem helicopters to account for landing gear, antennae, lights, and miscellaneous leakage. Momentum drag due to cooling airflow requirements is estimated at a representative 130 knots by scaling up known cooling requirements of existing helicopters by installed power. The drag of the external load is based on wind tunnel tests conducted by Sikorsky Aircraft on the S-60 and S-64 (CH-54A) crane helicopters with various types of external loads. These loads included simulated heavy trucks and trailers and produced a nominal drag increment of $f = 50$ square feet.

Vertical Drag

Because of the relatively large hovering time inherent in crane-type operation, where loads often must be transferred over rough terrain, hovering performance is particularly important. As a result, the payload-lifting decrement due to the drag of the airframe and load in the slipstream of the rotors must be accounted for. Through correlation of analytical

methods with model testing, Sikorsky Aircraft has developed a technique for predicting vertical drag. This technique has been used in this study. See Figure 3. It involves a strip analysis of the rotor slipstream impingement on the airframe and takes cognizance of slipstream contraction and the partial ground effect benefit produced by the airframe on the rotor.

Local slipstream velocities and drag coefficients are determined for each airframe area impinged upon by a given slipstream element, and drag is calculated and totalled. Since the fuselage exerts a partial ground effect on the rotor, one-third of the vertical drag is "recovered" in useful thrust. The net thrust loss is thus two-thirds of the airframe vertical drag.

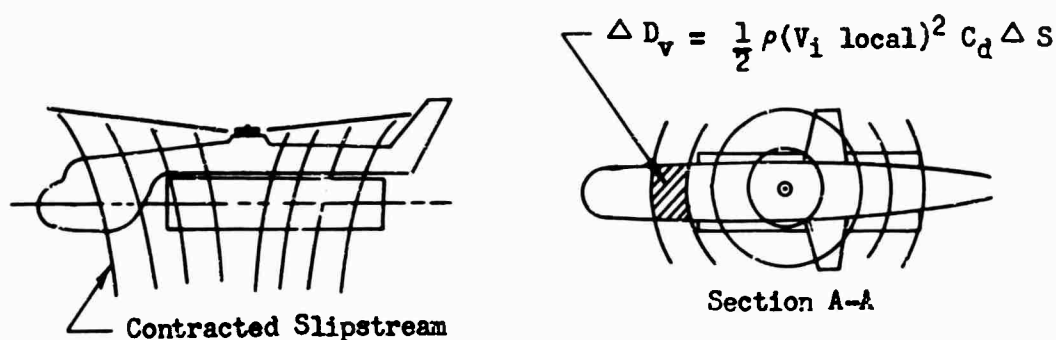


Figure 3 Slipstream Impingement on Airframe

The net vertical drag calculated for the single and tandem rotor configurations is shown in Table VIII with a 40-foot-x-12-foot load assumed as typical.

TABLE VIII
NET VERTICAL DRAG, PERCENT ROTOR THRUST

	Single Rotor	Tandem Rotor
Without external load	3.56	3.57
With 40 ft x 12 ft external load	3.81	4.89

The vertical drag in the unloaded configuration is nearly identical for the single and tandem rotor configurations. However, the external load for the tandem is positioned beneath the high slipstream velocity, overlapping rotor portions of the disk area, and thus imposes a greater penalty than for the single rotor helicopter. These values will not change significantly

as rotor disk loading varies. This is because the reduction in slipstream dynamic pressure resulting from a decreased disk loading is compensated for by the larger airframe necessary to support the rotor(s).

Drive System Efficiency and Accessory Power

The mechanical efficiency of the overall drive systems of both the single and tandem rotor configurations is assumed to be 96.3 percent, based on total engine power. The single rotor value is derived in the detailed analysis of the 12 to 20-ton crane transmission system described in Reference (8). The tandem system is assumed to be the same, since the number of rpm reduction stages between engines and lifting rotors is the same as for the single rotor, and the tandem's cross-shafting between rotors absorbs a relatively small transmission loss (most losses are associated with speed changing) which is equivalent to the tail rotor drive for the single rotor configuration. This is in disagreement with other published studies which show somewhat higher losses for the tandem.

Accessory power is assumed to be 100 HP for both configurations, consistent with that used in Reference (8).

Tandem Rotor Aerodynamic Interference and Asymmetric Loading

Aerodynamic interference between rotors of the overlapped tandem configuration increases the induced power required to produce a given total thrust over that for two isolated rotors of the same geometry. In the hovering regime, numerous tests, including those conducted by NASA and Sikorsky Aircraft, have resulted in an induced power correction factor as a function of rotor overlap which agrees reasonably well with theoretically derived trends. This is illustrated in Figure 4. The test data, representing rotors made up of blades with sections and twists consistent with standard practice (ie, not "ideal" twist, taper), fall between the theoretical curves for uniform and parabolic spanwise blade loading derived in NASA TN D-43, as would be expected. The correction factor for the 33 percent overlap assumed in this study is 1.12 (consistent with test points) or a 12-percent increase in induced power over what would be required of two isolated rotors producing the same total thrust.

In forward flight, the interference effect on induced power is considerably greater than in hover, since the air inflow is nearly horizontal, reducing the effective aspect ratio of the lifting system by about one-half, compared to two isolated rotors. The presence of tip losses reduces the diameter of the stream tube of inflowing air; and thus the effective aspect ratio is even less, so induced power correction factors of over 2.0 are possible, as pointed out in Reference (51). Since vertical displacement of

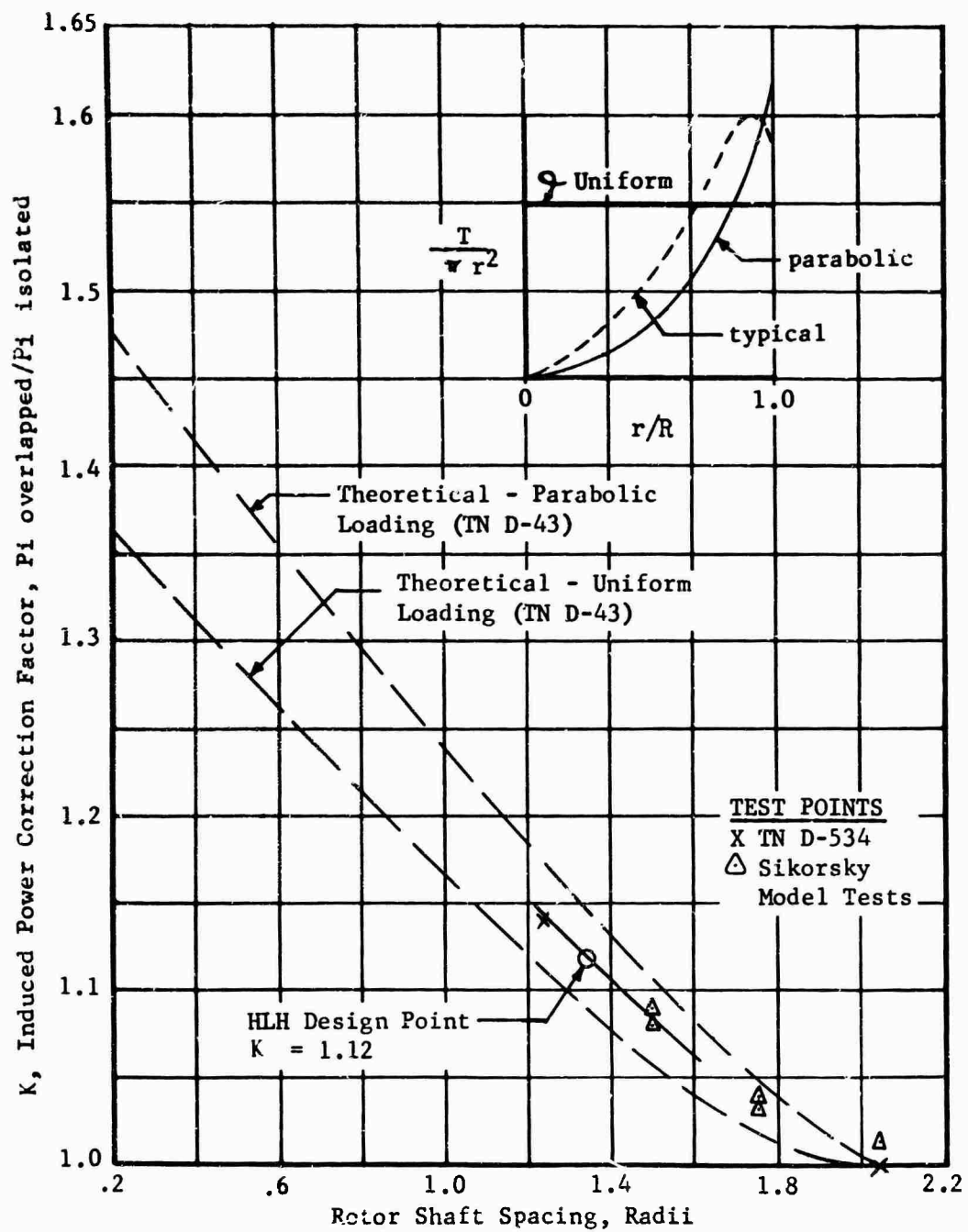


Figure 4 Hovering Induced Power Correction Due to Overlap

the front and rear rotors reduces the interference somewhat, a value of 2.0 is used for this study for forward speeds above 60 knots.

The requirement for + 2.5-foot longitudinal CG travel (refer to design criteria section) means that each rotor of the tandem configuration must be capable of lifting greater than half of the total weight. Thus, both rotor diameter (established by hover requirement) and blade area (established by cruise stall) must be greater than if each rotor had to support only half of the gross weight. This asymmetric loading results in the following empirical relationship:

$$T (\text{heavily loaded rotor}) = \frac{GW (1.667R + 5.0)}{3.333R} \quad (1)$$

This equation is used to establish the critical rotor lift loading for both hover and forward flight. Propulsive force distribution in cruise is assumed to be evenly split between the two rotors.

Tail Rotor and Horizontal Tail - Single Rotor Configuration

The tail rotor for the single rotor configuration is sized to provide both main rotor torque counteraction and a thrust margin for maneuvering capability. Diameter is established statistically by assuming that the tail rotor disk loading is the same as that on current helicopters. Since tail rotor moment arm is essentially proportional to main rotor radius, this relationship reduces to

$$(\text{Tail rotor diameter})^2 = \frac{K(HP)}{\Omega R_{MR}} \quad (2)$$

Figure 5 shows $(\text{Tail rotor diameter})^2$ plotted versus installed shaft power/main rotor tip speed ratio for various current helicopters and shows resultant boundary established. The expression for minimum tail rotor diameter then becomes

$$\text{Tail rotor diameter} = 5.5 \sqrt{\frac{HP}{\Omega R_{MR}}} \quad (3)$$

Of interest is the MIL Mi-6 point on Figure 5; it is the closest of existing helicopters to the 12-to 20-ton crane size, and appears somewhat inadequate on the basis of this criterion.

Tail rotor blade area is also established on the basis of existing helicopter designs. Current tail rotors have demonstrated adequacy at blade loadings of $C_T/\sigma = .15$ for severe maneuvers represented by a $.4 \text{ rad/sec}^2$ yawing acceleration in a 30-knot right sidewind at the critical density altitude ceiling. For the 12-to 20-ton crane, this C_T/σ is applied at 6,000

feet, 95-degrees Fahrenheit with yawing moment of inertia estimated by the relationship

$$I_{ZZ} = \left(\frac{DGW}{41.3} \right)^{1.85} \text{ slug - ft}^2 \quad (4)$$

and a fuselage aerodynamic yawing moment, based on CH-54A test data, of $7800 \left(\frac{R}{36} \right)^2$ foot-pounds. The resulting variation of tail rotor blade area with gross weight and main rotor radius is shown in Figure 6 for an assumed tail rotor tip speed of 700 feet per second. Thus Figures 5 and 6 define tail rotor geometry as a function of installed power, gross weight, and main rotor radius.

The steady-state hover power required by the tail rotor has been found to represent consistently 8 percent of total engine power. The constancy of this percentage with aircraft size is assured by the method described above for determination of diameter.

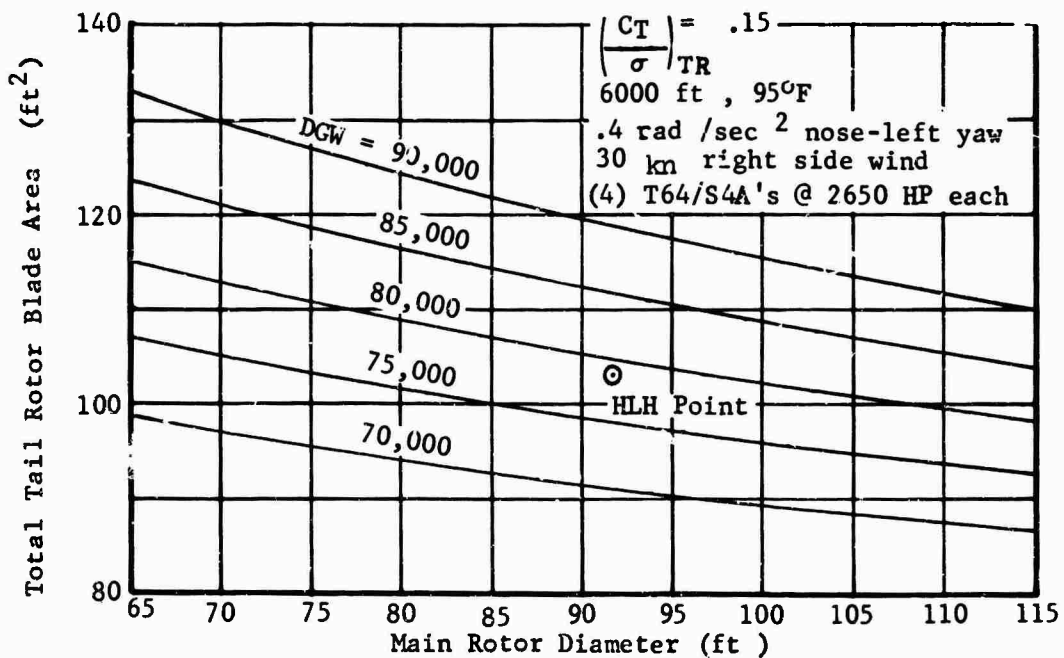
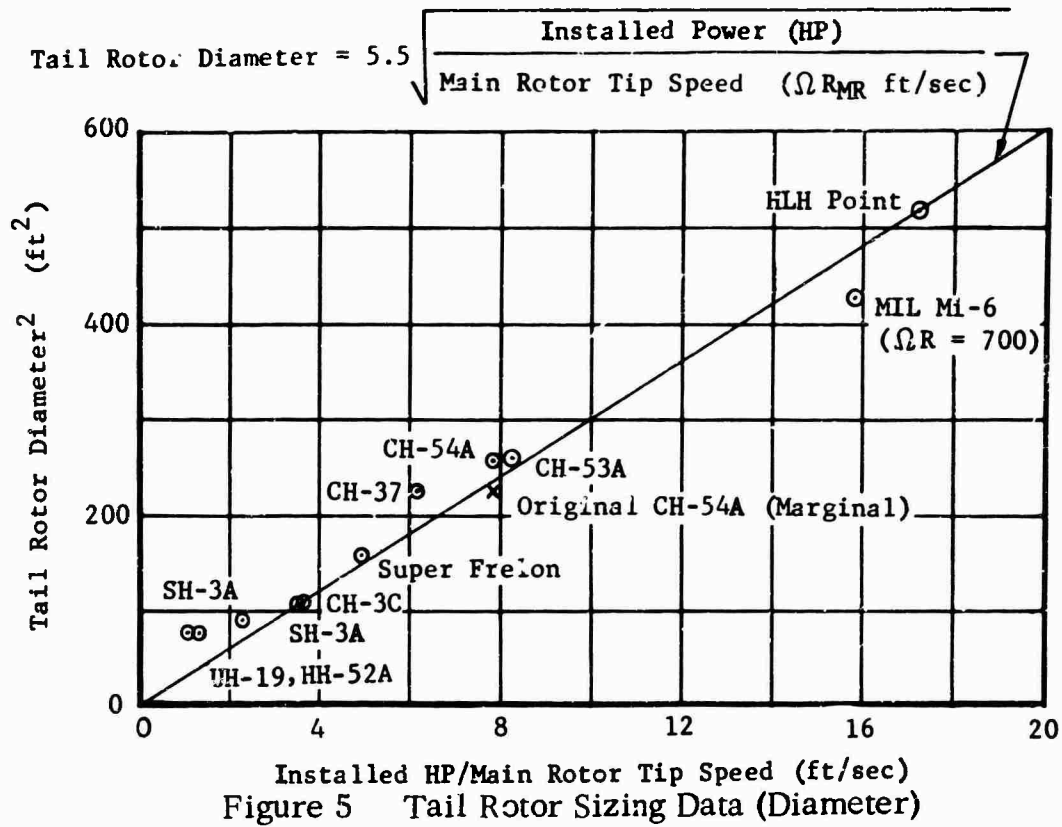
Horizontal tail area, like tail rotor size, is established by trends generated by existing helicopters. Figure 7 shows the product of tail area and main rotor radius, representative of the trim pitching moment capability, versus design gross weight. Conservative fairing of the data points yields the expression

$$\text{Tail area} = (.048 \text{ DGW} - 160) / R_{MR} \quad (5)$$

which is used to size the 12-to 20-ton crane tail for the single rotor configuration. The tandem rotor helicopter offers a shorter tail moment arm, and thus a tail sized by this same criterion would be large and would impose serious parasite and vertical drag penalties. Artificial stabilization is therefore assumed to provide adequate longitudinal stability in the tandem configuration.

Flapping Hinge Offset

Flapping hinge offset for the single rotor configuration is established by the + 2.5-foot longitudinal CG criterion. The amount of offset required depends on the mass and geometry of the blades, and, therefore, cannot be defined precisely until the rotor system geometry is established. While the use of offsets considerably larger than those required for control response offers the advantage of greater CG travel for helicopters weighing over 200,000 pounds, studies have indicated that for gross weights of interest in this study, a 25-percent offset would result in a rotor system weight increase of approximately 12 percent over a conventional system. Disadvantages associated with large offsets include greater gust sensitivity (particularly important for crane-type operation) and reduced rotor



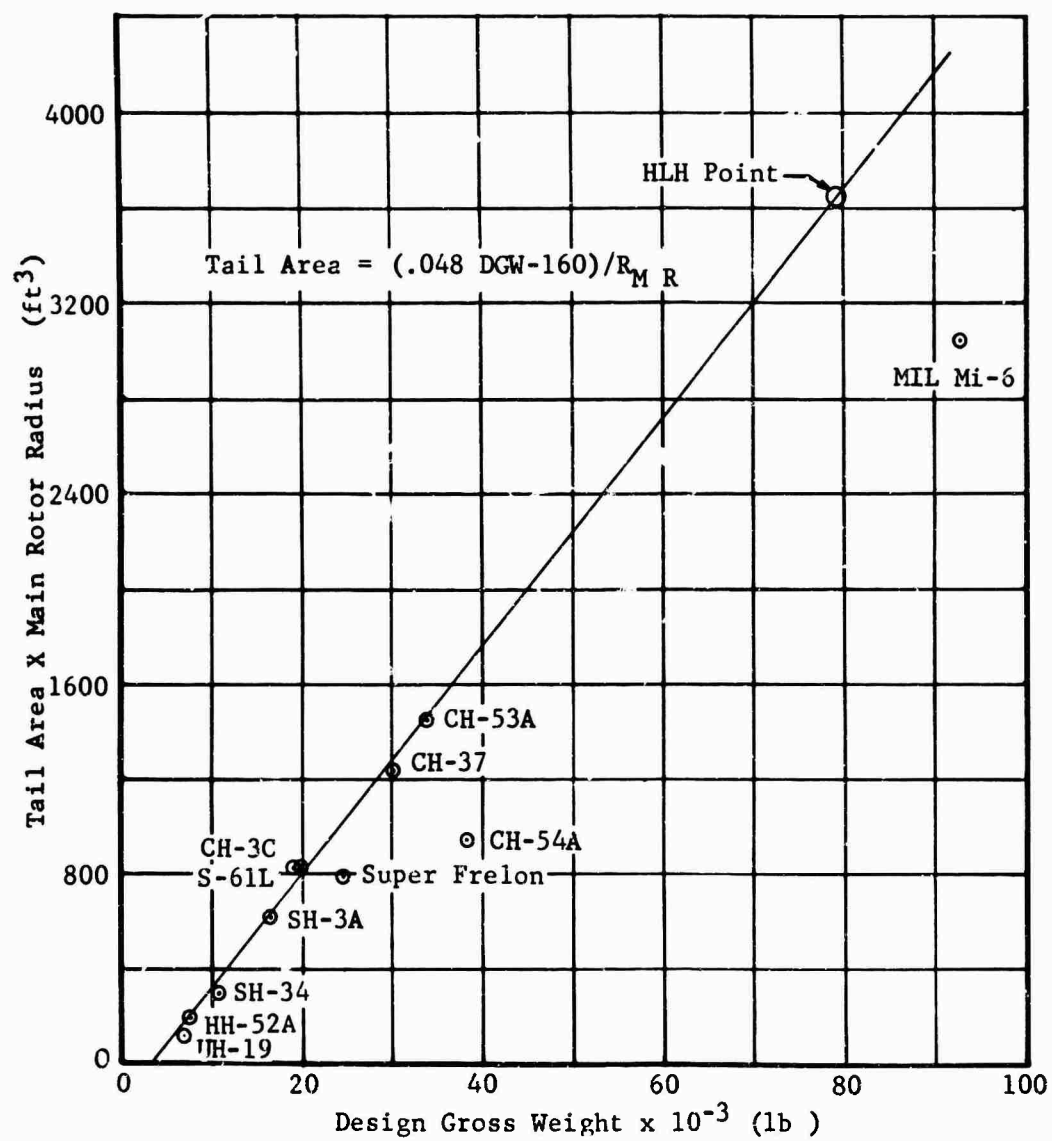


Figure 7 Horizontal Tail Sizing, Single Rotor

aerodynamic efficiency due to less lifting blade area and greater in-board cuff drag. For these reasons, 8 percent offset was assumed for the parametric study of the single rotor configuration. Since required offset depends not only on simple CG trim, but also on related factors such as hover and flare attitudes and resulting visibility and clearance, the approach used was to base the offset on hover attitude and blade flapping considerations. It has been found that a hover nose-up attitude of 6 degrees represents an average condition for an aft CG and does not produce unreasonable flare attitudes considering both visibility and tail rotor-to-ground proximity. The forward CG condition produces the same flapping stresses as the aft CG. Depending on the longitudinal shaft tilt, this can result in nose-down attitudes varying from 0 to -6 degrees. The shaft attitude initially selected for the single rotor crane is a 0 -degree tilt longitudinally and a 3-degree lateral (left) inclination to provide an optimum hovering work platform.

The 8-percent offset thus produces a head moment constant of 20,100 foot-pounds per degree, and results in less than ± 6 degrees of attitude change for ± 2.5 feet of CG travel. A smaller CG range would require less offset.

Flapping hinge offset for the tandem configuration is not required for longitudinal CG control, since differential rotor thrust provides this. However, some offset is necessary for adequate lateral CG and roll control. For this study, a tandem rotor flapping hinge offset of 1.5 percent, consistent with current practice, is assumed.

Summary

Table IX summarizes the basic design data derived in this section for both the single and tandem rotor configurations.

TABLE IX
SUMMARY OF BASIC DESIGN DATA

Item	Single Rotor	Tandem Rotor
Vertical drag with external load, % thrust	3.81	4.89
Vertical drag without external load, % thrust	3.56	3.57
Parasite drag with external load, f, ft ²	134	134
Parasite drag without external load, f, ft ²	84	84
Transmission efficiency, % engine power	96.3	96.3
Tail rotor power, hover, % engine power	8.0 (hover)	--
Tail rotor power, cruise, % engine power	4.0 (cruise)	--
Accessory power, HP	100	100
Isolated rotor induced power multiplication factor, hover	--	1.12 (hover)
Isolated rotor induced power multiplication factor, cruise	--	2.00 (cruise)
Tail rotor diameter, ft	$5.5\sqrt{HP/\Omega RMR}$ (Figure 5)	--
Tail rotor blade area, ft ²	(Figure 4)	--
Horizontal tail area, ft ²	$(.048 \text{ DGW-160})/R_{MR}$ (Figure 7)	--
Heaviest loaded rotor at CG extremes	--	$\frac{(1.667 R+5)}{3.33R} \times T_{\text{total}}$
Flapping hinge offset	.08R	.015 R

PARAMETRIC WEIGHT RELATIONSHIPS

This section presents the weight trends, in the form of equations, used in the parametric study. The equations and their correlation with existing helicopter weights are shown graphically in Figures 8 through 18.

For this study, the evaluation of the constants in the general equation, $W = KP^n$, is achieved for each weight group by first determining the exponent, n , using all available data. The coefficient, K , is then found using data from helicopters with characteristics similar to the type under consideration. The Sikorsky S-64 (CH-54A) Flying Crane provides an excellent hardware base for the crane concept and is therefore used extensively in determining realistic coefficients to the equations. The weight equations are written as functions of helicopter design variables which have significant, first-order effects on weight. Particular attention is given to the rotor parameters which constitute the base for this study. Design improvements such as the large weight savings gained by use of titanium components in the rotor systems of the S-65 (CH-53A) and S-61R (CH-3C) have been incorporated in the weight trends. Weight reductions in the drive system (Reference 8) have also been used, and the result has been significantly lower weight solutions than those shown in earlier studies.

Rotor Group

$$W_{rg} = K (RC)^{1.292} (b)^{1.27} + \Delta \quad (6)$$

where W_{rg} = Total main rotor group weight - lb

R = Main rotor radius - ft

C = Main rotor blade chord - ft

b = Number of blades per rotor

For the single rotor configuration,


K = 1.47 with titanium components

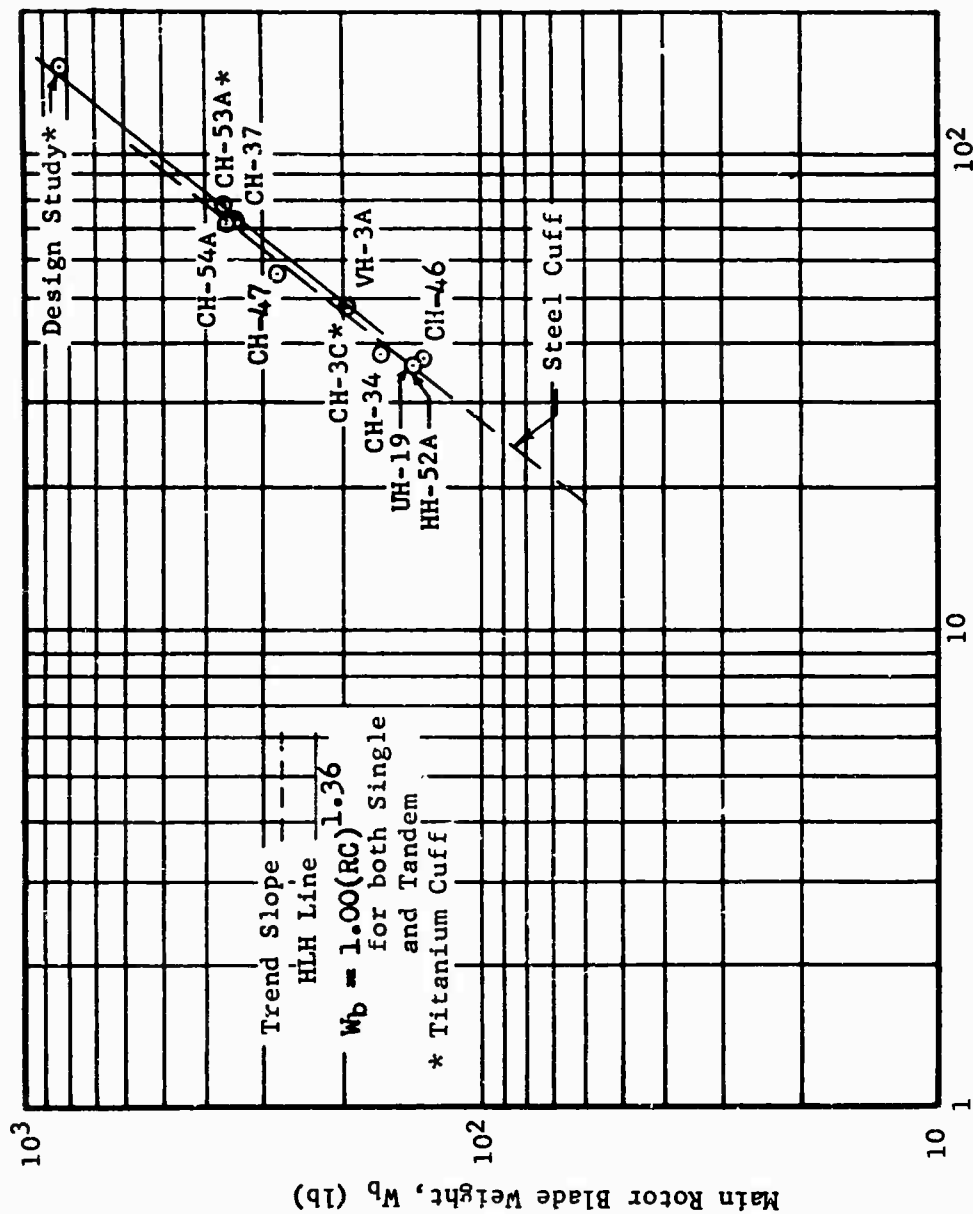
Δ = 20 lb for fairings

For the tandem rotors configuration,

K = 3.29 with titanium components

Δ = 30 lb for fairings

* United States Official Statutory Symbol for Identification of Registered Trade Mark



The general Sikorsky trend for main rotor blade weight, as shown in Figure 8, is given by

$$W_b = 1.092 (RC)^{1.36} \quad (7)$$

Since the coefficient of 1.092 corresponds to blades with steel cuffs, it is modified to reflect titanium cuffs by averaging coefficients obtained from the data points which have titanium cuffs (S-61R, S-65, and the Design Study, in Appendix). The resulting expression, applicable to both single rotors and tandem rotors, is

$$W_b = 1.0 (RC)^{1.36} \quad (8)$$

The rotor group weight trend is given by

$$W_{rg} = K (W_b)^{0.95} (b)^{1.27} \quad (\text{Figure 9}) \quad (9)$$

$$K = 1.69 \text{ for a single rotor}$$

$$K = 3.78 \text{ for tandem rotors}$$

The titanium weight savings is again incorporated into the expression by modifying the coefficient using the same data points. The expression for a single rotor configuration becomes

$$W_{rg} = 1.47 (W_b)^{0.95} (b)^{1.27} \quad (10)$$

Reducing the tandem coefficient to a comparable basis by the ratio

$$\frac{K}{3.78} = \frac{1.47}{1.69},$$

the tandem rotor group weight equation becomes

$$W_{rg} = 3.29 (W_b)^{0.95} (b)^{1.27} \quad (11)$$

In order to reduce the number of equations for the iterative process, Equation (8) is substituted into Equations (10) and (11), resulting in Equation (6).

Although a rotor group weight equation can be written more elaborately in terms of more or different variables, experience has shown that the simpler relationship shown in Equation (6) is a more effective weight prediction tool. It suffers little or nothing in accuracy, while its simplicity produces a decided advantage in the solution of iterative problems. The reason for its effectiveness lies in the fact that other variables which

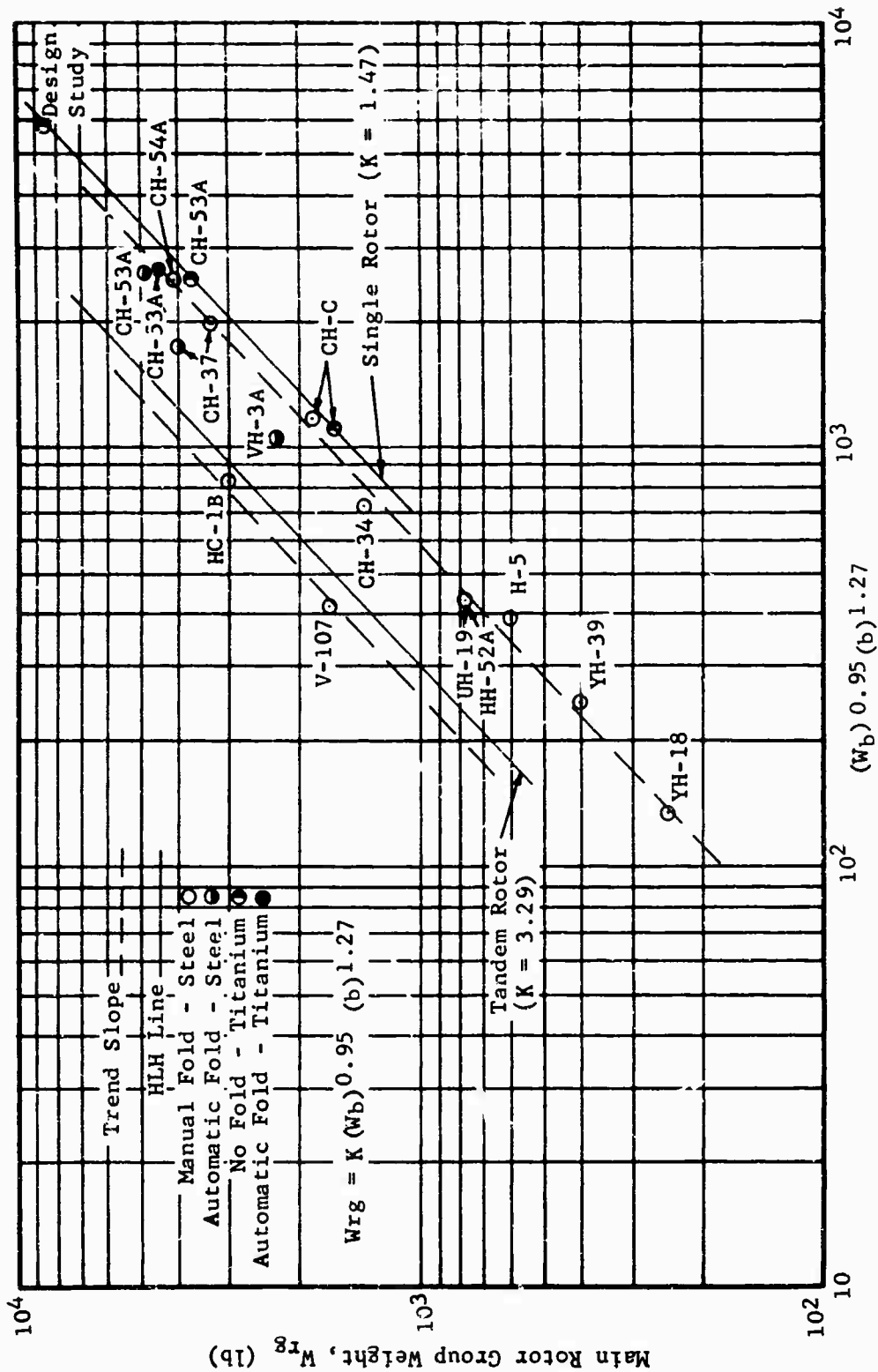


Figure 9 Rotor Group Weight

affect weight have either exhibited a historical dependence on the chosen parameters or have been held relatively constant. This same reason also may limit the application of Equation (6), as discussed below.

One variable which has been held relatively constant in the past is the aspect ratio of the rotor blades. Equation (6) is derived from data with an aspect ratio range of 16-20. Since the tandem rotors in this study have aspect ratios well below 16, a preliminary investigation of centrifugal force is made to achieve a qualitative evaluation of the effects of low aspect ratio blades on rotor group weight.

A measure of centrifugal force may be written as

$$F_c = K W_b \frac{V_t^2}{R} \quad (12)$$

where F_c = Measure of centrifugal force - lb

W_b = Unit blade weight - lb

V_t = Tip speed - ft/sec

R = Rotor radius - ft

K = Dimensional constant - sec²/ft

By assuming constant blade area, blade weight and tip speed, the equation may be rewritten as

$$F_c \propto \frac{1}{AR^{0.5}} \quad (13)$$

where AR = Blade aspect ratio

An increase in aspect ratio from 16 to 20, therefore, decreases the centrifugal force by 11 percent, while a decrease in aspect ratio from 16 to 9 increases the centrifugal force by 33.3 percent. This effect, which is oversimplified by the assumption of constant blade weight, is illustrated graphically in Figure 10.

To relate this to weight, we write

$$W_{rg} \propto (F_c)^n \quad (14)$$

or, by substitution,

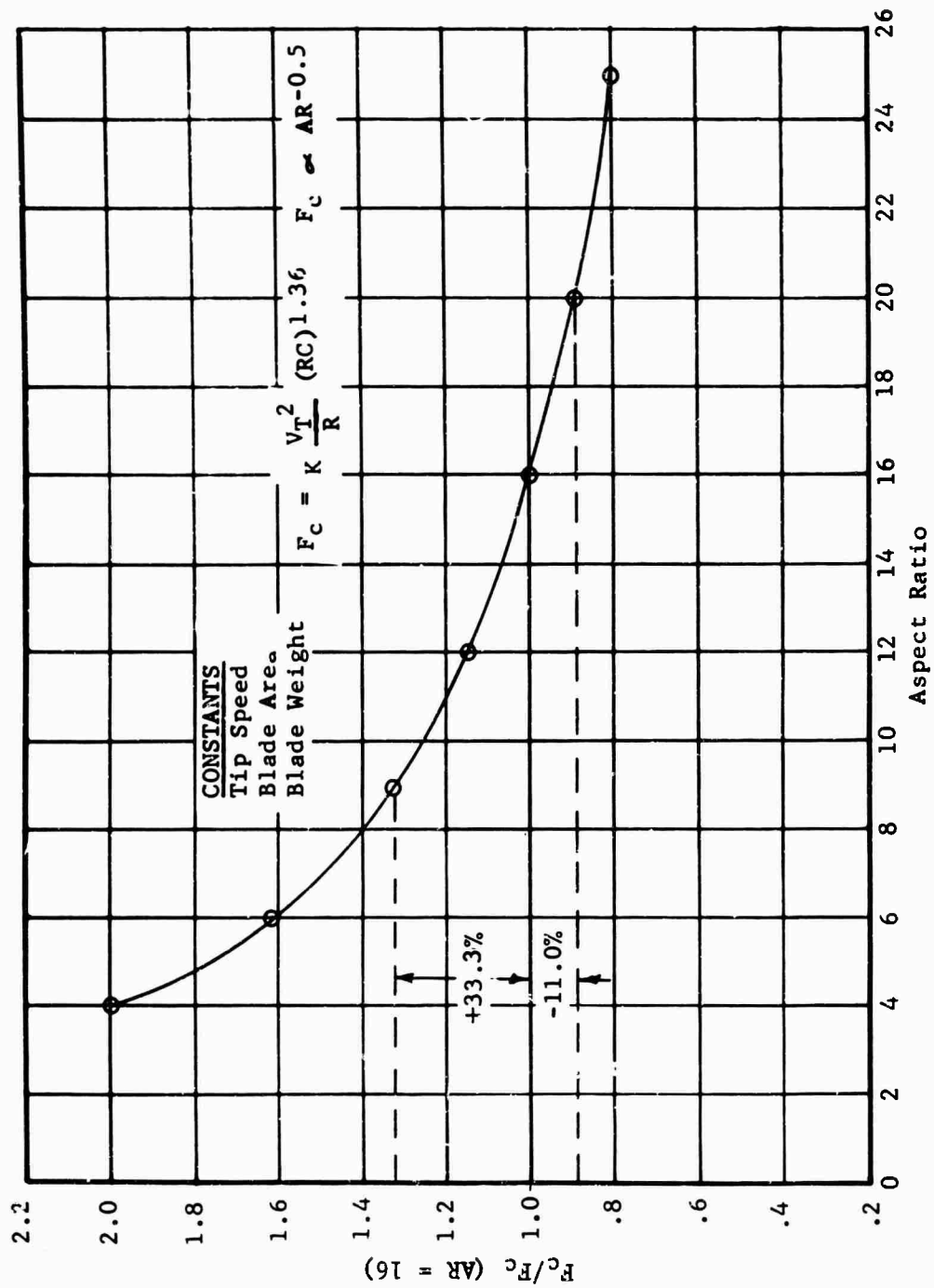


Figure 10 Variation of Centrifugal Force with Aspect Ratio

$$W_{rg} \propto \left(\frac{1}{AR}\right)^{0.5n} \quad (15)$$

Experience indicates that $1 < n < 1.5$. Taking the lower value results in a 33.3-percent weight increase by reducing aspect ratio from 16 to 9. Note that both the assumption of constant blade weight and the assumed value of n tend to minimize the effect of aspect ratio.

- The tandem rotor solution in this study has an aspect ratio of 9.4. For a constant tip speed, this could result in a rotor group weight 30 percent higher (2,200 pounds) than that predicted by Equation (6). A penalty of this magnitude requires verification based on detailed analysis and cannot be used prematurely in a quantitative manner. Equation (6) has therefore been used without modification for low aspect ratio blades.

Tail Rotor

$$W_{tr} = \left(0.236\right) \frac{A_{trb}^{1.938}}{T} + \Delta \quad (16)$$

where W_{tr} = Tail rotor weight - lb

A_{trb} = Tail rotor blade area (bRC) - ft²

T = A first-order measure of thrust as given by
 $\frac{HP}{(R)(rpm)}$ of the main rotor - R in ft

Δ = 20 lb for central oiling

The correlation of this equation with existing helicopter tail rotor weights is shown in Figure 11. The coefficient of 0.236 reflects the use of titanium components in the hub and titanium blade cuffs.

- Although this equation appears to imply an inverse relationship of weight to measure of thrust, T , such is not the case, since required blade area increases with thrust.

Stabilizer

$$W_s = 1.40 S_a^{1.15} \quad (17)$$

where W_s = Stabilizer weight - lb

S_a = Stabilizer area - ft²

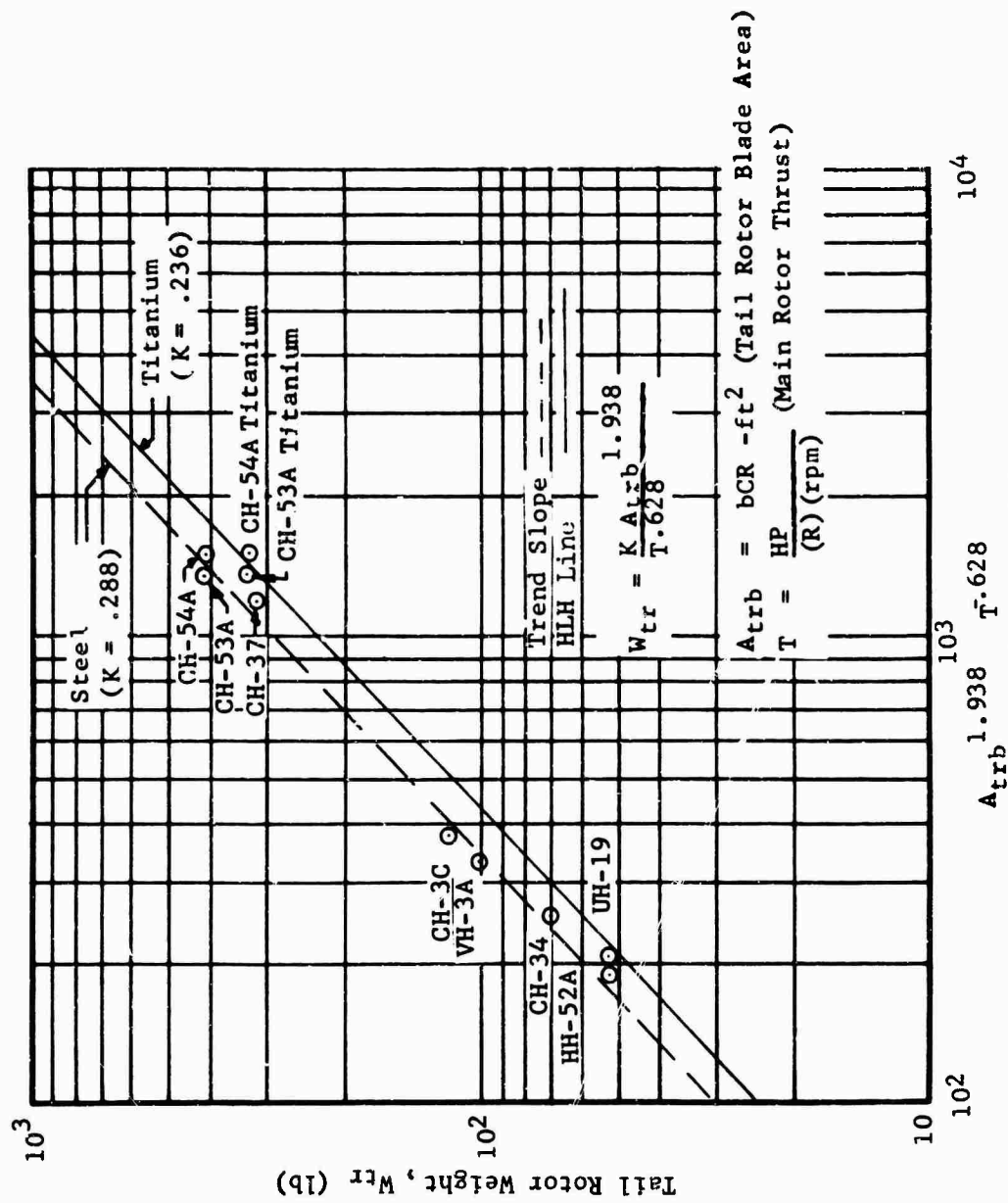


Figure 11 Tail Rotor Weight

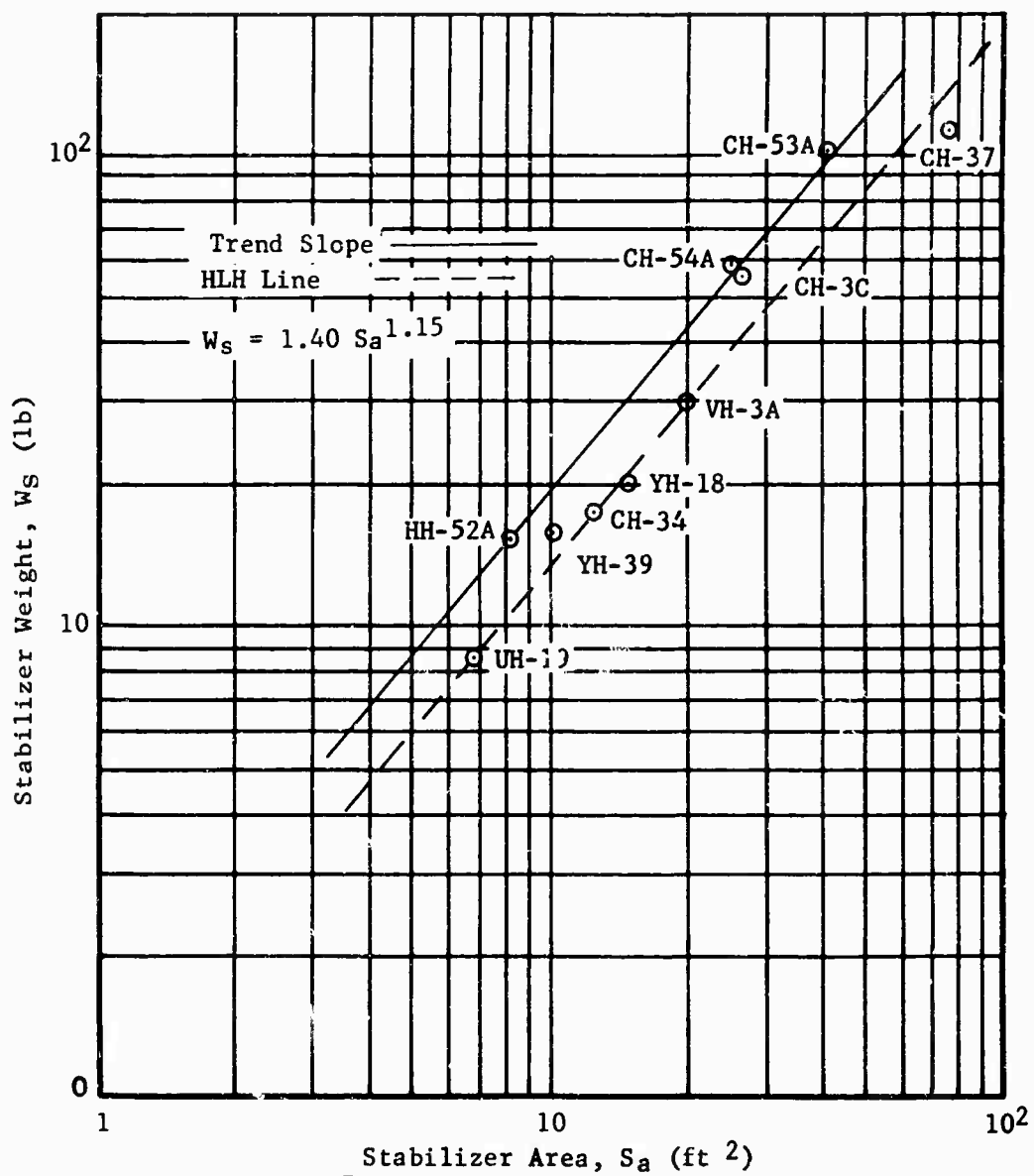


Figure 12 Stabilizer Weight

This equation is illustrated graphically in Figure 12.

Body Group

$$W_b = K (DGW)^{0.25} (R)^{1.84} \quad (18)$$

where W_b = Total body group weight - lb

DGW = Design gross weight - lb

R = Main rotor radius - ft

K = 0.272 for a single rotor crane configuration

K = 0.492 for a tandem rotor crane configuration

Equation (18) is derived by substituting

$$A_w = K R^{2.088} \text{ from Figure 14} \quad (19)$$

K = 0.727, single rotor

K = 1.230, tandem rotors

into $W_b = K (DGW)^{0.25} (A_w)^{0.88} \text{ from Figure 13} \quad (20)$

K = 0.360, single rotor

K = 0.410, tandem rotors

where A_w = Fuselage wetted area - ft²

The coefficient of 0.272 for the single rotor configuration is derived by using the CH-54A flying crane datum.

$$K = (0.360)(0.727)^{0.88} = 0.272 \text{ (Equation 18)}$$

The tandem crane coefficient in Equation (19) is obtained by applying the same ratio to the existing tandem coefficient that is obtained by comparing the single rotor crane coefficient to the coefficient for a single rotor cabin without a rear loading or front loading feature. The comparison is made to cabin bodies without rear or front loading capabilities, since this feature requires a local fuselage enlargement in a single rotor cabin and results in a larger wetted area for a given radius (evidenced by the CH-37, CH-3C and CH-53A data points in Figure 14) while for a tandem configuration, this feature requires little or no enlargement of fuselage. The lower single rotor

coefficient can, therefore, be used to derive a tandem crane coefficient. For Equation (19) then,

$$K = (1.374) \left(\frac{0.724}{0.812} \right) = 1.230 \text{ (Figure 14)}$$

The difference in coefficients shown in Equation (20) Figure 13, is attributable to the relatively constant tandem body depth as compared to the tapered body possible in a single rotor configuration. The tandem coefficient in Equation (18) then becomes

$$K = (0.410)(1.23)^{0.88} = 0.492$$

Alighting Gear

$$W_{alg} = 0.274 (DGW)^{0.83} + \Delta \quad (21)$$

where W_{alg} = Alighting gear group weight - lb

DGW = Design gross weight - lb

Single rotor Δ = 100 lb for tail skid and kneeling

Tandem rotors Δ = 60 lb for kneeling

See Figure 15 for the graph of this equation.

The 0.274 coefficient is used for both the single and tandem rotor configurations. The vertical centroid of the tandem configuration is generally higher than that of the single rotor configuration due to blade clearance requirements of the overlapping rotors. This would require a wider tread for the main landing gear on the tandem configuration to meet the same overturn requirements. If these requirements supersede load clearance criteria, the single rotor landing gear weight will be slightly less than that of the tandem.

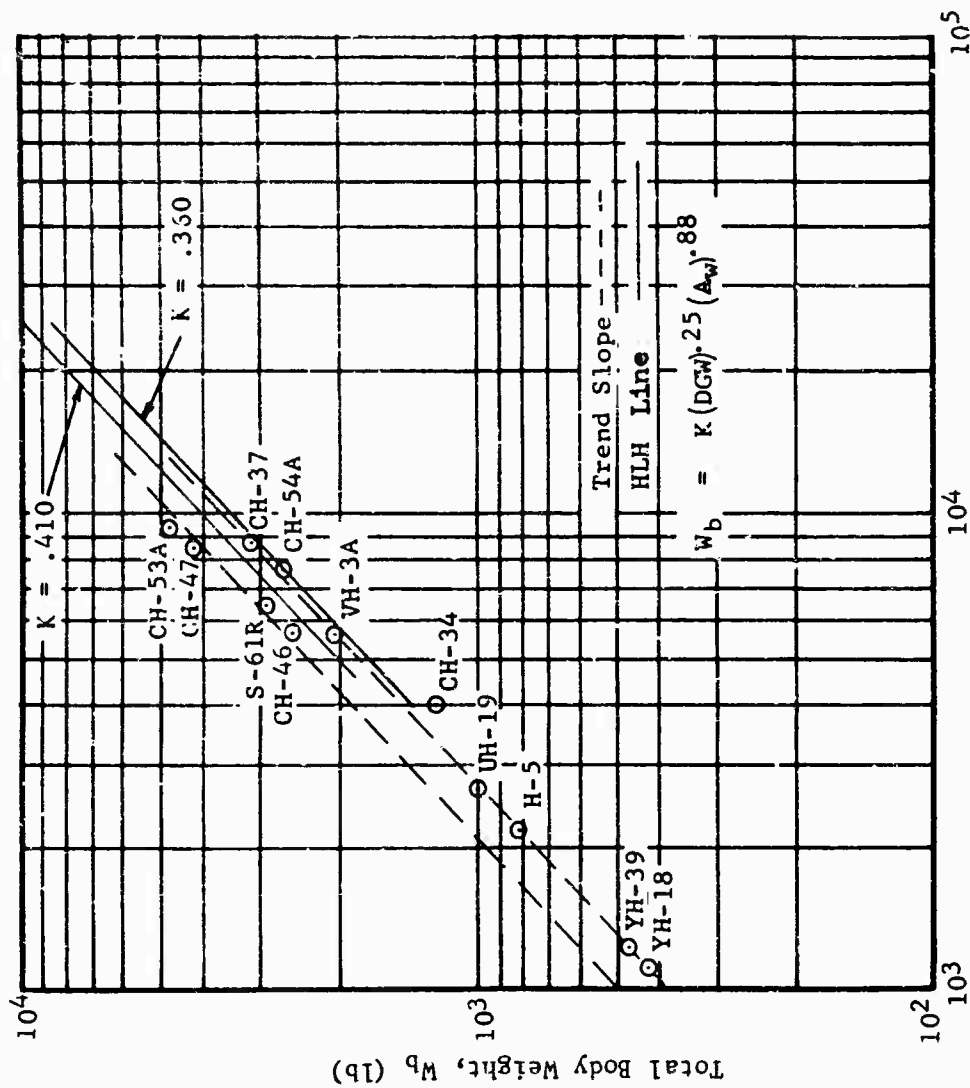
Flight Controls

$$W_{fc} = K (DGW)^{0.93} \text{ (Figure 16)} \quad (22)$$

where W_{fc} = Weight of flight controls group - lb

DGW = Design gross weight - lb

K = 0.066 (Single rotor configuration)



Total Body Weight, $(DGW)^{.25} (A_w)^{.88}$
Figure 13 Total Body Weight

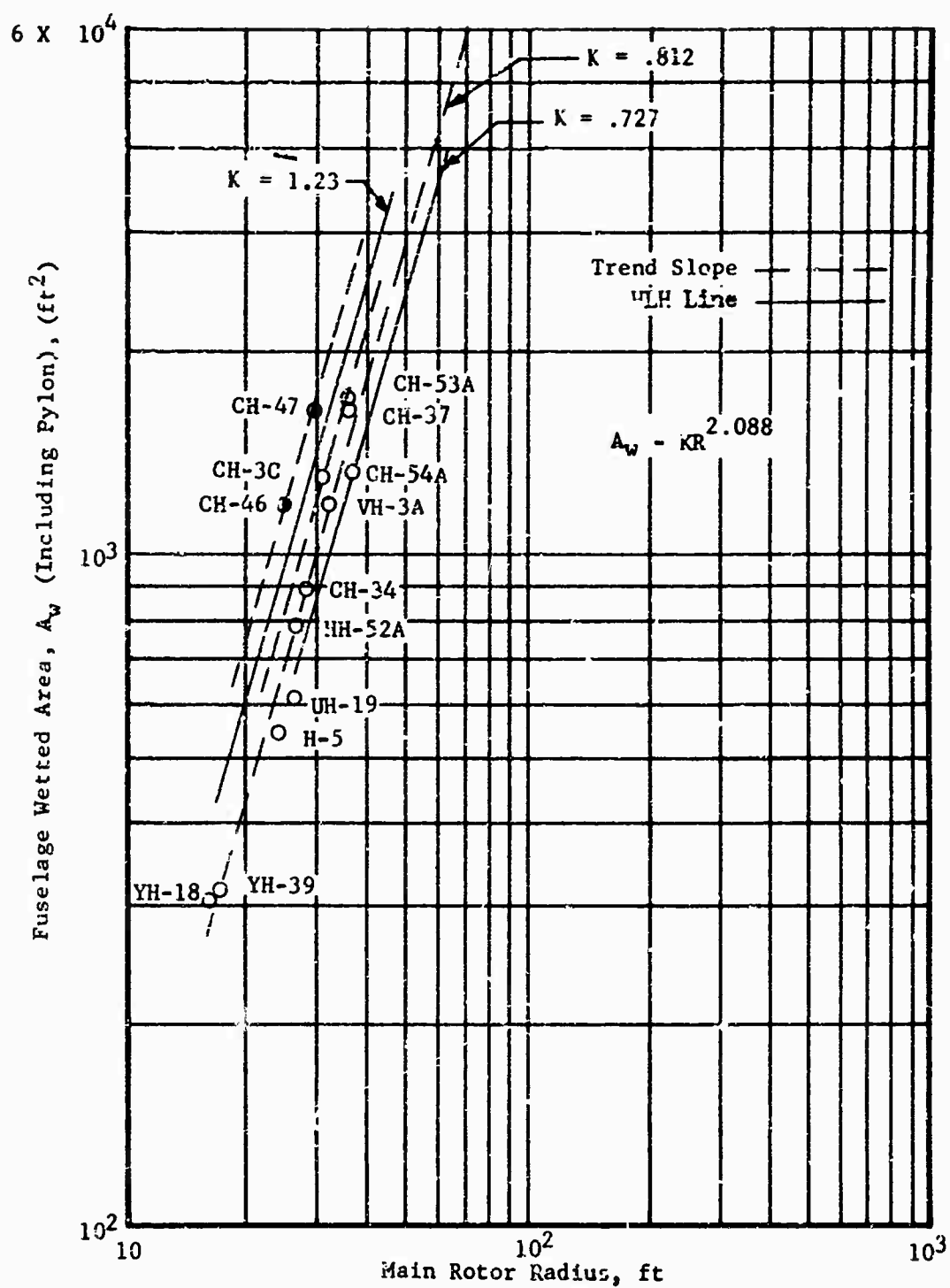
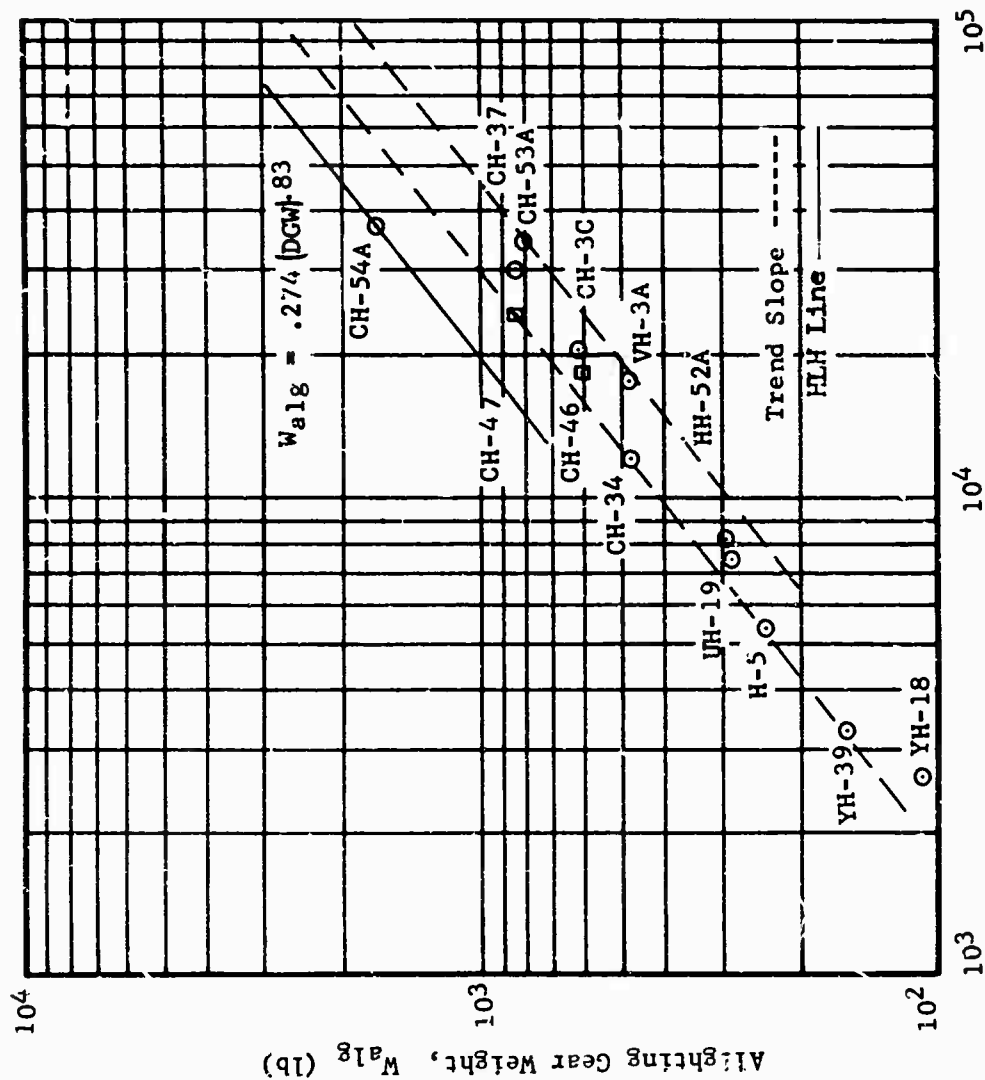
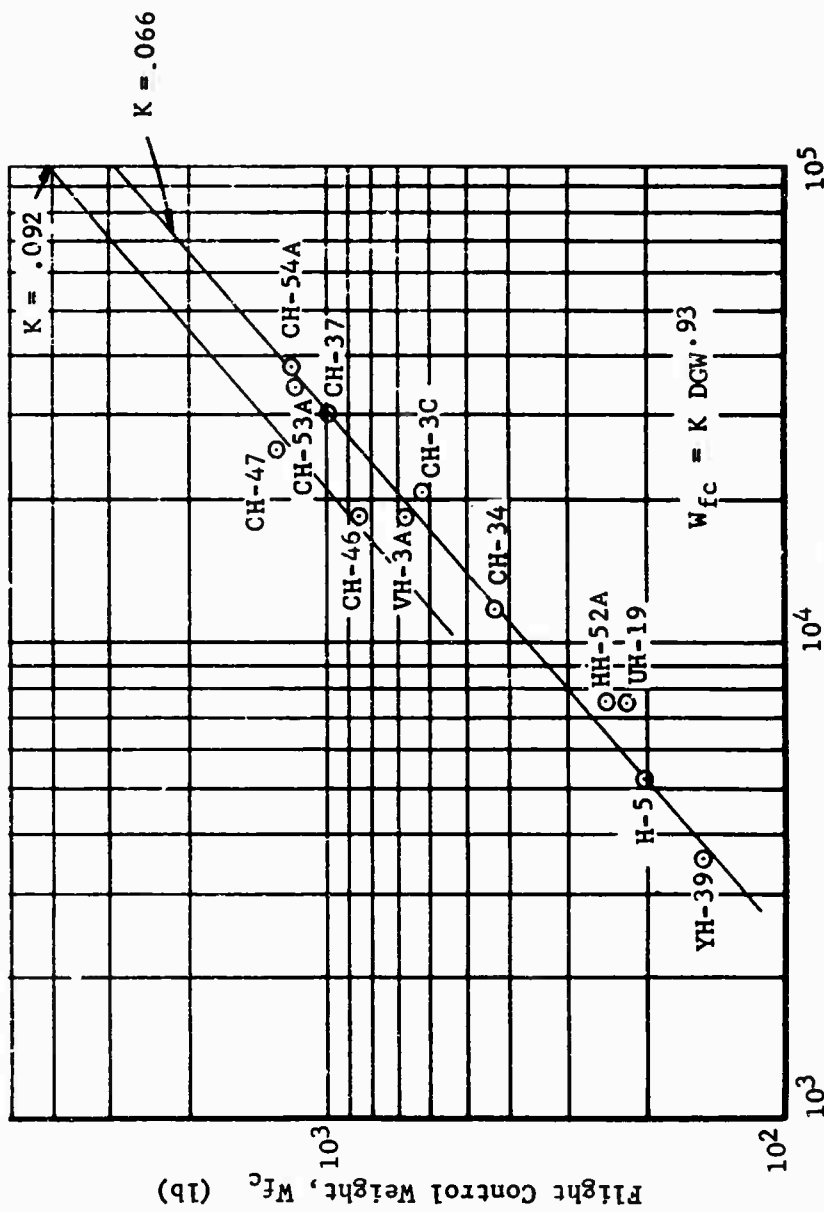


Figure 14 Fuselage Wetted Area



Design Gross Weight, DGW (lb)
Figure 15 Aligning Gear Weight



Design Gross Weight, DGW (lb)

Figure 16 Flight Controls Weight

$$K = 0.092 \text{ (Tandem rotor configuration)}$$

Automatic stabilization equipment is included in Equation (22).

Engines

The weight of the engines is taken from engine manufacturer's specifications. Five pounds per engine is added for residual fluids in compliance with MIL-W-25140 (ASG).

Fuel System

$$W_{fs} = 0.42 F_{cap} \quad (23)$$

where W_{fs} = Weight of fuel system - lb

F_{cap} = Fuel capacity - gal

This is consistent with a fuel system similar to that of the CH-54A Flying Crane.

Drive System

The drive system includes gearboxes, shafts, lubricating system, rotor brake, and transmission supports.

$$W_{ds} = K \left[\frac{(HP)(R)}{n_r V_t} \right]^{.795} \quad (24)$$

where W_{ds} = Drive system weight - lb

HP = Total horsepower required

R = Main rotor radius - ft

V_t = Main rotor tip speed - ft/sec

n_r = Number of rotors

K = 33.89 for the single rotor configuration

K = 78.31 for the tandem rotor configuration

This equation is derived by substituting $\text{rpm} = \frac{30 V_t}{\pi R}$ into

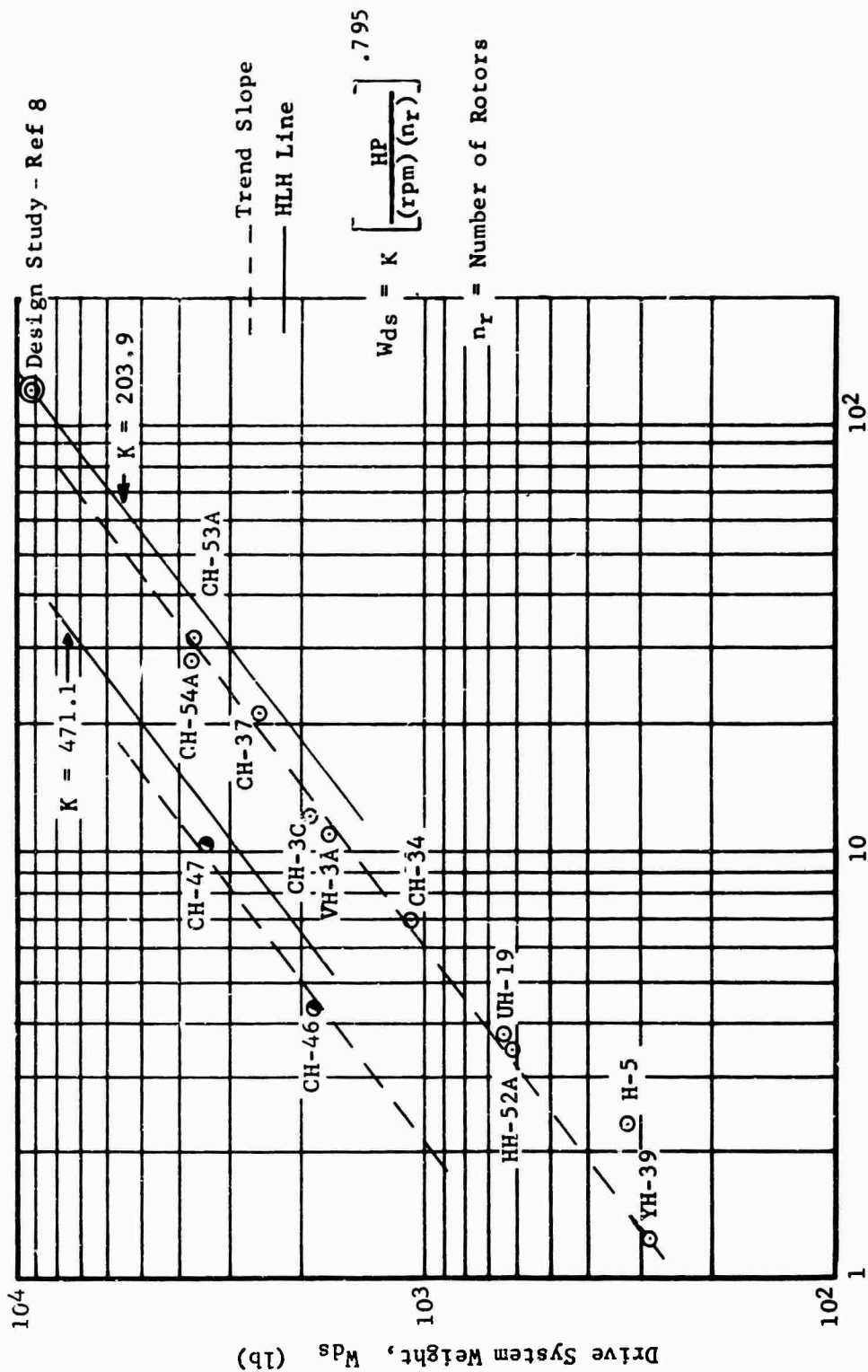


Figure 17 Drive System Weight

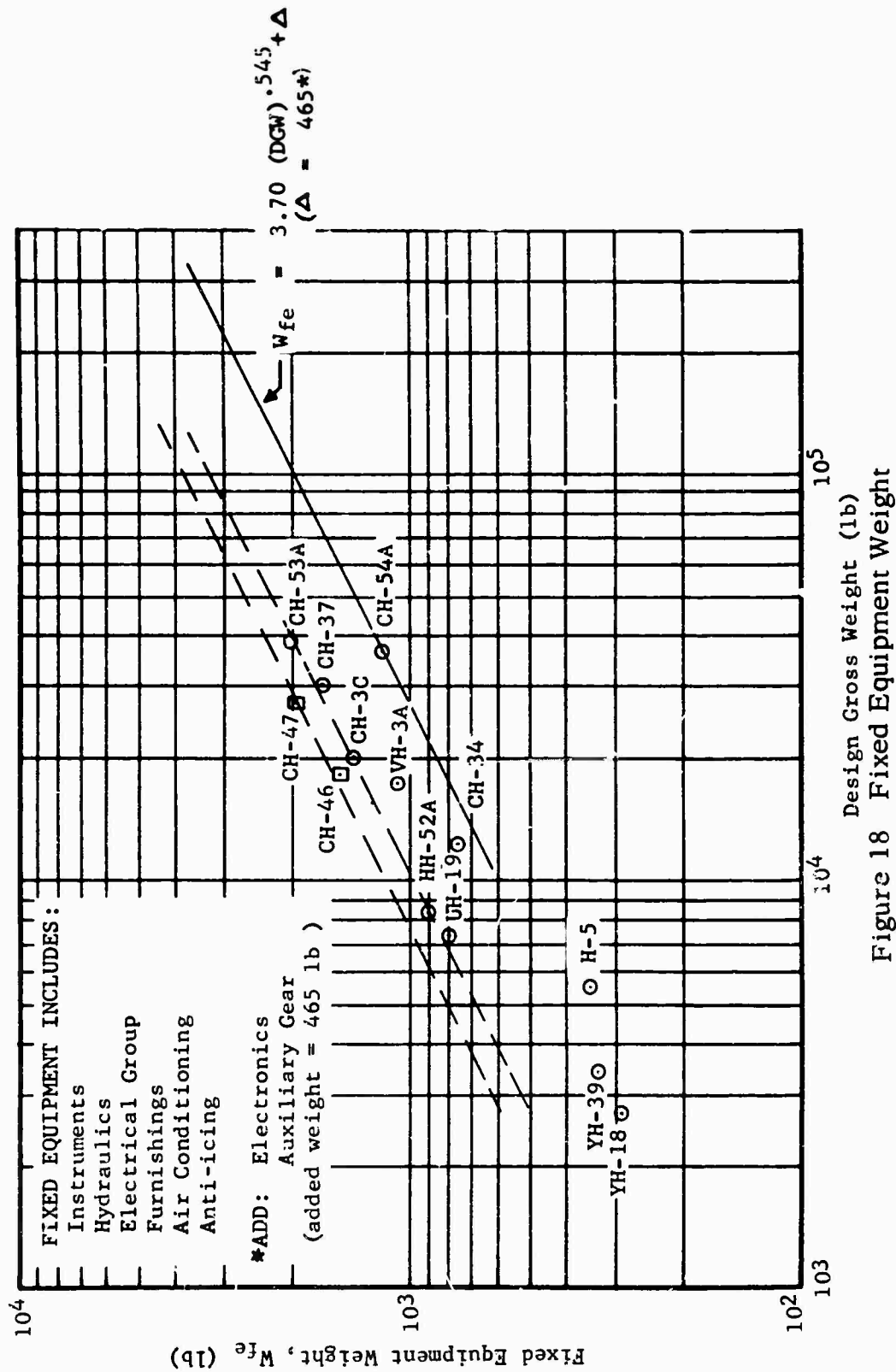


Figure 18 Fixed Equipment Weight

$$W_{ds} = K \left[\frac{HP}{(rpm)(n_r)} \right]^{0.795} \quad (\text{Figure 17}) \quad (25)$$

The coefficient for the single rotor equation is reduced as a result of the weight saving documented in the HLH Transmission Study (Reference 8). The statistical coefficient for the tandem rotor is reduced by the same percentage.

Fixed Equipment

$$W_{fe} = 3.70 (DGW)^{0.545} + 465 \quad (26)$$

Fixed Equipment, for the purpose of this study, includes:

- Instruments
- Hydraulics
- Electrical Group
- Electronics and Navigational Equipment
- Furnishings
- Air Conditioning
- Anti-Icing
- Auxiliary Gear

Although the weight of fixed equipment is primarily a function of mission requirements, there is a significant weight factor which is dependent on aircraft size. Figure 18 illustrates the anticipated weight growth from the CH-54A base point.

For simplicity, the same fixed equipment weight equation was used for both the single and tandem rotor configurations. A more accurate tandem prediction would result from the addition of dual transmission instrument weights and an allowance for the longer hydraulic lines necessitated by the remoteness of major hydraulic components from each other. These changes to the equation would, however, require a detailed design study for accurate results.

Fixed Weights

This group consists of weights which are held constant throughout this study. It includes the components of Table X.

TABLE X
FIXED WEIGHT COMPONENTS

Item	Weight - lb
Engine Section	770
Air Induction System	60
Exhaust System	60
Starting System	130
Lubricating System (Engines)	140
Engine Controls	50
<u>Auxiliary Power Plant</u>	<u>160</u>
Total Fixed Weights	1,370 lb

Balance

The selected single rotor and tandem rotor solutions were checked for balance characteristics, and both meet the center-of-gravity travel requirements of ± 2.5 feet.

ROTOR PERFORMANCE METHODS

Isolated rotor performance is determined for each parametrically assumed rotor geometry by the latest available analytical methods. These are the Goldstein-Lock Method for hovering and the Generalized Rotor Performance Method for forward flight. Both have been developed and refined by Sikorsky Aircraft and are computerized for rapid utilization. Each involves a strip analysis of the blade using two-dimensional airfoil data derived by full-scale wind tunnel testing. The elemental blade lift and in-plane forces are integrated spanwise and azimuthwise to determine total thrust and power for an assumed blade pitch. Local compressibility and stall are thus fully accounted for, and different airfoil sections are easily evaluated.

The Goldstein-Lock Method for determining hovering performance is a three-dimensional analysis which accounts for the effect of number of blades on the aerodynamic losses associated with the development of blade tip vortices. Thus "tip loss" is automatically accounted for and assumption of an arbitrary "tip loss factor," necessary in most simpler methods, is not required. This is particularly important for low aspect ratio blades and rotors with low numbers of blades, where tip losses are significant. Correlation with test-stand-measured performance of rotors with a wide range of geometries has demonstrated the accuracy of this method and has yielded the necessary correction factors for leading edge abrasion strips and spanwise flow effects. Figure 19 illustrates the good correlation obtained for two extremes of rotor geometry--a five-bladed, 62-foot-diameter rotor with aspect ratio 20.4 blades and a three-bladed, 51-foot-diameter rotor with aspect ratio 13 blades.

The Generalized Rotor Performance Method for forward flight is described in Reference 18 and is the method used to generate the nondimensional performance charts of Reference 55. This analysis solves the differential equation of blade flapping to trim the rotor and then integrates the elemental blade forces to determine total rotor lift and power. Good correlation with high speed (up to 190 knots) rotor data obtained in the Ames wind tunnel tests of the CH-34 main rotor has been demonstrated.

This method also provides a much more comprehensive retreating blade stall criterion than is possible with simpler methods. A stall parameter representing the maximum spanwise-integrated profile drag torque at the most critical retreating blade azimuth is calculated for each trimmed condition. More conventional criteria, dealing only with the blade tip at 270 degrees azimuth, for example, are inadequate for high speeds and blade loadings. By application of the bC_{Qd}/σ criterion, the blade stall and compressibility effects at all retreating side locations are fully recognized.

Test Stand Data Compared
to Goldstein-Lock
Calculations

(Sea Level Standard Day)

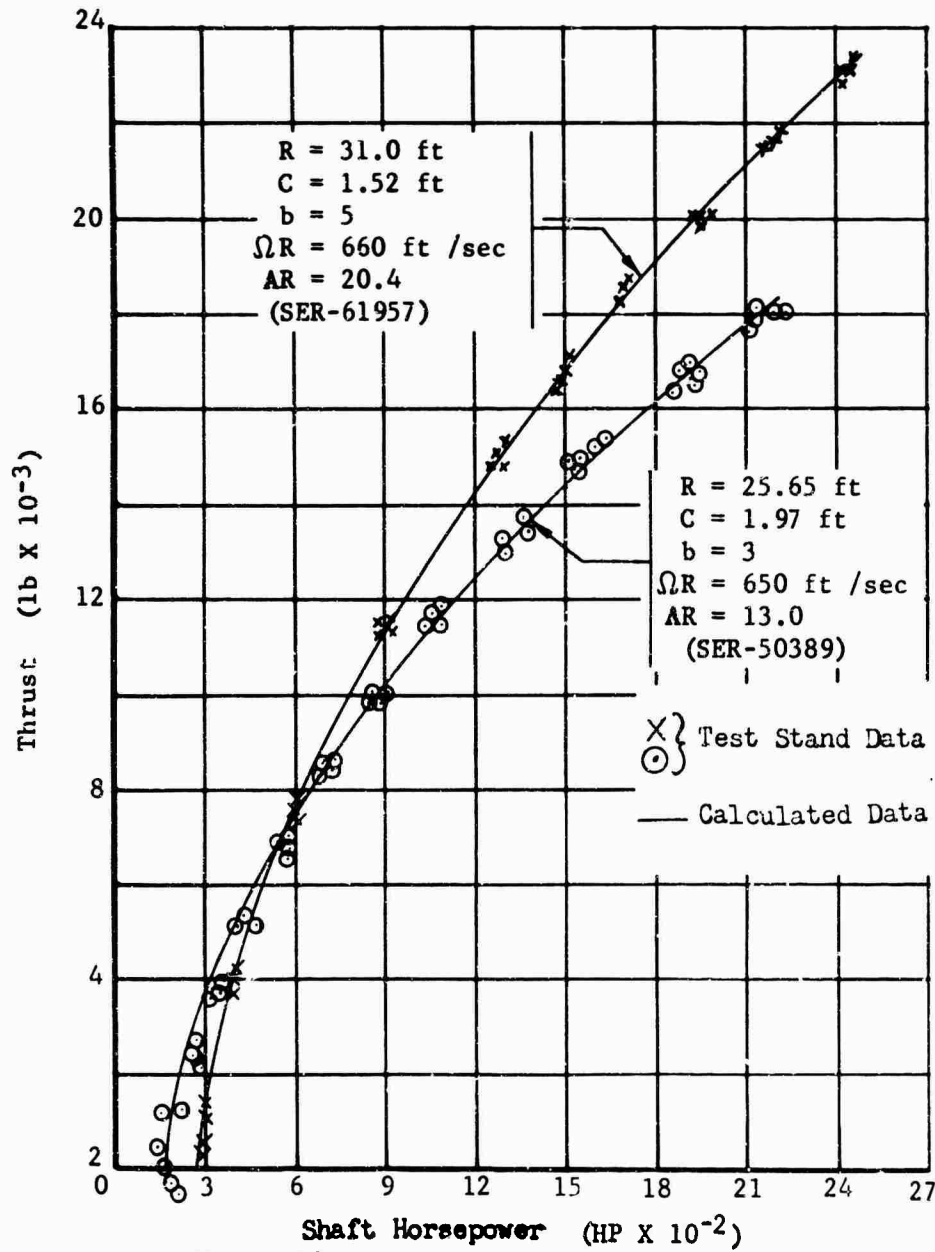


Figure 19 Hover Performance Correlation

A cruise blade tip loss factor of .97 is assumed throughout, since this has proved to be adequate in successful correlations of flight test data and the Ames wind tunnel results discussed above. This assumption is necessary until an accurate method for evaluating blade tip loss in forward flight is developed.

ENGINE SELECTION

Selection of the type and number of engines for the 12-to 20-ton crane helicopter is fundamental to the eventual parametric rotor system optimization and must therefore be established early in the study. The following engines were considered:

TABLE XI
ENGINE PERFORMANCE DATA

Engine	6000 feet, 95°F Max HP	Dry Weight	SLS, SFC at 1500 HP
T64/S4A	2650	708	.601
T64/S5A	3050	765	.639
LTC4B-11A	2640	640	.704
JFTD12A-5	3385	930	.935
T-78 548-C2	Performance classified		
T-78 548-D2 (regenerative)	Performance classified		

For each engine, various 6000-foot, 95-degree Fahrenheit powers were assumed (up to maximum available) and a rotor system was derived iteratively based on the required mission capability. Weight and performance were evaluated on the basis of preliminary data, including that of the 1962 study (Reference 27), since at this stage in the study fully refined relationships were not established, and rotor system refinement such as number of blades and solidity could not be defined pending completion of the rotor parametric study.

The results of the engine study are summarized in Figures 20 and 21, which show design gross weight (20-ton mission) versus installed power. Also shown is the disk loading variation. The T-78 engine curves are not shown since their performance is classified, but conclusions regarding their use are included herein.

It is apparent that gross weight continues to decrease as more installed power is assumed for a given engine; however, associated disk loading also increases rapidly.

NOTE: These curves are based on preliminary empty weight equations and rotor performance determination and do not illustrate fully optimized solutions for either the single or tandem rotor configuration.

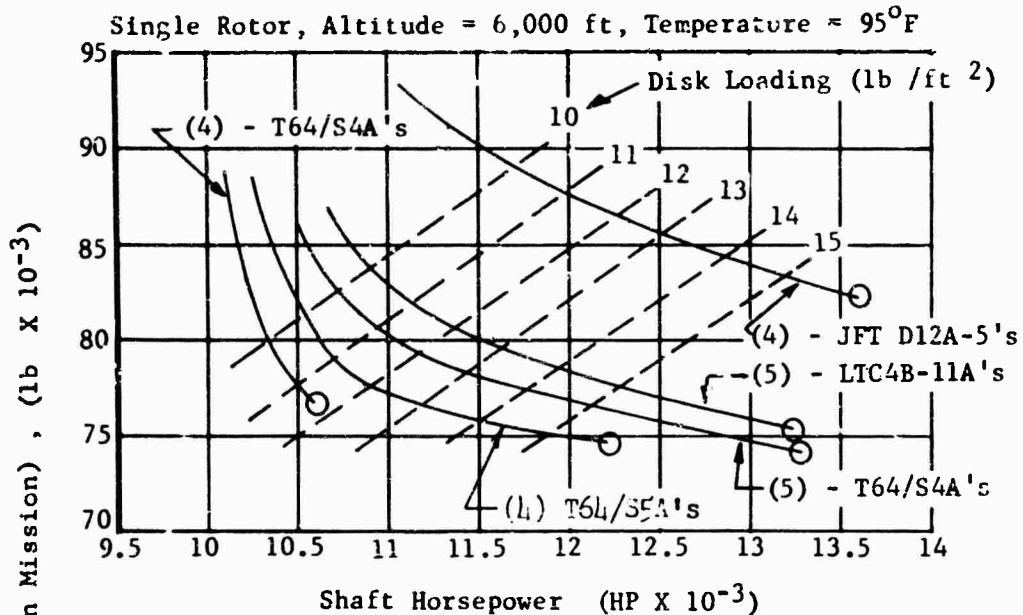


Figure 20 Single Rotor Engine Selection

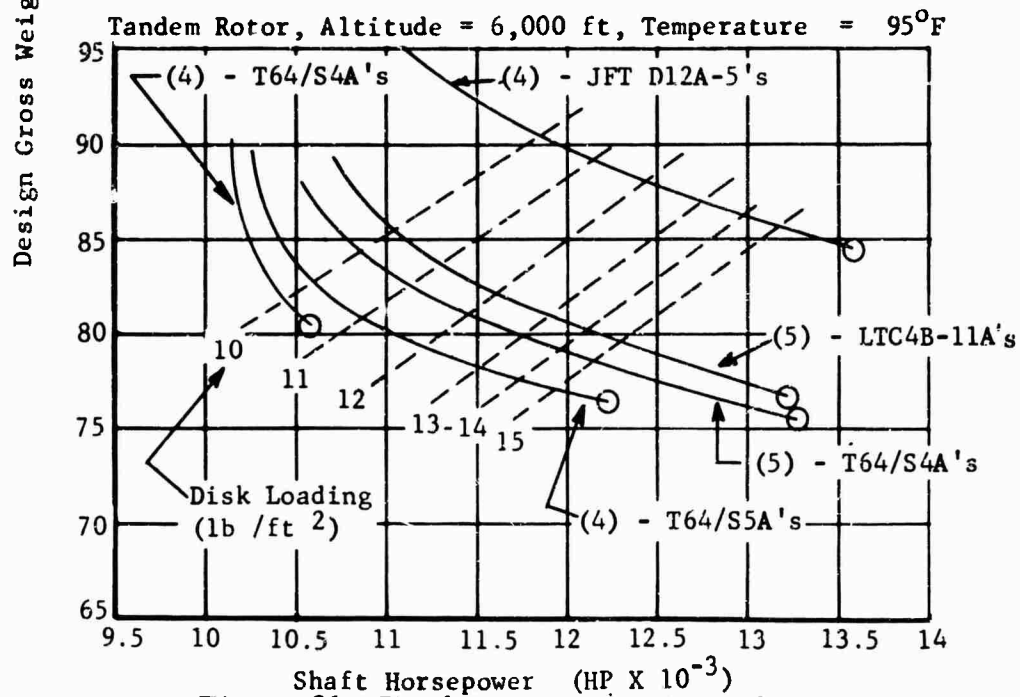


Figure 21 Tandem Rotor Engine Selection

On the basis of low gross weight and reasonable disk loading (12 pounds per square foot), four T64/S4A's rated at full maximum available power were selected for both the single and tandem rotor configurations. The JFTD12A-5 is unsatisfactory as a result of high fuel consumption and dry weight. The regenerative T-78 (548-D2) solution at the same disk loading was also attractive, but resulted in a slightly higher weight empty, which, combined with the uncertainty of the engine's future availability, eliminated it from consideration. The nonregenerative version of the T-78 (548-C2) is not as good a solution as the 548-D2. The LTC4B-11A, because of its higher fuel consumption, is not competitive with the T64/S4A, particularly since its gross weight disadvantage is magnified for the 12-ton mission. The T64/S5A, the next generation version of the T64/S4A, is a less desirable solution because of higher fuel consumption and dry weight.

However, if rotor and drive system weight reductions had not been achieved since the 1962 study (Reference 27), the higher gross weights of that solution, and corresponding higher power requirement, would have favored the T64/S5A.

The T64/S4A is a front-drive turboshaft engine rated at 3695 military power at sea level standard day. It will be available in its production version in mid-1967. Power available as a function of altitude and temperature is shown in Figure 22, and SFC versus power is shown in Figures 23 through 25.

GUARANTEED RATINGS

Sea Level Standard		Output Speed		6,000 ft., 95°F		Output Speed		Dry Weight
	Hover				Hover			lb.
HP	SFC ($\frac{\text{lb}}{\text{HP-hr}}$)	rpm	HP	SFC ($\frac{\text{lb}}{\text{HP-hr}}$)	rpm	rpm		
Max	3695	.476	2650	.493	13600	13600	708*	
Mil	3695	.476	2470	.499	13600	13600		
Norm	3230	.485	2100	.515	13600	13600		

* Includes Integral Oil System

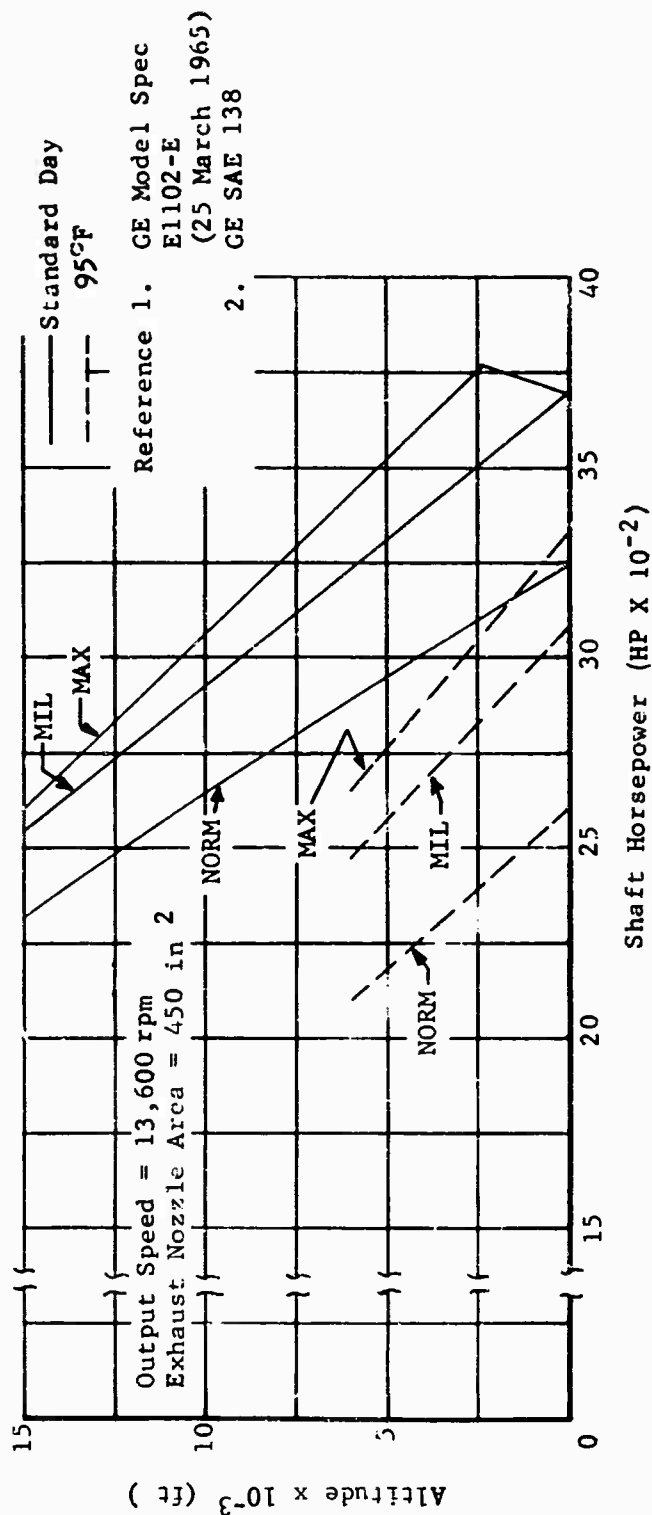


Figure 22 Estimated Minimum Performance of T64/S4A Engine Under Static Conditions

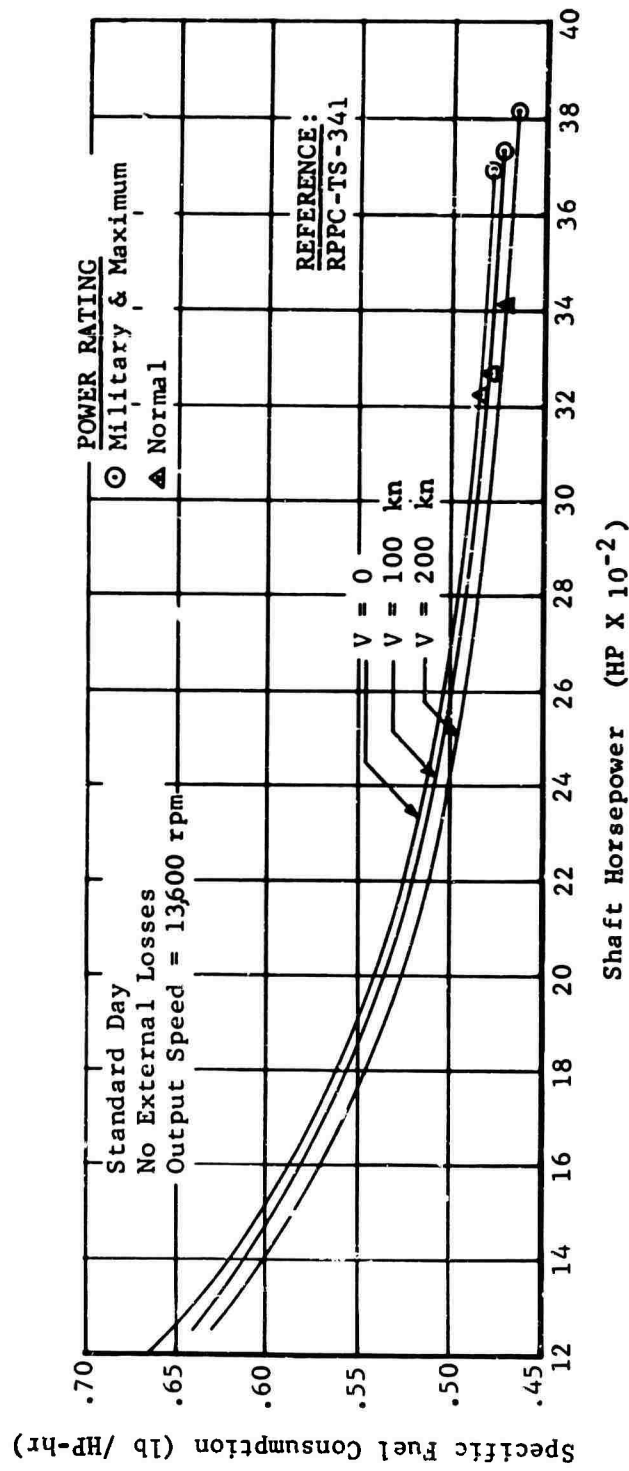


Figure 23 Estimated Minimum Performance of T64/S4A Engine at Sea Level

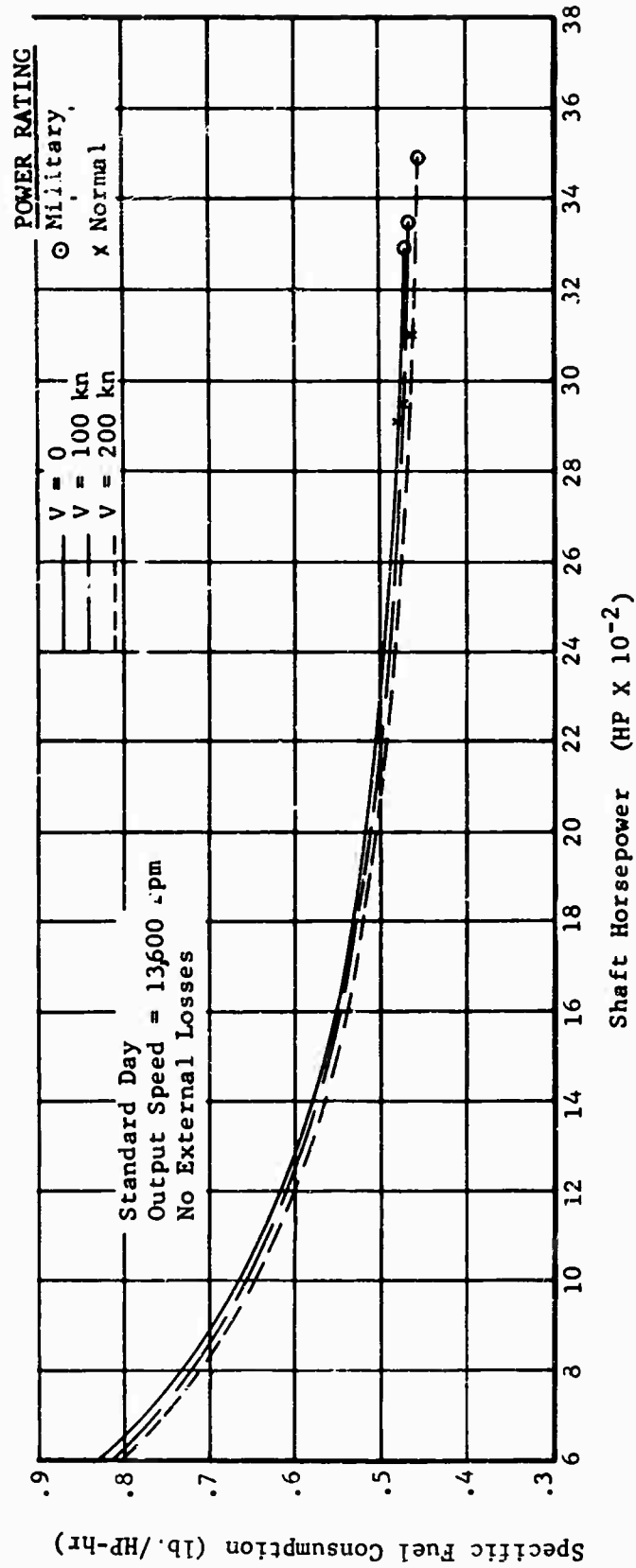


Figure 24 Estimated Minimum Performance of T64/S4A Engine at 5,000-Foot Altitude

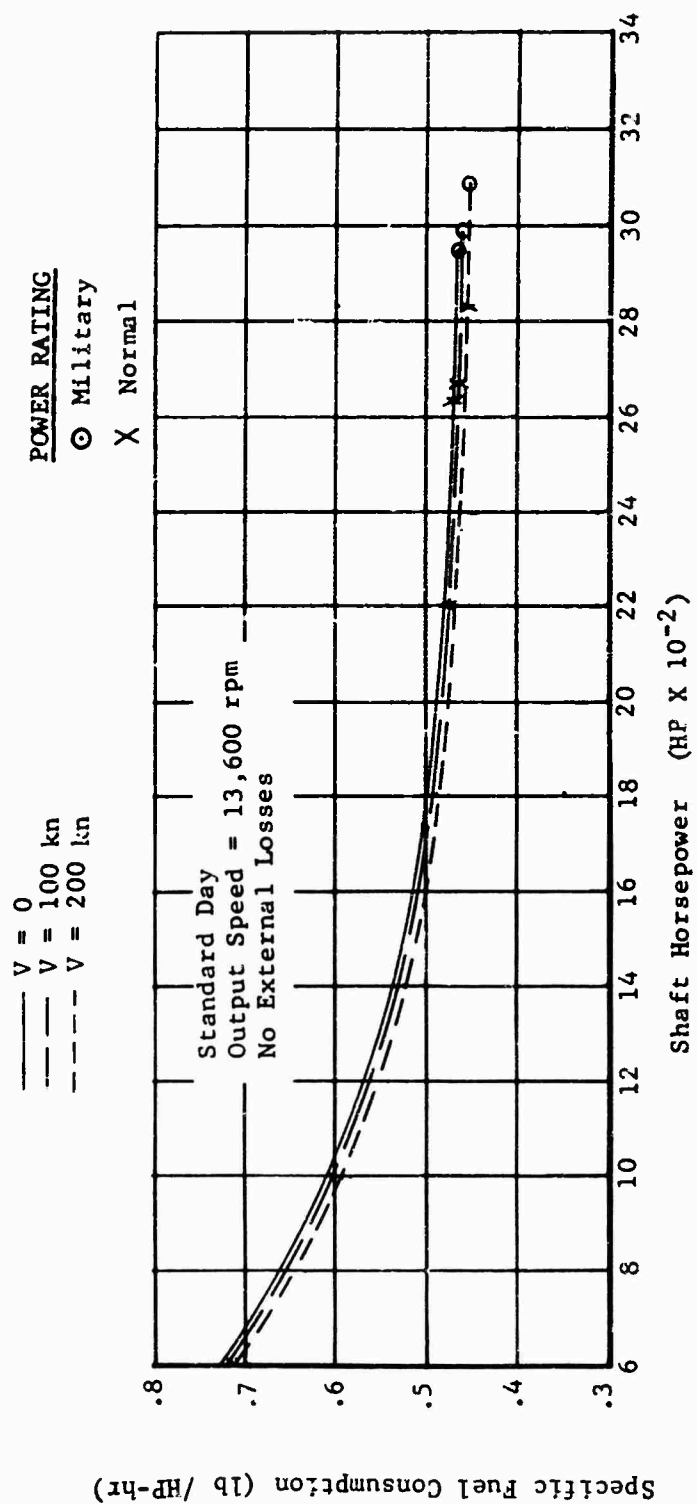


Figure 25 Estimated Minimum Performance of T64/S4A Engine at 10,000-Foot Altitude

ROTOR PARAMETRIC METHODOLOGY

The rotor parametric study includes optimization of rotor diameter, solidity, tip speed, number of blades, blade twist, and blade airfoil section for both single and tandem rotor configurations. Four T64/S4A engines, producing a total of 10,600 HP at 6,000 feet, 95 degrees Fahrenheit, are assumed (see engine selection section), and the parasite drag, vertical drag, rotor interference and asymmetrical loading, tail rotor and horizontal tail sizes, transmission losses, and accessory power described in the basic design data section are used.

To reduce the number of parametric combinations to a workable level, the twist, tip speed, and airfoil section variables are independently optimized at the beginning of the study, based on the rotor sized in the 1962 study (Reference 27). These three parameters are chosen for initial selection because their effect on aerodynamic performance and empty weight is small compared to diameter and solidity. Number of blades is a variable only for the single rotor configuration and is retained as a major variable. After the rotor systems are parametrically optimized, these variables are again investigated to confirm the initial selections.

With twist, tip speed, and airfoil section defined, diameter, solidity, and number of blades are systematically varied to produce 27 finite rotor systems for the single rotor configuration and 9 for the tandem (limited to three-bladed rotors). For each combination the hover gross weight capability, empty weight, and mission fuel are calculated to yield payload. Cross plots then yield the 12 to 20-ton payload solutions which, with boundary conditions superimposed, result in the optimum, minimum weight single and tandem rotor solutions. Boundary conditions include maximum blade loading (C_T/σ) allowable to prevent blade stall, and static blade droop considerations. The final configurations arrived at by this procedure are then checked to determine the validity of the initially selected twist, tip speed, and airfoil section values.

Figure 26 is a flow chart illustrating the parametric technique. The following pages discuss in greater detail the procedure followed.

Initial Twist, Tip Speed, Airfoil Section Selection

The rotor design optimized in the 1962 study (Reference 27) was used as a base for the investigation of twist, tip speed, and airfoil section effects. Criteria considered included hover, cruise power required, retreating blade stall, and blade stresses in cruise. Flight conditions required in three design missions (12-ton, 100-nautical-mile radius; 20-ton, 20-nautical-mile radius; and ferry) were first investigated at nominal values of twist (-11 degrees), tip speed (675 feet per second), and airfoil section (0012) to

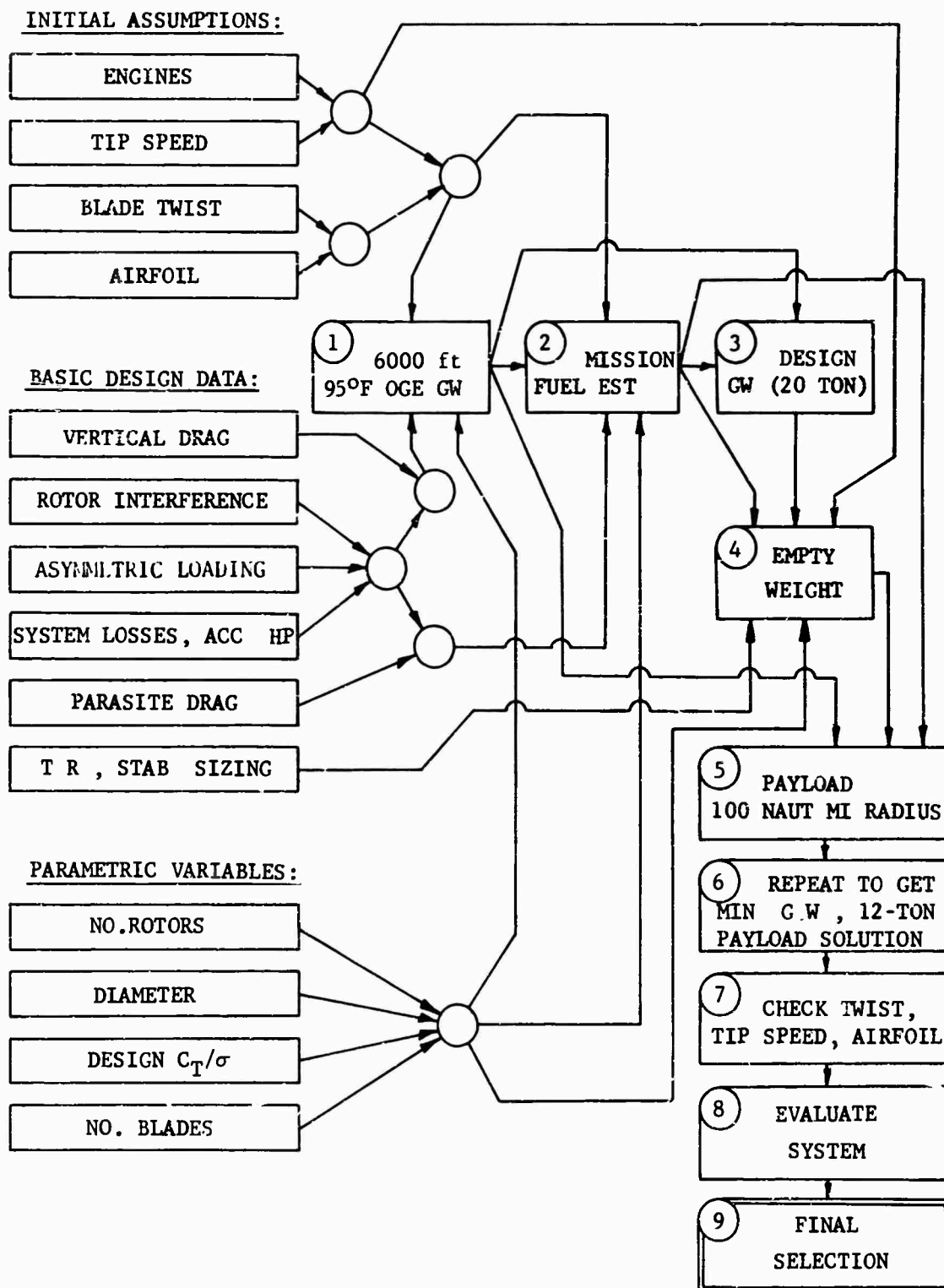


Figure 26 Rotor System Parametrics, Flow Chart

determine the critical flight condition for each criterion. These critical conditions are:

Hover power:	6000 feet, 95°F, OGE hover at GW = 76,000 pounds (12-ton hover)
Cruise power:	SLS, V = 95 knots at GW = 85,000 pounds, f = 200 square feet (20-ton outbound)
Cruise stall:	Same as cruise power
Cruise stresses:	SLS, V = 130 knots at GW = 48,000 pounds, f = 100 square feet (12, 20-ton inbound)

For these critical flight conditions, twist, tip speed, and airfoil section were each varied independently, holding the other two constant, to determine the effect on power, stall, and blade stress. The Goldstein-Lock and Generalized Rotor Performance methods described previously were used to determine hovering and cruise performance, respectively. The Coupled Blade Flatwise-Edgewise Torsional Aeroelastic Analysis developed by Sikorsky Aircraft (Reference 3) was used to calculate blade stresses in cruise.

Figures 27 through 29 show the results of this investigation. Avoidance of retreating blade stall in cruise requires a tip speed of over 665 feet per second for -11-degree twist and 680 feet per second for -8-degree twist. Both hover and cruise power are minimized at a tip speed of 680-700 feet per second. Blade stress decreases with increasing tip speed. High blade twist is desirable to minimize power and is also beneficial in terms of alleviating cruise blade stall. However, blade vibratory stresses in cruise are highly sensitive to twist, and this becomes the dominant factor in twist selection.

Four airfoil sections, varying in thickness from 10 percent to 12 percent chord, were investigated in terms of their influence on power required and retreating blade stall. The airfoil lift and drag characteristics used are the result of extensive two-dimensional wind tunnel testing by Sikorsky Aircraft. The 10, 11, and 12 percent thickness ratio airfoils have the same leading edge radius of 1.6 percent chord. In addition, a 10.7 percent thickness ratio, 1.0 percent chord leading edge radius airfoil--representing essentially that used on the CH-54A--was included to show the effect of a sharper leading edge. As Figures 27 through 29 illustrate, power required and blade stall are both improved with thicker sections. The sharper leading edge reduces power required still more, due to reduced advancing blade drag, but is less desirable in terms of retreating blade stall. Blade vibratory stresses increase with increasing thickness ratio. The selected 0012 section represents, for the 12-to 20-ton mission requirements, the best compromise between low power (high thickness ratios) and low blade stresses (low thickness ratios). It is noteworthy that

$\Omega R = 675$ ft /sec , NACA 0012 AIRFOIL
 Dia = 95 ft , b = 6, C = 2.95 ft (1962 Study - Reference 27)

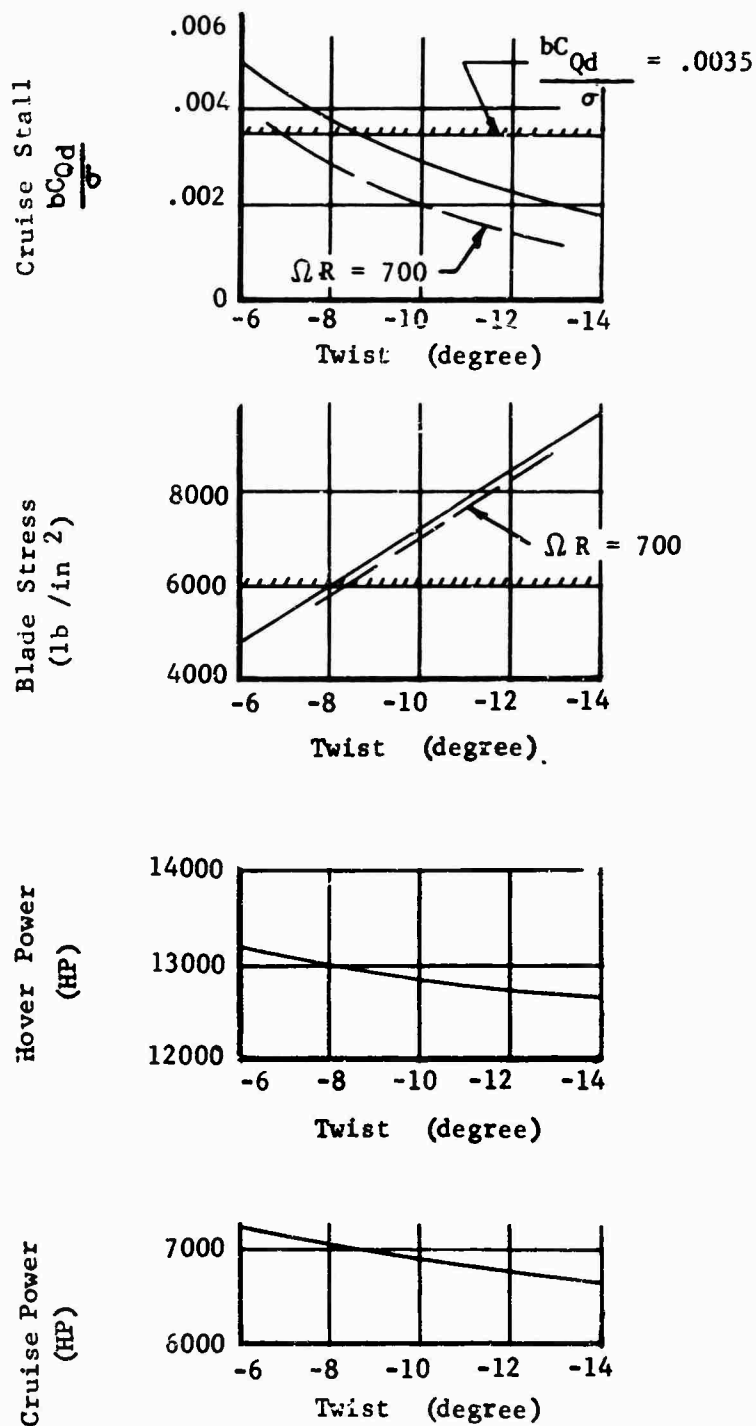


Figure 27 Preliminary Airfoil Selection, Twist Effect

$\theta_1 = 11^\circ$, NACA 0012 AIRFOIL
 Dia = 95 ft, b = 6, C = 2.95 ft (1962 Study - Reference 27)

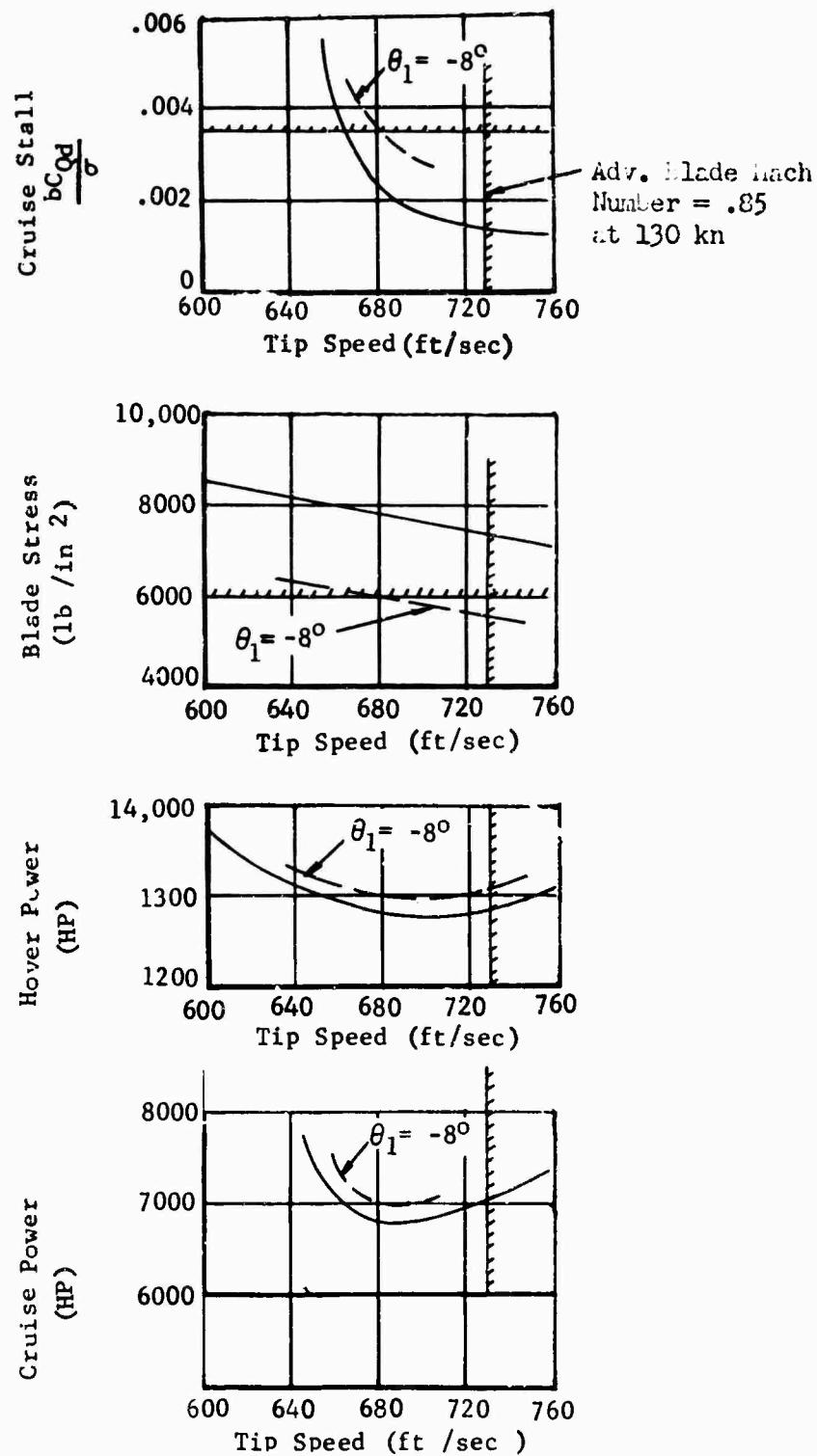


Figure 28 Preliminary Airfoil Selection, Tip Speed Effect

$\Omega R = 675 \text{ ft/sec} , \theta_1 = -11^\circ$
 Dia = 95 ft , b = 6, C = 2.95 ft (1962 Study - Reference 27)

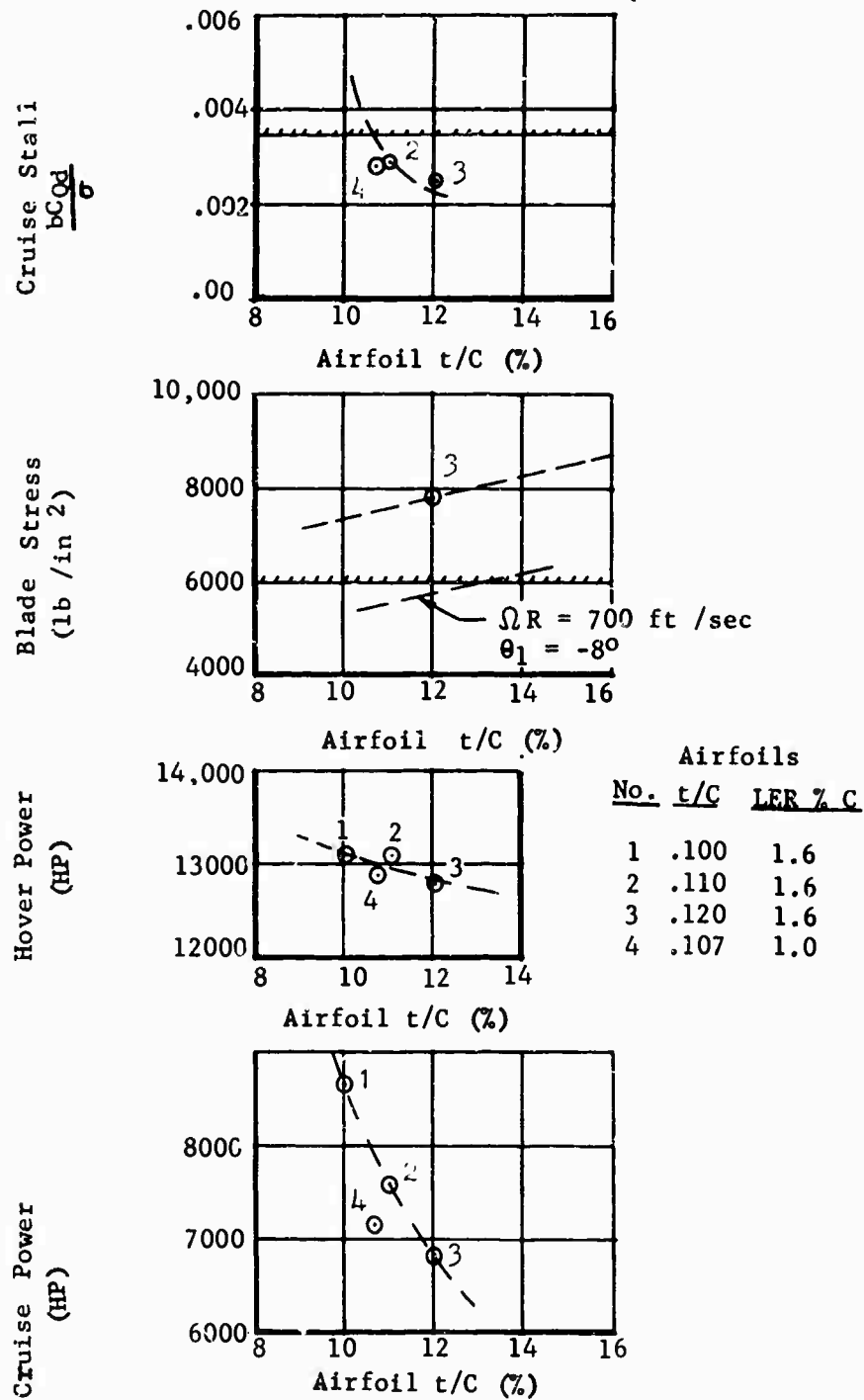


Figure 29 Preliminary Airfoil Selection, Airfoil Effect

this trade-off is different for helicopters designed for higher speed operation, which require a thinner optimum airfoil, such as the CH-53A.

Assuming a maximum allowable total blade vibratory stress of $\pm 6,000$ pounds per square inch, a retreating blade stall criteria of $\frac{bC_Qd}{\sigma} = .0035$ (see Reference 55), and power minimization in both hover and cruise, the following are selected:

Tip speed:	700 feet per second
Blade twist:	-8 degrees
Airfoil section:	0012

Although this analysis is based on the single rotor helicopter optimized in Reference 27, the same general conclusions are applicable to the tandem configuration, since the weights and drags are similar and the flight conditions are identical. Twist, tip speed, and airfoil section effects are rechecked for both configurations at the conclusion of the parametric study.

Diameter, Solidity, Number of Blades Investigations

With the twist, tip speed, and airfoil established, a systematic variation of rotor diameter, solidity, and number of blades was investigated for the single and tandem rotor configurations. Preliminary analysis yielded the range of diameters necessary to encompass a gross weight (20-ton, 6,000-foot, 95-degree Fahrenheit hover) range of from 60,000 to 80,000 pounds, within which the final configuration was expected to occur. Values

of $\frac{CT}{\sigma}$ from .075 to .115 were assumed, representing mean blade lift coefficients of approximately .50 to .75. The maximum value, $\frac{C_T}{\sigma} = .115$,

was picked to correspond to the highest blade loading demonstrated successfully by existing helicopters. Additional, special tests conducted by Sikorsky Aircraft with a three-bladed S-61 proved that no undesirable flying characteristics are encountered at this level (Reference 31). Six, eight, and ten blades were assumed for the single rotor configuration. For the tandem, the assumed 33-percent overlap eliminates consideration of more than three blades because of in-plane mechanical interference. Parametric variables that were considered are shown in Table XII.

For each combination, the Goldstein-Lock Method was used to calculate 6,000-foot, 95-degree Fahrenheit thrust capability as a function of power. This thrust capability was converted to gross weight at the power available (10,600 HP - four-T64/S4A's) by using the vertical drag, rotor interference,

TABLE XII
PARAMETRIC VARIABLES

	Single Rotor			Tandem Rotor		
Diameter	80	100	120 feet	60	75	90 feet
$\frac{C_T}{\sigma}$ (Representative of solidity)	.075	.095	.115	.075	.095	.115
Number of blades	6	8	10	3		
Total no. of parametric combinations	27			9		

asymmetric loading, tail rotor power, and transmission/accessory losses described previously. Fuel weight for both the 20- and 100-nautical-mile-radius missions was estimated for each combination of parameters through use of the nondimensional forward flight performance charts of Reference 55 by assuming 12- and 20-ton payload capability, respectively. Three-engine cruise, with the remaining engine shut down, is assumed for cruise, since two-engine flight is possible in case of engine failure, and a substantial fuel saving is obtained. As a result, the difference in weight between the 12-ton mission and the 20-ton mission was determined. This yielded design gross weight (20-ton mission) for each parametric combination for use in the empty weight equations. Also, the 12-ton-mission fuel defines integral tankage required. Transmission power was established as that required to hover OGE at sea level standard day at the 20-ton mission gross weight. Tail rotor and horizontal tail size were determined for the single rotor configuration by the method described in a previous section.

Thus the following information, necessary to determine empty weight, was established for each parametric point:

1. Rotor diameter
2. Rotor solidity
3. Rotor tip speed
4. Number of blades
5. Design gross weight (20-ton mission)
6. 12-ton mission fuel (integral fuel tankage required)
7. Tail rotor blade area and horizontal tail area
(single rotor configuration)

It is obvious that the assumed 12- and 20-ton payload, used to establish fuel required, will not be met exactly with all, or probably any, of the

specific parametric combinations assumed. However, since the finally selected configuration will by definition have this capability, and will be checked specifically, this procedure is valid.

With gross weight and empty weight established, the payload for each parametric point is determined by assuming 700 pounds for three crewmen and trapped fluids and 2000 pounds for a four-point, 20-ton capacity winch system. Tables XIII through XVI tabulate the weights derived for each assumed rotor system. Figures 30 and 31 show the resulting variation of payload for a 100-nautical-mile radius with rotor radius and number of blades for the single and tandem configurations, respectively. Figures 32 and 33 show the corresponding variation of takeoff gross weight. Figures 34 and 35 illustrate the cross-plotted solutions at 12-ton payload as a function of gross weight and rotor radius, which represent the results of the parametric study.

TABLE XIII
HELICOPTER WEIGHT BREAKDOWN,
SINGLE ROTOR, R = 40 FEET

	Weight, lb								
C _T /σ	.115	.095	.075	.115	.095	.075	.115	.095	.075
Number of blades	6	6	6	8	8	8	10	10	10
Gross weight	60330	61220	61920	60450	61380	62080	60510	61460	62120
Design gross weight	73350	74210	74880	73460	74360	75040	73520	74440	75080
RC blade area (each)(ft ²)	103.8	127.2	163.2	77.9	95.5	122.4	62.3	76.4	98.0
Transmission power (HP)	12250	12300	12270	12260	12340	12320	12300	12350	12330
Rotor group	5775	7505	10350	5735	7465	10310	5720	7420	10240
Tail rotor	1285	1305	1340	1285	1310	1340	1280	1310	1350
Stabilizer	229	231	234	229	231	235	230	231	235
Body group	3965	3980	3985	3975	3985	3990	3975	3985	3990
Alighting gear	3070	3120	3140	3075	3130	3140	3075	3130	3140
Flight controls	2200	2230	2255	2205	2235	2260	2205	2240	2260
Engines	2852	2852	2852	2852	2852	2852	2852	2852	2852
Drive system	6210	6225	6215	6210	6250	6235	6225	6255	6245
Fixed equipment group	2125	2140	2150	2125	2140	2150	2125	2140	2150
Fuel system	398	401	403	399	401	403	399	401	403
Fixed weights	1370	1370	1370	1370	1370	1370	1370	1370	1370
(1) Empty weight	29279	31359	34294	29460	31369	34285	29456	31334	34235
(2) Fixed useful load	2700	2700	2700	2700	2700	2700	2700	2700	2700
(3) Fuel (*)	6160	6200	6230	6170	6200	6230	6170	6210	6240
Gross weight	60330	61220	61920	60450	61380	62080	60510	61460	62120
(1) + (2) + (3)	38339	40259	43224	38330	40269	43215	38326	40244	43175
Payload (lb) (*)	21991	20961	18696	22120	21111	18865	22184	21216	18945
(tons)	10.996	10.481	9.348	11.060	10.556	9.433	11.092	10.608	9.473

* 100-nautical-mile radius, 6000 feet, 95°F, OGE hover at takeoff

TABLE XIV
HELICOPTER WEIGHT BREAKDOWN,
SINGLE ROTOR, R = 50 FEET

	Weight, lb									
C_T/σ	.115	.095	.075	.115	.095	.075	.115	.095	.075	.075
Number of blades	6	6	6	8	8	8	10	10	10	10
Gross weight	60980	70450	71230	69210	70650	71400	69240	70680	71450	71450
Design gross weight	81840	83800	83950	81970	83380	84120	82000	83410	84170	84170
RC blade area (each)(ft ²)	119	146.5	188.3	89.4	110	141.4	71.5	87.8	113	113
Transmission power (HP)	11770	11920	11900	11800	11970	11950	11810	11980	11960	11960
Rotor group	6860	8950	12300	6800	8880	12340	6800	8850	12300	12300
Tail rotor	1380	1415	1435	1375	1410	1440	1385	1410	1440	1440
Stabilizer	203	206	208	199	207	208	203	208	208	208
Body group	6105	6140	6150	6110	6142	6159	6110	6142	6160	6160
Alighting gear	3380	3428	3453	3382	3434	3460	3385	3435	3463	3463
Flight controls	2435	2482	2506	2439	2488	2512	2440	2488	2515	2515
Engines	2852	2852	2852	2852	2852	2852	2852	2852	2852	2852
Drive system	7180	7255	7242	7195	7277	7267	7199	7280	7270	7270
Fixed equipment group	2220	2240	2250	2220	2245	2255	2225	2245	2255	2255
Fuel system	418	419	431	418	420	431	418	420	431	431
Fixed weights	1370	1370	1370	1370	1370	1370	1370	1370	1370	1370
(1) Empty weight	34403	36757	40197	34360	36725	40294	34387	36700	40264	40264
(2) Fixed useful load	2700	2700	2700	2700	2700	2700	2700	2700	2700	2700
(3) Fuel (*)	6460	6490	6510	6460	6500	6510	6460	6500	6510	6510
Gross weight	69080	70450	71230	69210	70650	71400	69240	70680	71450	71450
(1) + (2) + (3)	43563	45957	49407	43520	45925	49504	43547	45900	49474	49474
Payload (lb) (*)	25517	24503	21823	25690	24725	21896	25693	24780	21976	21976
(tons)	12.758	12.252	10.912	12.845	12.363	10.948	12.847	12.390	10.988	10.988
(*) 100-nautical-mile radius, 6000 feet, 95°F, OGE hover at takeoff										

TABLE XV
HELICOPTER WEIGHT BREAKDOWN,
SINGLE ROTOR, R = 60 FEET

C _T /σ	Weight, lb									
	.115	.095	.075	.115	.095	.075	.115	.095	.075	.075
Number of blades	6	6	6	8	8	8	10	10	10	10
Gross weight	77390	78560	79640	77480	78680	79780	77500	78700	79800	79800
Design gross weight	90000	91150	92210	90090	91270	92350	90110	91290	92370	92370
RC blade area (each)(ft ²)	132.9	164	210	99.7	123	141.5	79.7	98.4	126	126
Transmission power (HP)	11590	11620	11600	11600	11680	11640	11610	11690	11640	11640
Rotor group	8050	10510	14490	7940	10420	14300	7900	10430	14350	14350
Tail rotor	1507	1541	1579	1504	1535	1572	1504	1533	1572	1572
Stabilizer	183	185	189	183	185	189	183	185	189	189
Body group	8830	8860	8890	8830	8860	8890	8830	8860	8890	8890
Alighting gear	3805	3850	3945	3805	3850	3950	3815	3850	3950	3950
Flight controls	2675	2715	2740	2675	2715	2755	2675	2715	2755	2755
Engines	2852	2852	2852	2852	2852	2852	2852	2852	2852	2852
Drive system	8130	8160	8140	8140	8280	8220	8150	8280	8220	8220
Fixed equipment group	2313	2325	2341	2313	2325	2344	2313	2333	2344	2344
Fuel system	428	429	430	428	429	430	428	429	430	430
Fixed weights	1370	1370	1370	1370	1370	1370	1370	1370	1370	1370
(1) Empty weight	40143	42797	46966	40040	42821	46872	40020	42837	46922	46922
(2) Fixed useful load	2700	2700	2700	2700	2700	2700	2700	2700	2700	2700
(3) Fuel (*)	6620	6640	6650	6620	6640	6650	6620	6640	6660	6660
Gross weight	77390	78560	79640	77480	78680	79780	77500	78700	79800	79800
(1) + (2) + (3)	49463	52137	56316	49360	52161	56222	49340	52177	56282	56282
Payload (lb) (*)	27927	26423	23324	28120	26519	23558	28160	26523	23518	23518
(tons)	13.964	13.212	11.662	14.060	13.260	11.779	14.080	13.262	11.759	11.759

(*) 100-nautical-mile radius, 6000 feet 95°F, OGE hover at takeoff

TABLE XVI
HELICOPTER WEIGHT BREAKDOWN,
TANDEM, THREE-BLADED ROTORS

	Weight, lb									
	.115	.115	.115	.095	.095	.095	.075	.075	.075	.075
Ct/σ	.115	.115	.115	.095	.095	.095	.075	.075	.075	.075
Radius	30	37.5	45	30	37.5	45	30	37.5	45	45
Gross weight	60720	69750	77235	61130	70370	78360	61230	70600	78922	78922
Design gross weight	73670	82440	89785	74060	83050	90890	74160	83270	91442	91442
RC blade area (each)(ft ²)	115.9	130.7	142.3	141.2	158.1	172.3	177.8	200.2	218.2	218.2
Transmission power (HP)	12240	11650	11050	12350	11770	11270	12210	11860	11500	11500
Rotor group	6210	7280	8110	8030	9230	10400	10780	12570	14030	14030
Body group	4210	6580	9370	4215	6580	9405	4220	6580	9420	9420
Alighting gear	3150	3490	3735	3185	3495	3760	3185	3500	3765	3765
Flight controls	3070	3440	3685	3100	3440	3740	3105	3470	3750	3750
Engines	2852	2852	2852	2852	2852	2852	2852	2852	2852	2852
Drive system	6545	7535	8350	6620	7610	8495	6545	7655	8590	8590
Fixed equipment group	2118	2215	2308	2128	2230	2318	2128	2236	2325	2325
Fuel system	415	434	442	415	435	444	415	435	444	444
Fixed weights	1370	1370	1370	1370	1370	1370	1370	1370	1370	1370
(1) Empty weight	29940	35197	40222	3191	37242	42784	34600	40668	46646	46646
(2) Fixed useful load	2700	2700	2700	2700	2700	2700	2700	2700	2700	2700
(3) Fuel (*)	6410	6710	6850	6430	6730	6870	6430	6730	6870	6870
Gross weight	60720	68750	77235	61130	70370	78360	61230	70600	78922	78922
(1) + (2) + (3)	39050	44607	49772	41045	46672	52354	43730	50098	56216	56216
Payload (lb) (*)	21670	25143	27463	20085	23698	26006	17500	20502	22706	22706
(tons)	10.835	12.571	13.732	10.043	11.849	13.003	8.750	10.251	11.353	11.353

(*) 100-nautical-mile radius, 6000 feet, 95°F, OGE hover at takeoff

100-Nautical-Mile-Radius Mission

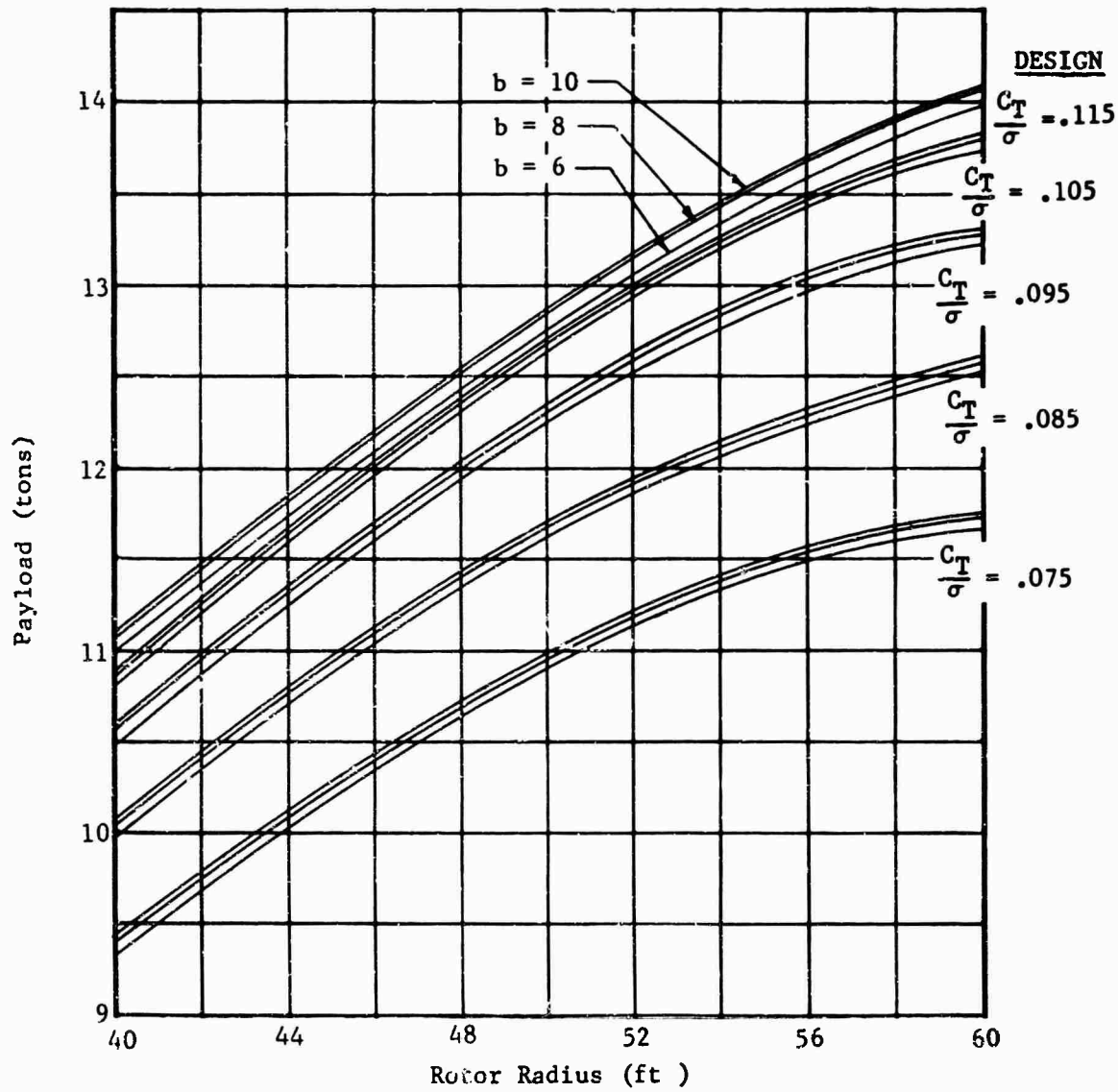


Figure 30 Payload Versus Rotor Radius, Single Rotor

100-Nautical-Mile-Radius Mission
 $b = 3$

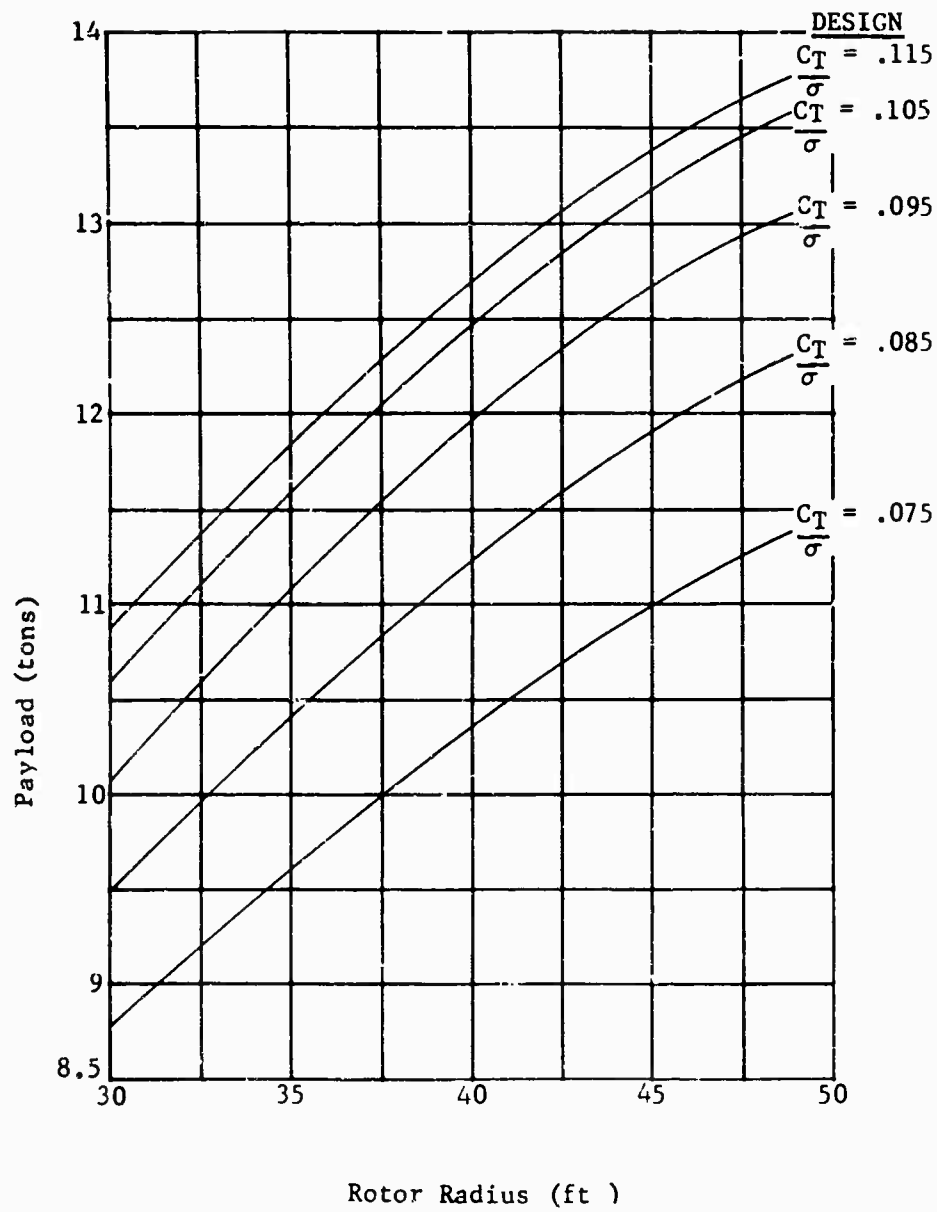


Figure 31 Payload Versus Rotor Radius, Tandem Rotor

100-Nautical-Mile-Radius Mission

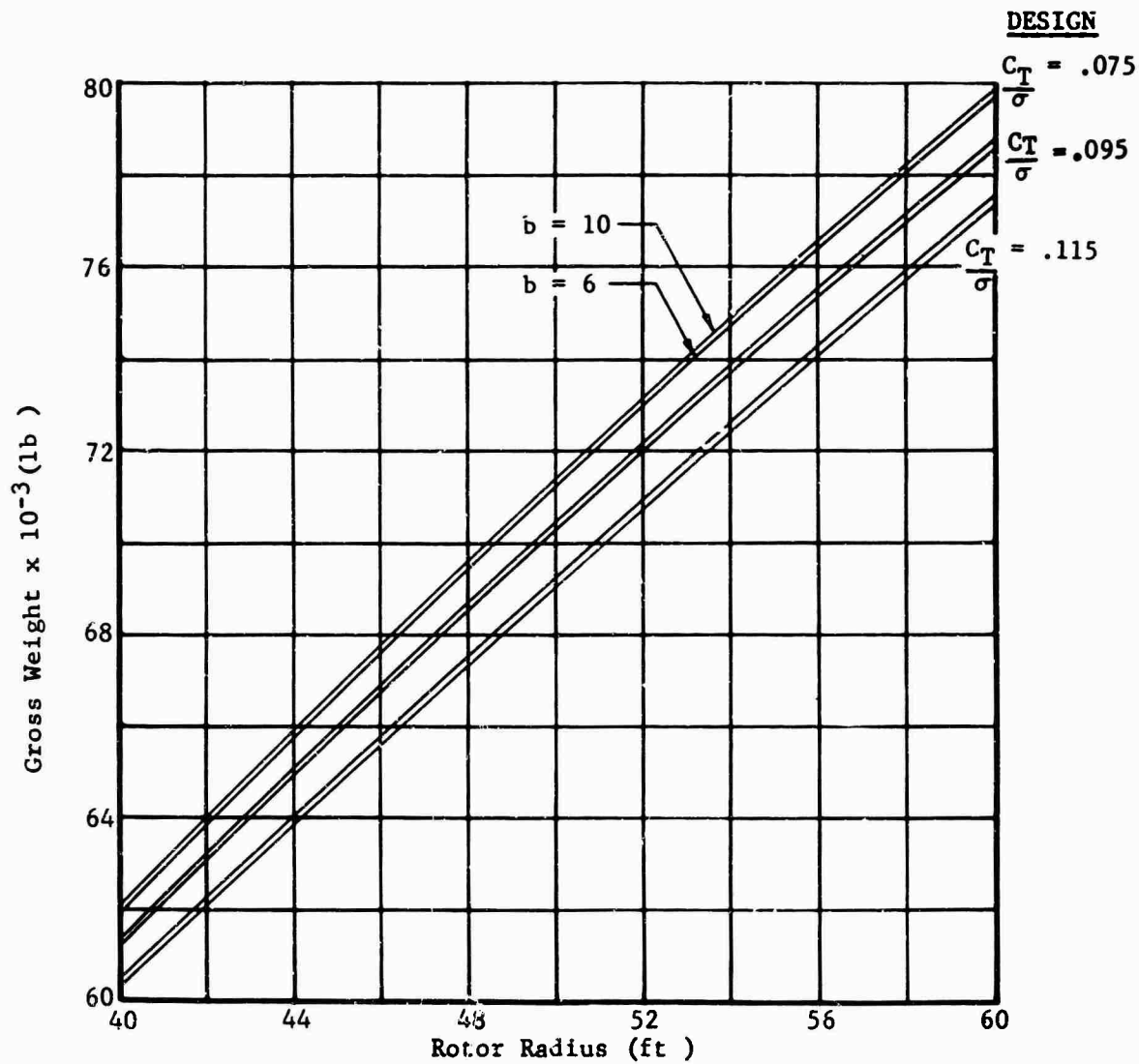


Figure 32 Takeoff Gross Weight Versus Rotor Radius, Single Rotor

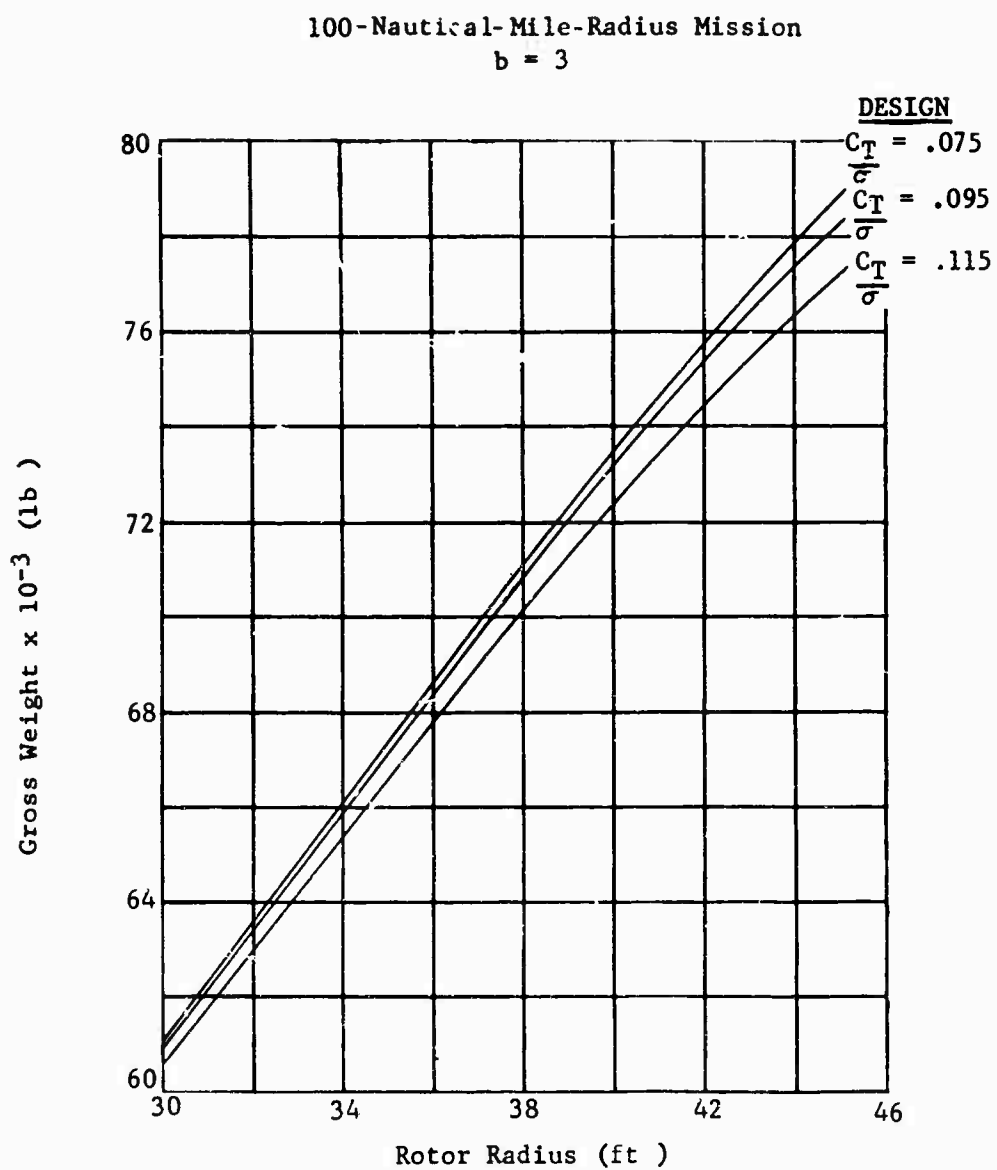


Figure 33 Takeoff Gross Weight Versus Rotor Radius, Tandem Rotor

100-Nautical-Mile-Radius Mission
12-Ton Payload

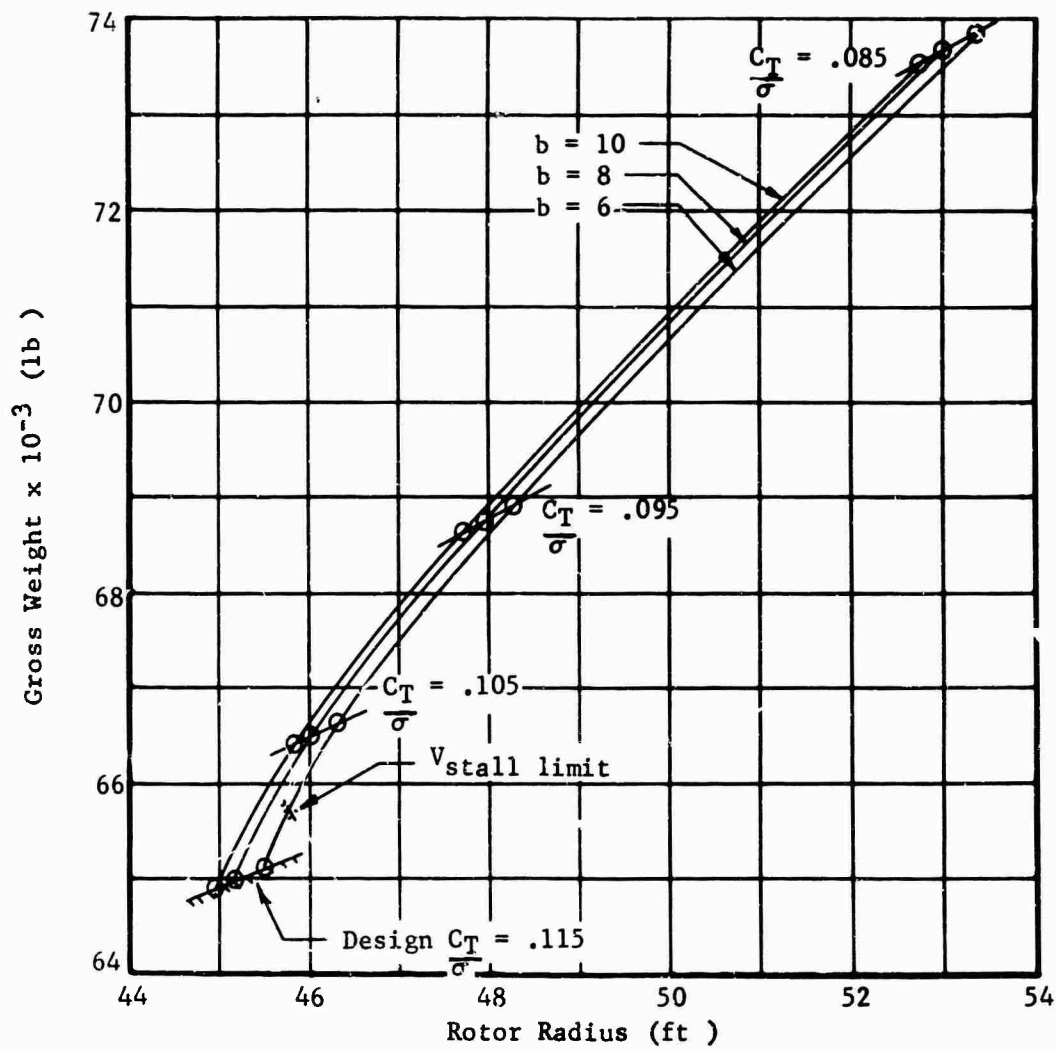


Figure 34 Gross Weight Versus Rotor Radius, Single Rotor

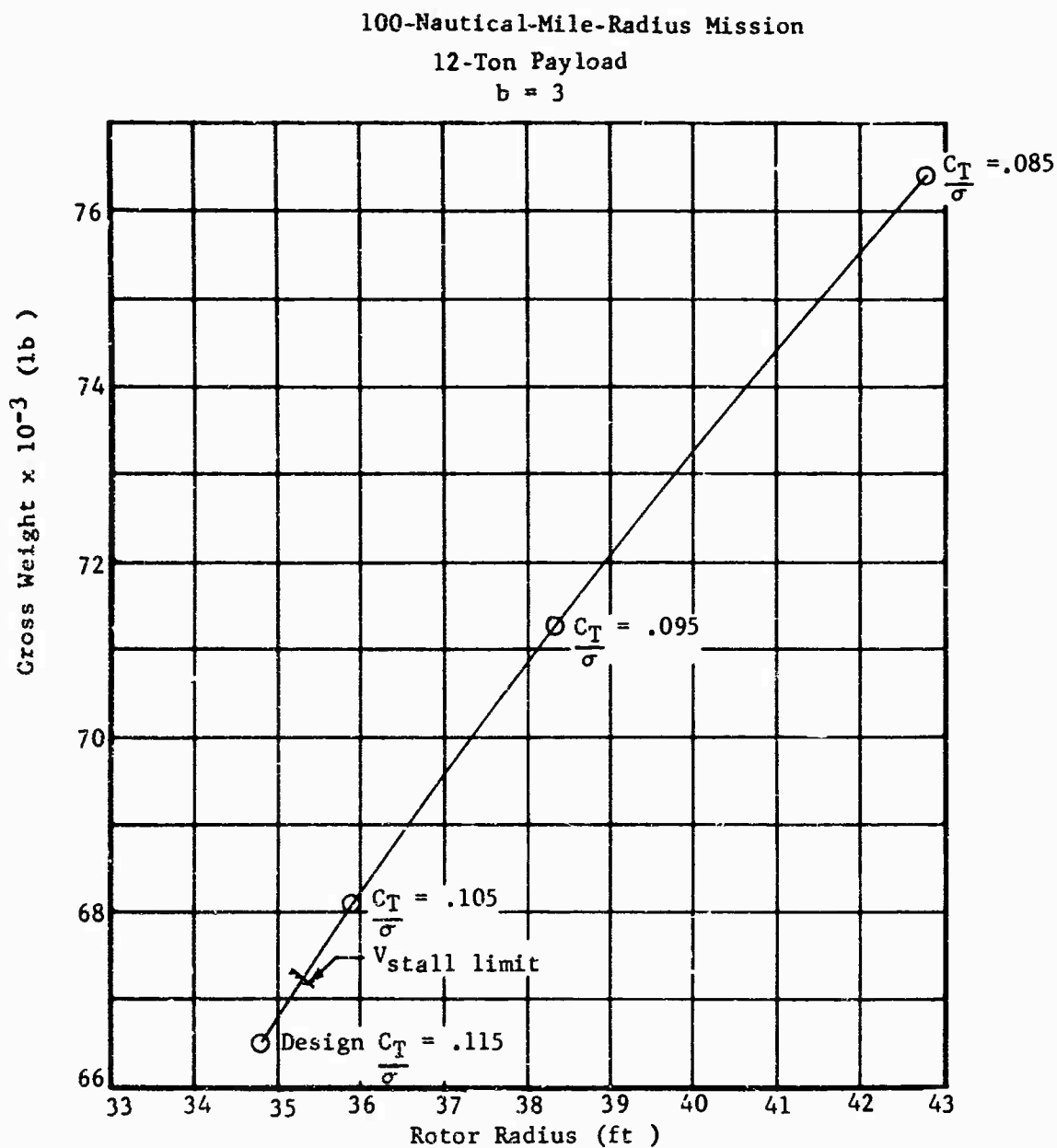


Figure 35 Gross Weight Versus Rotor Radius, Tandem Rotor

PARAMETRIC RESULTS

Figures 34 and 35, as discussed in the previous section, illustrate the results of the rotor parametric study for the single and tandem rotor configurations, respectively. General conclusions regarding diameter and solidity apply to both single and tandem rotor configurations.

Obviously, the lowest gross weight is obtained with the smallest diameter. However, as diameter decreases, so also does total blade area, since C_T/σ is increasing. The critical cruise condition of 95 knots with 20-ton payload dictates that on the basis of retreating blade stall a certain minimum blade area, resulting in a maximum allowable blade loading, or $C_T/\sigma = .110$, is required. This limit is shown on Figures 34 and 35 and establishes the minimum gross weight solution obtainable. It should be noted that higher stall-limited cruise speeds are attainable with lower C_T/σ (more blade area). However, this results in a gross weight penalty of about 340 pounds per knot and an .8-foot-diameter increase per knot and is therefore not considered herein.

Concerning number of blades, another factor becomes important for the single rotor configuration. Although a large number of blades, with resulting long, narrow, high aspect ratio geometry, improves both hovering efficiency and blade weight, other factors must be considered. The reduced flatwise stiffness of extremely high aspect ratio blades increases the rotor-fuselage clearance required to allow for static and dynamic blade droop. Large numbers of blades also increase the complexity of the rotor head and, after a point, probably increase both rotor head weight and drag beyond what is considered in the parametric analysis. The logistics problems associated with many blades are also a consideration. With these factors in mind, and because of the relatively small weight reduction indicated by the parametric weight trends (200 pounds going from six to ten blades), six blades are selected for the single rotor solution.

The selected single and tandem rotor solutions are shown in Table XVII.

TABLE XVII
DESIGN PARAMETERS FOR SELECTED ROTORS

	Single Rotor	Tandem Rotor
Rotor diameter, ft	91.6	70.6
Rotor design C_T/σ (6000 ft, 95°F)	.110	.110
Rotor solidity, $bC/\pi R$.108	.102
Blade chord, ft	2.58	3.76
Number of blades	6	3 per rotor
Blade aspect ratio	17.7	9.4
Flapping hinge offset, ft	3.64	.53

With the two rotor systems defined parametrically, weight empty and mission fuel were checked. In this case, fuel was determined by calculating cruise power required rigorously rather than by use of the nondimensional charts of Reference 55. The weight breakdown and resulting gross weight were in close agreement with the parametrically determined values.

Table XVIII shows the fuel breakdown for the two design missions, including average gross weight and power for each mission leg.

The weight breakdown for both the single and tandem configurations is shown in Table XIX.

For the selected configurations, variation in twist, tip speed, and airfoil section were again investigated to confirm the initially selected values. Figures 36 through 38 show the results of this study in similar form to Figures 27 through 29. Although the weights and drags for the critical flight conditions are different from those in the initial study which was based on the rotor system of Reference 27, it is apparent that the same factors which influenced the initial selection of 700-foot-per-second tip speed, -8-degree twist, and a 0012 airfoil section also apply to the optimized diameter-solidity-number of blades solutions for both the single and tandem configurations and that the same values are desirable.

With the geometry of the two selected configurations established, three-view sketches were made to illustrate weight balance, rotor clearances, and landing gear geometries. These are shown in Figures 39 and 40 for the single and tandem rotor configurations, respectively. It should be noted that establishment of the elaborate details of fuselage design and component arrangement was not undertaken at this time. The sketches can therefore be considered rigorously accurate only in those details studied on the parametric analysis.

TABLE XVIII
MISSION FUEL BREAKDOWN

12-Ton Payload Mission						
Mission Breakdown (SLS)	Single Avg GW	TOGW Avg HP	65, 800 lb Fuel	Tandem Avg GW	TOGW Avg HP	67, 300 lb Fuel
1. 2-Min Warm-up & TO at NRP (a)	65700	11980	205	67200	11860	205
2. 3-Min Hover at TO	65470	9050	250	66970	9050	248
3. Cruise Out 100 naut mi at 110 kn (c)	63900	5300	2890	65250	6300	3150
4. 2-Min Hover at Midpoint	62300	8500	175	63590	8400	170
5. Cruise Back 100 naut mi at 130 kn (b) (c)	37200	4300	2150	38350	5000	2275
Total Fuel Used			5670			6048
10% Fuel Reserve (a)			630			672
TOTAL FUEL			6300			6720
20-Ton Payload Mission						
Mission Breakdown (SLS)	Single Avg GW	TOGW Avg HP	78, 750 lb Fuel	Tandem Avg GW	TOGW Avg HP	80, 050 lb Fuel
1. 2-Min Warm-up & TO at NRP (a)	78650	11980	205	79950	11860	205
2. 5-Min Hover at TO	78290	11850	510	79600	11600	508
3. Cruise Out 20 naut mi at 95 kn (c)	77650	5850	730	78900	7250	880
4. 10-Min Hover at Midpoint	76750	11450	1030	77950	11350	1020
5. Cruise Back 20 naut mi at 130 kn (b) (c)	36050	4250	450	37200	5000	510
Total Fuel Used			2925			3123
10% Fuel Reserve (a)			325			347
TOTAL FUEL			3250			3470
(a) Required per MIL-C-5011A (b) Return cruise with zero payload (c) Three-engine cruise						

TABLE XIX
WEIGHT BREAKDOWN

	Weight, lb	
	Single Rotor	Tandem Rotor
Rotor group	6,820	7,375
Tail rotor group	1,330	--
Horizontal stabilizer	213	--
Body group	5,190	5,810
Alighting gear	3,275	3,270
Flight controls	2,360	3,320
Engines	2,852	2,852
Drive system	6,795	7,265
Fuel system	408	434
Fixed equipment	3,555	3,555
Empty weight	32,798	33,881
4-point, 20-ton-capacity winch	2,000	2,000
Crew (3) and trapped fluids	700	700
GW less fuel, payload	35,498	36,581
<u>100-naut-mi-radius mission</u>		
Payload	24,000	24,000
Fuel	6,300	6,720
Gross weight	65,798	67,301
<u>20-naut-mi-radius mission</u>		
Payload	40,000	40,000
Fuel	3,250	3,470
Gross weight	78,748	80,051
<u>Ferry mission (1500 naut mi)</u>		
Payload	0	0
Fuel	36,200	41,220
Aux Tankage	2,300	2,700
Gross weight	72,000*	78,500*
* Without winch		

Perturbations are based on selected single, tandem rotor solutions. Except as noted, single and tandem trends are the same. $\Omega R = 700$ ft /sec , NACA 0012 Airfoil

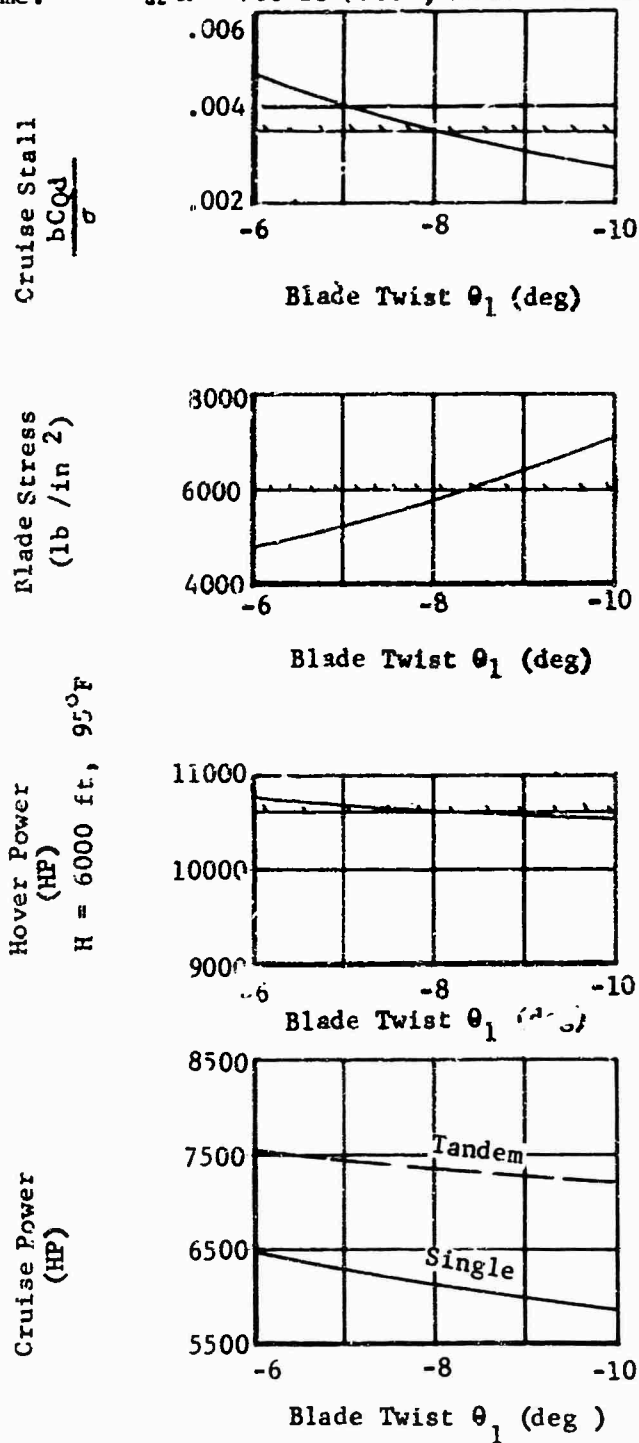


Figure 36 Final Perturbations, Twist Effect

Perturbations are based on selected single, tandem rotor solutions. Except as noted, single and tandem trends are the same. $\theta_1 = -8^\circ$, NACA 0012 Airfoil

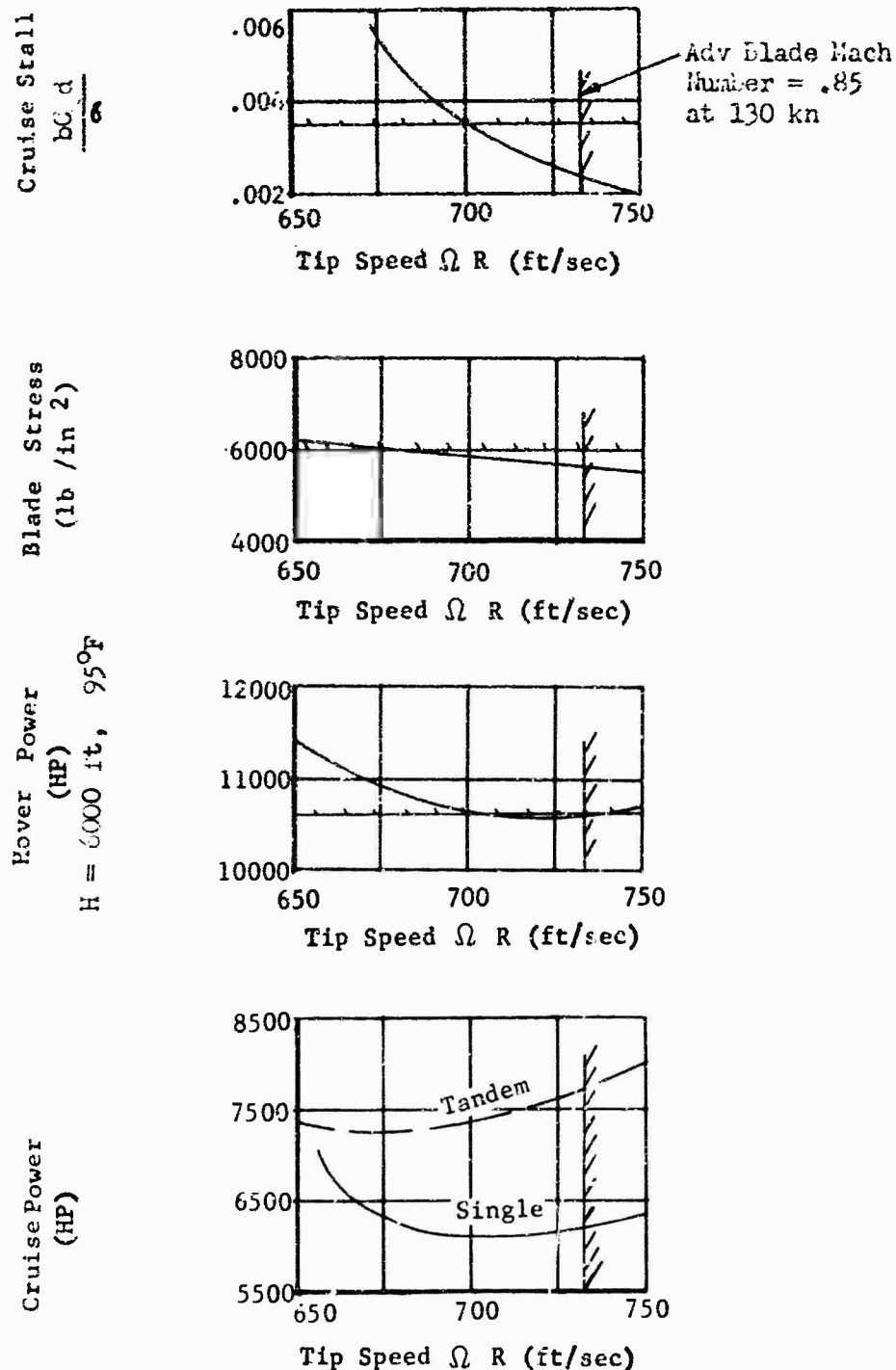


Figure 37 Final Perturbations, Tip Speed Effect

Perturbations are based on selected, single, tandem rotor solutions. Except as noted, single and tandem trends are the same.

$$\theta_1 = -8^\circ, \Omega R = 700 \text{ ft/sec}$$

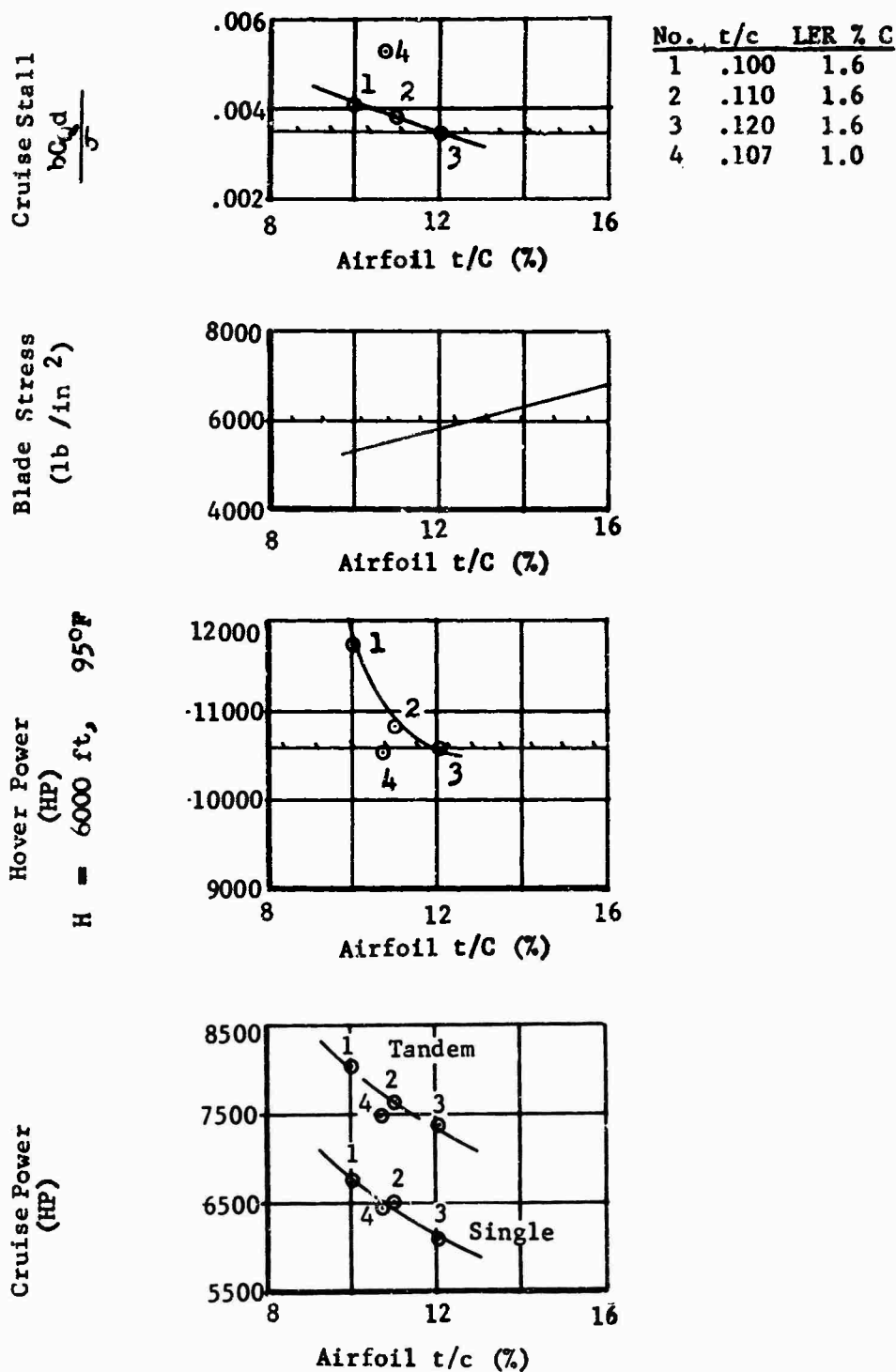


Figure 38 Final Perturbations, Airfoil Effect

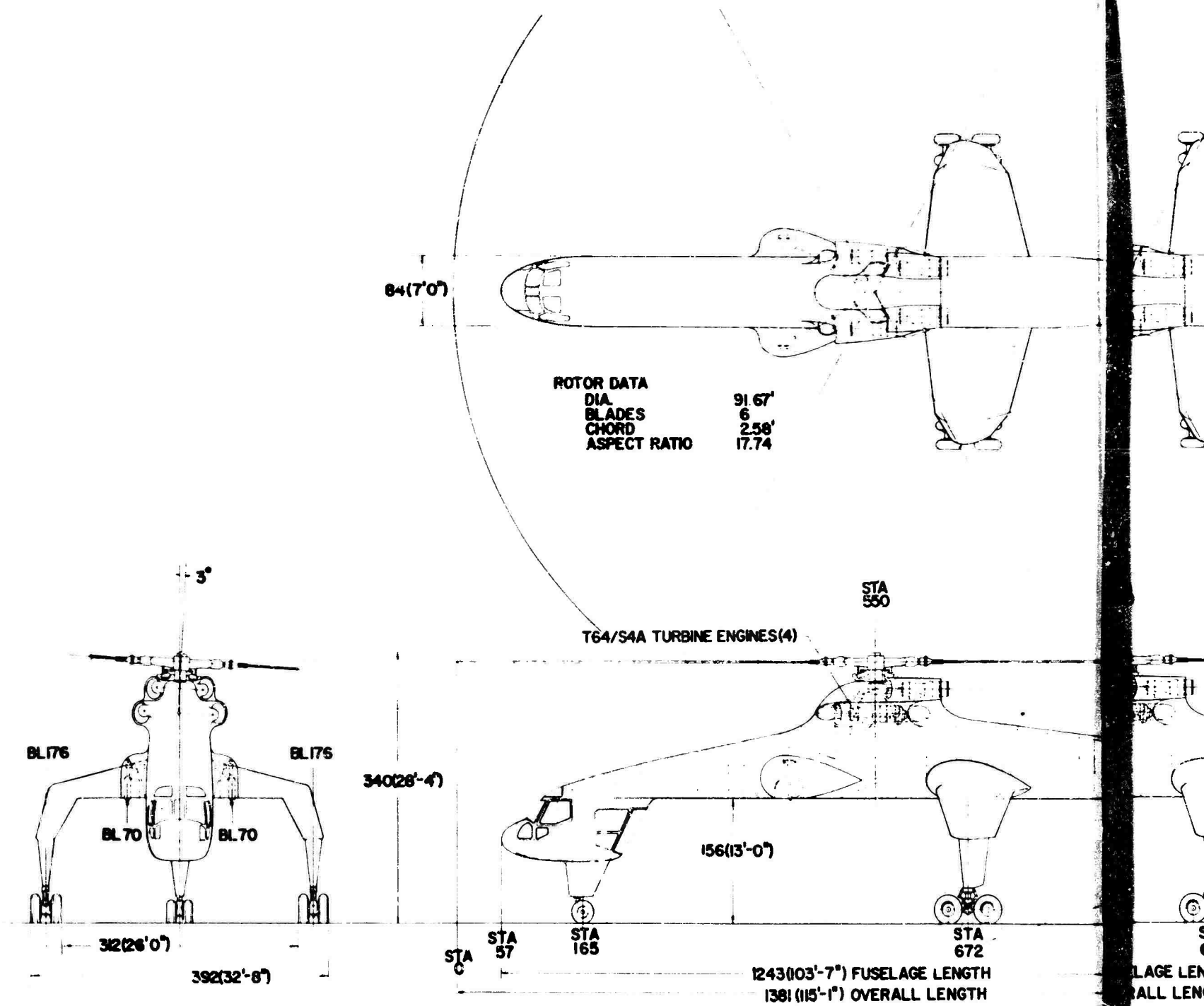
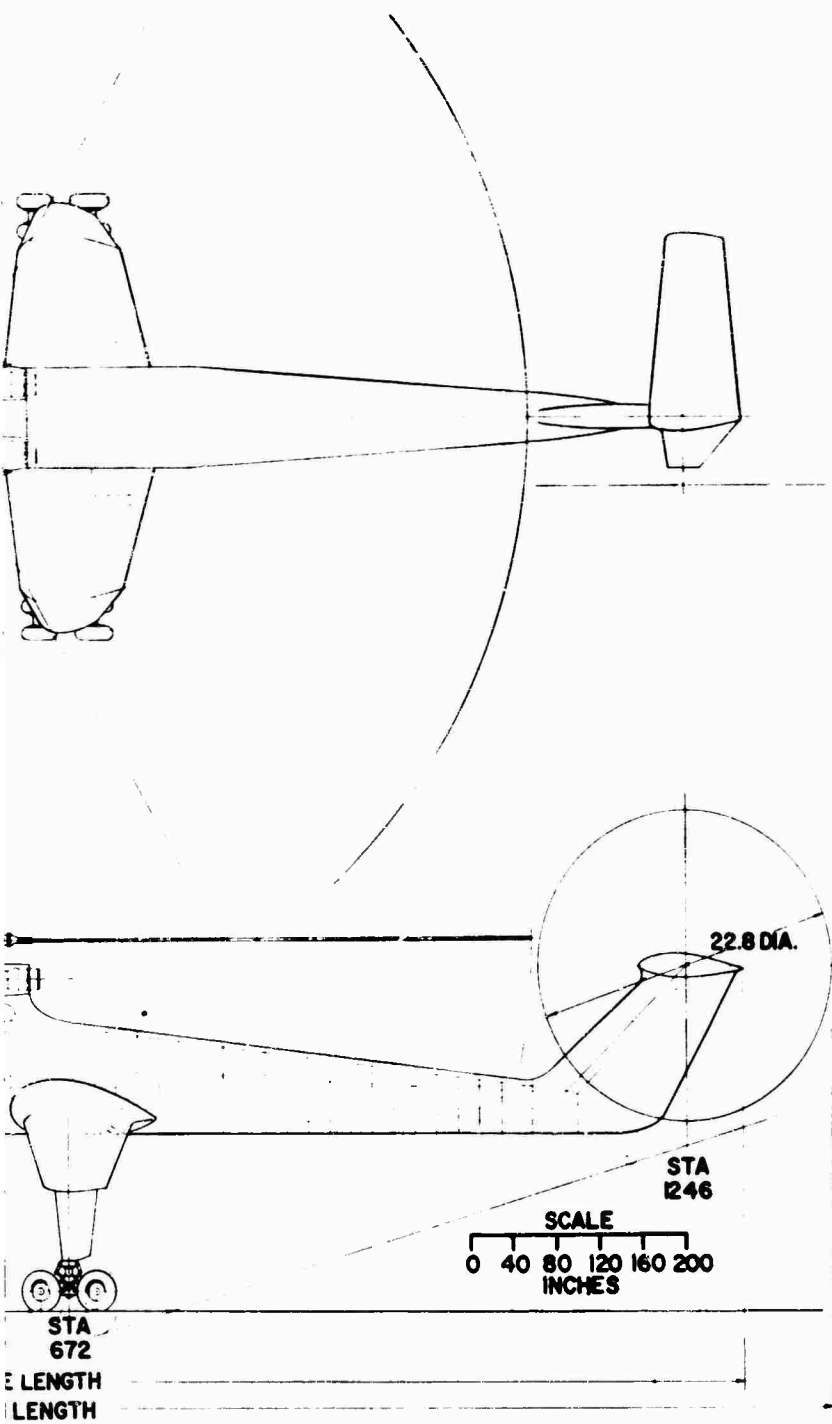
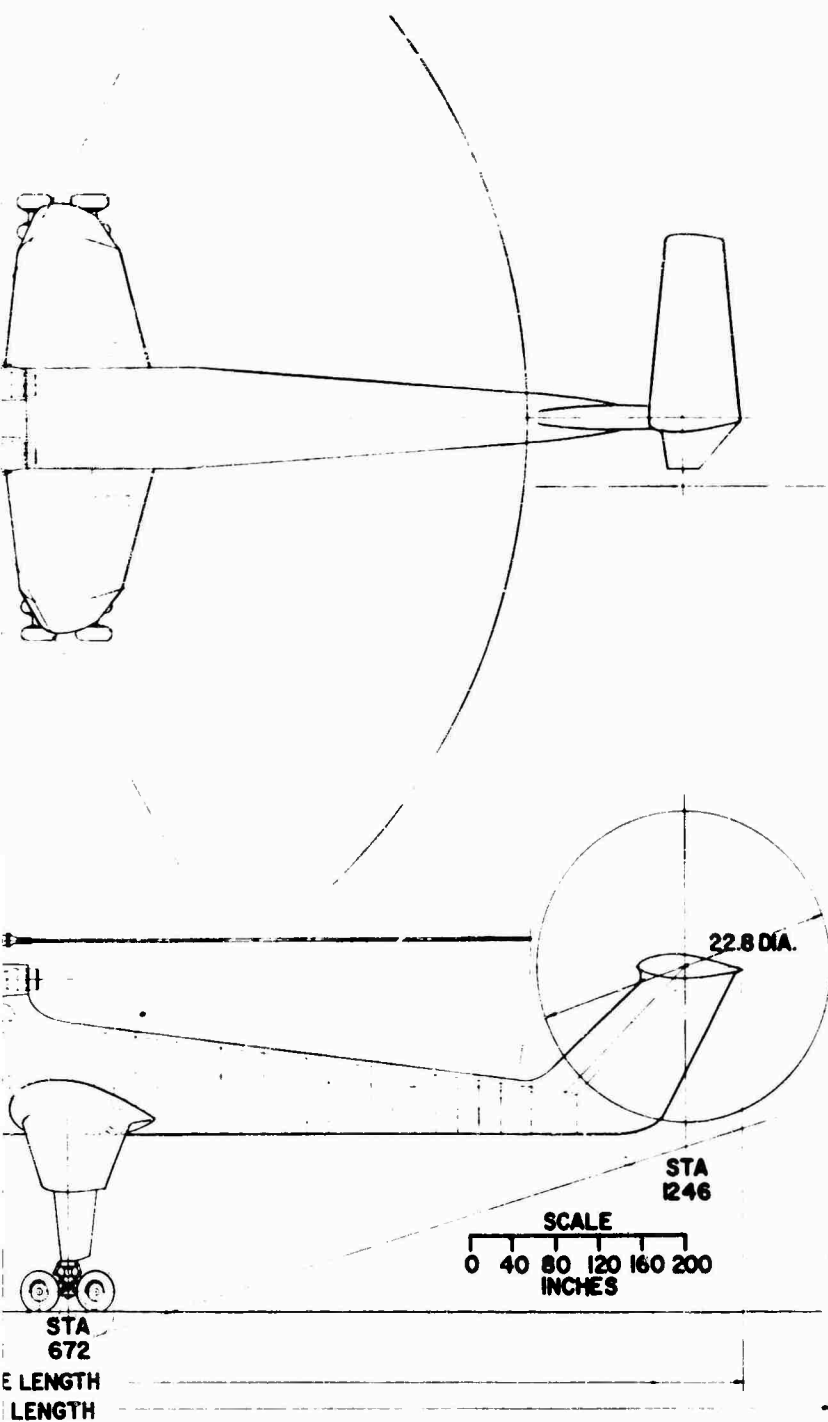


Figure 39 General Arrangement, Single Rotor,
 12-20-Ton Skycrane ©



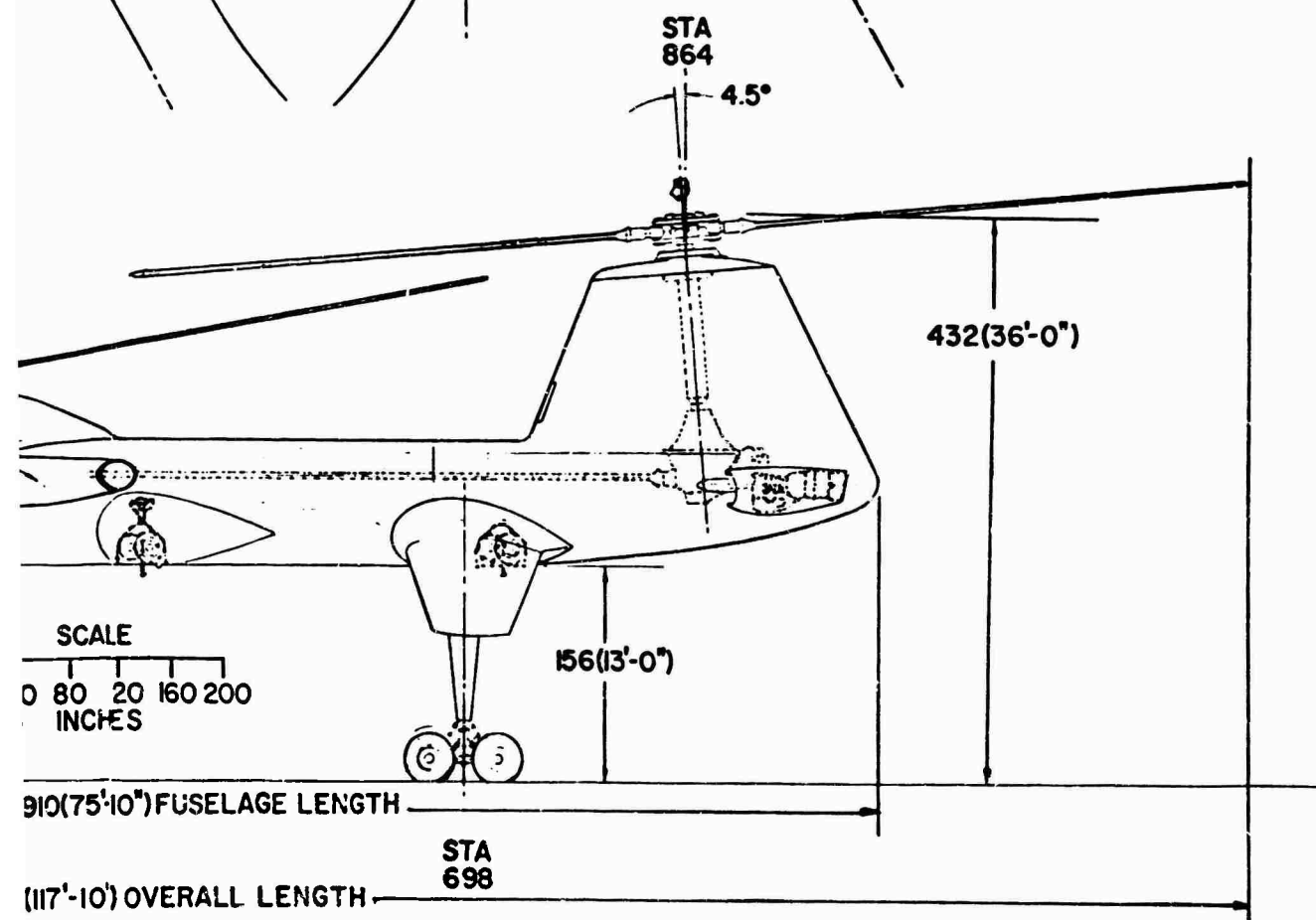
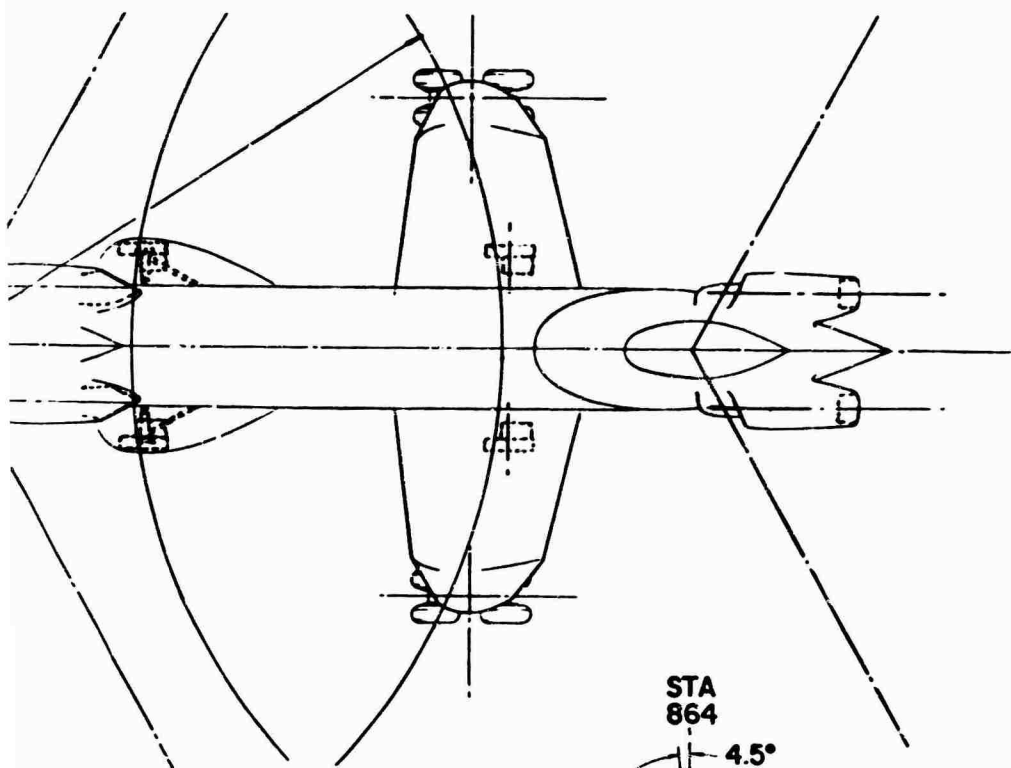
DESIGN NO.	REV.	DATE	BY
12-20	1	10/1/57	WJH
GENERAL ARRANGEMENT SINGLE ROTOR 12-20 TON SKYCRANE			
DESIGNED BY	CHECKED BY	APPROVED BY	DATE
WJH	WJH	WJH	10/1/57

B



PROJECT NO.	06-157-01-1
DATE	12/21
GENERAL ARRANGEMENT SINGLE ROTOR 12-20 TON SKYCRANE	
DESIGNED BY	1
CHECKED BY	1

B



13

EVALUATION OF OPTIMIZED CONFIGURATIONS

This section summarizes the side-by-side characteristics of the optimized single and tandem rotor configurations. Table XX lists the basic physical characteristics of both.

Other factors which must be considered in evaluation of the two configurations are off-design performance, stability and control, vibration, and reliability/maintainability characteristics. These factors are discussed in the following pages.

Performance

Hover ceilings for standard and 95-degree Fahrenheit temperatures, power required at various gross weights versus speed, maximum speed capability, and climb performance were determined as functions of gross weight for each configuration. These are illustrated in Figures 41 through 49.

Since the mission hovering requirements were used to size the rotor systems parametrically, OGE hover capability is nearly identical for the single and tandem helicopters for the same useful load. Single rotor gross weight hover capability is somewhat less, since less gross weight is required for the same payload. The single rotor configuration has a greater in-ground-effect advantage, since the ratio of rotor height above ground to rotor diameter is lower for the same wheel clearance. This is illustrated in Figures 41 and 42.

Cruise power required is somewhat less for the single rotor helicopter (at equal gross weight) with a corresponding increase in specific range. In cruise, the tail rotor absorbs 4 percent of engine power in the single rotor configuration. The tandem configuration has no tail rotor, but its induced power is greater than for the single rotor because of its shorter span. Induced power is inversely proportional to span squared, as follows:

$$P_i = \frac{kL^2}{\rho V b^2} \quad (27)$$

where $b = \text{span} = 2R$

$$k = 2/550$$

Table XXI illustrates the relative tail rotor and induced power increments for the single and tandem configurations at various forward speeds. A gross weight of 60,000 pounds is assumed for both.

The effective span of the tandem helicopter can be increased by sideslipping; however, this increases parasite drag and is impractical except

TABLE XX
SUMMARY OF PHYSICAL CHARACTERISTICS

	Single	Tandem
Gross weight, 12-ton mission, lb	65,800	67,300
Gross weight, 20-ton mission, lb	78,750	80,050
Weight empty, lb	32,800	33,880
Rotor diameter, ft	91.6	70.6
Number of blades per rotor	6	3
Blade chord, ft	2.58	3.76
Rotor solidity, $bc/\pi R$.108	.102
Blade aspect ratio	17.7	9.4
Blade airfoil section	0012	0012
Blade twist, deg	-8	-8
Rotor tip speed, ft/sec	700	700
Flapping hinge offset, % radius	8	1.5
Maximum rotor $C_{T/\sigma}$, 6000 ft, 95°F, 12-ton GW	.110	.110
Maximum blade mean C_l , 95°F, 12-ton GW	.7(a)	.7(a)
Disk loading, 20-ton GW, lb/ft ²	12.4	12.0(b)
Parasite drag, no external load, ft ²	84	84
Parasite drag with external load, ft ²	134	134
Parasite drag, ferry configuration, ft ²	94(c)	94(c)
Vertical drag, no external load, % thrust	3.56	3.57
Vertical drag with external load, % thrust	3.81	4.89
Power plants	T64/S4A's	T64/S4A's
No. of engines	4	4
Fuselage length, ft	103.6	75.8
Ground clearance, ft	13	13
Rotor overlap, % diameter	--	33
Tail rotor diameter, ft	22.7	--
Horizontal stabilizer area, ft ²	80	--
Integral fuel tankage, gal	970	1035
NOTES: (a) Approximate		
(b) Based on projected disk area		
(c) Without fairings		

for short periods at low speed.

Power required versus speed and gross weight is shown in Figures 43 through 46. The power limitations imposed by four-, three-, and two-engine utilization are shown in these plots, illustrating the feasibility of the three-engine cruise assumed for the design missions.

In climb capability the single rotor configuration has an advantage over the tandem, again because of the induced power penalty for the latter. As a result, the best rate of climb of the single is about 600 feet per minute more than the tandem at equivalent useful load. Maximum endurance and service ceiling are correspondingly greater for the single rotor configuration. Relative climb capability is illustrated in Figure 47.

TABLE XXI
TAIL ROTOR AND INDUCED POWER INCREMENT

GW = 60,000 lb, SLS	95 kn	110 kn	130 kn
Single rotor:			
tail rotor power	146	165	210
induced power	1,300	1,120	950
total	1,446	1,285	1,160
Tandem:			
induced power	2,190	1,885	1,600

For the same payload, the stall-limited cruise speed capabilities of the two configurations are similar, again because this was a determining factor in the rotor parametric analysis. This is shown in Figure 49.

Performance is compared for the two configurations, single and tandem rotor, in Table XXII. For comparative purposes, hover, cruise, and climb capabilities are shown for each at the gross weights necessary to perform the two design missions.

Ferry range, the third mission requirement, is illustrated for the two configurations in Figure 49 as a function of takeoff gross weight. Optimum altitude (up to 10,000 feet) and cruise speed are assumed, with a 1-percent reduction in best specific range per MIL-C-5011A. Three-engine cruise after takeoff is used to conserve fuel. Fuel for normal rated power climb at 500 feet per minute in two 5000-foot increments is included. A 10-square-foot drag penalty is applied to both configurations to account for externally mounted auxiliary fuel tankage. This value is felt to be conservative and is based on the size tankage required to take advantage of full

TABLE XXII
DESIGN MISSION PERFORMANCE

	Single Rotor f = 134	Tandem Rotor f = 134
<u>12-ton, 100-naut-mi-radius mission:</u>		
Gross weight, lb	65,800	67,300
OGE hover ceiling, 95°F, ft	6,000*	6,000*
IGE hover ceiling, 95°F, ft (10-ft wheel clearance)	8,400	7,100
OGE hover ceiling, std temp, ft	11,000	11,550
IGE hover ceiling, std temp, ft	13,850	12,750
Max cruise speed, stall, SLS, kn	134	134
OEI max speed, SLS, kn	141	138
OEI max ROC, NRP, SLS, ft/min	2,210	1,600
OEI max specific range, SLS, naut mi/lb fuel	.0353	.0315
<u>20-ton, 20-naut-mi-radius mission:</u>		
Gross weight, lb	78,750	80,050
OGE hover ceiling, std temp, ft	SL*	SL*
IGE hover ceiling, std temp, ft	7,100	3,900
Max cruise speed, stall, SLS, kn	95*	95*
OEI max speed, NRP, SLS, kn	122	119
OEI max ROC, NRP, SLS, ft/min	1,380	700
OEI max specific range, SLS, naut mi/lb fuel	.0285	.0244

* Parametric design points

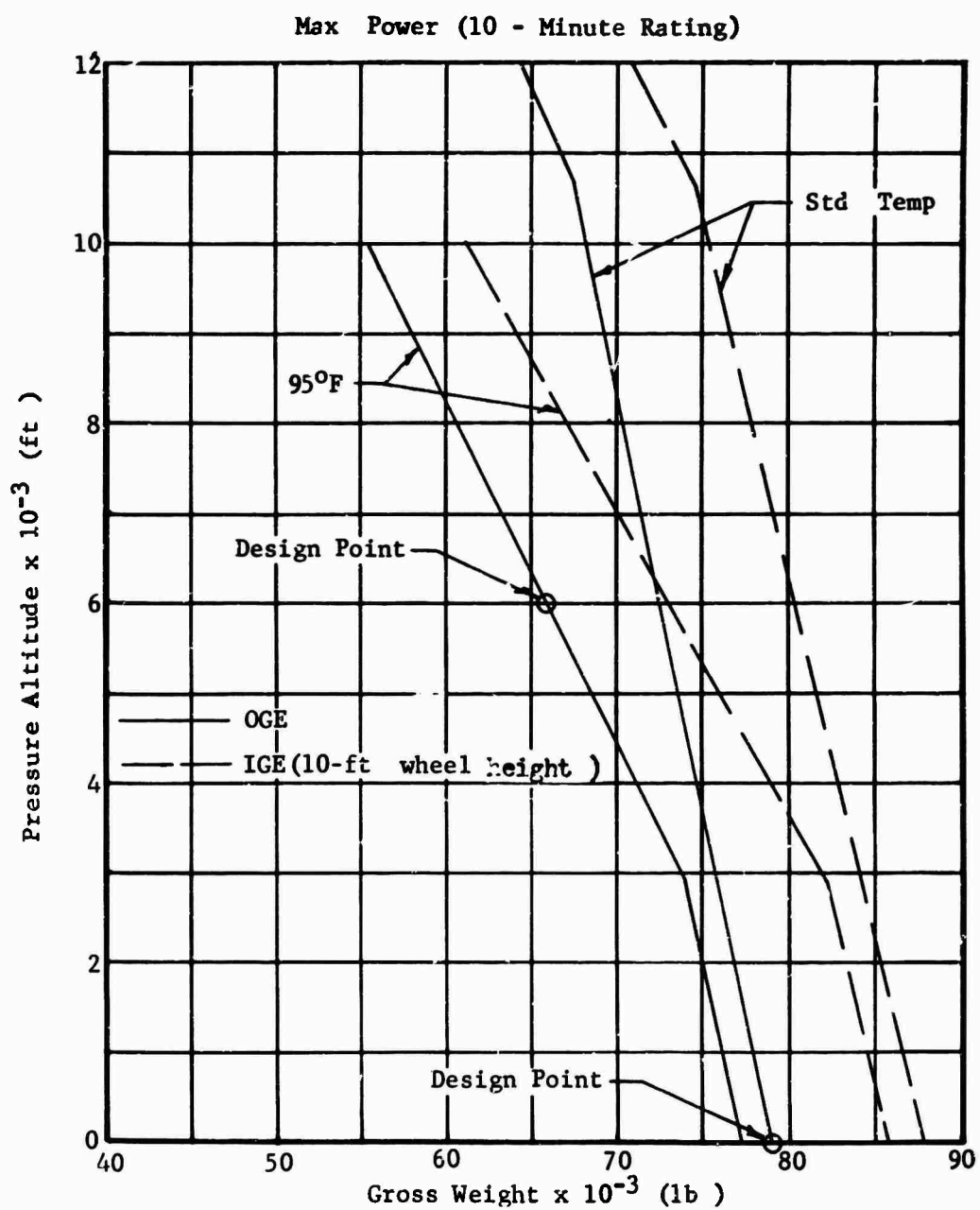


Figure 41 Hover Ceiling Versus Gross Weight, Single Rotor

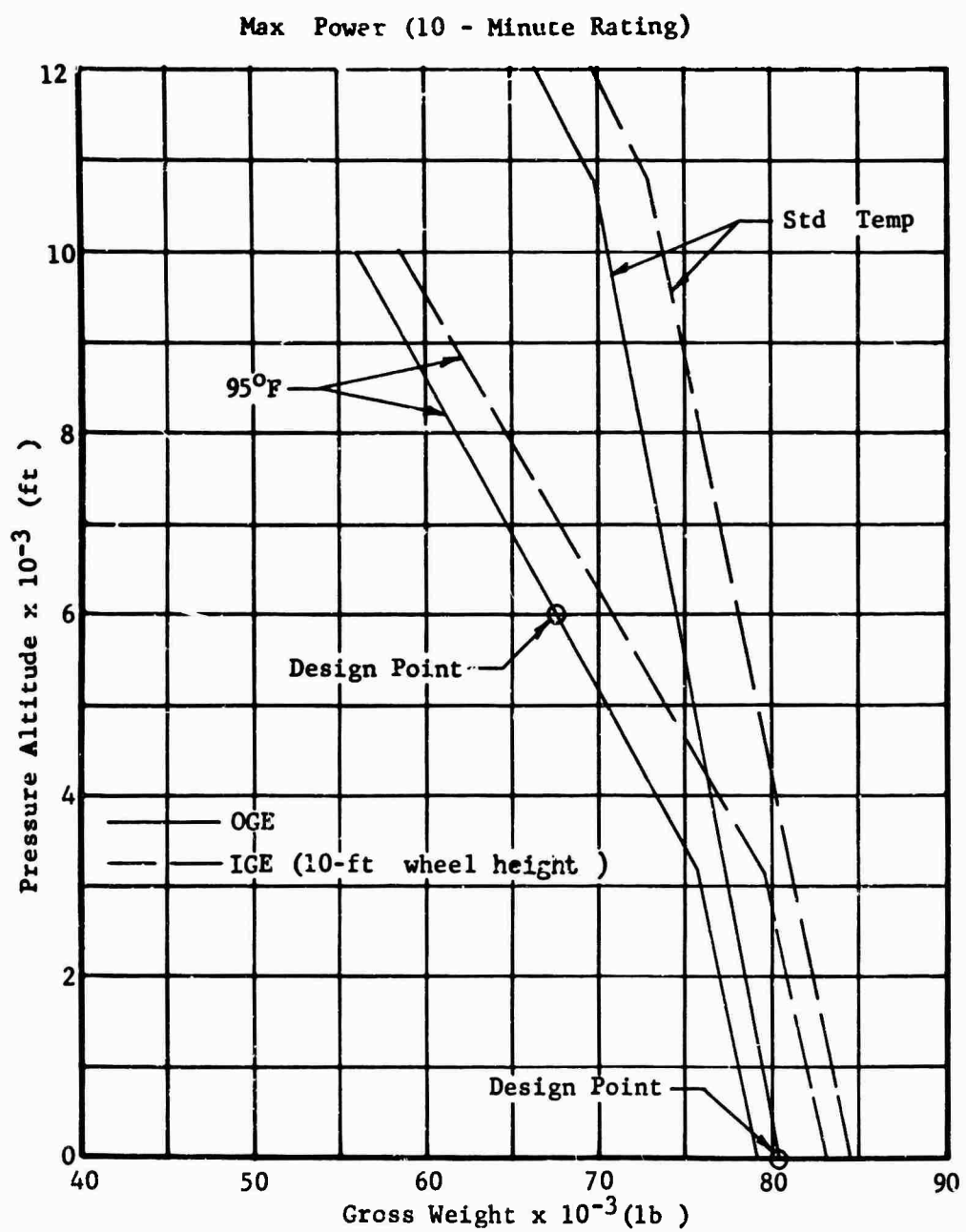


Figure 42 Hover Ceiling Versus Gross Weight, Tandem Rotor.

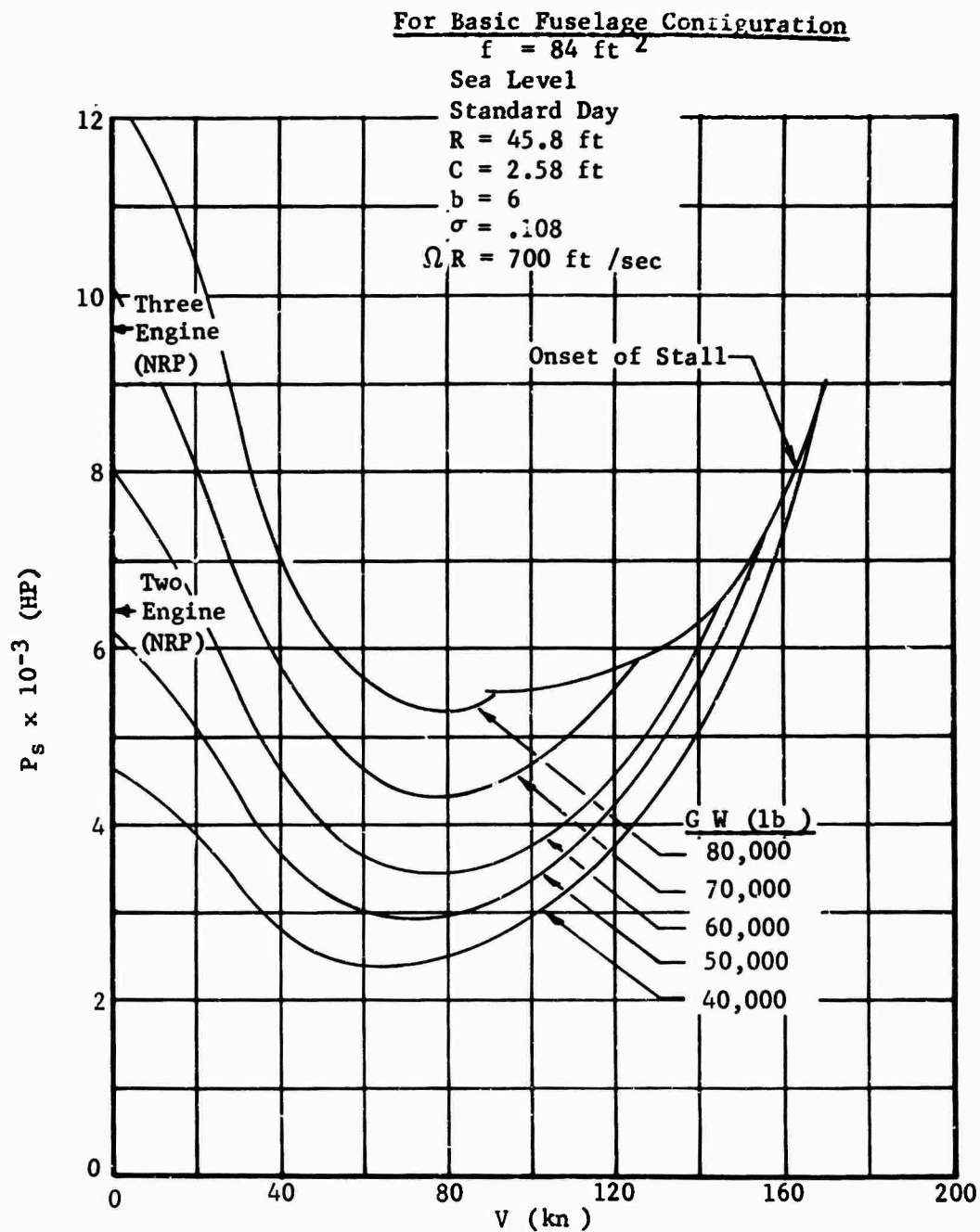


Figure 43 Forward Flight Characteristics, Single Rotor
 Basic Fuselage Configuration

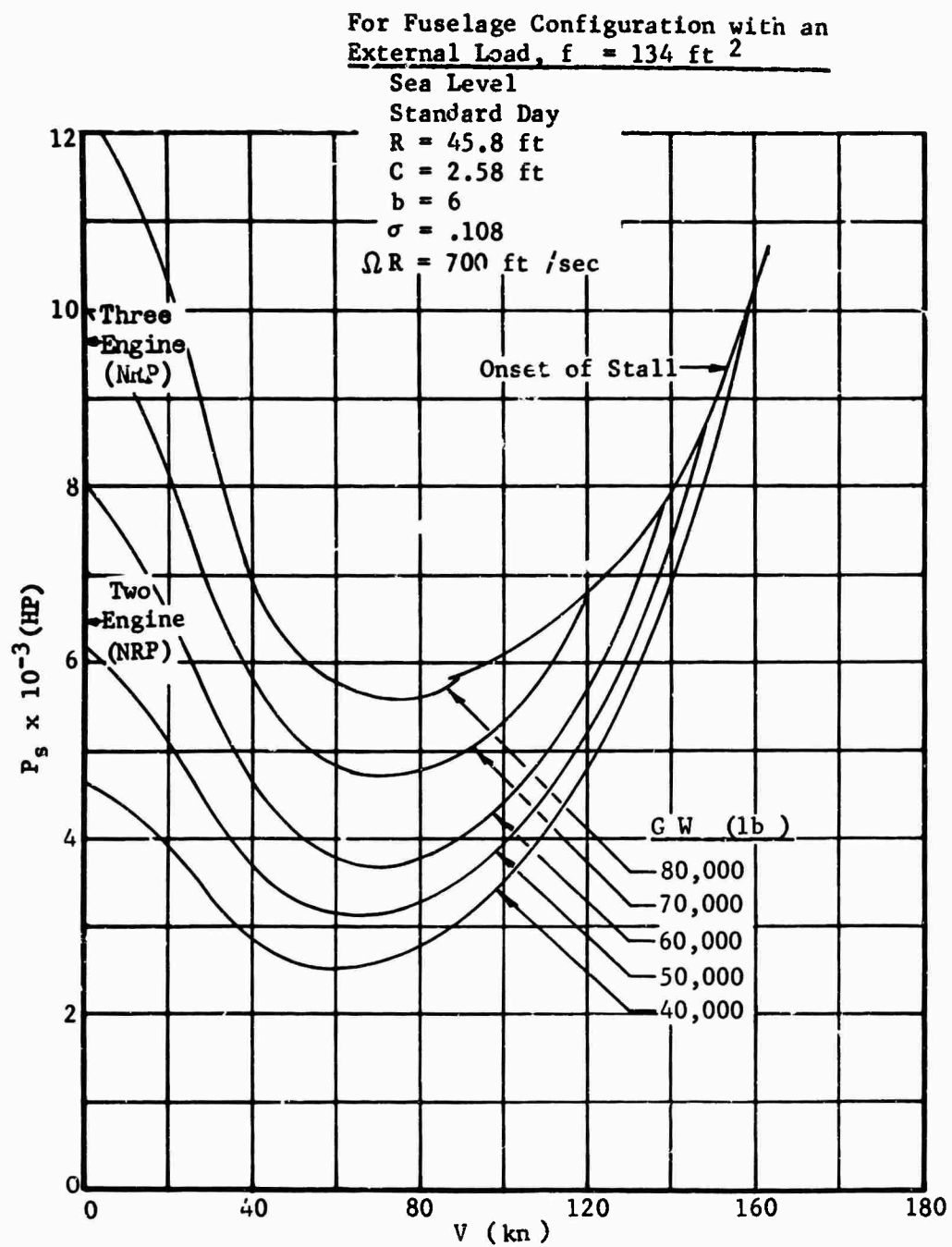


Figure 44 Forward Flight Characteristics, Single Rotor
External Load Configuration

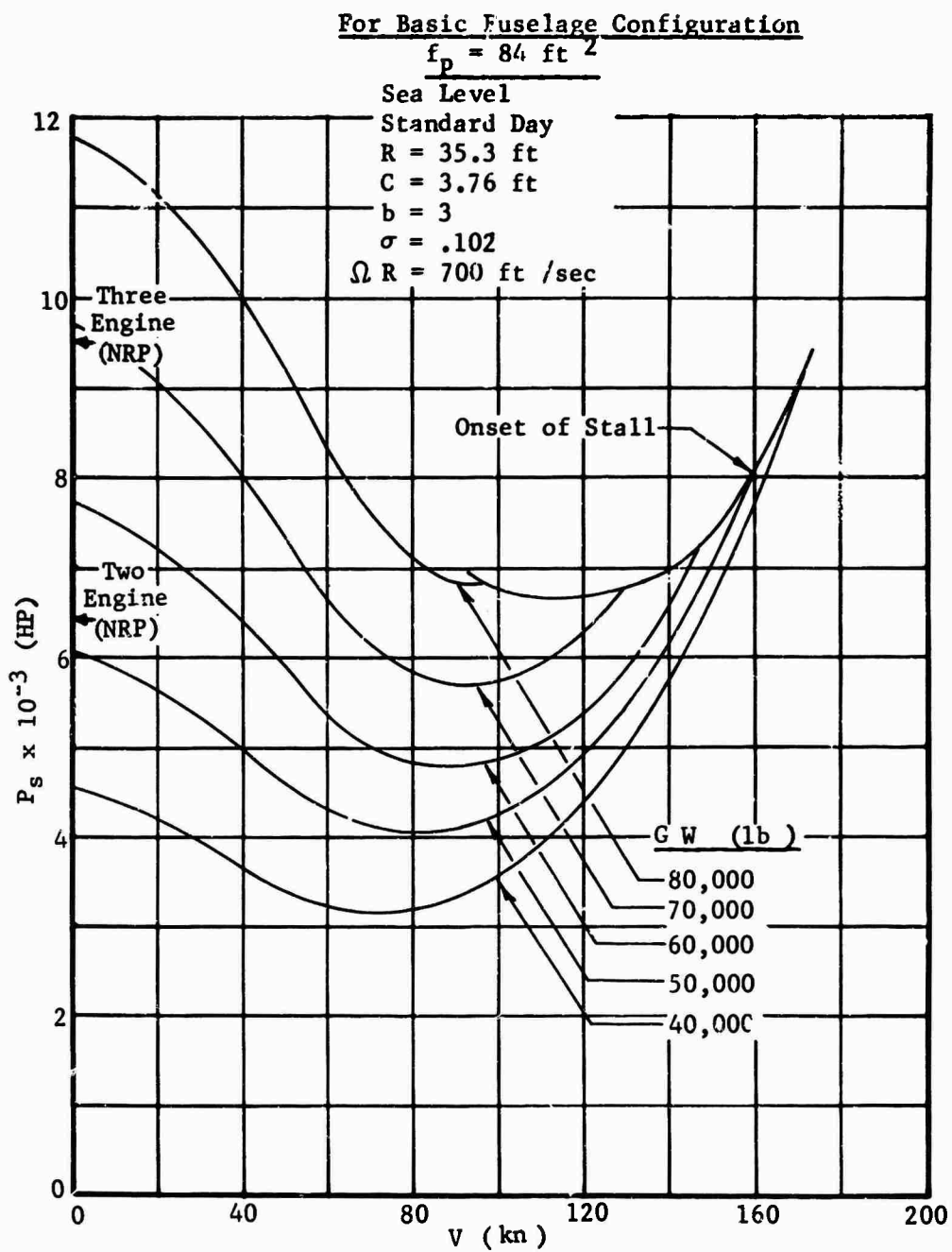


Figure 45 Forward Flight Characteristics, Tandem Rotor Basic Fuselage Configuration

For Fuselage Configuration with an
External Load, $f_p = 134 \text{ ft}^2$

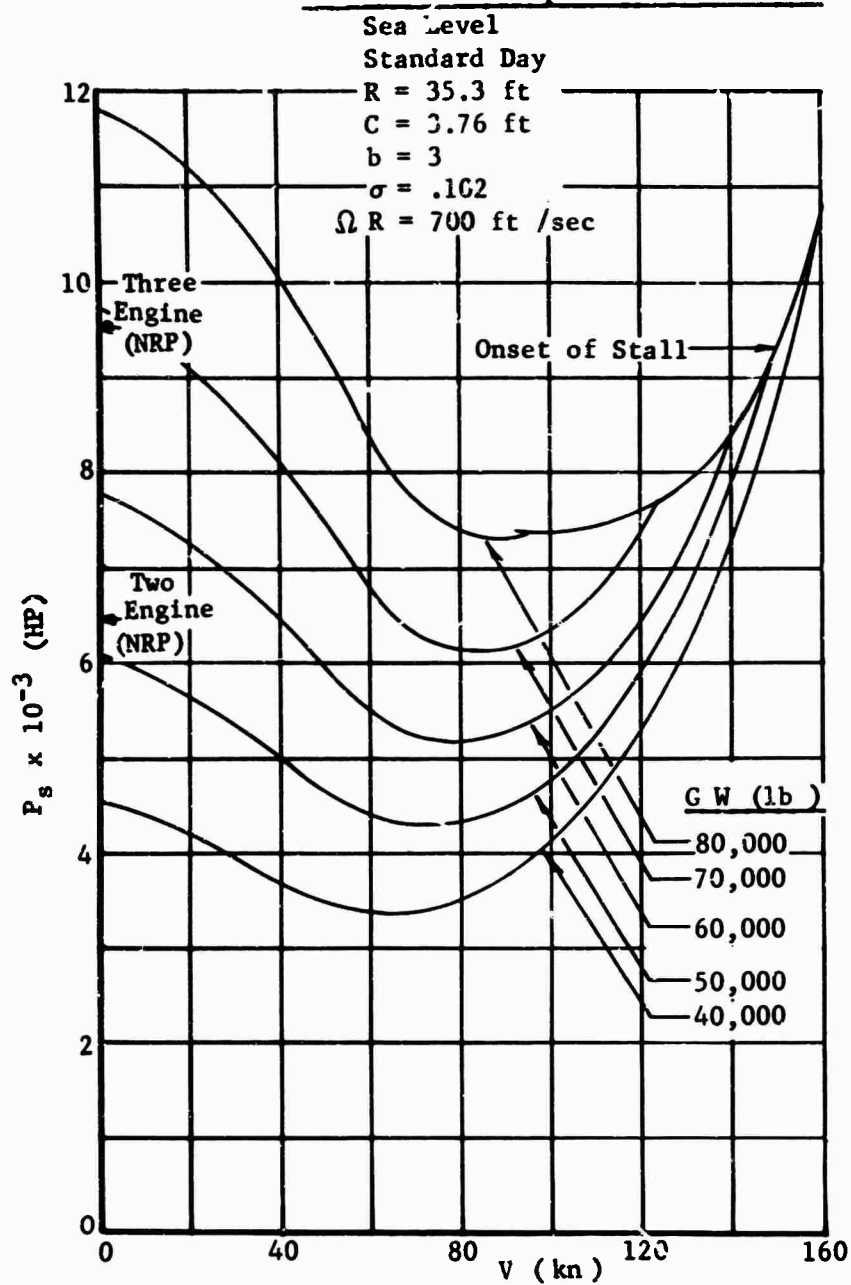


Figure 46 Forward Flight Characteristics, Tandem Rotor
External Load Configuration

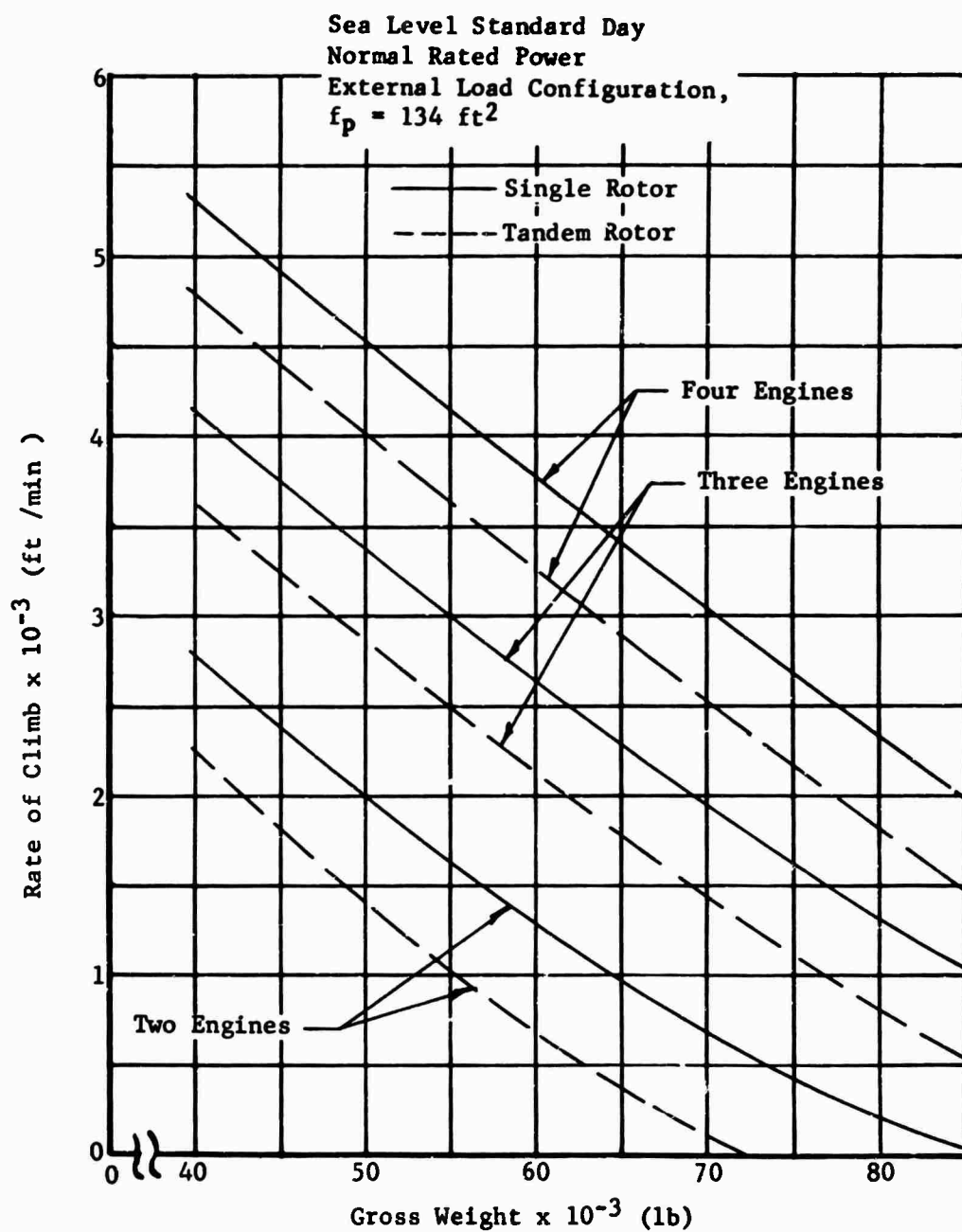


Figure 47 Best Rate of Climb Versus Gross Weight

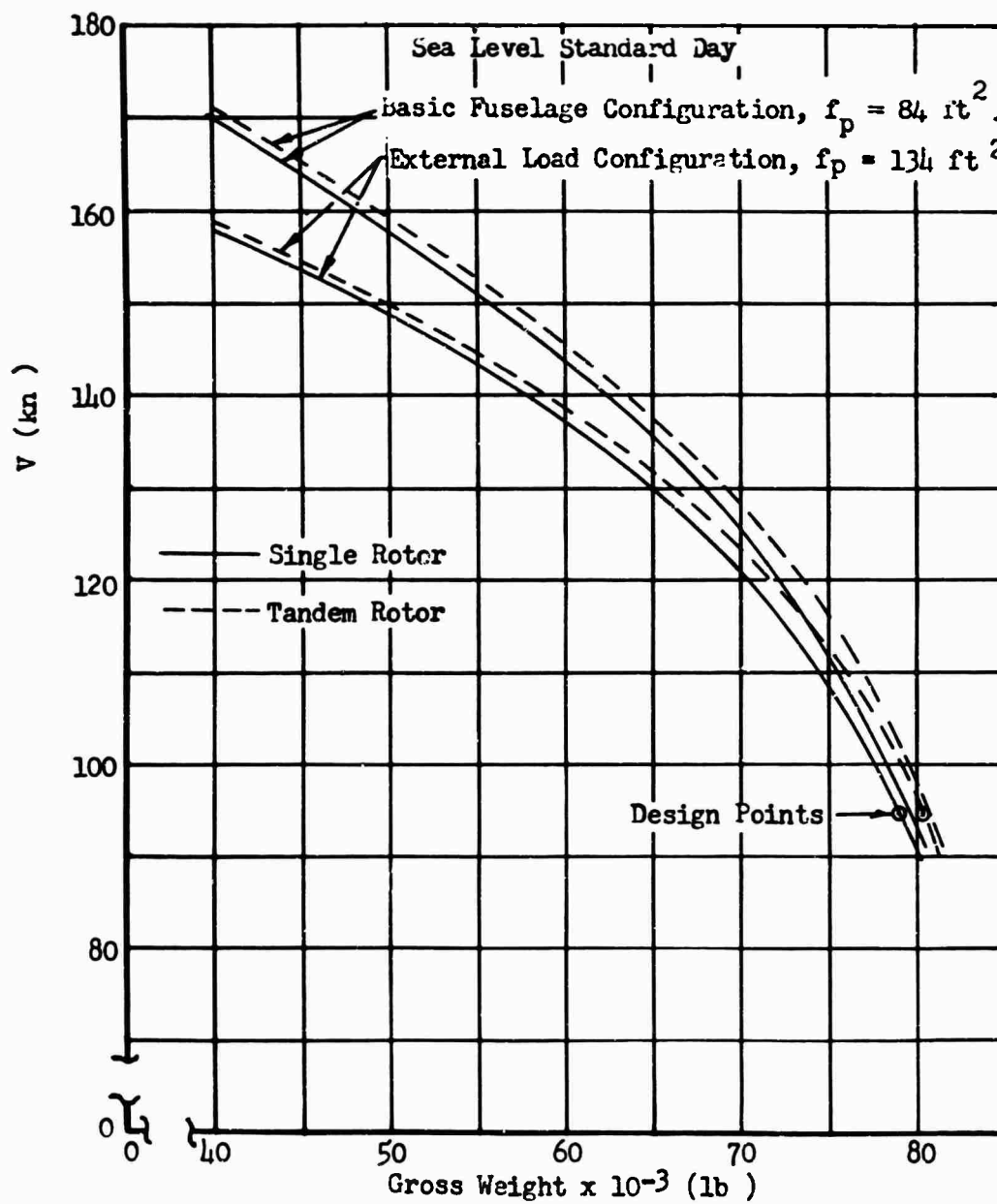


Figure 48 Speed at Onset of Stall

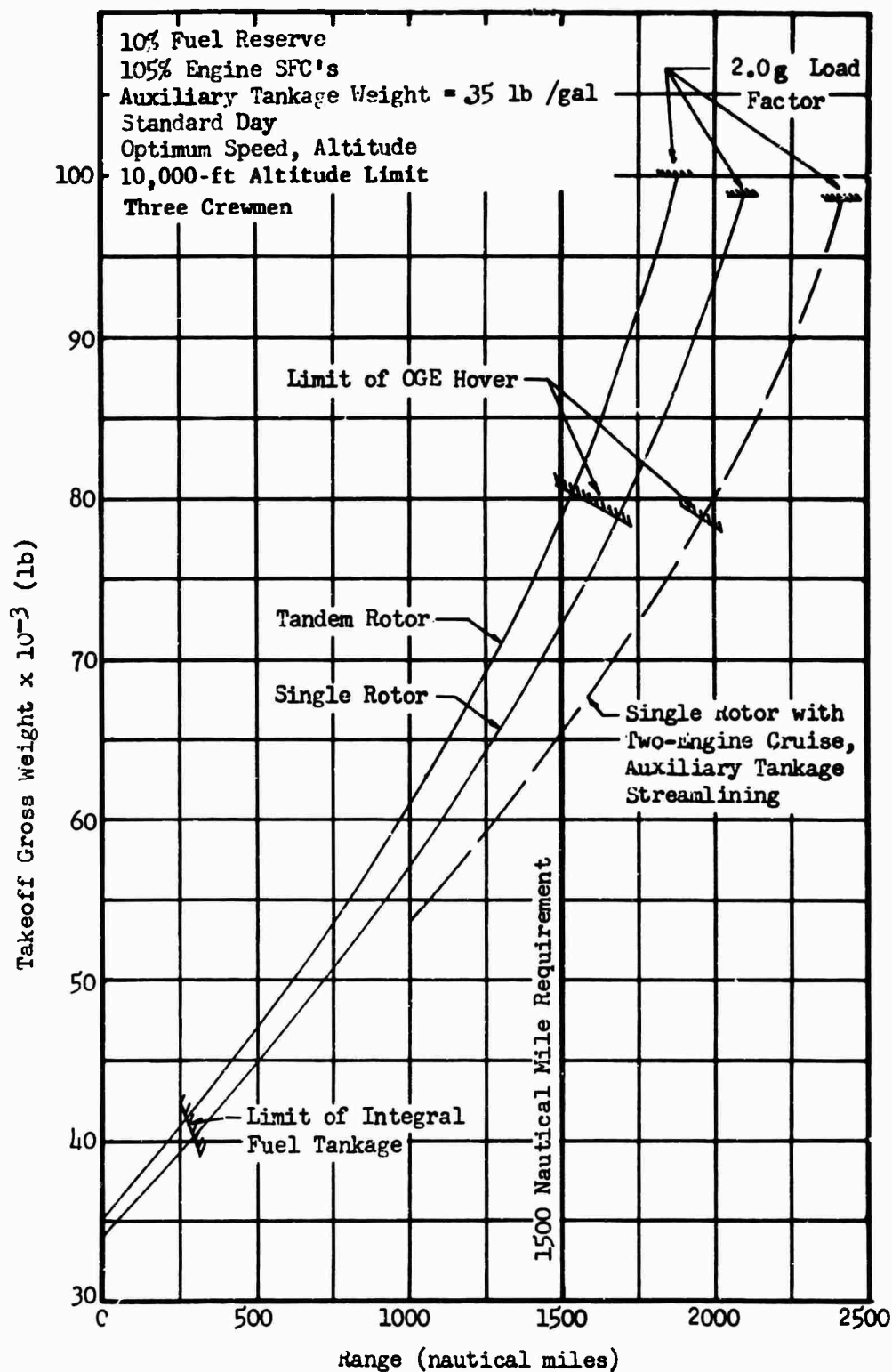


Figure 49 Ferry Range Versus Takeoff Gross Weight

ferry range capability at maximum allowable gross weight (2.0g load factor).

Because of the excellent fuel consumption characteristics of the T64/S4A engine, the 1500-nautical-mile Army requirement is easily met and imposes no limitation on the design of the helicopters. Of particular interest is the fact that for 1500 nautical miles, vertical takeoff is possible, since the gross weights are lower than those required for the 20-ton payload mission which has OGE, SLS hover capability. At maximum takeoff gross weight, defined by a load factor of 2.0g, the obtainable ferry ranges are 2080 and 1870 nautical miles for the single and tandem configurations, respectively.

Additional investigation of the single rotor configuration shows that considerable extension of cruise range can easily be accomplished. Simply by cruising on two engines for the latter part of the flight, an 11-percent range increase can be obtained. The external fuel tank can be streamlined to act as a fairing, cutting down fuselage drag instead of increasing it, resulting in still another 5-percent increase. The resulting 16-percent range improvement increases capability at a 2.0g load factor takeoff weight to over 2400 nautical miles, as shown by the dashed line in Figure 49. It should be noted that the only special equipment required to achieve the ranges shown by this curve is the external tank kit and that the helicopter, which does not have to be stripped or faired, arrives at its destination ready to go to work. Because the ferry tank is external, it is quickly disconnected and removed, as if it were any other payload. Further range improvement is possible through use of droppable fuel tanks, additional component fairings, removal of nonessential equipment, and cruise above 10,000-foot altitude. However, since the two changes investigated result in greater range than that required to ferry from San Francisco to Hawaii, from Hawaii to Wake, or from Midway to Tokyo, no additional range improvement measures were investigated. Similar range extension changes in the tandem configuration are estimated to increase its ferry range to slightly over 2100 nautical miles, sufficient for ferrying across the Pacific via Guam and the Phillipines, but possibly inadequate for the trip from Midway to Tokyo.

In summary, key performance--hover capability, speed, payload/range--are nearly equivalent for the single and tandem rotor designs, since each is configured to the same mission requirements. The single rotor configuration excels in climb and low speed flight and has a substantial in-ground effect hour advantage. Ferry range capability of the single rotor design is also superior due to its lower cruise power.

STABILITY AND CONTROL CHARACTERISTICS

The characteristic configuration of tandem and single rotor helicopters results in different inherent levels of stability and control for otherwise comparable design solutions. However, automatic electronic stabilization is used to obtain essentially equivalent stability and control for the two configurations. Although a complete check against (Reference 4) MIL-H-8501A has not been made, it appears that for the speeds involved, both optimized configurations possess adequate stability and control characteristics, ie., equivalent to those of the CH-54A (single rotor) and CH-47A (tandem).

The single rotor arrangement has been equipped with an 80-square-foot horizontal surface for longitudinal stability and an 84-square-foot vertical fin for directional stability.

The tandem rotor arrangement has no horizontal stabilizing surfaces except for the main landing gear support fairings, which contribute only a small influence. In this respect, the design criteria for the two configuration types differ, as they do for current production helicopters. Because a stabilizing surface on a tandem rotor helicopter would have to work at a short moment arm, a very large stabilizer would be required. Consequently, it is assumed that artificial stabilization will be used to provide satisfactory longitudinal stability in the tandem rotor helicopter. In all probability, a redundant AFCS would be used in the tandem machine while a single system would be employed in the single rotor version for pilot unburdening. These are the approaches taken in the CH-47A and CH-54A, respectively.

Since the two design solutions are typical of current design trends for these two types of helicopters, the general static characteristics of each will be discussed in light of experience with existing helicopters. The four types of static stability are speed stability, angle of attack stability, directional stability, and effective dihedral.

Speed Stability

Generally, single rotor helicopters are stable with speed; that is, an increase in forward speed produces a nose-up moment on the helicopter. The resulting nose-up attitude tilts the rotor thrust rearward and tends to return the helicopter to its trim speed. The source of the single rotor helicopter's speed stability is the rotor.

The tandem is usually unstable with speed. Although the individual rotors tend to produce stability, as on the single rotor ship, variations of thrust of the rear rotor with speed produce an unstable moment. This variation of rear rotor thrust with speed is caused by the front rotor downwash. In

forward flight, the rear rotor operates in the downwash of the front rotor and is trimmed accordingly. As forward speed increases, the downwash angle is reduced because of the lower lift coefficient (larger mass flow of air) of the front rotor. The reduction of downwash angle with increasing speed causes an increase in the rear rotor angle of attack and an increased rear rotor thrust. The increased thrust on the rear rotor causes an unstable nose-down moment.

Angle of Attack Stability

The helicopter rotor is unstable with angle of attack; that is, a nose-up change in angle of attack produces a nose-up moment. The helicopter fuselage is also unstable with angle of attack. Therefore, helicopters require some device to provide angle of attack stability.

The single rotor helicopter generally has a horizontal tail stabilizer of sufficient size to provide approximately neutral angle of attack stability at high speeds. Figure 7 indicates that generous use of tail moment coefficient was applied in sizing the single rotor aircraft's horizontal tail to be sure this quality was maintained.

A tandem helicopter has an additional source of instability with angle of attack, which is related to the operation of the rear rotor in the downwash field of the front rotor. When the helicopter angle of attack is increased, the rear rotor angle of attack, and hence the rear rotor thrust, increase less than the angle of attack and thrust of the front rotor because of the increased downwash from the front rotor. The result is a nose-up, and hence unstable moment.

A heavy lift tandem crane helicopter in the 12-20-ton payload class utilizing S-64 dynamic components was investigated on the Sikorsky V/STOL simulator and several observations were noted concerning static stability. The presence of positive static stability is displayed in the form of a positive stick gradient with speed. From these studies it was found that a combination of collective and cyclic control biases was necessary as a function of dynamic pressure "q" to provide a positive longitudinal control gradient throughout the speed range. The stick gradient of a single rotor aircraft is generally stable in all but a small area between 50 and 80 knots, where some reversal is the result of nonuniform inflow.

Directional Stability

The desired directional stability characteristic is a moment which tends to return the helicopter to its unyawed heading. The lifting rotor(s) of a single or tandem helicopter do not contribute significant yawing moments due to sideslip. The helicopter fuselage is generally unstable directionally;

that is, if the fuselage is yawed to the right, a yawing moment to the right (unstable) is produced. For this reason, the helicopter requires vertical stabilizing surfaces. Generally, the tail rotor of the single rotor shaft-driven helicopter provides sufficient directional stability due to its change in thrust with yaw. The concern for the stability of the helicopter to make a safe landing following a tail rotor malfunction or loss requires adequate vertical fin area to provide a stable fuselage gradient.

The tandem rotor HLH fuselage appears to be only mildly unstable directionally because of the large amount of overlap (short fuselage) and the large rear pylon. When the two rotors are equally loaded, they contribute little to directional stability. For forward center-of-gravity locations, however, the greater speed stability of the more heavily loaded forward rotor generates a strong directional instability which can ultimately limit the usable range of forward CG.

In general, stable tandem operation requires sideslip measurement coupled with a stability and augmentation system, while stable single rotor operation does not.

Effective Dihedral

A large amount of effective dihedral, which is related to the rolling moment produced by a sideslip, is not desired for dynamic reasons.

In a single rotor helicopter, the primary source of effective dihedral is the rotor. The effective dihedral of the rotor is produced in the same manner as speed stability. For example, a sideslip to the left tilts the rotor plane to the right because of differences in velocity between the forward and rearward blades. The tilt of the rotor plane produces a rolling moment to the right.

On a tandem helicopter, the rotors also produce effective dihedral. In addition, the fuselage contributes effective dihedral due to side forces acting on the aft pylon which is above the center of gravity.

The result of this dihedral is that if the helicopter encounters a disturbance in roll or yaw, it will undergo an oscillation involving simultaneous variations in roll and sideslip (Dutch roll). In single rotor helicopters this oscillation is damped to a greater degree than in tandems. The difference is related to the larger ratio of rolling to yawing moment of inertia in tandem helicopters.

In summary, the inherent (not electronically augmented) stability characteristics of the single and tandem rotor configurations compare as shown in Table XXIII.

TABLE XXIII
STABILITY CHARACTERISTICS

	Single Rotor	Tandem Rotor
Speed stability	stable	unstable
Longitudinal (angle of attack) stability	neutral ^(a)	unstable
Directional stability	stable	unstable
Effective dihedral (Dutch roll)	damped	less damped
(a) Unstable at low forward speeds		

Electronic stabilization can be utilized to obtain positive stability in all modes. In fact, complete reliance on automatic stabilization would lessen the necessity for large tail surfaces and would thereby reduce airframe weight of the single rotor configuration in particular. Penalties in complexity and reliability, however, are necessarily associated with such automatic stabilization. In practice, the tandem utilizes comprehensive redundant Automatic Flight Control Systems, and the single augments inherent stability with limited AFCS. They obtain essentially the same overall stability. Since these assumptions are used in the parametric weight equations, the two configurations must be considered equivalent in terms of stability and control characteristics.

DYNAMIC CHARACTERISTICS

Presented in this section are the results of a dynamic analysis of the single and tandem rotor crane configurations. Results of rotor blade aerodynamic analysis are presented in Figures 50 and 51, and results of airframe vibration analysis are shown in Figures 52 through 58.

ROTOR BLADE ANALYSIS

The preliminary design study of a rotor blade for a six-bladed, 95 foot diameter rotor, which was conducted early in the HLH program, showed that resonant frequencies of large blades follow the same patterns observed frequently in present production helicopters. Figures 52 and 53 show the relationships of frequencies and rotor speeds. In Table XXIV, the HLH blade first-mode frequencies at normal operating speeds are compared with three production blades.

TABLE XXIV
FIRST-MODE FREQUENCIES AT NORMAL ROTOR SPEED FOR
SEVERAL MAIN ROTOR BLADES

Model	Main Rotor Radius (ft)	First-Mode Flatwise	Frequencies (cycles/rev)
			Edgewise
H-34	28	2.6	3.4
SH-3A	31	2.8	3.4
H-37	36	2.7	3.3
HLH Design Study	47.5	2.7	3.6

It is apparent that the flatwise or edgewise natural frequency of a wide range of blade geometries is the same, or about three cycles, per revolution. Therefore the tandem configuration, which utilizes three-bladed rotors, will experience greater n-cycles-per-revolution blade loads than the single rotor design with six blades.

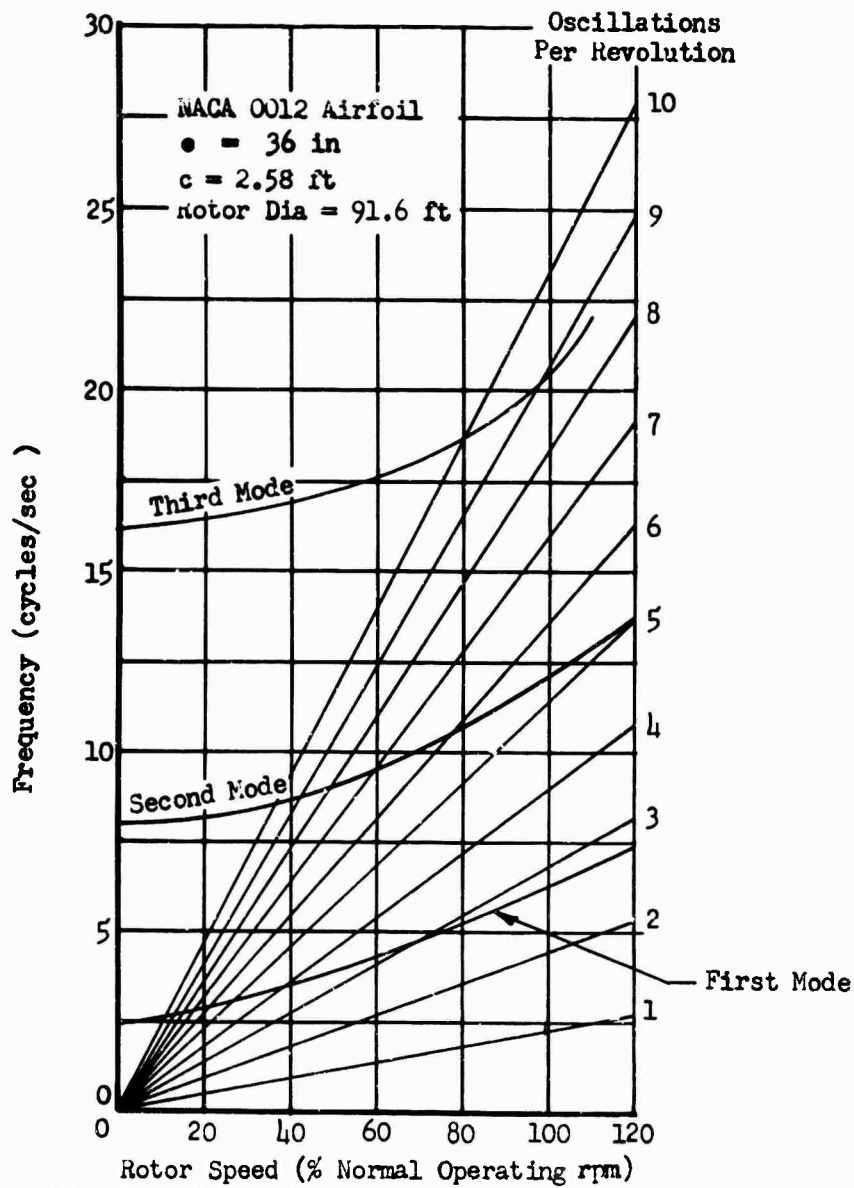


Figure 50 Blade Natural Frequency, Flapwise Bending

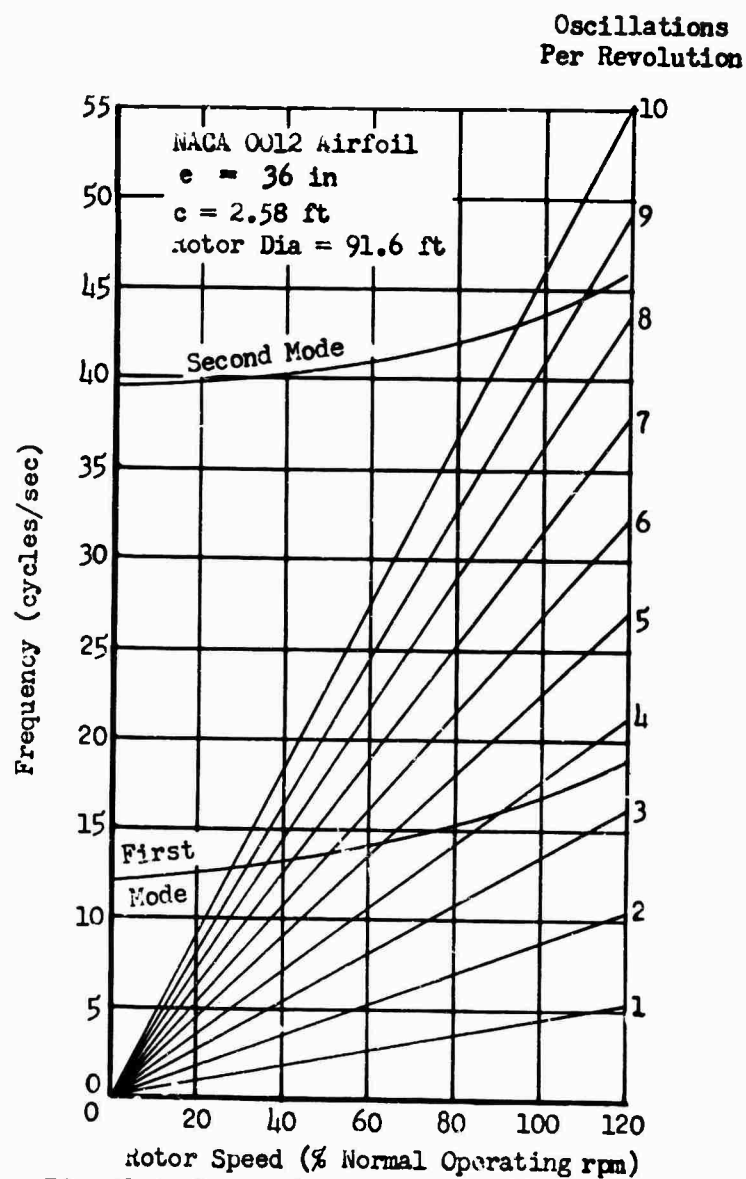


Figure 51 Blade Natural Frequency, Edgewise Bending

AIRCRAFT VIBRATION

A dynamic analysis was conducted to determine the vibration characteristics and predicted in-flight response of the single and tandem configurations. Results of this investigation are based upon preliminary parametric design information which did not describe local stiffness effects of transmission support and payload support structure.

The dynamic models of the two configurations are shown in Figure 52. As shown, only the vertical and pitch degrees of freedom of the aircraft were considered, since frame support structural stiffnesses, which significantly control lateral and torsional modes, were unknown.

The single rotor model was described with 19 degrees of freedom and the tandem rotor model with 23 degrees of freedom. Airframe resonances were generated by a computer iteration procedure. Rotor excitation was extrapolated from previous test data. Forced response, in-flight vibration characteristics were derived from application of the predicted rotor loads to airframe forced response sensitivities.

AIRFRAME VIBRATION CHARACTERISTICS

The vertical airframe modes of the single and tandem rotor configurations are presented in Figures 53 and 54. Figure 55 presents a comparison of the proximity of these modes to primary excitation frequencies. As shown, the modes of both configurations are removed from primary excitation frequencies.

One-cycle-per-revolution and n-cycles-per-revolution forced response results are presented in Figures 56 through 58. One-cycle-per-revolution rotor loads (rotor loads are presented in appendix) were computed for a 1-inch out-of-track condition. Tandem one-cycle-per-revolution rotor loads are higher because of heavier blade mass. These rotor loads were applied to forced response sensitivities to predict aircraft one-cycle-per-revolution vibration for a 1-inch out-of-track condition. The results shown in Figure 56 reveal that, as expected, tandem one-cycle-per-revolution vibration is higher than the single rotor configuration, since the applied load for the tandem is higher and airframe impedance is lower.

N-cycles-per-revolution rotor loads were derived from measured SH-3A rotor loads (Reference 59) and H-21 rotor loads (Reference 25) for the single and tandem configurations, respectively. The measured rotor loads for both configurations were scaled up by a $C_{T/\sigma}$ (representative of mean blade lift coefficient) relationship. This procedure, while lacking somewhat in quantitative accuracy, yields good comparative loads.

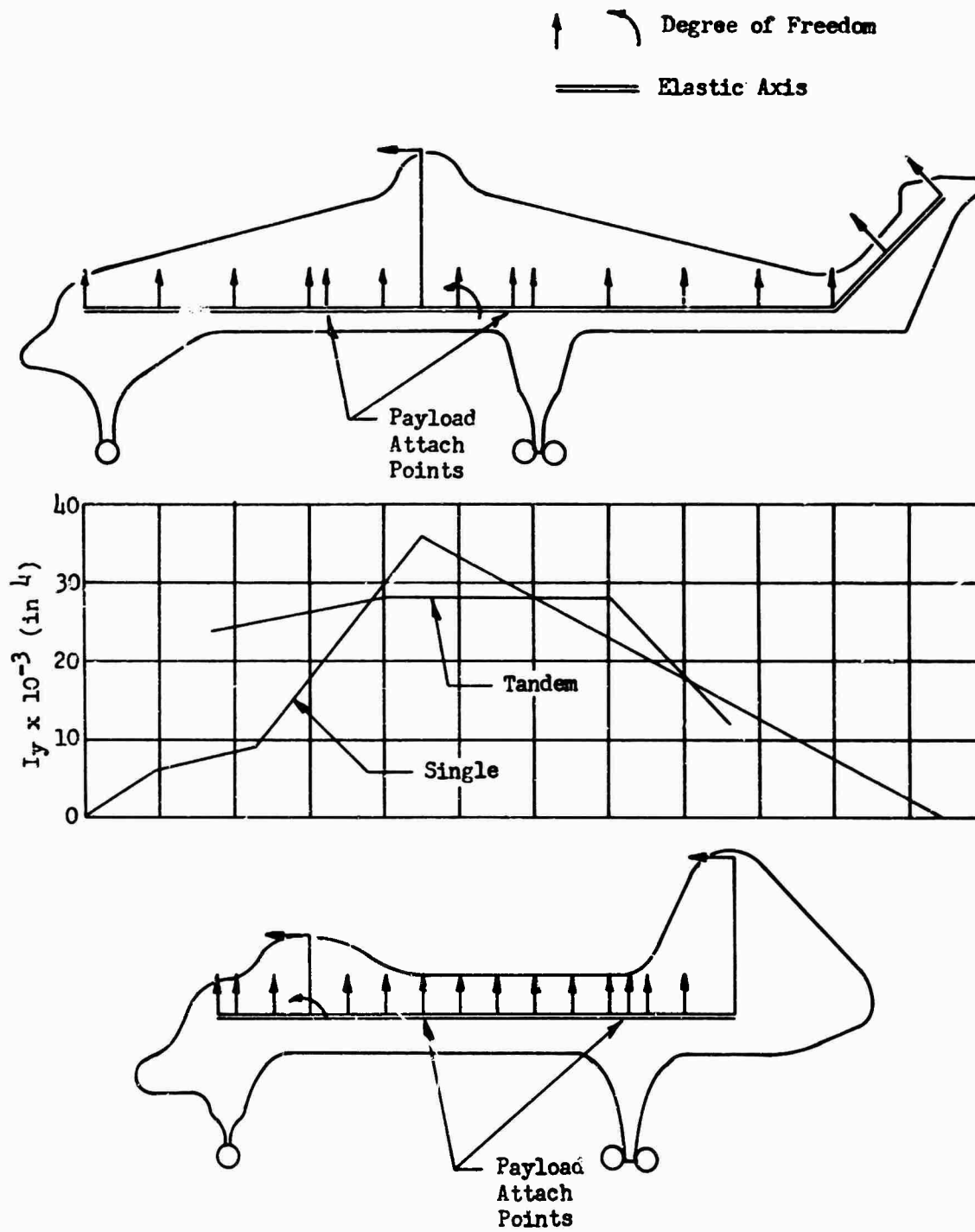


Figure 52 Dynamic Analysis Models

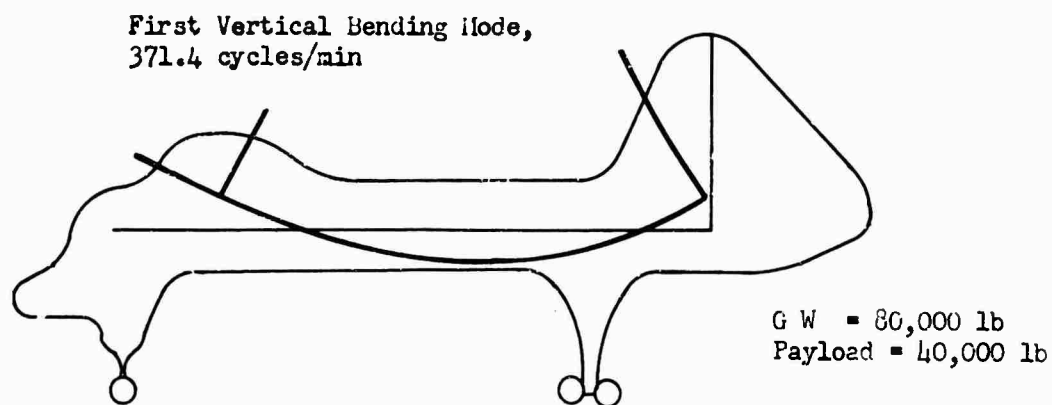
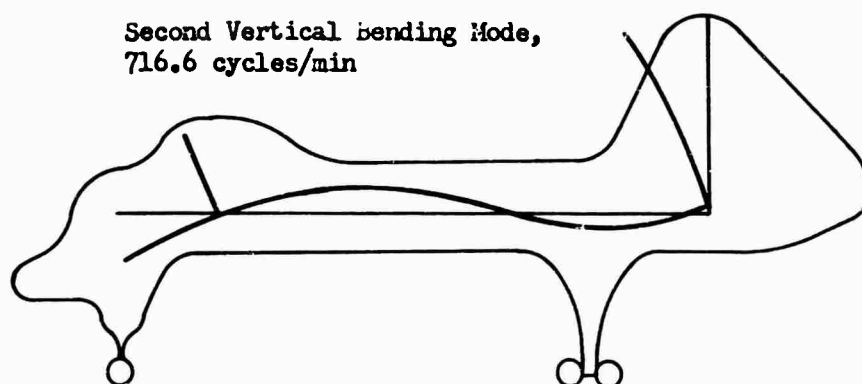
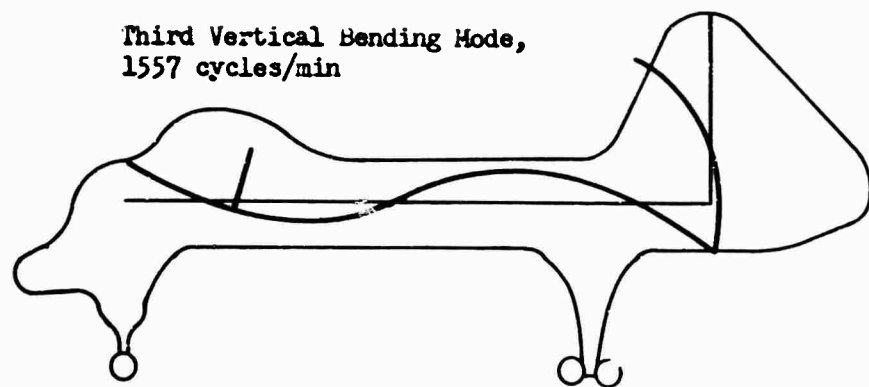


Figure 53 Fuselage Dynamic Analysis, Tandem Rotor

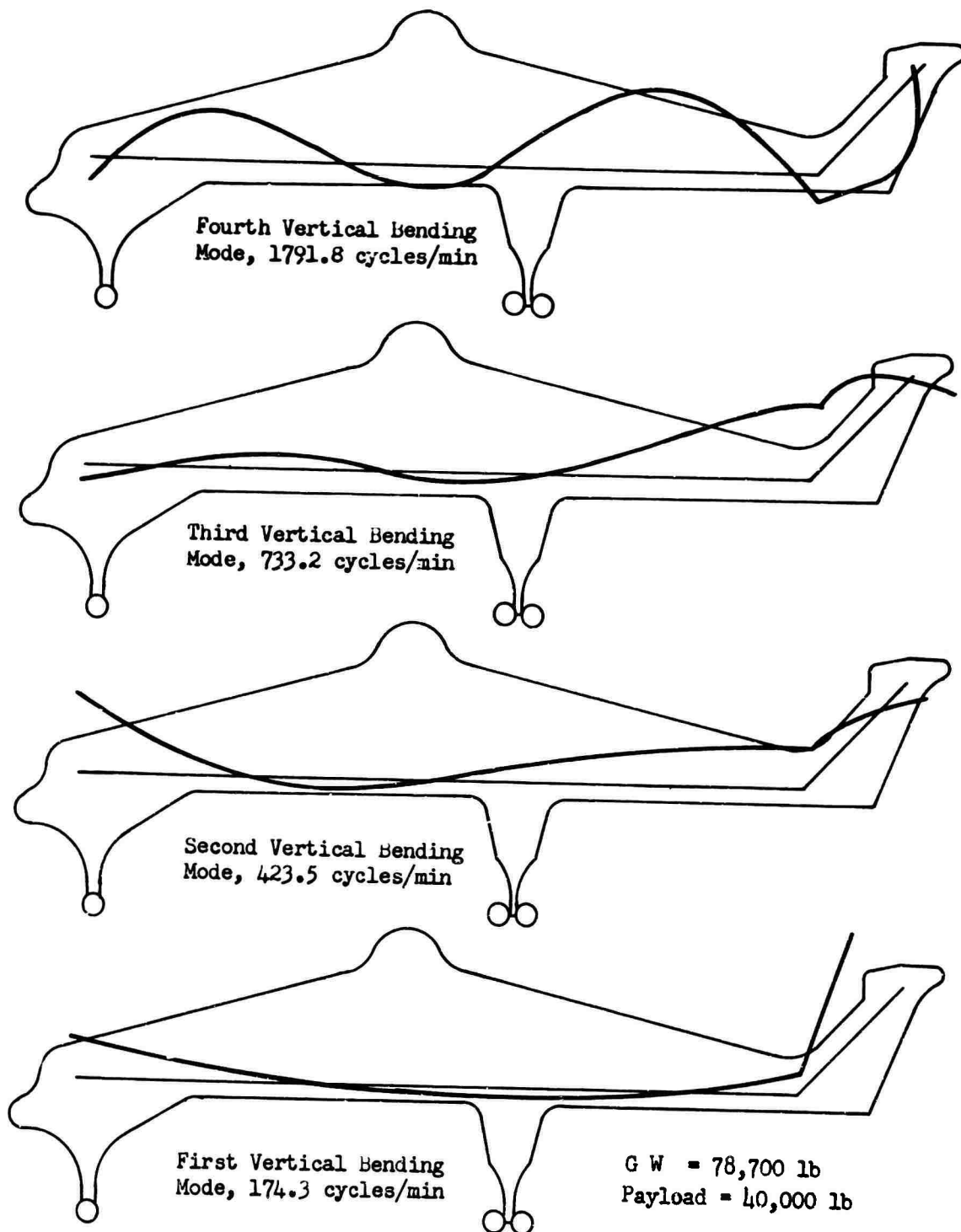


Figure 54 Fuselage Dynamic Analysis, Single Rotor

Single Rotor

Tandem Rotor

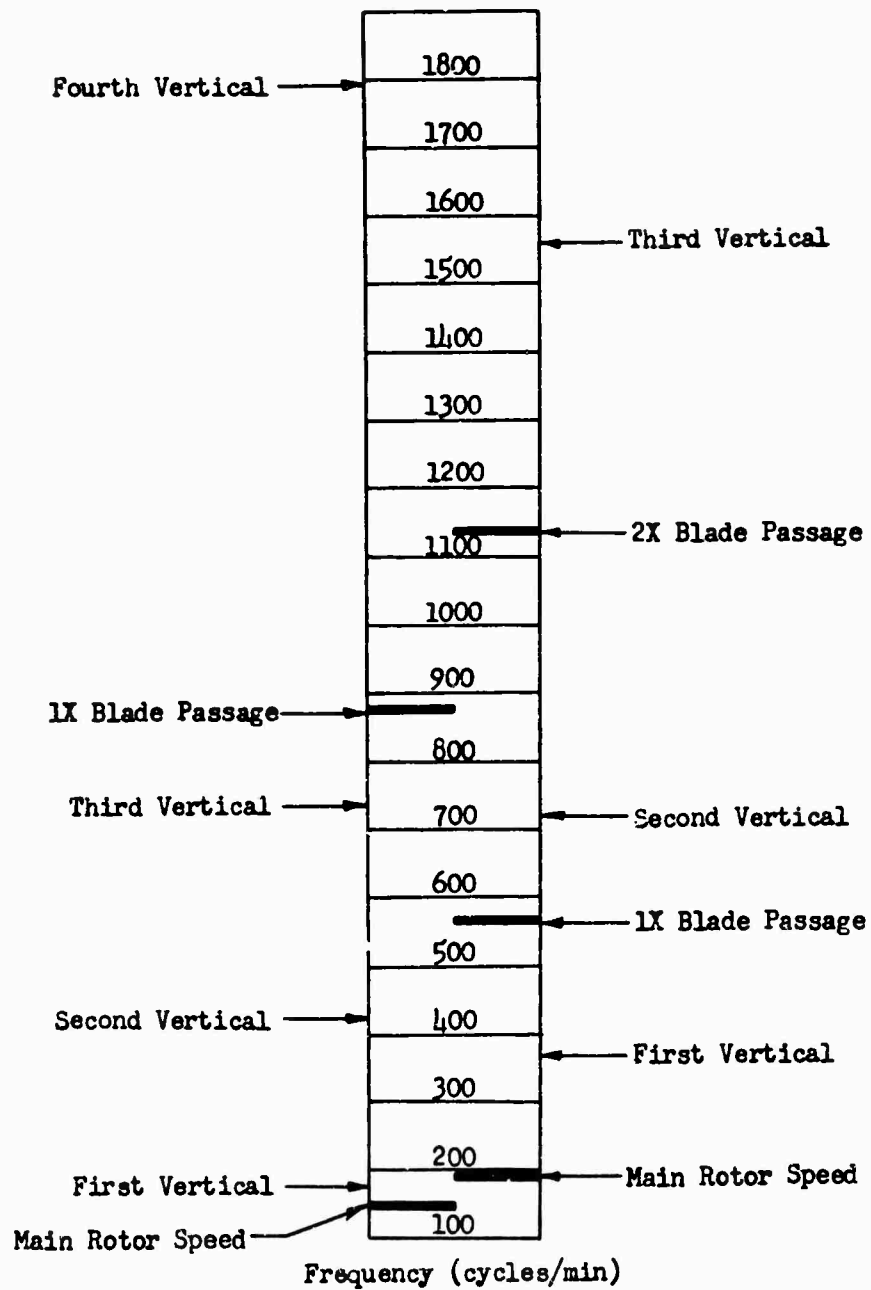
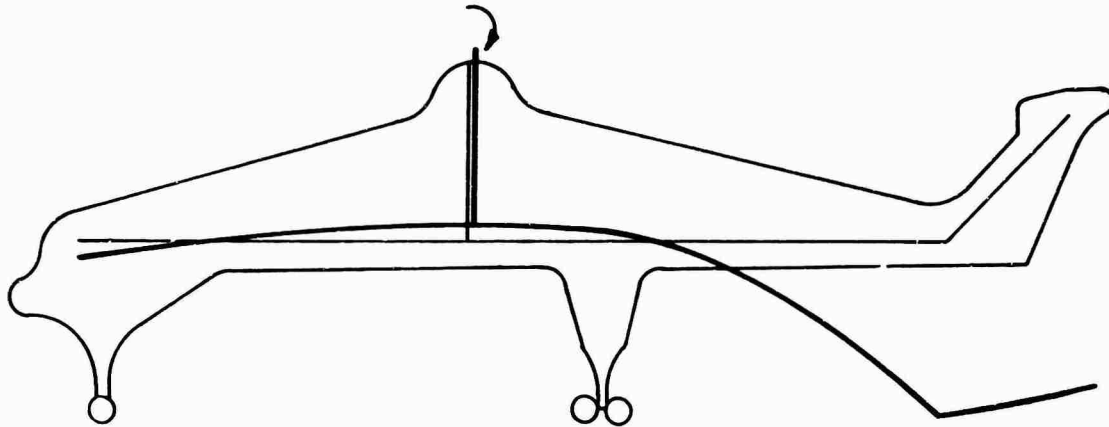


Figure 55 Vertical Bending Mode Frequencies

Moments are due to one blade's being 1 inch out of track



Note: Only moments due to out of track are considered. Result is conservative estimate of 1/rev response

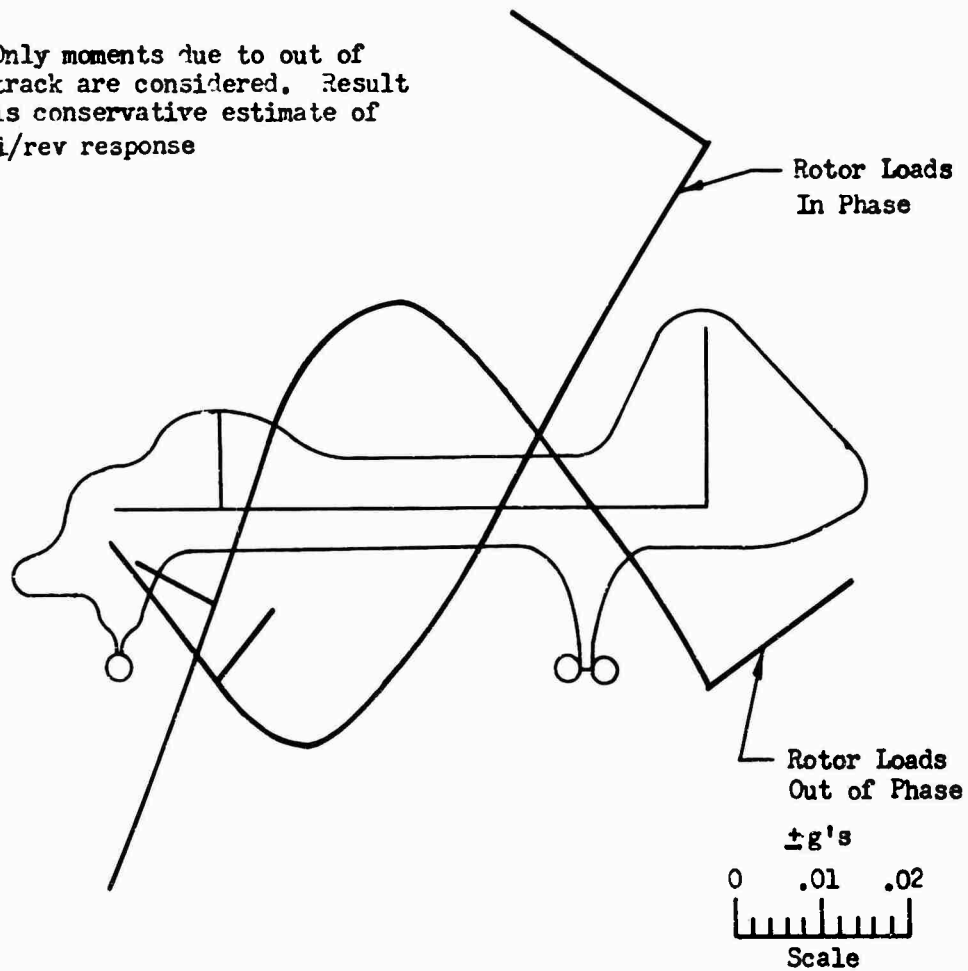
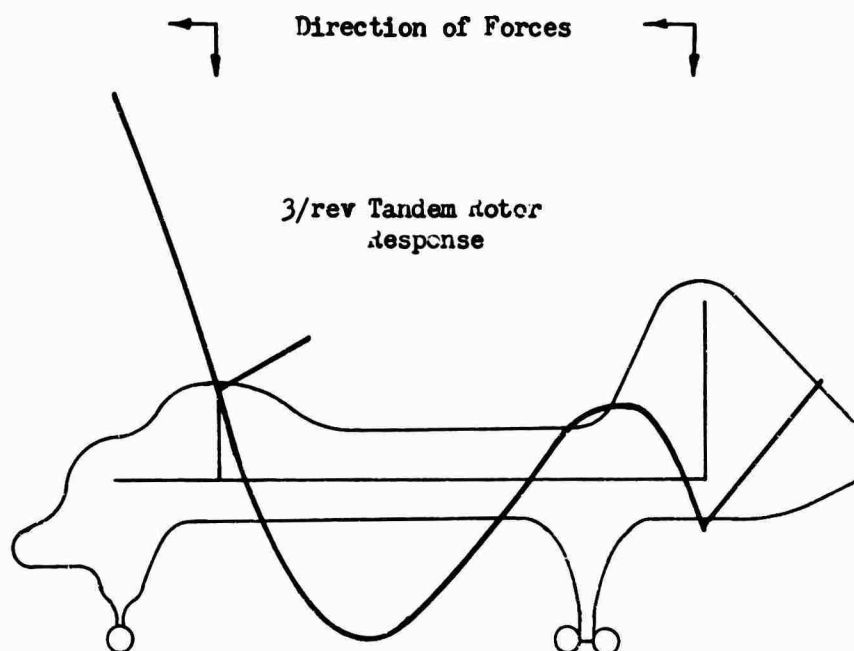
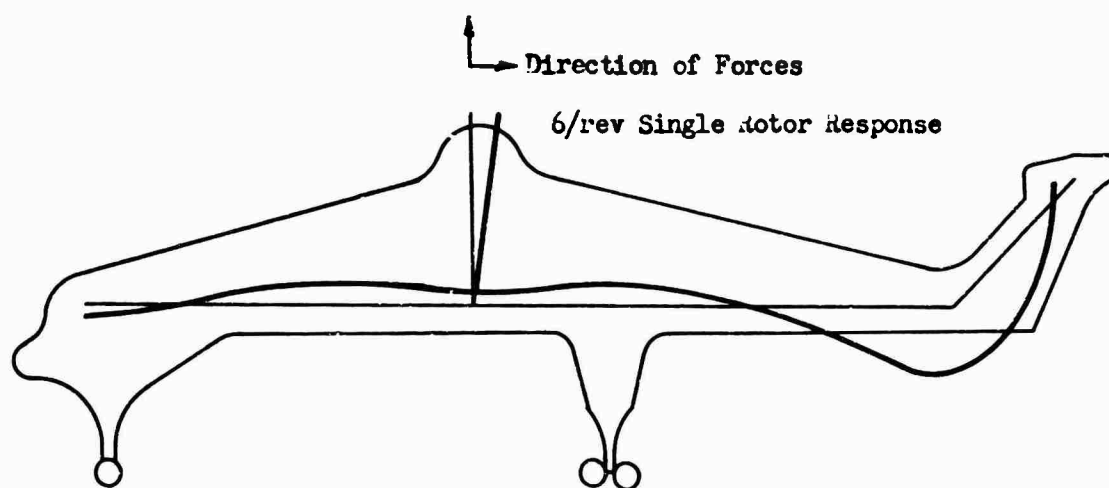


Figure 56 1/rev Response Due to Out-of-Track Moment



Rotor Loads are Phased for Highest Cockpit Vibration

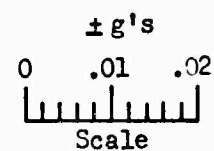
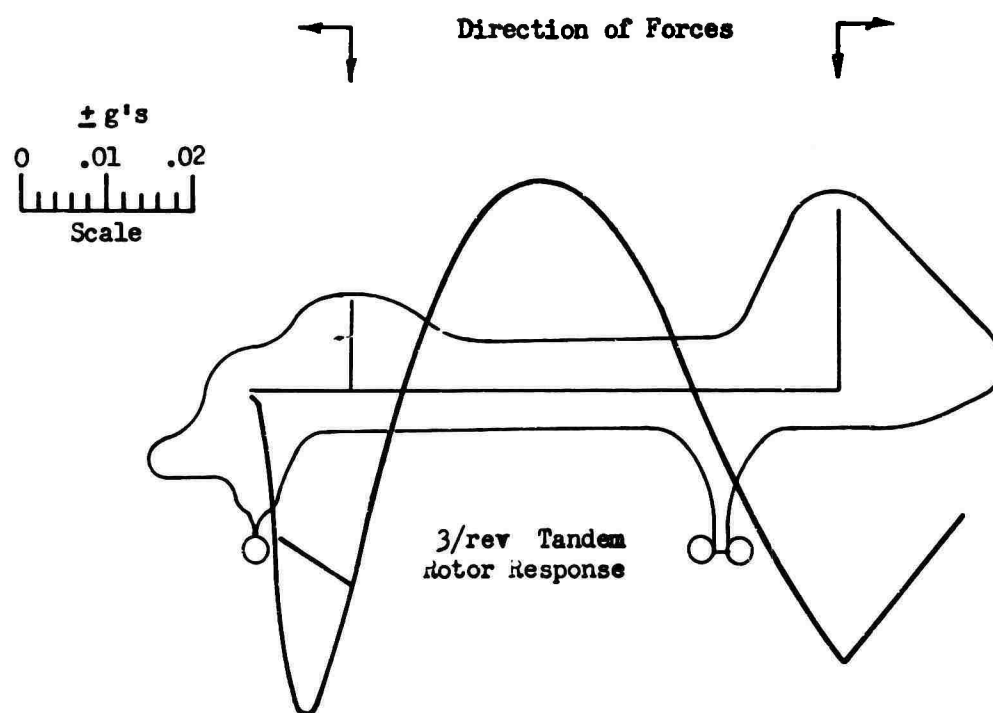
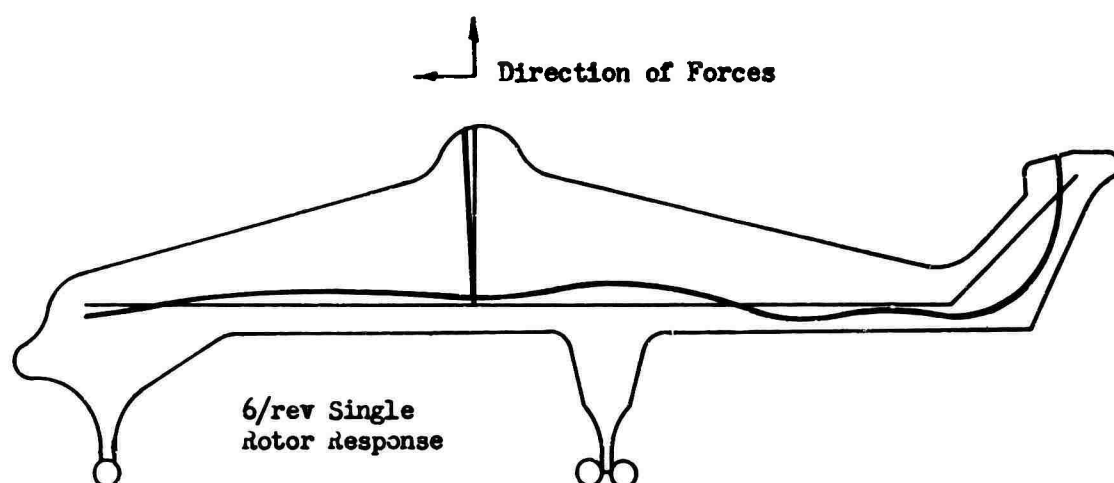


Figure 57 N/rev Response, Highest Cockpit Vibration



Rotor Loads are Phased for Lowest Cockpit Response

Figure 58 N/rev Response, Lowest Cockpit Vibration

The estimated n-cycles-per-revolution rotor loads were applied to n-cycles per-revolution forced response sensitivities for an in-flight aircraft vibration comparison. The results presented in Figures 57 and 58 show aircraft n-cycles-per-revolution response with both the most favorable and unfavorable phase addition of rotor loads. As shown, tandem configuration vibration was much higher than with the single rotor configuration. This can be attributed to higher tandem rotor loads and the contribution of two airframe modes which bracket three cycles per revolution. In the single rotor design, only one mode appreciably contributes to six-cycles-per-revolution response.

Since the analytical results presented are based on preliminary design information which did not account for some important areas which significantly control aircraft response, a review of potential problem areas and an evaluation of penalties involved in mitigating them are necessary.

Potential Problem Areas

As shown in Figure 55, the basic vertical resonances of both the single and tandem rotor designs are removed from one-cycle-per-revolution. However, the first coupled lateral-torsional resonance of the tandem configuration may be much closer to one cycle per revolution. This occurs because of the large concentrations of mass and inertia at the ends of the tandem aircraft. To mitigate this problem, the EI distribution of the center span of the aircraft could be increased. However, as shown in Figure 52, center section EI is quite large, and small percentage changes in that area will result in a considerable weight penalty.

The first coupled lateral-torsional mode of the single rotor design is much higher, since the large concentration of mass and inertia occurs at the stiffest portion of the aircraft, the transmission support structure. In the single rotor configurations, however, the first vertical bending resonance may approach one cycle per revolution. Tail stiffness can be employed to relieve this. As shown in Figure 52, the EI distribution at the tail is small, so reshaping of the tail beam for more efficient beam stiffness can be incorporated as a solution with a negligible weight increase.

In summary, if a one-cycle-per-revolution problem exists with both configurations, resolution can be much more efficiently achieved for the single rotor design, since the ratio of $\frac{\text{percent stiffness change}}{\text{percent weight increase}}$ will be much higher for the single rotor design.

Another area of concern is local transmission support flexibility. Since the transmission of the single rotor design is mounted in the stiffest portion

of the aircraft, the transmission modes will be well above six cycles per revolution and will have no adverse affect on one-cycle-per-revolution response.

The tandem rotor transmissions are mounted on the most flexible portions of the aircraft. Transmission modes can therefore affect the proximity to one cycle per revolution of the lateral-torsional mode of the tandem. Considerable local beef-up of the transmission supports may be required, but care is necessary to prevent the transmission modes from occurring near three cycles per revolution. Keeping the transmission modes between one cycle per revolution and three cycles per revolution may be difficult in the design cycle, since accurate knowledge of local flexibilities is needed.

As shown in Figure 55, single rotor airframe resonances are well separated from six cycles per revolution. However, the first and second bending modes of the tandem bracket three cycles per revolution. The advantages of having the modes well separated as opposed to close coupling of modes is shown in Figures 59 and 60.

As shown in Figure 59, one of the most important problems in helicopter designs has been the presence of excitation frequencies occurring at the lowest response sensitivity between resonances (mode tuning). Operation between coupled modes results in response sensitivities which far exceed rigid body response. Therefore, even favorable mode tuning may not prevent a comfort problem. The tandem characteristics are similar to the characteristics shown in Figure 59, since the first and second modes closely bracket three-cycles-per-revolution. However, with the modes well separated as in the single rotor aircraft design, a low, wide band is available at six cycles per revolution for comfort levels approaching rigid body response. These comparative characteristics explain the cause of higher tandem three-cycles-per-revolution response.

The final significant area of concern is transmission resonance. For the single rotor configuration, the transmission modes will be well above six-cycles per revolution, as previously explained. The transmission modes for the tandem design will probably be placed between one and three cycles per revolution, since elevating these modes above three cycles per revolution will be very difficult because of the low airframe flexibility at the ends of the tandem design.

In summary, the tandem configuration, because of two vibration exciters at the ends of the fuselage, presents a more difficult vibration problem than the single rotor design where the rotor is mounted at the less sensitive center of the fuselage beam. Heavier tandem rotor blades produce greater excitation forces, and the lesser number of blades places this excitation closer to the blade natural frequency than for the single rotor design. The weight penalties necessary to mitigate possible one-cycle-per-

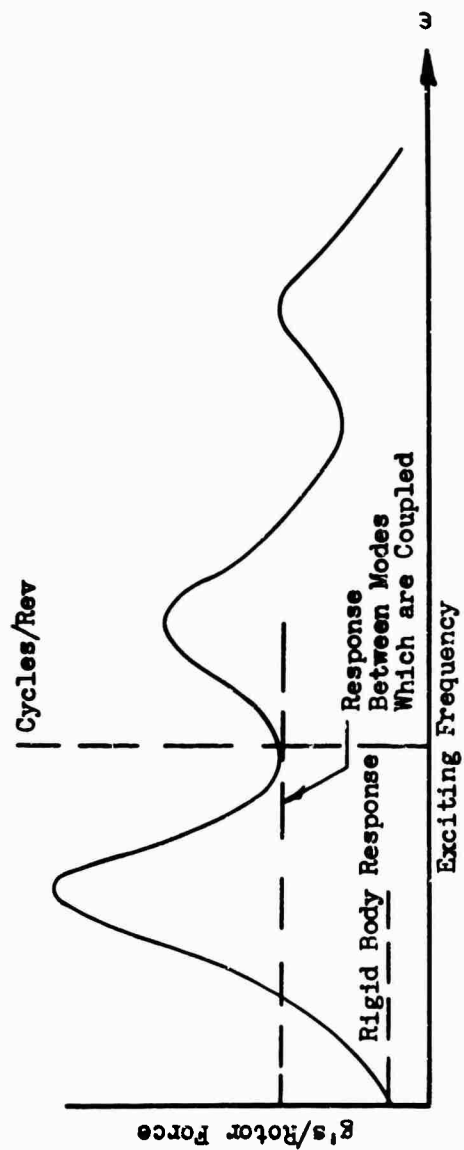


Figure 59 Typical Response Between Coupled Modes

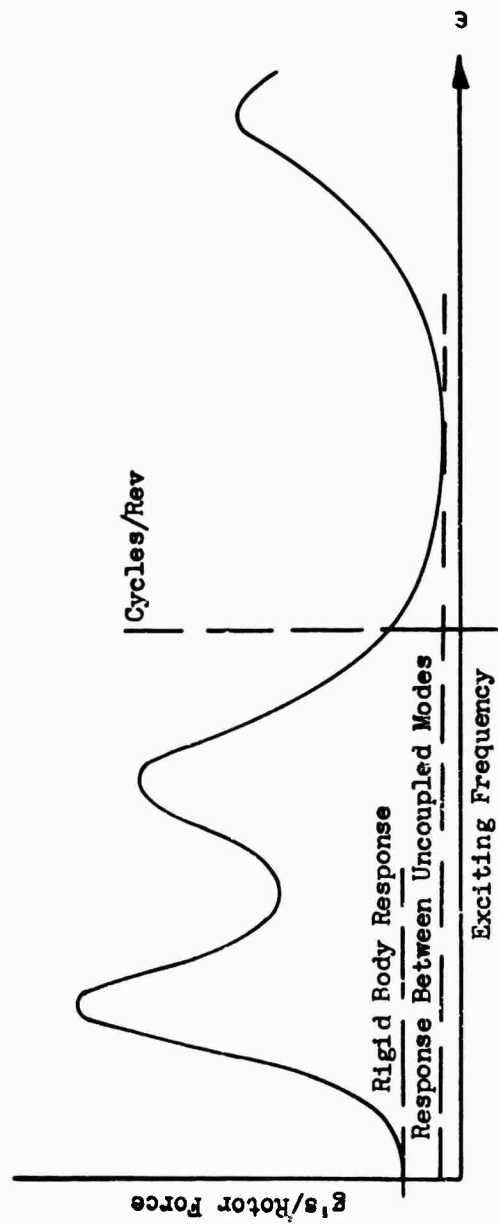


Figure 60 Typical Response Between Uncoupled Modes

revolution vibration problems encountered during detail airframe designs are generally less for the single than for the tandem rotor configuration, since stiffness in the appropriate mode is more easily obtained.

RELIABILITY

A comparison of flight safety of single and tandem helicopter rotor-drive and control configurations shows the overall risk of catastrophe to be approximately 50 percent less in the single rotor configuration. The tandem with redundant shafting, although appreciably safer than the basic tandem, requires a substantial weight increase which was not considered in the parametric study.

The following facts were the governing factors in the determination of the risks.

1. The tandem configuration has fifteen items in the rotor-drive region that are catastrophic by nature in that the rotor system will be rendered totally useless instantly or within a few seconds after failure. The overlapped rotors must remain synchronized, so that any failure in the connecting drive system is catastrophic. Incorporation of redundant shafting reduces this figure to twelve, but at the expense of four additional gearboxes and three shaft assemblies. In relation to six of these items (the rotor blades), the probability of failure has been reduced to a negligible figure by the incorporation of BIM[®]. The six-bladed single rotor configuration has eight rotor-drive system items catastrophic by nature. This number is reduced to two with BIM[®].
2. The relative safety of the mechanical flight control system slightly favors the single, for, where the tandem requires four distinct primary servo inputs all sustaining heavy flight loads and all catastrophic upon failure, the single requires three such primary servo inputs and a normally noncritical tail servo input. The single rotor configuration contains the additional items of the tail rotor system that have catastrophic implications. The catastrophic risk is minimized by providing sufficient fin area to allow adequate aircraft stability in the event of tail rotor drive/control loss at a reasonable cost in weight and complexity.

The following is a more detailed discussion of the catastrophic risk involved in each configuration. Engines, accessory gearboxes, and hydraulic portions of the flight controls have not been considered in the comparison due to the similarity that exists between the two configurations and the redundancy of the engines and hydraulic portions of the flight controls.

1. Single Main Rotor Configuration, Figure 61

Three- or four-bladed rotor heads cannot tolerate partial blade loss. However, in the two known cases of partial blade loss involving five-bladed aircraft, the rotor head has remained intact and retained, for a time, a minimum control over the aircraft. Though the six-bladed head will strengthen this margin of control to a degree that it is no longer clearly catastrophic, it is considered that the risk of catastrophe upon blade separation is very high. The risk of a blade fatigue progressing to blade separation, however, has been minimized to a negligible figure with the incorporation of the BIM[®] monitoring system, which, through a pressurized blade indication system, assures the early detection of fatigue cracks. Structural fatigue fracture of either the main rotor hub or the main shaft is clearly catastrophic. Loss of any of the main rotor control rods, linkages, or control mechanisms clearly renders the aircraft out of control. Failure statistics show that loss of components in the tail rotor power train (from main gearbox aft) or loss of tail rotor control results in a relatively small risk of catastrophe. The total number of catastrophic risk areas is thus two.

2. Tandem Rotor Configuration Without Redundant Shafting, Figure 62

Three-bladed rotor heads cannot tolerate partial blade loss. Risk of blade loss, however, is negligible due to the incorporation of BIM[®]. Structural fatigue fracture of either the forward or aft rotor hubs or shafts is clearly catastrophic. Loss of any of the forward or aft rotor control rods, linkages, or control mechanisms clearly renders the aircraft out of control. Failure of any of the power train components will immediately result in blade interference of the two rotors and is clearly catastrophic. Total number of catastrophic risk areas is thus nine.

3. Tandem Rotor Configuration With Redundant Shafting, Figure 63

Redundant shafting allows the tandem to sustain a shaft failure in the drive system without catastrophic risk, reducing the number of catastrophic risk areas to six but with a weight penalty not considered in the parametric weight equations.

The modes of failure considered are:

<u>ITEM</u>	<u>MODE</u>
1. Blade	Blade separation
2. Hub assembly	Loss of retention qualities
3. Shafts, gearboxes	Loss of continuity
4. Control mechanisms	Failure rendering a control channel inoperative

Application of failure statistics to the above listed failure modes results in the two catastrophic risk areas of the single rotor configuration yielding approximately 50 percent less overall risk than the nine areas of the tandem.

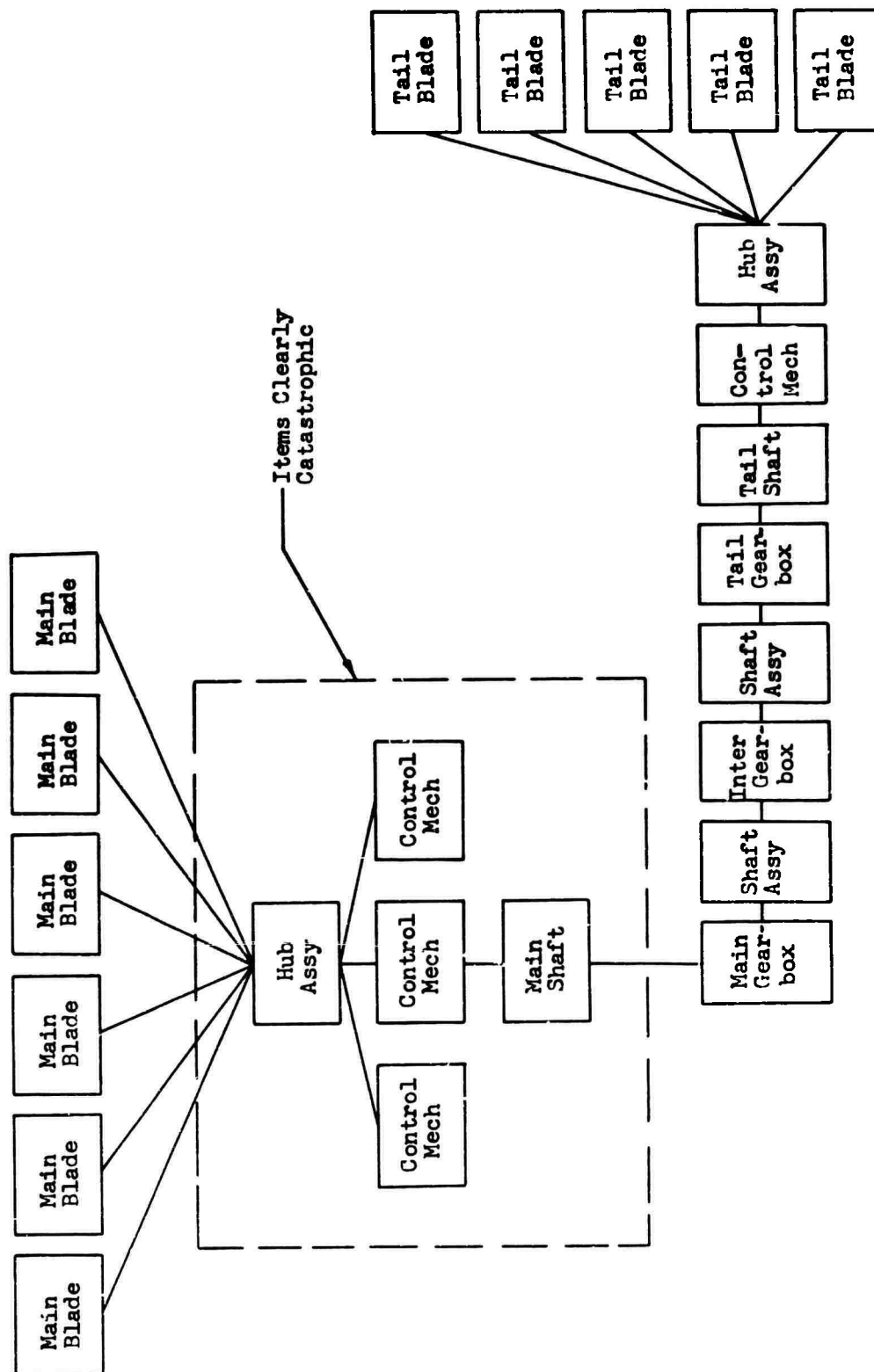


Figure 61 Rotor Drive and Control System, Single Rotor

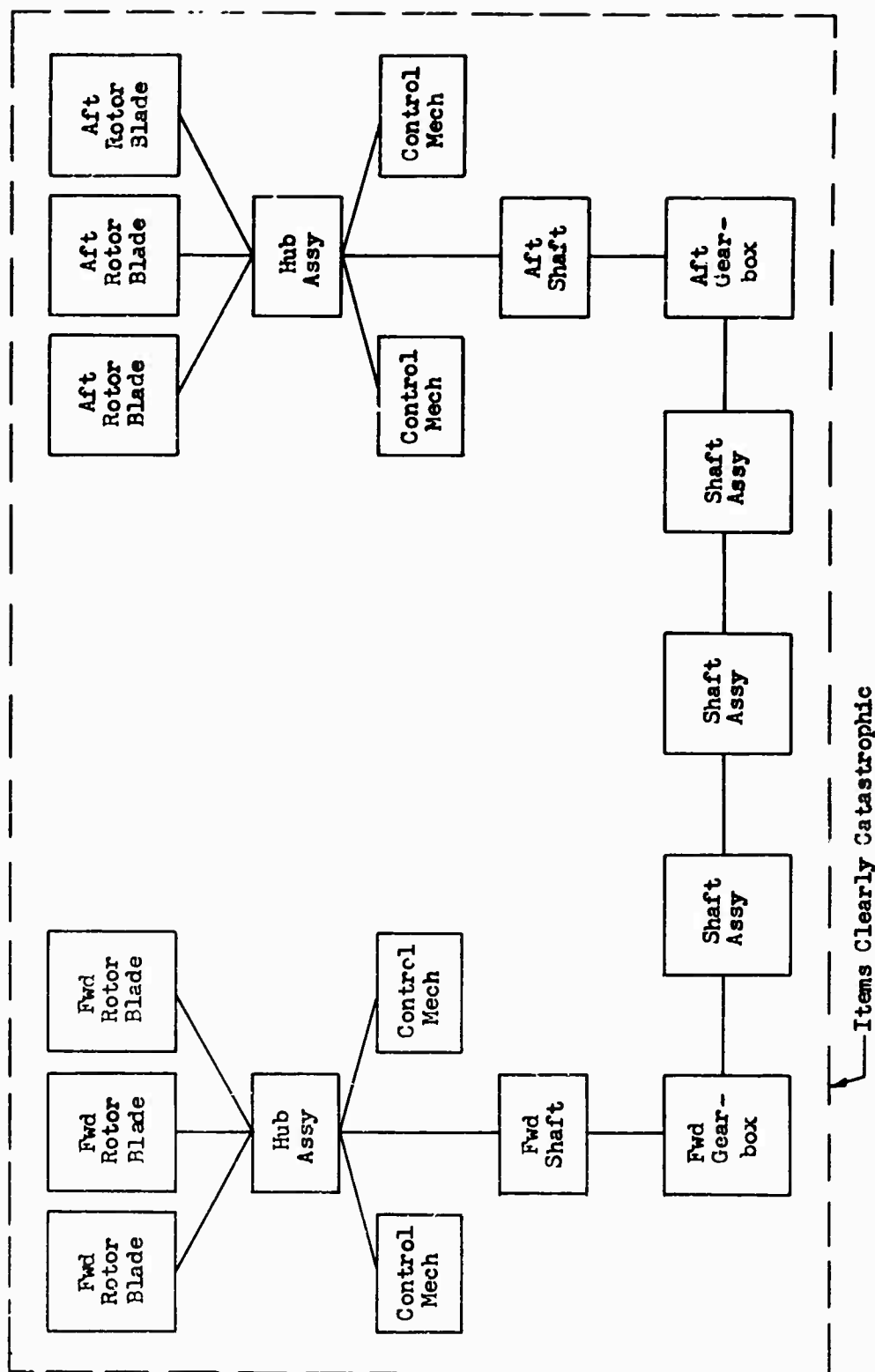


Figure 62 Rotor Drive and Control System, Tandem Rotor

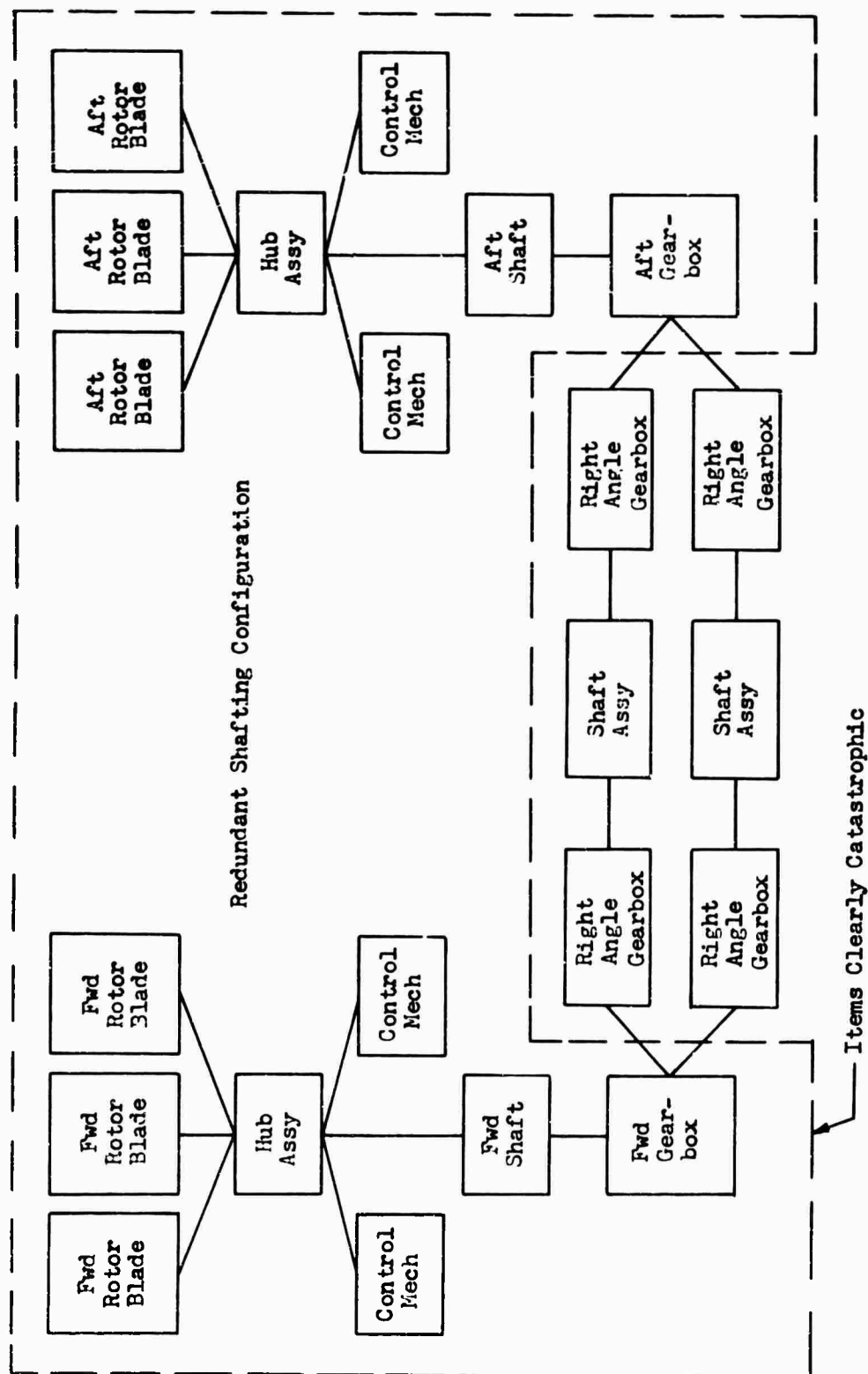


Figure 63 Rotor Drive and Control System, Redundant Tandem Rotor

FINAL CONFIGURATION SELECTION

On the basis of gross weight required to perform the design missions, and considerations of off-design performance, stability and control, vibration, and reliability, the single rotor configuration is recommended for detailed study in this contract. The relative merits of the single and tandem configurations are summarized below:

<u>Factor</u>	<u>Evaluation</u>
Design mission gross weight	Single rotor 2 percent lighter than tandem
Off-design performance	Single rotor superior by small margin
Stability and control	Single rotor superior
Reliability (catastrophic risk)	Single rotor superior

The tandem configuration has the advantage of greater compactness (with blades folded), and field maintenance is facilitated by the need to supply only one type of spare blade, as compared to the single rotor which has the same number of main rotor blades with the addition of smaller tail rotor blades. The optimized single rotor solution possesses a greater implicit confidence level, since both weight and performance uncertainties exist for low aspect ratio rotor blades and tandem rotor aerodynamic interference complicates performance and blade load analyses.

DESIGN PERTURBATIONS

Effect of Cruise Speed

The effect on payload-radius of varying the cruise speeds from those set forth for the design missions was investigated for the selected single rotor configuration. Very little improvement in payload-radius capability is obtained through speed variations, since the basic design speeds fall very close to the best range speeds at the mission weights. Higher speed cruise is of course possible, but only at the expense of reduced payload or radius.

Figure 64 shows speed versus gross weight, including best range and maximum cruise (stall-limited) speed for both loaded and unloaded drag conditions. The gross weight range for outbound and inbound legs of the basic design missions is shown, as are the design mission speeds. Figure 65 shows specific range (nautical miles per pound fuel) versus gross weight for the same speed conditions.

Figures 66 and 67 are plots of payload versus radius for takeoff gross weights representing OGE hover at (a) 6000 feet, 95 degrees Fahrenheit (65,800 pounds) and (b) sea level standard (78,750 pounds). For these weights, total hover times of 5 and 15 minutes, respectively, are assumed for consistency with the design missions. Payload is carried outbound only.

The influence of speed shown on these plots is summarized in Table XXV.

It is apparent that best range cruise improves payload-radius very little over the design mission speeds. Productivity is also relatively unaffected, since best range speed is slightly higher outbound, and slightly lower inbound, than the design speeds and yields about the same average overall speed. Some gain in productivity is possible, particularly for longer radii, by utilizing maximum cruise speed, but there is a penalty of reduced payload. It can be concluded that the design mission speeds result in a near-minimum gross weight solution for the required payload-radius capabilities.

It is noteworthy that external loading, crane-type operation considerably reduces the time required to load and unload at the start and mid-point of the missions compared to internal loading. This substantially improves the mission productivity in terms of the total time required to deliver a given amount of payload from point a to b.

Sea Level
Standard Day

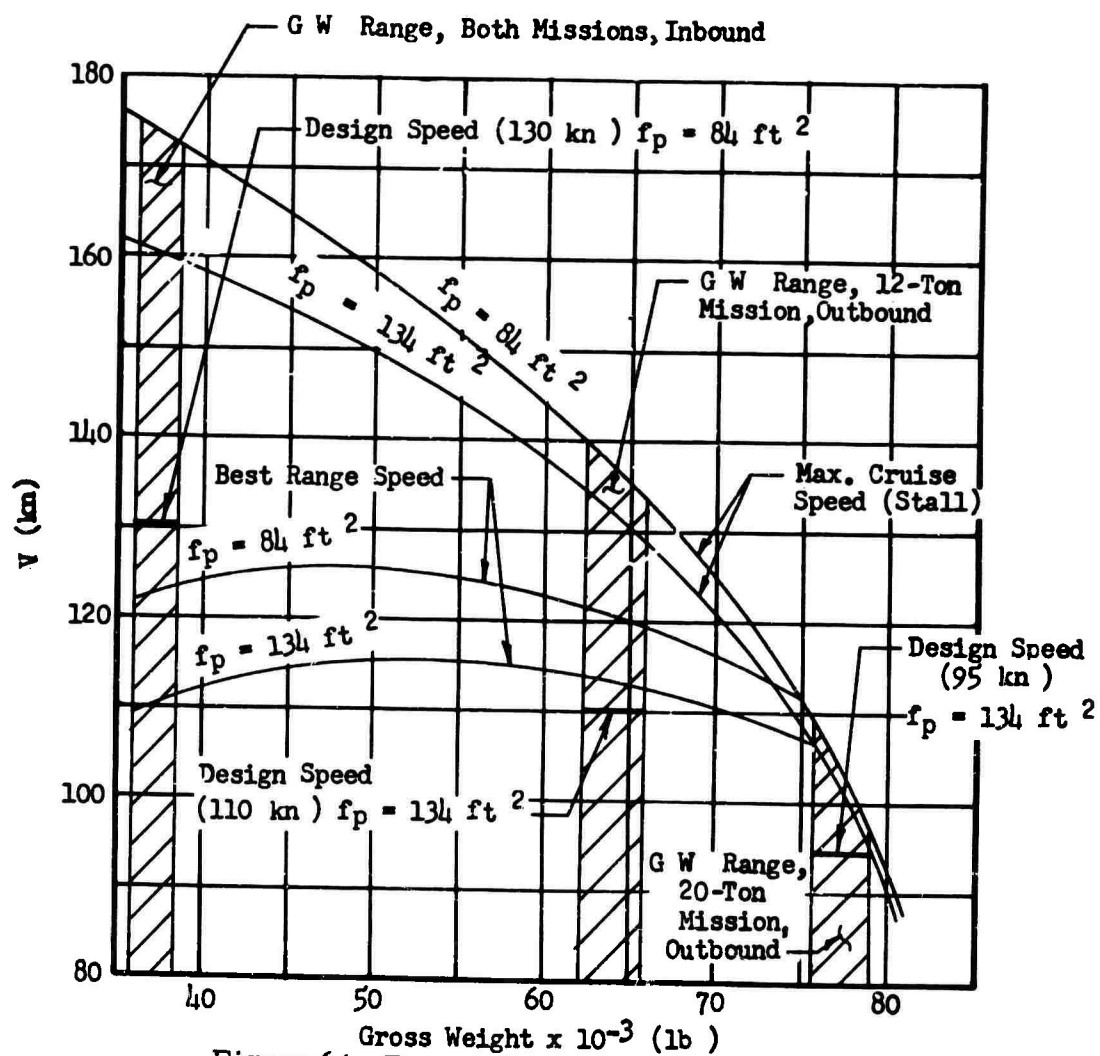


Figure 64 Forward Speed Versus Gross Weight

Sea Level Standard Day

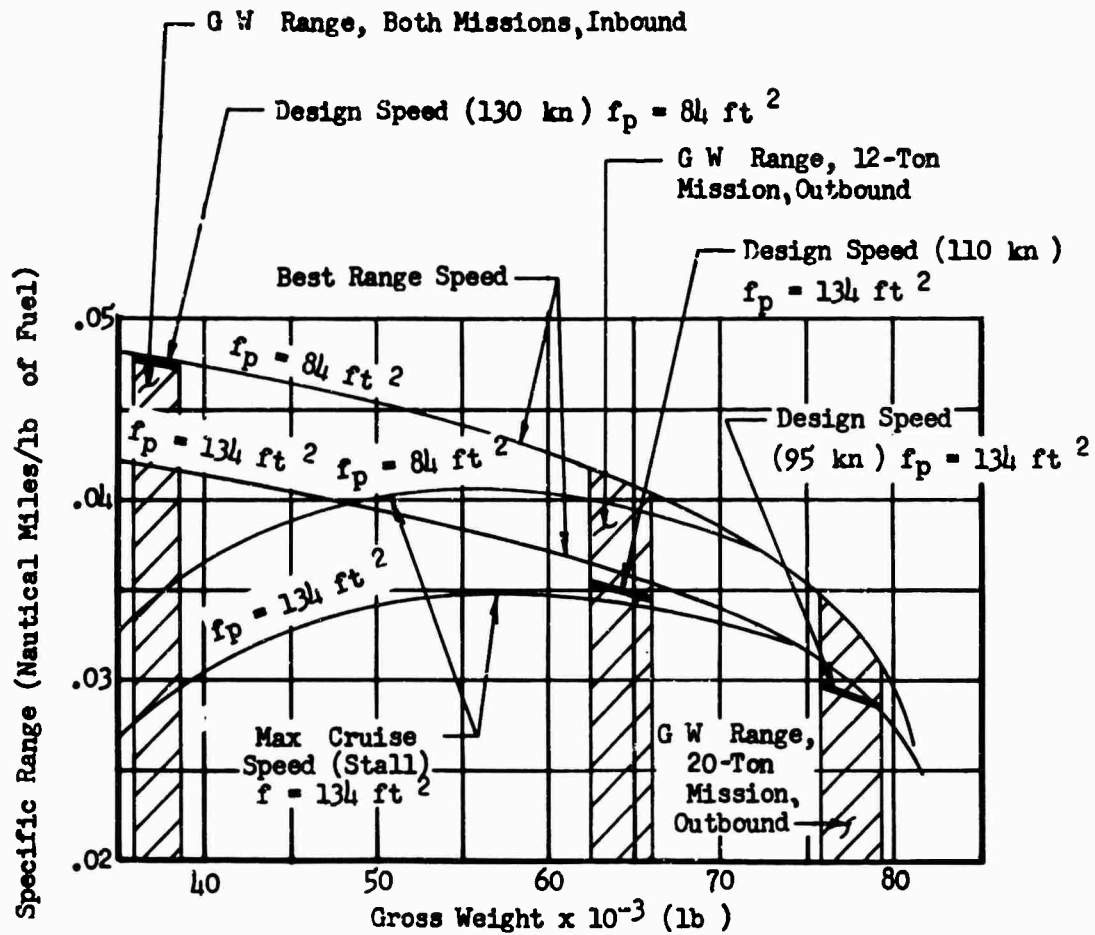


Figure 65 Specific Range Versus Gross Weight

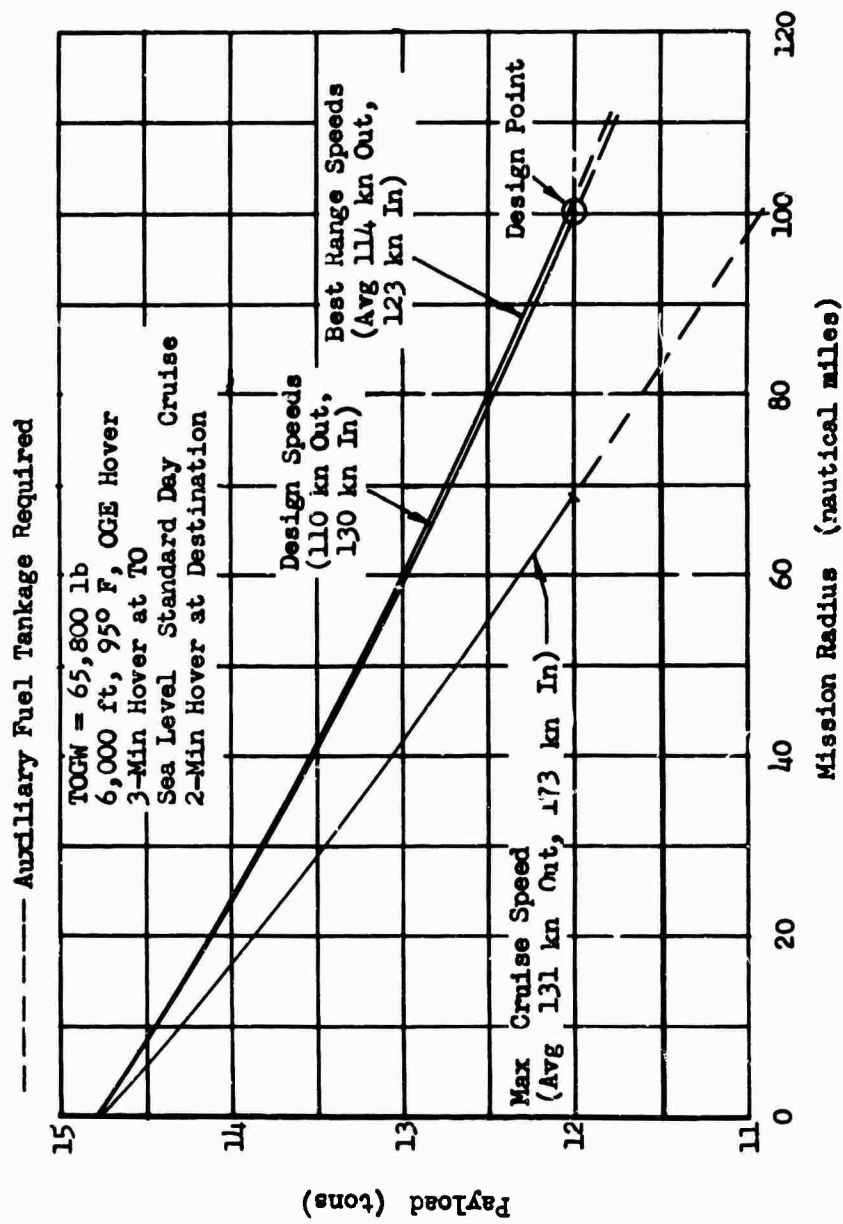


Figure 66 Payload Versus Mission Radius, 12-Ton Mission

TOGW = 78,750 lb
 Sea Level, Standard Day, OGE Hover
 5-Min Hover at TO
 Sea Level, Standard Day Cruise
 10-Min Hover at Destination

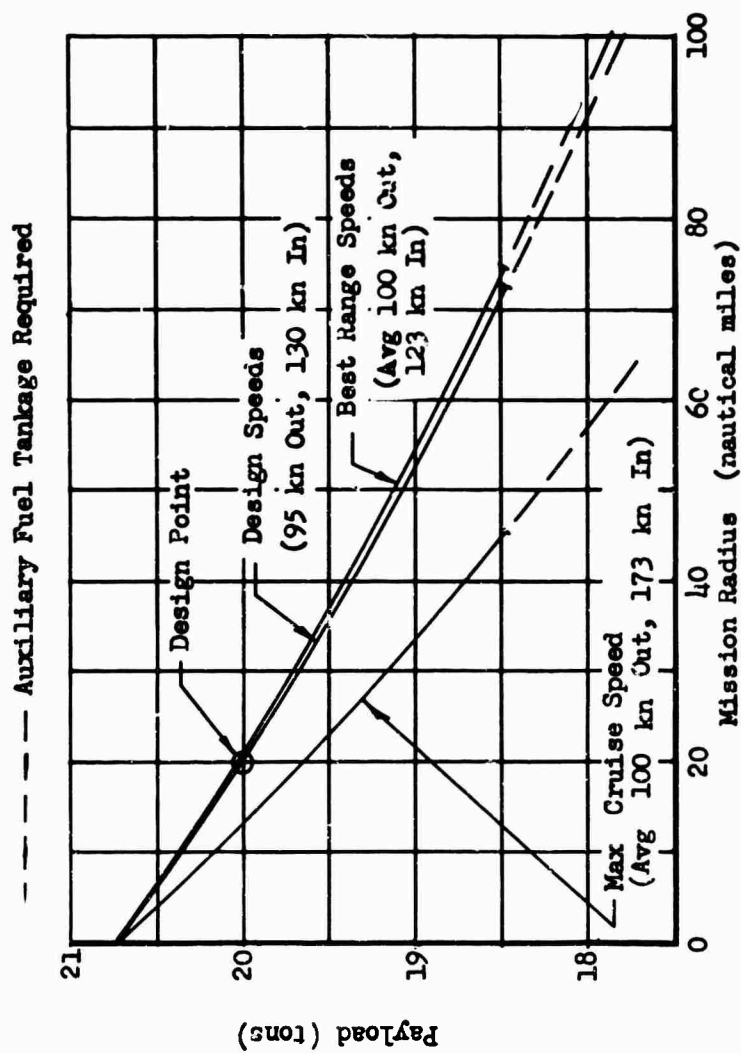


Figure 67 Payload Versus Mission Radius, 20-Ton Mission

TABLE XXV
INFLUENCE OF SPEED ON MISSION PERFORMANCE

Takeoff Hover Condition, GW	Speed Condition	Average Speed, kn out/in	Payload, tons	Radius, naut mi	Productivity (a) ton-naut mi radius hr
6000 Ft, 95°F, OGE (65, 800 lb)	Design	110/130	12.0	100	680
	Best range	114/123	12.0	101	676
	Best range	114/123	12.04	100	679
	Max cruise	131/173	12.0	69	821
	Max cruise	131/173	10.92	100 (b)	767
SLS, OGE (78, 750 lb)	Design	95/130	20.0	20	652
	Best range	98/123	20.0	21	662
	Best range	98/123	20.03	20	651
	Max cruise	98/173	20.0	13	570
	Max cruise	98/173	19.65	20	691

NOTES:

(a) Includes hover time: 5 min for low GW, 15 min for high GW

(b) Requires additional fuel tankage

Effect of Transmission Power Rating

The transmission rating assumed in the parametric analysis is equal to the power required for sea level, OGE hover at the 20-ton-mission gross weight. For the optimized configuration, this is slightly under 12,000 horsepower. Two other possible criteria are total engine power available at sea level standard day and the power required for 6000-foot, 95-degrees Fahrenheit OGE hover at the 12-ton-mission gross weight (this is higher than that for sea level standard, OGE hover at 16-ton, 20-nautical-mile-radius gross weight). Drive system weight is increased approximately .47 pound per additional horsepower for the 91.6-foot-diameter rotor. However, this weight increase requires a larger diameter rotor to meet the mission requirements, resulting in a total empty weight growth of about 2.5 times this, or 1.2 pounds per horsepower. Gross weight increases at a slightly faster rate due to the increased fuel required. Table XXVI summarizes the approximate influence of transmission power rating on weight and rotor size.

TABLE XXVI
INFLUENCE OF TRANSMISSION POWER RATING
ON WEIGHT AND ROTOR SIZE

Transmission Rating (HP)	Condition	Empty Weight (lb)	Design Gross Weight (lb)	Rotor Diameter (ft)
11,980 (assumed)	SLS, OGE hover, 20-ton GW	32,800	78,750	91.6
14,780	Full available SLS,T64/S4A HP	36,140	82,150	99.4
10,600	6000 Ft, 95°F, OGE hover, 12-ton GW	31,140	77,000	87.6

The increment in off-design performance obtained by designing transmission capability to utilize full SLS engine power is offset by a 3400-pound weight penalty and a larger overall helicopter. On the other hand, SLS OGE hover capability for the 20-ton mission at takeoff is believed to be a reasonable lower limit on usable power.

WEIGHT/SIZE GROWTH FACTORS

This writeup is intended to provide some insight into the effect of an individual component weight increment on the resulting size and weight helicopter required to perform the design missions. For a given gross weight, each additional pound of component weight represents a corresponding pound reduction in payload. As a result, gross weight must be increased to maintain required payload. However, as gross weight increases, the rotor diameter required to maintain hover capability also increases, resulting in a higher rotor system weight. In addition, those components whose weight is dependent on gross weight (ie, alighting gear, body group, etc) also become heavier. Thus, an increase in the weight of an individual component represents a substantially higher empty and gross weight increment, accompanied by a larger diameter. Table XXVII summarizes those growth factors for both the single and tandem rotor configurations.

TABLE XXVII
SUMMARY OF GROWTH FACTORS,
SINGLE AND TANDEM ROTORS

	Single	Tandem
Diameter increase per pound component weight, ft/lb	.0058	.0048
Empty weight increase per pound component weight, lb/lb	2.50	2.80
Gross weight increase per pound component weight, lb/lb	2.55	2.85

Gross weight is increased by slightly more than empty weight, since mission fuel is somewhat greater. Single and tandem rotor diameters are increased by 5.8 and 4.8 feet per 1000 pounds of component weights, respectively.

MISSION PERFORMANCE FOR DRAG (f) = 100, 200 SQUARE FEET

In fulfillment of a verbal understanding with USAAVLABS, and to facilitate comparison with competitive solutions, the HLH mission payload-radius capability of the optimized single rotor configuration with assumed parasite drag values of 200 square feet and 100 square feet (with and without external load, respectively) is presented. Since the corresponding drag values were estimated from the three-view drawing of the optimized HLH

to be 134 square feet and 84 square feet, respectively, this assumption results in payload-radius capability somewhat less than that required in the design missions and is believed to be overly conservative.

The higher drag assumption increases cruise fuel consumption by about 10 percent for the 12-ton 100-nautical-mile mission and 7 percent for the lower speed, 20-ton 20-nautical-mile mission. At the same takeoff weight, which is defined by required hover capability, this increase in fuel represents a corresponding decrease in payload for the same mission radius. Conversely, for the same payload, mission radius is reduced. Table XXVIII summarizes these trade-offs.

TABLE XXVIII
SUMMARY OF MISSION TRADE-OFFS

Takeoff GW (lb)	Takeoff Hover Condition	Drag Loaded/Unloaded (ft ²)	Mission Radius (naut mile)	Mission Payload (ton)
65, 800	6000 ft, 95°F, OGE	134/84	100.0	12.0
		200/100	100.0	11.77
			90.8	12.0
78, 750	SLS, OGE	134/84	20.0	20.0
		200/100	20.0	19.96
			18.65	20.0

Obviously, if the helicopter were to be reoptimized using the higher drag values, a large diameter, heavier solution would result in order to maintain the required hover capability for the design missions. Table XXIX shows this estimated growth

TABLE XXIX
GROWTH ESTIMATION USING HIGHER DRAG VALUES

	Drag (f) (ft ²)	
	84, 134	100, 200
Rotor diameter, ft	91.6	94.9
Empty weight, lb	32, 800	34, 220
Design gross weight, lb	78, 750	80, 200

It is noteworthy that, because of its higher gross weight to component weight growth factor, the tandem rotor configuration suffers a greater penalty (about 12 percent more) for the conservative drag assumption than does the single rotor design.

Ferry range, assuming a basic drag of 100 square feet rather than the 84 square feet derived in the study (and adding 10 square feet to both values for external fuel tankage), is reduced by about 4 percent at the same take-off weight. This results in a range of 2000 nautical miles for the single rotor configuration at a 2.0g load factor takeoff weight, which is still well above the required 1500 nautical miles.

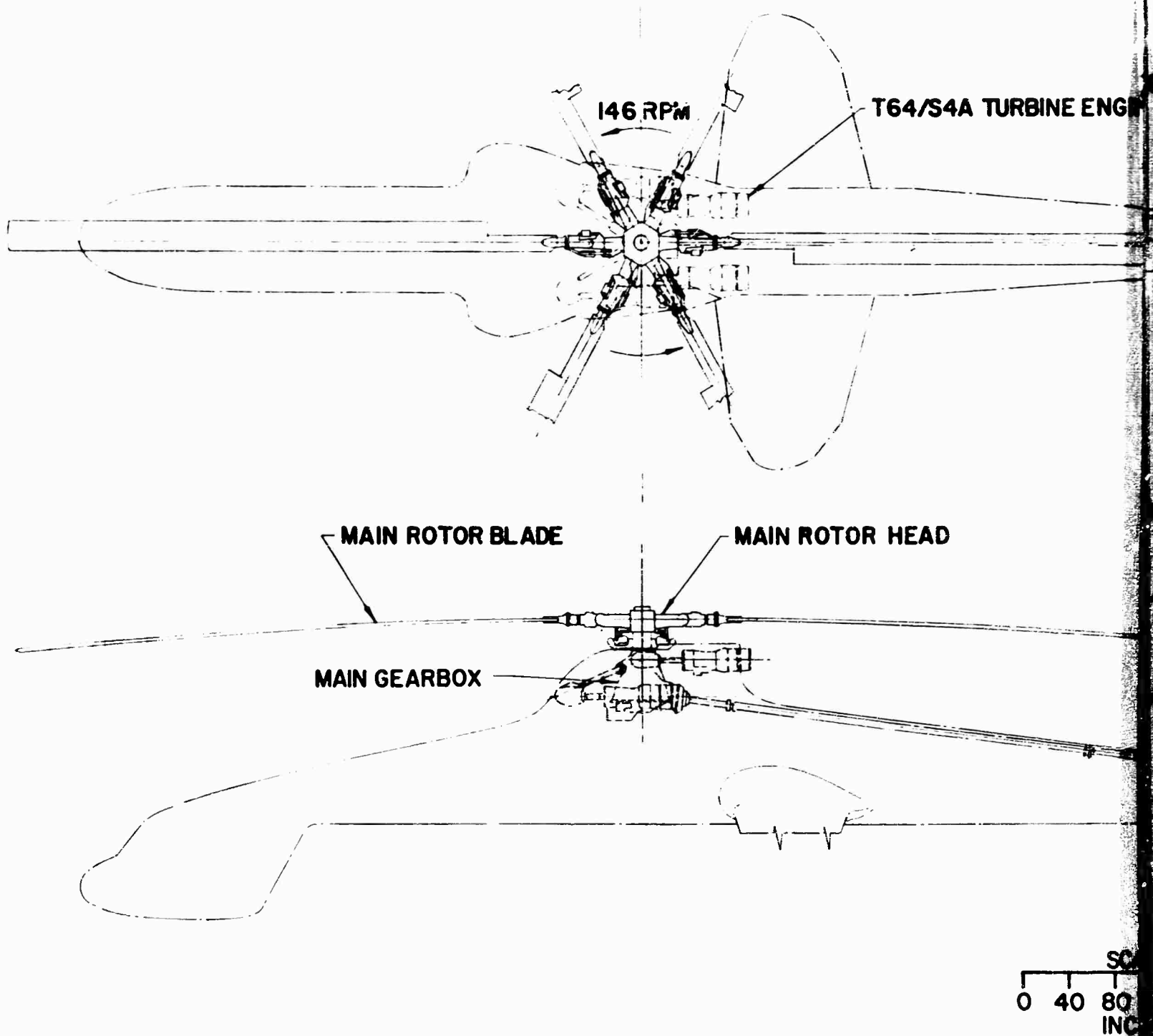
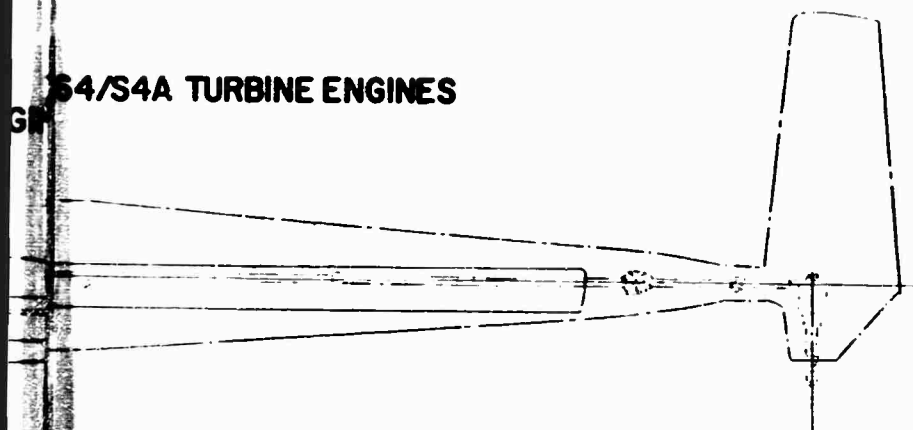
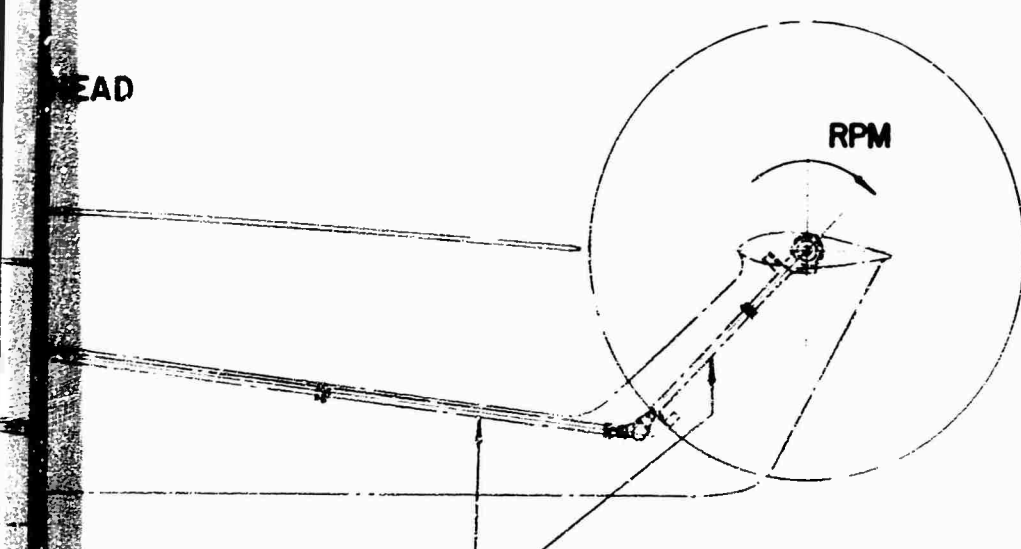


Figure 68 Dynamic System Schematic, Single Rotor,
12-20-Ton Skycrane®

GP S4/S4A TURBINE ENGINES



HEAD



TAIL ROTOR DRIVE SHAFTING

SCALE
0 40 80 120 160 200
INCHES

REPORT NO.	10-100-1000	FIGURE NO.	
DESIGNER	J. K. Kopp	SYSTEM	
TECHNICAL	J. K. Kopp	ADJ. DESIGN	
		PRD. DESIGN	
		DESIGNER	J. K. Kopp
		DATE	
REPORT NO.		FIGURE NO.	
ROTOR SYSTEM SCHEMATIC SINGLE ROTOR 12-20 TON SKYCRANE			
Sikorsky Aircraft		DS-137-01-2	
U		SCALE 1/40	REV.
A		5000	0

B

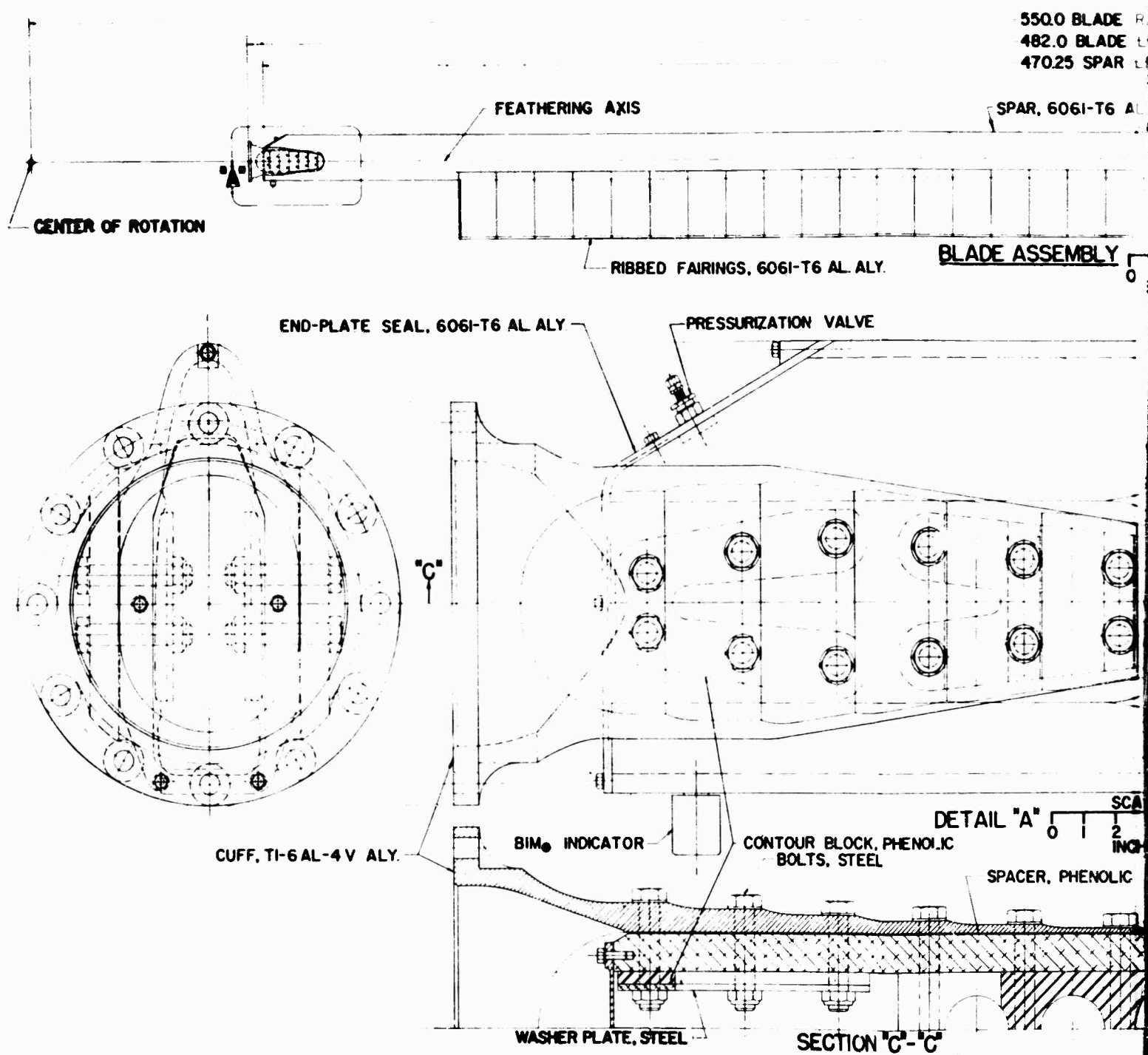


Figure 69 Flex-Rotor™ Blade, 12-20-Ton Skycrane®

550.0 BLADE RADIUS
482.0 BLADE LENGTH
470.25 SPAR LENGTH

SPAR, 6061-T6 AL. ALY.

ABRASION SHIELD, 302 STAINLESS STEEL

BED FAIRINGS, 6061-T6 AL. ALY.

BLADE ASSEMBLY

SCALE

0 10 20 30 40 50
INCHES

PRESSURIZATION VALVE

COUNTERWEIGHTS, STEEL

BALANCE WEIGHT RETAINING BLOCK, 6061-T6 AL. ALY.
COUNTERWEIGHT RETAINING BLOCK, 6061-T6 AL. ALY.
BM₂ SEAL

RIVETS, AL

FEATHERING

SEAL RETAINER, 6061-T6 AL. ALY.

BALANCE WEIGHT RETAINING BLOCK, 6061-T6 AL. ALY.

"C"

FEATHERING AXIS

31.0 CHORD

DETAIL "A"

SCALE

0 1 2 3 4 5
INCHES

CONTOUR BLOCK, PHENOLIC
BOLTS, STEEL

SPACER, PHENOLIC

SPACER, PHENOLIC

DETAIL "B"

SCALE

0 5
INCHES

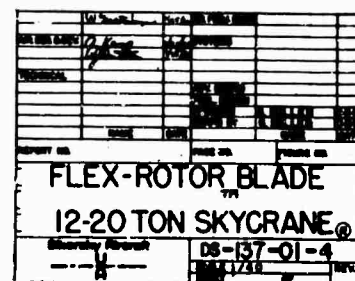
SECTION "C-C"

STEEL

ane ©

B

02 STAINLESS STEEL



PRELIMINARY DESIGN AND STRUCTURAL ANALYSIS

BLADE DESIGN

Construction

Figure 68 shows the general arrangement of the rotor system and Figure 69 shows the detailed breakdown of the blade parts. The blade, which is essentially all metal, has a structure consisting of two primary members, a spar which runs nearly the full length of the blade, and a cuff which retains the spar and transfers loads to the rotor head. Four secondary structural members retain leading edge counterweights and shim weights used for spanwise and chordwise balance. All other parts are non-structural and are included for balancing, abrasion-resistance, sealing, or aerodynamic purposes. They consist of trailing edge fairings, root and spacer blocks, a tip cap, leading edge counterweights, outboard shim weights, abrasion strips, and spar and fairing seals.

The spar, which is 6061-T6 aluminum alloy material extruded in the shape of a hollow "D", forms the leading edge of the airfoil section and is the main structural member (see Figure 70). It has a constant inner contour

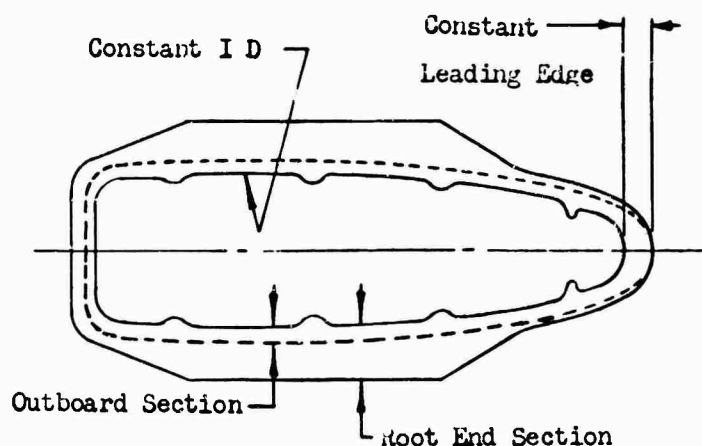


Figure 70 Spar Section

over the full length of the blade, while the outer contour varies slightly to allow the sidewall and backwall thicknesses to increase from thin sections at the outboard end to an appropriately thick root end of sufficient strength to carry all centrifugal, torsional, and bending stresses.

The leading edge thickness is constant over the entire spar. The blade chord is constant, while the airfoil thickness increases gradually from 12 percent of chord at the outboard end to 13.1 percent of chord at the termination of the airfoil. A short tip cap covers the outboard end of the spar which retains the balance weights, while an end plate seals the inboard end of the spar. An abrasion strip is structurally bonded to the outboard portion of the leading edge of the spar; a short abrasion strip is also bonded to the leading edge of the tip cap.

The aft portion of the airfoil contour is formed by sheet metal fairings bonded to the aft portion of the spar. Closely spaced reinforcing ribs stiffen the fairings and prevent local panel flutter. The fairings are non-structural units, each one 12 inches long, consisting of 6061-T6 aluminum alloy formed ribs and outer skins adhesively bonded together (see Figures 71 and 72). Spaces between fairings are sealed with wedges of closed cell, nitrogen-filled neoprene sponge. The inboard end of the

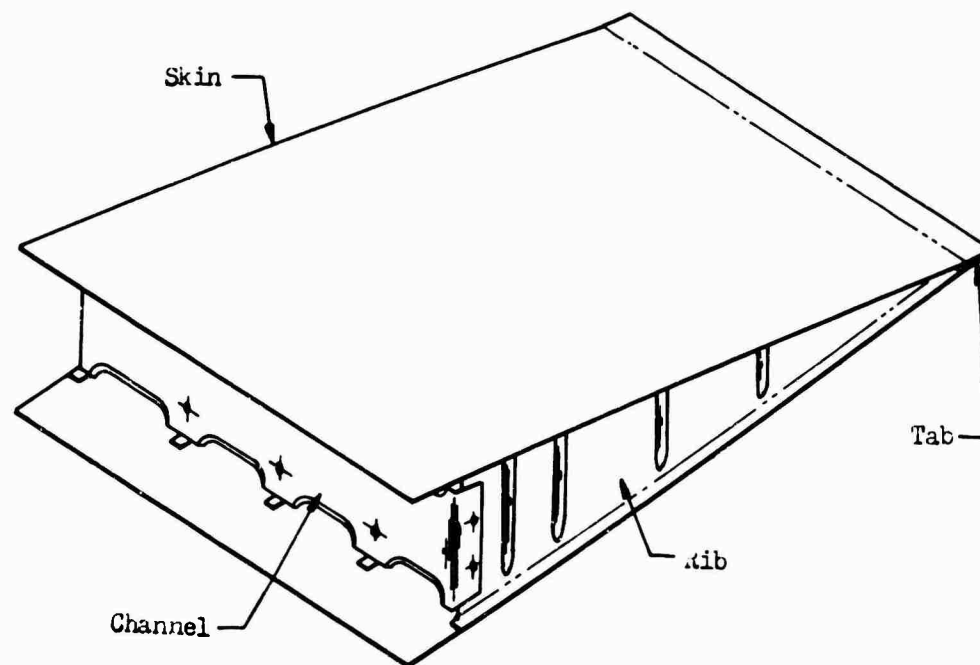


Figure 71 Fairing

blade has no fairings. In this region the spar thickness increases gradually to a thick attachment region.

The cuff, made of Ti-6Al-4V alloy, is retained to the root end of the spar by six bolts loaded in double shear and twelve bolts loaded in single

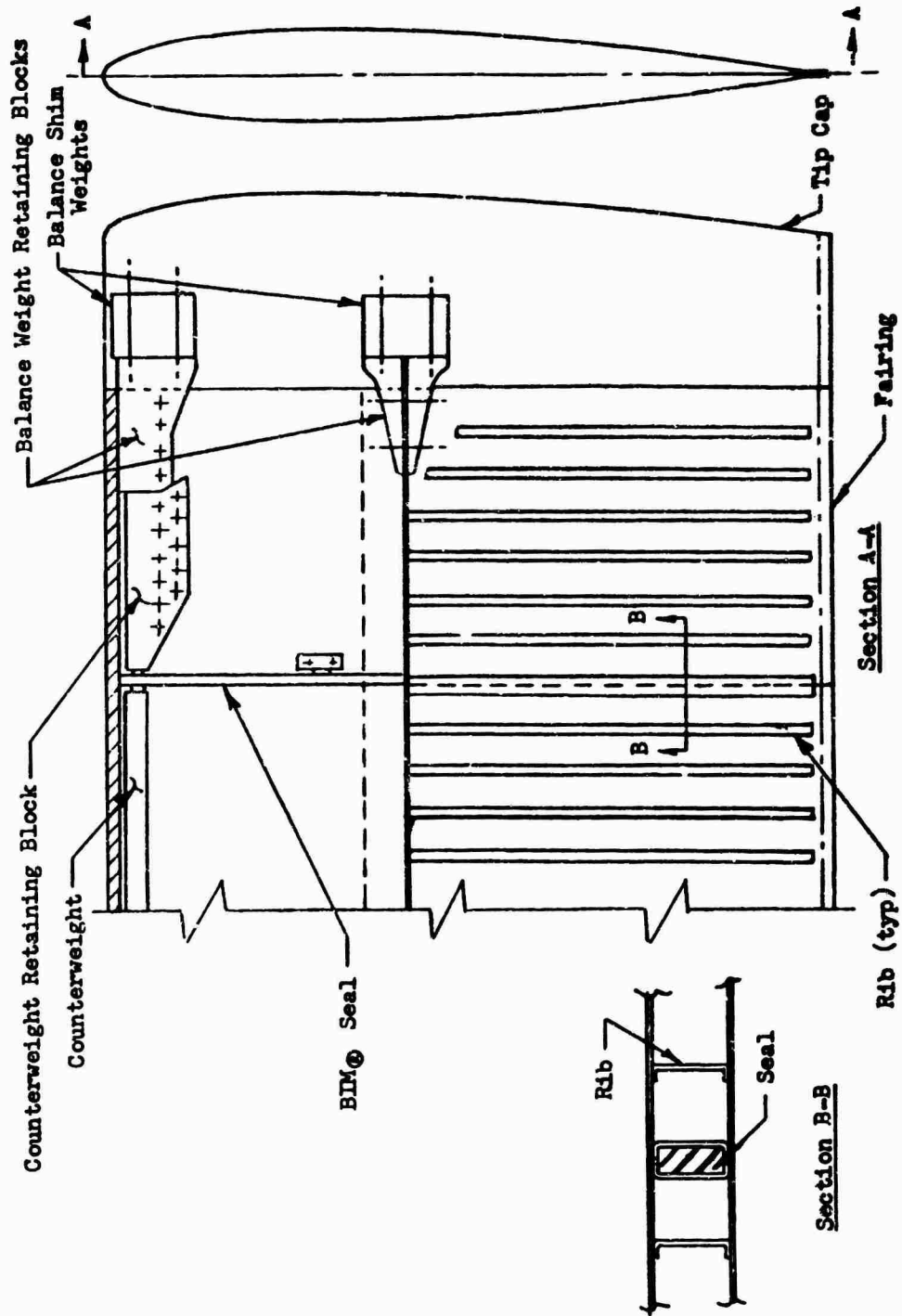
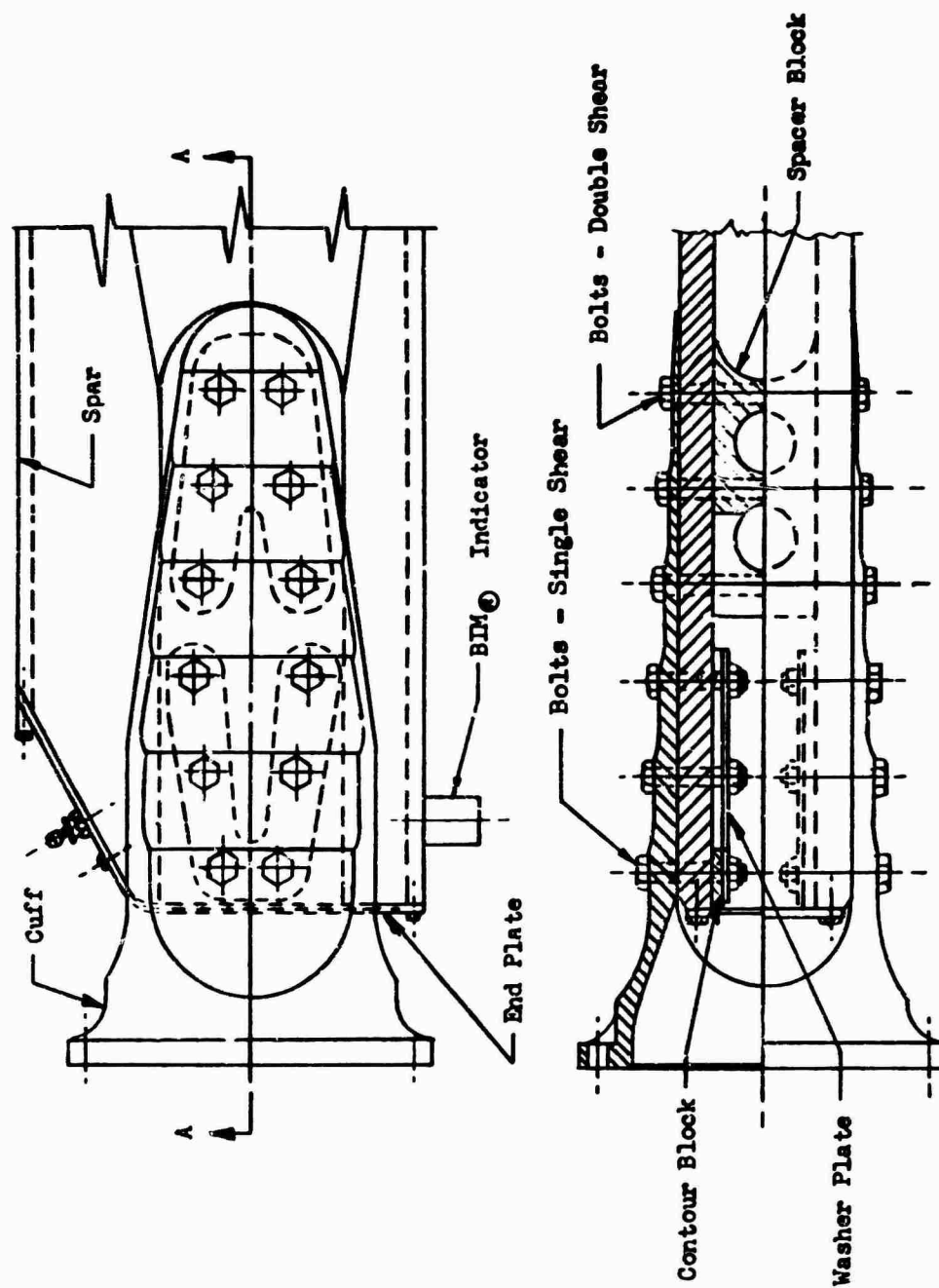


Figure 72 Blade Tip Assembly



Section A-A
Figure 73 Cuff-Spar Attachment

shear (see Figure 73). The cuff plates are tapered to distribute the centrifugal force of the blade in approximately equal shear loads to all of the bolts. The inboard end of the cuff has a circular flange which is bolted to the rotor head.

Nonstructural counterweights are installed in the leading edge of the spar (Figure 74). They are steel bars 12 inches long, each covered with a molded-on jacket of rubber to allow an interference fit in the spar

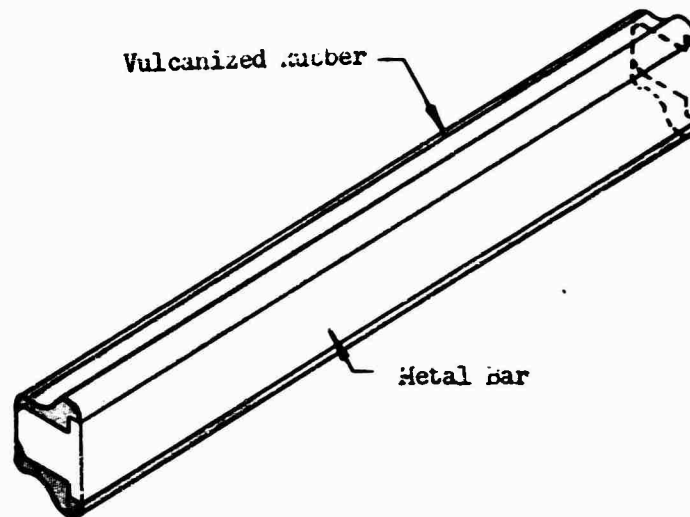


Figure 74 Counterweight

without metal-to-metal contact. These counterweights provide the capability to balance each section of the blade about the feathering axis, different weights being used as required. Longitudinal beads in the extruded inner contour of the spar hold the counterweight in position, while their centrifugal force is reacted by a retaining block riveted in the spar near the tip.

At the blade tip end (Figure 72), shim weights used to balance each blade against a master are retained by aluminum alloy brackets. The forward bracket is riveted to the nose of the spar, while the aft brackets are secured with bolts to the backwall of the spar. The tip cap is a non-structural fairing formed from a chem-milled aluminum alloy sheet. Each cap is statically balanced to a standard moment to permit interchangeability.

The blade is equipped with Sikorsky's structural monitoring device, BIM®. The blade spar is sealed and pressurized from its root end to a point just inboard of the counterweight retaining block (Figure 75).

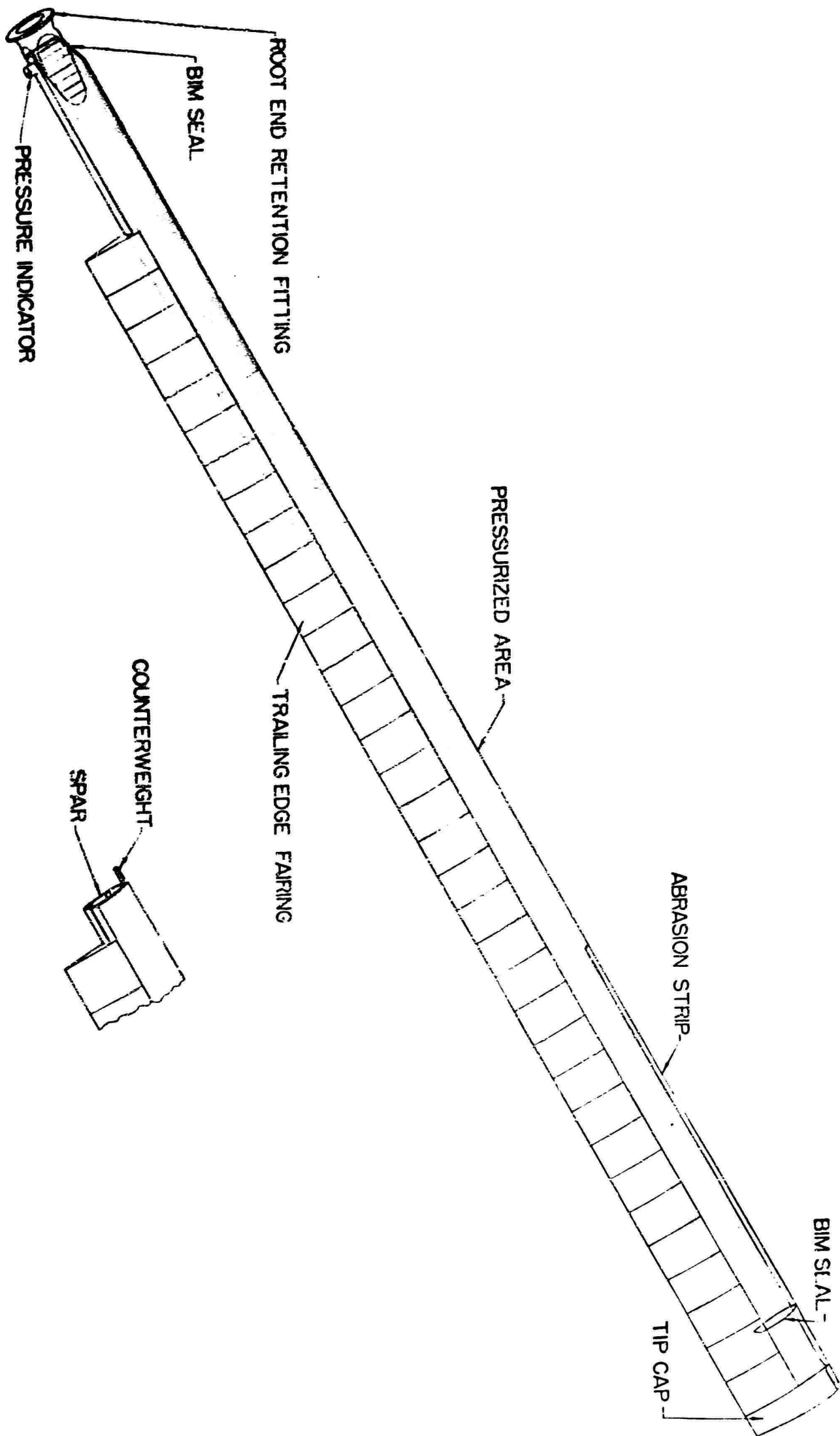


Figure 75 Flex-Rotor™ Pressurized Blade,
12-20-Ton Skycrane®

A device to indicate pressure loss visually, by showing red, is installed near the root end, where it is visible from the ground.

Design Philosophy

The blade design is dictated primarily by reliability and stability requirements, which were systematically applied in a process of elimination, to determine the structural scheme.

The structure is exposed to dynamic and aerodynamic loadings resulting from its rotational, flapping, and translational motions, while the non-structural components serve mainly to fair the blade to an airfoil shape capable of generating lift and propulsive forces to maneuver and support the aircraft. The primary loadings are tension, flexure in two planes, and torsion. The structure which reacts these loads must be light, feasible to manufacture to close tolerances and high quality standards, readily inspectable, and capable of fabrication with prescribed spanwise variations in its structural properties. While a few different types of construction fill all of these requirements well, a close examination of some of the more subtle points of blade design discloses that the field of satisfactory design solutions is narrow.

Before the structural scheme can be selected, the various axes of the blade must first be located. Since the airfoil envelope is symmetrical about the mean chord, and since no significant advantages can be gained by placing the material asymmetrically about the mean chord, this line is taken as the chordwise centerline of symmetry of all sections of the blade structure. This leaves the axes perpendicular to the mean chord to be located: the flexural (or neutral) axis for edgewise bending, the shear center, the feathering axis, the center of tensile restraint, and the mass centroid (or center of gravity) of the entire blade.

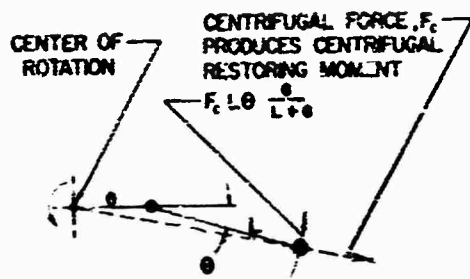
Flutter avoidance requires that all vibratory forces act approximately through the center of feathering motion of the blade. At any section, feathering motion is a combination of motion about the feathering hinge bearings of the rotor head and torsional deflection of the part of the blade inboard of the section being considered. The coincidence of loads with the center of feathering motion thus demands, first, that the structural shear center and feathering hinge axis coincide. Aerodynamic transients act through the aerodynamic center, located at 25 percent of chord. Dynamic (or inertial) transients act through the combined mass centroid of the structural and nonstructural components, at any section. Thus, the second step is to place the mass centroid of every section at the aerodynamic center, and the third step is to merge the feathering/shear center axis and aerodynamic center/mass centroid axis together at 25 percent of chord. The coincidence of these axes can be approximate,

with the closeness of the approximation depending mostly on the torsional stiffness, which in turn depends strongly on the blade aspect ratio.

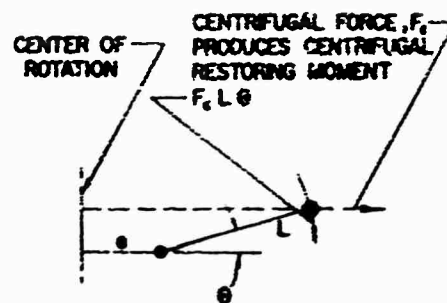
The tensile reaction required to equalize centrifugal force is most conventionally located in line with the feathering hinge to minimize the bending moments in the hinge components. This implies coincidence of rotor head hinge axes and also locates the axis of tensile forces along the 25-percent-chord line by acting through the mass centroidal axis, as would be expected. With this arrangement, the only way for a straight blade to stay straight under centrifugal tension is for the flexural axis of each section to be at 25 percent chord also. As in the flutter consideration, the coincidence can be approximate, with aspect ratio being the primary indicator of how closely the approximation must approach the ideal at any section.

The cluster of points at 25 percent chord places severe restrictions on the structural schemes that can be used. For example, the coincidence of flexural axis and shear center rules out the use of a C-shaped spar, which could easily be designed with a flexural axis at 25 percent chord, but would then have a shear center outside the airfoil section, ahead of the leading edge.

Because the cyclic bending moments result from inertial effects and airloads, they tend to vary in proportion to blade stiffness. If the blade were infinitely flexible, every section of the blade would be able to assume a position in line with the resultant of the dynamic and aerodynamic loads on it; no bending moments would be generated, nor would any be required to equilibrate the blade. Conversely, a very stiff blade would experience very large cyclic bending moments. It should also be noted that transverse loads on the blade are not reacted by bending moments alone. The stiffness of the rotating blade is, in fact, largely due to centrifugal force, which tends to pull the blade out straight. This stiffening effect does not contribute equally to flatwise and edgewise stiffness; as shown in Figure 76, any mass deflected through equal cone and lag angles from a radial position experiences a stronger centrifugal restoring moment in the vertical plane of rotation. It follows that an appropriate selection of relative blade flexural stiffnesses would be a large edgewise stiffness (to combine with a small in-plane centrifugal restoring moment) and a small flatwise stiffness (to combine with a large vertical plane centrifugal restoring moment). This, of course, implies that the structural portion of the blade should be wider in the chordwise direction than in the direction perpendicular to the chord; the desired solution is not a round tube, a square box beam, or a slender rod.



Point Mass Displaced in Plane of Rotation



Point Mass Displaced out of Plane of Rotation

Figure 76

The combination of flexural and torsional loads favors the use of a monocoque structure or a very close approximation of a monocoque structure to place the material as far away as possible from the neutral axis (See Figure 77). Certainly the simplest monocoque is a thin-walled member of uniform wall thickness, occupying the full airfoil

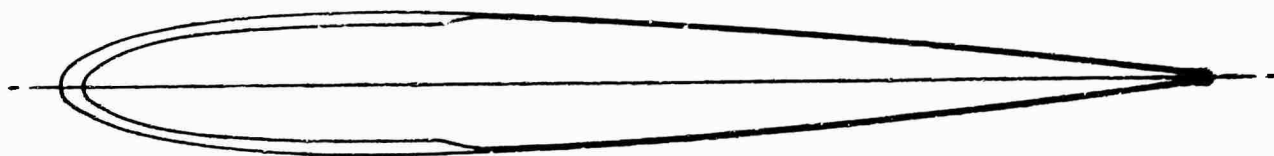


Figure 77 Full Span Monocoque Blade Structure

contour. This is immediately found deficient, in that its centroid is at about 45 percent chord. Adding material to the nose and thinning down the tail corrects the centroid to 25 percent chord.

The structure now looks good for flatwise bending, but edgewise bending produces high stresses at the trailing edge. In this plane, the knife-edged beam is exactly opposite to the I-beam philosophy of putting most of

the material as far as possible from the neutral axis. It is, in fact, like an I-beam lying on its side. The logical remedy is to pull in on the aft extremity of the structure, forming a "D" section. This reduces the edgewise moment of inertia, and thus reduces the bending moments; but if the structure now extends about 15 percent chord aft of the neutral axis (as compared to 75 percent aft of the axis in the full-chord monocoque), the edgewise bending stresses at the aft of the structure have been reduced about 80 percent. Higher edgewise stresses can be tolerated at the nose, since flatwise bending produces lower stresses there than at the aft corners. With this configuration of the blade spar, the ratio of edgewise to flatwise stiffness is about 8:1, which is appropriate for the HLH application.

The aft end of the blade now needs to be faired to the proper airfoil shape, but the fairing must be nonstructural; if a continuous fairing were added, it would undo all of the advantage gained by switching from a full-chord monocoque to a 40-percent-chord "D" spar. To prevent the trailing edge from reacting edgewise moments, it is segmented into individual fairings 12 inches long, separated by elastomeric blocks which also prevent airflow between top and bottom surfaces of the airfoil at the pocket joints.

The addition of nonstructural fairings moves the mass centroid aft of 25 percent chord. This cannot be balanced with structural mass at the leading edge, however, or the flexural axis of the spar will be displaced. A nonstructural leading edge counterweight is therefore used, supported in the spar by a vulcanized elastomeric jacket.

Material selection for the resulting design was accomplished by trade-off studies. Aluminum alloy 6061-T6 was selected for the spar, largely for its ability to perform well in adverse environmental conditions and for its excellent crack propagation resistance. The same alloy was selected for the fairing skins and ribs, positively eliminating corrosion and differential thermal expansion due to use of dissimilar metals. Each pocket is bonded together and then bonded to the spar to accomplish an efficient attachment without introducing stress concentrations from mechanical fasteners.

Operations in heavily wooded and jungle areas expose the blades to the possibility of frequent impacts with various foreign objects, ranging in size from tiny dust specks to large tree trunks. It is clearly beyond the state of the art to design an aircraft that can safely be flown head on into a stone wall; however, normal environmental hazards have been a primary factor in establishing the design of the outboard portion of the blade, with the object of allowing minor impacts to be treated as normal operation and allowing repair of heavy impact damage without replacing

blades. Only repeated contact with large, stationary objects should necessitate blade replacement, but the aircraft should still be flyable after all but the extreme cases of repeated impacts.

Protection against damage by impacts with rain, sand, small gravel particles, and leaves and twigs of trees accidentally contacted in nap-of-the-earth operation has been provided by leading edge reinforcement. The leading edge of the spar is .5 inch thick, and the outboard end of the blade is covered with a strip of 1/4 hard, type 302 stainless steel .020 inch thick.

In the event of a solid impact with a large object, the tip cap is designed to deform or break away without causing any serious damage to the spar. The tip cap can be replaced in the field. The shim weight retaining hardware is designed to break away from the spar without disturbing the leading edge counterweight retaining block. This type of damage leaves the aircraft flyable but requires blade replacement.

The design feature most important to the reliability of the HLH blade is the BIM® system, which constantly inspects the condition of the blade spar, providing a complete check of structural integrity at a glance. BIM® was developed to provide a continuous indication of the structural integrity of the blade. With the BIM® system, a main rotor blade is continued in service as long as the indicator shows that it is structurally sound. Arbitrary retirement life is eliminated. The highest degree of rotor blade reliability and lowest rotor blade cost are thus achieved. The philosophy rests on making an evaluation of the condition of each individual blade, based on an actual structural inspection, rather than on judging a large population of blades on the basis of statistical calculations, as would be necessary under the "safe-life" concept. By inspecting each blade, the using unit can reach a valid conclusion on its condition, without assumptions of the effect of operating conditions, material composition, loading history, manufacturing tolerances, or any of the other variables that may make two apparently identical components behave differently.

The concept of BIM® is quite simple. The blade is sealed and pressurized with dry nitrogen. Before each flight, the pressure indicators are visually checked. No judgment is required; the indicators show either white (normal) or red (Figure 78). Even persons with poor color perception can tell the difference at a glance. The indicators can be observed from the ground on a walk-around inspection and visual inspection of the whole blade is not required. The reliability of a blade is not dependent on the accuracy of logging and totaling of flight hours, nor on the judgment used in evaluating the severity of overspeeds and severe maneuvers, nor on the proficiency employed in the application of

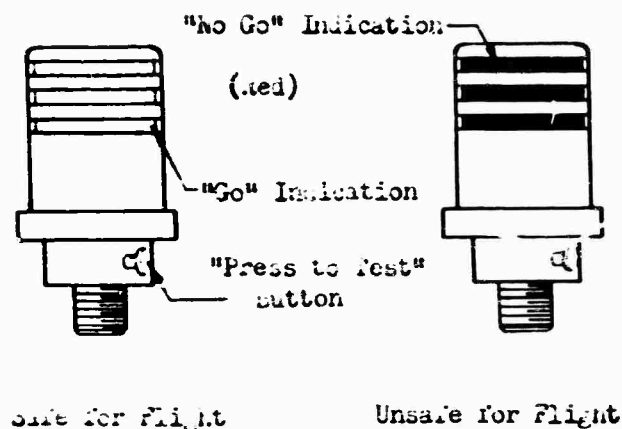


Figure 78 BIM[®] Indicator

delicate instruments on intricate test procedures. The effect of logistics can be deduced from the fact that most blades will outlast the aircraft on which they are delivered, while under the "safe-life" concept two or three sets of blades will be required during the useful life of the aircraft under the same conditions.

During the development of the BIM[®] concept, it was necessary to substantiate four basic premises on which the inspection is based: (a) Any defect capable of destroying the blade's usefulness will create a discernible leak in the sealed cavity; (b) Leaks can be detected reliably by a simple indicator; (c) Sufficient time will elapse from indication to fracture so that a mission can be completed even though a defect is indicated at the instant of start-up; (d) Sealing methods and indicator characteristics of sufficient quality can be applied to keep false indications to a tolerably low level, thereby safeguarding the logistics advantages of BIM[®] and simultaneously maintaining personnel confidence in the system.

The first premise was satisfied inductively. The behavior of fatigue cracks in metal blade spars has been observed carefully during approximately 1,000 full-size spar fatigue tests conducted by Sikorsky Aircraft. In every case, the crack was observed to break through the wall, well before fracture of the spar. Thus, it was concluded that leak detection is a valid inspection tool.

Satisfactory leak detection indicators have required extensive testing and development. Simple, positive, reliable, lightweight indicators are tailored to the volume of the spar, so that the pressure loss corresponding to the presence of a crack of noncritical length will be detected. Tem-

perature compensation and absolute pressure indication are obtained by comparing the spar cavity pressure with the pressure in a reference volume within the indicator. A "press-to-test" feature is incorporated which isolates the indicator from the spar cavity and then reduces the sensed pressure to actuate the indicator. The test is performed by one man, with no tools, and consumes about 10 seconds per blade.

The crack propagation rates of 6061-T6 aluminum alloy blade spars have been determined by over 300 full-size spar fatigue tests conducted during the past 16 years. Testing of small plate specimens has also been conducted under USAAVLABS sponsorship. Other material was compared to 6061-T6 aluminum alloy. It was found that 6061-T6 extrusions, procured to Sikorsky Aircraft's rigid procurement specifications, provided longer crack propagation time than any other material (for more than enough time to get the aircraft back from the longest transport mission contemplated).

The fourth premise, that the blade can be sealed well enough to prevent false indications, demands that almost perfect sealing be achieved. The amount of leakage normally experienced in a rubber tire just because of the permeability of the rubber cannot be tolerated in a BIM® equipped blade. The seals used on the HLH blade consist of a plate screwed and bonded to the root end and a rubber-lipped plate sealed into the blade tip end with a pourable, elastomeric sealing compound. The techniques of design and application of the tip-end seal have been carefully evolved by comparative testing from six earlier seal types. The sealing of the cuff attachment bolts is a more delicate consideration, since the sealing device must not preclude continuous inspection of the attachment region. This is accomplished by phenolic spacer blocks with slightly oversize holes, filled with an extrudable elastomeric sealant. Because the sealant covers only that portion of the spar immediately adjacent to the bolts, defects in the bolt region can be detected satisfactorily. BIM® sealing and indicating methods are covered by U. S. Patents 2,134,445; 3,136,369; and 3,168,144; with other patents pending.

ROTOR HEAD DESIGN

Construction

The rotor head assembly, mounted directly above the main gearbox, consists of a hub assembly and a control system swashplate assembly (Figures 79 through 89).

Hub Assembly

Six equally spaced conical members are rigidly fastened to the outboard faces of the gearbox main rotor shaft (Figures 79 through 83). These hub arms, made from Ti-6Al-4V, support the blades and their respective free motion hinges. The outboard end of each hub arm retains rolling element needle bearings. These bearings permit free motion of the flapping blade to relieve inboard bending stresses and provide the flapping hinge offset. The HLH rotor head is designed with a 36-inch distance or offset between the vertical centerline of the main rotor shaft and the flapping hinge axis. This offset allows aircraft center-of-gravity variation and provides overall aircraft controllability.

The Ti-6Al-4V alloy flapping hinge (Figure 84) is attached to the offset hinge axis by its two lugs and a flapping pin. Integral bosses, on both the hub arms and flapping hinge inboard center sections, provide physical droop stops for the HLH blades during periods of rotor shutdown. A resilient, replaceable pad is attached to the contacting surfaces to withstand the blade impact loads and provide for easy replacement if worn or damaged.

The outboard bore of this flapping hinge houses rolling element bearings identical to the ones used in the hub arms. These bearings provide another degree of full blade freedom, that of movement of the blade in the plane of rotation. This motion permits the blade to assume an equilibrium position determined by centrifugal and drag forces and also to hunt forward and rearward under the influence of vibratory Coriolis forces.

A hinge pin is supported inside the bearing bore and retains the inboard lug of the spindle (Figure 85). The Ti-6Al-4V alloy spindle has an integral damper attachment arm. Its cylindrical shank supports five angular-contact thrust bearings and one preload bearing. The bearings allow the rotor head's sleeve to rotate about its feathering (pitch-change) axis and permit constant mechanical control of the lifting force on each blade. The inboard section of the spindle's central bore and the integral tang on the outboard section of the flapping hinge provide physical lead-lag stops for the blades. These stops permit free motion, approximately

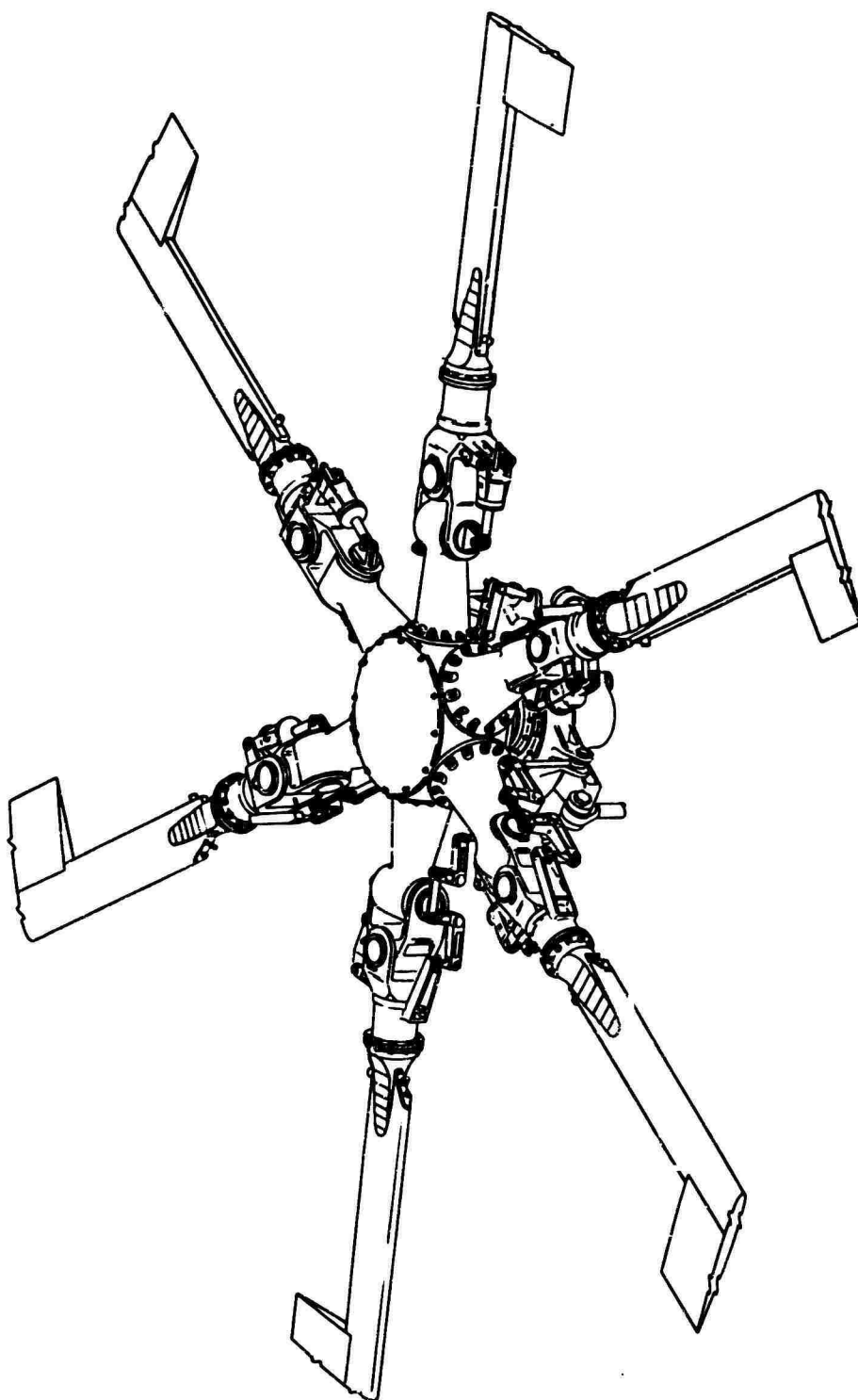


Figure 79 Rotor System

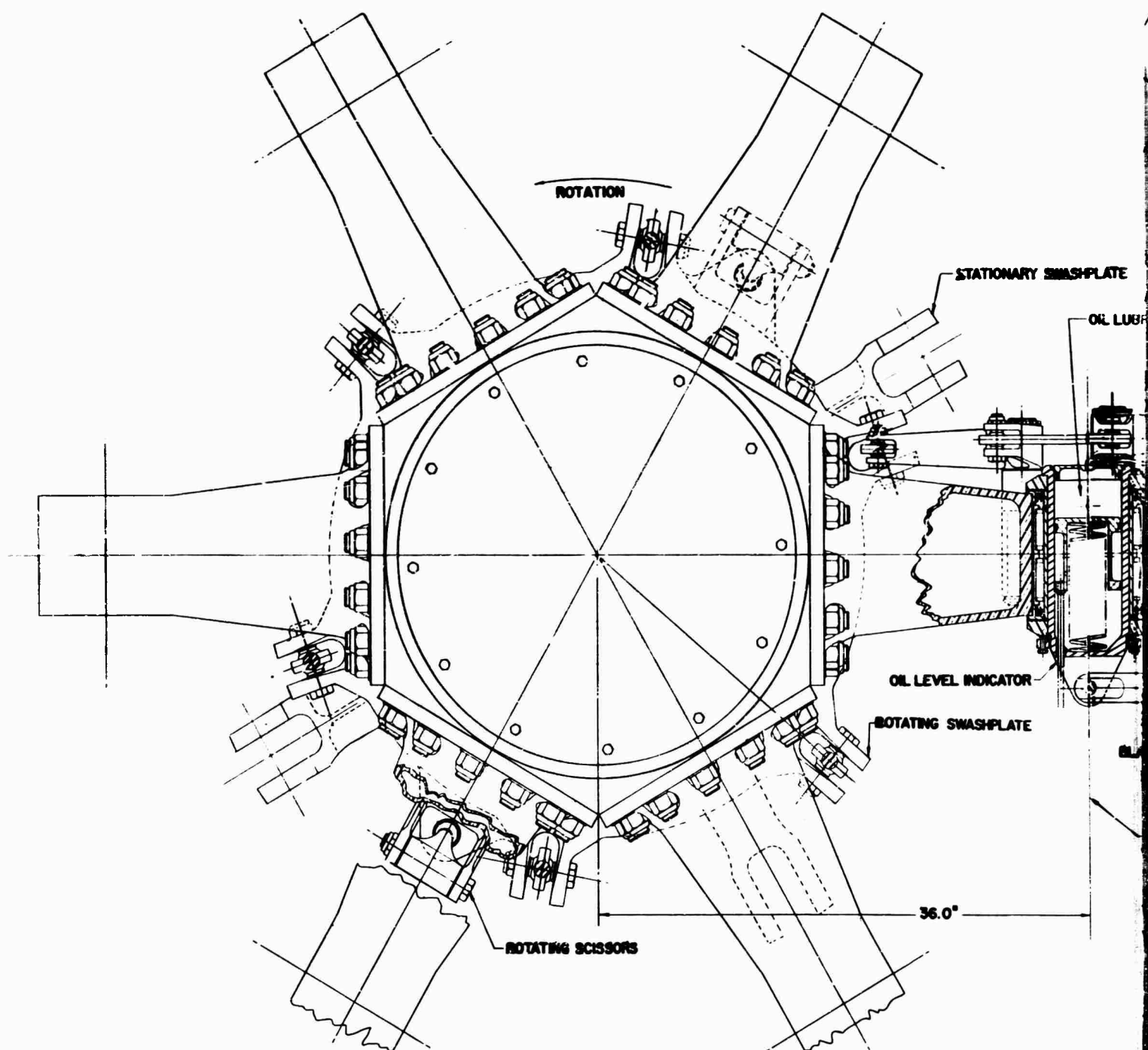
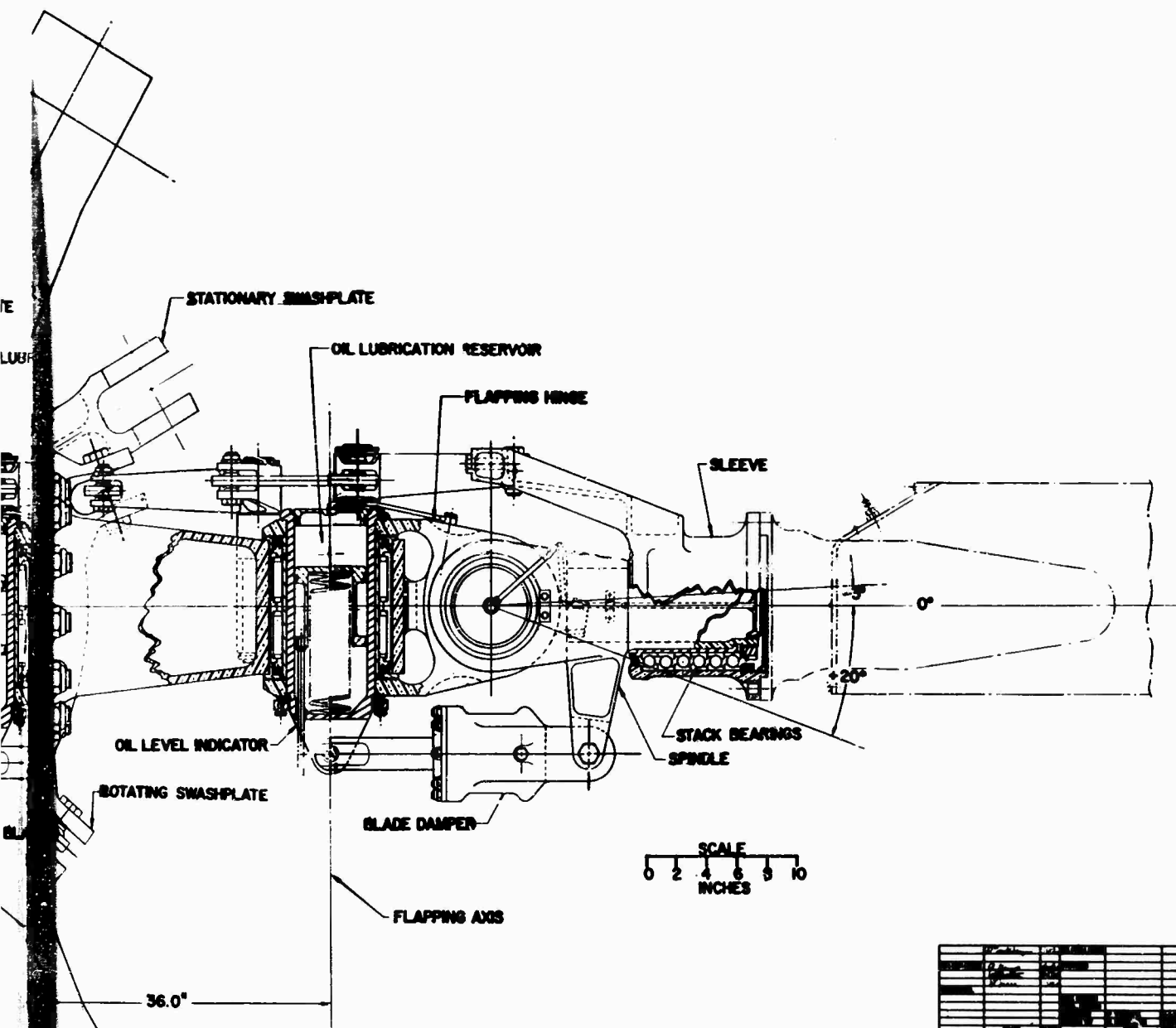


Figure 80 Flex-Rotor_{TM} Head, Plan View,
12-20-Ton Skycrane[®]



DESIGNED BY	DATE	REVISION
DRAWN BY	DATE	REVISION
CHECKED BY	DATE	REVISION
APPROVED BY	DATE	REVISION
FLEX-ROTOR HEAD		
PLAN VIEW		
12-20 TON SKYCRANE		
PROJECT NO.	08-07-01-3	
SCALE	1/2" = 1'-0"	

B

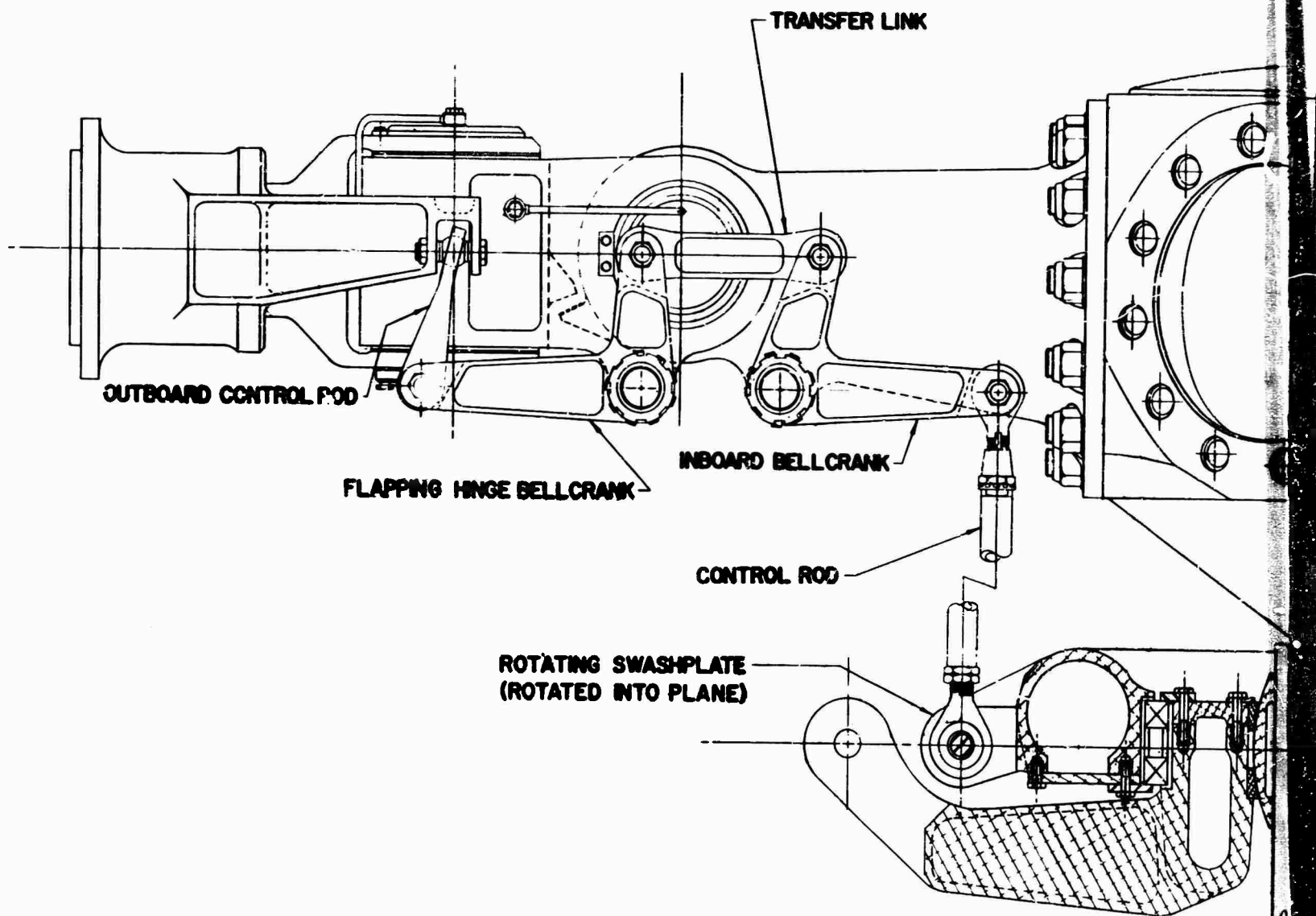
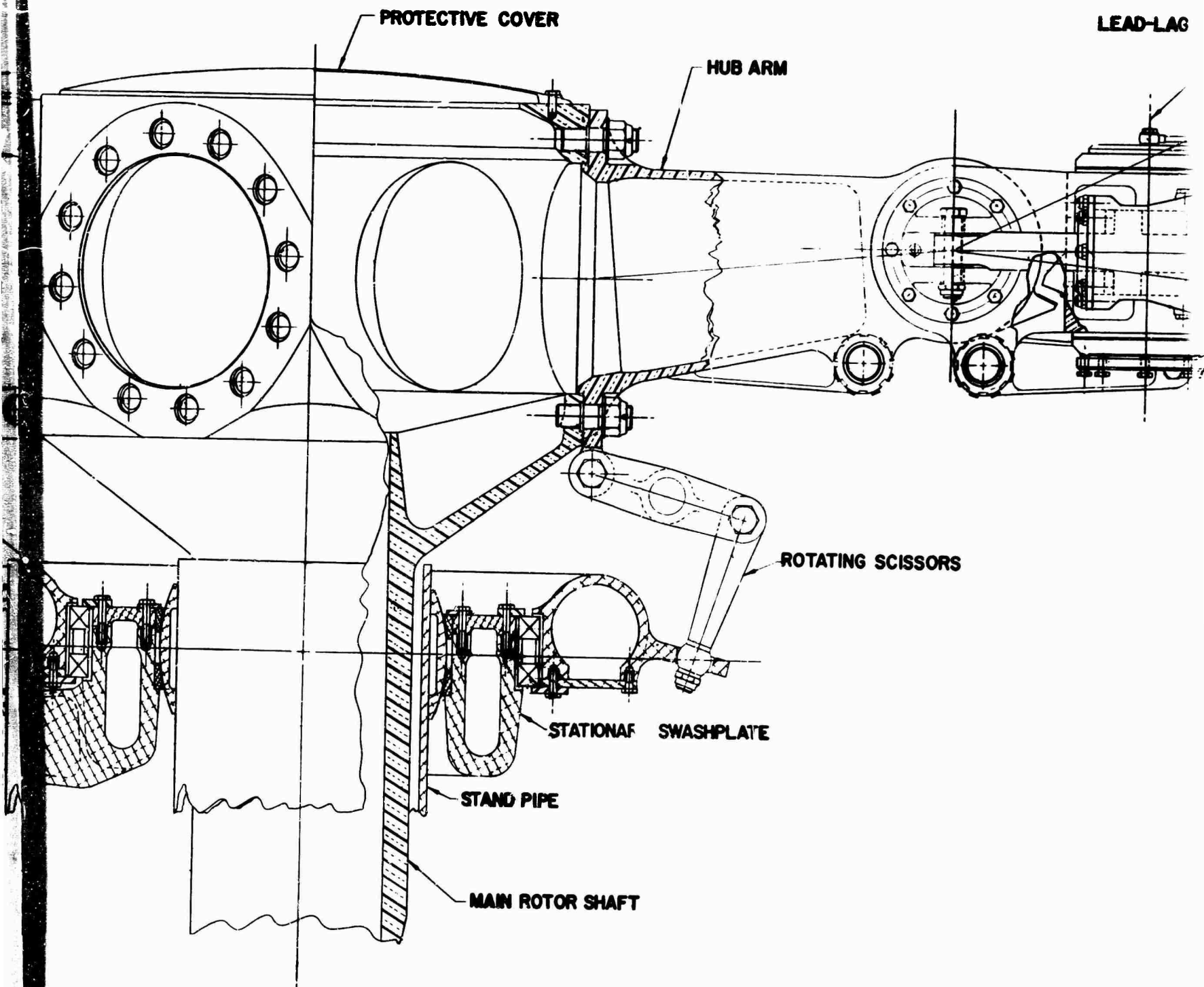


Figure 81 Flex-Rotor™ Head, Elevation View,
12-20-Ton Skycrane®

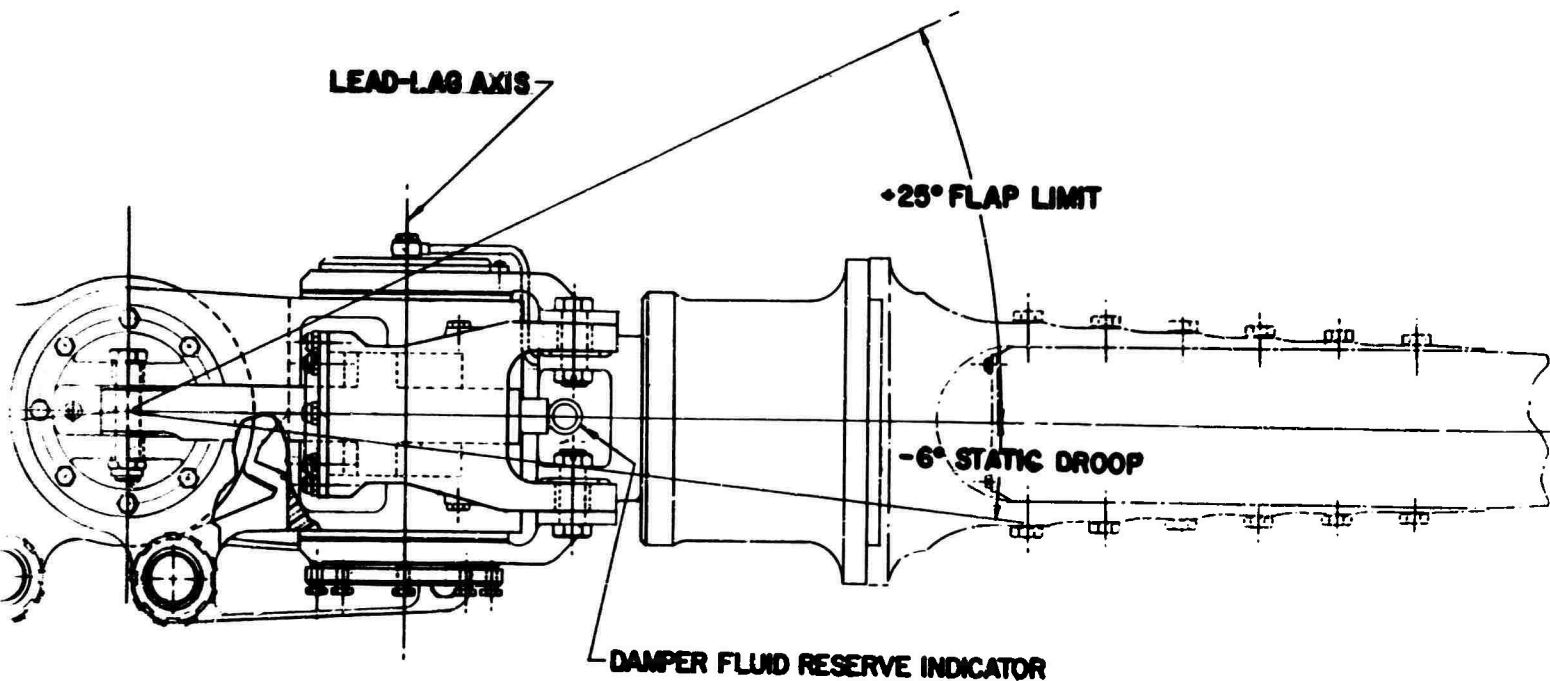


B

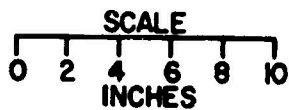
AG

IN
IN
IN

IN
IN
IN



SCISSORS



DESIGN NAME	DATE	BY	CHKD BY	DATE
DESIGN NO.	DATE	BY	CHKD BY	DATE
REPORT NO.	DATE	BY	CHKD BY	DATE
<p>FLEX-ROTOR HEAD ELEVATION VIEW 12-20 TON SKYCRANE</p>				
<p>DS-137-01-3</p>		<p>REV.</p>		

C

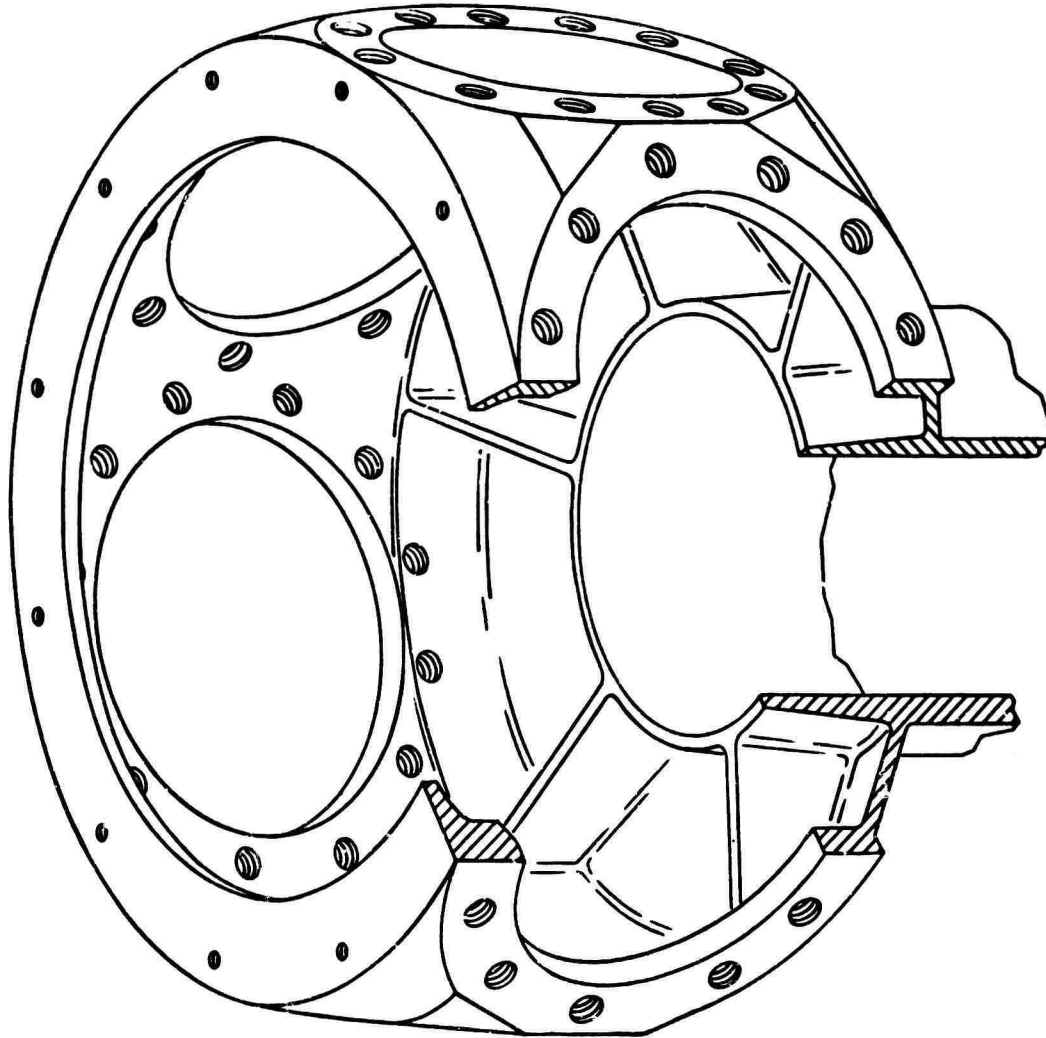


Figure 82 Integral Hub-Shaft Main Gearbox

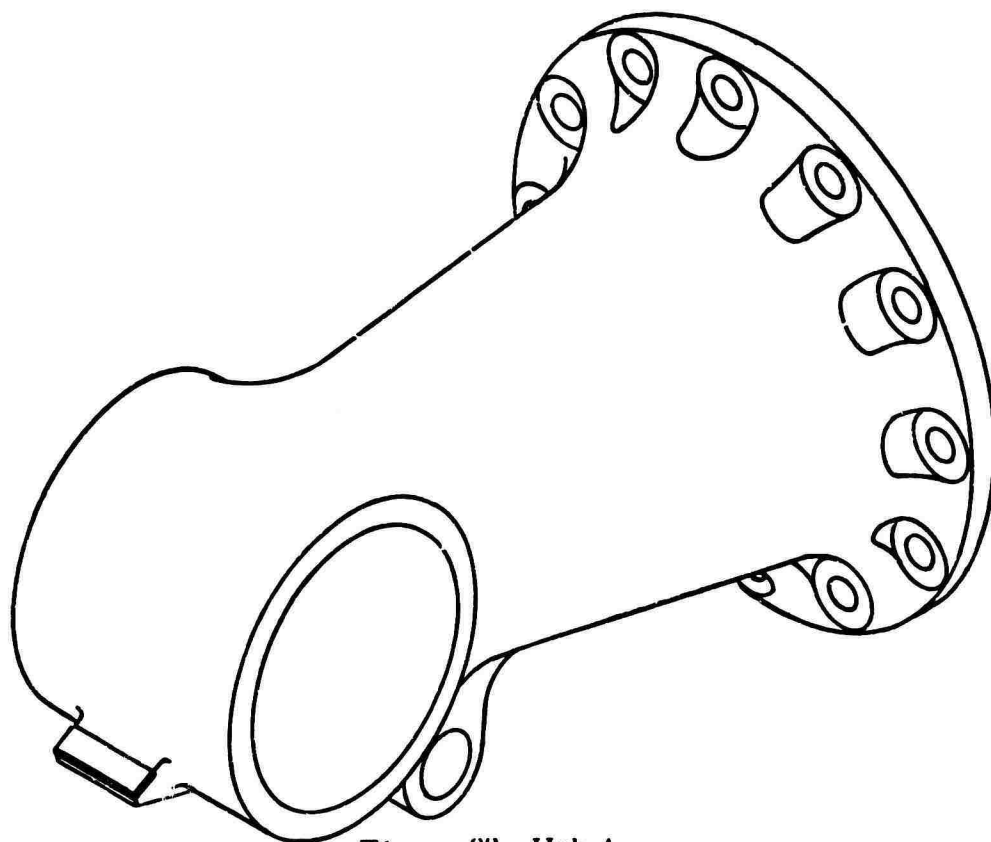


Figure 83 Hub Arm

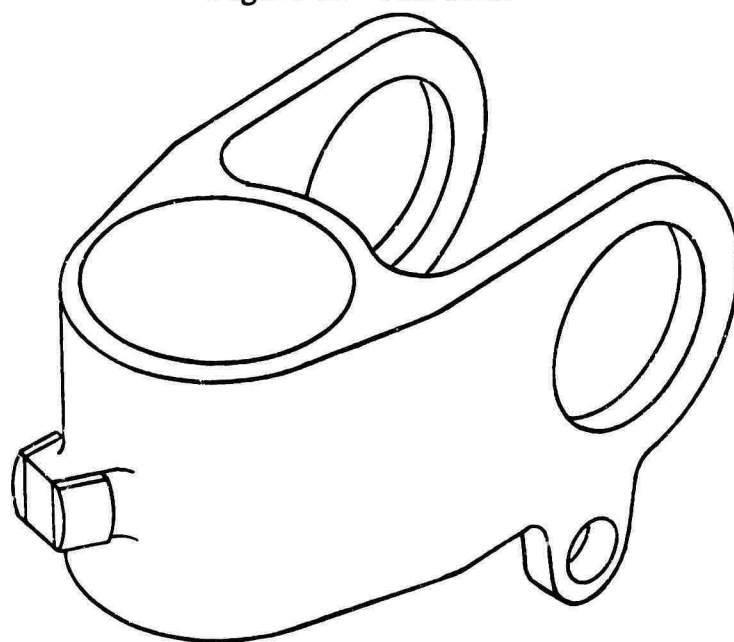


Figure 84 Flapping Hinge

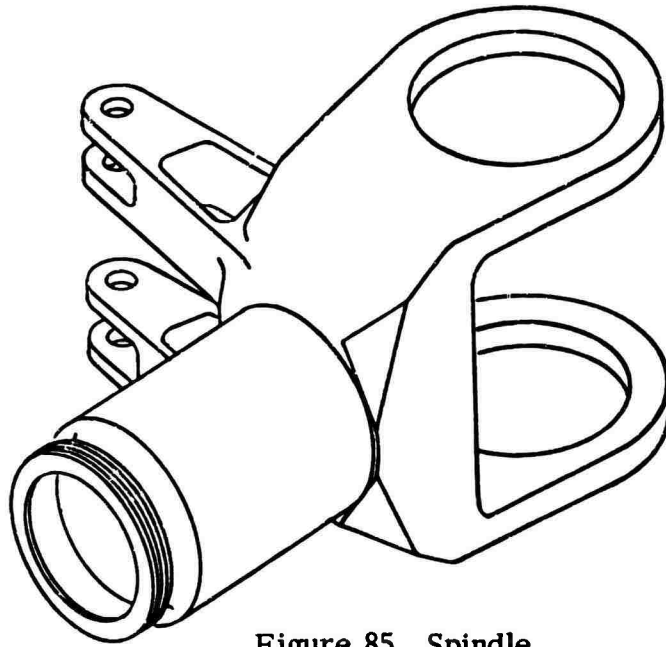


Figure 85 Spindle

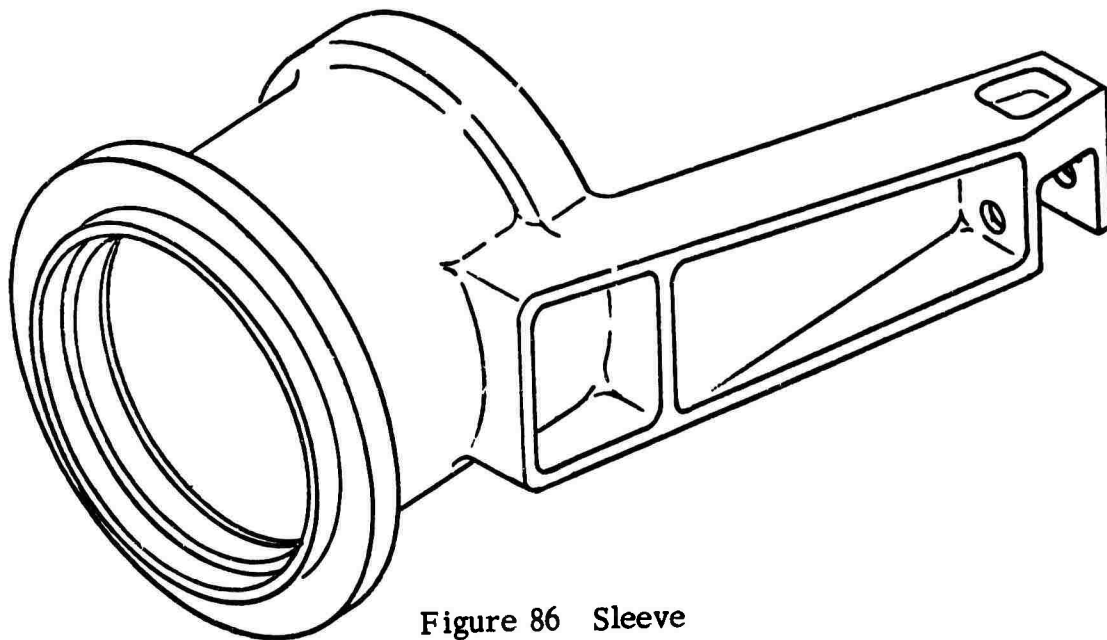


Figure 86 Sleeve

3 degrees forward and about 20 degrees aft of the radial line. Again, replaceable resilient pads are used on the contacting surfaces to reduce impact loads during main rotor starting and stopping conditions. These stops also prevent all of the starting and stopping loads from being reacted by the blade damper assemblies.

Divergent blade hunting oscillations are prevented by linear hydraulic damper assemblies located between the end of the flapping pin and the spindle's attachment arm. Relief valves inside the piston limit the magnitude of the lead-lag loading experienced by the main rotor blades. A replaceable orifice plate in the piston controls the stiffness characteristics of the damper.

The forged, Ti-6Al-4V alloy sleeve is a hollow, cylindrical component whose outboard section contains a flange to which the main rotor blade cuffs are easily installed or removed (Figure 86). The inboard section of the sleeve has an integral arm (horn) which is activated by the control system linkages and produces feathering motion of the sleeve and attached blade relative to the main rotor spindle.

The HLH main rotor oil lubrication system, developed by Sikorsky Aircraft, provides a complete bath of oil for all of the rolling element bearings. This permanent and complete bath of oil adds to the overall reliability of these bearings. There are no periodic greasing intervals to be forgotten or intentionally extended, which would normally reduce the service time expected from these bearings. Also, the system uses no flexible oil lines which could possibly break or become loose while in the oscillating blade motion environment.

Every oil lubrication system requires reliable, long-lasting seals to guarantee operation without field maintenance. A new oil sealing principle, developed by Sikorsky Aircraft, is in production on the CH-53A helicopter. This unique, one-piece, channel-shaped diaphragm seal (Figure 87) has no rubbing seal surfaces to wear out or collect grit and no relative motion between sealing elements. The one-piece design is possible since the normal oscillating motion of the rotor head's hinges is extremely small and there are no requirements for complete rotation of any hinge.

Swashplate Control System

The angle of attack or pitch of the main blades is controlled by the flight control system. This system is connected to the blades through a swashplate assembly located below the hub assembly (Refer to Figures 80, 81, 88, and 89). The swashplate assembly consists of an upper (rotating) swashplate driven by the main rotor hub's two rotating scissor assemblies and a lower, nonrotating (or so-called "stationary") swashplate

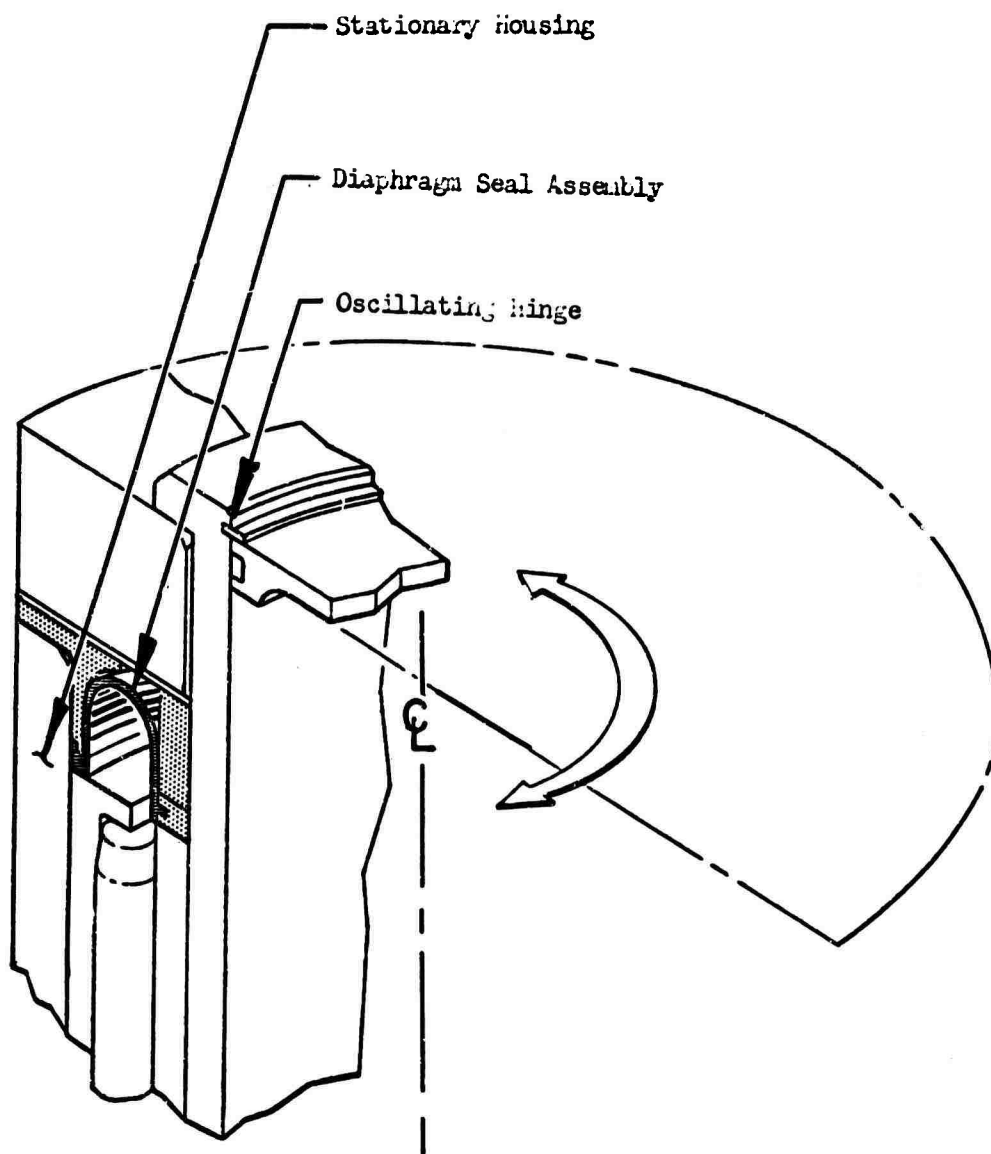


Figure 87 Typical Diaphragm Seal Installation

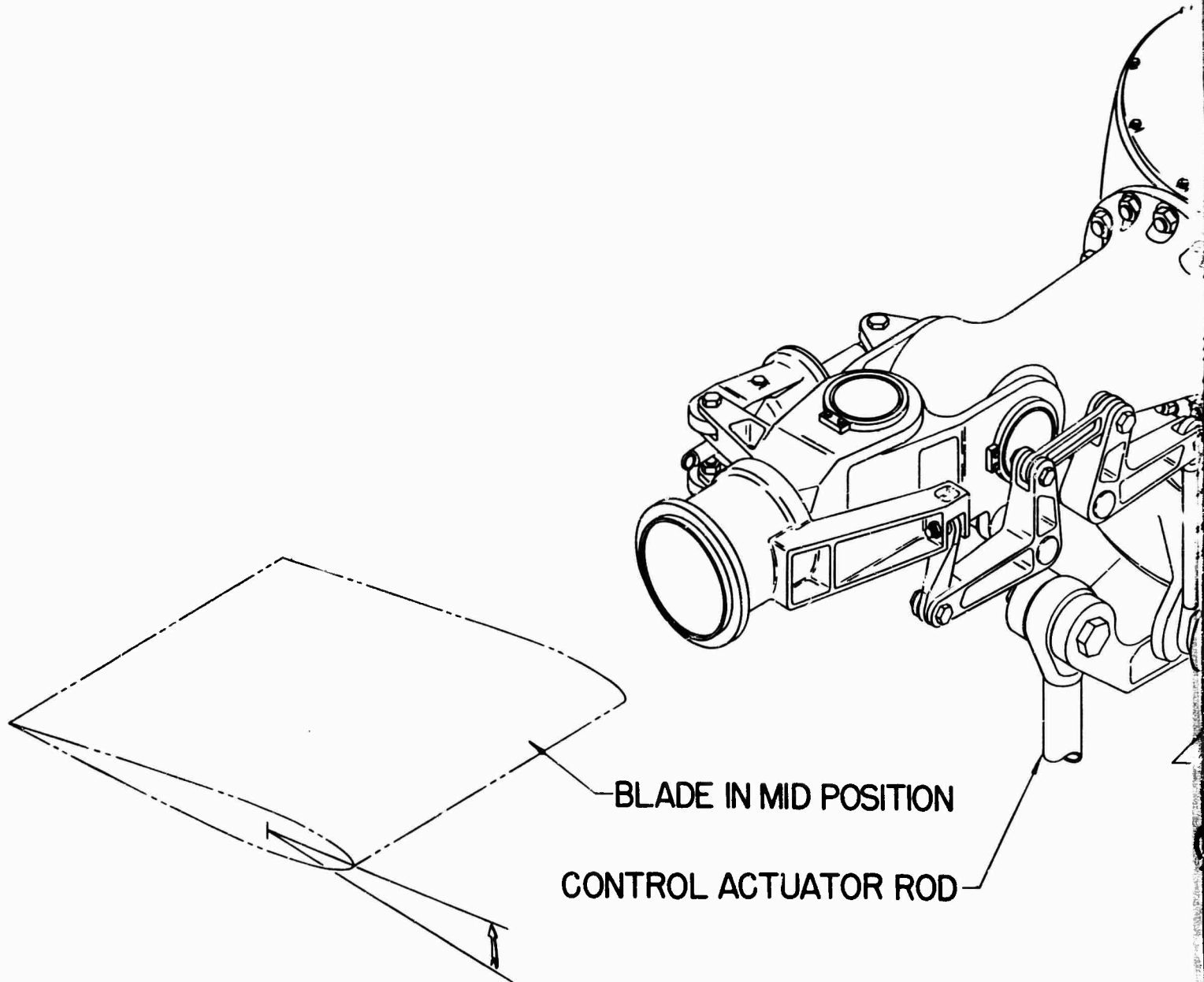
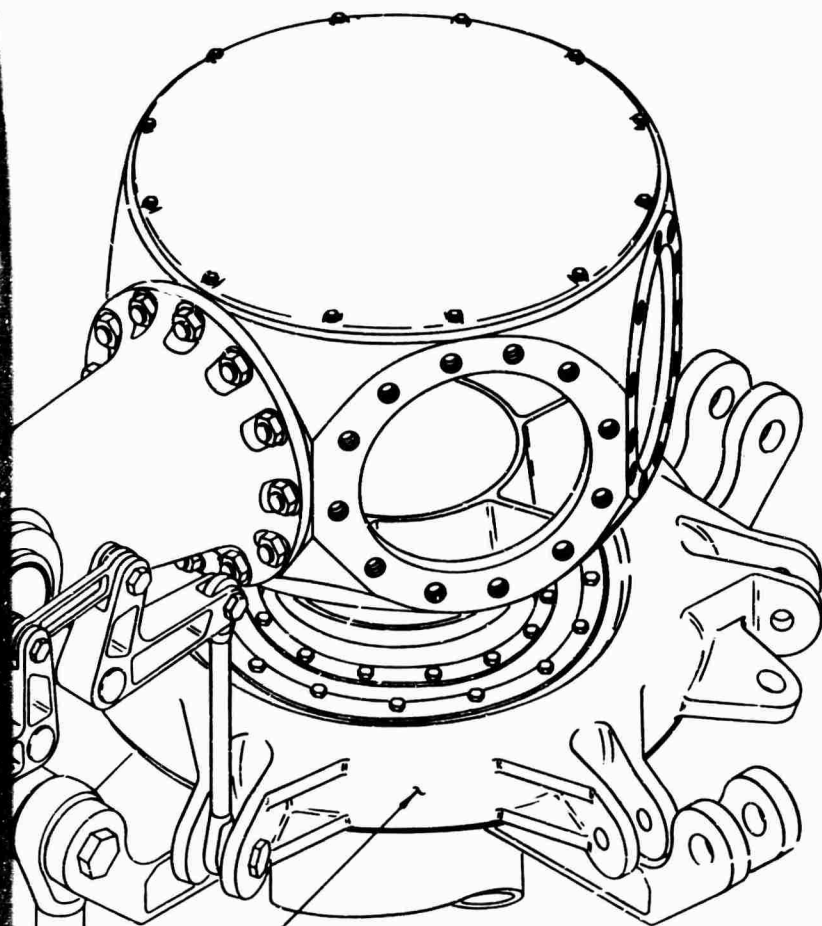


Figure 88 Control System, Mid Pitch, Flex-Rotor_{TM} Head,
12-20-Ton Skycrane®



SWASHPLATE ASSY POSITIONED
IN CENTER OF VERT TRAVEL
(PLANE OF SWASHPLATES PERPENDICULAR
TO ROTOR SHAFT)

DESIGN & DEV		CHECKED BY		DATE	
TECHNICAL		APPROVED BY		DATE	
NAME		DATE		NAME	
REPORT NO.		PAGE NO.		FIGURE NO.	
CONT. SYS.-MID PITCH FLEX-ROTOR™ 12-20 TON SKYCRANE®					
Sikorsky Aircraft		DS-137-01-8		REV.	

B

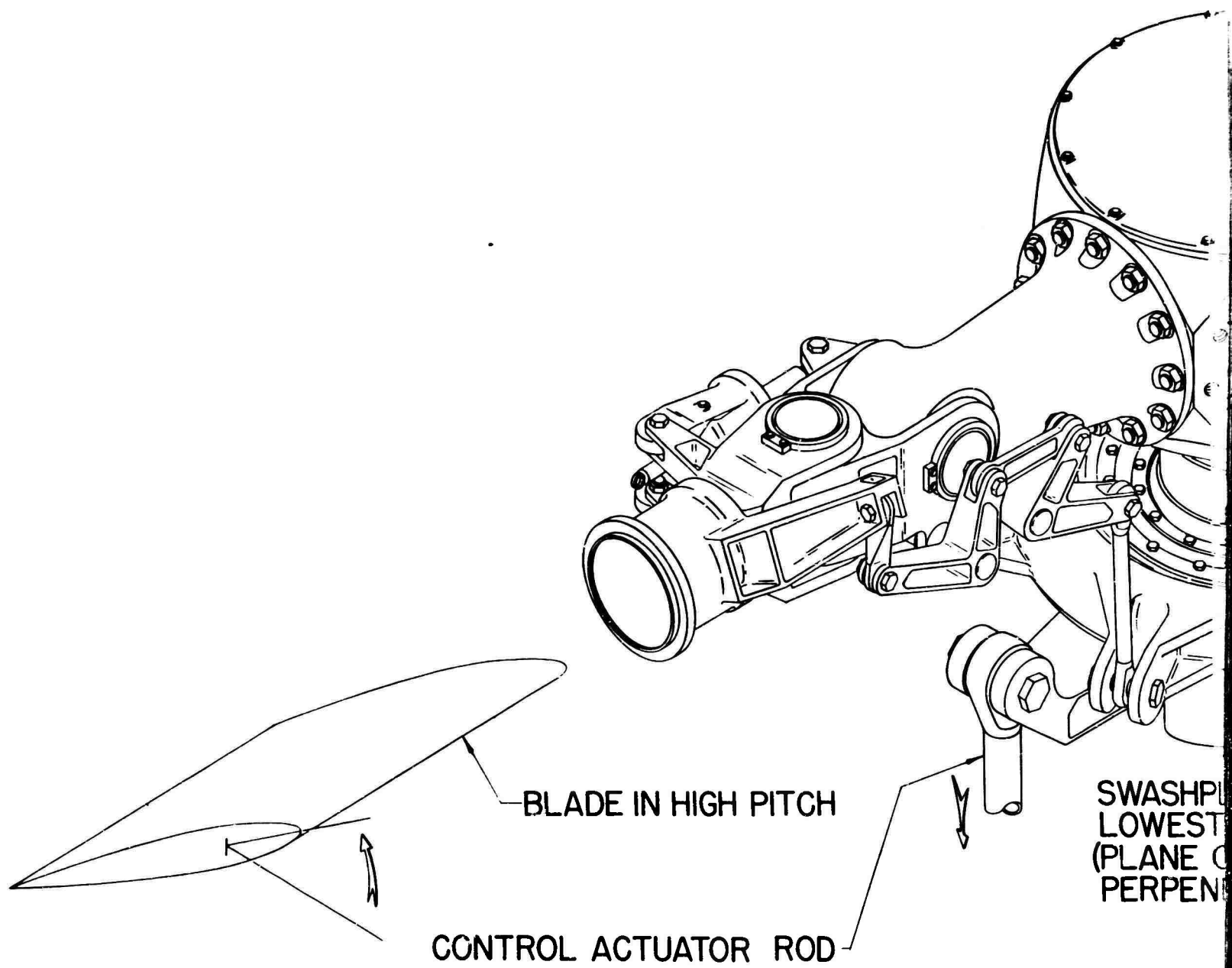
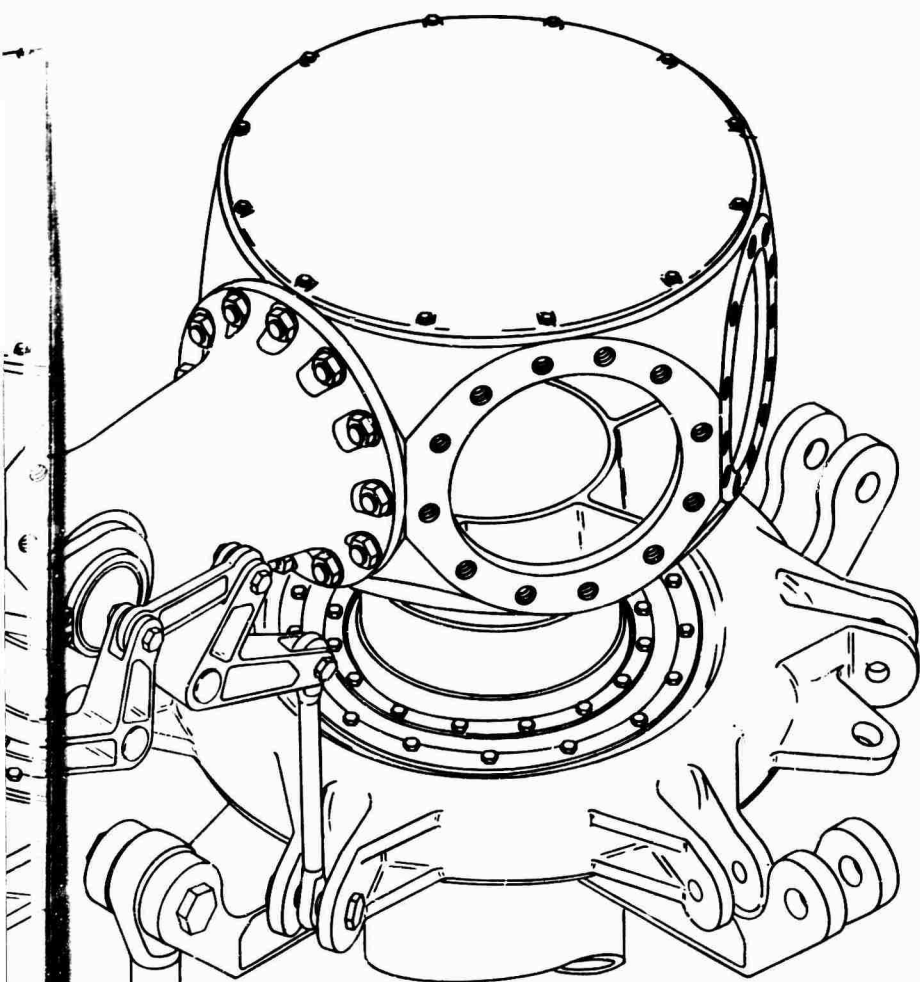


Figure 89 Control System, High Pitch, Flex-RotorTM Head,
12-20-Ton Skycrane®



SWASHPLATE ASSY IN
LOWEST VERT. POSITION
(PLANE OF SWASHPLATES
PERPENDICULAR TO ROTOR SHAFT)

DESIGNER	DATE	BY	DATE	BY	DATE
APPROVED	DATE	BY	DATE	BY	DATE
TECHNICAL	DATE	BY	DATE	BY	DATE
REPORT NO.		PAGE NO.		FIGURE NO.	
CONT. SYS.-HIGH PITCH FLEX-ROTOR™ 12-20 TON SKYCRANE®					
Shorek Aircraft		DS-137-01-8		REV.	
---		---		---	

secured by another scissors assembly to the main gearbox. The non-rotating scissors attachment is incorporated into the attachment fitting of the fore-and-aft servo. Both swashplates are fabricated from 7075-T73 aluminum alloy forgings. The swashplate assembly pivots at its center on a sliding ball and socket joint, which allows it to be tilted, raised, or lowered simultaneously by control rods of the flight control system which connect to arms on the lower (stationary) swashplate. Cyclic or collective pitch changes introduced at the stationary swashplate are transmitted to the blades by control rods and bell cranks between the rotating swashplate arms and horn assemblies attached to each blade's feathering sleeve.

The control linkage is so arranged that pitch variations resulting from flapwise blade motion (delta 3 effect) and from lagwise blade motion (alpha 1 effect) are minimized in the region of normal power-on operation. A novel feature of the linkage is that the coupling of pitch motion to the other blade motions can be altered, without any changes to major structural components, simply by altering control rod and bell crank dimensions. This provision allows for minor developmental changes to be incorporated during flight testing, to alter handling qualities, without the expenses and inconvenience of a major redesign. Similarly, control sensitivity can be modified, over part or all of the pitch range, merely by slight alterations to the control linkage geometry.

Considered as a whole, the rotor head is at once a specialized design, tailored exactly to the HLH requirements, and yet is a combination of proven design concepts, already developed and in production. The light overall weight and low drag area of the head result from its unique structural scheme. However, the material and bearing selections, and the detail design methods employed locally at all points of attachment and articulation, are firmly based on precedent, with no areas of risk or uncertainty.

ALTERNATE BLADE AND ROTOR HEAD DESIGNS

Alternate Blade Design

An alternate blade design evaluated for this application uses a spar built up of several members fastened together by structural adhesive bond. Referring to Figure 90, the spar consists of three main structural members fabricated from extruded aluminum alloy 6061-T6. The members are internally and externally machined to produce the desired wall thicknesses and the closely controlled fits required for bonding. The external contour surfaces on all three pieces are machined with a taper to provide for a thicker wall on the inboard end of the spars. The internal surfaces of the leading and trailing edge members are tapered (adjacent to the quarter chord) to provide for thicker walls at the inboard end of the spar. To assemble the spar, the pieces are mated, installed in a contoured "clamshell" fixture, and structurally bonded under controlled conditions of temperature and pressure.

The required thick root end is obtained by gradually laminating up the sidewalls of the inboard end of the spar with bonded-on aluminum alloy sheets.

Sikorsky has been engaged in the development of this type of spar for the past 5 years. Many multi-piece-type configurations held together by structural adhesives have been studied, and different types of structures have been designed. Two types of spar specimens have been fabricated and bonded in the manner described above and have then been fatigue tested. One of the specimens tested (Figure 91, U.S. Application Serial No. 474598) had a configuration closely resembling the alternate HLH spar.

The specimens were subjected to fatigue testing under simulated centrifugal tension and reversed bending moments. In every test conducted, metal fracture occurred before bond separation, indicating the feasibility of the design concept. The most pronounced advantage obtained is control of crack propagation, leading to significant improvements in reliability, particularly when coupled with BIM®. The crack propagation control, obtained by both the shape of the components and the use of low modulus, viscoelastic adhesives, results in a definite "crack dwell" at each point where a new crack must be initiated at an interface. This effect has been verified both by direct test observation and by electron microfractography of the fractured parts.

The open sections employed in all of the spar components permit close, accurate inspection of the entire structure before assembly and rework

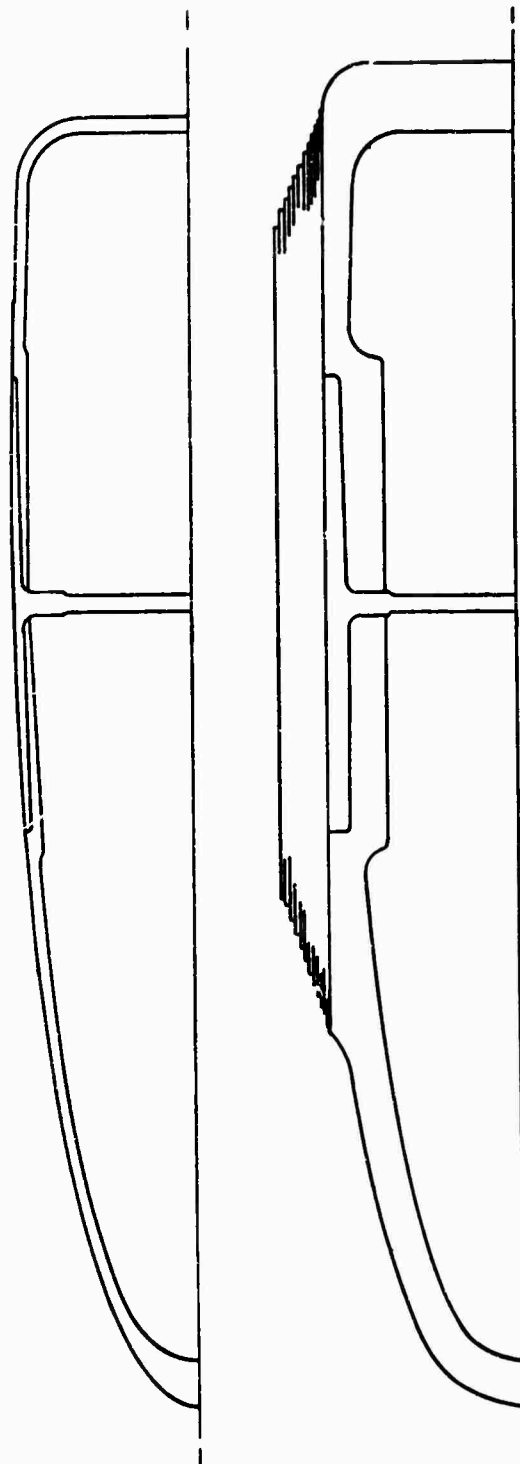


Figure 90 Alternate Blade Design

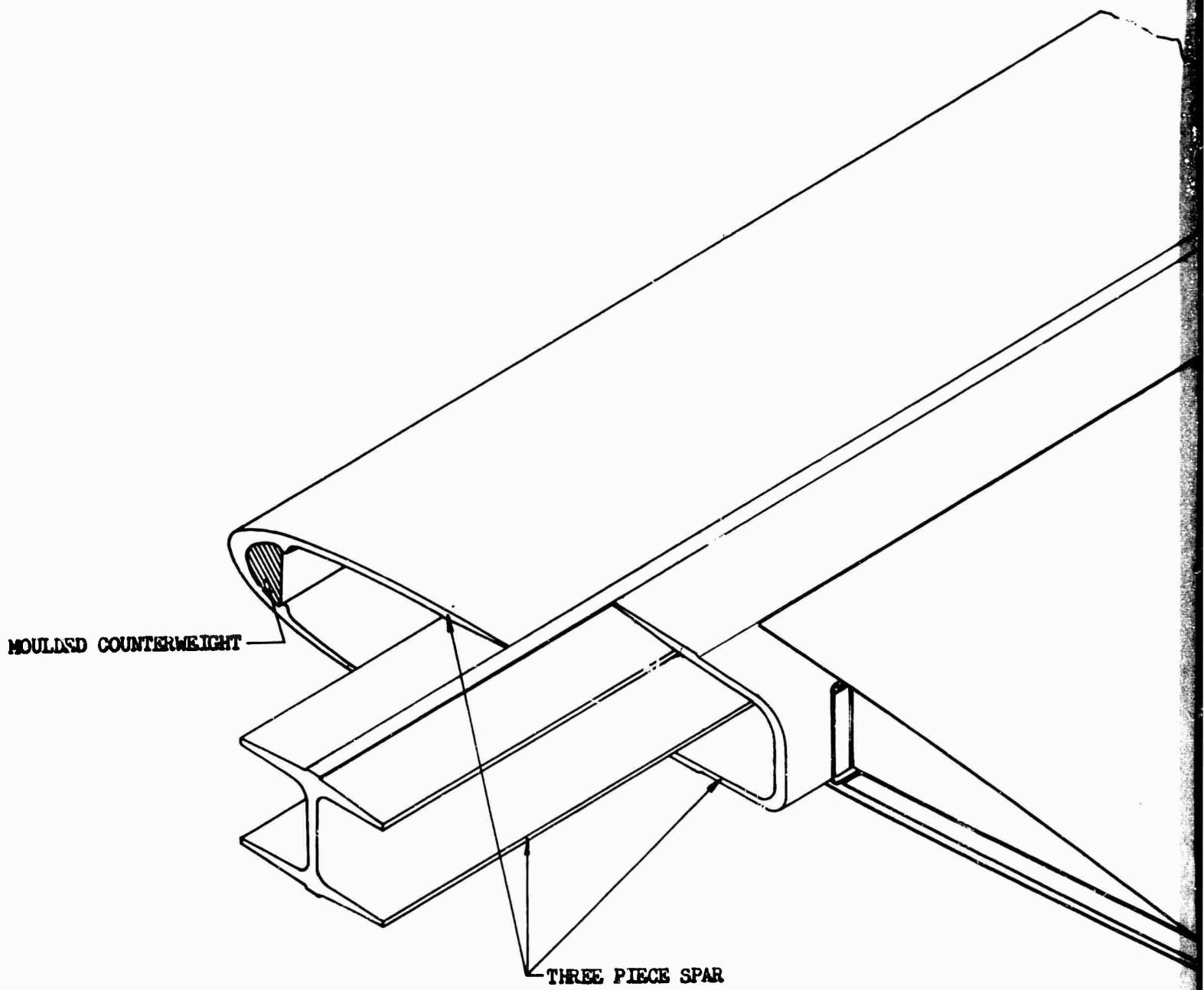
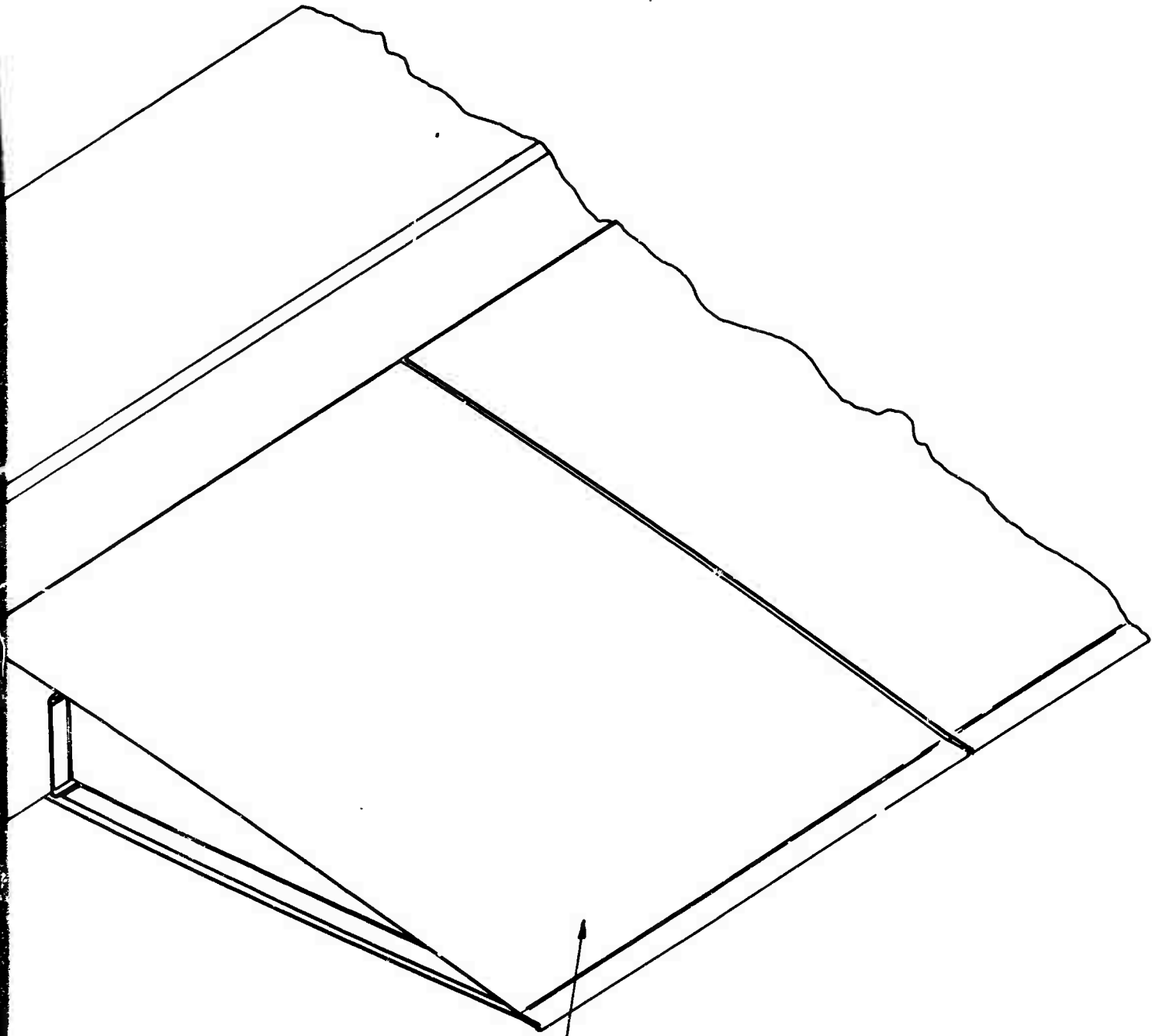


Figure 91 Built-Up Spar Configuration



TRAILING EDGE FAIRING

3

of flaws, nicks, and other surface blemishes inaccessible (and therefore requiring rejection) in a "D" section spar. The end result is inevitably higher reliability.

Another advantage of a redundant spar is that the inside of the spar segments may be machined; machining is not limited to the outside contour above as it is presently limited on extruded "D" section spars. With open sections, both the inside and outside of the parts can be tapered to whatever shape is required by design; Figure 90, which compares an outboard section and a root end section, shows how material can be added to the spar at various blade stations. In addition, the open sections provide easy access to the inside, for cleaning, anodizing, and painting of parts. Closer wall thickness tolerances are possible, resulting in blades even more closely matched elastically and aerodynamically than in present designs.

The weight penalty for spar redundancy is small, amounting to approximately 4 percent of blade weight. This is an increase of 173 pounds in the total weight of the six blades. Accompanying enlargement of rotor head structure to compensate for increased hub forces resulting from the increases of centrifugal force and blade inertia would add another 100 pounds, approximately. The total increase in rotor system weight is thus about 270 pounds. The further development of the redundant spar HLH blade appears to be warranted.

Alternate Leading Edge Counterweight

Counterweights are required in the leading edge of the rotor blade to balance the nonstructural trailing edge fairings. To avoid disturbance of the structural centroid, the leading edge counterweights must be essentially nonstructural. The design solution used for many years is a segmented counterweight of steel bars, suspended in elastomeric jackets in the forward extremity of the spar cavity. These counterweights are loaded in compression by centrifugal force and are retained by a solid block attached to the spar near the blade tip. While this counterweight system has been thoroughly proven, the construction of the alternate blade spar permits another method to be used, introducing several significant improvements.

The alternate counterweight is cast in place in the leading edge cavity. Composed of lead particles in an elastomeric, organic matrix, the counterweight bonds itself in place as the matrix cures.

The nonstructural nature of the cast counterweight is provided by its low elastic modulus, which is only about 2 percent of the spar modulus. The counterweight has about the same density as steel. Because it com-

pletely conforms to the inner contour of the spar, the cast counterweight centroid is farther forward than that of a conventional counterweight, achieving a given balance moment with less mass. In addition, it is self-supporting over its entire length, so that no tip block is required, and even severe ballistic damage to a local area has no effect on the structural integrity of the rest of the counterweight.

Cast counterweights have been made with several matrix materials. Static tests, fatigue tests, and flight tests of small lengths have all produced satisfactory results. Further development of this concept is required, particularly to substantiate the properties of the matrix as a function of calendar time. The counterweight is the subject of U. S. Patent Application Serial No. 429408.

Alternate Hub Configuration

Figure 92 shows an exploded view of an alternate rotor hub assembly which incorporates a separate titanium alloy hub member located between the main drive shaft and the individual hub arms. Spline teeth in the hub's central bore transmit the main rotor shaft torque to the blades. An integral, conical surface, located directly above the hub splines, accurately centers the entire rotor head assembly on the main rotor shaft.

The required preload force necessary to seat the hub tightly on the shaft is provided by a special bolt-preloaded nut assembly. A standard torque wrench and socket are the only tools required to install and preload this nut assembly. A separate beryllium-copper conical element, driven between the hub's lower skirt section and the main rotor shaft, completes the lift system's rigid attachment to the aircraft. This redundant securing system design prevents hub and shaft surface fretting resulting from aerodynamic head moments induced by the flapping action of the blades.

This alternate design approach simplifies the fabrication of the main rotor shaft and allows easier installation and removal of the control system's swashplate assembly. The gearbox and rotor head can be split apart at a low echelon into two separate packages weighing approximately 5000 and 3800 pounds, respectively.

This alternate design increases the complexity of the rotor hub and adds several new components. The precision machining of the spline and the conical seating surfaces would probably make the alternate design more costly than the integrated hub and shaft. The shaft weight is reduced by 410 pounds, while the rotor head weight is increased by 680 pounds. This results in a 270-pound net weight increase. Because all of the

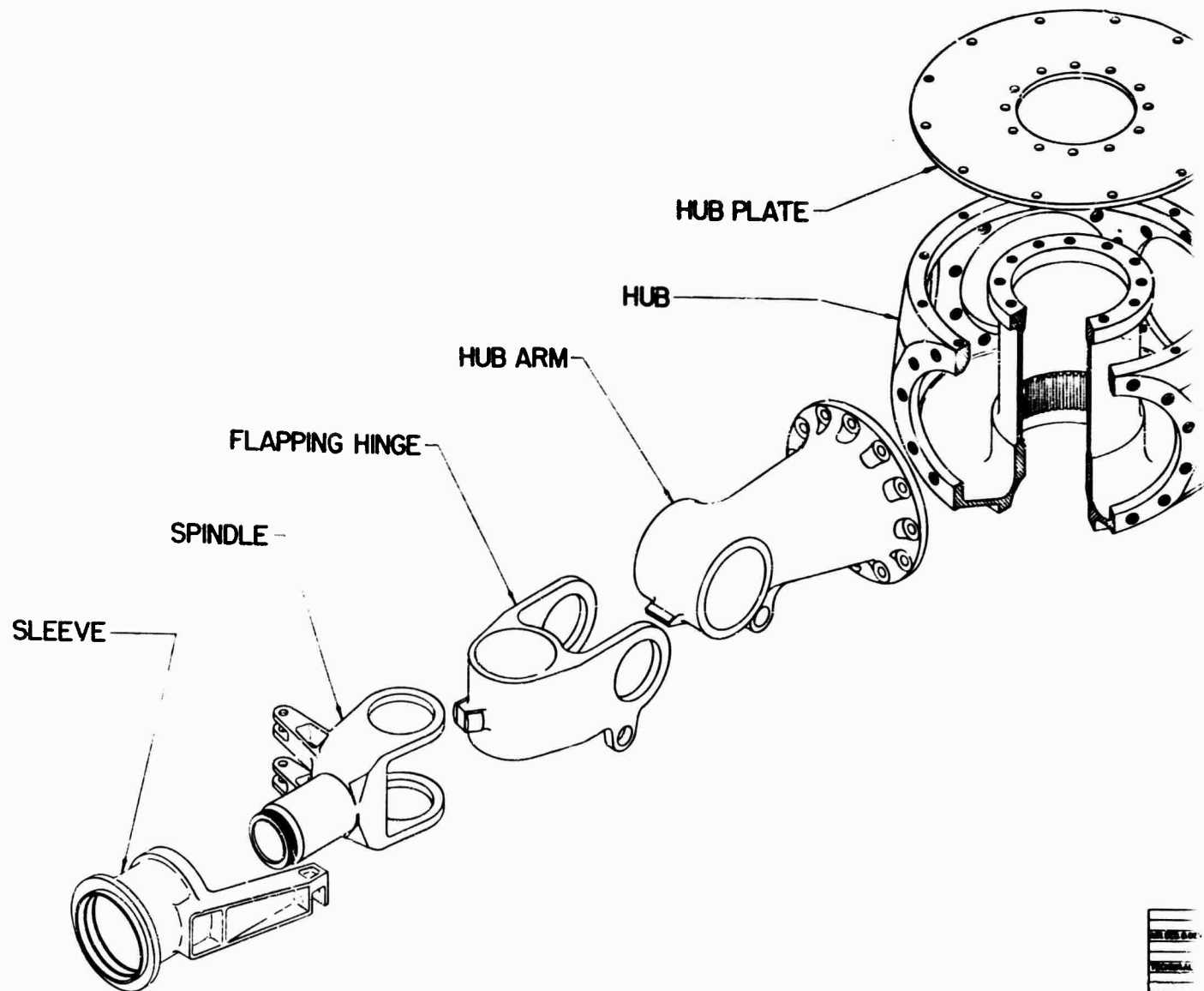


Figure 92 Alternate Hub Assembly, Flex-Rotor™ Head,
12-20-Ton Skycrane ©

A-

design principles used are well established, the splined hub does not involve any added risk.

Fabric Journal Bearings

Sikorsky Aircraft is now testing, on the Model CH-53A main rotor head, a fabric bearing which is a direct replacement for the production rolling element bearings. Preliminary results from this development program indicate that each of the HLH flapping and lead-lag rolling element bearings could be replaced by equivalent load capacity fabric bearings. The use of these fabric bearings would eliminate two areas now requiring oil lubrication and would save approximately 120 pounds in weight by reducing the bearing outer diameters at the flapping and hunting hinges. Because bearing friction would be greater than in rolling element bearings, less damping would be required, so that the blade dampers and associated hardware could perhaps be reduced in size and weight also. The possibility exists that the hunting journal bearings could be designed especially to provide sufficient friction so that the damper could be totally eliminated.

The CH-53A bearings have been laboratory tested, and some whirl testing was accomplished in 1965. The concept is not completely proven and still requires some development to verify its advantages and characteristics. Experience to date has been successful, however, indicating that it is not a high risk alternate design.

Alternate Rotor Control System

The size of the HLH permits consideration of an "internal" control system, in which the control inputs are introduced to the rotor head by mechanism located within the rotor shaft. The swashplate assembly, or its equivalent mechanism, is located at the top of the hub. Two typical internal systems were investigated in Reference 54, in which it was found that rotor drag area could be reduced by slightly less than 1 square foot by either system. An added advantage is that the control mechanism is mostly located within the shaft or above the hub components so that an appreciable degree of protection from ballistic damage can be offered the control components.

Functionally, the major problems involved in the design of a successful internal control system stem from the small diameter of the shaft bore, as compared with the wide spacing of the nonrotating control inputs in the conventional arrangement. The internal system thus tends toward larger control loads and smaller displacements, with large motion multiplication taking place on top of the hub. Free motion in the mechanism within the shaft is multiplied considerably, so that for a

given amount of free blade motion, the free input motion must be held to about 20 percent of the tolerable amount for a conventional system. For the Hafner system, in which two separate members in the shaft tilt and elevate a swashplate, two sliding contact ball and socket joints, one gimball joint, and two bushings are employed within the shaft, so that small lost motion is not an inherent tendency in the design. The double eccentric system, which imparts vertical motion to a central member for collective pitch input and uses a pair of hollow eccentric shafts to displace the member radially for cyclic pitch inputs, is better suited for operation with very little free motion.

While the design requirements of the systems analyzed for the present HLH configuration differ slightly from those of Reference 42, the relative weights of the various designs follow the same general trend. For the rotor system of this study, the Hafner system weighs about 100 pounds more than the conventional system. The double eccentric system weighs about the same as the conventional system. Thus, of the two internal systems studied, the double eccentric arrangement appears to be the more promising. The advantages gained in drag should be weighed against the development required for this mechanism in forming the decision of whether to proceed with its reduction to practice. For the low forward speeds encountered in the HLH design missions, the development penalty does not appear warranted.

Alternate Rotor System

Investigation of several rotor design concepts which provide mechanical simplicity by substituting flexible members for bearings has led to a family of alternate designs. The evolutionary trend of these design efforts can be noted in a chronological listing of the most significant of the various means investigated for allowing the blade to pitch, flap, and hunt:

- a) Conventional arrangement of separate antifriction bearings for each of the three motions. This type is currently in production on many models.
- b) Spherical hydrostatic bearings, one per blade, each permitting three degrees of freedom. This rotor was built and extensively ground and flight tested.
- c) Separate elastomeric bearings for each motion. Laboratory testing of full-size components has been accomplished on this concept.
- d) Spherical elastomeric bearings, one per blade, analogous to the hydrostatic bearing. This was tested in the laboratory at full size.
- e) Flexure members, acting as cantilever beams, for flapping

motion, combined with various bearing and flexure arrangements for pitching and hunting.

- f) Flexible straps, deflecting over radius blocks, in arrangements basically similar to the last method above.
- g) Laminated flexible members for flapping, with pitch bearings, and edgewise blade flexibility to permit hunting.
- h) Slender flexible members, whose deformation permits all three motions, guided by spherical radius blocks moving in a rigid framework.

In addition to the methods listed above, which essentially form a continuum of development effort, gimbaled rigid rotors have been designed, and rotors without hunting bearings have been designed and produced, including two-bladed teetering rotors. For the HLH, consideration of all of the available alternate design solutions led to the conclusion that the design which has the best chance of competing with a freely hinged rotor is a rigid rotor (no hinges in the flapping and hunting planes) with pitching permitted by a bearing arrangement placed well inboard to minimize control system weight, and blade flexibility permitting flapping and hunting motions. Two variants were investigated, having high and low values of in-plane blade stiffness. The hub has built-in pre-cone and pre-lag, selected for average operating regimes.

Study of previously tested rotors led to the conclusion that the high second harmonic content in the motions of the blade would result in transmission of large vibratory forces to the fuselage by a three-bladed rotor. The need for sizeable hub moments to facilitate control of a large helicopter ruled out a two-bladed rotor. At the other end of the spectrum, the required solidity dictates increasingly slender blades as the number of blades increases (aspect ratio approximately 30 at 10 blades, for example), which in turn poses static droop problems. Since large blade droop would require the addition of weight, either in the fuselage to raise the rotor or in the rotor to restrain the blade, the use of aspect ratios in excess of 25 was avoided. The alternate solution was thus constrained to use between four and eight blades.

Selection of satisfactory edgewise stiffness is influenced by the absence of a lag damper. A strong tendency is observed to oscillate in-plane in the first mode at a frequency close to one cycle per revolution. To avoid ground resonance, it is desirable to design either a stiff blade edgewise (with a frequency at or above 1.4 cycles per revolution) or a blade with an extremely low edgewise stiffness (with a frequency below 0.75 cycle per revolution). Both of these families of design solutions were investigated for the HLH rotor.

Preliminary studies of stiff in-plane systems disclosed that severe weight penalties were experienced in six-bladed rotors of the same solidity as the selected design solution. While a drastic reduction in the number of blades appeared to offer a better design, the use of a low in-plane stiffness system was selected as a better approach for this rotor. Two rotor systems were then studied in more detail, both having the same diameter and solidity as the freely hinged, six-bladed design; one of these has six blades, the other eight, with aspect ratios of 17.7 and 23.7, respectively.

The weight trends observed in the investigation are shown in Figure 93. Hub weights for three-bladed rotors have historically enjoyed a considerable weight advantage over larger numbers of blades, which is borne out by the curves shown. Elementary beam design considerations rule out efficient stiff in-plane blades of high aspect ratio and very flexible in-plane blades of low aspect ratio. Thus, two families of design solutions for flexible blades retained by rigid hubs are compared with the various freely hinged rotor solutions. Although continuous curves are shown, only integral numbers of blades can actually represent solutions. The correspondence of numbers of blades and aspect ratio values is based on the HLH design solidity of 0.108.

The observed trends indicate that in the HLH size, the region in which the flexible blade and rigid hub enjoy a weight advantage over the freely hinged rotor is when the number of blades is greater than seven. These findings correlate approximately with trends observed in similar rotors of smaller diameter, implying that weight-size trends are equivalent to those for freely hinged rotors.

The main difference between the ground resonance response of a hingeless as opposed to a hinged rotor system is in the magnitude of the exciting natural frequency. For a freely hinged rotor, this frequency is of the order of $.7\Omega$ (102 cycles per minute), which permits the design of a landing gear arrangement which has lateral, pitch, and roll rigid body frequencies well removed from the exciting ground resonance frequency. This separation assures freedom from ground resonance instability under all operating conditions.

For the rigid rotor configuration, the exciting ground resonance frequency was found to be equal for $.3\Omega$ (45 cycles per minute) (see Figure 94). Using the landing gear configuration designed for the hinged rotor as a base, coincidence of the rigid body lateral mode with the exciting frequency at normal operating speed (146 revolutions per minute) is indicated and will result in unstable oscillations.

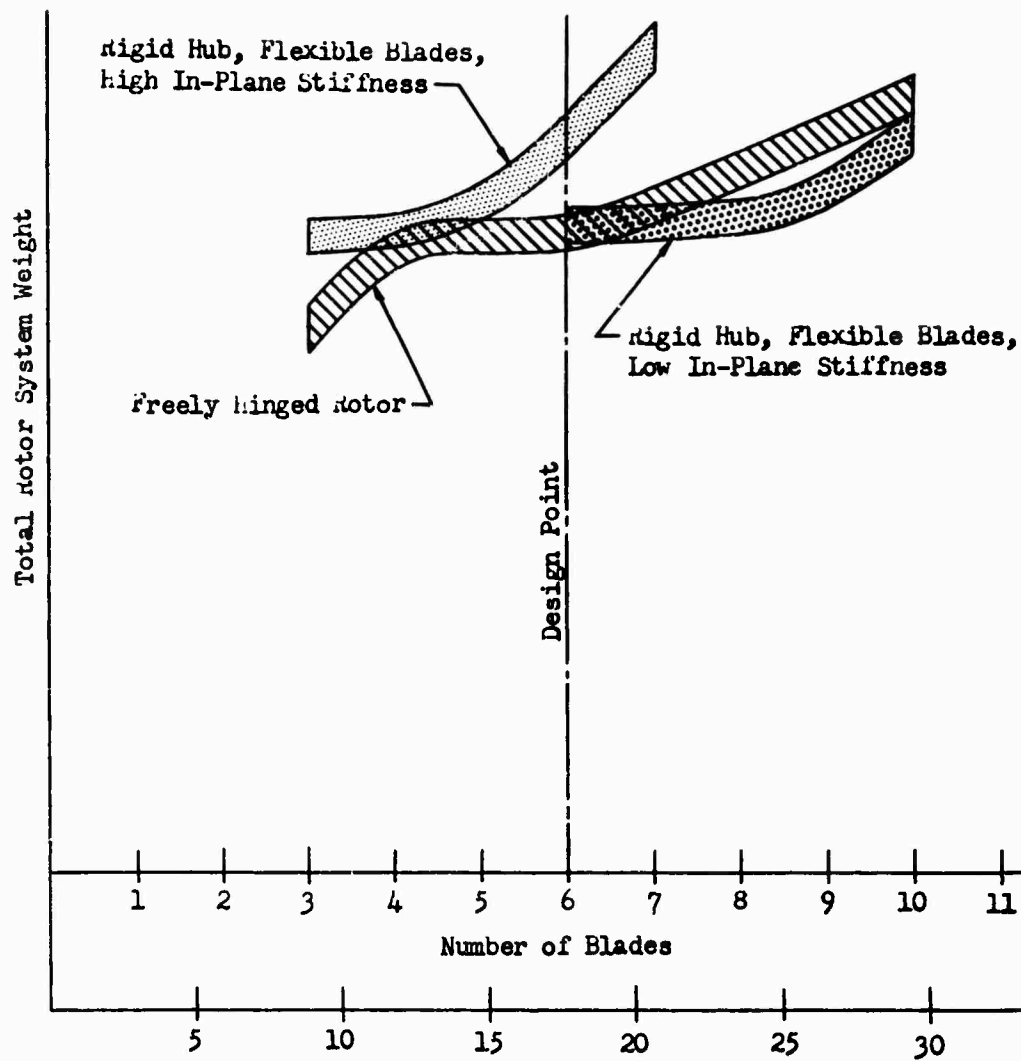


Figure 93 Number of Blades and Blade Aspect Ratio Versus Total Rotor System Weight

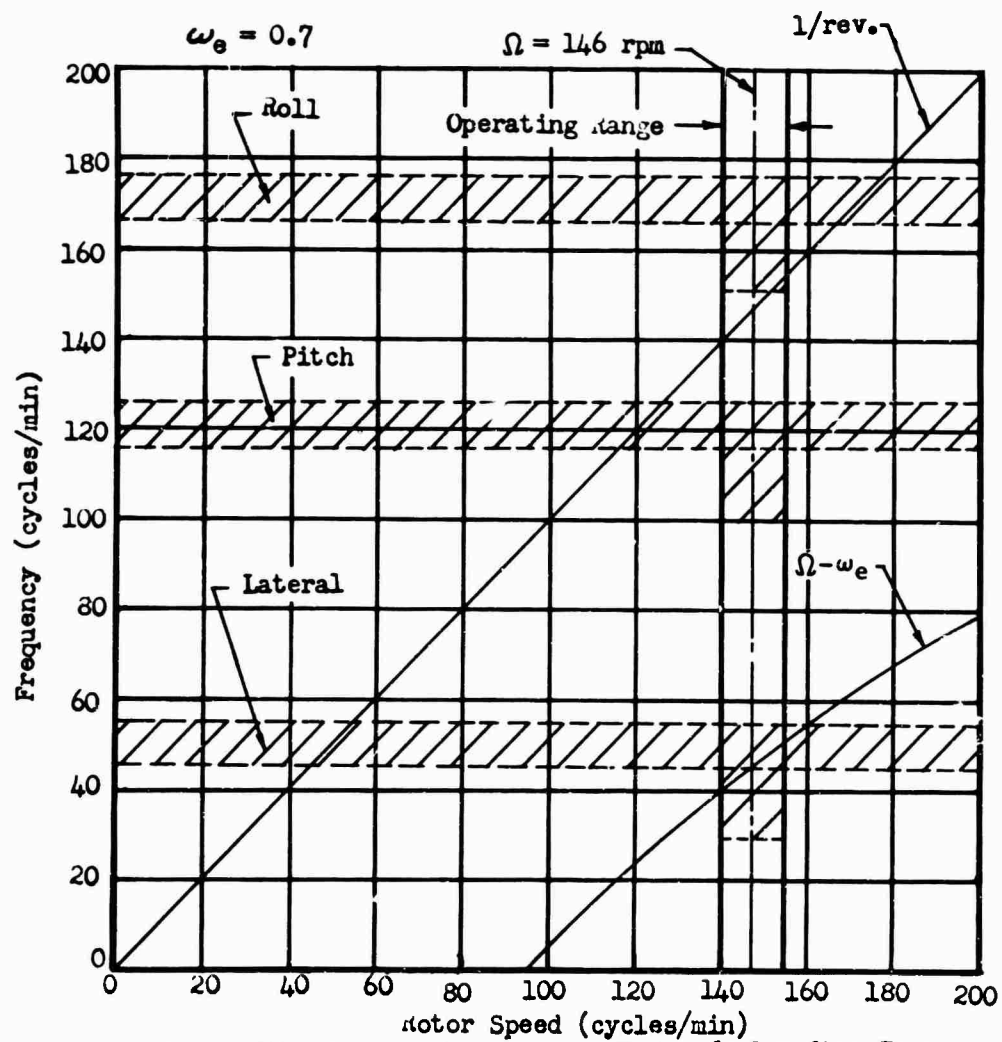


Figure 94 Ground Resonance, Tricycle Landing Gear, HLH Alternate Rotor Design

Basically, three ways exist to alleviate this condition of instability. The first consists of changing the first edgewise natural frequency to produce some separation of the exciting frequency from the first lateral mode. Because very little flexural deformation is experienced in this mode, alteration of the first edgewise frequency of the blade by changing its stiffness can result in only a very narrow frequency range. As a result, significant relief from instability cannot be obtained with this approach. An alternate second approach is to lower the lateral fuselage mode by designing a landing gear configuration with high lateral flexibility. However, this poses the problem of passing through an unstable band during rotor runup and shutdown, at a high percentage of rotor rpm. The third solution for this instability problem, which appears to be the most practical approach, is to raise the lateral rigid body fuselage mode by designing a landing gear configuration with high lateral stiffness. One such possible configuration would be a four-point system with a stiff, split fore landing gear configuration as shown in Figure 95. Besides eliminating the problem of ground resonance, this four-point system would allow for total load straddling capability, permitting the aircraft to taxi forward over the load. This landing gear change also removes all definite restrictions on the length of a straddled load, since it allows the load to project both forward and aft of the fuselage. The maximum load length then depends on its shape and other characteristics and the terrain characteristics at the landing site. To capitalize on the load straddling capability, raising the cockpit might also be considered, the resulting configuration being as shown in Figure 95.

The primary disadvantage encountered in the alternate rotor designs is the large effective offset. If the offset could be reduced as the hingeless blade concept is developed, it would make this design competitive with hinged rotors in the areas of aircraft attitude and handling characteristics, control load, and "off-design" operational stresses.

Aircraft attitude is related to effective offset by the hub moment resulting from tilting the rotor thrust vector to provide propulsive force. For a first approximation, the moment can be considered proportional to offset. Aircraft attitude changes with changes of speed or direction are therefore greater than normal design practices dictate.

The preliminary study of the two alternate designs indicates that for both six and eight blades, the effective offset is about 25 percent as compared to 6-1/2 percent for the hinged rotor. This would create a head moment on the alternate systems on the order of 4 times greater than the normal hinged design.

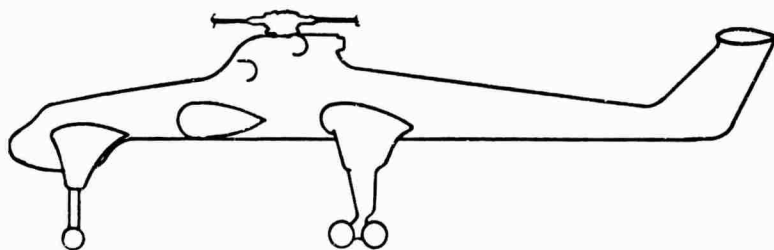
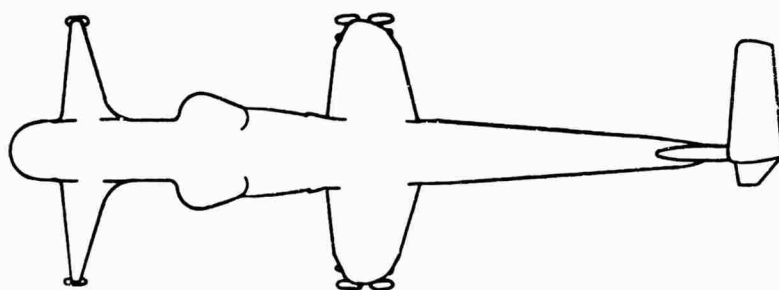
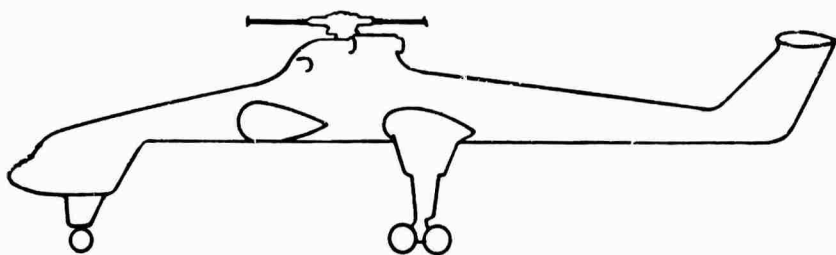
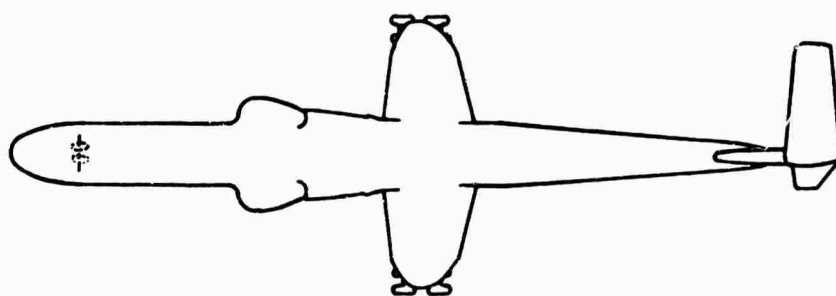


Figure 95 Comparison of Tricycle and Quadracycle Landing Gear

Selection of pre-cone and pre-lag angles requires an exact knowledge of operating conditions, both for design missions and for off-design applications. Since optimization of these angles for the most severe conditions could place cruise or ferry operation in the fatigue damaging regime, a complete spectrum of operating variables is necessary for good design in this area.

Both steady and vibratory stresses have been found to vary significantly with pre-cone angle, as shown in Figure 96.

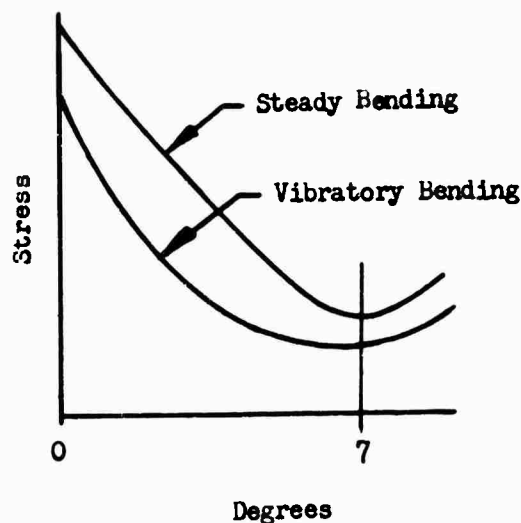


Figure 96 Pre-Cone Angle Versus Stress

The optimum pre-cone angle is the same angle the blade would assume if freely hinged. It is roughly proportional to the lift per blade divided by the centrifugal force at the blade root. Therefore, for a given blade and operating rpm, the optimum pre-cone angle is directly proportional to gross weight. It becomes apparent that if the aircraft gross weight is changed significantly, the optimum coning angle for minimum blade stress should also change by the same percentage. But since the pre-cone angle is fixed, a stress penalty (roughly proportional to the relative change in gross weight) is then incurred. Should the aircraft have a pre-cone angle of 7 degrees optimized on a gross weight of 80,000 pounds, flight at its no-payload weight of about 40,000 pounds results in a pre-cone angle reduction of about 3-1/2 degrees too large, so a 35-percent bending stress increase (both steady and vibratory) results. This stress increase can accumulate considerable fatigue damage on the blade. Any other equivalent change in gross weight, such as 2.0 or 2.5 g maneuver load, would similarly create increased static and vibratory stresses and their associated fatigue damage.

For the purpose of this analytical investigation, blade loadings were limited to those for the 20-ton mission cruise at 95 knots and 78,750-pound gross weight. Two hingeless rotors were designed and investigated, one a six-bladed rotor (Blade I) and the other an eight-bladed rotor (Blade II). Stiffness distributions and steady and vibratory stresses for both configurations are shown in Figures 97 through 102.

For the six-bladed rotor, the inboard portion of the blade was kept considerably more flexible than the normal hinged blade design, with an I_{yy}/I_{xx} ratio of approximately 2 to 1. The resulting stresses were found to be satisfactory for titanium alloys such as Ti-6AL-4V and Ti-6AL-6V-2 Sn. Steady and vibratory stresses experienced would cause accumulative fatigue damage inboard if aluminum were selected, giving an unsatisfactory blade life and replacement time. Investigation of pre-cone and pre-lag angles for the flight condition yielded 7 degrees pre-cone and 5 degrees pre-lag, measured at 5 percent of rotor radius, as the best combination. In this position, the blade is in approximately the natural equilibrium attitude it would seek if it were freely hinged.

It was also noted that due to flapwise-edgewise coupling, the effect of pre-coning on edgewise stresses (and of pre-lagging on flapwise stresses) must be accounted for in the final iterations. The benefits gained in lowering flapwise stresses by a small increase in pre-cone angle may be negated by a rise in edgewise stresses due to the coupling effect. Final selection of both angles must be evaluated over the entire spectrum of flight maneuvers.

The titanium alloys tentatively selected can sustain the induced fatigue stresses with a 4σ deviation included in the computation of allowable working stress curves. The final alloy to be chosen should be determined by ability of the material to be worked to the proper form, ease of maintenance, and cost. The first-mode edgewise frequency is 0.7 cycle per revolution. The blade static droop is 27.4 inches, slightly more than the hinged blade, but the 7-degree pre-cone angle elevates the blade tip approximately 5-1/2 feet, so no interference with the aircraft fuselage will occur.

During the investigation of the six-bladed rotor configuration, it became apparent that some benefit could be derived from a heavier blade with more flexibility. The most efficient method available for effecting these changes was to increase the blade's aspect ratio. Relative to the root end section properties, the added length of blade in a high aspect ratio design increases the relief moment of centrifugal force, while the increased flexibility reduces bending moments and stresses. The reduction of vibratory stresses is significant, since it can be seen from the slope of a modified Goodman diagram that a

steady stress gradient can be tolerated more readily than an equal vibratory stress change.

In order to maintain the rotor performance as the six-bladed rotor, the existing rotor radius and solidity were not changed; an eight-bladed rotor with a narrower chord (23.25 inches) resulted.

The pre-cone angle of 7 degrees and pre-lag angle of 5 degrees at 5-percent offset were found to be optimum values for this rotor, just as in the six-bladed design. This coincidence stems from the fact that total blade weights are the same for both rotors, and lift to drag ratios are equal.

A stress survey of the spar of the narrow chord blade showed that 6061-T6 aluminum alloy could be used for the structural member. Inboard, in the hub attachment area, bending loads require the use of titanium alloy attachment components. In this region the stiffness and section modulus requirements necessitate deviation from the "D" shaped spar section.

Analysis of the natural frequencies shows the first-mode edgewise frequency to be 0.72 cycle per revolution. The first-mode flapwise frequency is 1.1 cycles per revolution, but amplification of flapwise response is negligible due to large aerodynamic damping.

Static droop for this blade is approximately the same as the elevation of the blade tip due to the pre-cone angle, so that no fuselage-blade tip interference will occur.

Preliminary calculations show also that dynamic response may be improved by the addition of a concentrated mass at the tip of both blades should the amplification of response exceed that predicted in the design criteria. The need for such a tip weight was not indicated by the analysis performed on either of the alternate designs, but the possible benefits of its use should be investigated in a more detailed study to determine a trade-off point of benefit versus added weight. This addition of tip mass will have an effect on blade stresses similar to the effect of an increase in blade aspect ratio, but it is an inefficient method of changing the blade frequencies since it adds parasite weight, incapable of supporting itself or adding to the blade structure.

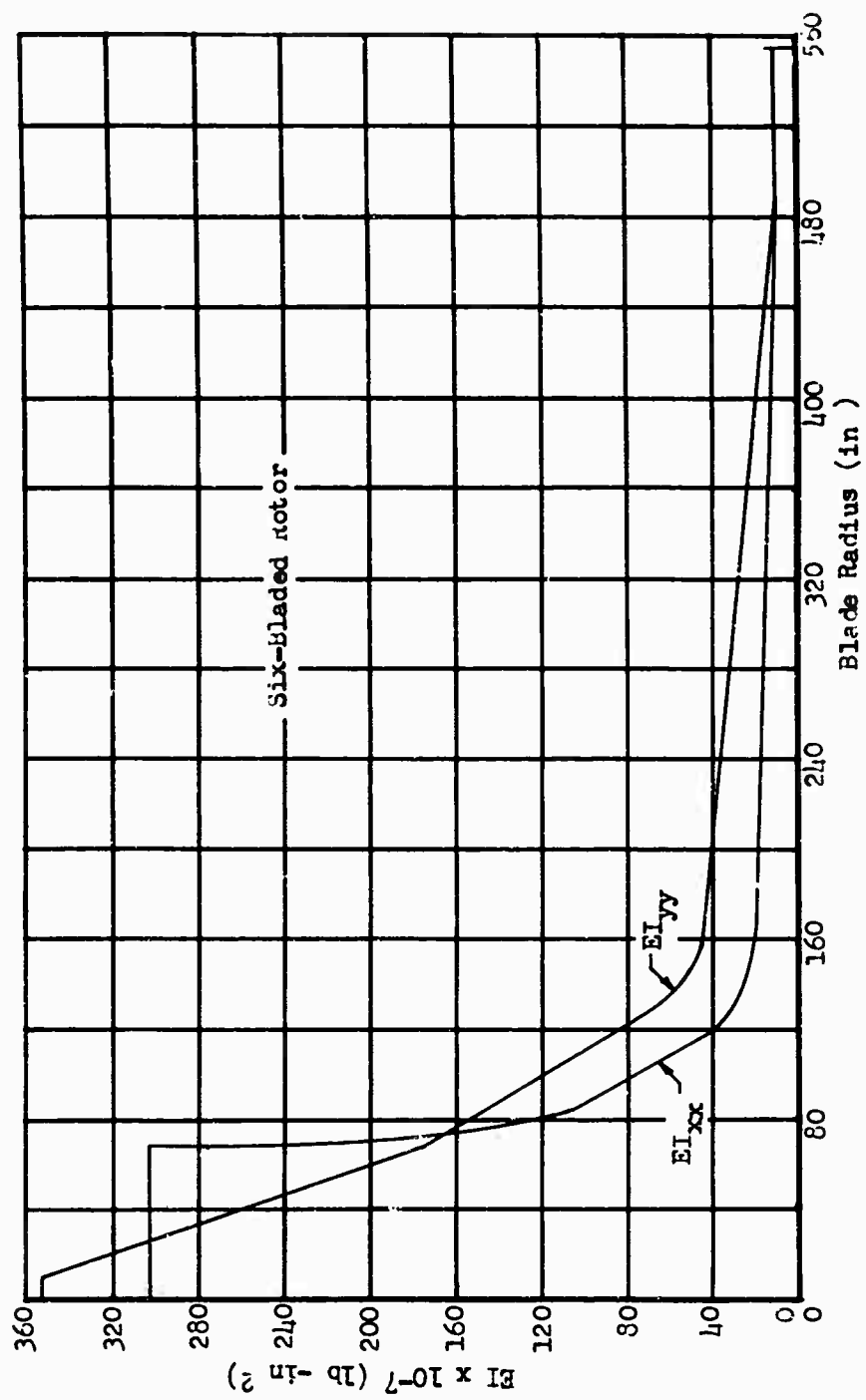


Figure 97 Stiffness Distribution, Hingeless Blade I

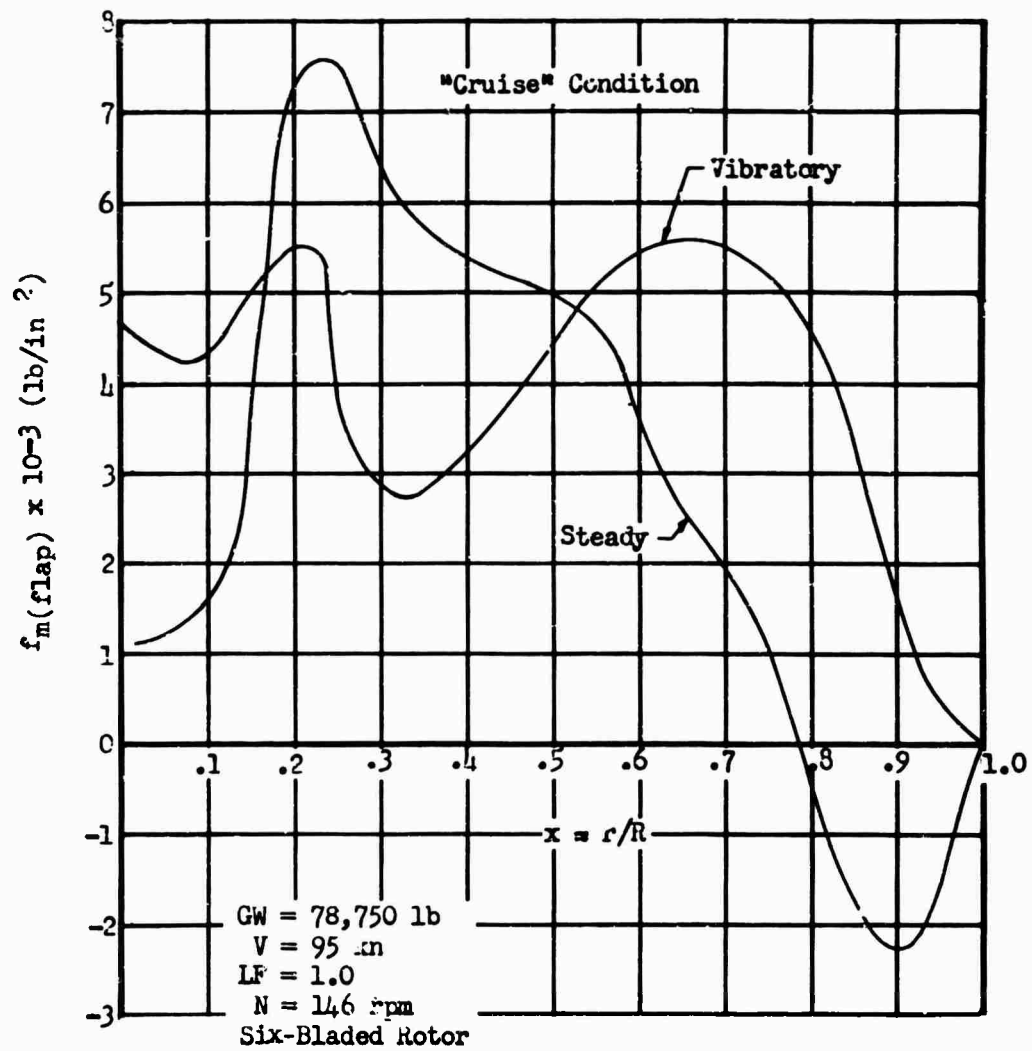


Figure 98 Flapwise Stress Distribution, Hingeless Blade I

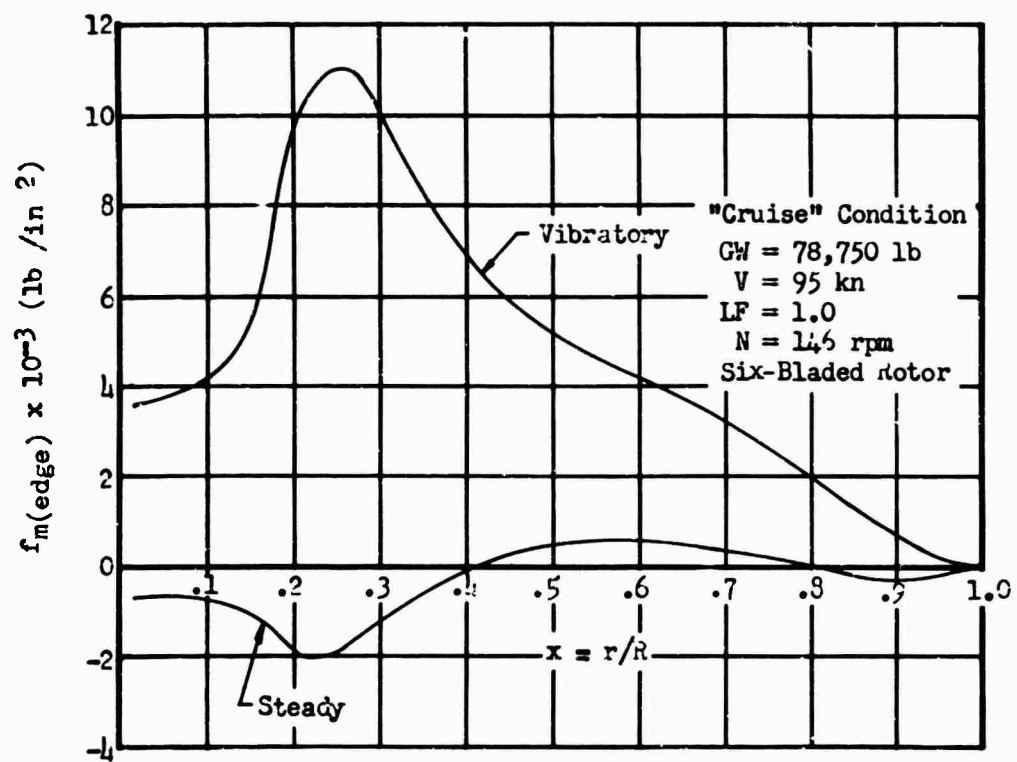


Figure 99 Edgewise Stress Distribution, Hingeless Blade I

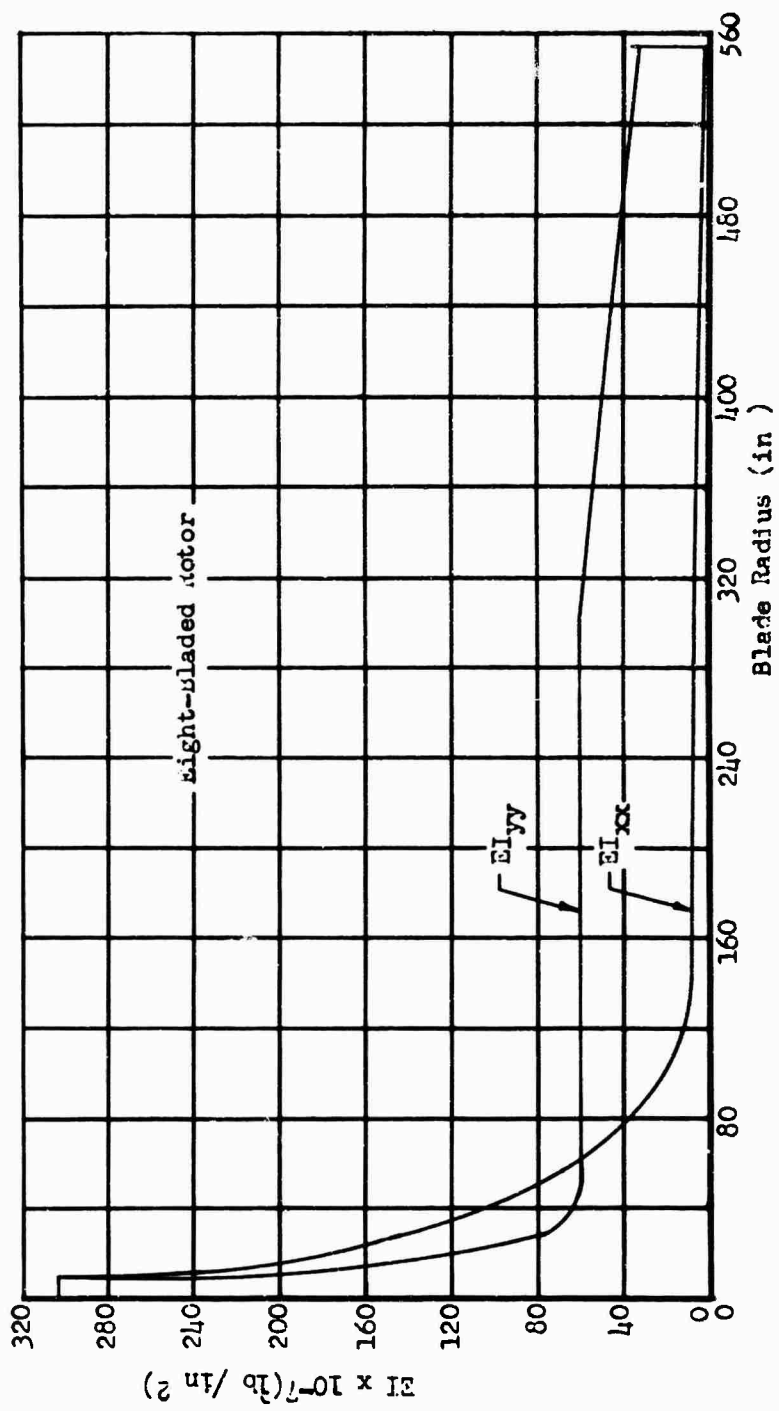


Figure 100 Stiffness Distribution, Hingeless Blade II

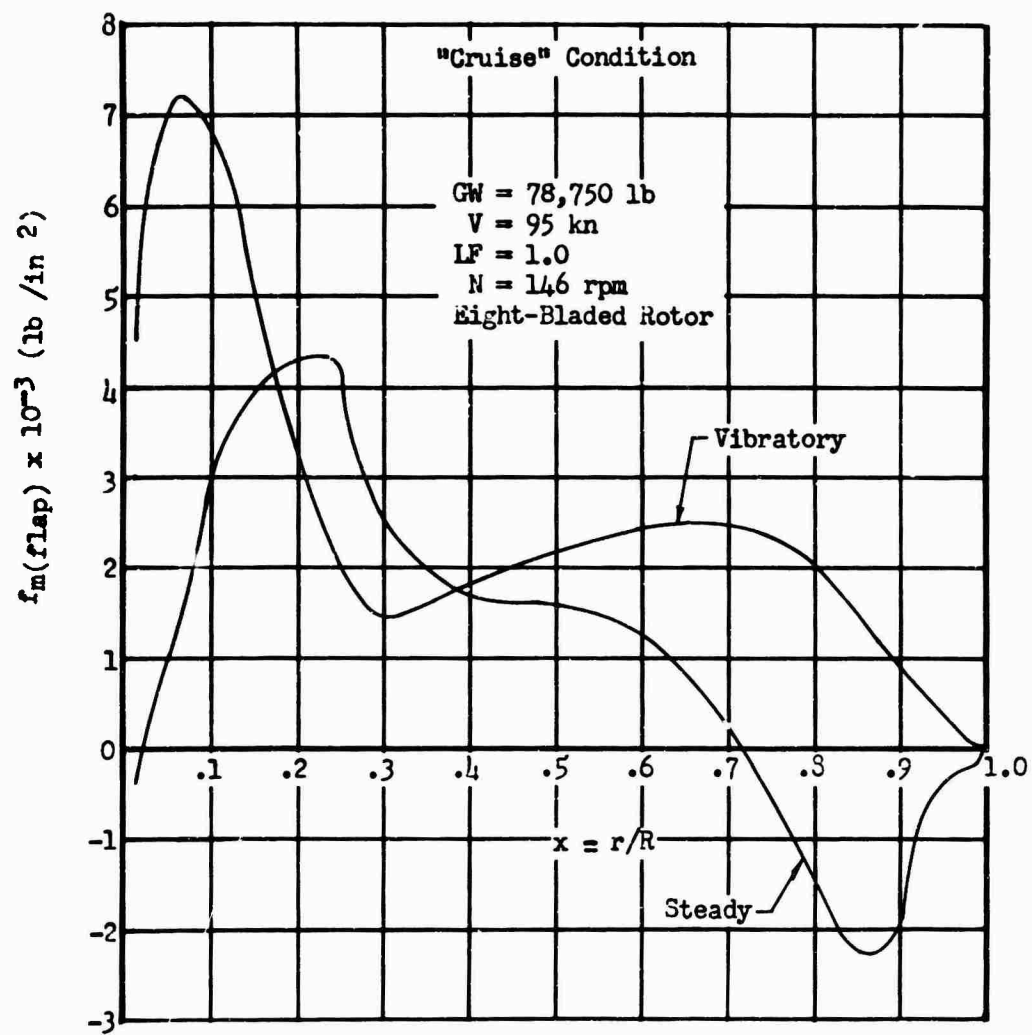


Figure 101 Flapwise Stress Distribution, Hingeless Blade II

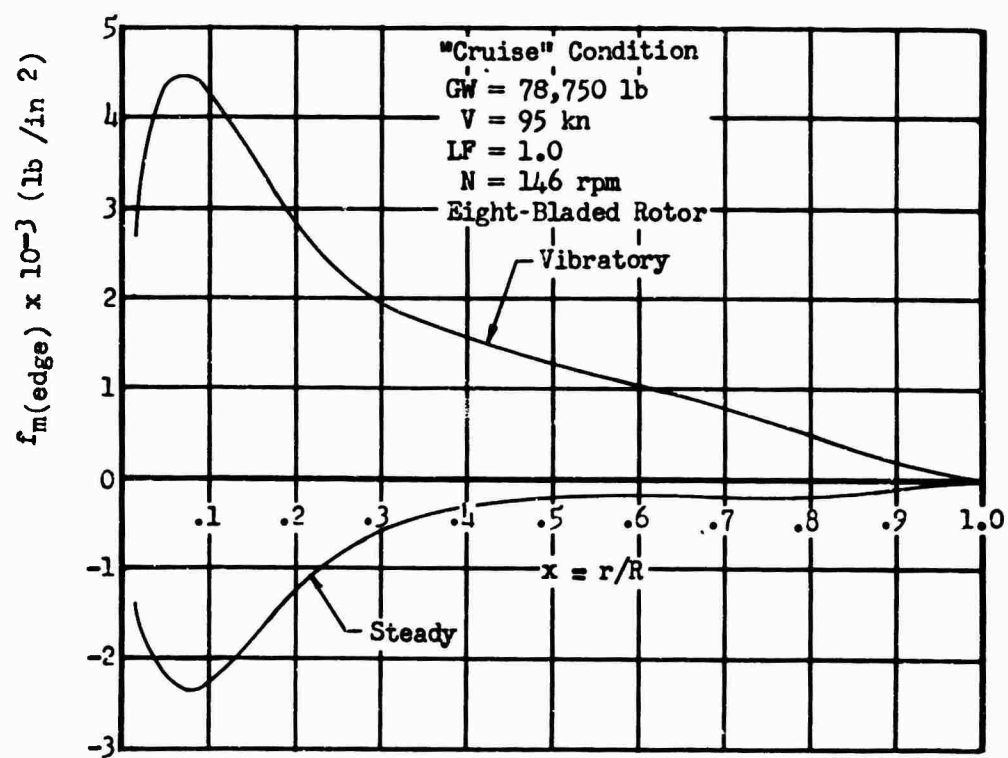


Figure 102 Edgewise Stress Distribution, Hingeless Blade II

ARTICULATED ROTOR BLADE STRUCTURAL ANALYSIS

Results

A summary of the rotor blade structural analysis showing the margins of safety is presented in Table XXX. These margins are typical of those on in-service blades and show the blade to be structurally adequate for the anticipated flight and ground operations.

The fatigue analysis calculated shows a blade life far in excess of the specified 3600 hours.

Description

In Figure 103 the (1) Cuff, a "U" shaped 6AL-4V titanium attachment fitting, joins the blade to the sleeve component of the rotor head. The two stepped tangs and the double trapezoidal bolt pattern of the cuff are designed to provide an efficient, redundant load path between the cuff and the main structural member of the blade, the (2) spar.

The spar, a hollow "D" section extrusion of 6061-T6 aluminum alloy, forms the leading edge of a modified NACA 0012 airfoil while segmented, nonstructural (3) Fairings are bonded to the spar backwall, completing the aft portion of this contour.

(4) Counterweights, located in the leading edge and held in place at the outboard end of the spar by a (5) Retaining Block, are required to keep the mass of the blade balanced about the feathering axis. To produce completely interchangeable blades, every blade is balanced, at the factory, against a master blade. This is accomplished with the (6) Tip Balance Assembly, which consists of two sets of shim weights, one forward and one aft, attached to the (7) Balance Assembly Support Blocks. The number of weights fore and aft is varied to adjust edgewise balance and to trim the dynamic characteristics of the blade, while the total number of weights adjusts the spanwise balance.

The tip of the blade is faired to a smooth airfoil contour by a (8) Tip Cap to improve tip efficiency and reduce noise levels.

At the inboard end of the spar, the blade's (9) BIM[®] Indicator provides a visual check of the spar's structural integrity by indicating the pressure level of an inert gas atmosphere. The gas is contained within the spar by the (10) BIM[®] Seal Assembly which seals the internal cavity at the outboard end of the spar and by a contoured cover plate at the inboard end.

TABLE XXX
SUMMARY OF MARGINS OF
SAFETY FOR MAIN ROTOR BLADE COMPONENTS

1. Analysis of Cuff Attachment to Rotor Head Sleeve

Bolts (combined stress) MS = .85

2. Analysis of Cuff-Spar Attachment Region

Inboard Bolt Holes

Cuff (combined stress)	MS _{prin} = .93
	MS _{shear} = 1.37
Cuff (in bearing)	MS = HIGH
Spar (in bearing)	MS = 1.66
Spar Tear-cut (through end)	MS = HIGH
Bolts	MS _{shear} = .57

Outboard Bolt Holes

Spar (combined stress)	MS _{prin} = .07
	MS _{shear} = .34
Spar (in bearing)	MS = 1.69
Cuff (in bearing)	MS = .59
Cuff Tear-out (through end)	MS = HIGH
Bolts	MS _{bending} = .34

3. Analysis of Spar Outboard of Attachment Region

Blade Station X = r/R	MS min @ Condition #
.9	.94 @ 4a
.8	.49 @ 4a
.7	.26 @ 4a
.6	.10 @ 4a
.55	.03 @ 4a
.5	.01 @ 4a
.45	.02 @ 4a
.4	.05 @ 4a
.35	.13 @ 4a
.3	.22 @ 4a
.25	.26 @ 5a
.2	.48 @ 5a

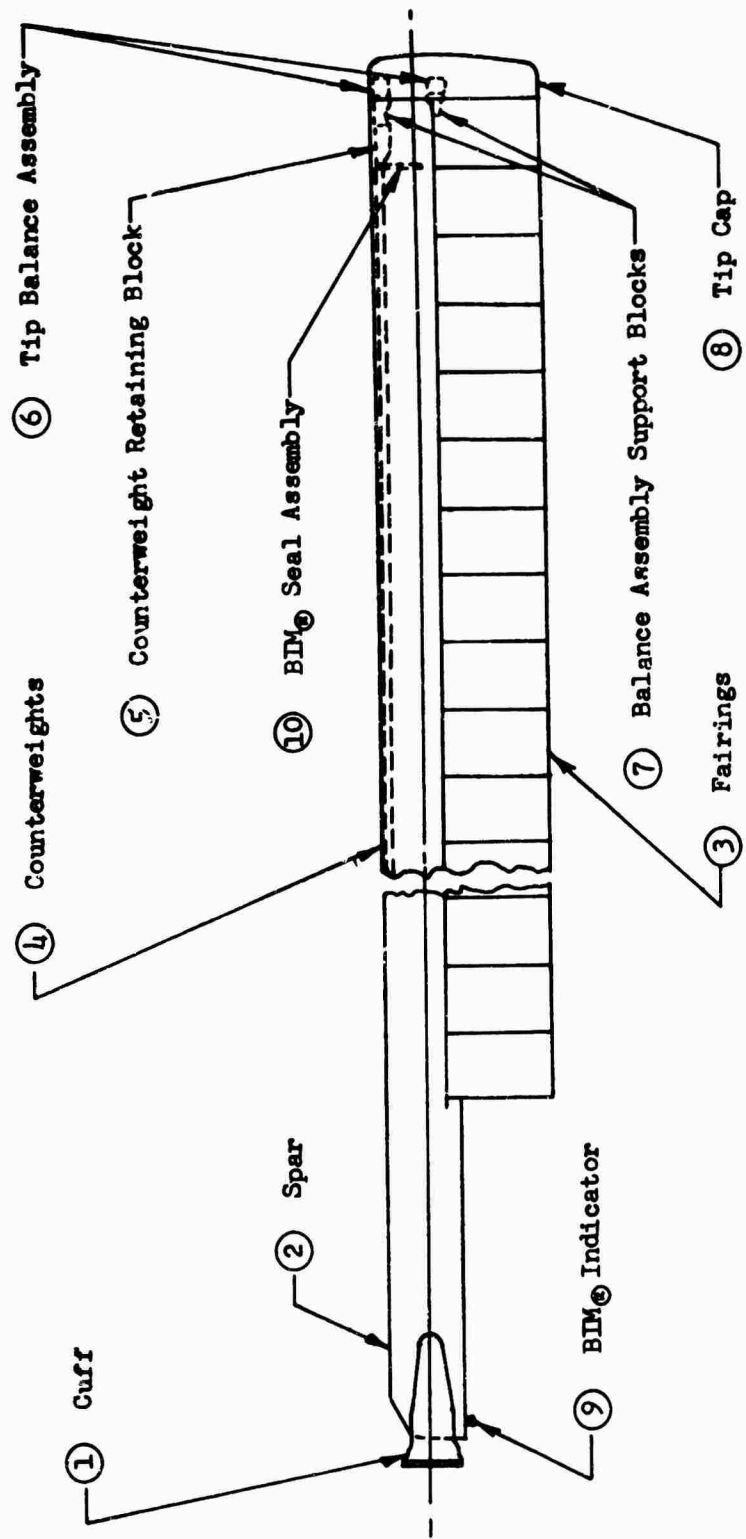
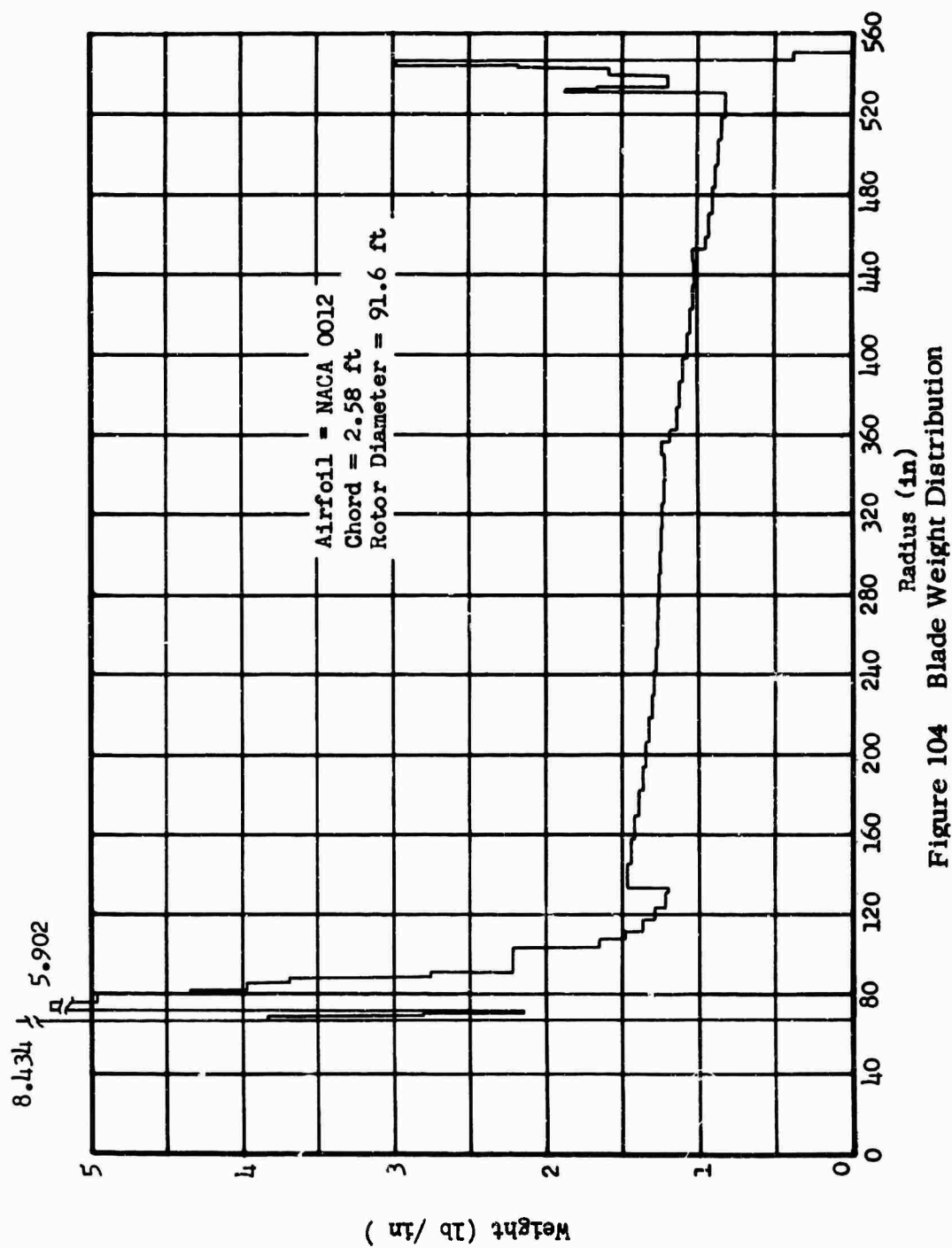


Figure 103 Rotor Blade, General Arrangement



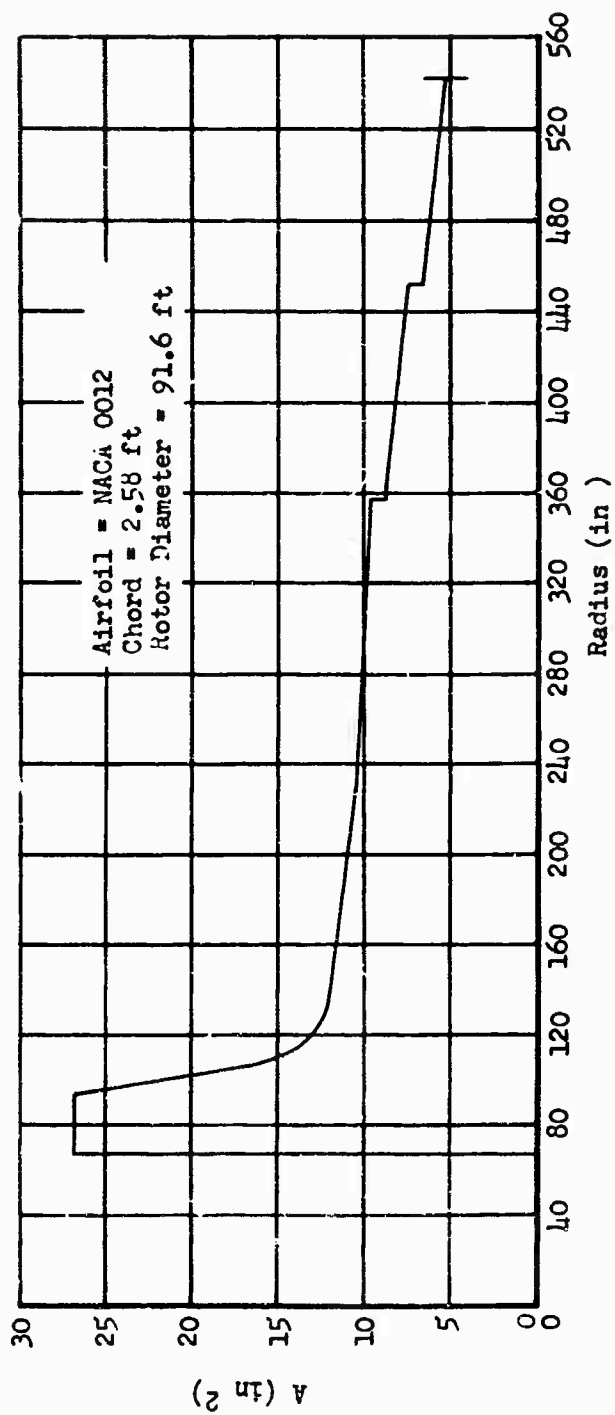


Figure 105 Spar Area Distribution

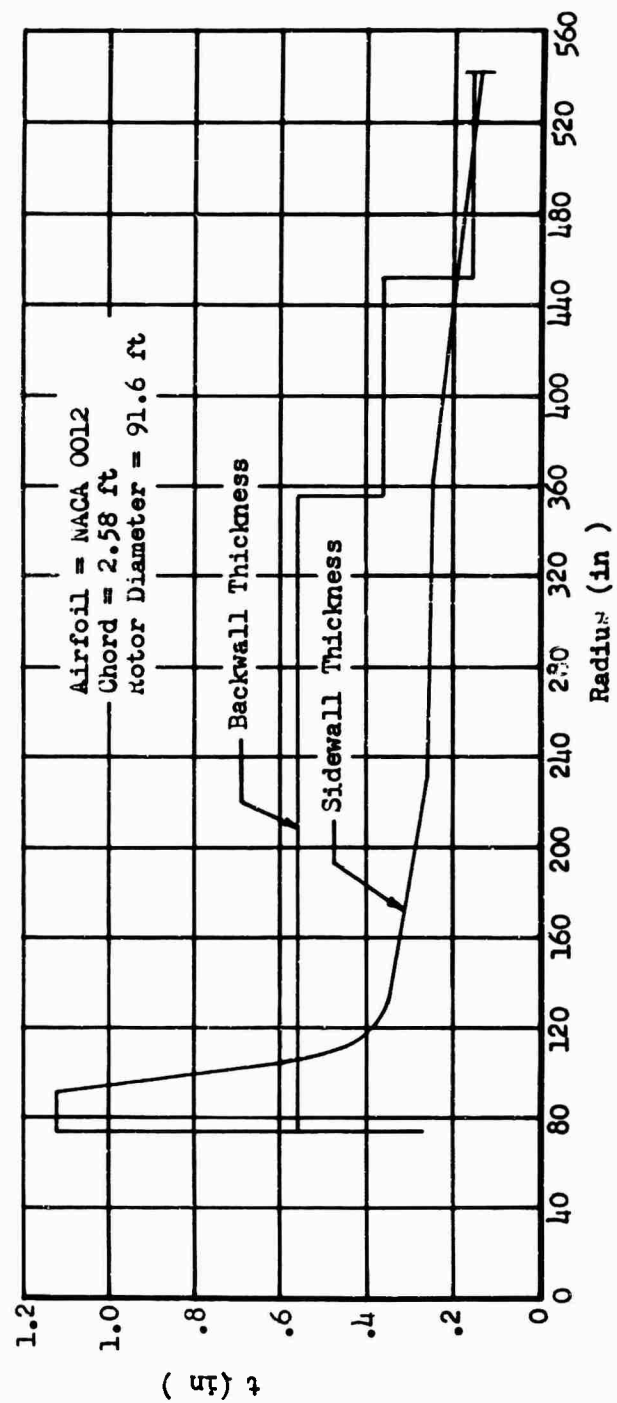


Figure 106 Spar Thickness Distribution

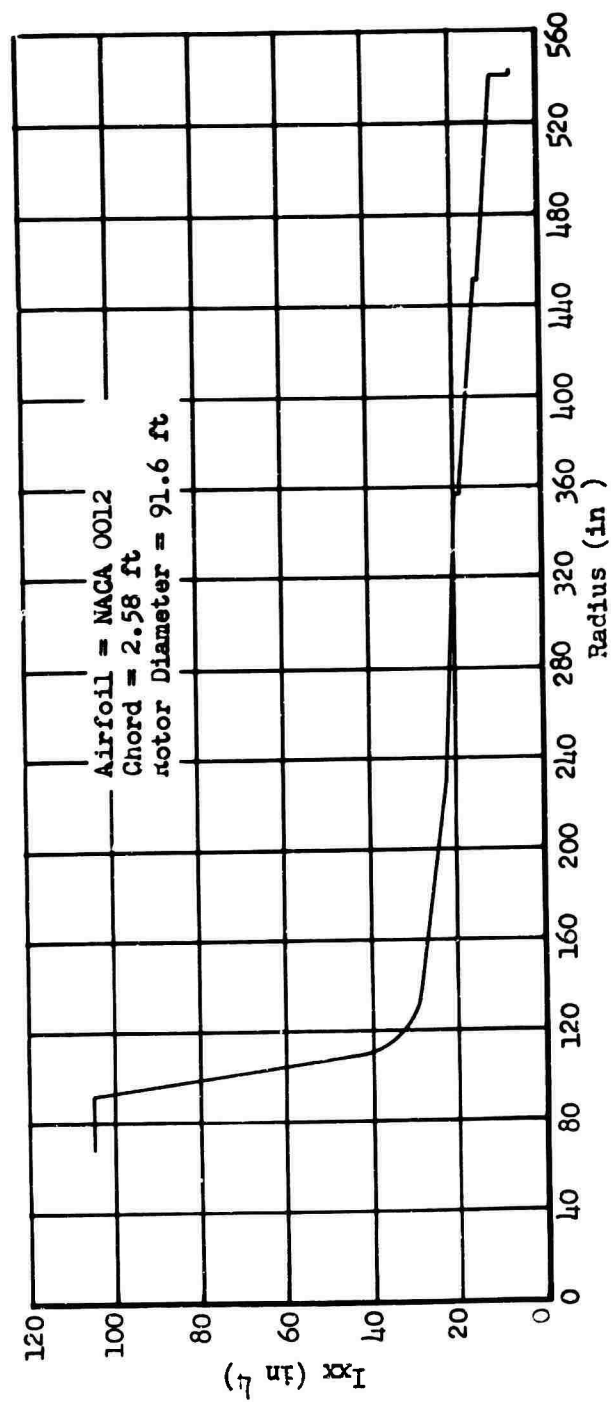


Figure 107 Spar Flapwise Moment of Inertia Distribution

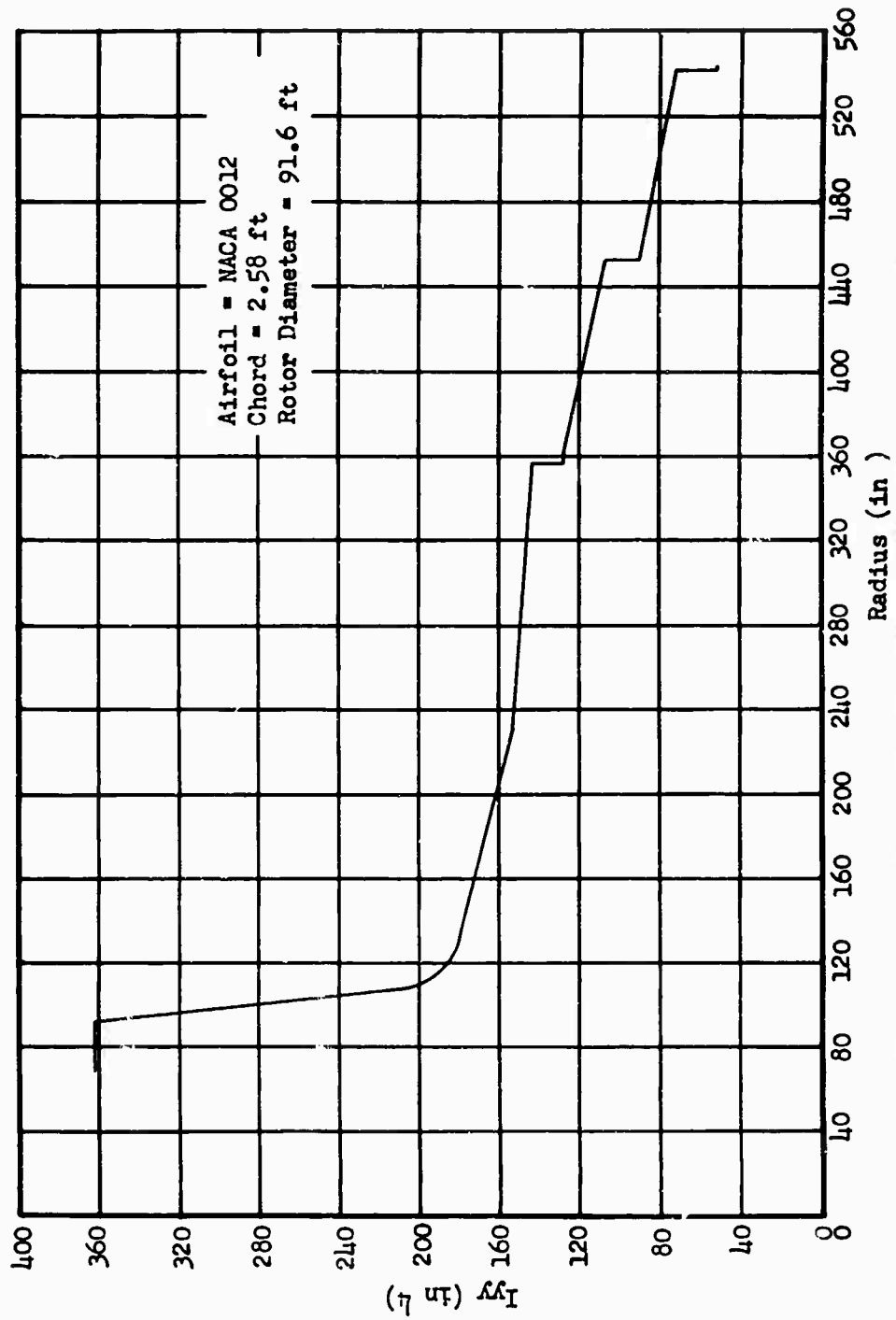


Figure 108 Spar Edgewise Moment of Inertia Distribution

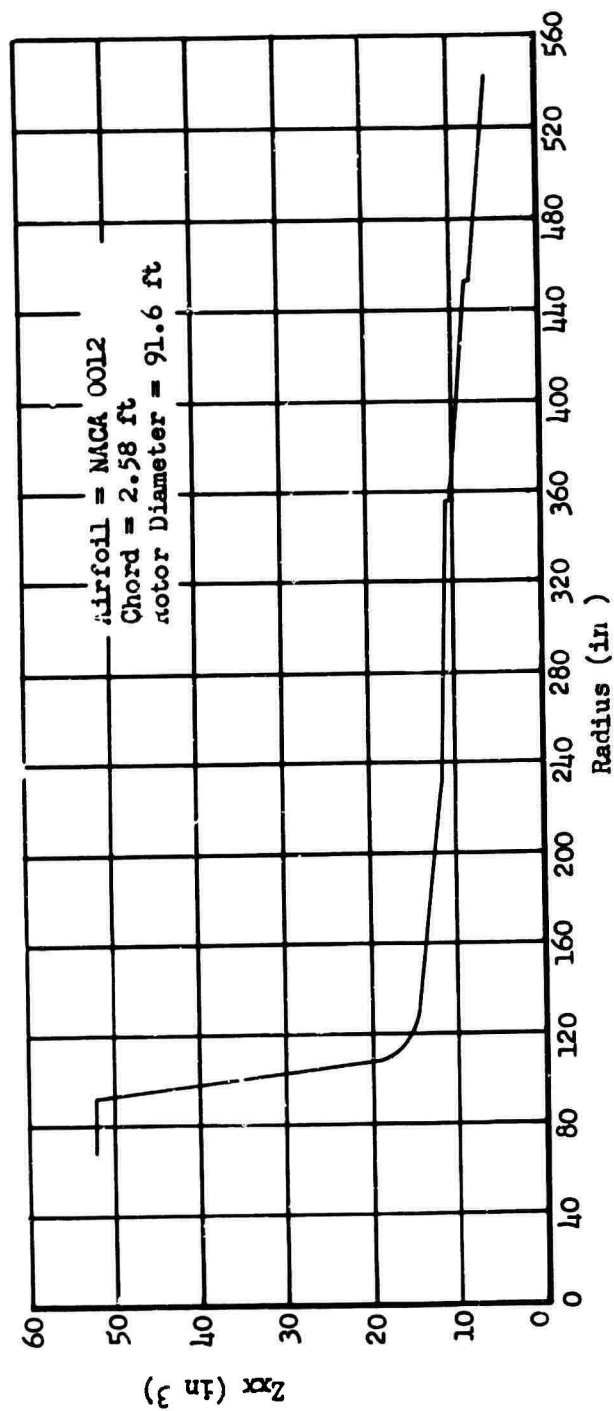


Figure 109 Spar Flapwise Section Modulus Distribution

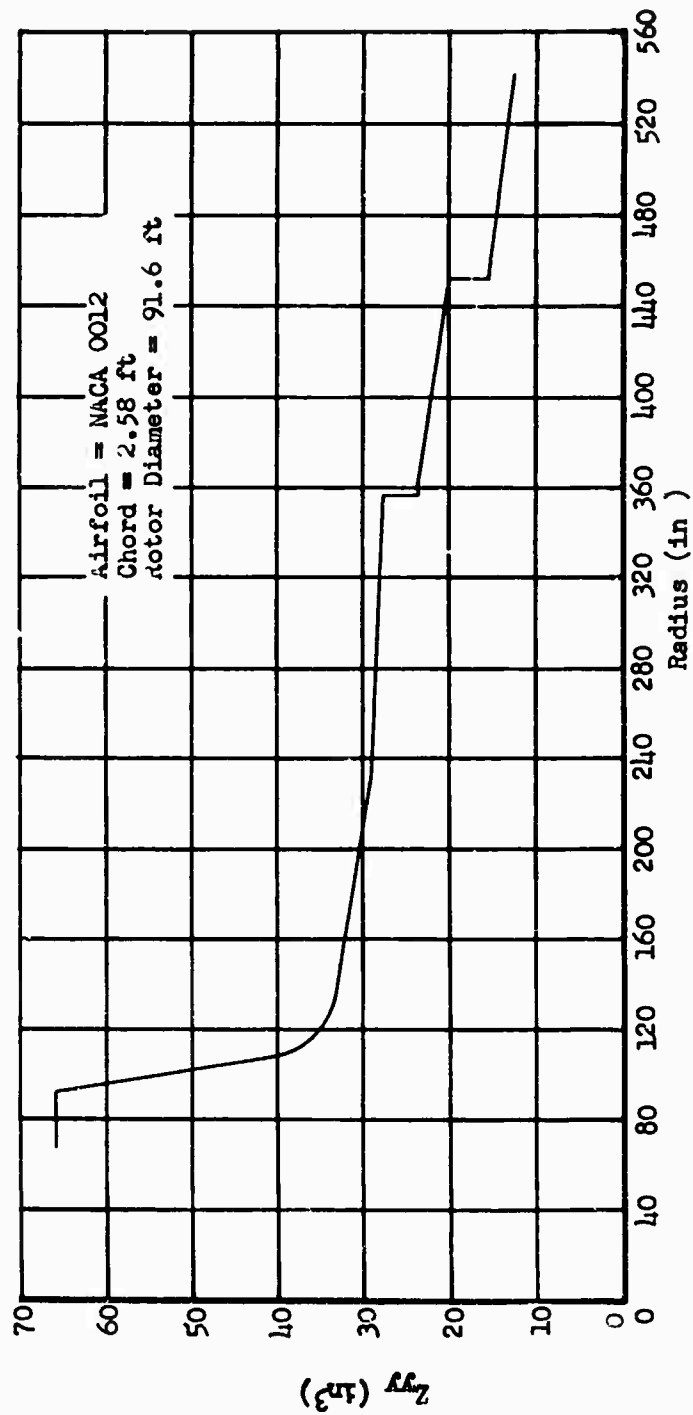


Figure 110 Spar Edgewise Section Modulus Distribution

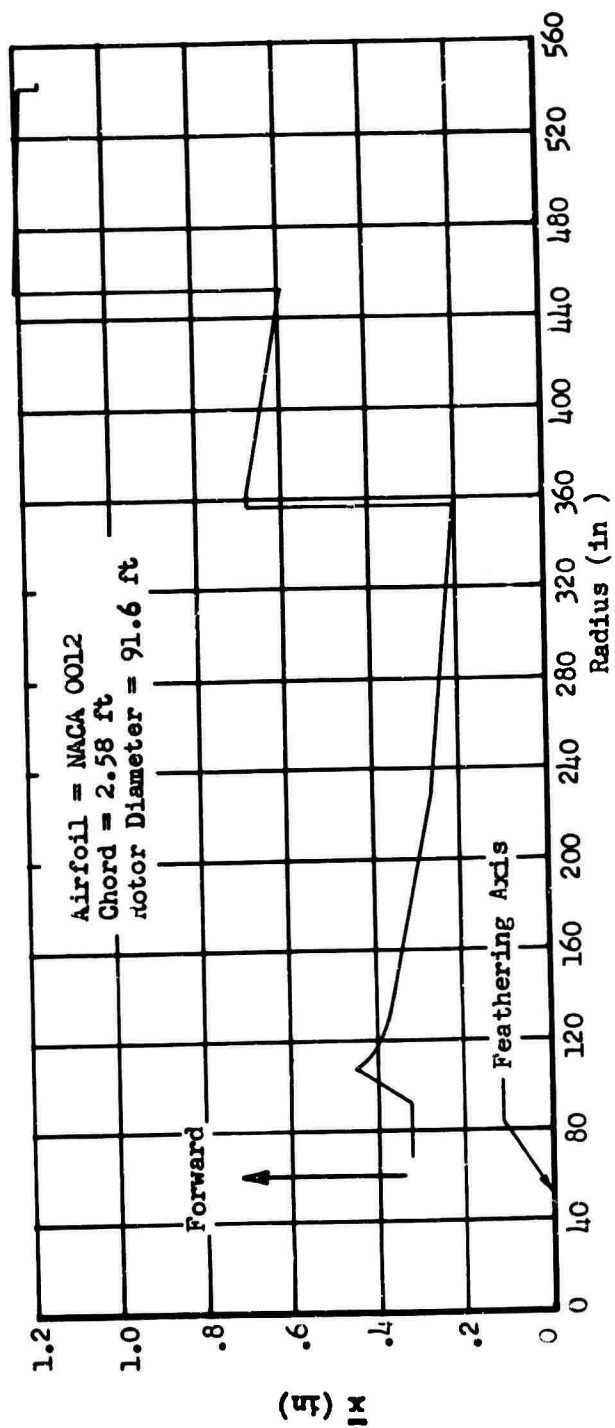


Figure 111 Spar Sectional Center-of-Gravity Variation

In Figures 104 through 111 are shown the physical properties of the spar. The curves include: the spar weight, area and thickness distributions, the spar flapwise and edgewise moments of inertia distributions and spar section modules and sectional center-of-gravity variations.

Torsional Behavior of the Spar

Introduction

The spar is essentially a single cellular monocoque structure. Its torsional behavior during operation depends on the distribution of the internal resisting shear, the spanwise distribution of section shear centers, and torsional stiffness.

Determination of Shear Flow and Shear Center Distribution

Using the analysis given in Reference 7, the shear flow distribution and shear center of the spar at various spanwise stations were determined. The shear center is located approximately at the feathering axis, the actual positions being shown in Figures 112 and 113.

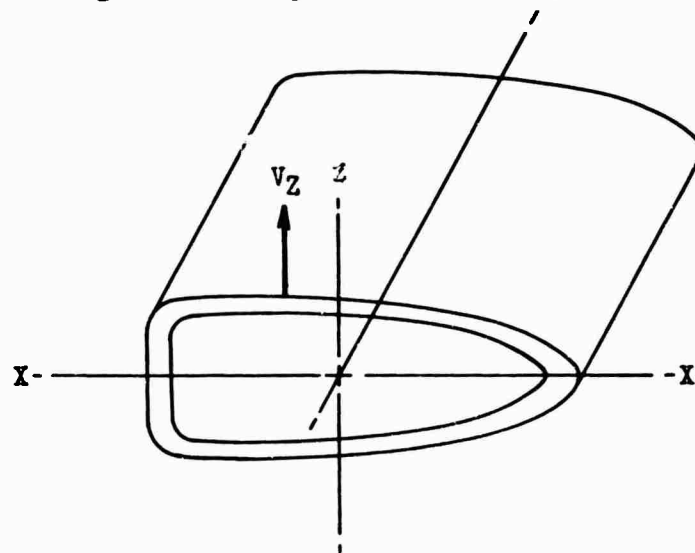


Figure 112 Spar Shear Flow Determination

Given the spar, with an external load V_Z , the shear flow per unit of length is determined by

$$q = \frac{VZ}{I_x} \sum ZA \quad (28)$$

where I_x = Moment of inertia about X axis, in⁴
 Z = Distance to centroid of element, in
 A = Area of the element, in²

The spar was divided into 56 elements and the shear flow distribution around the spar was determined. The equation for the angular twist θ per unit length of beam is

$$\theta = \frac{1}{2AG} \sum q_{avg} \frac{L}{t} \quad (29)$$

where L = Length of element, in
 t = Thickness, in
 G = Modulus of rigidity, psi
 $q_{avg} = \frac{(q_i + q_{i+1})}{2}$

Since the shear center is the point where bending occurs without twist, θ must be cancelled by adding a constant shear flow q around the section such that

$$\frac{1}{2AG} \left[\sum q_{avg} \frac{L}{t} - \sum q' \frac{L}{t} \right] = 0 \quad (30)$$

The resulting shear flow pattern is shown in Figure 113. For this ($q_{avg} + q'$) distribution, the sum of moments about any arbitrary moment center must equal zero. The shear center e_2 is then determined from

$$e_2 = \frac{\sum M}{\sum VZ} = \frac{2 \sum (q_{avg} + q')_{avg} AK}{VZ} \quad (31)$$

where e_2 = Distance from moment center to shear center
 AK = Enclosed area under the element to the moment center

This analysis was applied at several stations along the blade, and the resulting spanwise distribution of the shear center is shown in Figure 114.

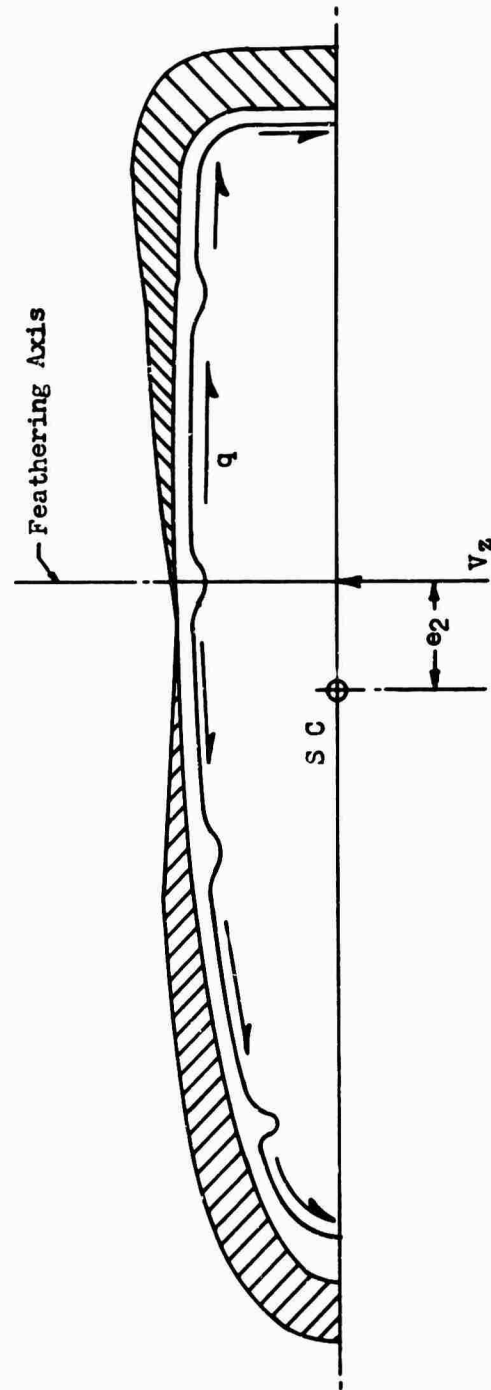


Figure 113 Typical Shear Flow Distribution

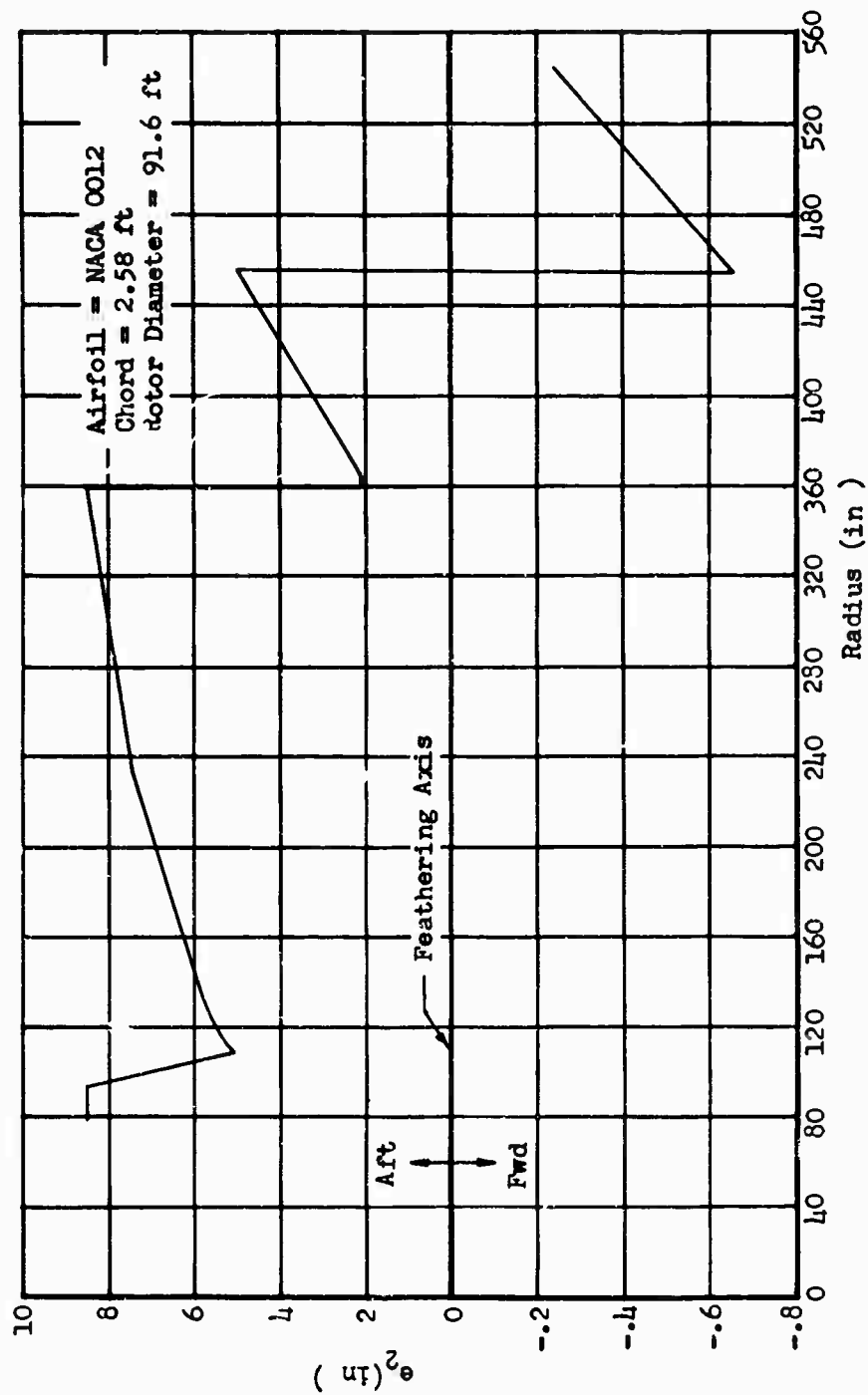


Figure 114 Spar Shear Center Variation

Determination of Torsional Stiffness

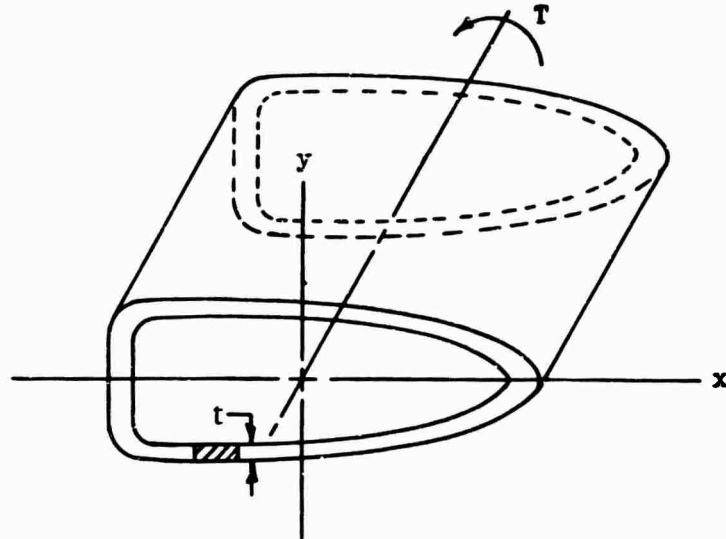


Figure 115 Spar Section Loaded in Torsion

Consider a unit square cut (see Figures 115 and 116) from the wall of the spar. The shear force q on the edge of the square is

$$q = (f_s t) (1) = f_s t \quad (32)$$

where f_s = Torsional stress, lb/in²
 t = Wall thickness, in

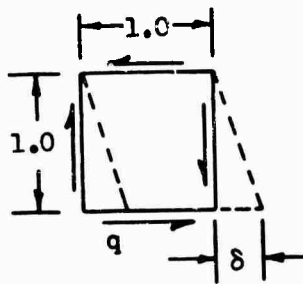


Figure 116 Shear on Spar Element (Reference Figure 115)

The shear deformation δ is

$$\delta = \frac{f_s}{G} \quad (33)$$

where G = Modulus of rigidity, lb/in²

The work done by the shear force,

$$W = \frac{(f_s t) (l)}{2} \delta = \frac{f_s^2 t}{2G} \text{ lb-in} \quad (34)$$

The torsional stress for a single cell, thin walled closed section was determined by Prandtl to be

$$f_s = \frac{T}{2A't} \text{ lb/in}^2 \quad (35)$$

where A' = Enclosed area formed by the center line of the contour walls, in² (See Figure 117)

T = Resisting moment, lb-in

Substituting this value of f_s into the expression for W ,

$$W = \frac{T^2}{8 (A')^2 G t} \quad (36)$$

The total work for the entire cross section per length of spar, then, equals

$$W_{\text{total}} = \frac{T^2 P}{8 (A')^2 G t} \text{ lb-in} \quad (37)$$

where P = is the perimeter of the section, in

The work, however, is also $= \frac{T\theta}{2}$, where θ = Angle of twist per length of blade

Hence,

$$\frac{T\theta}{2} = \frac{T^2 P}{8 (A')^2 t G} \quad \text{or,} \quad (38)$$

$$\theta = \frac{TP}{4 (A')^2 t G} = \frac{T}{KG}$$

$$\text{where } K = \frac{4(A')^2 t}{P}$$

K is generally referred to as the torsion constant, since it is a function only of the geometrical shape for the spar section; since t varies for different parts of the section, this expression then becomes

$$K = \frac{4(A')^2}{\oint \frac{dP}{t}} \quad (39)$$

The spar shear stiffness (KG) was plotted versus blade radius for several stations along the span and is shown in Figure 118.

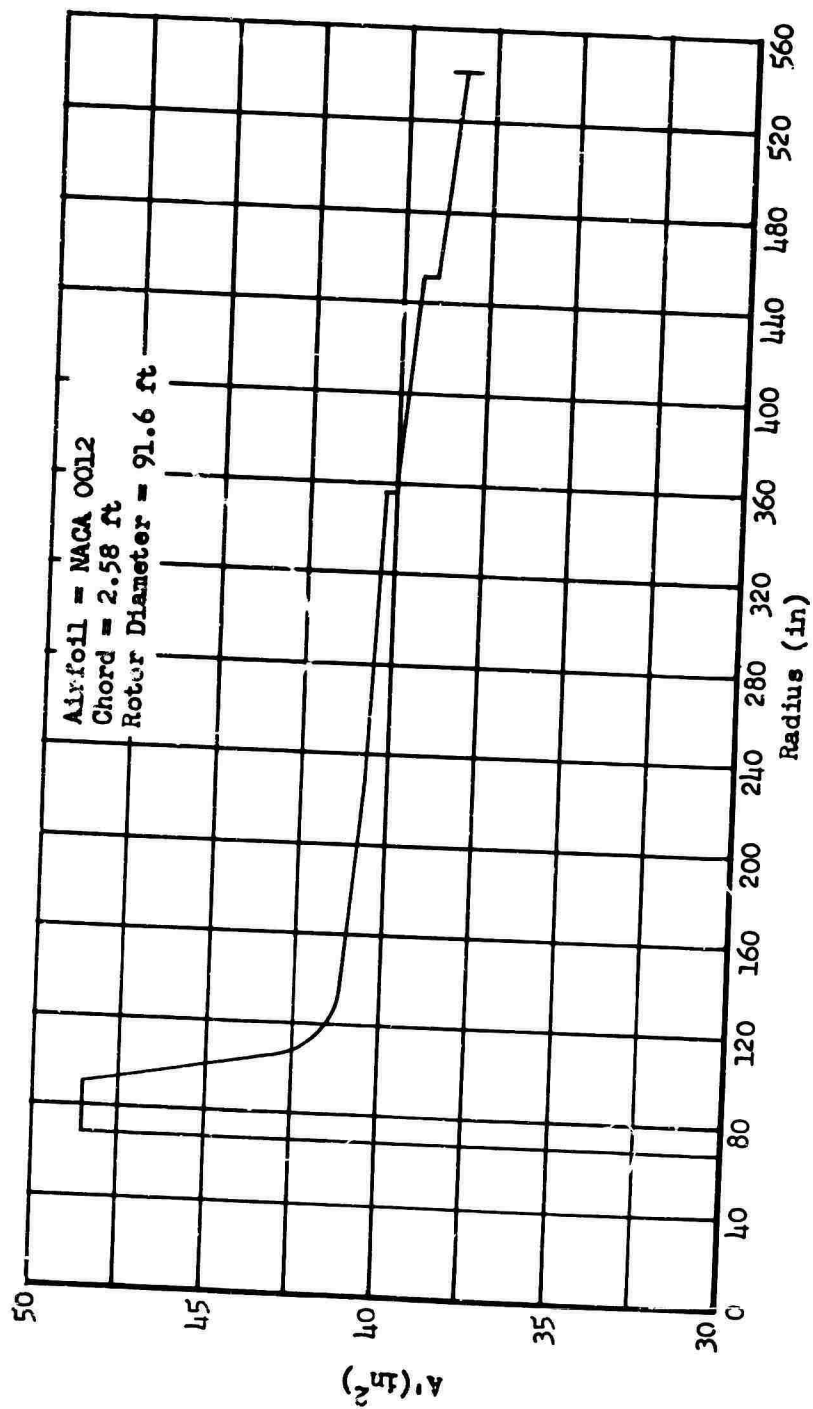


Figure 117 Distribution of Enclosed Area Within Mean Line of Spar Wall

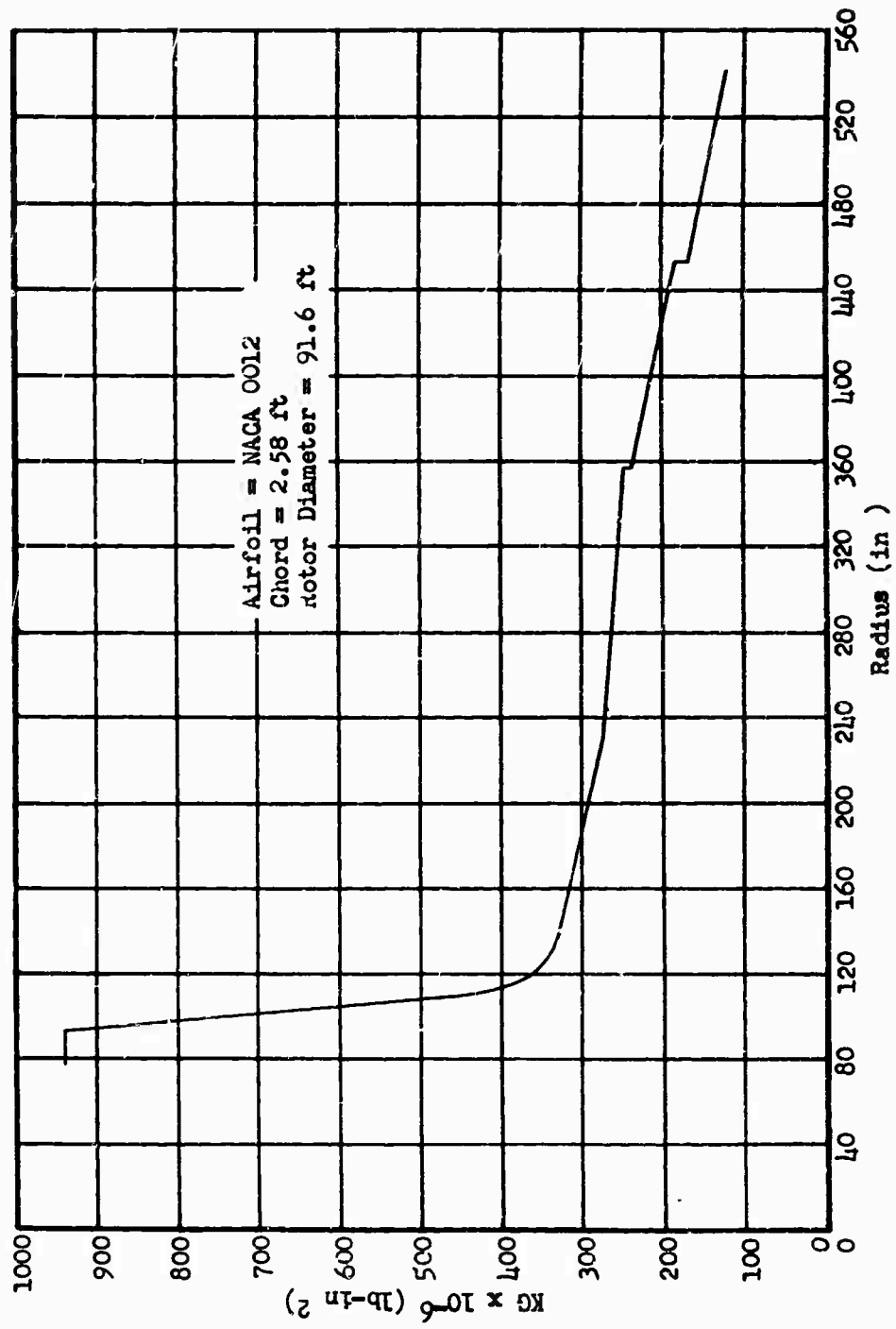


Figure 118 Spar Torsional Stiffness Distribution

ROTOR BLADE LOADS

Calculation Of Airloads

The basic thrust equation for the flapwise airload distribution on a rotor blade in forward flight is given by

$$\frac{dT}{dr} = 1/2 \left[\rho aC(\Omega R)^2 (\theta - \phi) \right]$$

The combined forward velocity of the aircraft and the rotational velocity of the blade produces an harmonic variation in the velocity at each blade element. The basic thrust equation has been expanded to allow for these harmonic variations in velocity and the resultant flapping motion of the blade. The expanded equation (Fourier Series) for the thrust distribution then becomes

$$\begin{aligned} \frac{dT}{dr} = 1/2 \rho aC(\Omega R)^2 & \left[\left\{ \lambda x + \theta_x (x^2 + 1/2 \mu^2) + 1/4 \mu^2 b_2 + \right. \right. \\ & \left. \left. 1/2 e \mu a_1 \right\} \right. \\ & + \cos \psi \left\{ -\mu a_0 x - 1/2 \mu a_2 x + b(x^2 + 1/4 \mu^2) - e b_1 + e \mu a_2 \right\} \\ & + \sin \psi \left\{ \mu \lambda + 2 \mu x \theta_x + a_1 (1/4 \mu^2 - x^2) - 1/2 \mu x b_2 + \right. \\ & \left. e (a_1 x + b_2 \mu) \right\} \\ & + \cos 2 \psi \left\{ -1/2 \mu^2 \theta_x + \mu x a_1 + 2x^2 b_2 x - \frac{1}{2} e \mu a_1 \right\} \\ & \left. + \sin 2 \psi \left\{ -1/2 \mu^2 a_0 - 2x^2 a_2 + \mu x b_1 + 2e x a_2 - \frac{1}{2} e \mu b_1 \right\} \right] \\ \text{where } \theta_x = \theta_0 + \theta_1 \end{aligned} \quad (40)$$

In order to solve the thrust equation, the unknown parameters - the inflow coefficient (λ), pitch angle at the blade root (θ_0), and the flapping coefficients (a_0, a_1, a_2, b_1, b_2) - must be determined.

The inflow coefficient (λ) is determined from an analysis by J. F. Bailey (Reference 6), which is basically derived from the equation for torque equilibrium. This analysis assumes a constant induced inflow over the entire rotor disk.

Since the flapping motion of the blade is harmonic with a period of 2π radians, the flapping angle (β_f) may be represented by a Fourier series function of azimuth angle (ψ). Harmonics higher than two have been found to be negligible.

$$\beta_f = a_0 - a_1 \cos \psi - b_1 \sin \psi - a_2 \cos 2\psi - b_2 \sin 2\psi \quad (41)$$

Successive differentiation of the expression for flapping angle yields the flapping velocity $\dot{\beta} = \frac{d\beta_f}{dt}$ and the flapping acceleration

$$\ddot{\beta} = \frac{d^2\beta_f}{dt^2} \quad (42)$$

The boundary condition at the blade root causes the flapwise moments due to thrust, blade weight, centrifugal and inertia forces to vanish at the flapping hinge. The resultant dynamic motion equation becomes

$$M_{\text{thrust}} - M_{\text{weight}} - M_{\text{centrifugal force}} - M_{\text{inertia}} = 0 \quad (43)$$

$$\text{where } M_{\text{thrust}} = \int_0^R \frac{1}{2} \rho a c (\theta U_T^2 + U_p U_T) (r - e) dr$$

$$M_{\text{weight}} = \int_0^R m g r dr$$

$$M_{\text{centrifugal force}} = \int_0^R m \Omega^2 r (r \beta_f) dr$$

$$M_{\text{inertia}} = \int_0^R \left[m \ddot{\beta} (r - e) \right] (r - e) dr$$

Substituting the expressions for β_f , $\ddot{\beta}$, U_p and U_T into these moment relations and setting $M_{\text{thrust}} - M_{\text{weight}} = M_{\text{centrifugal force}} + M_{\text{inertia}}$, the resulting expression may be written as a matrix consisting of five equations and seven unknowns (a_0 , a_1 , a_2 , b_1 , b_2 , λ , θ_0).

The matrix is then solved for the flapping coefficients in terms of θ_0 and λ , and takes the form $a_0 = a_{01} \theta_0 + a_{02} \lambda + a_{03}$. λ (Lambda) is a known quantity, having been previously calculated from the torque balance equation. The pitch angle is determined by integrating the thrust equation around the azimuth, which yields an expression containing θ_0 , a_1 and b_2 as unknowns. The relations for a_1 and b_2 from the matrix above are substituted into the thrust equation, which is solved for θ_0 .

This determines all the parameters in the thrust equation, so it is now possible to calculate the radial thrust distribution at any azimuth position.

Drag Distribution

The drag distribution or edgewise airload is calculated from an expansion of the basic drag relation

$$\frac{dD}{dr} = \frac{1}{2} \rho C (C_d - C_L \phi) U_T^2 \quad (44)$$

This equation is expanded to include the effects of blade flapping on the inflow angle ϕ and velocity U_T in much the same manner as the thrust equation was expanded.

Method

A digital computer is utilized in order to facilitate the computation of lambda (λ), pitch angle (θ_0), flapping coefficients (a_0 , a_1 , a_2 , b_1 , b_2), thrust ($\frac{dT}{dr}$), and drag ($\frac{dD}{dr}$) distributions.

ROTOR BLADE RESULTANT AIRLOADS, SHEARS AND MOMENTS

Table XXXI is a summary of the flight conditions analyzed and Table XXXII shows the list of design constants used for the investigations. Subsequent Tables XXIII through XLIX and Figures 122 through 178 graphically represent the resultant airloads, shears and moments for each flight condition.

TABLE XXXI
BLADE CONDITIONS INVESTIGATED

Condition	Title and Basic Parameters
1a	"Hover", 20-Ton Mission V=0, N=161 rpm, LF=1.0, GW=78,750 lb
1b	"Hover", 12-Ton Mission V=0, N=161 rpm, LF=1.0, GW=65,800 lb
1c	"Hover", Ferry Mission V=0, N=161 rpm, LF=1.0, GW=72,000 lb
2a	"Vertical Takeoff", 20-Ton Mission V=0, N=161 rpm, LF=2.0
2b	"Vertical Takeoff", 12-Ton Mission V=0, N=161 rpm, LF=2.0
2c	"Vertical Takeoff", Ferry Mission V=0, N=161 rpm, LF=2.0

TABLE XXXI (Contd)
BLADE CONDITIONS INVESTIGATED

Condition	Title and Basic Parameters
3a	"Cruise", 20-Ton Mission $V_{cr}=95$ kn, $N=146$ rpm, $LF=1.0$
3b	"Cruise", 12-Ton Mission $V_{cr}=110$ kn, $N=146$ rpm, $LF=1.0$
3c	"Cruise", Ferry Mission $V_{cr}=130$ kn, $N=146$ rpm, $LF=1.0$
4a	"Symmetrical Dive and Pullout", 20-Ton Mission $V_D=121$ kn, $N=146$ rpm, $LF=2.5$
4b	"Symmetrical Dive and Pullout", 12-Ton Mission $V_D=159$ kn, $N=146$ rpm, $LF=2.5$
4c	"Symmetrical Dive and Pullout", Ferry Mission $V_D=145$ kn, $N=146$ rpm, $LF=2.0$
5a	"Autorotative Dive and Pullout", 20-Ton Mission $V_D=121$ kn, $N=168$ rpm, $LF=2.5$
5b	"Autorotative Dive and Pullout", 12-Ton Mission $V_D=159$ kn, $N=168$ rpm, $LF=2.5$
5c	"Autorotative Dive and Pullout", Ferry Mission $V_D=145$ kn, $N=168$ rpm, $LF=2.0$
6	4g Weight Moment: Ground Handling

TABLE XXXII
SUMMARY OF BASIC DESIGN CONSTANTS FOR ALL CONDITIONS

Constant	Symbol	Value
Altitude	ρ	Sea Level
Density	ρ	.002378 slugs/ft. ³
Rotor Radius	R	45.8 ft
Flapping Hinge Offset	e	3.0 ft
Number of Blades	b	6
Gross Weight:	GW	
20-Ton Mission		78,750 lb
12-Ton Mission		65,800 lb
Ferry Mission		72,000 lb
Chord	C	2.583 ft
Equivalent Chord (Thrust)	Ceq(T)	2.560 ft
Equivalent Chord (Torque)	Ceq(Q)	2.577 ft
Tip Loss Factor	B	0.97
Inner Aerodynamic Limit	X ₁	0.244
Moment of Inertia of Flapping Mass About Center of Rotation	I _{mcr}	13,484 ft-lb-sec ²
Mass Moment of Flapping Mass About Center of Rotation	M _{mcr}	496.5 ft-slugs
Weight Moment of Flapping Mass About Flapping Hinge	M _{wFH}	13,175 ft-lb
Blade Weight (with cuff)	W _b	666.5 lb
Rotor Speed, rpm	N	
Normal Operating		146 rpm
Limit, Power On (1.10 N)		161 rpm
Power Off (1.15 N)		168 rpm
Forward Velocity, Knots	V	
20-Ton Mission:		
Dive Velocity	V _D	121 kn
Maximum Velocity	V _H	105 kn
Cruise Velocity	V _{cr}	95 kn
12-Ton Mission:		
Dive Velocity	V _D	159 kn
Maximum Velocity	V _H	138 kn
Cruise Velocity	V _{cr}	110 kn
Ferry Mission:		
Dive Velocity	V _D	145 kn
Maximum Velocity	V _H	126 kn
Cruise Velocity	V _{cr}	130 kn

Condition 1 - Hover

The conditions investigated were:

1a: 20-Ton Mission

1b: 12-Ton Mission

1c: Ferry Mission

These conditions are presented for the purpose of supplying data for performance calculations in hover. The airloads encountered are free of harmonics and therefore do not vary with azimuth position. The steady airload, shears and moments which occur are presented on the following pages.

TABLE XXXIII
CONDITION 1a, HOVER,
20-TON MISSION,
BASIC DESIGN PARAMETERS

Parameter	Symbol	Value
Airspeed	V	0
Rotor rpm	N	161 rpm
Angular Velocity	Ω	16.857 rad/sec
Linear Tip Velocity	ΩR	772 ft/sec
Gross Weight	TW	78,750 lb
Load Factor	LF	1.0
Thrust	T	78,750 lb
Tip Speed Ratio	μ	0.0
Blade Pitch Angle at Hub	θ_0	0.2735 rad
Twist Angle	θ_1	-0.1396 rad

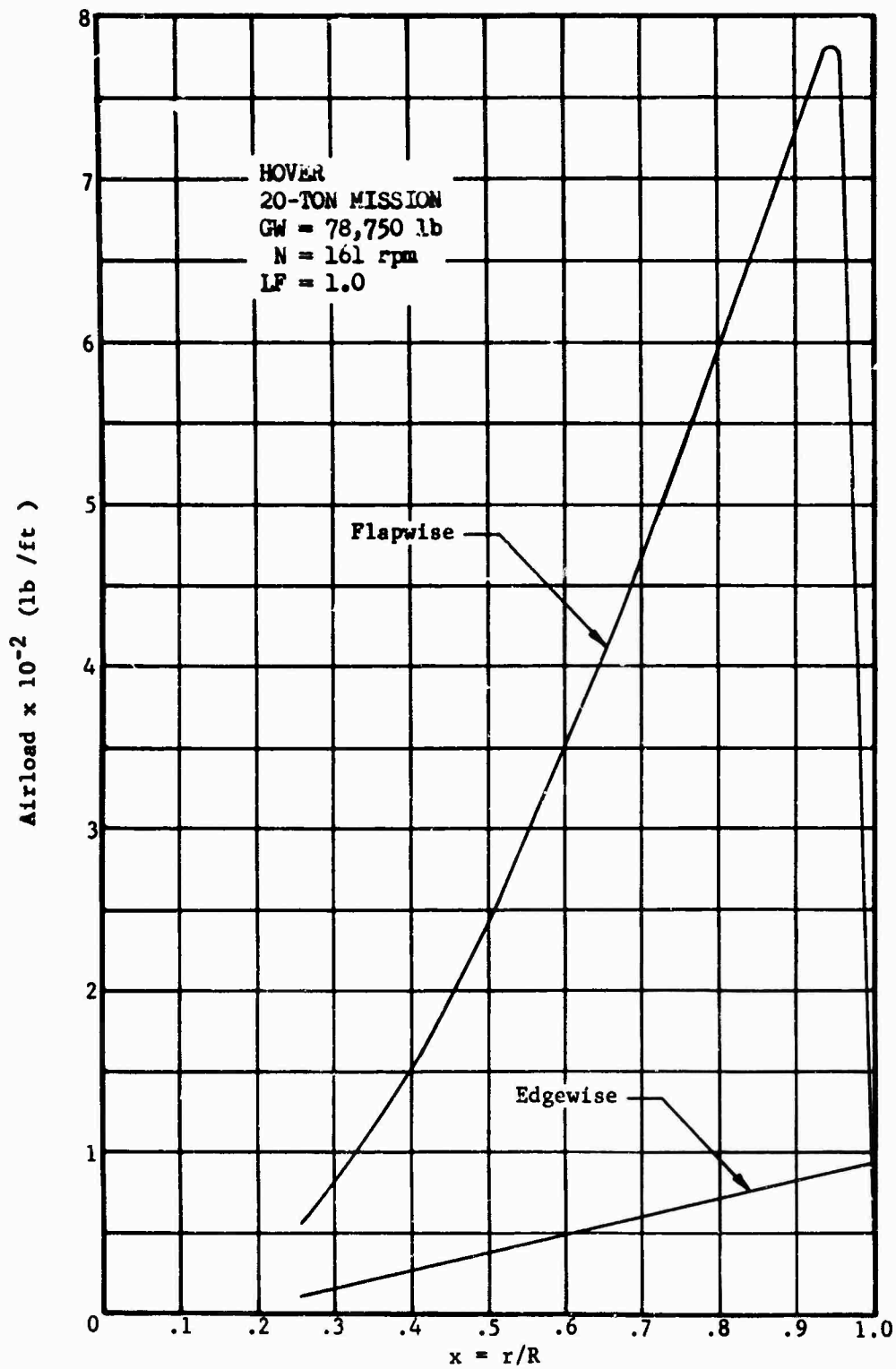


Figure 119 Airload Distribution, Condition 1a

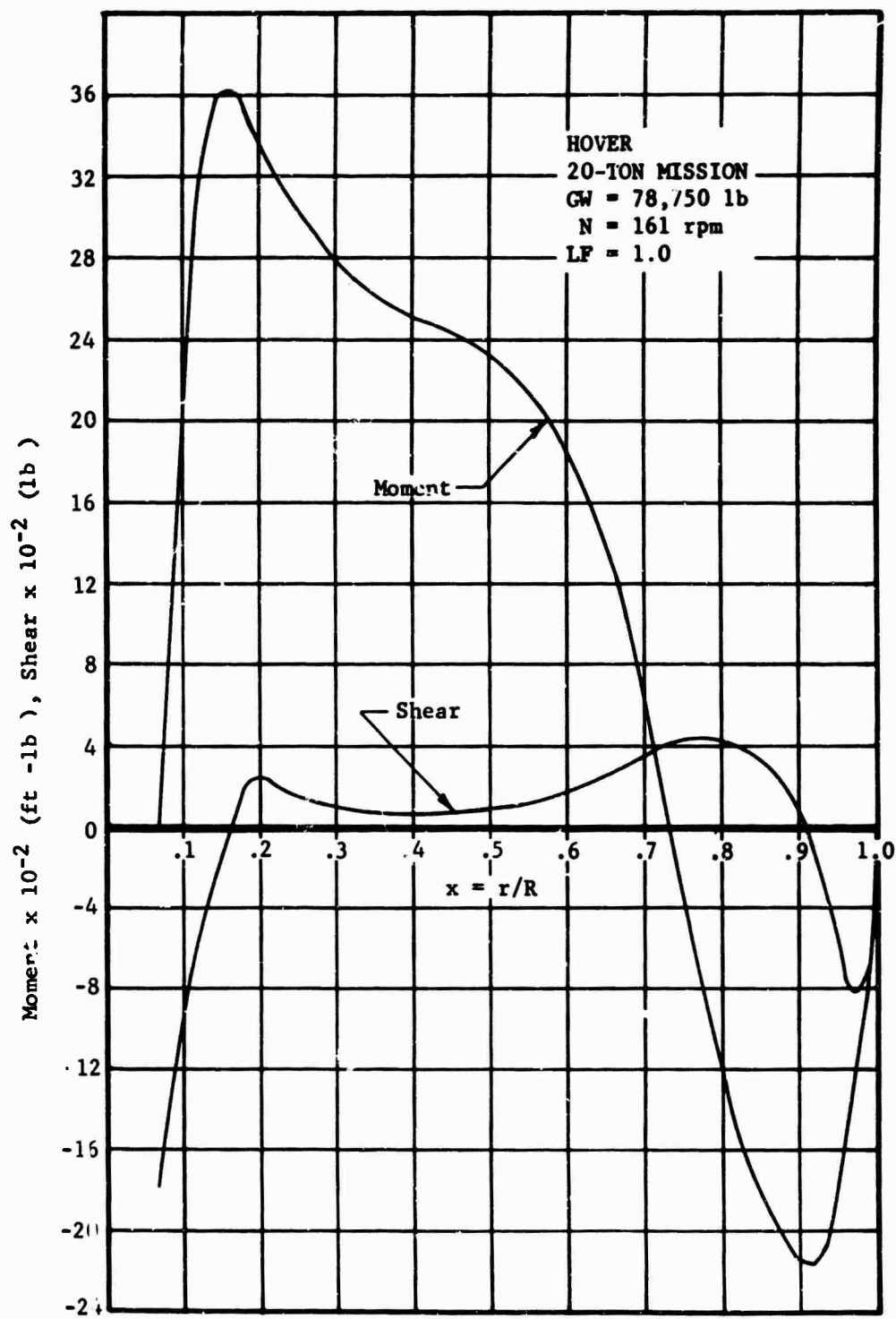


Figure 120 Flapwise Shear and Moment Distribution, Condition 1a

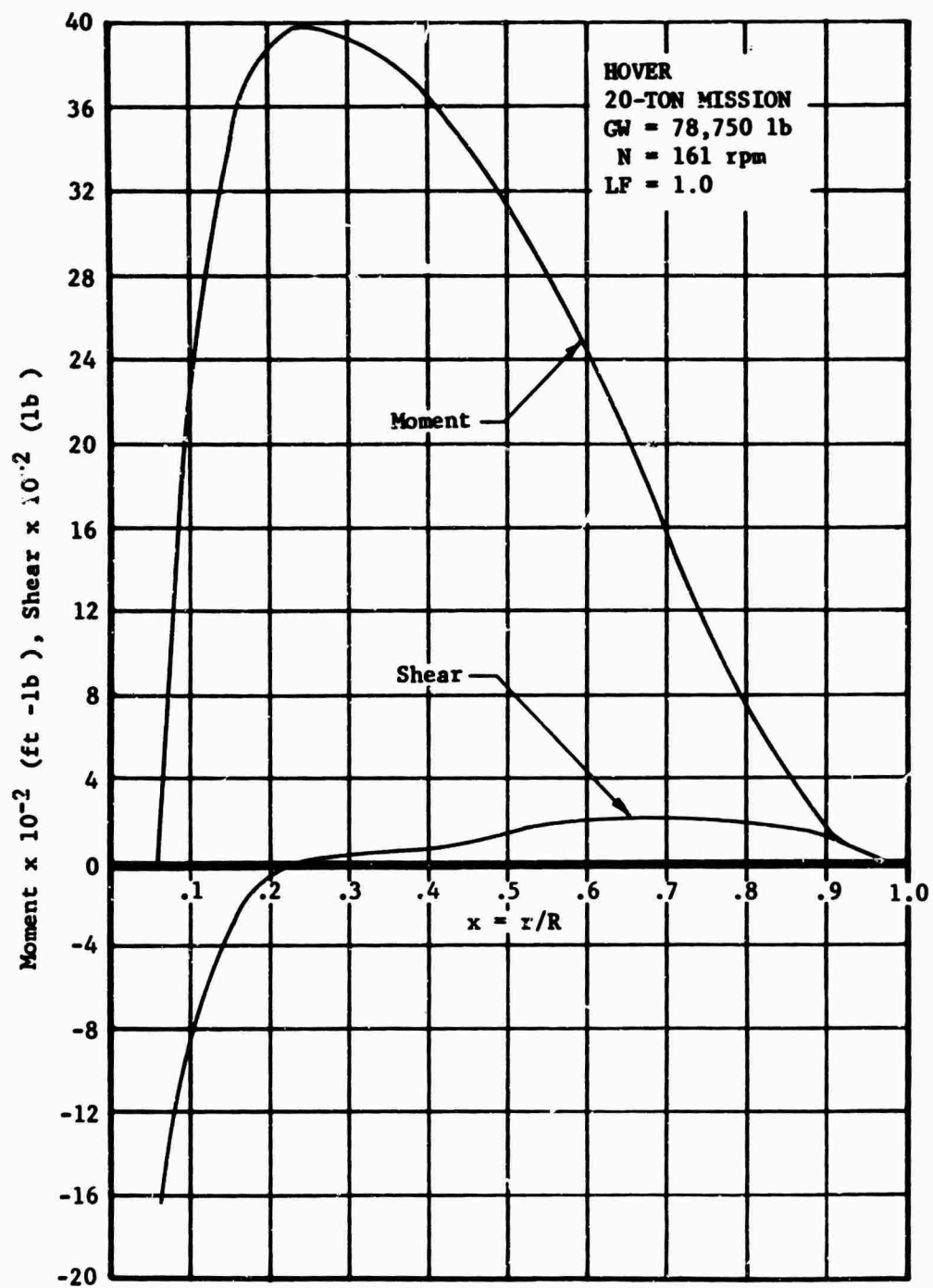


Figure 121 Edgewise Shear and Moment Distribution, Condition 1a

TABLE XXXIV
CONDITION 1b. HOVER,
12-TON MISSION,
BASIC DESIGN PARAMETERS

Parameter	Symbol	Value
Airspeed	V	0
Rotor rpm	N	161 rpm
Angular Velocity	Ω	16.857 rad/sec
Linear Tip Velocity	ΩR	772 ft/sec
Gross Weight	GW	65,800 lb
Load Factor	LF	1.0
Thrust	T	65,800 lb
Tip Speed Ratio	μ	0.0
Blade Pitch Angle at Hub	θ_0	0.2536 rad
Twist Angle	θ_1	-0.1396 rad

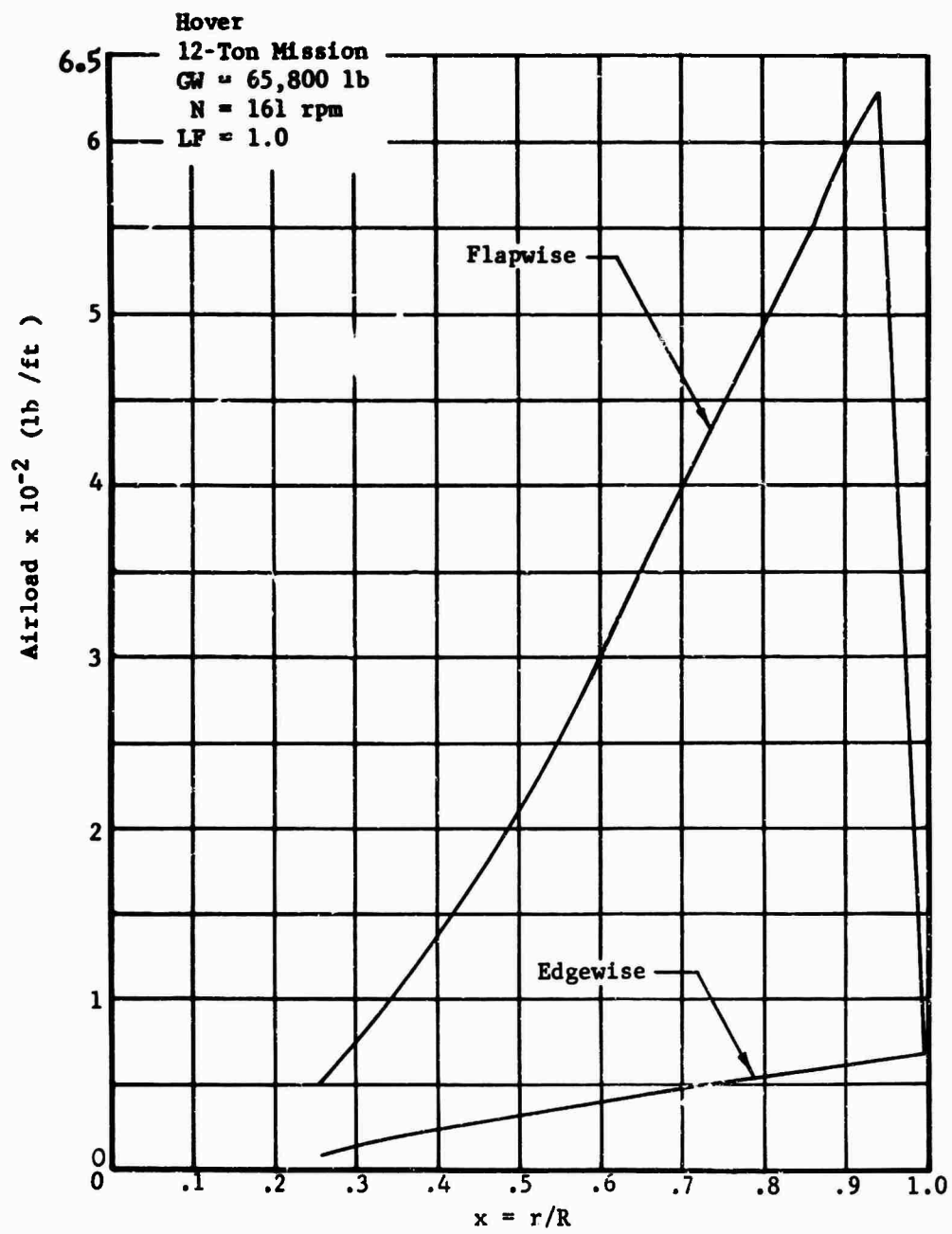


Figure 122 Airload Distribution, Condition 1b

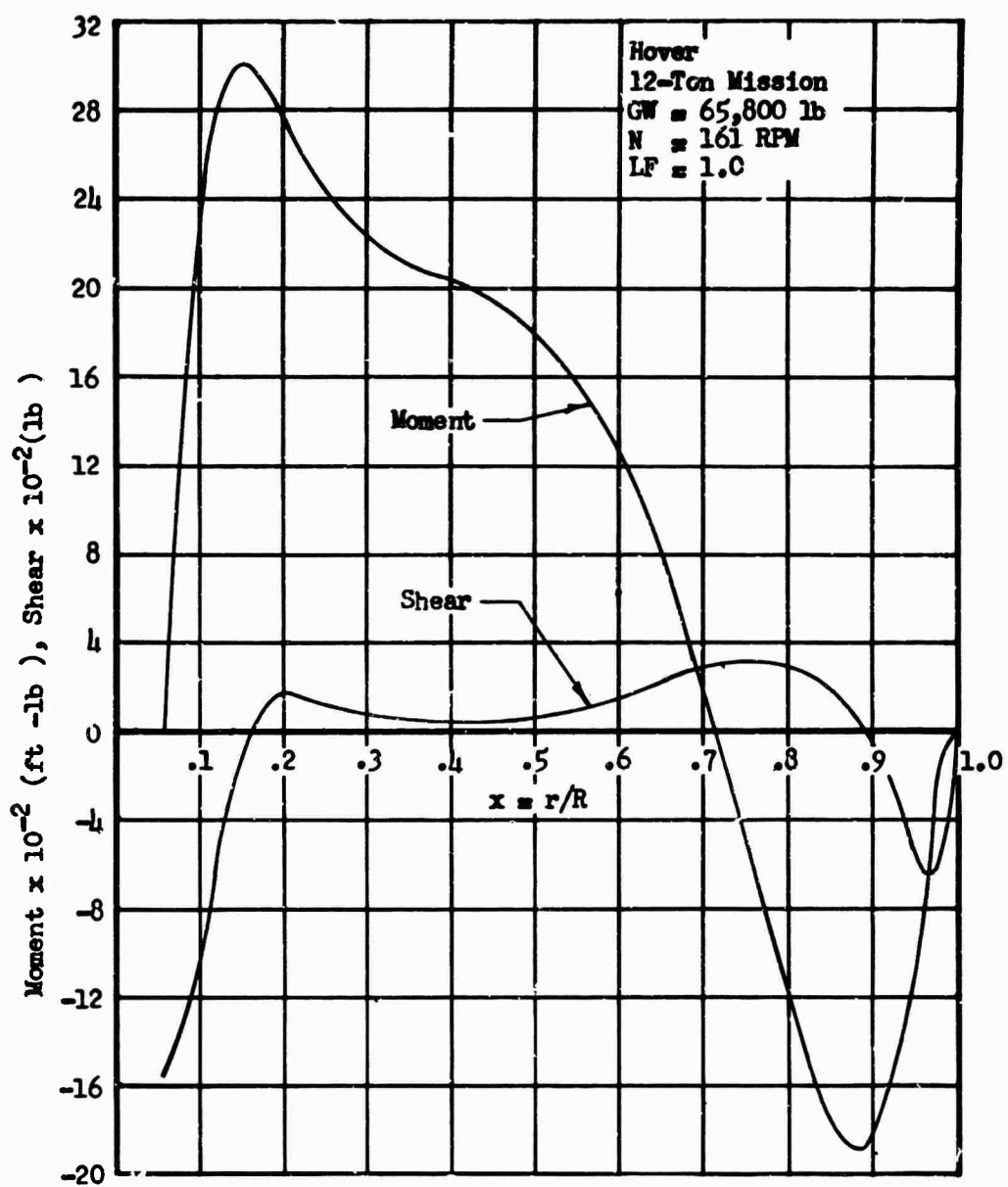


Figure 123 Flapwise Shear and Moment Distribution, Condition 1b

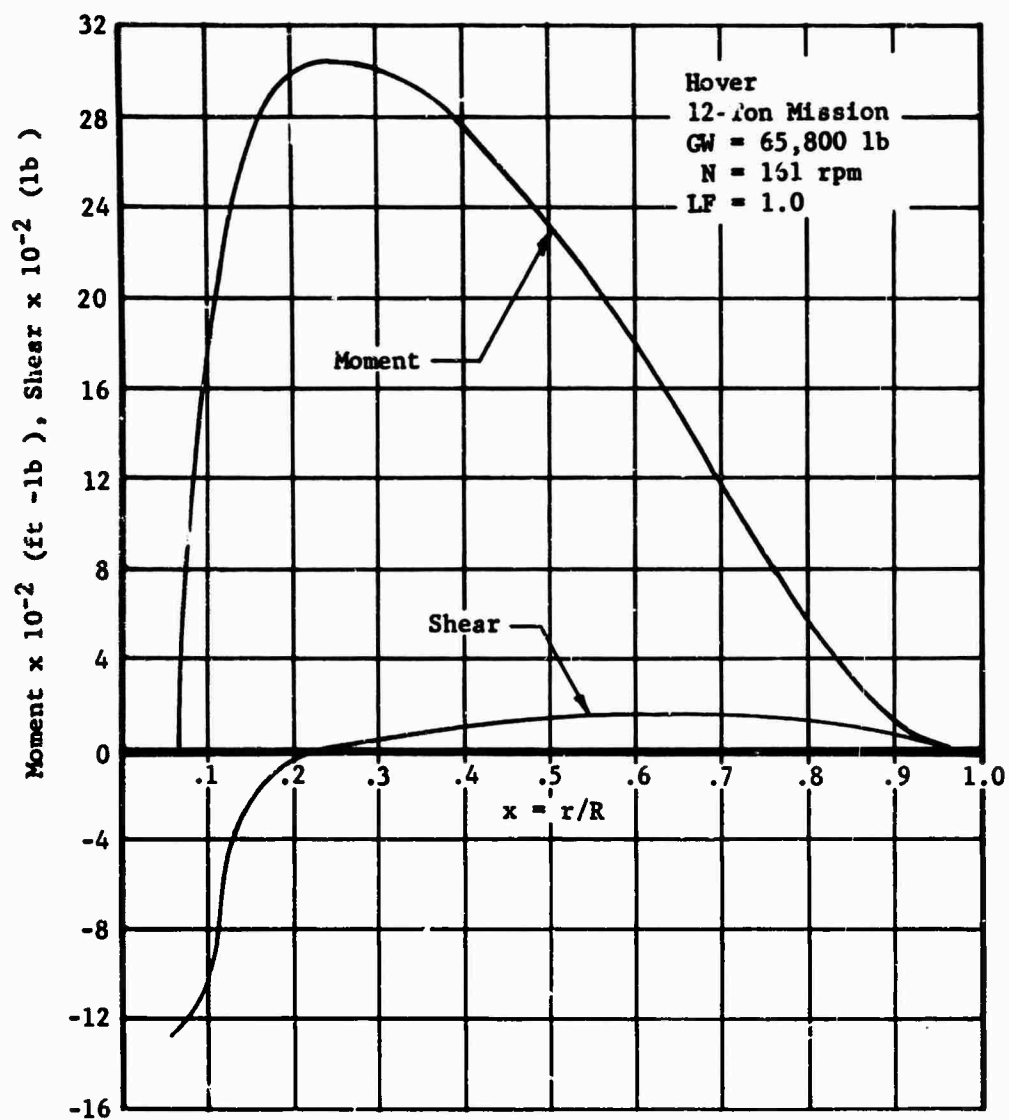


Figure 124 Edgewise Shear and Moment Distribution, Condition 1b

TABLE XXXV
CONDITION 1c, HOVER,
FERRY MISSION,
BASIC DESIGN PARAMETERS

Parameter	Symbol	Value
Airspeed	V	0
Rotor rpm	N	161 rpm
Angular Velocity	Ω	16.857 rad/sec
Linear Tip Velocity	ΩR	772 ft/sec
Gross Weight	GW	72,000 lb
Load Factor	LF	1.0
Thrust	T	72,000 lb
Tip Speed Ratio	μ	0.0
Blade Pitch Angle at Hub	θ_0	0.2632 rad
Twist Angle	θ_1	-0.1396 rad

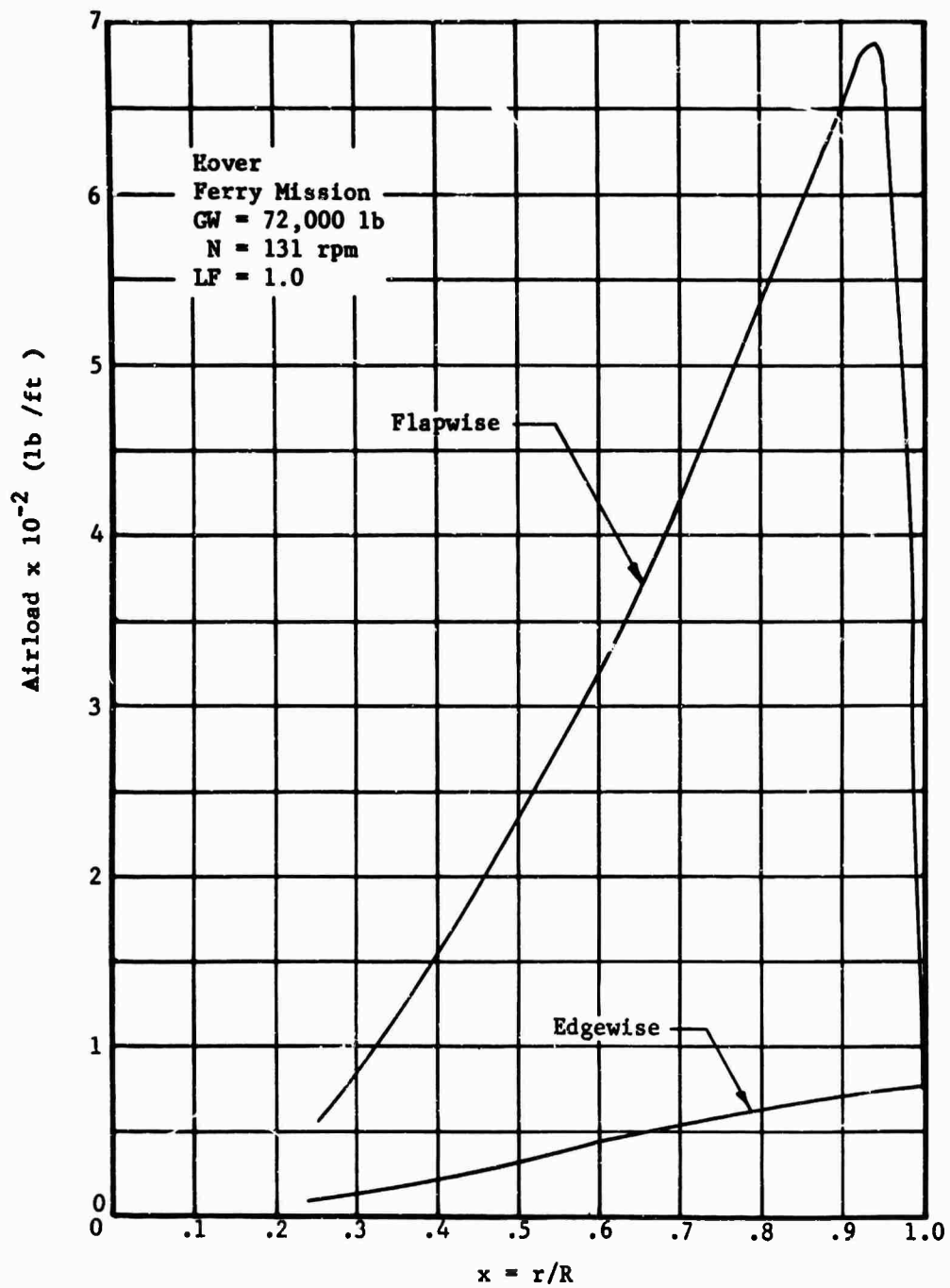


Figure 125 Airload Distribution, Condition 1c

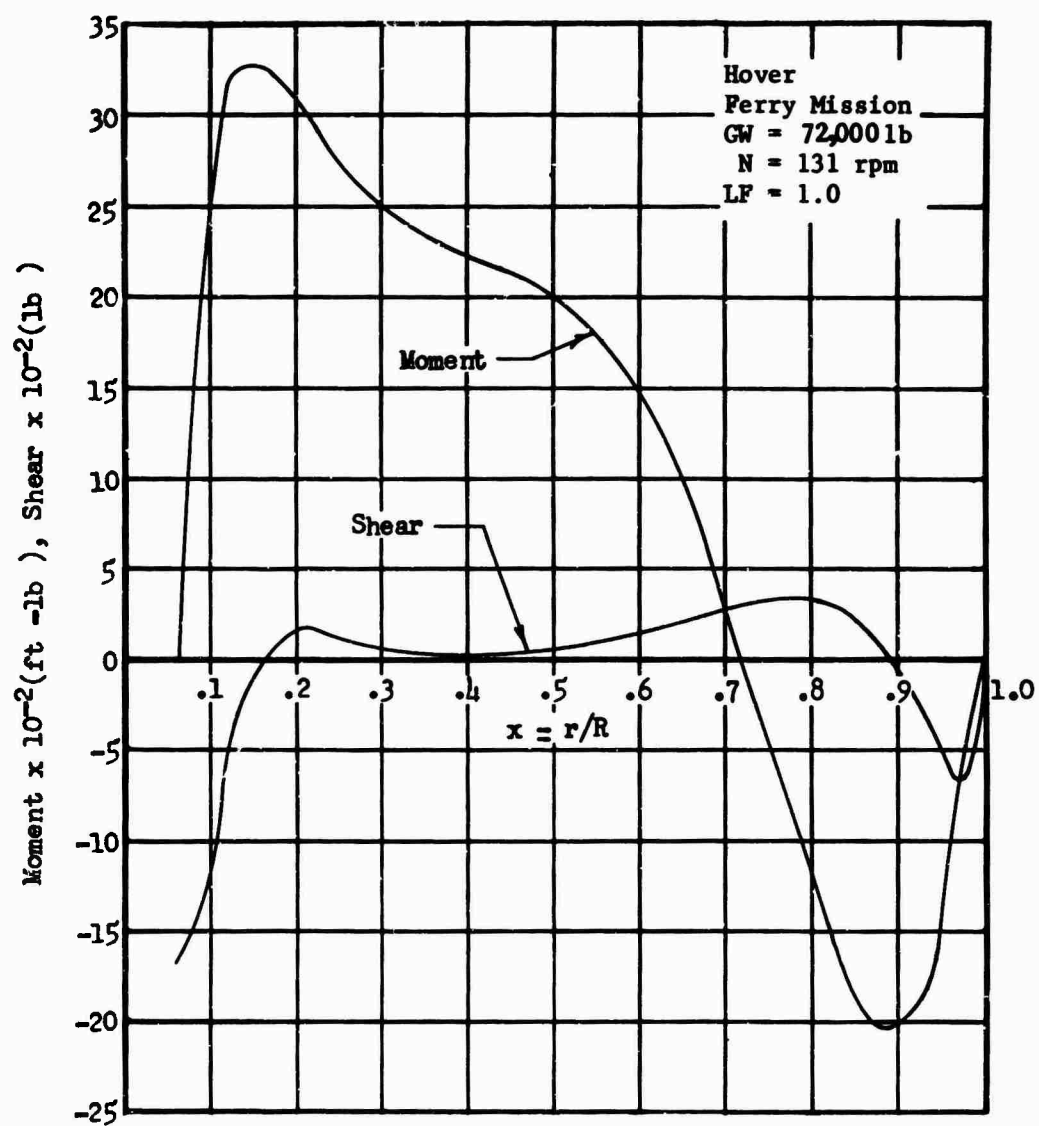


Figure 126 Flapwise Shear and Moment Distribution, Condition 1c

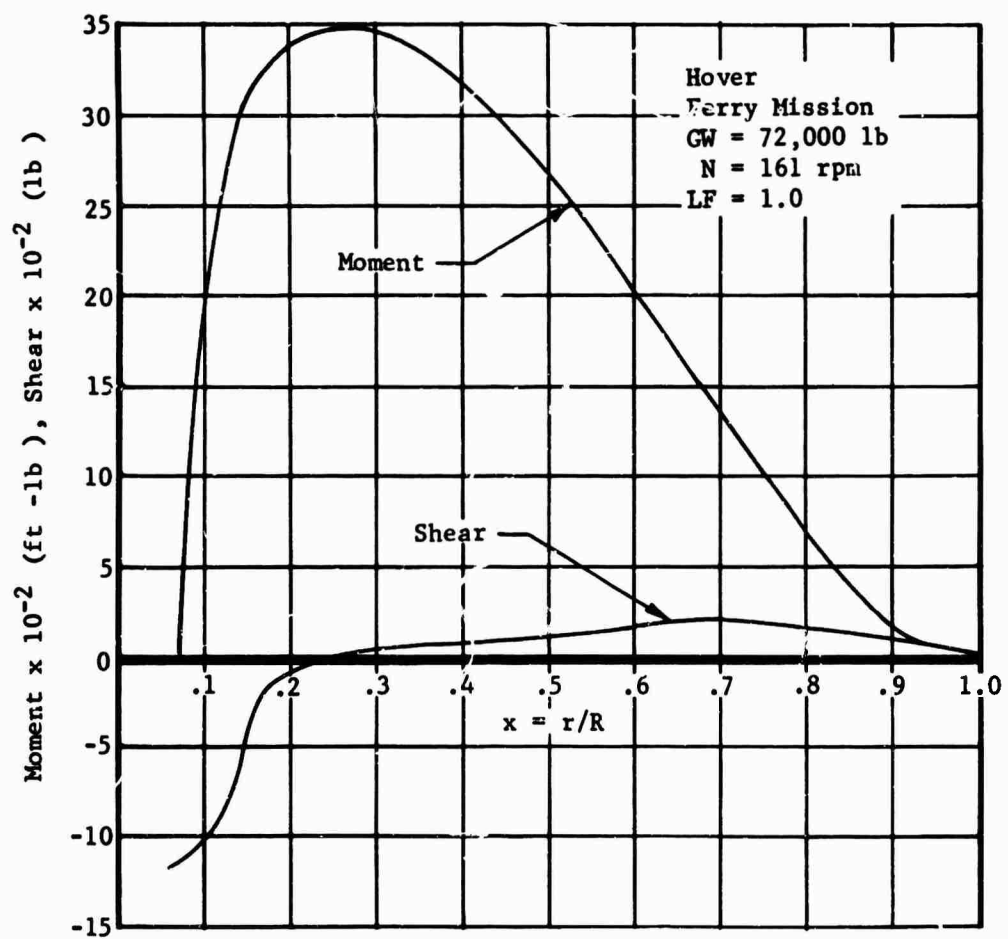


Figure 127 Edgewise Shear and Moment Distribution, Condition 1c

Condition 2 - Vertical Takeoff

The conditions investigated were:

2a: 20-Ton Mission

2b: 12-Ton Ferry

2c: Ferry Mission

Vertical takeoff, like hover, is analyzed as a steady-state condition. The only difference between the two is a climb velocity which has a negligible effect on the rotor inflow when compared to the effect due to blade rotational velocity. The load factor 2.0 applied to the gross weight in accordance with the requirements of Reference 34 accounts for the vertical acceleration experienced at the start of the ascent.

TABLE XXXVI
CONDITION 2a, VERTICAL TAKEOFF,
20-TON MISSION,
BASIC DESIGN PARAMETERS

Parameter	Symbol	Value
Airspeed	V	0
Rotor rpm	N	161 rpm
Angular Velocity	Ω	16.857 rad/sec
Linear Tip Velocity	ΩR	772 ft/sec
Gross Weight	GW	78,750 lb
Load Factor	LF	2.0
Thrust*	T	157,500 lb
Tip Speed Ratio	μ	0.0
Blade Pitch Angle at Hub	θ_0	0.3835 rad
Twist Angle	θ_i	-0.1396 rad
*Considered momentary for load factors other than unity		

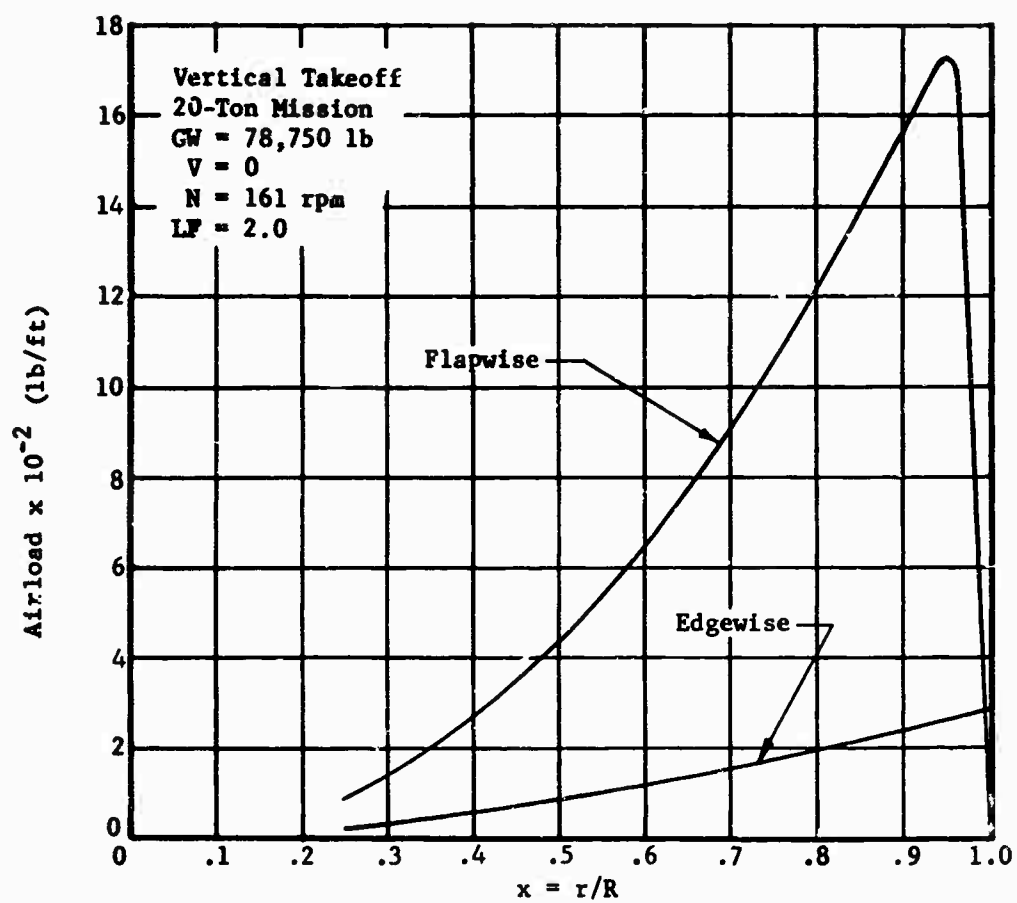


Figure 128 Flapwise and Edgewise Airload Distribution, Condition 2a

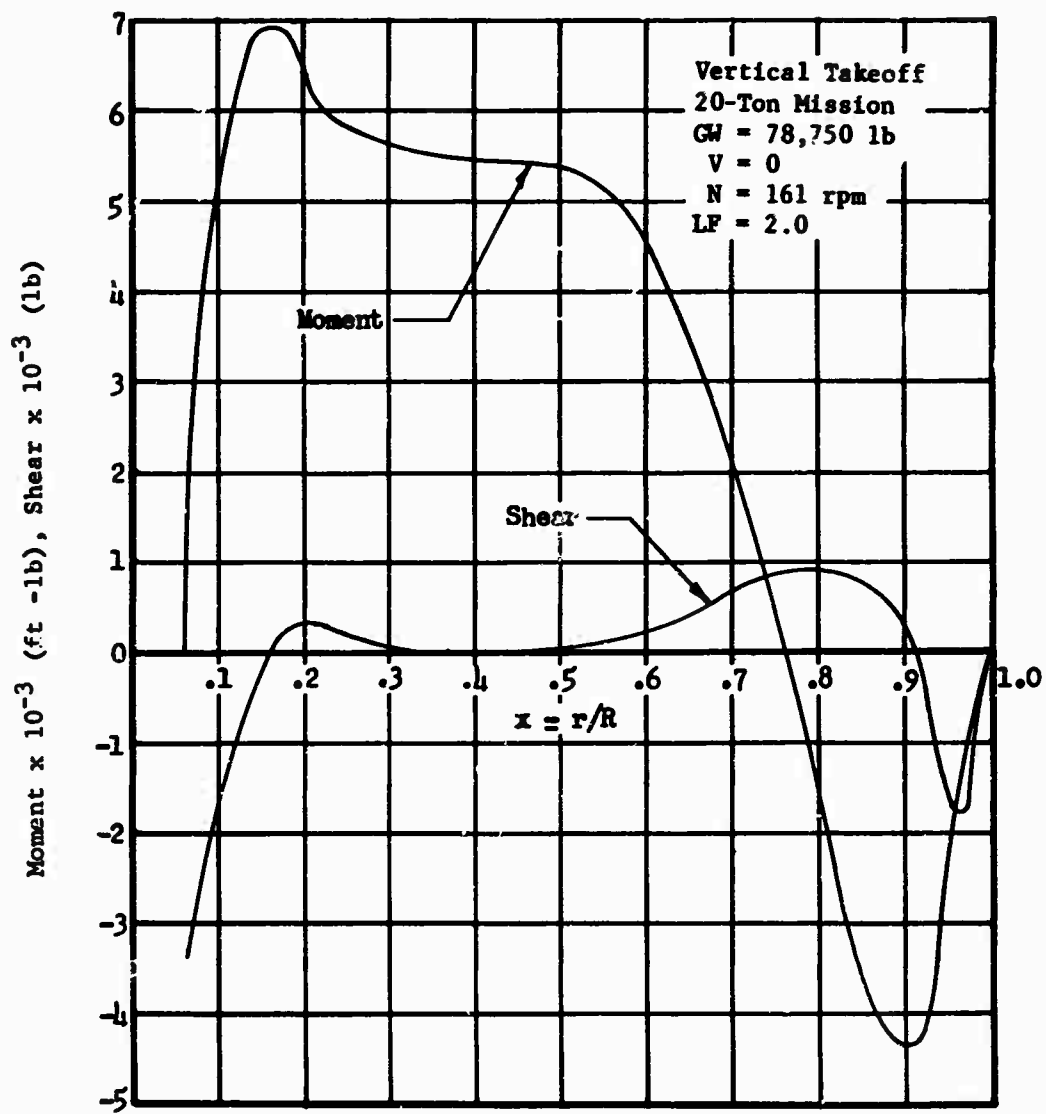


Figure 129 Flapwise Shear and Moment Distribution, Condition 2a

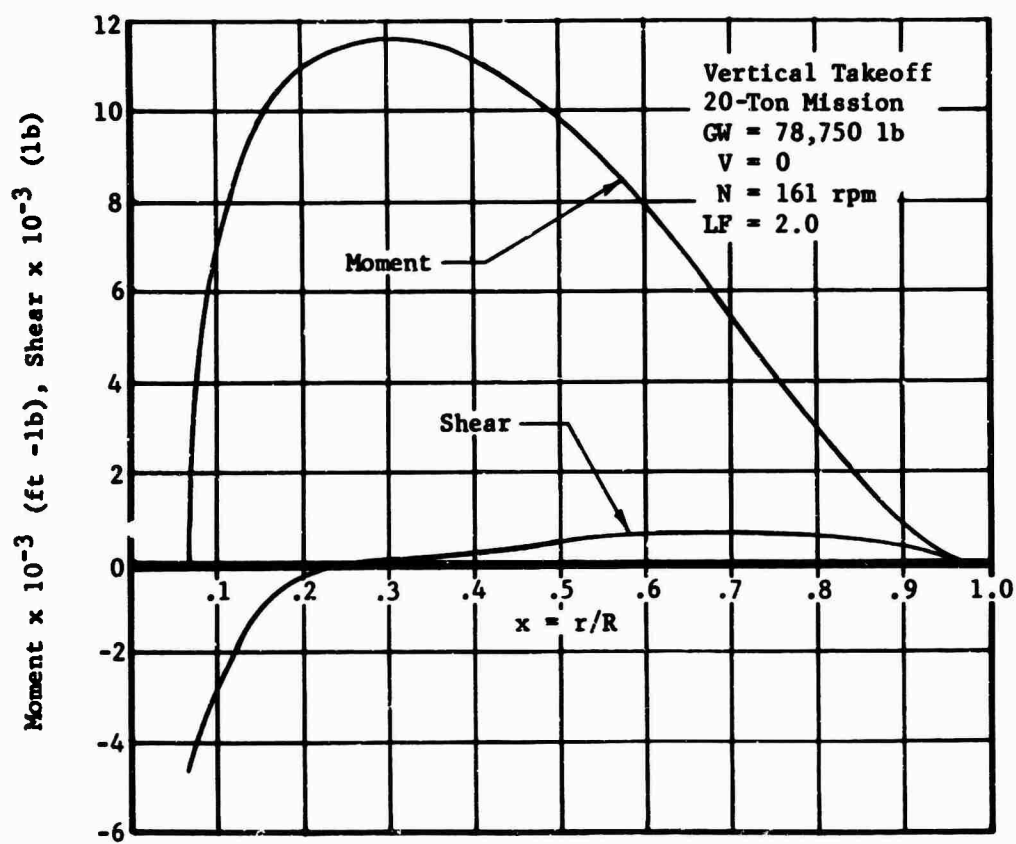


Figure 130 Edgewise Shear and Moment Distribution, Condition 2a

TABLE XXXVII
CONDITION 2b, VERTICAL TAKEOFF,
12-TON MISSION,
BASIC DESIGN PARAMETERS

Parameter	Symbol	Value
Airspeed	V	0
Rotor rpm	N	161 rpm
Angular Velocity	Ω	16.857 rad/sec
Linear Tip Velocity	ΩR	772 ft/sec
Gross Weight	GW	65,800 lb
Load Factor	LF	2.0
Thrust *	T	131,600 lb
Tip Speed Ratio	μ	0.0
Blade Pitch Angle at Hub	θ_0	0.3487 rad
Twist Angle	θ_i	-0.1396 rad
*Considered momentary for load factors other than unity.		

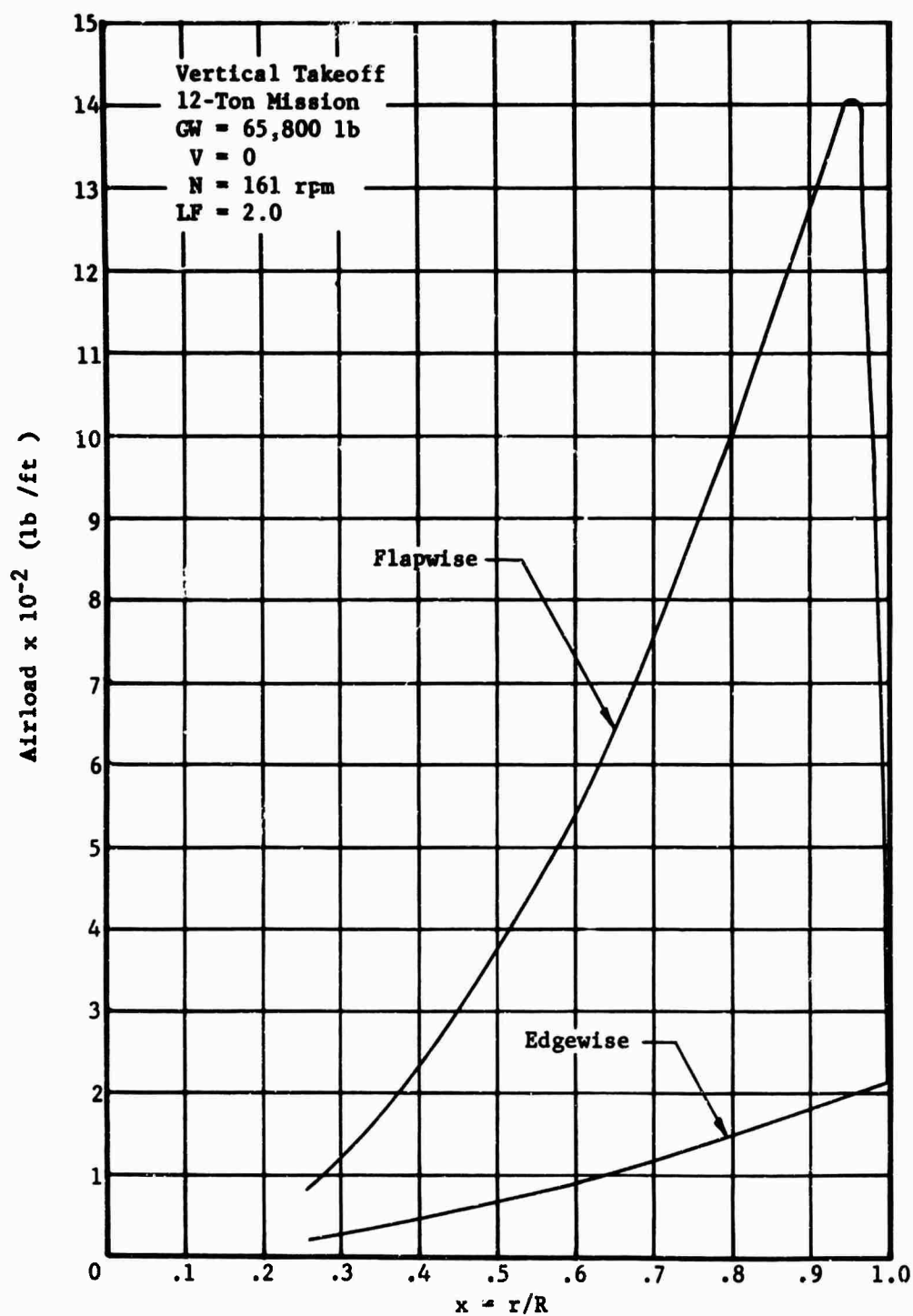


Figure 131 Flapwise and Edgewise Airload Distribution, Condition 2b

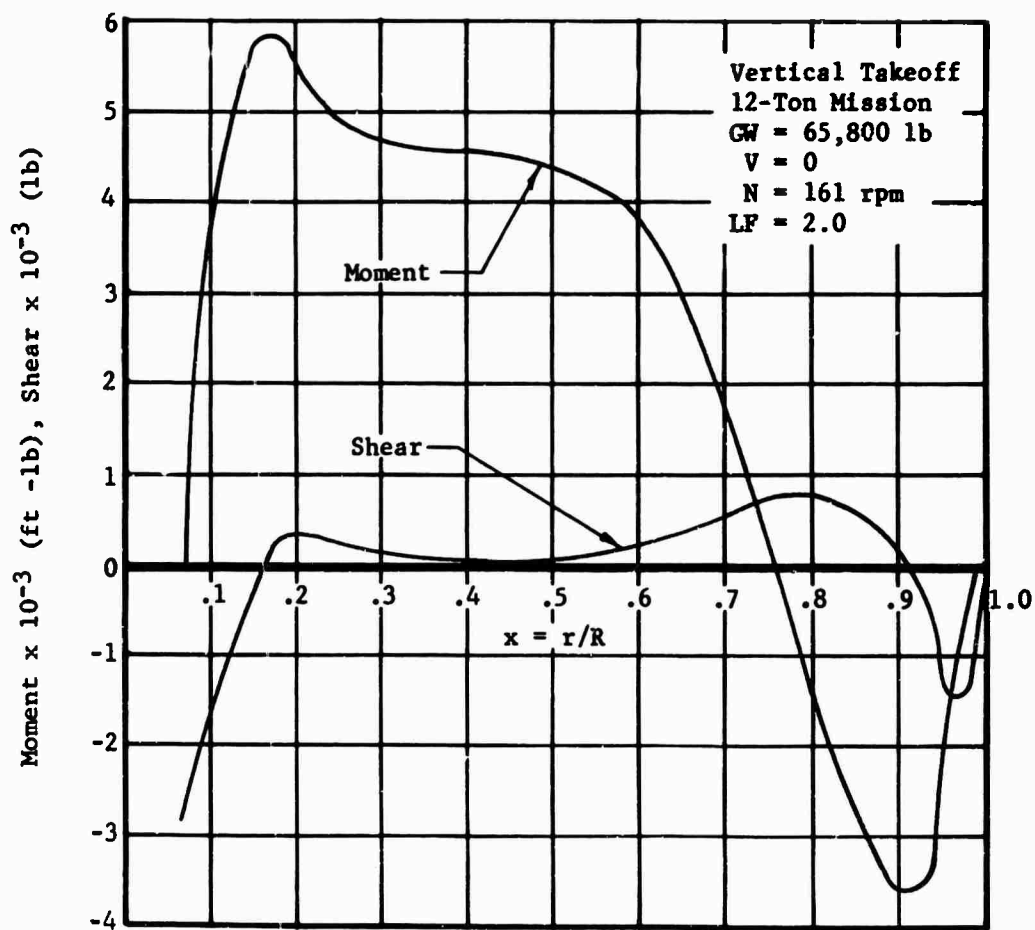


Figure 132 Flapwise Shear and Moment Distribution, Condition 2b

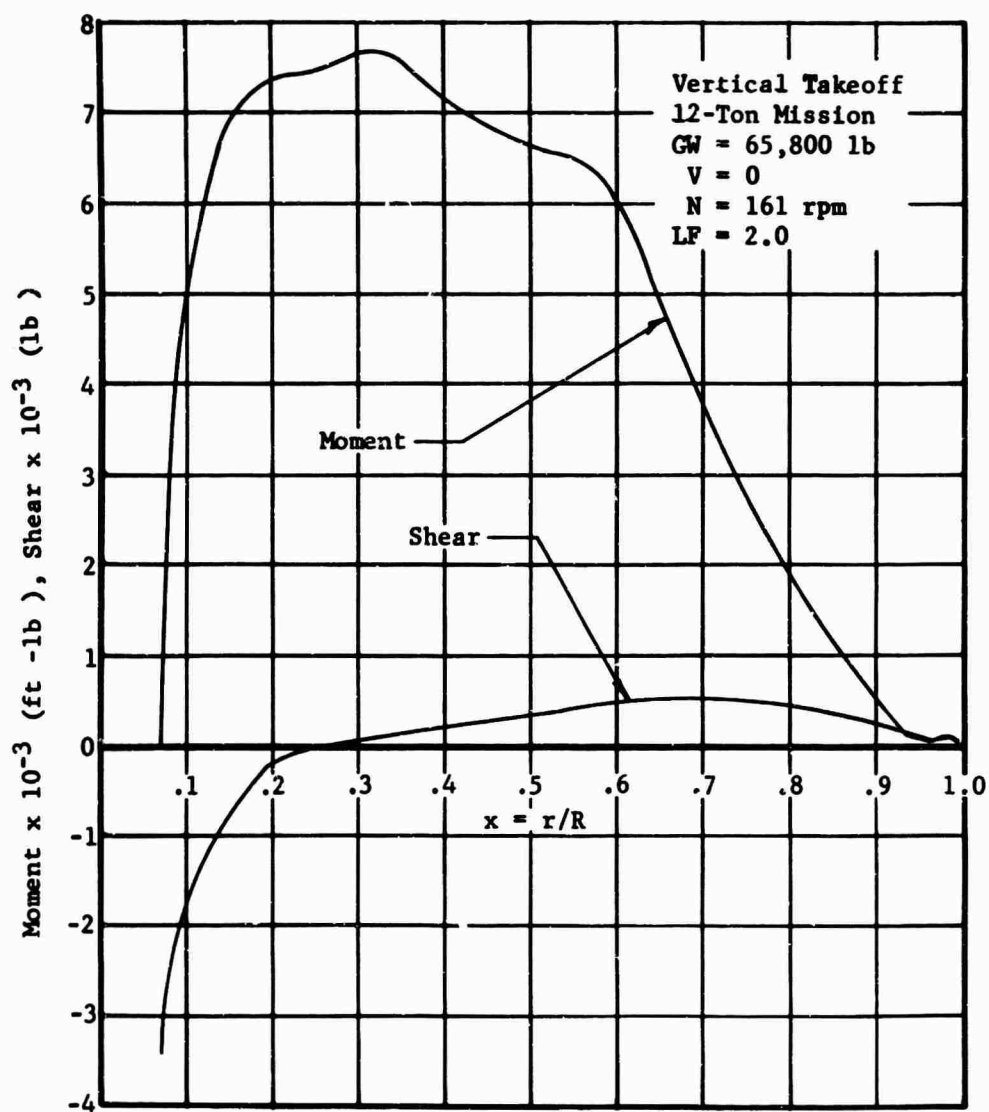


Figure 133 Edgewise Shear and Moment Distribution, Condition 2b

TABLE XXXVII
CONDITION 2c, VERTICAL TAKEOFF,
FERRY MISSION
BASIC DESIGN PARAMETERS

Parameter	Symbol	Value
Airspeed	V	0
Rotor rpm	N	161 rpm
Angular Velocity	Ω	16.857 rad/sec
Linear Tip Velocity	ΩR	772 ft/sec
Gross Weight	GW	72,000 lb
Load Factor	LF	2.0
Thrust *	T	144,000 lb
Tip Speed Ratio	μ	0.0
Blade Pitch Angle at Hub	θ_0	0.3655 rad
Twist Angle	θ_1	-0.1396 rad

* Considered momentary for load factors other than unity.

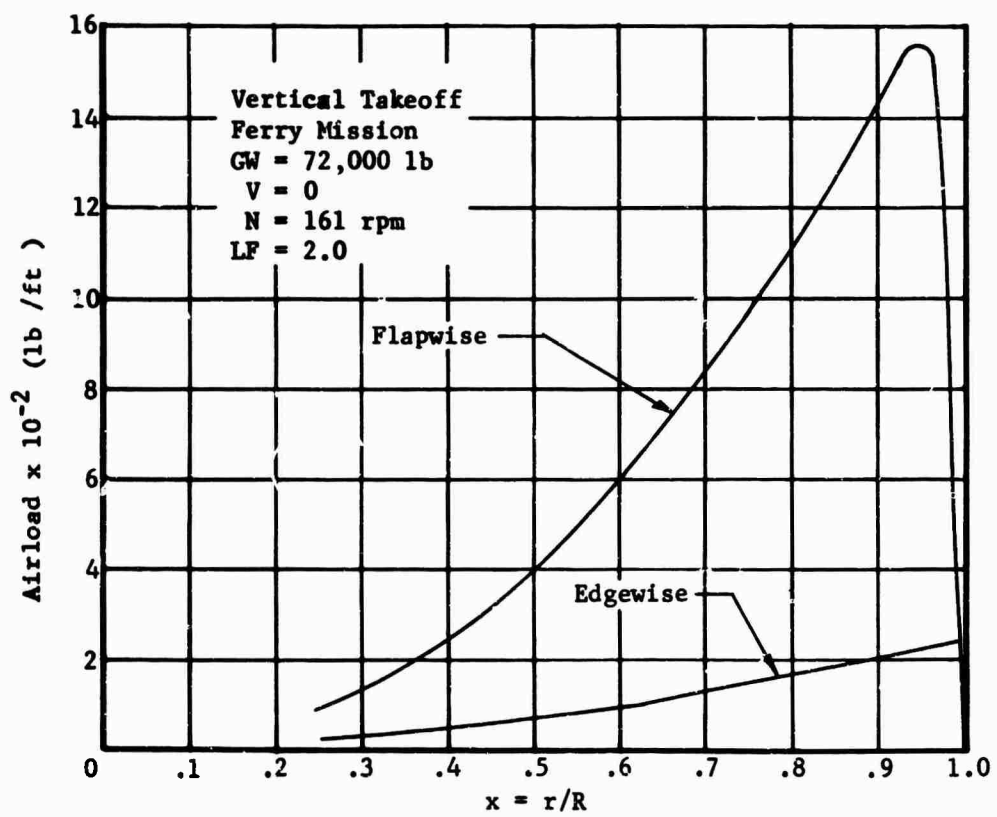


Figure 134 Flapwise and Edgewise Airload Distribution, Condition 2c

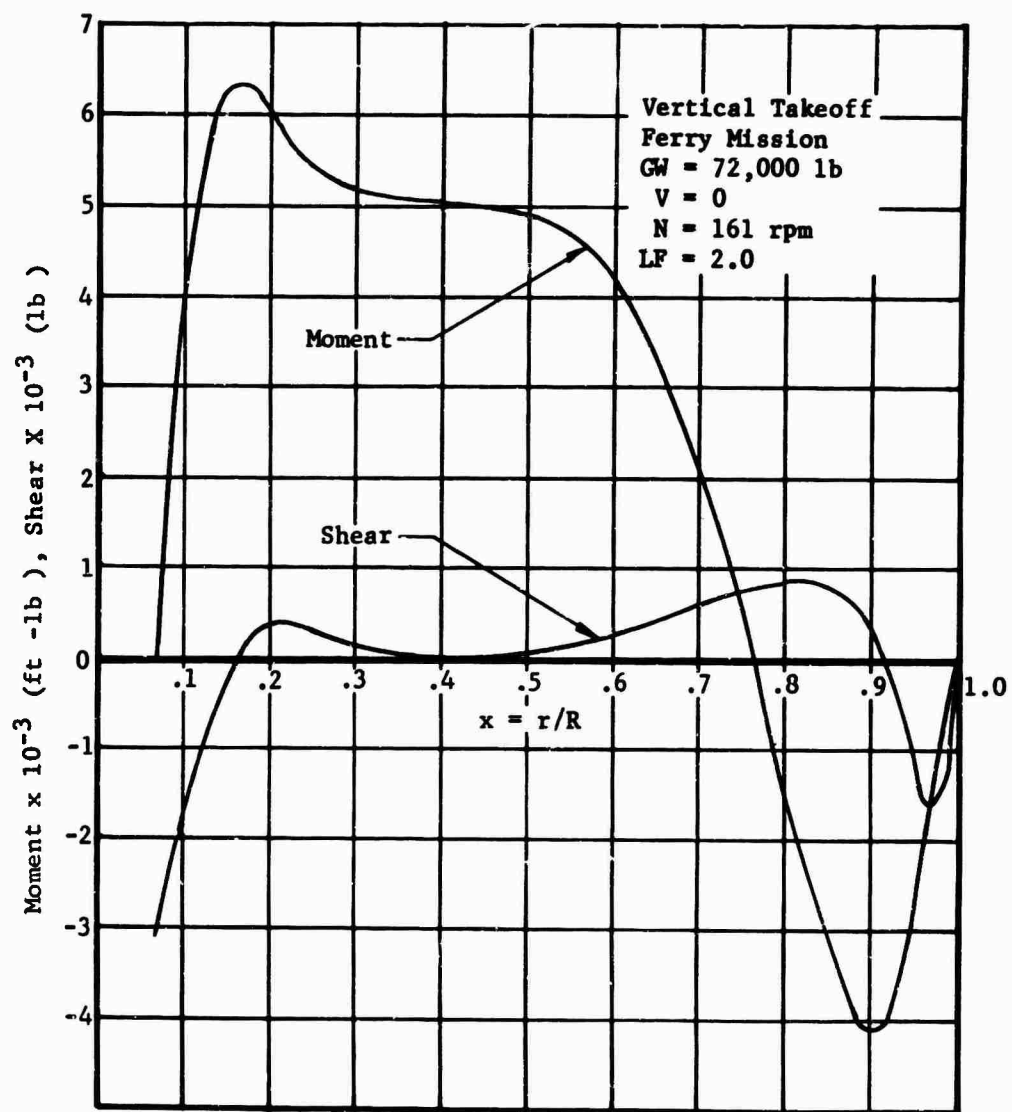


Figure 135 Flapwise Shear and Moment Distribution, Condition 2c

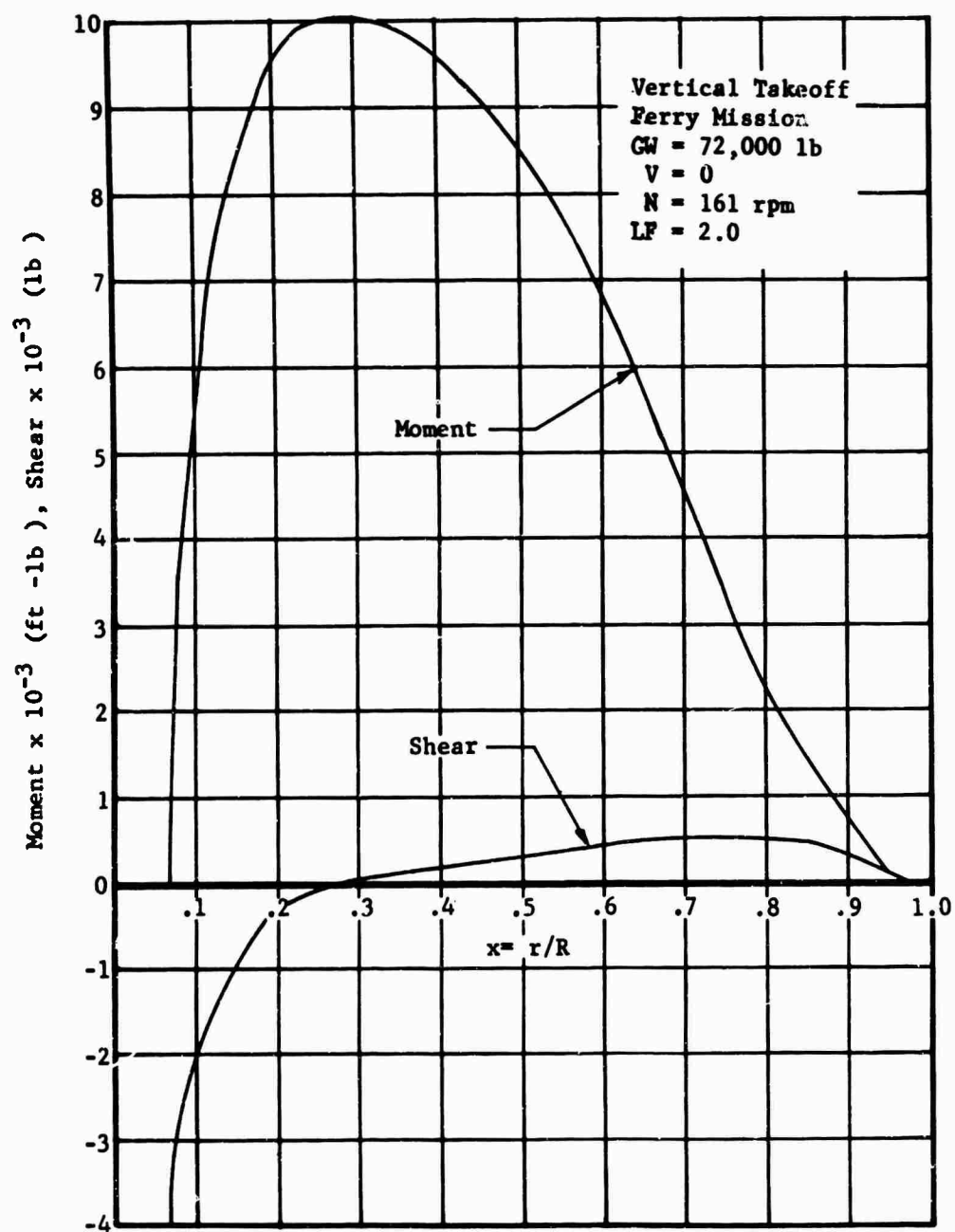


Figure 136 Edgewise Shear and Moment Distribution, Condition 2c

Condition 3 - Cruise (Level Flight)

The conditions investigated were:

3a: 20-Ton Mission

3b: 12-Ton Mission

3c: Ferry Mission

These conditions, although not critical ones, are presented because the majority of the flight time spectrum is spent in forward level flight. The airloads, shears, and moments presented here cover the entire performance requirements of the aircraft for all three missions at forward speeds of 95, 110, and 138 knots. These loads are applied to the blade in the spar fatigue analysis section of the structures report to determine blade life.

TABLE XXXIX
CONDITION 3a, CRUISE,
20-TON MISSION,
BASIC DESIGN PARAMETERS

Parameter	Symbol	Value
True Airspeed	V	95 kn
Rotor rpm	N	146 rpm
Angular Velocity	Ω	15.286 rad/sec
Linear Tip Velocity	ΩR	700 ft/sec
Load Factor	LF	1.0
Gross Weight	GW	78,750 lb
Thrust	T	78,750 lb
Lift Curve Slope	a	6.90
Tip Speed Ratio	μ	0.2290
Blade Pitch Angle at Hub	θ_0	0.2424 rad
Twist Angle	θ_1	-0.1396 rad
Inflow Factor	λ	-0.0400
Coning Coefficient	a_0	0.1325 rad
Flapping Coefficients		
cos ψ component	a_1	0.0798 rad
sin ψ component	b_1	0.0388 rad
cos 2 ψ component	a_2	0.0057 rad
sin 2 ψ component	b_2	-0.0035 rad

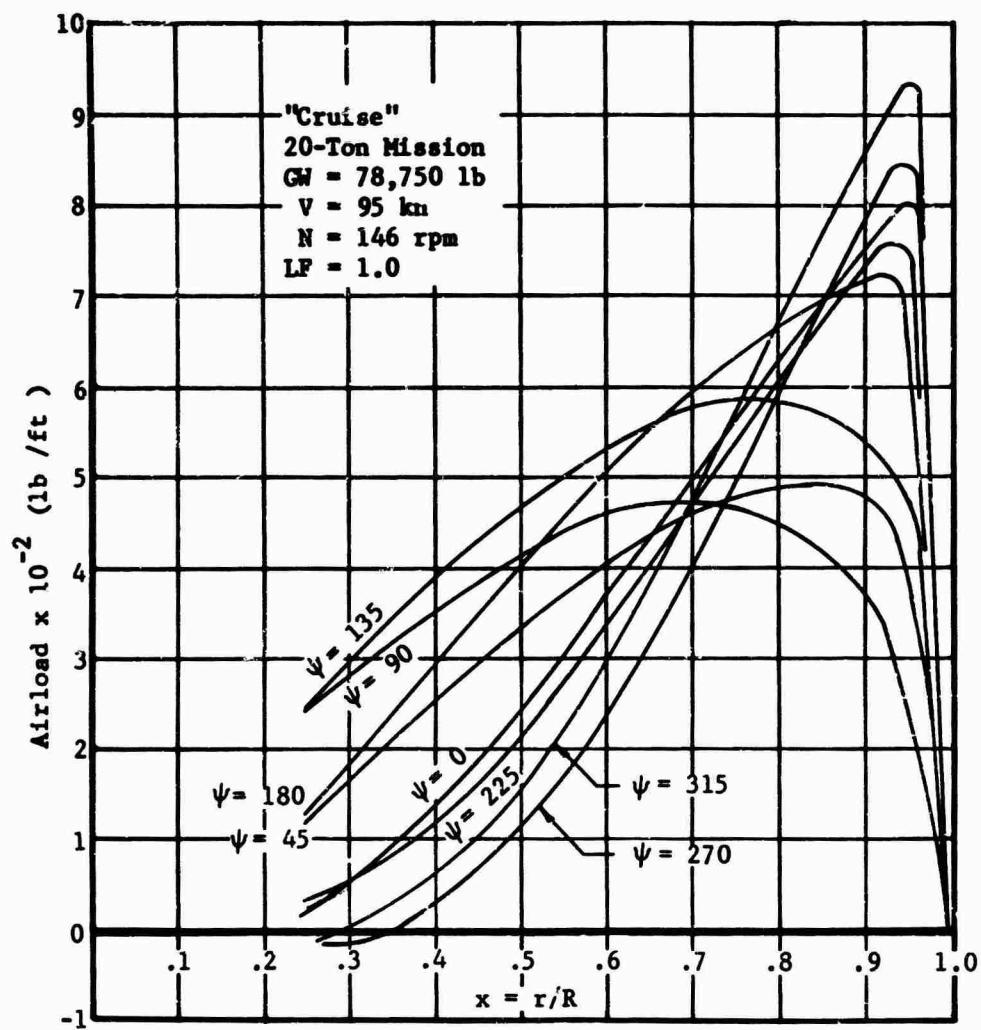


Figure 137 Flapwise Airload Distribution, Condition 3a

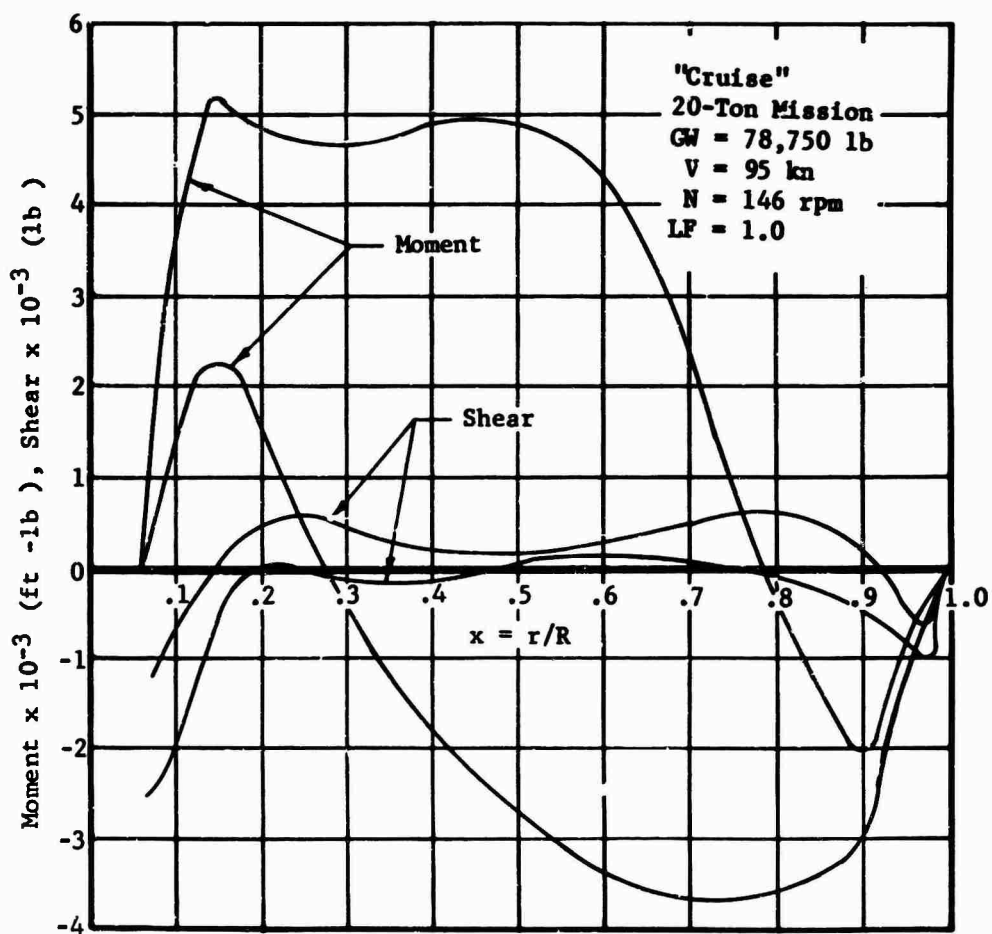


Figure 138 Flapwise Shear and Moment Envelope, Condition 3a

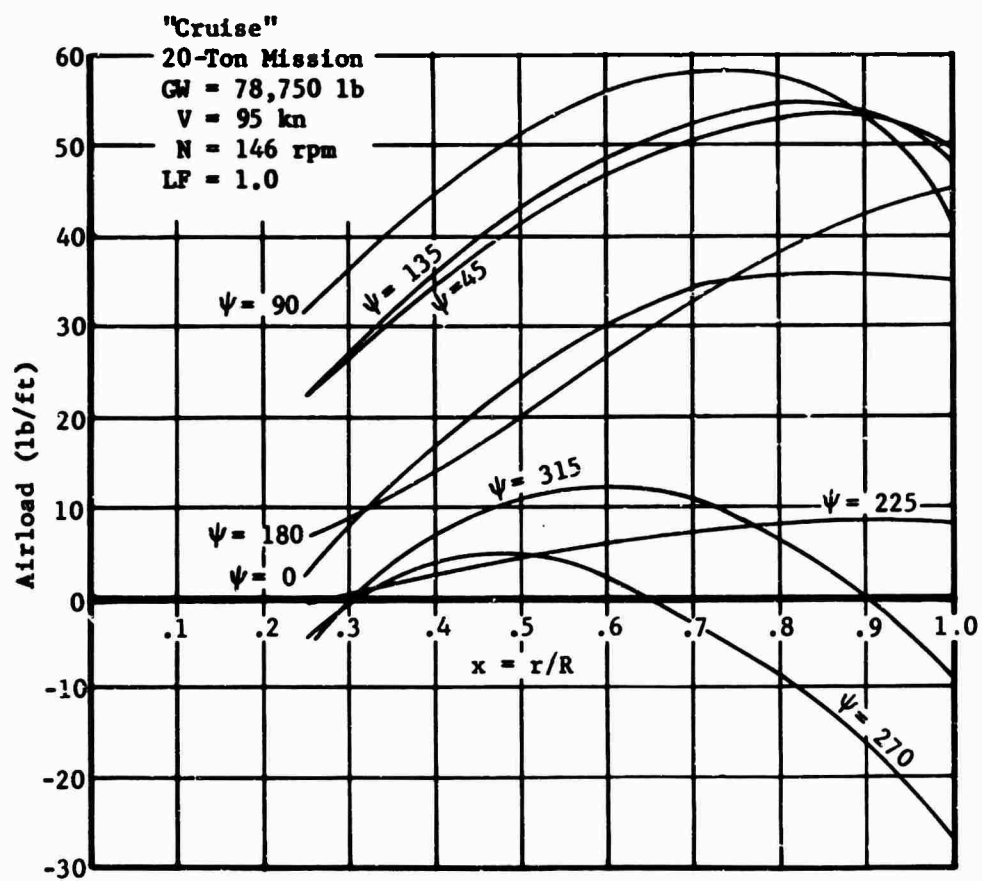


Figure 139 Edgewise Airload Distribution, Condition 3a

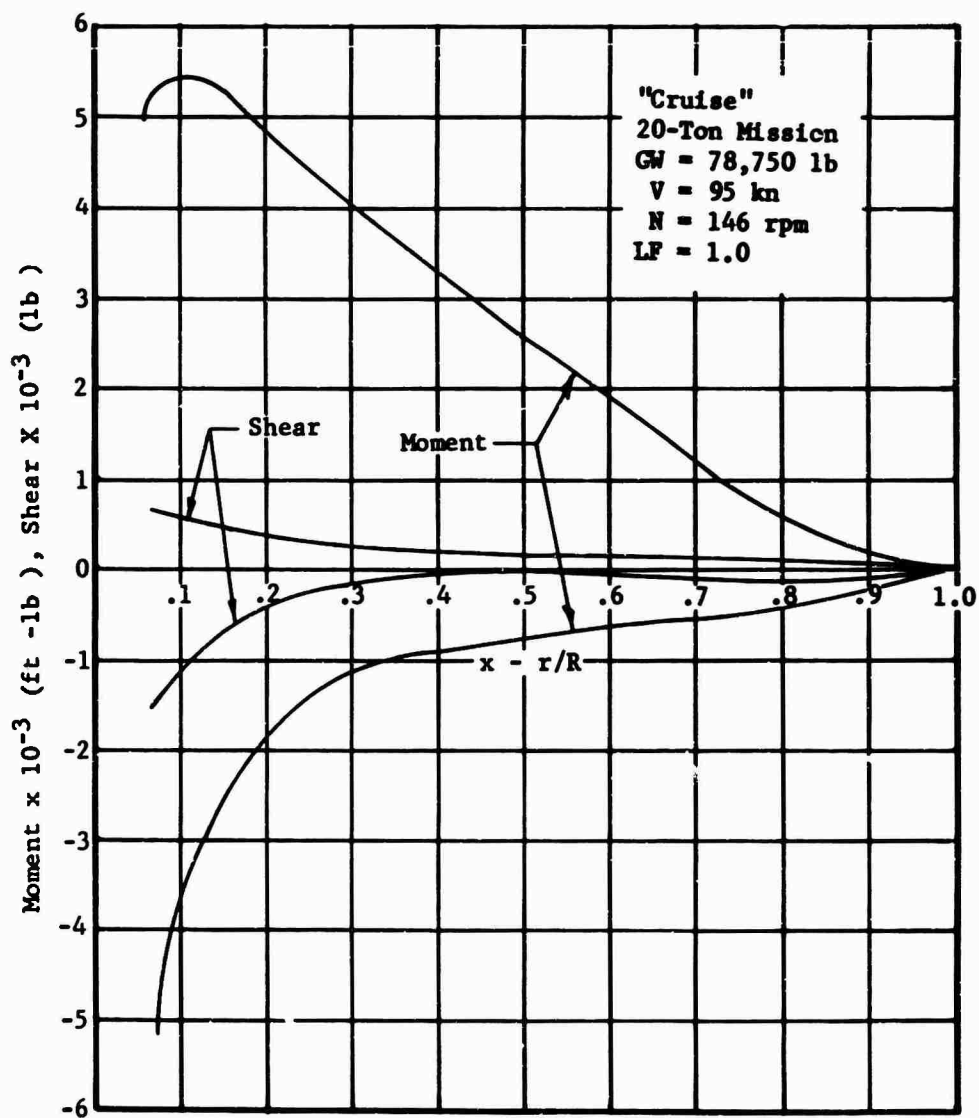


Figure 140 Edgewise Shear and Moment Envelope, Condition 3a

TABLE XXXX
CONDITION 3b, CRUISE,
12-TON MISSION,
BASIC DESIGN PARAMETERS

Parameter	Symbol	Value
True Airspeed	V	110 kn
Rotor rpm	N	146 rpm
Angular Velocity	Ω	15.286 rad/sec
Linear Tip Velocity	ΩR	700 ft/sec
Load Factor	LF	1.0
Gross Weight	GW	65,800 lb
Thrust	T	65,800 lb
Lift Curve Slope	a	6.90
Tip Speed Ratio	μ	0.265
Blade Pitch Angle at Hub	θ_0	0.2221 rad
Twist Angle	θ_1	-.1396 rad
Inflow Factor	λ	-.0378
Coning Coefficient	a_0	0.1076 rad
Flapping Coefficients		
cos ψ component	a_1	0.0776 rad
sin ψ component	b_1	0.0362 rad
cos 2 ψ component	a_2	0.0063 rad
sin 2 ψ component	b_2	-0.0040 rad

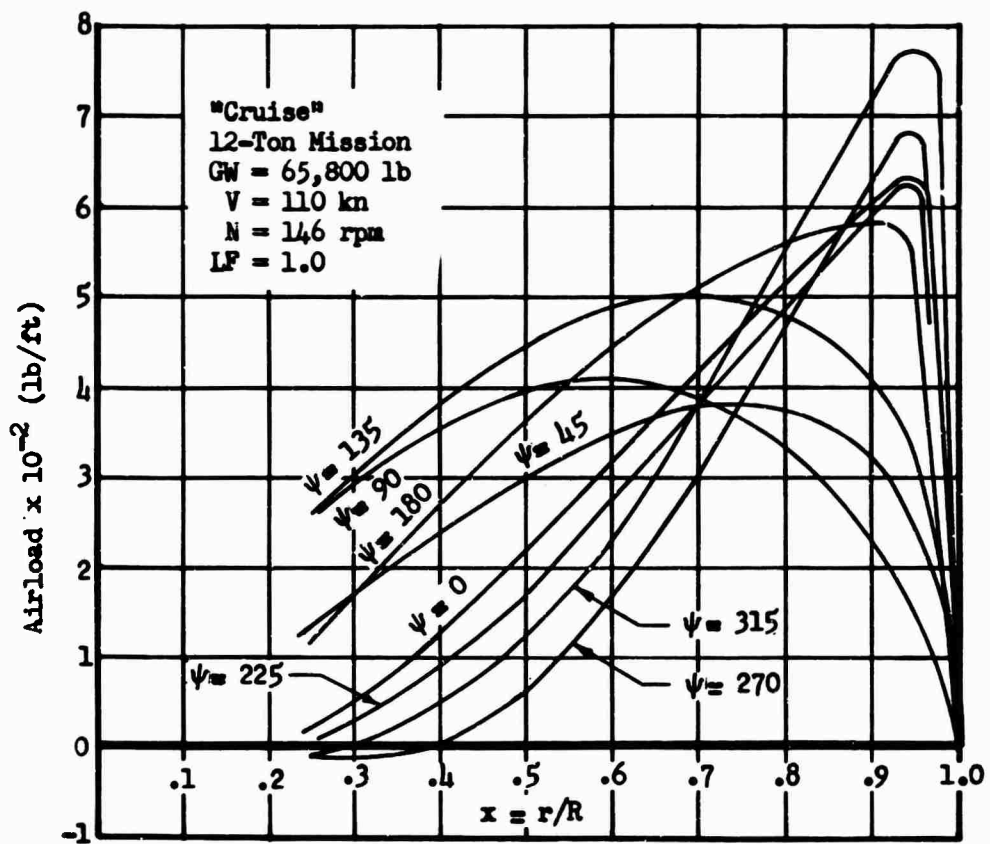


Figure 141 Flapwise Airload Distribution, Condition 3b

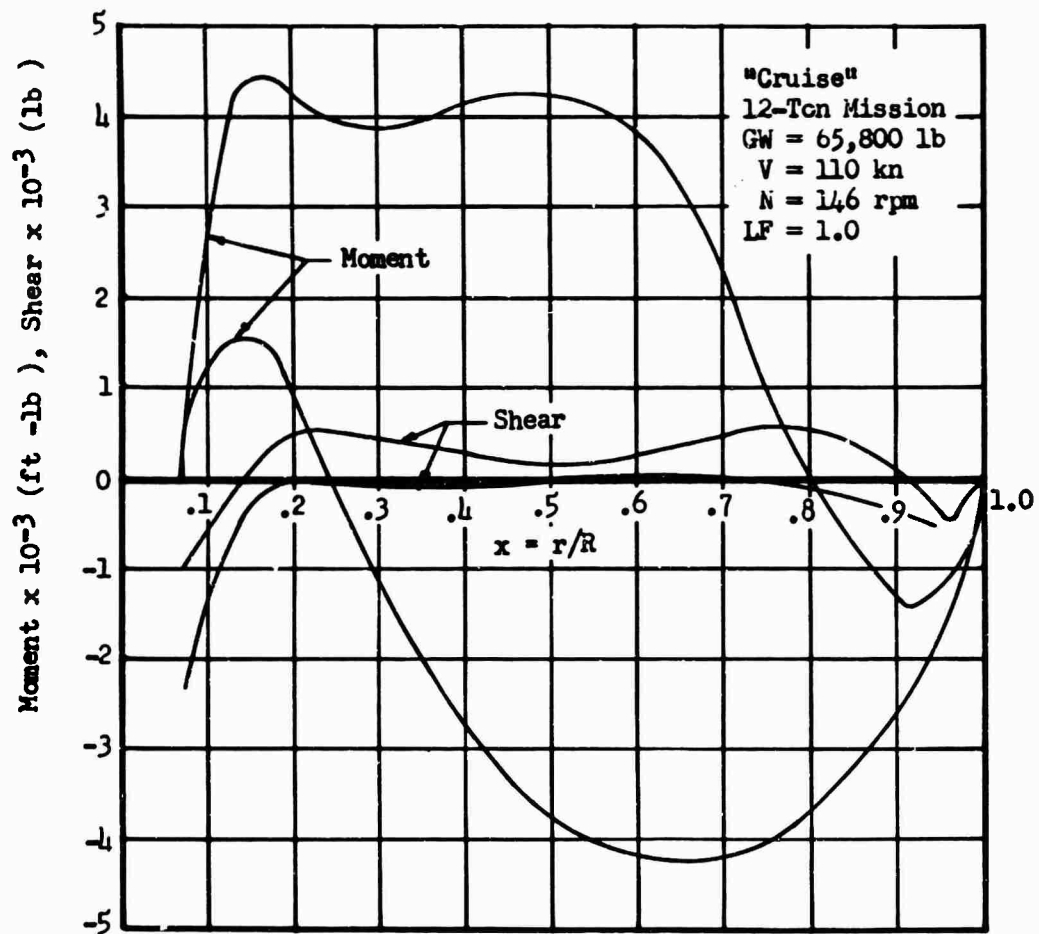


Figure 142 Flapwise Shear and Moment Envelope, Condition 3b

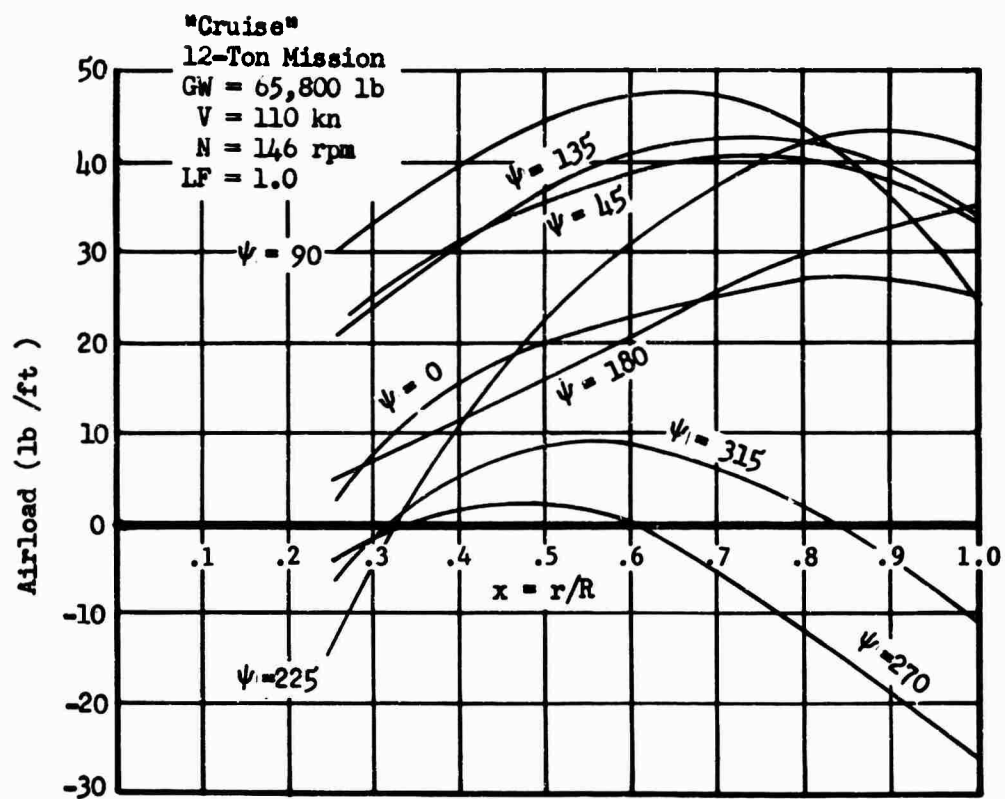


Figure 143 Edgewise Airload Distribution, Condition 3b

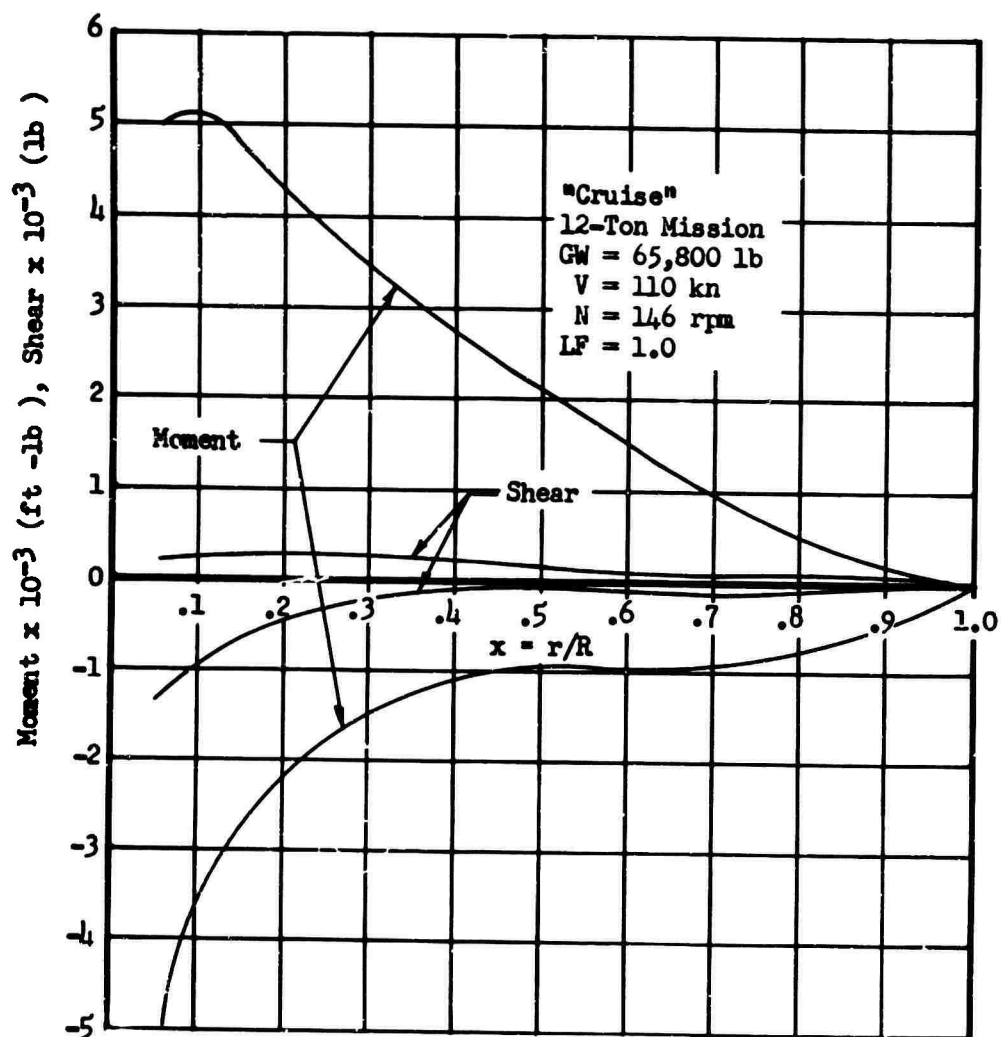


Figure 144 Edgewise Shear and Moment Envelope, Condition 3b

TABLE XXXXI
CONDITION 3c, CRUISE,
FERRY MISSION,
BASIC DESIGN PARAMETERS

Parameter	Symbol	Value
True Airspeed	V	130 kn
Rotor rpm	N	146 rpm
Angular Velocity	Ω	15.286 rad/sec
Linear Tip Velocity	ΩR	700 ft/sec
Load Factor	LF	1.0
Gross Weight	GW	72,000 lb
Thrust	T	72,000 lb
Lift Curve Slope	a	6.90
Tip Speed Ratio	μ	0.314
Blade Pitch Angle at Hub	θ_0	0.2127 rad
Twist Angle	θ'	-.1396 rad
Inflow Factor	λ	-.0292
Coning Coefficient	a_0	0.1155 rad
Flapping Coefficients		
cos ψ component	a_1	.0906 rad
sin ψ component	b_1	.0463 rad
cos 2 ψ component	a_2	.0091 rad
sin 2 ψ component	b_2	-.0055 rad

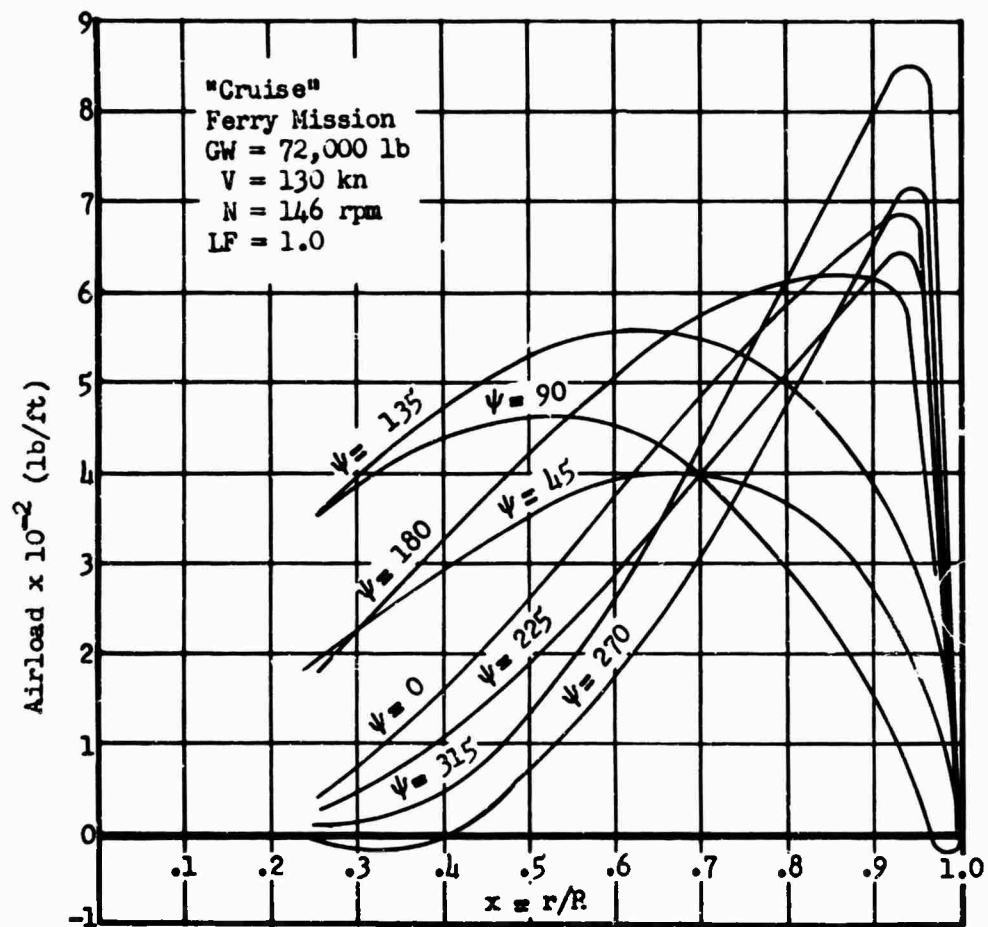


Figure 145 Flapwise Airload Distribution, Condition 3c

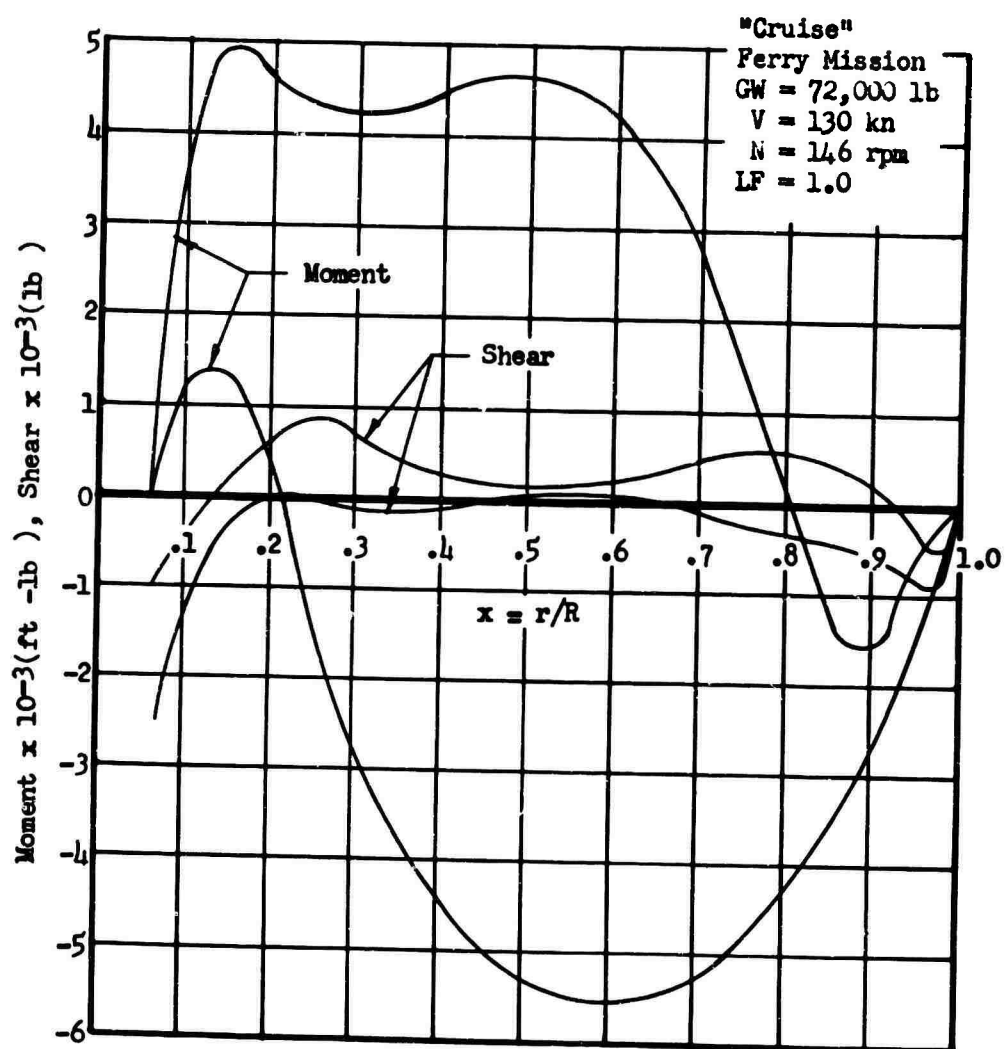


Figure 146 Flapwise Shear and Moment Envelope, Condition 3c

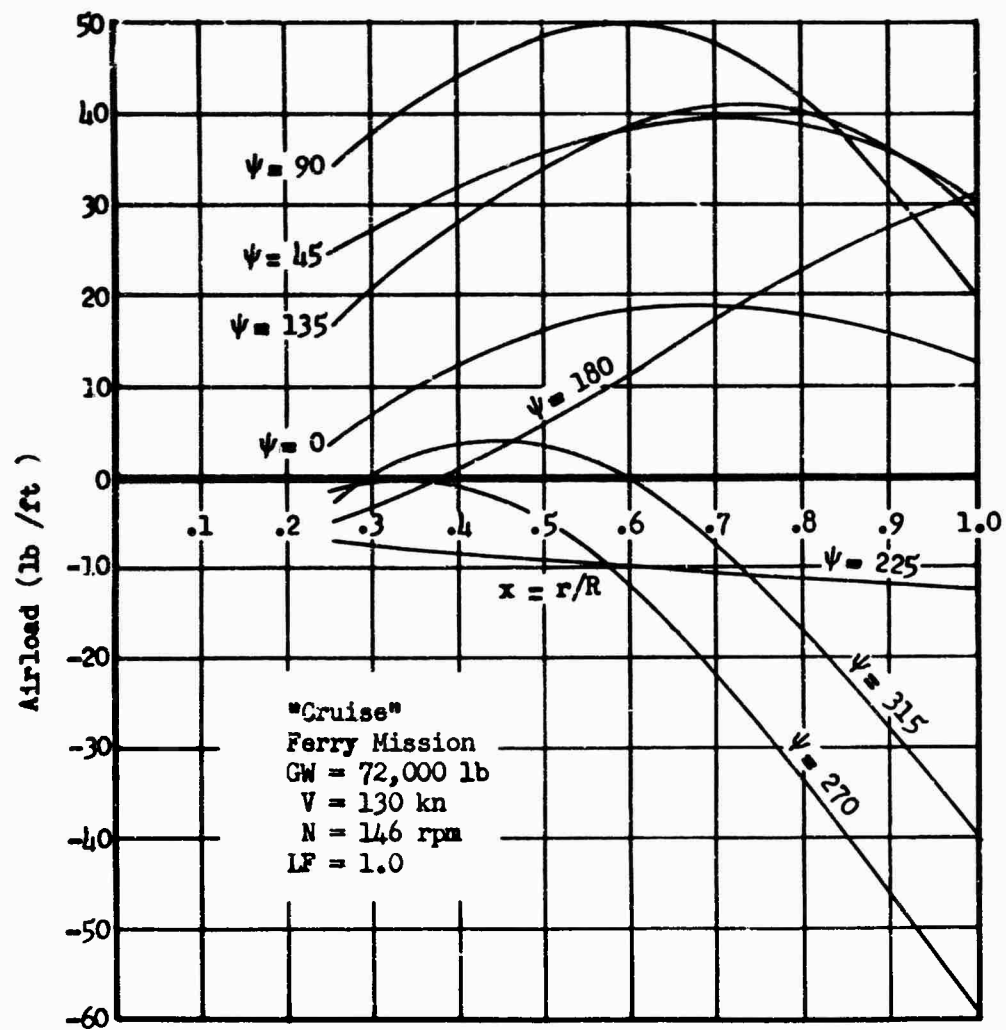


Figure 147 Edgewise Airload Distribution, Condition 3c

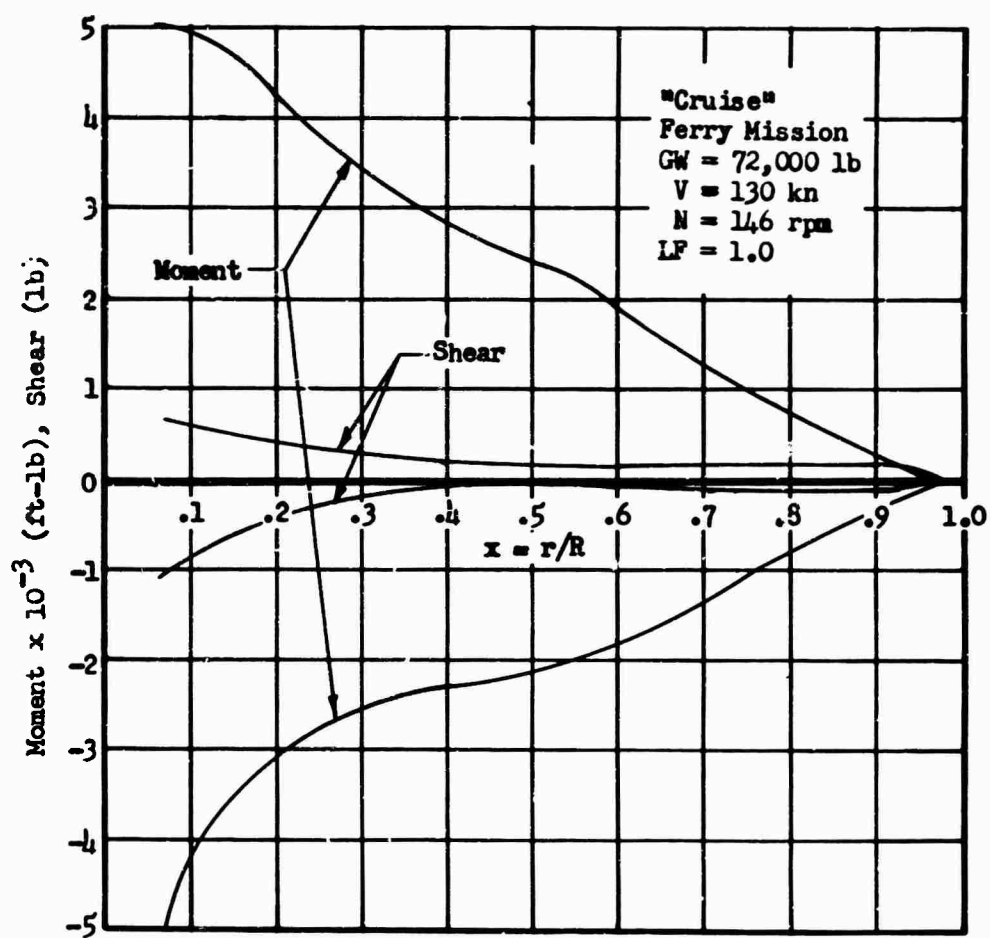


Figure 148 Edgewise Shear and Moment Distribution, Condition 3c

Condition 4 - Symmetrical Dive And Pullout

The conditons investigated were:

- 4a: 20-Ton Mission
- 4b: 12-Ton Mission
- 4c: Ferry Mission

The airloads for this maneuver are calculated as outlined earlier on page 207. This condition generates the highest combination of loads on the outboard 75 percent of the blade. In accordance with Reference 34, the net airload over the aft 30 percent of the airfoil section has been increased by a uniformly distributed "compressibility increment". This analysis of change in airload intensity, as presented in Reference 34, is applied to that portion of the blade where the Mach number exceeds 0.6. The net total airload is considered unaltered, so the analysis is limited to determining the torsional moment developed along the blade.

TABLE XXXXII
CONDITION 4a, SYMMETRICAL DIVE AND PULLOUT,
20-TON MISSION,
BASIC DESIGN PARAMETERS

Parameter	Symbol	Value
True Airspeed	V	121 kn
Rotor rpm	N	146 rpm
Angular Velocity	\dot{n}	15.286 rad/sec
Linear Tip Velocity	nR	700 ft/sec
Load Factor	LF	2.5
Gross Weight	GW	78,750 lb
Thrust*	T	196,875 lb
Lift Curve Slope	a	6.90
Tip Speed Ratio	μ	0.291
Blade Pitch Angle at Hub	θ_0	0.3909 rad
Twist Angle	θ_1	-.1396 rad
Inflow Factor	λ	-0.0640
Coning Coefficient	a_0	0.3448 rad
Flapping Coefficients		
cos ψ component	a_1	0.2298 rad
sin ψ component	b_1	0.1302 rad
cos 2 ψ component	a_2	0.0228 rad
sin 2 ψ component	b_2	-0.0130 rad

*Considered momentary for load factors other than unity

TABLE XXXXIII
COMPRESSIBILITY INCREMENT,
CONDITION 4a

r_k	x_k	MN_k	V_k	q_k	k	C_{lk}	MN_{cr}	$MN_{cr} \left(\frac{MN_k}{MN_{cr}} - 1 \right)^{1/2}$	W_k	$r_{k+1} - r_k$	S_k	M_k
ft			ft/sec	lb/ft ²	degree				lb/in	in	lb	in-lb
30.7	.67	.604	674	540	7.31	.731	.420	.662	8.07	16.8	141	38,818
32.1	.70	.623	695	575	7.07	.707	.430	.670	8.70	27.6	252	36,196
34.4	.75	.654	730	635	6.40	.640	.450	.673	9.60	27.6	279	31,508
36.6	.80	.684	764	694	5.93	.593	.470	.675	10.59	27.6	310	26,319
38.9	.85	.716	799	760	5.36	.536	.485	.690	11.84	27.6	336	20,553
41.2	.90	.747	834	828	4.83	.483	.515	.671	12.55	38.4	520	14,303
44.4	.97	.791	883	928	4.23	.423	.535	.692	14.51	16.8	249	4,631
45.8	1.00	.810	905	974	3.99	.399	.550	.688	15.13	-	-	-

209

$$W_k = .02259 \left(\frac{MN_k}{MN_{cr}} - 1 \right)^{1/2} q$$

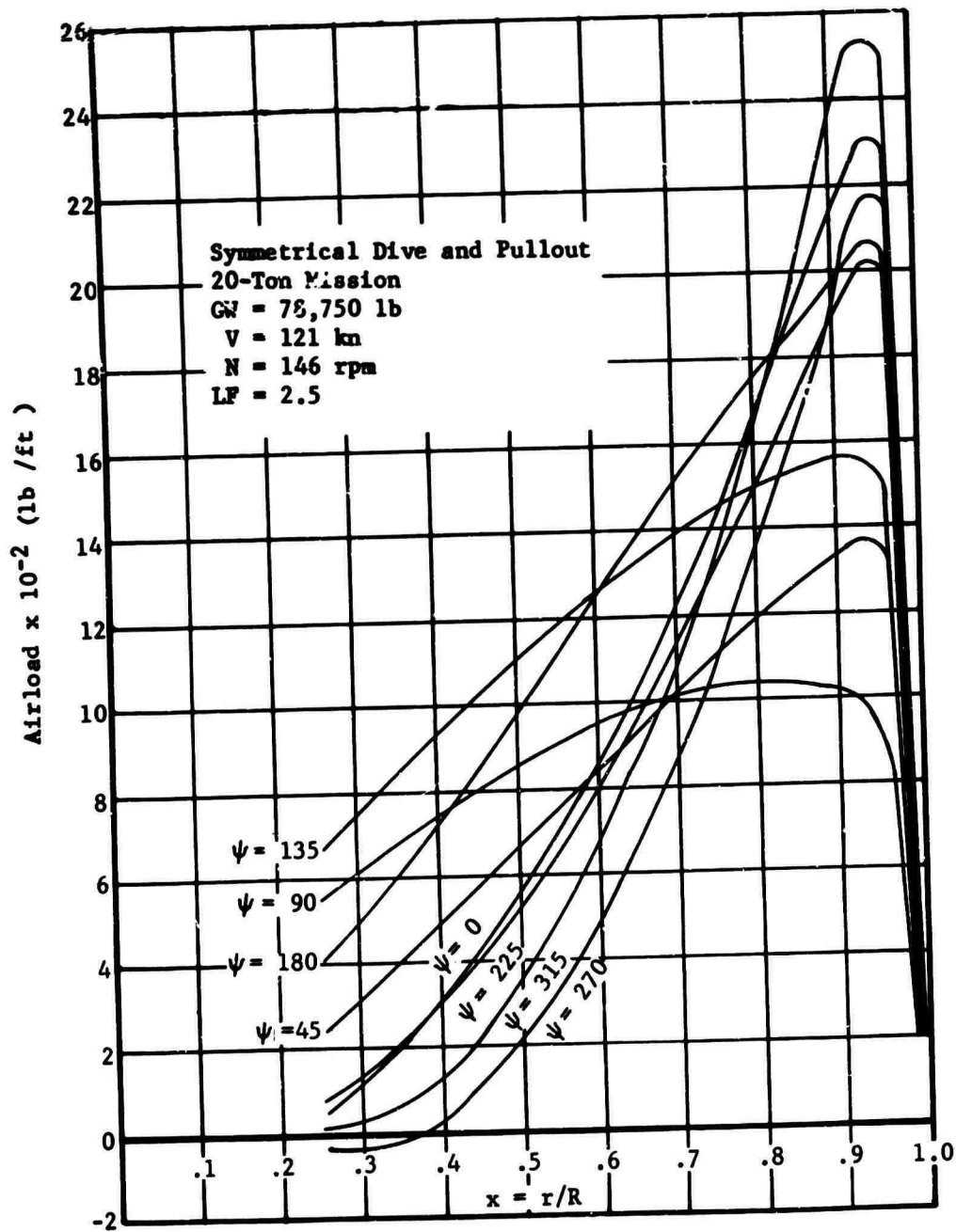


Figure 149 Flapwise Airload Distribution Condition 4a

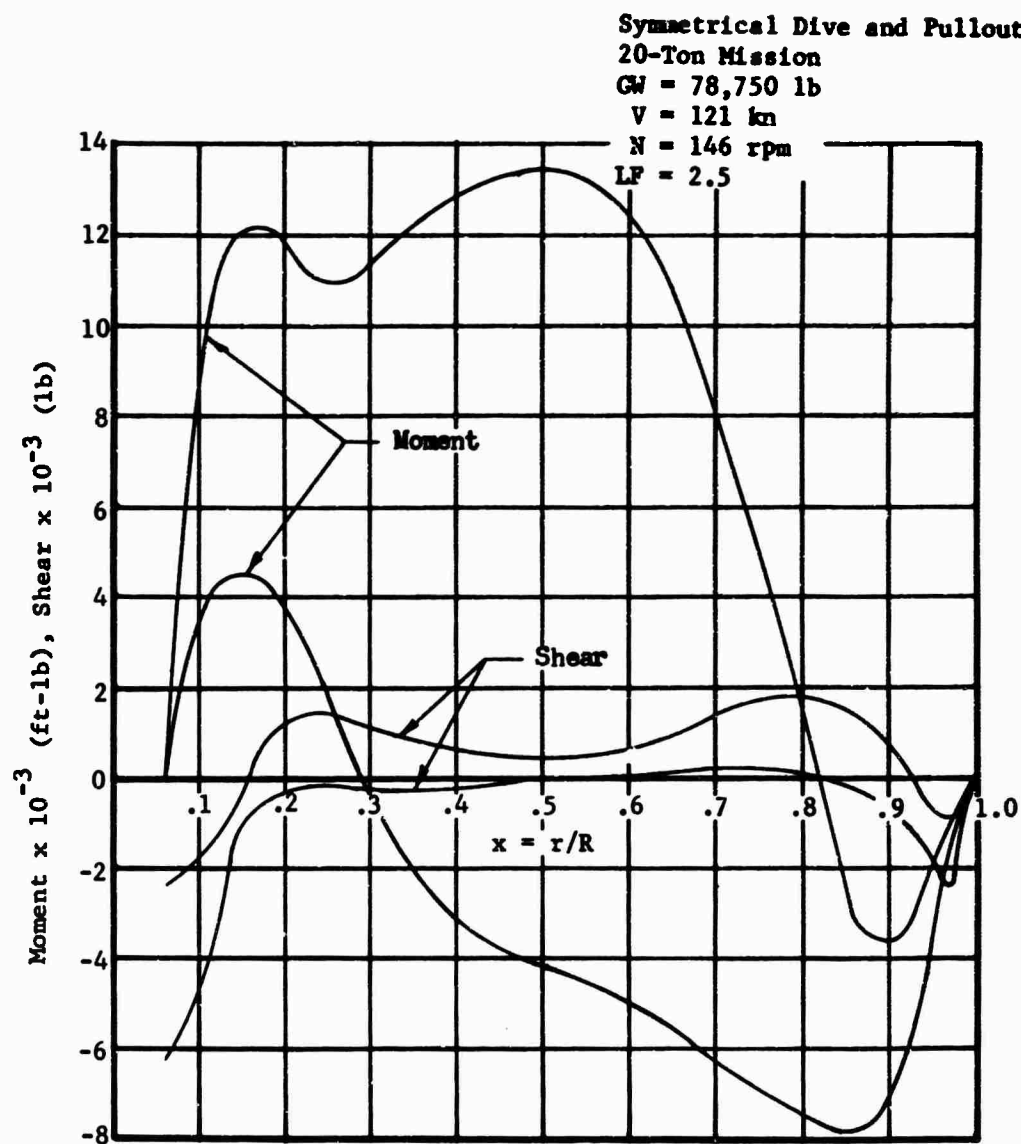


Figure 150 Flapwise Shear and Moment Envelope, Condition 4a

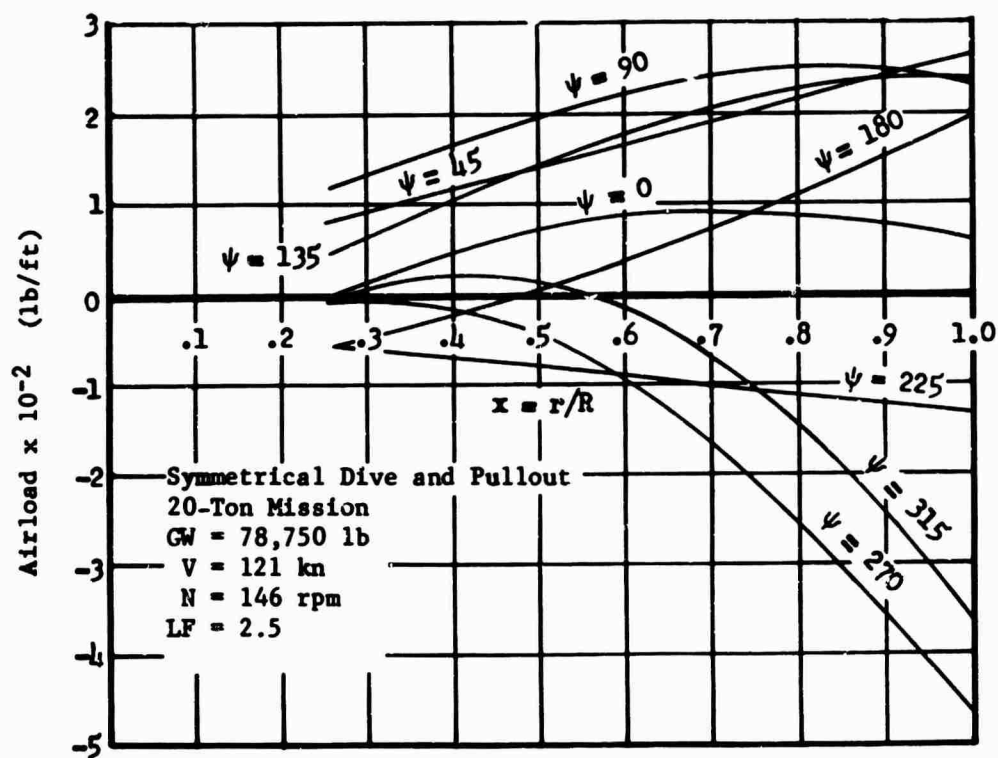


Figure 151 Edgewise Airload Distribution, Condition 4a

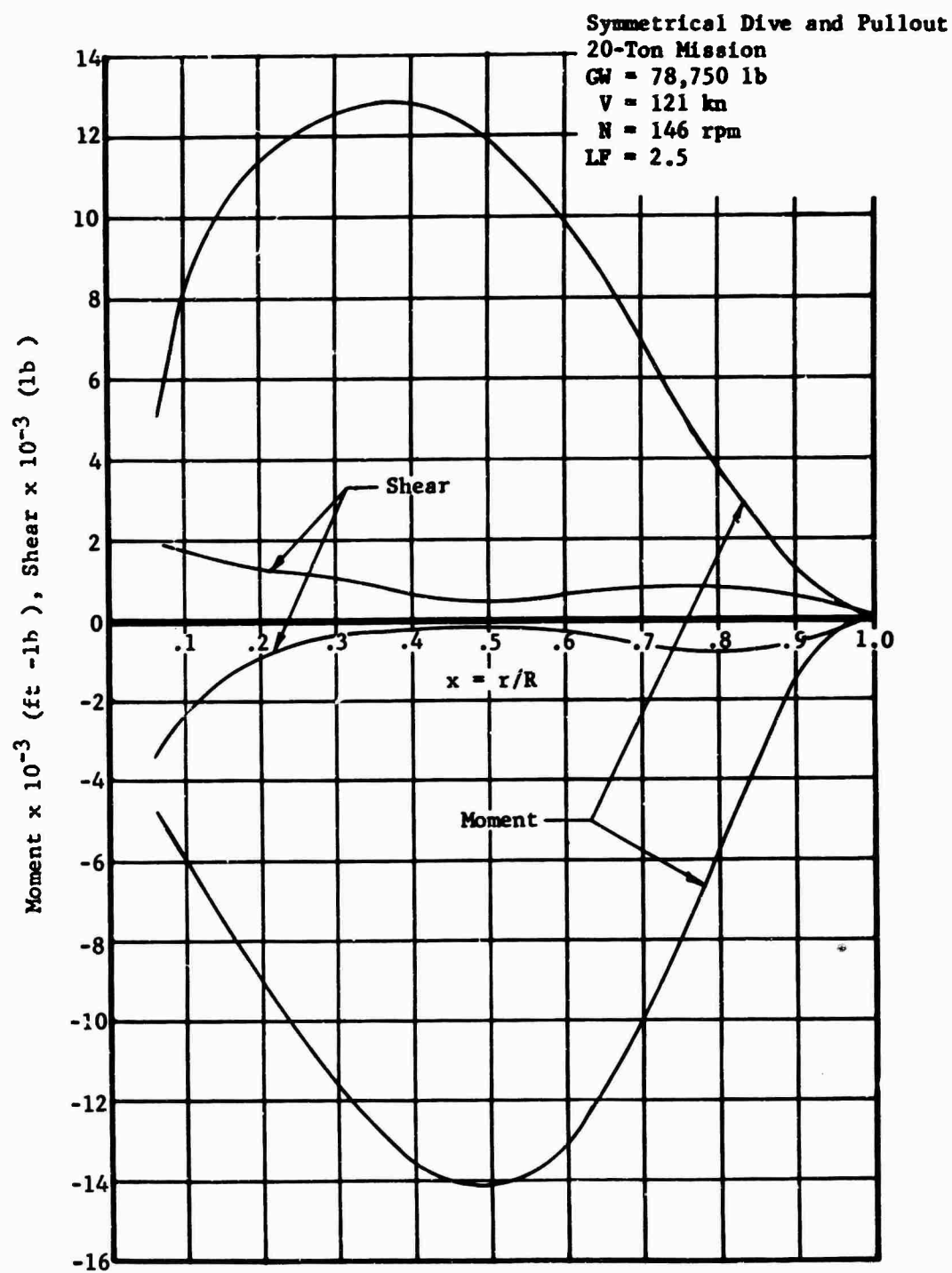


Figure 152 Edgewise Shear and Moment Envelope, Condition 4a

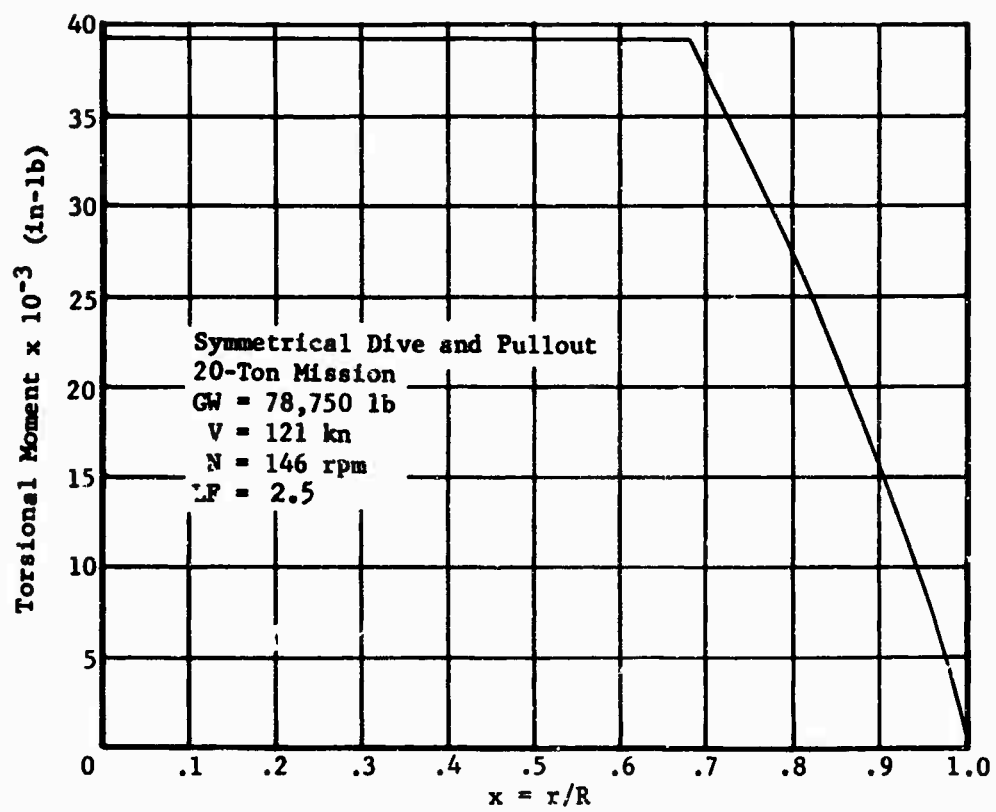


Figure 153 Compressibility Increment, Condition 4a

TABLE XXXXIV
CONDITION 4b, SYMMETRICAL DIVE AND PULLOUT,
12-TON MISSION,
BASIC DESIGN PARAMETERS

Parameter	Symbol	Value
True Airspeed	V	159 kn
Rotor rpm	N	146 rpm
Angular Velocity	Ω	15.286 rad/sec
Linear Tip Velocity	ΩR	700 ft/sec
Load Factor	LF	2.5
Gross Weight	GW	65,800 lb
Thrust	T	164,500 lb
Lift Curve Slope	a	6.90
Tip Speed Ratio	μ	0.383
Blade Pitch Angle at Hub	θ_0	0.4034 rad
Twist Angle	θ_1	-0.1396 rad
Inflow Factor	λ	-0.1167
Coning Coefficient	a_0	0.2867 rad
Flapping Coefficients		
cos ψ component	a_1	0.2805 rad
sin ψ component	b_1	0.1391 rad
cos 2ψ component	a_2	0.0337 rad
sin 2ψ component	b_2	-0.0207 rad

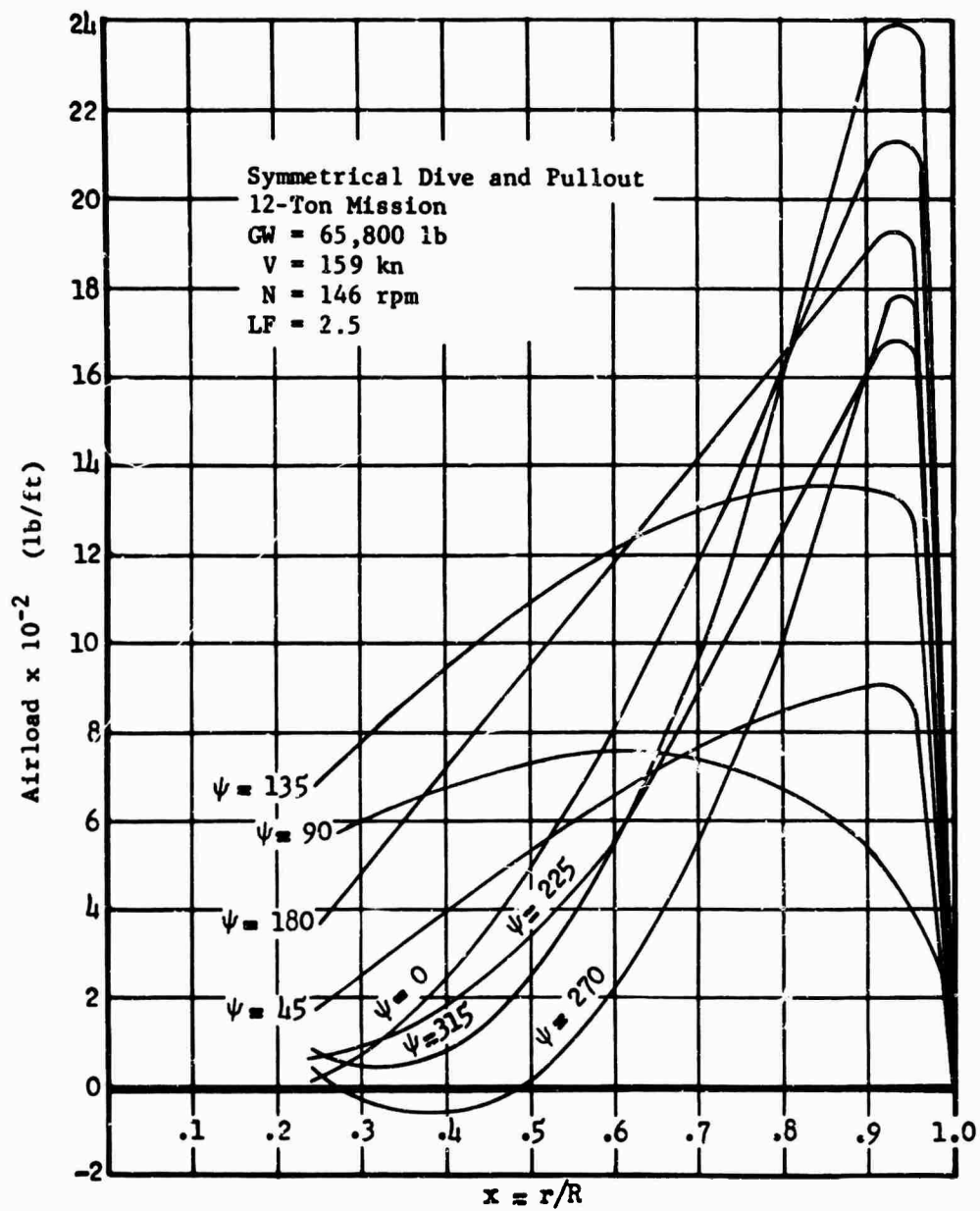


Figure 154 Flapwise Airload Distribution, Condition 4b

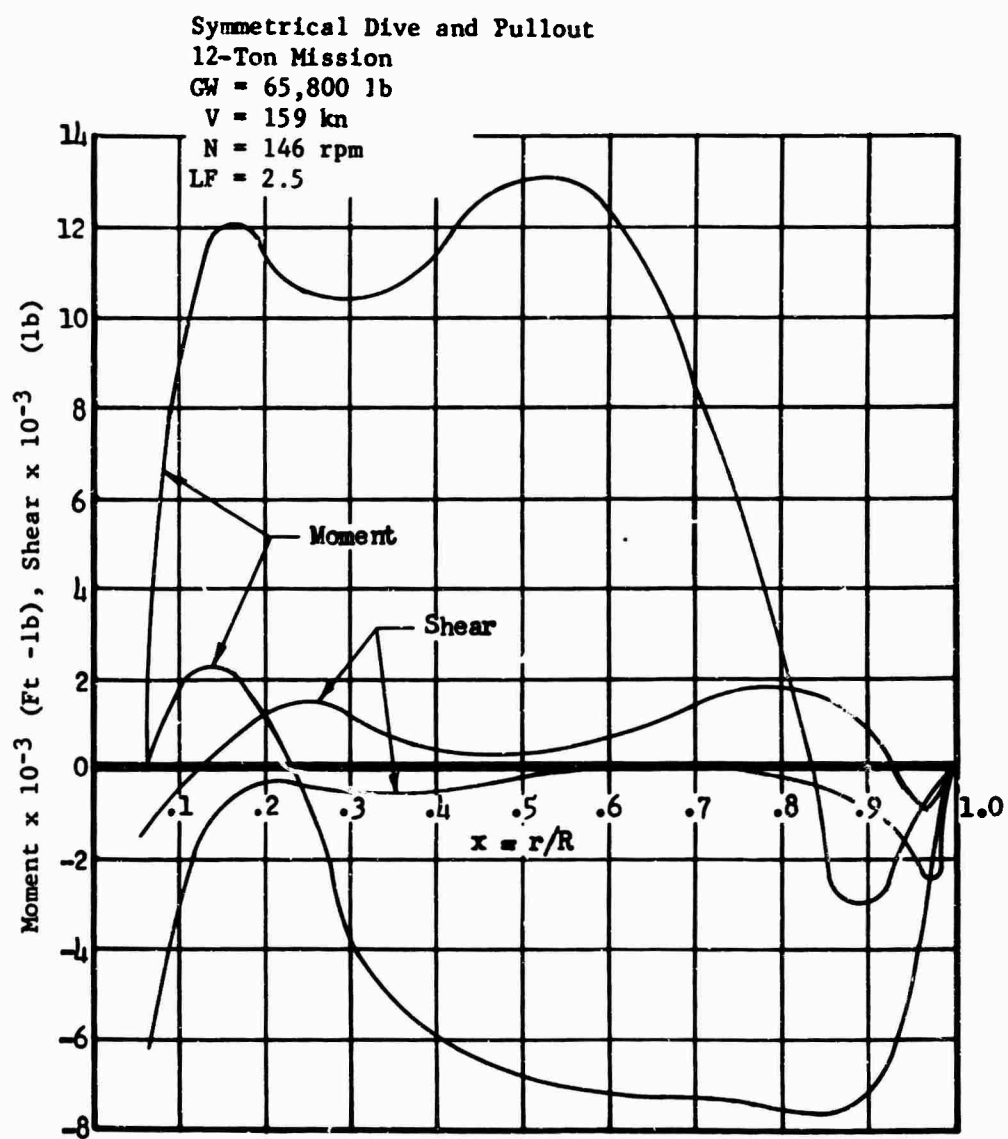


Figure 155 Flapwise Shear and Moment Envelope, Condition 4b

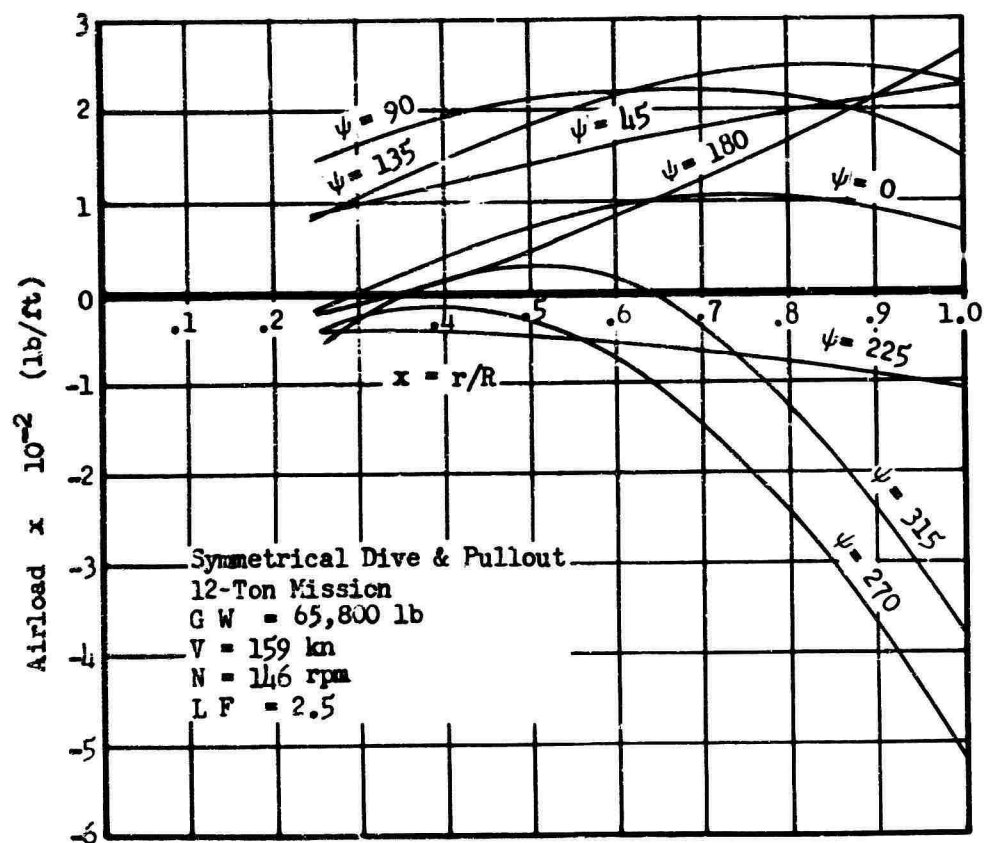


Figure 156 Edgewise Airload Distribution, Condition 4b

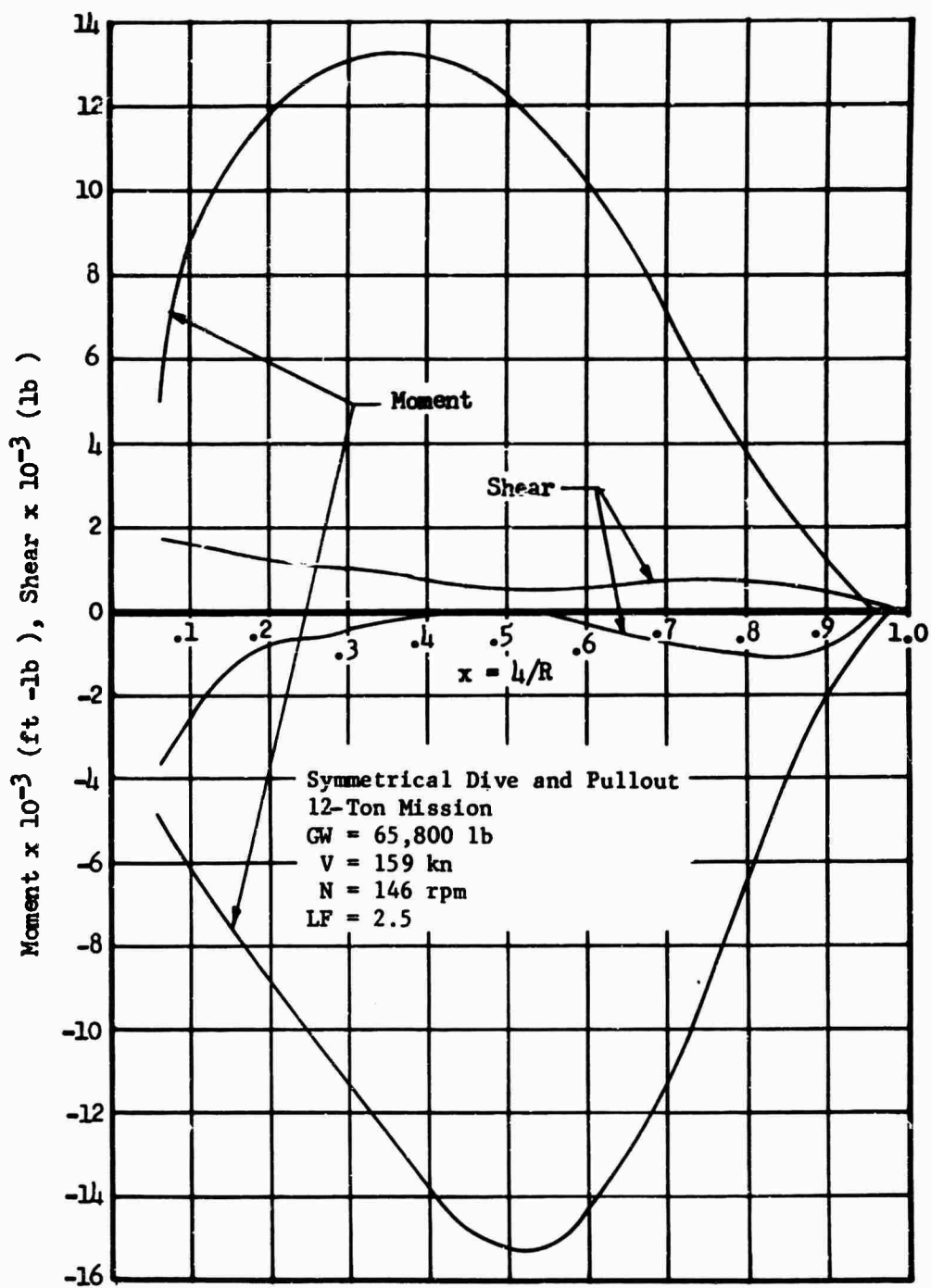


Figure 157 Edgewise Shear and Moment Envelope, Condition 4b

TABLE XXXXV
CONDITION 4c, SYMMETRICAL DIVE AND PULLOUT,
FERRY MISSION,
BASIC DESIGN PARAMETERS

Parameter	Symbol	Value
True Airspeed	V	145 kn
Rotor rpm	N	146 rpm
Angular Velocity	Ω	15.286 rad/sec
Linear Tip Velocity	ΩR	700 ft/sec
Load Factor	LF	2.0
Gross Weight	GW	72,000 lb
Thrust*	T	144,000 lb
Lift Curve Slope	a	6.90
Tip Speed Ratio	μ	0.350
Blade Pitch Angle at Hub	θ_0	0 rad
Twist Angle	θ_1	-0.1396 rad
Inflow Factor	λ	-0.0943
Coning Coefficient	a_0	0.2505 rad
Flapping Coefficients		
cos ψ component	a_1	0.2236 rad
sin ψ component	b_1	0.1112 rad
cos 2 ψ component	a_2	0.0246 rad
sin 2 ψ component	b_2	-0.0151 rad
*Considered momentary for load factors other than unity.		

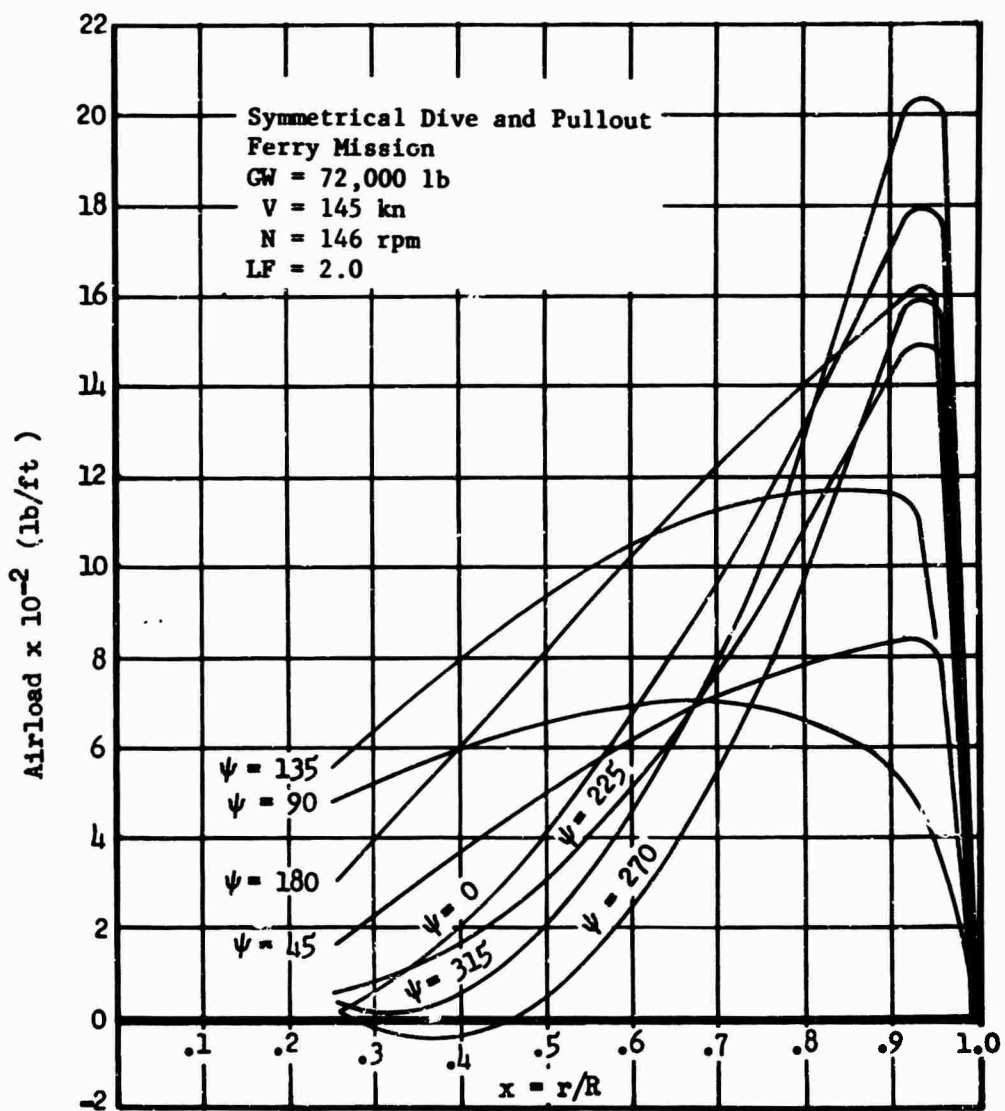


Figure 158 Flapwise Airload Distribution, Condition 4c

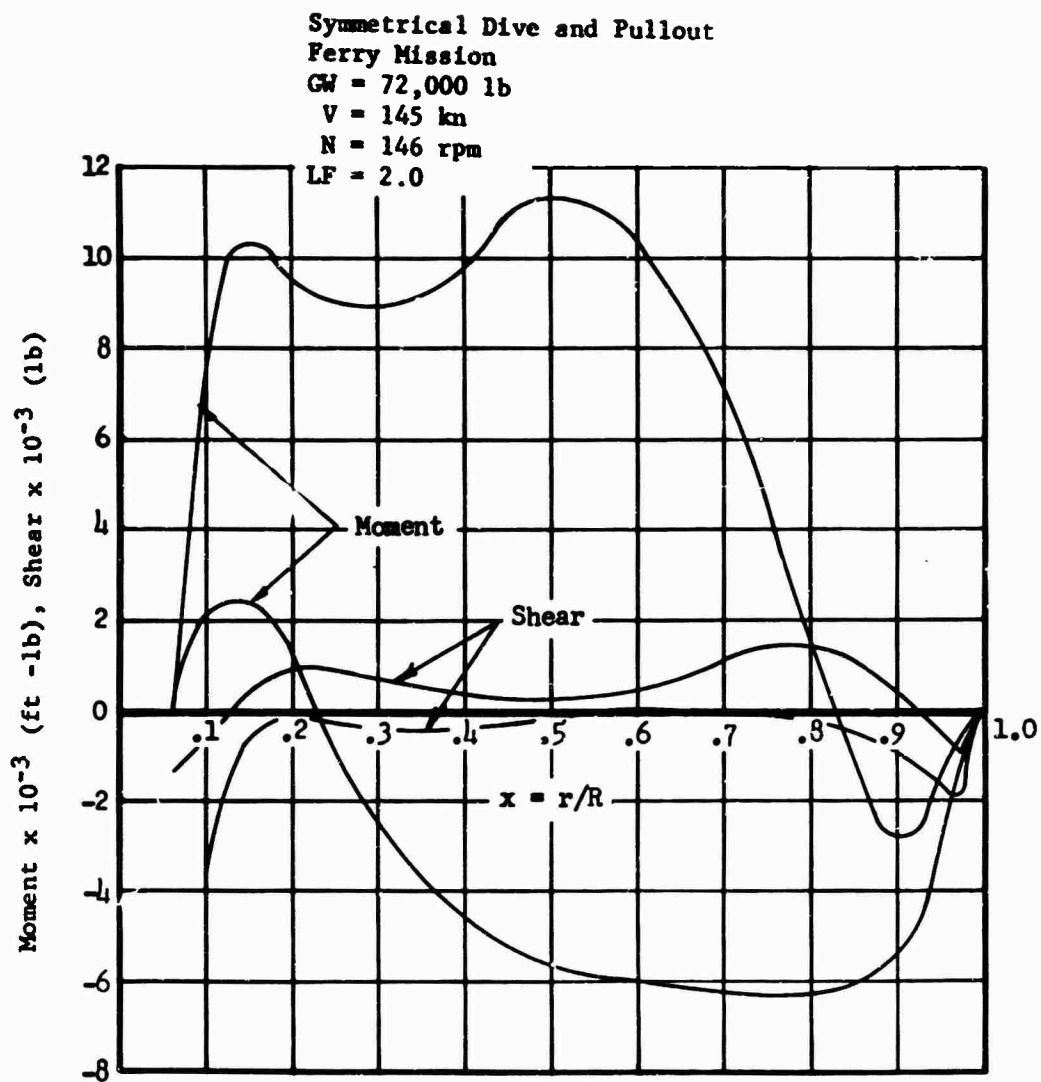


Figure 159 Flapwise Shear and Moment Envelope, Condition 4c

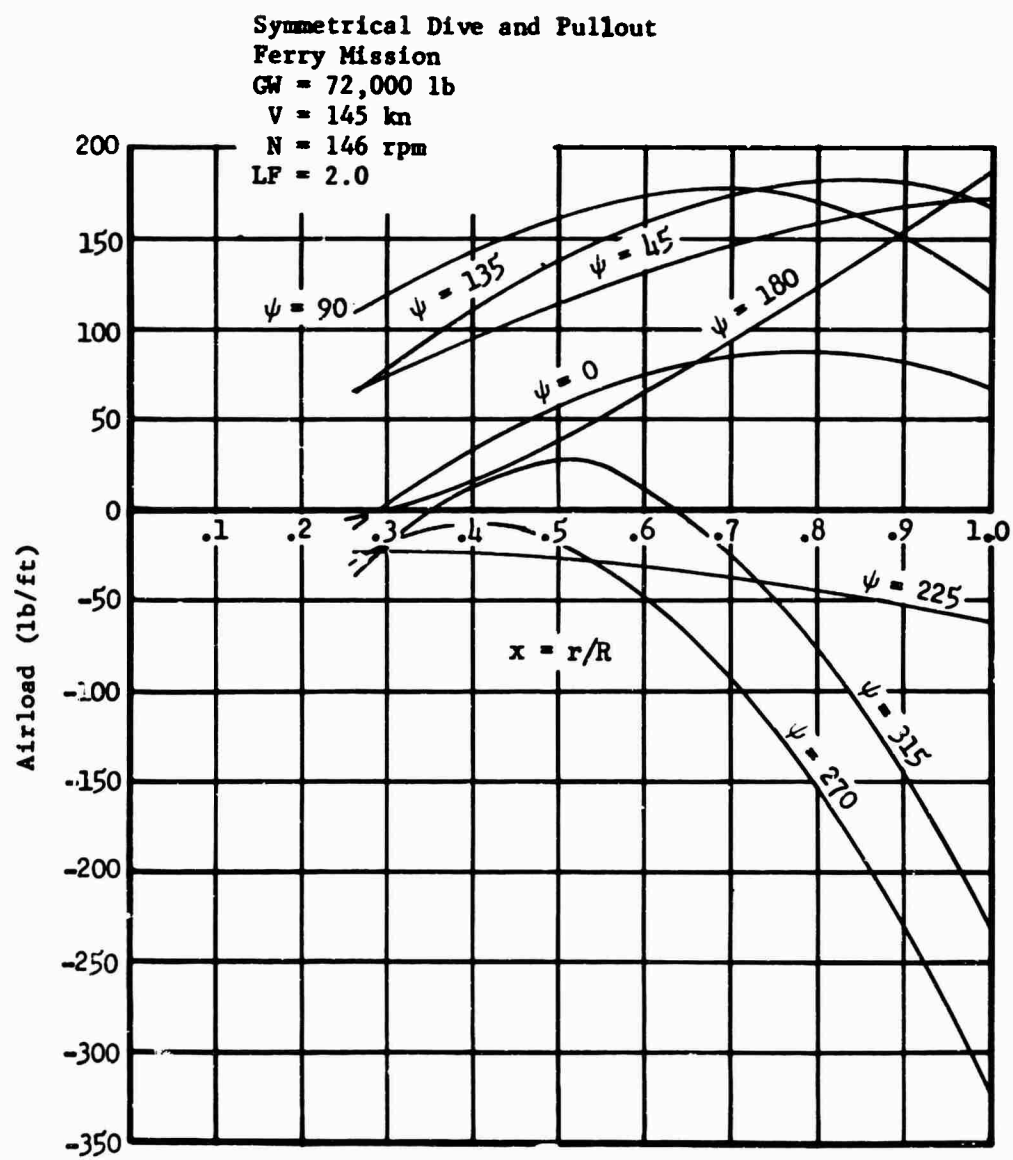


Figure 160 Edgewise Airload Distribution, Condition 4c

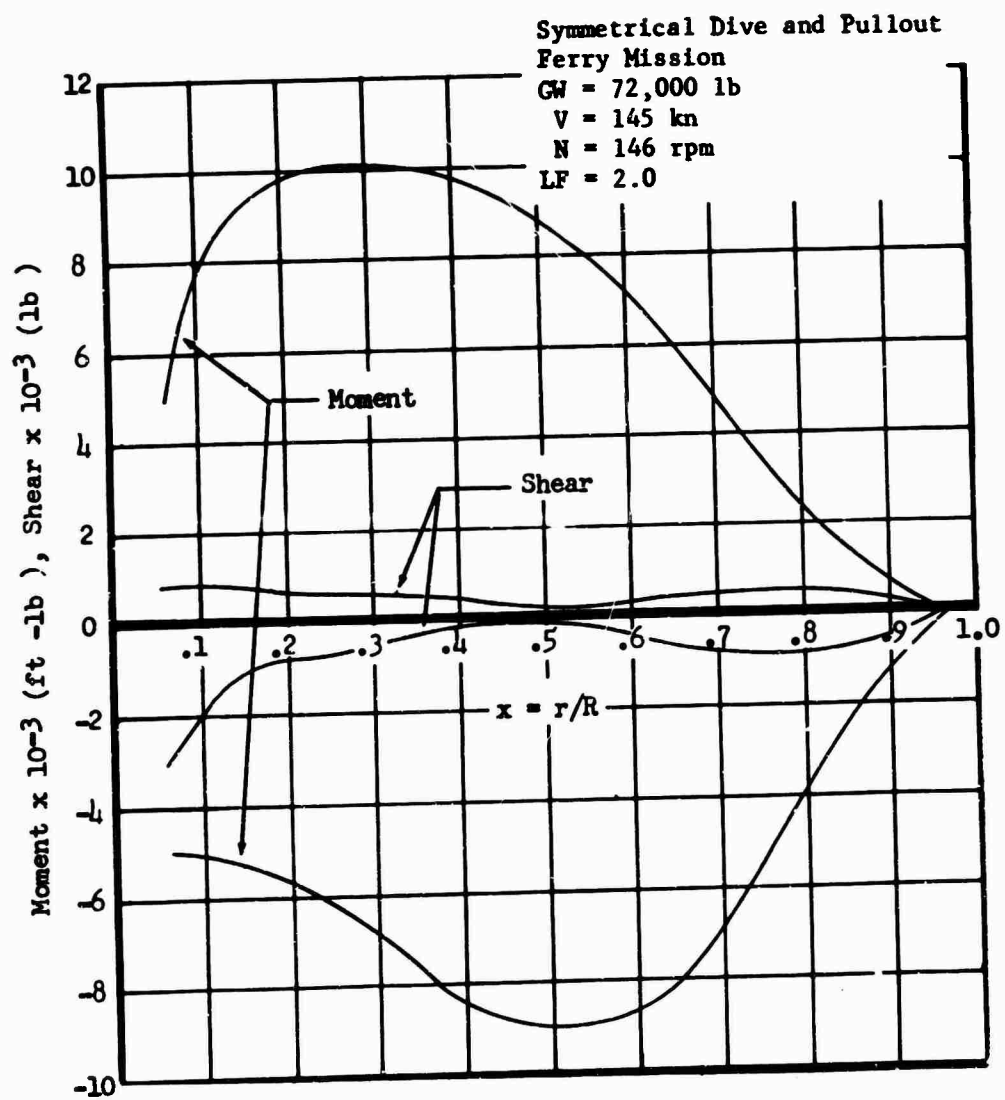


Figure 161 Edgewise Shear and Moment Envelope, Condition 4c

Condition 5 - Autorotative Dive and Pullout

The conditions investigated were:

5a: 20-Ton Mission

5b: 12-Ton Mission

5c: Ferry Mission

The autorotative dive and pullout maneuver produces the highest load combination on the inboard 25 percent of the blade and is presented here to complete the blade loading envelope. The torsional moment due to the compressibility increment is calculated as outlined in Condition 4, Symmetrical Dive and Pullout, and the results are presented in Table XXXXVI, and Figure 166.

TABLE XXXXVI
CONDITION 5a, AUTOROTATIVE DIVE AND PULLOUT,
20-TON MISSION,
BASIC DESIGN PARAMETERS

Parameter	Symbol	Value
True Airspeed	V	121 kn
Rotor rpm	N	168 rpm
Angular Velocity	Ω	17.59 rad/sec
Linear Tip Velocity	ΩR	806 ft/sec
Load Factor	LF	2.5
Gross Weight	GW	78,750 lb
Thrust *	T	196,875 lb
Lift Curve Slope	a	7.35
Tip Speed Ratio	μ	0.2540
Blade Pitch Angle at Hub	θ_0	0.2271 rad
Twist Angle	θ_1	-.1396 rad
Inflow Factor	λ	0.0175
Coning Coefficient	a_0	0.2482 rad
Flapping Coefficients		
cos ψ component	a_1	0.1125 rad
sin ψ component	b_1	0.0842 rad
cos 2ψ component	a_2	0.0114 rad
sin 2ψ component	b_2	-0.0058 rad

* Considered momentary for load factors other than unity.

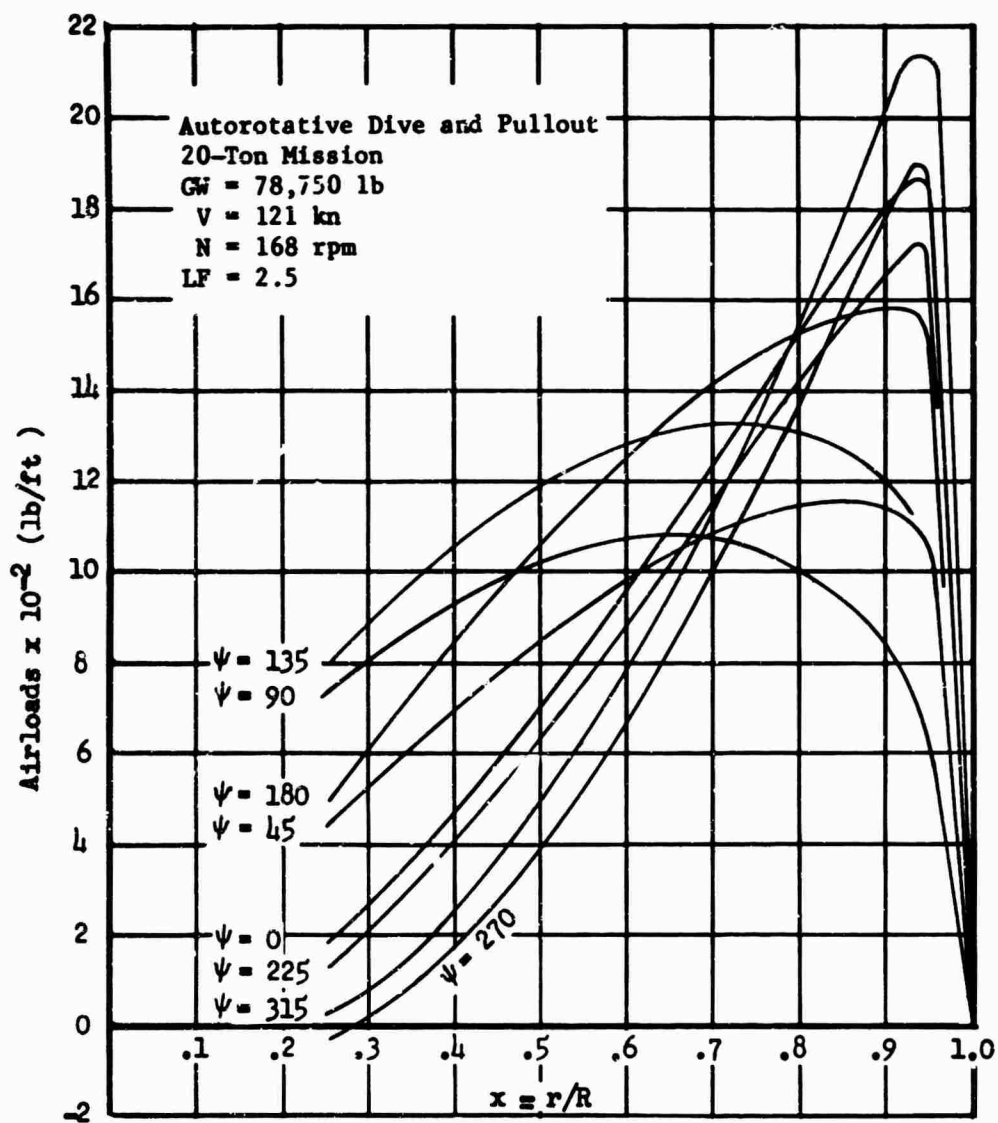


Figure 162 Flapwise Airload Distribution, Condition 5a

Autorotative Dive and Pullout
 20-Ton Mission
 GW = 78,750 lb
 V = 121 kn
 N = 168 rpm
 LF = 2.5

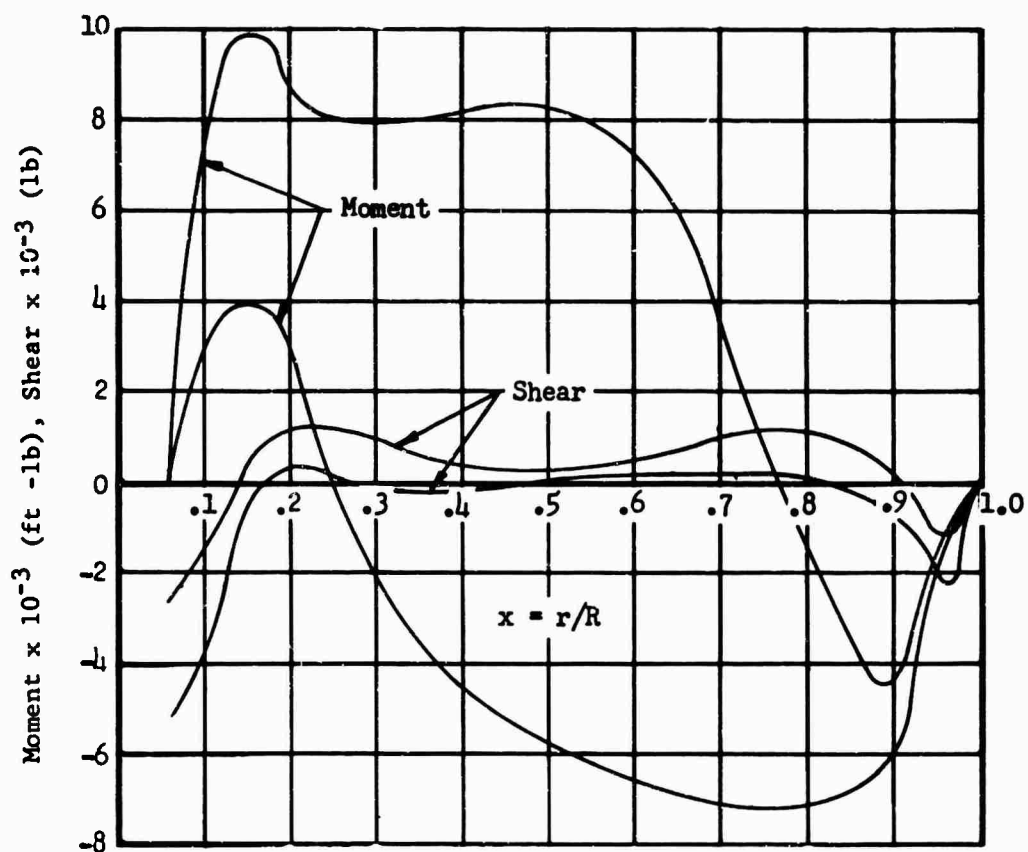


Figure 163 Flapwise Shear and Moment Envelope, Condition 5a

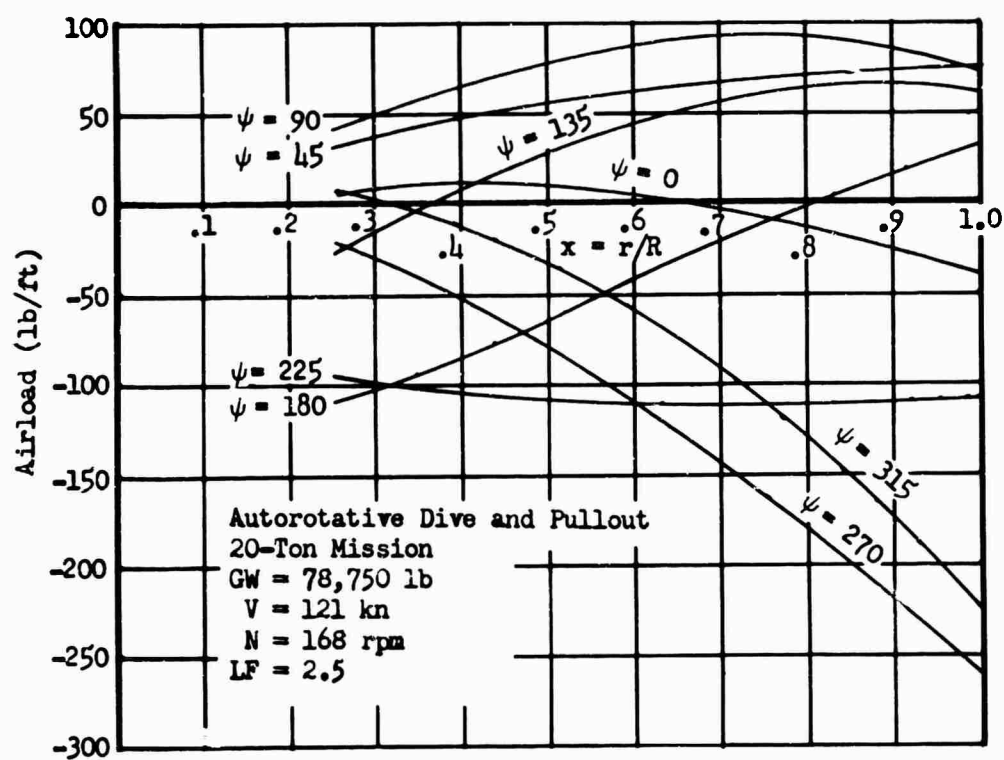


Figure 164 Edgewise Airload Distribution, Condition 5a

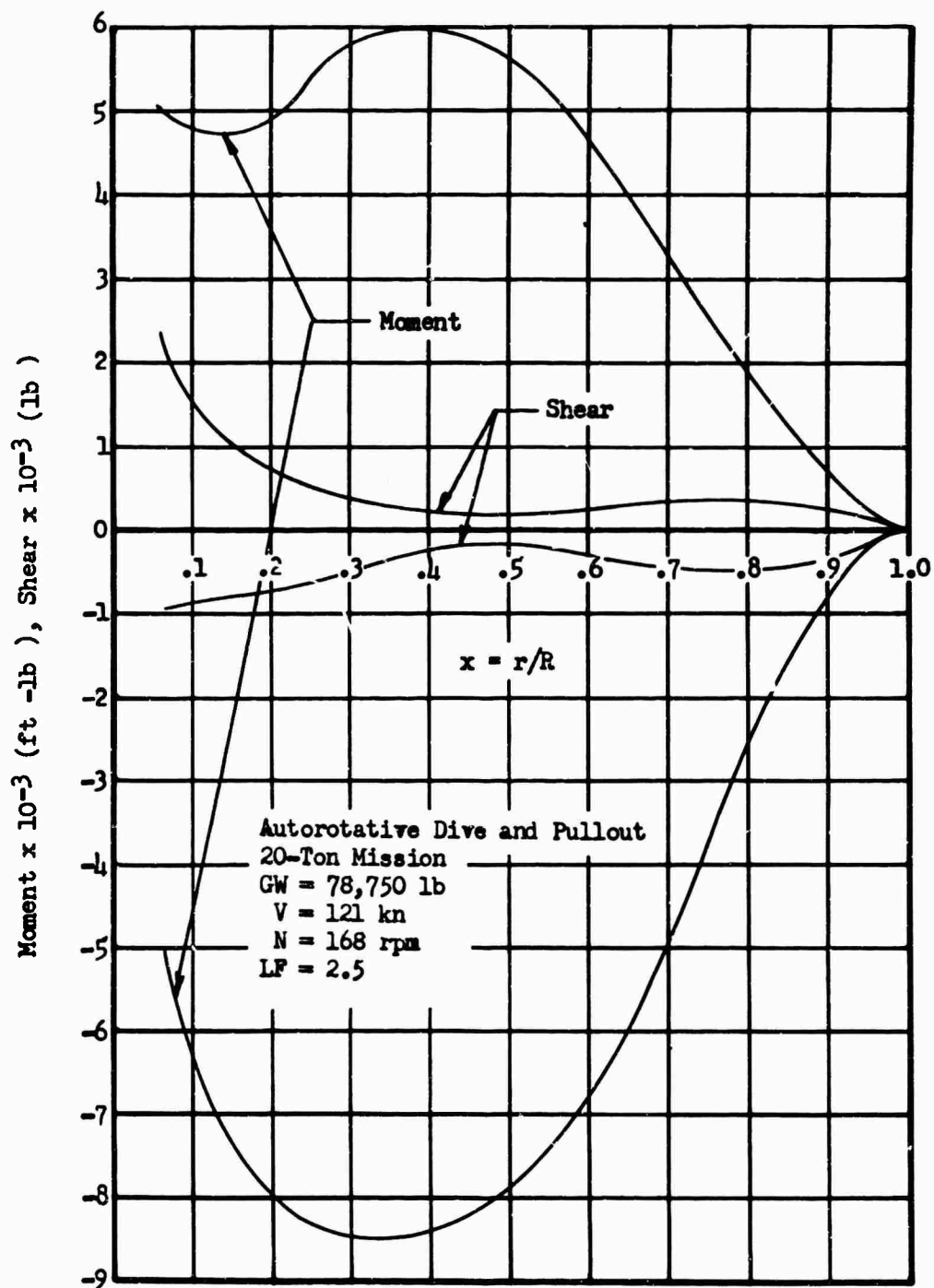


Figure 165 Edgewise Shear and Moment Envelope, Condition 5a

TABLE XXXXVII
COMPRESSIBILITY INCREMENT,
CONDITION 5a

CONCLUSION 34												
r_k	x_k	MN_k	V_k	q_k	α_k	C_{lk}	MN_{Cr}	$\left(\frac{MN_k}{MN_{Cr}} - 1\right)^{\frac{1}{2}}$	W_k	$r_k + 1 - r_k S_k$	M_k	
ft			ft/sec	lb/ft ²	degree				lb/in	in	lb	in-lb
26.4	.58	.600	669	533	7.05	.705	.430	.629	7.57	13.2	102	51,710
27.5	.60	.616	688	563	6.63	.663	.445	.620	7.88	55.2	497	49,997
32.1	.70	.689	769	704	5.25	.525	.490	.637	10.13	54.0	602	40,753
36.6	.80	.760	848	856	4.10	.410	.545	.628	12.1	55.2	727	29,555
41.2	.90	.832	929	1027	2.84	.284	.605	.612	14.20	38.4	581	16,033
44.4	.97	.883	985	1156	2.15	.215	.640	.616	16.08	16.2	281	5,227
45.8	1.00	.905	1010	1214	1.89	.189	.645	.635	17.41			

$$W_k = .02259 \left(\frac{MN_k}{MN_{cr}} - 1 \right)^{\frac{1}{2}} q$$

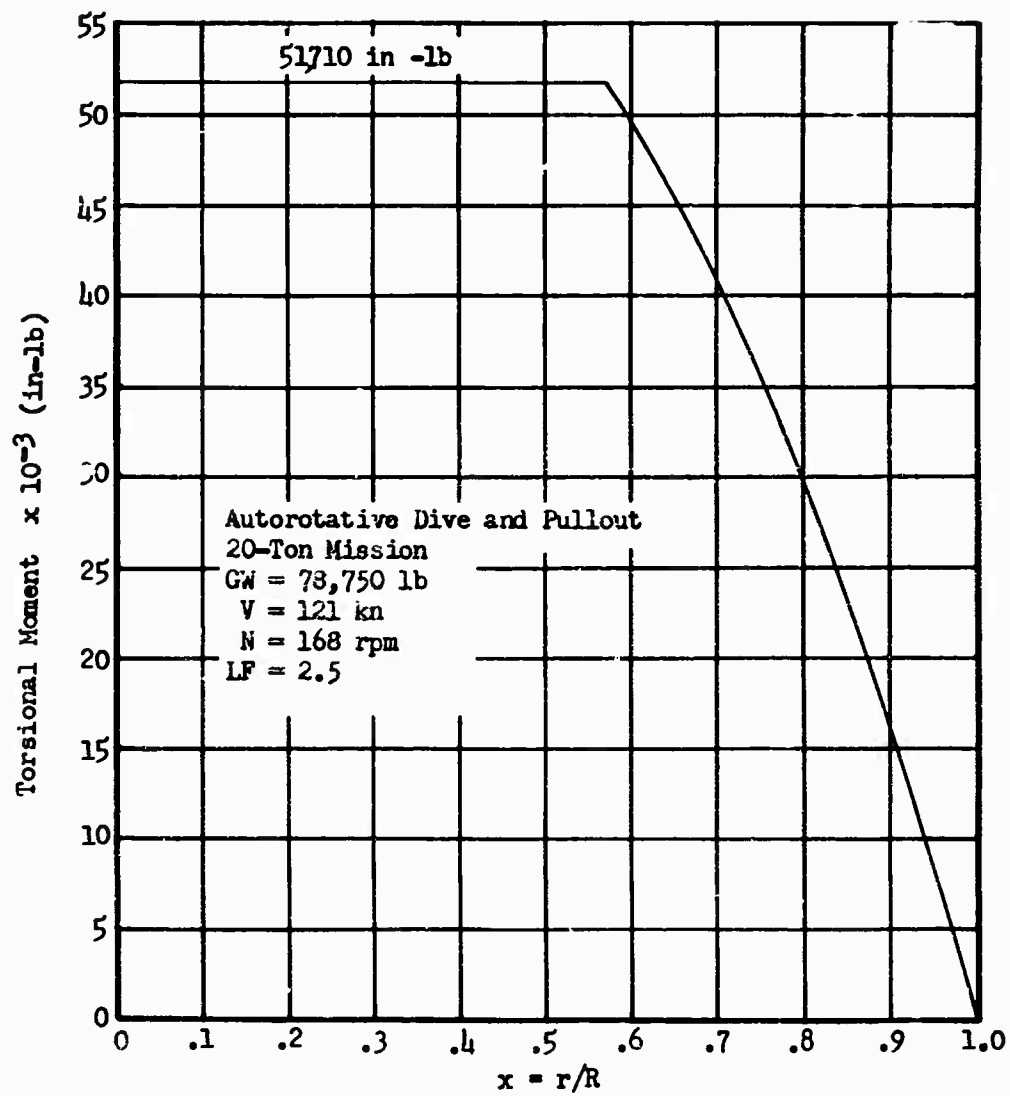


Figure 166 Compressibility Increment, Condition 5a

TABLE XXXXVIII
CONDITION 5b, AUTOROTATIVE DIVE AND PULLOUT,
12-TON MISSION,
BASIC DESIGN PARAMETERS

Parameter	Symbol	Value
True Airspeed	V	159 kn
Rotor rpm	N	168 rpm
Angular Velocity	Ω	17.59 rad/sec
Linear Tip Velocity	ΩR	806 ft/sec
Load Factor	LF	2.5
Gross Weight	GW	65,800 lb
Thrust *	T	164,500 lb
Lift Curve Slope	a	7.35
Tip Speed Ratio	μ	0.333
Blade Pitch Angle at Hub	θ_0	0.1920 rad
Twist Angle	θ_1	-0.1396 rad
Inflow Factor	λ	0.0205
Coning Coefficient	a_0	0.2008 rad
Flapping Coefficients		
cos ψ component	a_1	0.1162 rad
sin ψ component	b_1	0.0889 rad
cos 2 ψ component	a_2	0.0158 rad
sin 2 ψ component	b_2	-0.0081 rad

* Considered momentary for load factors other than unity.

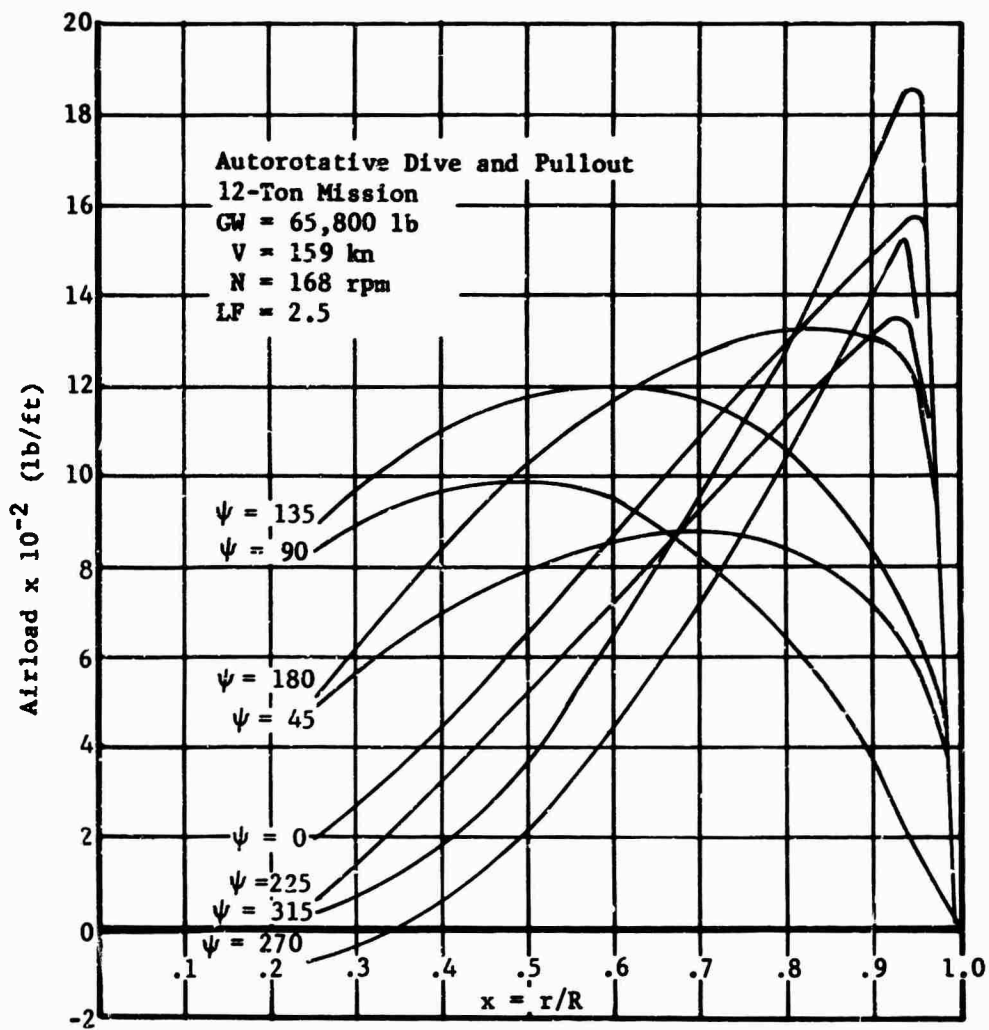


Figure 167 Flapwise Airload Distribution, Condition 5b

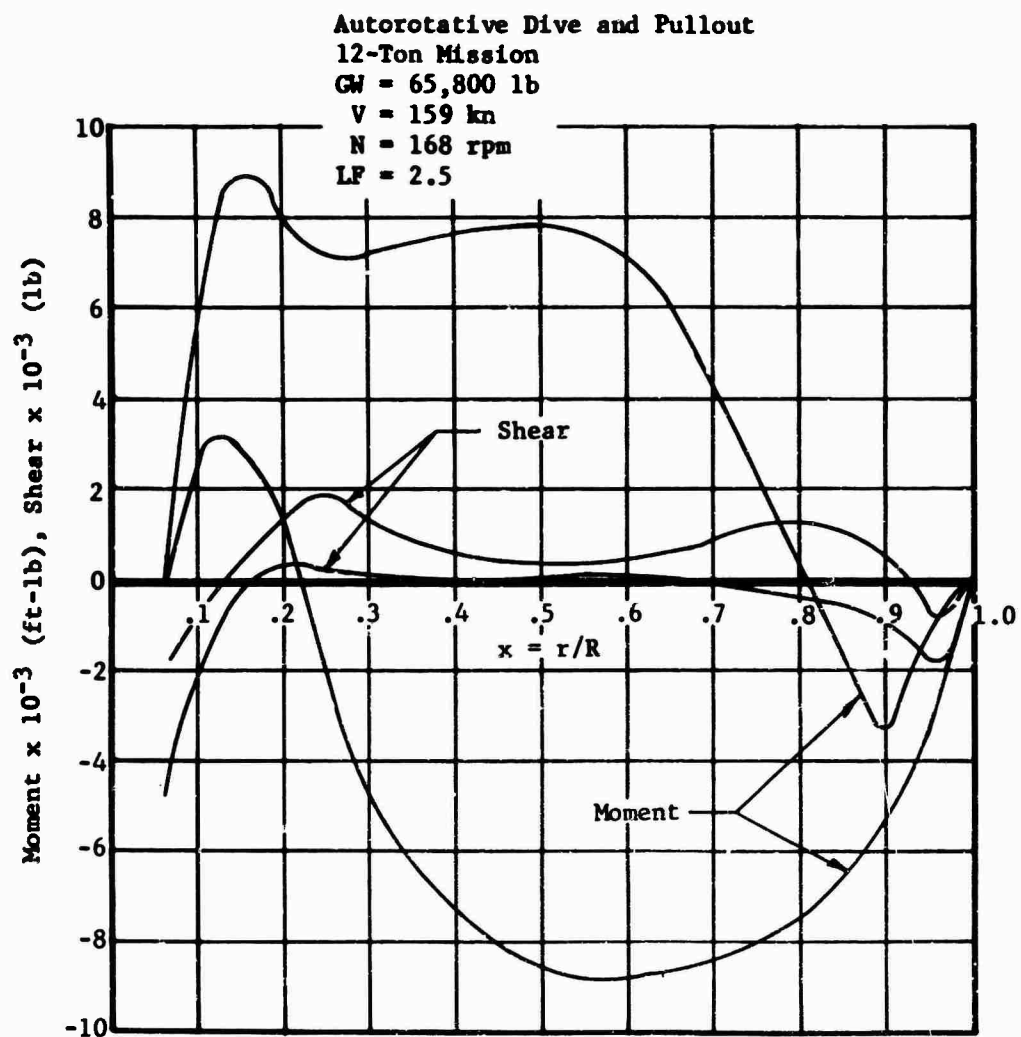


Figure 168 Flapwise Shear and Moment Envelope, Condition 5b

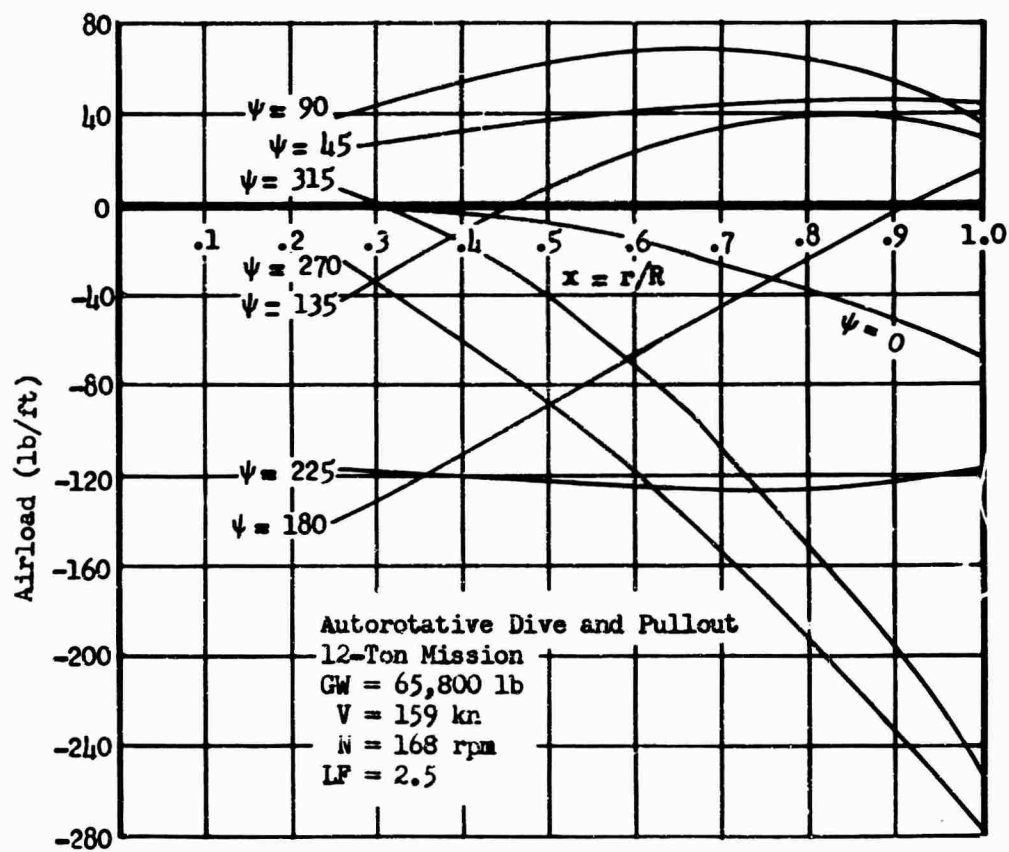


Figure 169 Edgewise Airload Distribution, Condition 5b

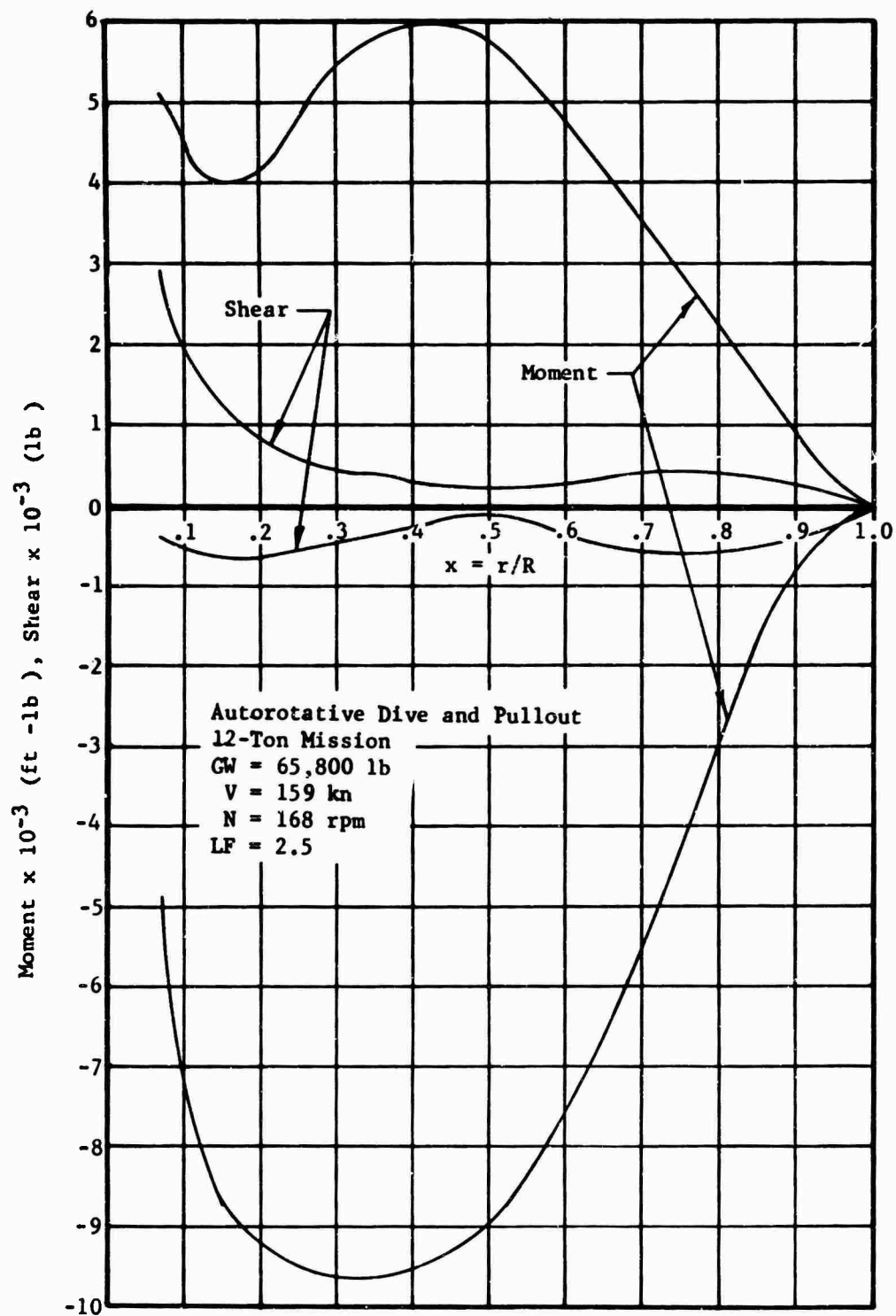


Figure 170 Edgewise Shear and Moment Envelope, Condition 5b

TABLE XLIX
CONDITION 5c, AUTOROTATIVE DIVE AND PULLOUT,
FERRY MISSION,
BASIC DESIGN PARAMETERS

Parameter	Symbol	Value
True Airspeed	V	145 kn
Rotor rpm	N	168 rpm
Angular Velocity	Ω	17.59 rad/sec
Linear Tip Velocity	ΩR	806 ft/sec
Load Factor	LF	2.5
Gross Weight	GW	72,000 lb
Thrust *	T	180,000 lb
Lift Curve Slope	a	7.35
Tip Speed Ratio	μ	0.304
Blade Pitch Angle at Hub	θ_0	0.1830 rad
Twist Angle	θ_1	-0.1396 rad
Inflow Factor	λ	0.0178
Coning Coefficient	a_0	0.1748 rad
Flapping Coefficients		
cos ψ component	a_1	0.0934 rad
sin ψ component	b_1	0.0708 rad
cos 2 ψ component	a_2	0.0115 rad
sin 2 ψ component	b_2	-0.0059 rad

* Considered momentary for load factors other than unity.

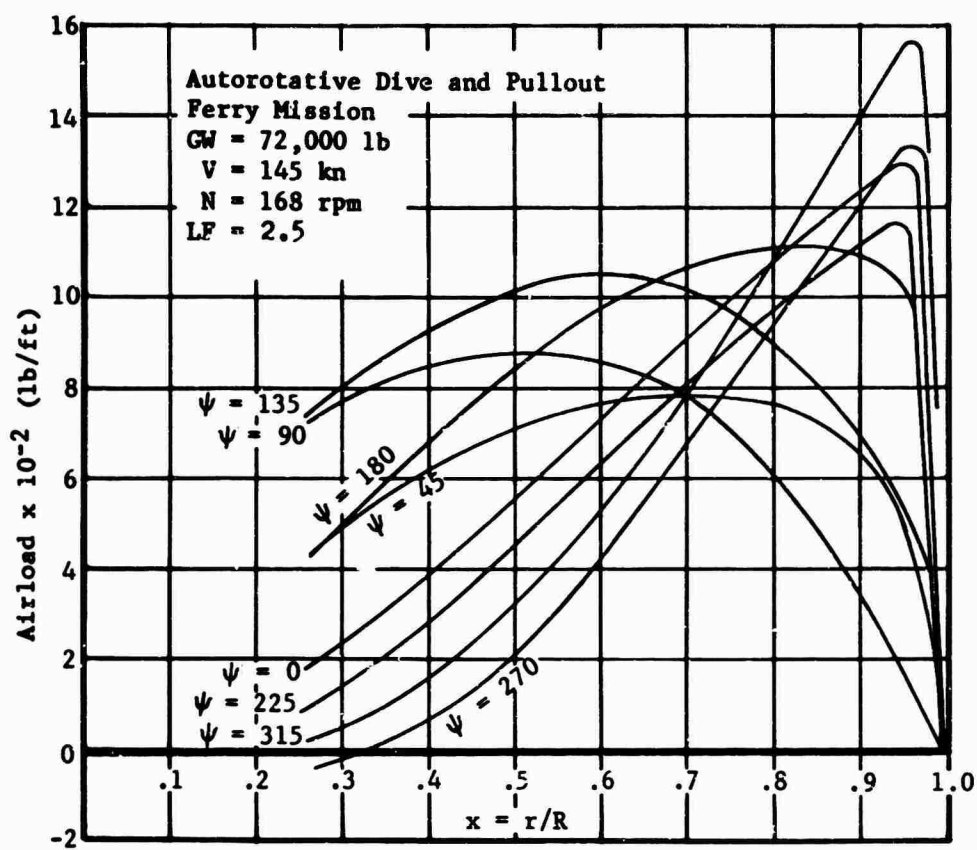


Figure 171 Flapwise Airload Distribution, Condition 5c

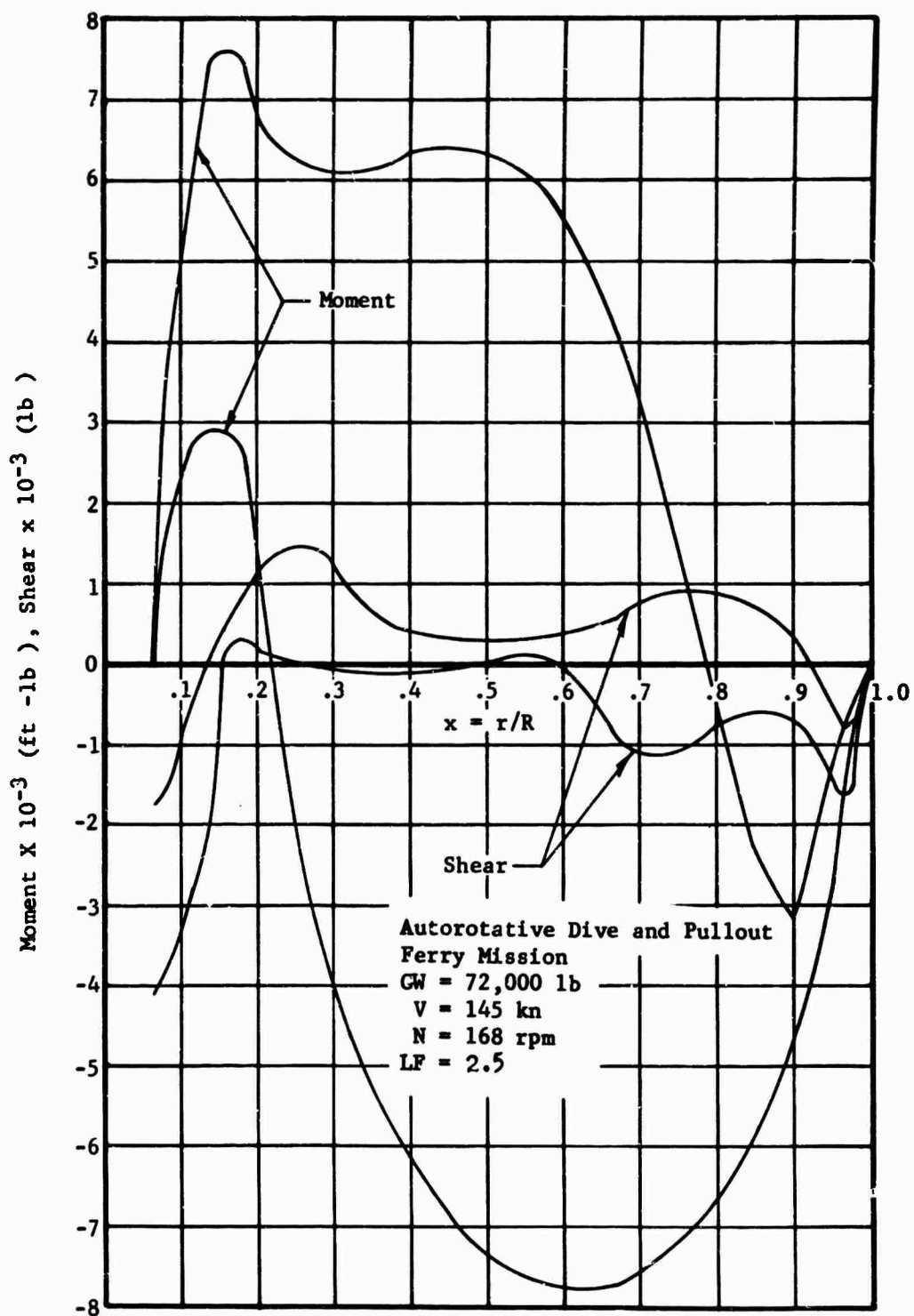


Figure 172 Flapwise Shear and Moment Envelope, Condition 5c

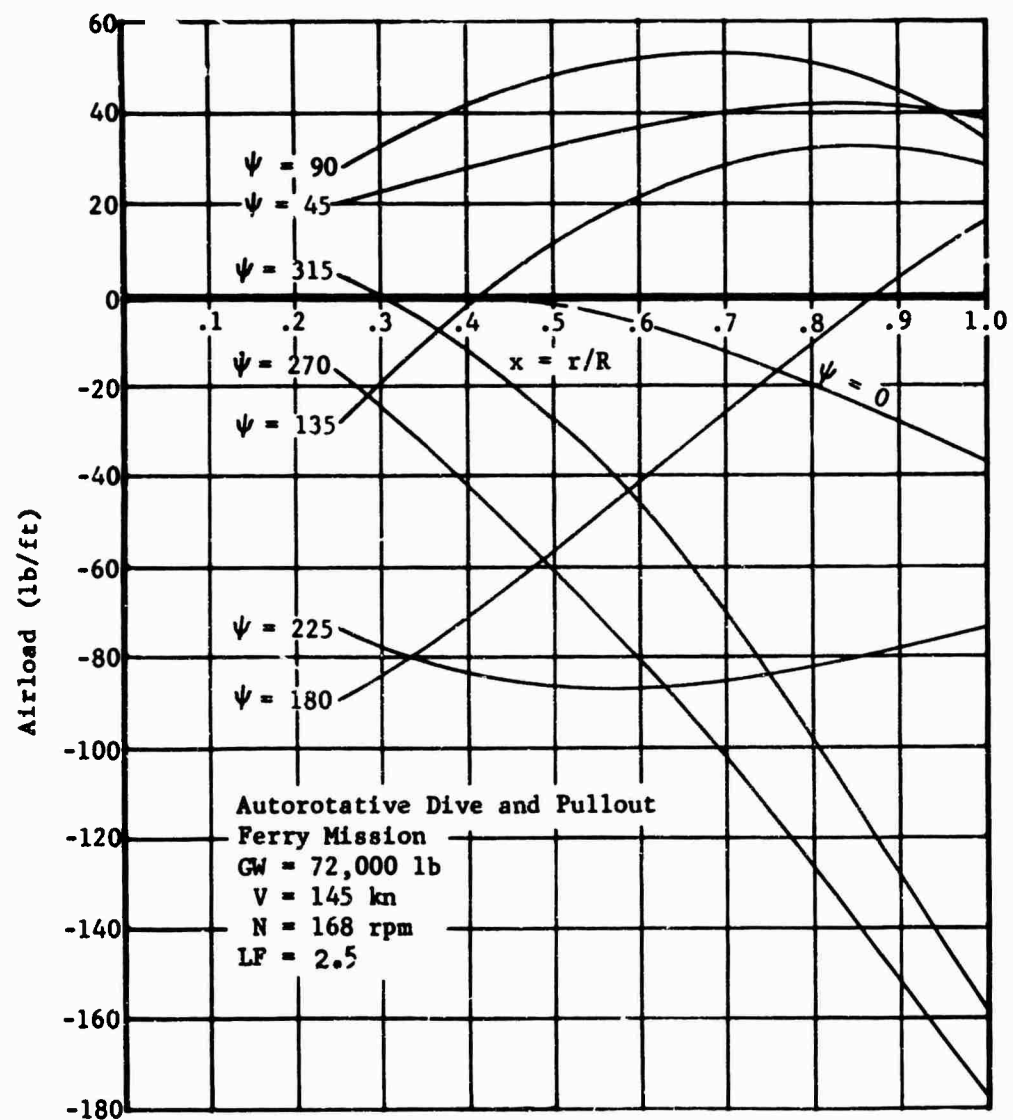


Figure 173 Edgewise Airload Distribution, Condition 5c

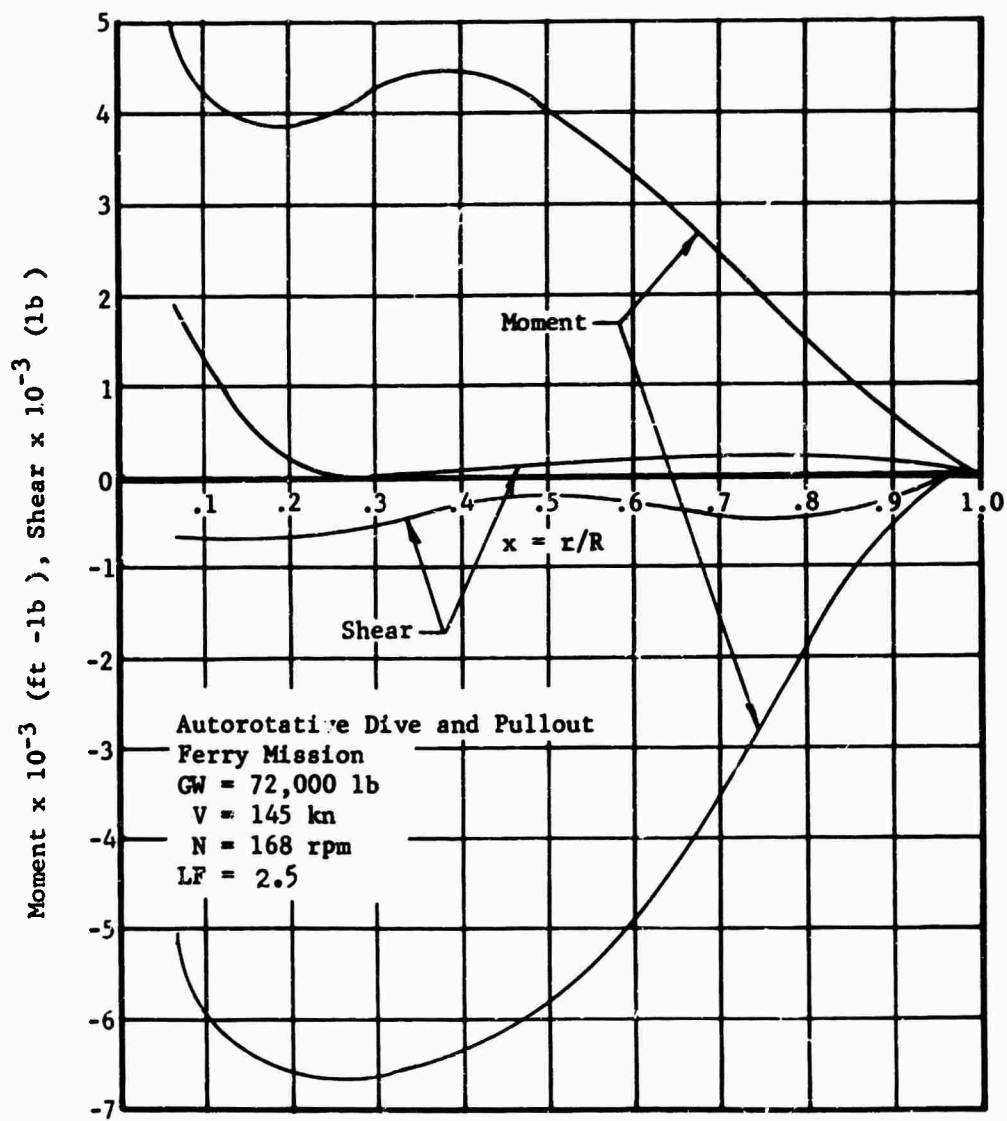


Figure 174 Edgewise Shear and Moment Envelope, Condition 5c

Condition 6 - 4g Weight Moment: Ground Handling

This condition contains the calculation of the static shear, moment, and deflection due to blade weight. A 4g moment curve was calculated to cover maximum vertical forces occurring in any ground handling operations with the rotor stopped.

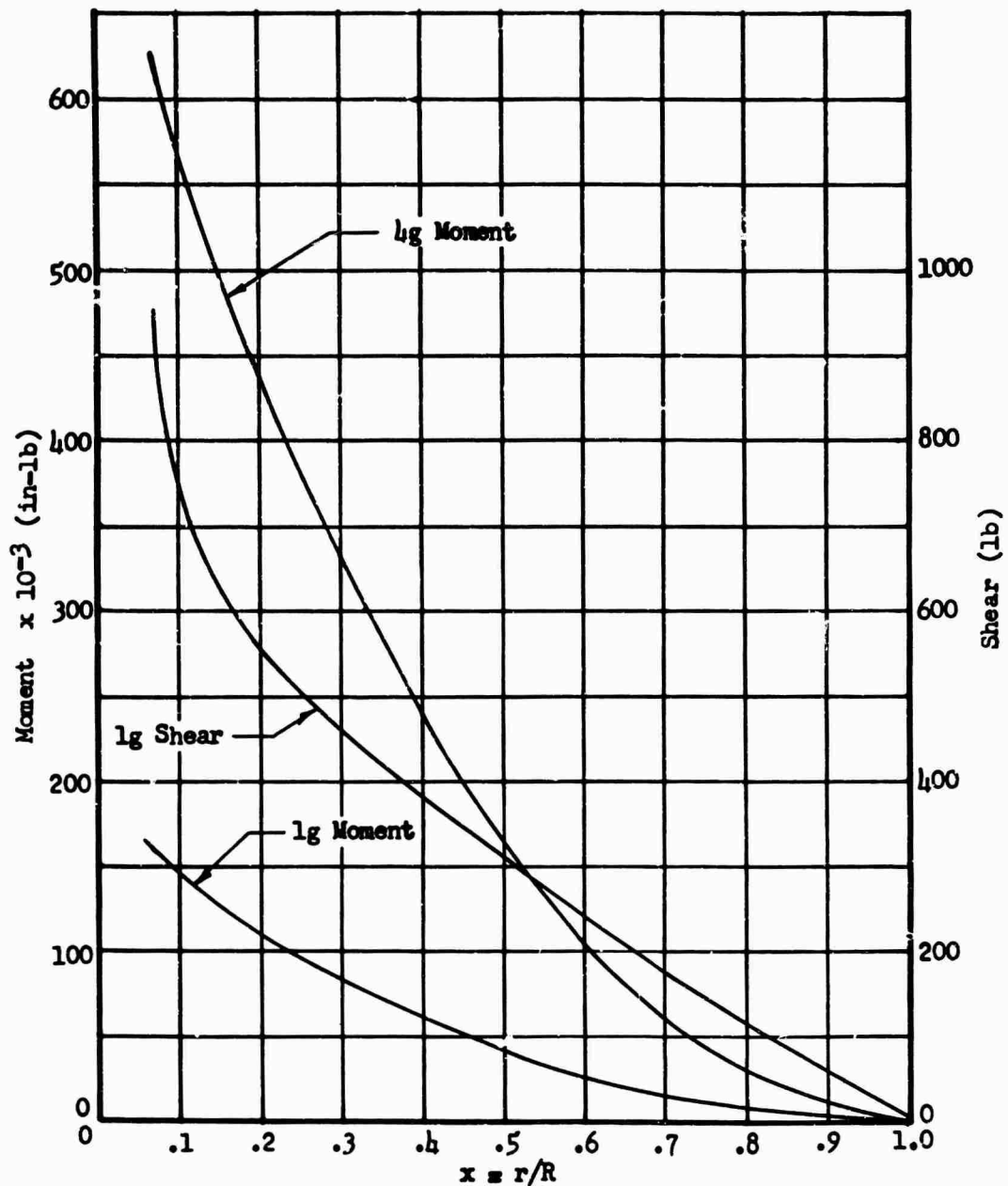


Figure 175 Shear and Bending Moment Due to Weight, Condition 6

ROTOR BLADE STRUCTURAL ANALYSIS

In this section, the structural integrity of the main rotor blade and cuff is substantiated.

A comparison of rotor blade loads shows that the 20-ton mission generates highest static blade stresses; the highest bending stresses occur along the outboard 75 percent of the blade during the symmetrical dive and pullout maneuver, and the highest centrifugal stresses occur along the inboard 25 percent of the blade during the autorotative dive and pullout maneuver.

An analysis of the fatigue stresses generated on the spar for the flight spectrum is also presented to substantiate the replacement life of the spar.

The blade and cuff are analyzed for the shear and moment envelopes developed from Condition 1 through Condition 6. These envelopes are determined by surveying all azimuth positions to determine the maximum shear and bending moments which occur at each radial blade section. The azimuth at which the maximum shear for a given blade station occurs is never the azimuth where maximum bending occurs; and since maximum edgewise and flapwise loadings rarely occur simultaneously at one given azimuth, this method of load combining is very conservative.

The forces to be considered may be categorized as aerodynamic, dynamic, and gravitational. The aerodynamic forces consist of lift

$$\frac{\Delta L}{\Delta r} = \frac{1}{2} \rho C \left[(C_{l0} + C_{l\alpha}) V_T^2 + U_P U_T \right] \quad (45)$$

and drag

$$\frac{\Delta D}{\Delta r} = \frac{1}{2} \rho C \left[(C_{d0} + C_{d\alpha}) U_T^2 \right] \quad (46)$$

The dynamic forces are centrifugal tension,

$$F_c = \int_0^R M \Omega^2 r \, dr \quad (47)$$

inertia,

$$F_{in} = \int_0^R M(r - e') \ddot{\beta} \, dr \quad (48)$$

and Coriolis forces

$$F_{Cor} = -2 \int_e^R \beta \dot{\beta} \frac{w}{g} (r - c') dr; \quad (49)$$

and the gravitational force is expressed as

$$\text{Weight} = \int_e^R w dr \quad (50)$$

Sign Convention

The sign convention for blade motion, shown in Figure 176, will be used throughout the blade discussion. It is a standard method of notation used in all Sikorsky Aircraft blade analysis reports.

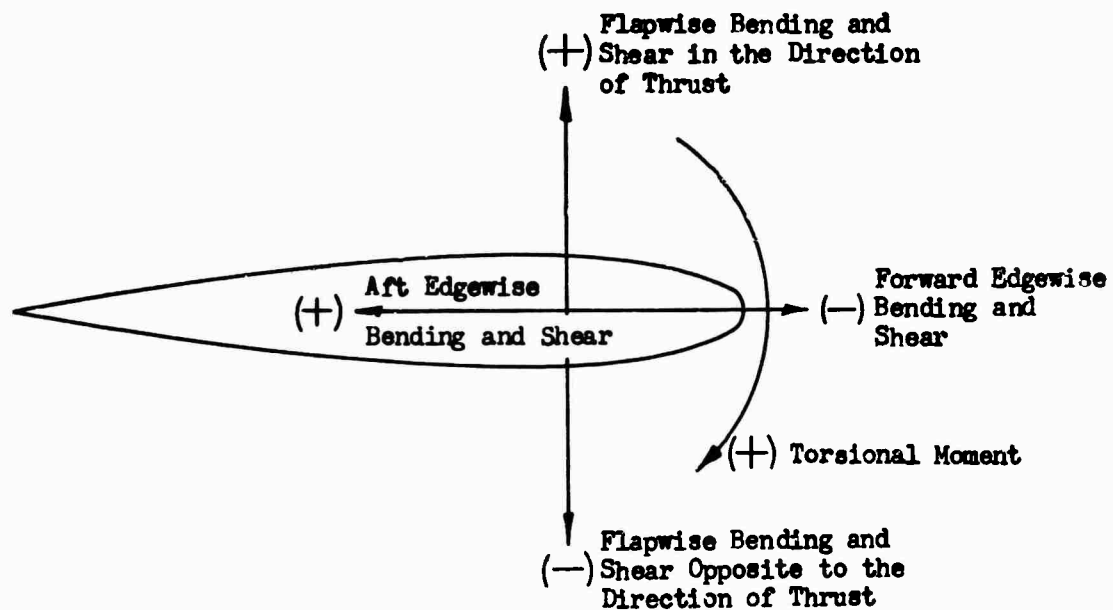


Figure 176 Sign Convention for Blade Motion

Analysis of Cuff-to-Sleeve Attachment

The analysis of the cuff-sleeve joint presented here assumes that the joint is sufficiently rigid to prevent any significant deflections of the cuff flange or the hinge at attachment. If the deflections remain small, the bolts will be loaded in tension and shear only. For large deflections, bending deflections in the bolts cause changes in the distribution of bolt loads. The inboard portion of the cuff, as designed, possesses sufficient rigidity to make the bolt analysis valid.

To determine the loading on the bolts resulting from the applied loads on the joint, an equivalent moment of inertia must be found for the entire joint. Figure 177 is a sketch of the section showing the cuff flange bolt pattern and the equivalent flange areas used in the derivation of the equivalent moments of inertia. The method of calculation of the bolt loads is as follows:

1. Locate a neutral axis so that the area moment of the resisting flange area above the axis will equal the area moment of the bolts below the axis.
2. Locate an equivalent flange area so that its area moment equals that of the bolts.
3. Determine the moment of inertia of the total equivalent system about the neutral axis.
4. Determine the stress in the bolts according to the relation

$$f = \frac{M c}{I_{eq}} \quad (51)$$

where

$$\begin{aligned} f &= \text{unit stress, lb/in}^2 \\ M &= \text{bending moment, in-lb} \\ c &= \text{distance from neutral axis to bolt, in} \\ I_{eq} &= \text{moment of inertia of the equivalent system, in}^4 \end{aligned}$$

The loads and moments used in the analysis were taken from condition 5a. Preliminary investigations showed that the high centrifugal loading of this maneuver produces the largest combination of stresses on this joint.

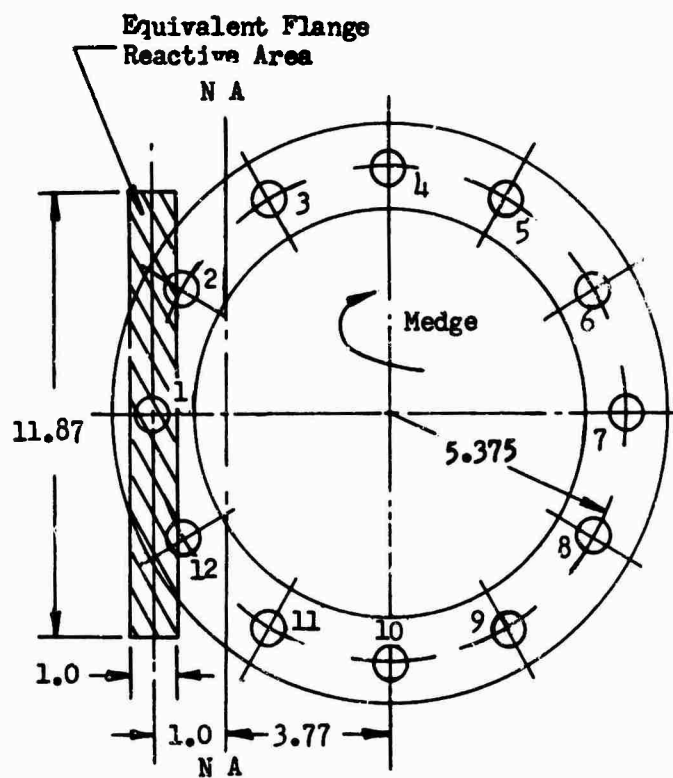
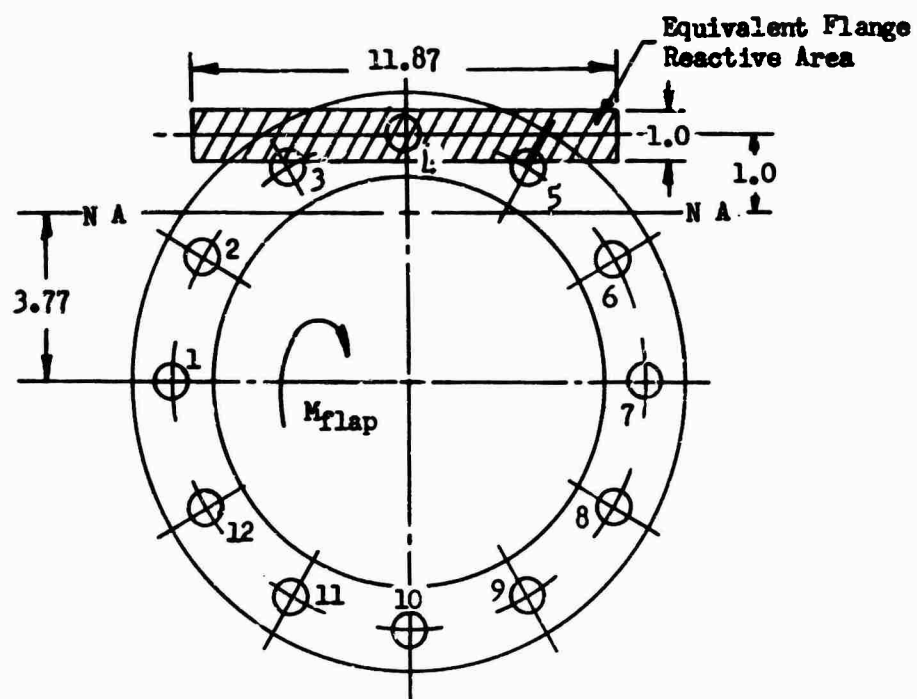


Figure 177 Equivalent Cuff Area Resisting Bending

Neutral Axis Determination

By iteration, the neutral axis is found to be 3.77 inches from the axis of symmetry of the flange (see Figure 177).

Determination of I_{eq}

$$\begin{aligned}\text{Bolt Area} &= .3068 \text{ in}^2; d = 0.625 \text{ in}; 9 \text{ bolts} \\ \text{Minor Dia} &= .5568 \text{ in}; \text{Minor Dia Area} = .2435 \text{ in}^2 \\ M_A \text{ bolt} &= 11.87 \text{ in}^3; 9 \text{ bolts}\end{aligned}$$

For simplicity of calculations, let the equivalent flange area be a rectangle 11.87 inches x 1.0 inch, centered 1.00 inch from the neutral axis.

$$\text{Then } M_A \text{ flange} = 11.87 \text{ in}^3$$

Calculate the moment of inertia of the bolts and flange about the neutral axis (I_{eq}).

$$I_{eq} = I_{NA} + Ar^2 \quad (52)$$

Bolts:

$$\begin{aligned}I_{eq \text{ bolts}} &= \frac{9\pi(.5568)^4}{64} + (2)(.2435) \left[(1.0825)^2 + (3.77)^2 \right. \\ &\quad \left. + (6.458)^2 + (8.425)^2 \right] + (.2435)(9.145)^2\end{aligned}$$

$$I_{eq \text{ bolts}} = .137 + 63.124 + 20.36 = 83.62 \text{ in}^4$$

$$\begin{aligned}I_{eq \text{ flange}} &= \frac{1}{12} 11.87(1)^3 + 11.87(1)(1)^2 \\ &= 9892 + 11.87 = 12.859 \text{ in}^4\end{aligned}$$

$$I_{eq} = I_{eq(\text{bolts})} + I_{eq(\text{flange})} = 83.62 + 12.859 = 96.48 \text{ in}^4$$

Loads and Moments @ $r = 68 \text{ in}$, $X = .124$

- a) Centrifugal Force $F_C = 142,418 \text{ lb}$ (Figure 178)
- b) Flapwise Bending Moment $M_{\text{flap}} = +108,000 \text{ in-lb}$
- c) Edgewise Bending Moment $M_{\text{edge}} = -82,300 \text{ in-lb}$
- d) Torsional Moment $M_T = 51,710 \text{ in-lb}$

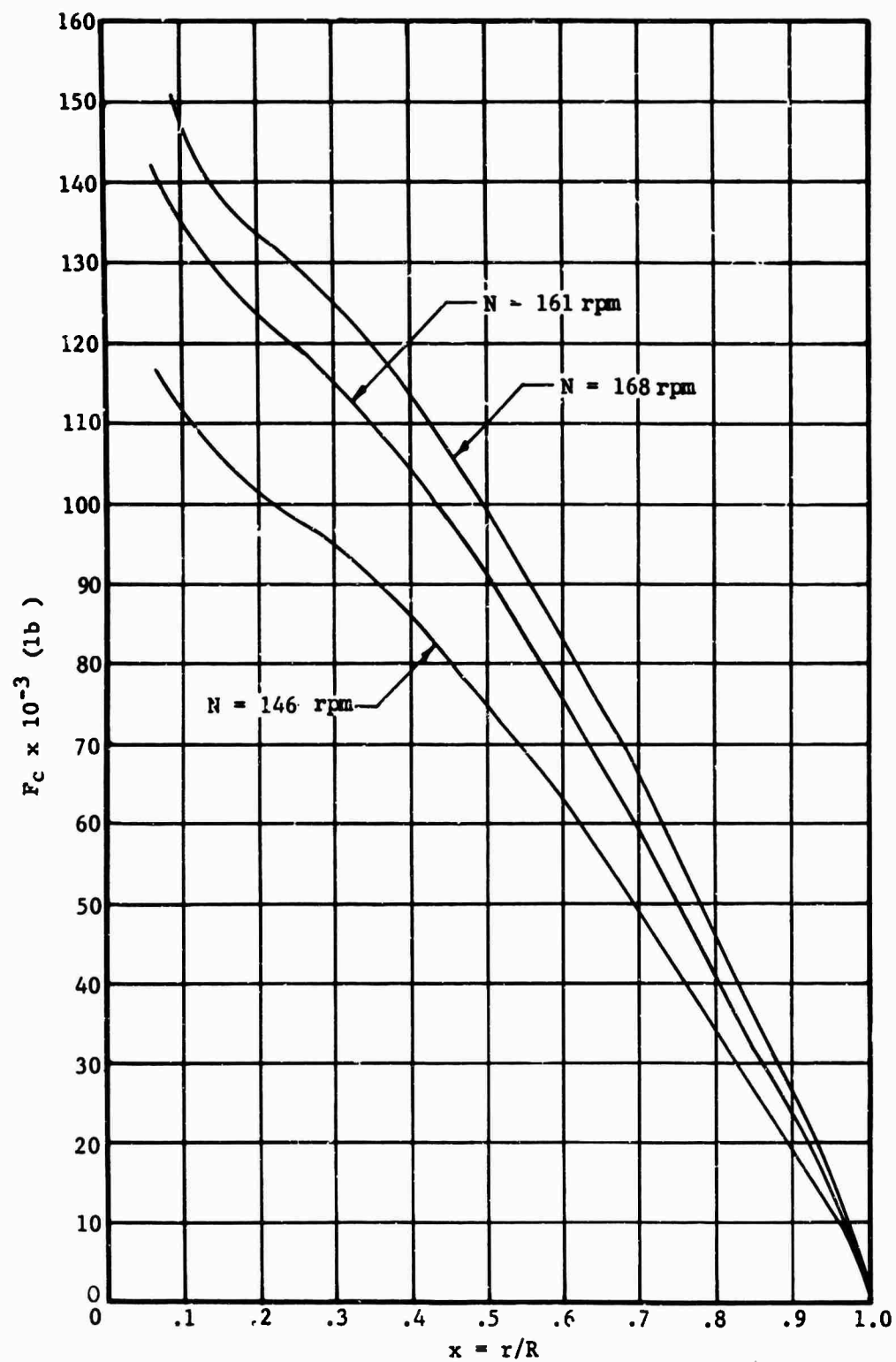


Figure 178 Centrifugal Tension

- e) Flapwise Shear $S_{flap} = -2,400 \text{ lb}$
 f) Edgewise Shear $S_{edge} = 1,300 \text{ lb}$

Calculations of Loads and Stresses

a) Centrifugal Tension

$$F_c = \frac{142,418}{12} = 11,868 \text{ lb/bolt}$$

$$f_c = \frac{11,868}{.2435} = 48,739 \text{ lb/in}^2$$

b) Flapwise Bending Moment

$$f_{flap} = \frac{108,000 \times (c)}{96.48} = 1120 \text{ (c) lb/in}^2$$

Bolt No.	1120 x (c)	=	Stress - lb/in ²
1	(1120)(3.77)	=	4,222
2	(1120)(1.0825)	=	1,212
6	(1120)(1.0825)	=	1,212
7	(1120)(3.77)	=	4,222
8	(1120)(6.4575)	=	7,232
9	(1120)(8.4249)	=	9,436
10	(1120)(9.145)	=	10,242
11	(1120)(8.4249)	=	9,436
12	(1120)(6.4575)	=	7,232

c) Edgewise Bending Moment

$$f_{edge} = \frac{82,800 \text{ (c)}}{96.48} = 858 \text{ (c) lb/in}^2$$

Bolt No.	858 x (c)	=	Stress - lb/in ²
3	(858)(1.0825)	=	929
4	(858)(3.77)	=	3,235
5	(858)(6.4575)	=	5,541
6	(858)(8.4249)	=	7,228
7	(858)(9.145)	=	7,846
8	(858)(8.4249)	=	7,228
9	(858)(6.4575)	=	5,541
10	(858)(3.77)	=	3,235
11	(858)(1.0825)	=	929

d) Torsion

$$\text{Load on Each Bolt} = \frac{51,710}{12 (5.375)} = 802 \text{ lb}$$

$$f_t = \frac{4}{3} \left(\frac{V}{A} \right) = \frac{4(802)}{3(.3068)} = 3384 \text{ lb/in}^2$$

e) and f) Flapwise and Edgewise Shear (Figure 179)

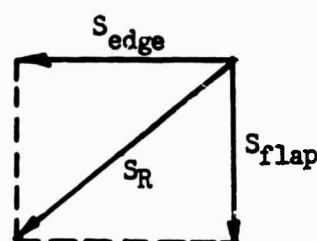


Figure 179 Flapwise and Edgewise Shear Vector

$$S_R = \sqrt{S_{\text{flap}}^2 + S_{\text{edge}}^2} \quad (53)$$

$$S_R = \sqrt{(2400)^2 + (1300)^2} = 2729 \text{ lb}$$

$$S_R(\text{per bolt}) = \frac{2729}{12} = 227 \text{ lb/bolt}$$

$$f_s = \frac{227}{.3068} = 740 \text{ lb/in}^2$$

Combined Tensile Stress on Bolts, lb/in²

Bolt No.	f_c	+	f_{flap}	+	f_{edge}	=	$f_{\text{total lb/in}^2}$
1	48,739	+	4,222	+	0	=	52,961
2	48,739	+	1,212	+	0	=	49,951
3	48,739	+	0	+	929	=	49,668
4	48,739	+	0	+	3,235	=	51,974
5	48,739	+	0	+	5,541	=	54,280
6	48,739	+	1,212	+	7,228	=	57,179
7	48,739	+	4,222	+	7,846	=	60,807

Bolt No.	f_c	$+ f_{flap}$	$+ f_{edge}$	=	$f_{total} \text{ lb/in}^2$
8	48,739	+ 7,232	+ 7,228	=	63,199
9	48,739	+ 9,436	+ 5,541	=	63,716
10	48,739	+ 10,242	+ 3,235	=	62,216
11	48,739	+ 9,436	+ 929	=	59,104
12	48,739	+ 7,232	+ 0	=	55,971

Maximum loaded bolt is number 9, $f = 63,716 \text{ lb/in}^2$

Additional Stress on Bolts Due to Preload

Bolt Dia = .625 in $E_{bolt} = 30 \times 10^6 \text{ lb/in}^2$

Bolt Area = .3068 in^2 $E_{flange} = 16 \times 10^6 \text{ lb/in}^2$

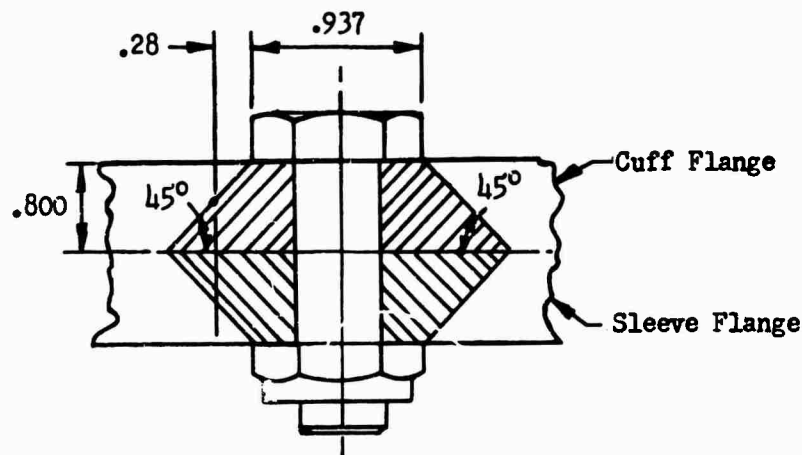


Figure 180 Bolt Loading Distribution

The stress distribution in the flange is assumed to be triangular.
See Figure 180. The average flange area under the bolt is

$$A = \frac{\pi}{4} \left[.937 + .565 \right]^2 - .3068$$

$$A = 2.3868 - .3068 = 2.08 \text{ in}^2$$

$$\text{Preload} = 15,520 \text{ lb}$$

$$\text{Maximum load on bolt number 9} = 63,716 (.3068) = 19,548 \text{ lb} = Q$$

$$\text{Therefore, the total tensile load} = P + Q \left[1 - \frac{1}{\frac{(AE)_b}{(AE)_F} + 1} \right] \quad (54)$$

$$\frac{(AE)_{\text{bolt}}}{(AE)_{\text{flange}}} = \frac{.3068 (30 \times 10^6)}{2.08 (16 \times 10^6)} = .276$$

$$\text{Total Tensile Load} = 15,520 + 19,548 \left[1 - \frac{1}{1.276} \right] = 19,742 \text{ lb}$$

$$\text{Maximum Tensile Stress} = \frac{19,742}{.3068} = 64,350 \text{ lb/in}^2$$

Maximum Shear on any bolt:

$$f_s(\text{tot}) = f_t + f_s = 740 + 3384 = 4124 \text{ lb/in}^2$$

Margin of Safety

$$R_1 = \frac{64,350 (1.5)}{180,000} = .536$$

$$R_2 = \frac{4124 (1.5)}{109,000} = .057$$

$$M_S = \frac{2}{(.536) + \sqrt{(.536)^2 + 4(.057)^2}} - 1 = .85$$

Ground Conditions - 4g Moment and Load

$$M_{\text{flap}} = 529,884 \text{ in-lb (Reference Figure 175)}$$

Stress on maximum loaded bolt number 4

$$f_{\text{flap}} = \frac{529,884 (9.145)}{96.48} = 50,226 \text{ lb/in}^2$$

Preload (P = 15,520 lb):

$$\text{Load on bolt number 4} = 50,226 (.3068) = 15,409 \text{ lb}$$

$$\text{Total Tensile Load} = 15,520 + 15,409 \left[1 - \frac{1}{1.276} \right] = 18,853 \text{ lb}$$

$$\text{Maximum Tensile Stress} = \frac{18,853}{.3068} = 61,451 \text{ lb/in}^2$$

$$MS = \frac{180,000}{61,451 \times 1.5} - 1 = .95$$

Structural Analysis of Cuff-Spar Attachment Region

The cuff-spar joint is one of the most highly loaded sections of the blade. Static loads and moments reach a maximum in the attachment region and stress concentration factors associated with the fastener holes create peak stresses at the bolt holes rather than the extreme fibers of the cuff and spar.

Structural fastening of the cuff and spar is accomplished with eighteen 1/2-inch-diameter bolts. The three outboard rows use through bolts, while the three inboard rows use shorter bolts, each loaded in single shear. See Figure 181.

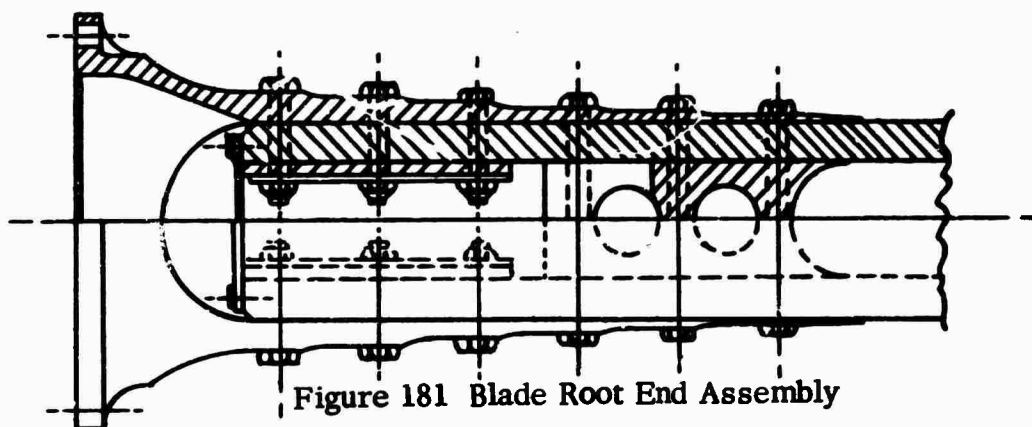


Figure 181 Blade Root End Assembly

The bolts are assumed to transfer the loads from the spar to the cuff by shear; bearing between cuff and spar, as well as friction between mating surfaces, is conservatively neglected.

Two cross sections will be analyzed: one through the inboard bolt holes where the entire load has been transferred to the cuff, and a second through the outboard bolt holes where the spar absorbs all the loading.

The most severe loads on this portion of the blade are generated in Condition 5a, "Autorotative Dive and Pullout".

Design Data - Allowable Stresses:

Aluminum Alloy (6061-T6)

$$F_{tu} = 38,000 \text{ lb/in}^2$$

$$F_{su} = 24,000 \text{ lb/in}^2$$

$$F_{bry} = 56,000 \text{ lb/in}^2$$

Titanium Alloy (6AL-4V)

$$F_{tu} = 130,000 \text{ lb/in}^2$$

$$F_{su} = 80,000 \text{ lb/in}^2$$

$$F_{bru} = 248,000 \text{ lb/in}^2$$

NAS Steel Bolts

$$F_{tu} = 160,000 \text{ lb/in}^2$$

$$F_{bru} = 300,000 \text{ lb/in}^2$$

Analysis of Cuff-Spar Joint

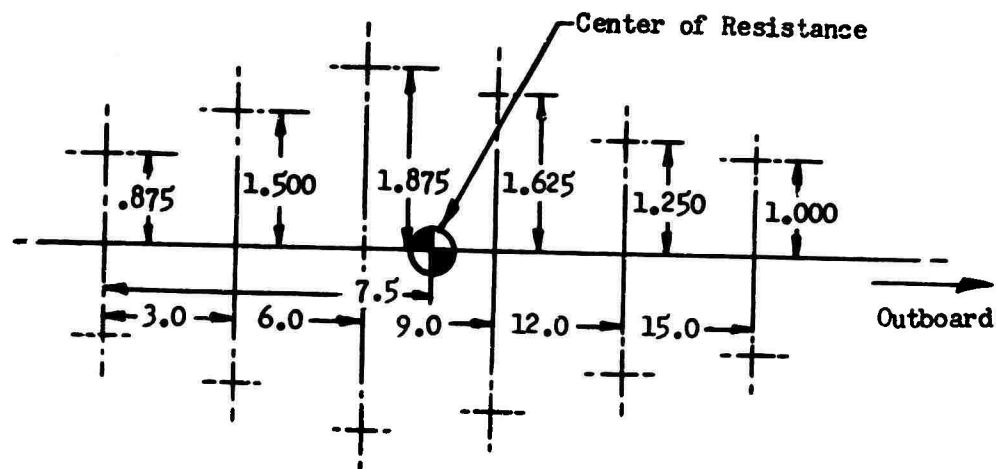


Figure 182 Cuff-to-Spar Attachment Bolt Pattern

$$\text{Center of Resistance} = \frac{3 + 6 + 9 + 12 + 15}{6} = 7.5 \text{ in (See Figure 182)}$$

$$\Sigma X^2 = 4(157.5) = 630 \text{ in}^2, \quad \Sigma Y^2 = 4(11.7343) = 46.9372 \text{ in}^2 \quad (55)$$

$$I_p = (\Sigma X^2 + \Sigma Y^2) = 676.937 \text{ in}^2$$

Inboard Bolts, See Figure 183.

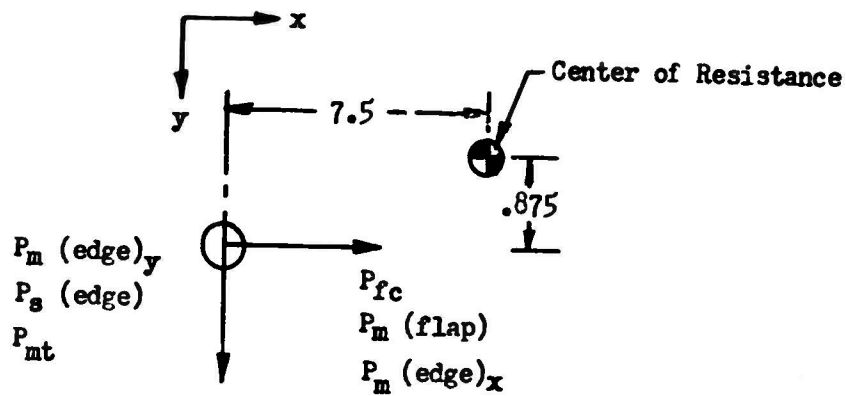


Figure 183 Inboard Bolt Loading

Loads: $r = 74,125$ in $x = .135$

$F_c = 141,000$ lb

$M_{\text{flap}} = 116,400$ in-lb

$M_{\text{edge}} = 84,000$ in-lb

$M_t = 51,710$ in-lb

$S_{\text{edge}} = 1200$ lb

Loads on bolts:

$P_{fc} = \frac{F_c}{24} = \frac{141,000}{24} = 5875$ lb/bolt

$P_{m\text{flap}} = \frac{M_{\text{flap}}}{12 h} = \frac{116,400}{12(5.64)} = 1720$ lb/bolt

$P_{s(\text{edge})} = \frac{S_{\text{edge}}}{24} = \frac{1200}{24} = 50$ lb/bolt

$P_{mt} = \frac{M_t}{12 h} = \frac{51,710}{12(5.64)} = 764$ lb/bolt

$$P_{m(edge)x} = \frac{M_{edge Y}}{I_p} = \frac{84,000 \times .875}{676.937} = 108 \text{ lb}$$

$$P_{m(edge)y} = \frac{M_{edge X}}{I_p} = \frac{84,000 \times 7.5}{676.937} = 931 \text{ lb}$$

$$P_x = F_{fc} + P_{mflap} + P_{m(edge)x} = 5875 + 1720 + 108 = 7703 \text{ lb/bolt}$$

$$P_y = P_{sedge} + P_{mt} + P_{m(edge)y} = 50 + 764 + 931 = 1745 \text{ lb/bolt}$$

$$P = \sqrt{P_x^2 + P_y^2} = \sqrt{(7703)^2 + (1745)^2} = 7898 \text{ lb/bolt} \quad (56)$$

Outboard Bolts, See Figure 189.

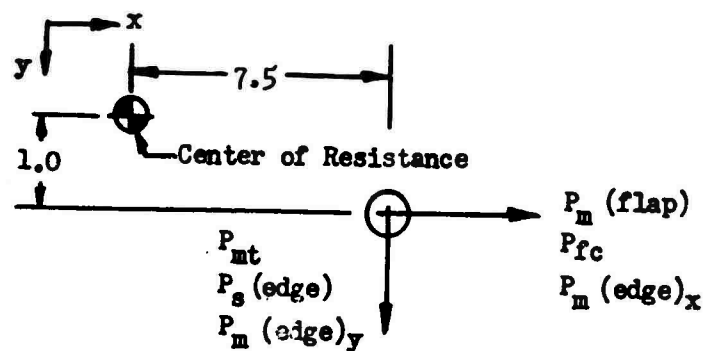


Figure 184 Outboard Bolt Loading

Loads: $r = 89.125 \text{ in}$ $x = .162$

$F_c = 137,000 \text{ lb}$

$M_{flap} = 118,800 \text{ in-lb}$

$M_{edge} = 90,000 \text{ in-lb}$

$M_t = 51,710 \text{ in-lb}$

$S_{edge} = 900 \text{ lb}$

Loads on bolts:

$$P_{fc} = \frac{F_c}{24} = \frac{137,000}{24} = 5708 \text{ lb/bolt}$$

$$P_{m\text{flap}} = \frac{M_{\text{flap}}}{12 h} = \frac{118,800}{12 \times 5.64} = 1755 \text{ lb/bolt}$$

$$P_{\text{sedge}} = \frac{S_{\text{edge}}}{24} = \frac{900}{24} = 38 \text{ lb/bolt}$$

$$P_{mt} = \frac{M_t}{12 h} = 764 \text{ lb/bolt}$$

$$P_{m(\text{edge})x} = \frac{M_{\text{edge } Y}}{I_p} = \frac{90,000 \times 1.0}{676.937} = 133 \text{ lb}$$

$$P_{m(\text{edge})y} = \frac{M_{\text{edge } X}}{I_p} = \frac{90,000 (7.5)}{676.937} = 997 \text{ lb}$$

$$P_x = 5,708 + 1,755 + 133 = 7596 \text{ lb}$$

$$P_y = 38 + 764 + 997 = 1799 \text{ lb}$$

$$P = (7,596)^2 + (1,799)^2 = 7806 \text{ lb}$$

Margin of Safety for Inboard Bolt Analysis

Inboard Bolts in Shear:

$$P = 7898 \text{ lb} \quad P_{all} = 18,650 \text{ lb} \quad (\text{Reference 51})$$

$$MS_{\text{min}} = \frac{18,650}{7898(1.5)} - 1 = .57$$

Cuff in Bearing:

$$P_{br} = 7,898 \text{ lb} \quad f_{br} = \frac{7,898}{.45} = 17,551 \text{ lb/in}^2$$

$$MS = \frac{248,000}{(1.5)(17,551)} - 1 = \text{High}$$

Spar in Bearing:

$$f_{br} = \frac{7898}{.5 (1.125)} = 14,041 \text{ lb/in}^2$$

$$MS = \frac{56,000}{(1.5)(14,041)} - 1 = 1.66$$

Tear-out through End of Spar - Shear:

$$f_s = P/A = \frac{7703}{(1.125) (2) (1.125)} = 3,044 \text{ lb/in}$$

$$MS = \frac{24,000}{1.5 (3,044)} - 1 = \text{High}$$

Margin of Safety for Outboard Bolt Analysis

Outboard Bolts in Bearing:

$$f_{br} = \frac{7806}{.50 (.15)} = 104,080 \text{ lb/in}^2$$

$$f_{bru} = 300,000 \text{ lb/in}^2$$

$$MS = \frac{300,000}{(1.5)(104,080)} - 1 = .92$$

Outboard Bolts in Bending:

$$L = \frac{2 t_{cuff}}{4} + t_{shim} = .075 + .05 = .125 \text{ in}$$

$$M = PL = .125 (7,806) = 976 \text{ in-lb}$$

$$f = M/Z = \frac{976 (.25)}{.00307} = 79,479 \text{ lb/in}^2$$

$$MS = \frac{160,000}{(1.5) 79479} - 1 = .34$$

Spar in Bearing:

$$P = 7806 \text{ lb}, f_{br} = \frac{7806}{(1.125)(.5)} = 13,877 \text{ lb/in}^2$$

$$MS = \frac{56,000}{(1.5)(13,877)} - 1 = 1.69$$

Cuff in Bearing:

$$f_{br} = \frac{7806}{(.15)(.5)} = 104,080 \text{ lb/in}^2$$

$$MS = \frac{248,000}{1.5(104,080)} - 1 = .59$$

Tear-out through End of Cuff - Shear:

$$\text{Load } P = 7596 \text{ lb}$$

$$f_s = P/A = \frac{7596}{2(.2644)} = 14,364 \text{ lb/in}^2$$

$$MS = \frac{80,000}{1.5(14,364)} - 1 = \text{High}$$

Figure 185 shows cross sections of inboard and outboard bolt holes analyzed in the previous pages.

Analysis of Cuff through Inboard Bolt Holes

Cuff Section Properties: $r = 74.125 \text{ in}$ (See Figure 185)

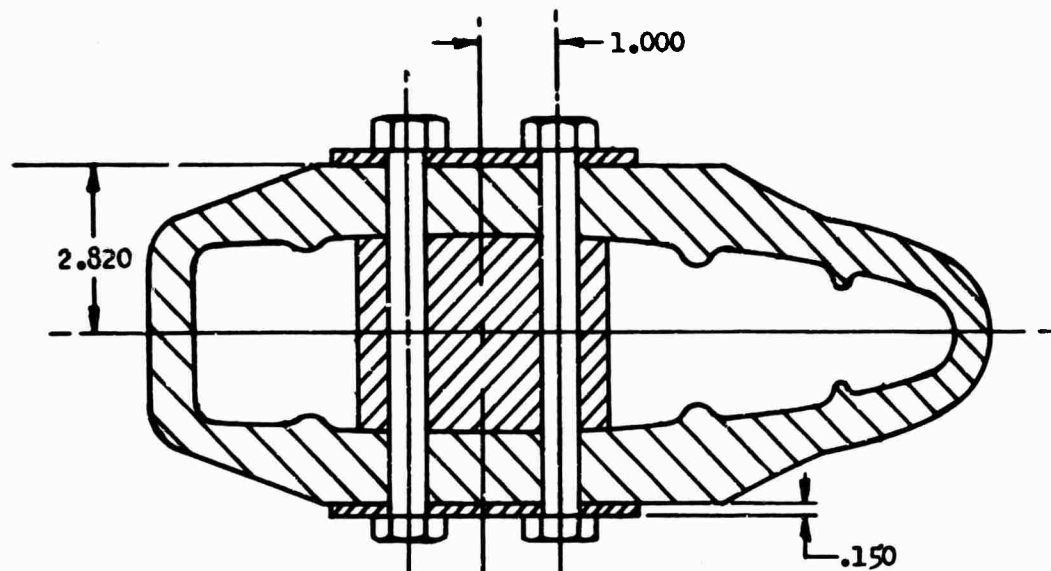
$$A = 11.75 \text{ in}^2$$

$$I_{xx} = 96.7 \text{ in}^4 \quad c = 3.72 \text{ in}$$

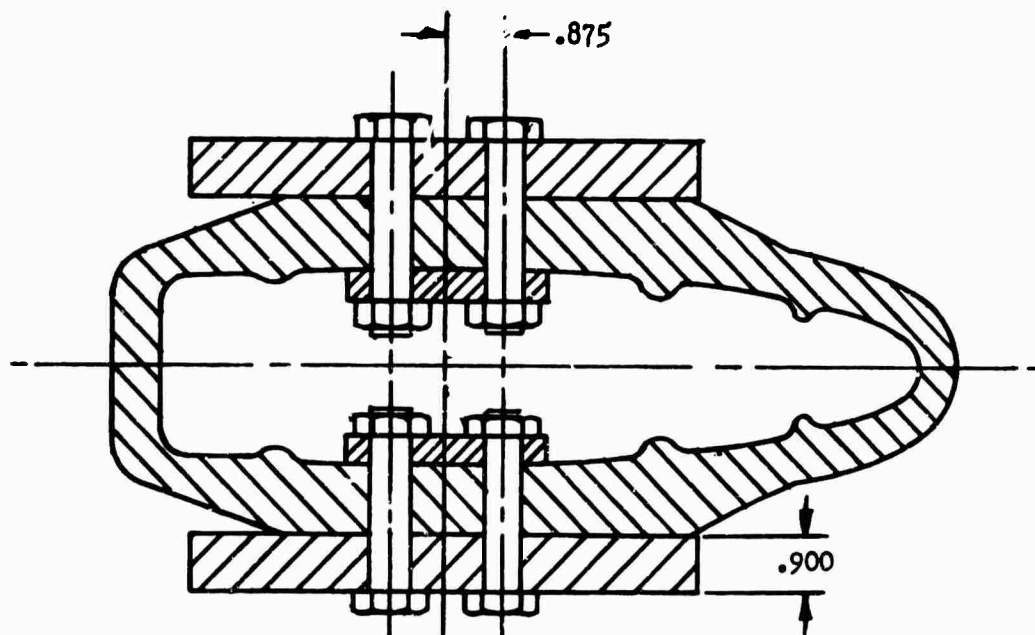
$$I_{yy} = 68.17 \text{ in}^4 \quad c = 1.125 \text{ in}$$

$$Z_{xx} = 25.995 \text{ in}^3$$

$$Z_{yy} = 60.604 \text{ in}^3$$



Section at Outboard Bolt Holes



Section at Inboard Bolt Holes

Figure 185 Spar-Cuff Sections with Maximum Stress

$$K_f = 0 \text{ at extreme surface}$$

$$K_c = .09 \text{ at neutral axis}$$

$$K = (\text{stress concentration factor}) = 2.5 \text{ for hole (Reference 41)}$$

Loads:

$$F_c = 141,000 \text{ lb}$$

$$M_{\text{flap}} = 116,400 \text{ in-lb}$$

$$M_{\text{edge}} = 84,000 \text{ in-lb}$$

$$S_{\text{edge}} = 1200 \text{ lb}$$

$$S_{\text{flap}} = 2000 \text{ lb}$$

$$M_t = 51,710 \text{ in-lb}$$

Stresses:

$$f_t = \frac{F_c}{A} = \frac{141,000}{11.75} = 12,000 \text{ lb/in}^2$$

$$f_{m\text{flap}} = \frac{M_{\text{flap}}}{Z_{xx}} = \frac{116,400}{25.995} = 4478 \text{ lb/in}^2$$

$$f_{m\text{edge}} = \frac{M_{\text{edge}}}{Z_{yy}} = \frac{84,000}{60.604} = 1386 \text{ lb/in}^2$$

$$f_n = f_t + f_{m\text{flap}} = 17,864 \text{ lb/in}^2$$

$$f_{nk} = f_n (K) = 2.5 (17,864) = 44,660 \text{ lb/in}^2$$

$$f_{s\text{edge}} = S_{\text{edge}} (K_c) = 1200 (.09) = 108 \text{ lb/in}^2$$

$$f_{s(\text{torsion})} = \frac{M}{h (A)} = \frac{51,710}{11.75 (4.08)} = 1079 \text{ lb/in}^2$$

$$f_s = f_{s\text{edge}} + f_{s(\text{torsion})} = 1187 \text{ lb/in}^2$$

$$f_{sk} = K f_s = 2.5 (1187) = 2968 \text{ lb/in}^2$$

$$f_{(\text{prin})} = \frac{44,660}{2} + \sqrt{\left(\frac{44,660}{2}\right)^2 + (2968)^2} = 44,856 \text{ lb/in}^2$$

$$f_{s(max)} = \sqrt{\frac{(44,660)^2}{2} + (2968)^2} = 22,526 \text{ lb/in}^2$$

Cuff Margin of Safety:

$$MS_{prin} = \frac{130,000}{(1.5) 44,856} - 1 = .93$$

$$MS_{shear} = \frac{80,000}{(1.5) 22,526} - 1 = 1.37$$

Analysis of Spar Through Outboard Bolt Holes

Spar Section Properties: (See Figure 185)

$A = 24.29 \text{ in}^2$	$r = 89.125 \text{ in}$
$I_{xx} = 98.09 \text{ in}^4$	$A^1 = 48.51 \text{ in}^2$
$I_{yy} = 359.35 \text{ in}^4$	$K_f = 0.0$
$Z_{xx} = 35.37 \text{ in}^3$	$K_c = .372$
$Z_{yy} = 227.87 \text{ in}^3$	$K = 2.5$

Loads:

$F_c = 137,000 \text{ lb}$
$M_{flap} = 118,800 \text{ in-lb}$
$M_{edge} = 90,000 \text{ in-lb}$
$S_{flap} = 400 \text{ lb}$
$S_{edge} = 900 \text{ lb}$
$M_t = 51,710 \text{ in-lb}$

Stresses:

$$f_t = \frac{137,000}{24.29} = 5640 \text{ lb/in}^2$$

$$f_{mflap} = \frac{118,800}{35.37} = 3359 \text{ lb/in}^2$$

$$f_{\text{medge}} = \frac{90,000}{227.87} = 395 \text{ lb/in}^2$$

$$f_n = f_t + f_{\text{mflap}} + f_{\text{medge}} = 9394 \text{ lb/in}^2$$

$$f_{nK} = K f_n = 2.5 (9394) = 23,845 \text{ lb/in}^2$$

$$f_{\text{sedge}} = 900 (.372) = 335 \text{ lb/in}^2$$

$$f_{\text{storsion}} = \frac{M}{2A't} = \frac{51,710}{2(48.514)(1.125)} = 474 \text{ lb/in}^2$$

$$f_s = f_{\text{sedge}} + f_{\text{storsion}} = 809 \text{ lb/in}^2$$

$$f_{sk} = K f_s = 2.5 (809) = 2022 \text{ lb/in}^2$$

$$f_{\text{prin}} = \frac{23,485}{2} + \sqrt{\frac{23,485^2}{2} + (2022)^2} = 23,657 \text{ lb/in}^2$$

$$f_{\text{smax}} = \sqrt{\frac{23,485^2}{2} + (2022)^2} = 11,915 \text{ lb/in}^2$$

Spar Margin of Safety:

$$MS_{\text{prin}} = \frac{38,000}{1.5 (23,657)} - 1 = .07$$

$$MS_{\text{shear}} = \frac{24,000}{1.5 (11,915)} - 1 = .34$$

Analysis of Blade Spar Outboard of Root End Attachment

Static Analysis of the Spar

The HLH main rotor blade was analyzed at 12 stations along the span to determine the stresses and margins of safety resulting from the applied loadings discussed below.

Investigation of loads and section moduli about the spar periphery shows the highest combination of stresses to occur at the entrance to the spar backwall radius. This will be the point of analysis for each blade section.

Loading:

The spar will be analyzed for the following loads:

- (a) Centrifugal force - F_c (See Figure 178)
 - (b) Flapwise bending moment - M_{flap}
 - (c) Edgewise bending moment - M_{edge}
 - (d) Flapwise shear - S_{flap}
 - (e) Edgewise shear - S_{edge}
 - (f) Torsional moment due to compressibility - M_t
 - (g) Moment due to the eccentricity of centrifugal force from the spar neutral axis - M_e (See Figure 186)
- } Condition 4a
and Condition 5a

The spar was investigated for loading conditions covering the entire spectrum of flight and ground operations. A survey of these conditions indicates that a complete substantiation of the spar need only consider two of these conditions, since the remaining will produce less severe moments and loads (See Figure 187).

From Station $x = .25$ outboard, condition 4a, "Symmetrical Dive and Pullout - 20-Ton Mission", produces the largest flapwise and edgewise bending moments on the blade and, therefore, the highest combination of stresses in this area.

Condition 5a, "Autorotative Dive and Pullout - 20-Ton Mission", because of the high centrifugal stresses, produces the highest stress condition for the inboard 25 percent of the spar.

Since the point to be analyzed on the periphery of the spar is approximately the extreme fiber in both the flapwise and edgewise directions, the stresses due to S_{flap} and S_{edge} are negligible.

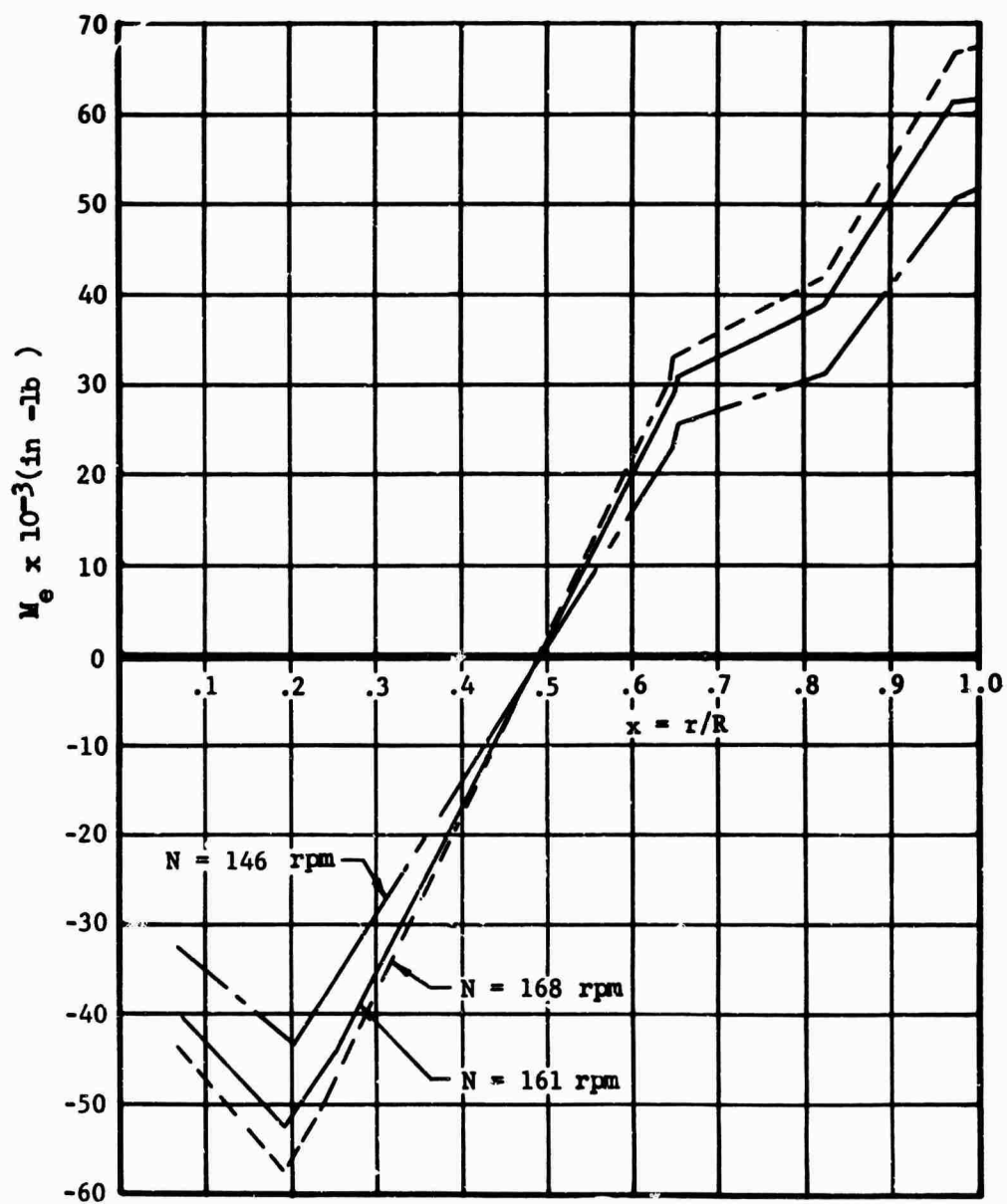


Figure 186 Eccentric Moment of Blade Mass About the Elastic Axis

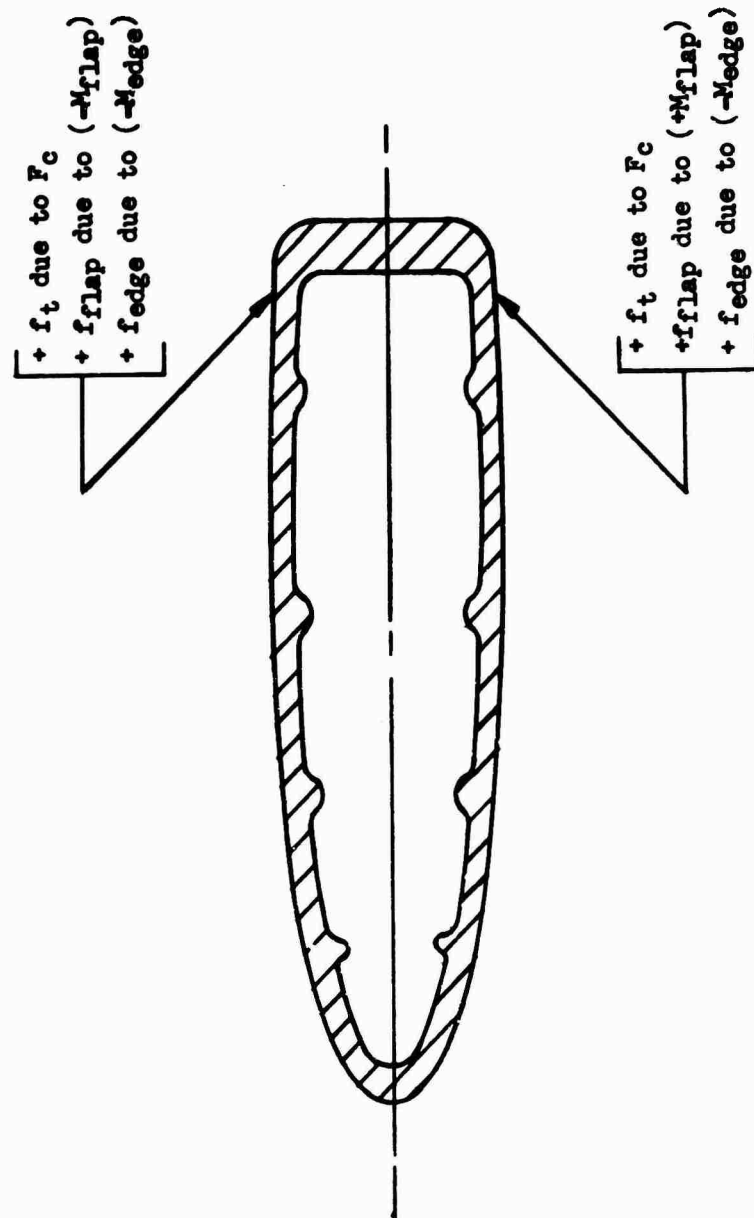


Figure 187 Spar Loading

Section properties are taken from the basic data given on pages 208 through 214.

Margins of Safety:

Margins of safety are calculated by a method using 1/R stress ratios (Reference 51).

Moduli of rupture in bending were derived from flapwise and edgewise bending tests of full-sized spar specimens loaded to rupture. Using the MIL HNDBK-5 ultimate tensile strength of 38,000 pounds per square inch, the ratio of resultant rupture stress/ultimate tensile strength was plotted against a parameter (D/t) derived from spar cross section dimensions. A plot of these ratios for several models established curves of flapwise and edgewise values of F_{rup} , as shown in Figure 188.

Separate stress ratios are then determined for each of the tension and bending stresses (times a 1.5 safety factor). The stress ratio for tension is obtained by dividing stress by the ultimate tensile stress. For the stress ratio due to bending, the bending stress is divided by the ultimate tensile stress multiplied by the ratio of F_{rup}/F_{ult} obtained from Figure 188.

These stress ratios are combined into the following formula to obtain the margins of safety for various stations along the blade:

$$MS = \frac{2}{R_t + \left[R_t^2 + 4 R_s^2 \right]^{\frac{1}{2}}} - 1 \quad (57)$$

(where R_t is the tensile stress ratio and R_s is the shear stress ratio).

The calculations of the required parameters and the resultant ratios and margins of safety are shown in Tables L and LI.

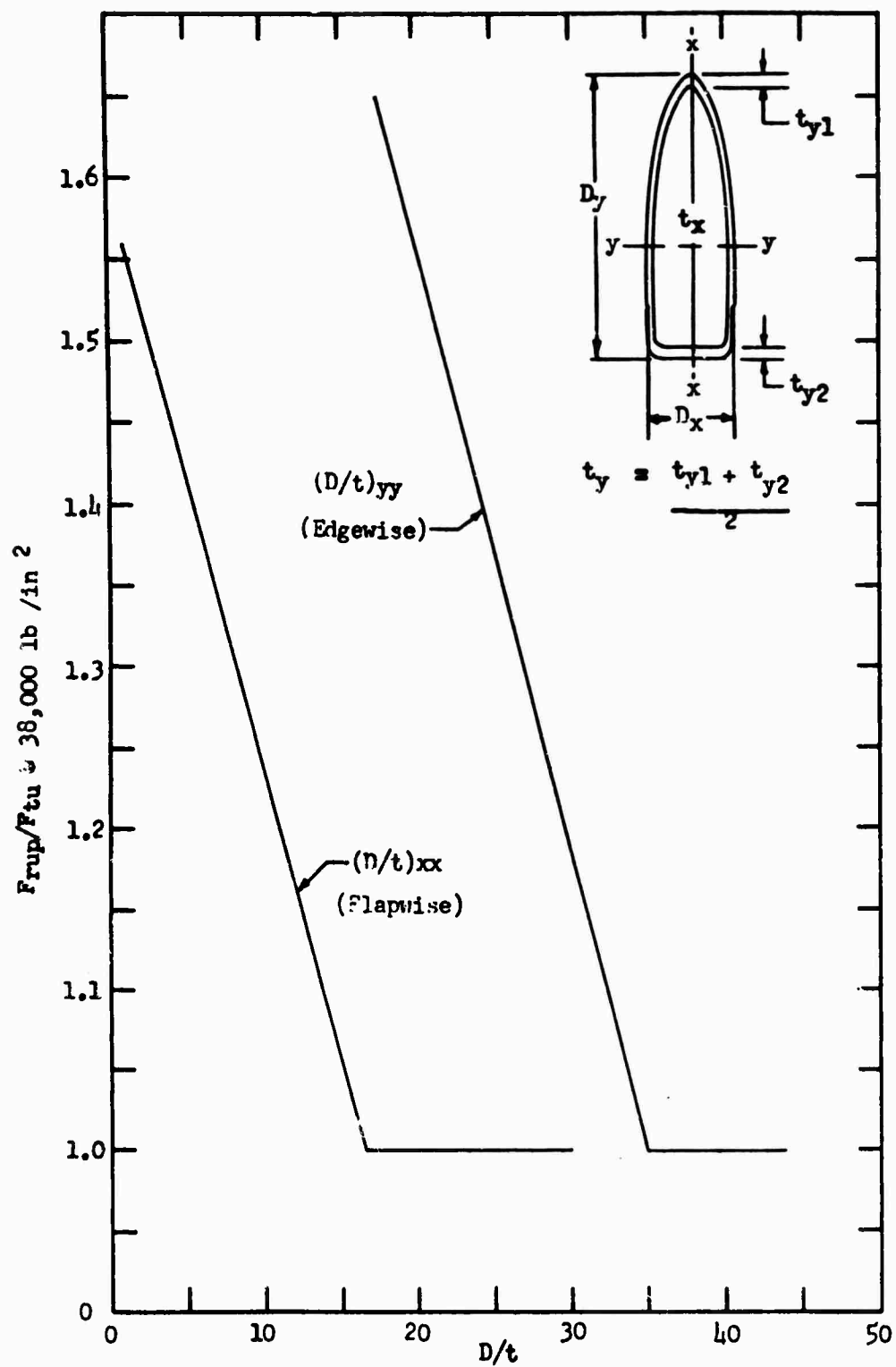


Figure 188 Form Factors for "D" Section Extrusion

SUMMARY OF LOADS, MOM

STATION x r	P _o	A	f _t	R ₁	M _{flap}	Z _{xx}	f _{m(flap)}	$\frac{D}{t}$ xx	$\frac{F_{rup}}{F_{tu}}$ xx	R ₂	M _{edge}
in	lb	in ²	lb/in ²		in-lb	in ³	in/lb ²				in-lb
.9 495	18,000	6.0	3,000	.118	84,000	7.25	11,586	21.8	1.0	.457	16,800
.8 440	33,000	7.6	4,342	.171	91,200	8.5	10,729	18.8	1.0	.424	64,800
.7 385	48,000	8.4	5,714	.226	100,800	9.5	10,610	16.0	1.02	.411	117,600
.6 330	62,000	9.8	6,326	.250	148,800	11.0	13,527	14.9	1.06	.504	156,000
.55 302	68,000	10.0	6,800	.268	158,400	11.25	14,080	14.9	1.06	.524	166,800
.5 275	74,000	10.1	7,327	.289	160,800	11.5	13,983	14.5	1.075	.513	170,400
.45 248	80,000	10.3	7,767	.306	158,400	11.75	13,481	14.2	1.085	.490	168,000
.4 220	85,000	10.6	8,019	.316	153,600	12.25	12,539	13.6	1.105	.448	163,200
.35 192	90,000	11.2	8,036	.317	144,000	12.75	11,294	12.9	1.13	.394	153,600
.3 165	94,000	11.6	8,103	.320	134,400	13.5	9,956	12.2	1.16	.339	140,400
.25 138	97,000	12.2	7,951	.314	130,800	14.25	9,179	11.6	1.175	.308	124,800
.2 110	101,000	15.0	6,733	.266	141,600	16.5	8,582	9.49	1.25	.271	110,400

$$R_1 = \frac{f_t(1.5)}{F_{tu}}$$

$$R_2 = \frac{f_m(flap)(1.5)}{(F_{rup})_{xx}}$$

$$R_3 = \frac{[f_m(edge) + (f_{te})]^{1.5}}{(F_{rup})_{yy}}$$

$$R_s = \frac{f_{st}(1.5)}{F_{su}}$$

$$R_t =$$

A

HOME

edge

TABLE L
SUMMARY OF LOADS, MOMENTS, AND STRESSES FOR CONDITION 4a

in-lb	M _{flap}	Z _{xx}	f _{m(flap)}	$\frac{D}{t}$ _{xx}	$\frac{F_{rup}}{F_{tu}}$ _{xx}	R ₂	M _{edge}	Z _{yy}	f _{m(edge)}	M ₀	f _{te}	$\frac{D}{d}$ _{yy}	$\frac{F_{rup}}{F_{tu}}$
in-lb	in ³	in/lb ²					in-lb	in ³	lb/in ²	in-lb	in/lb ²		
5,800													
5,800	34,000	7.25	11,586	21.8	1.0	.457	16,800	14.0	1,200	-41,000	-2929	40.67	1.0
7,600	41,200	8.5	10,729	18.8	1.0	.424	64,800	20.5	3,161	-30,000	-1463	31.2	1.1
5,800	40,800	9.5	10,610	16.0	1.02	.411	117,600	22.5	5,227	-26,000	-1156	31.2	1.1
0,400	48,800	11.0	13,527	14.9	1.06	.504	156,000	28.0	5,572	-16,000	- 571	25.3	1.3
5,000	58,400	11.25	14,080	14.9	1.06	.524	166,800	28.5	5,853	- 9,000	- 316	25.3	1.3
5,200	60,800	11.5	13,983	14.5	1.075	.513	170,400	28.5	5,979	- 1,000	- 35	25.3	1.3
5,600	58,400	11.75	13,481	14.2	1.085	.490	168,000	29.0	5,793	+ 6,000	207	25.3	1.3
5,400	53,600	12.25	12,539	13.6	1.105	.448	163,200	29.5	5,532	14,000	474	25.3	1.3
5,800	44,000	12.75	11,294	12.9	1.13	.394	153,600	31.0	4,955	21,000	677	25.3	1.3
5,400	34,400	13.5	9,956	12.2	1.16	.339	140,400	32.0	4,388	29,000	906	25.3	1.3
	30,800	14.25	9,179	11.6	1.175	.308	124,800	33.0	3,782	36,000	1091	25.3	1.3
	41,600	16.5	8,582	9.49	1.25	.271	110,400	38.0	2,905	44,000	1158	25.3	1.3

$$R_3 = \frac{[f_m(\text{edge}) + (f_{te})]^{1.5}}{(F_{rup})_{yy}}$$

$$R_8 = \frac{f_{st} (1.5)}{F_{su}}$$

$$R_t = R_1 + R_2 + R_3$$

$$MS = \frac{2}{R_t + [R_t^2 + 4 (R_s)^2]^{\frac{1}{2}}} - 1$$

13

E L
ID STRESSES FOR CONDITION 4a

	$f_m(\text{edge})$	M_e	f_{te}	$\frac{D}{d}$ yy	$\frac{F_{rup}}{F_{tu}}$ yy	R_3	M_t	$2A't$	f_{st}	R_s	R_t	MS
	lb/in ²	in-lb	in/lb ²				in-lb	in ³	lb/in ²			
	1,200	-41,000	-2929	40.67	1.0	-.068	14,303	13.17	1,086	.068	.507	.94
1.0	3,161	-30,000	-1463	31.2	1.15	.058	26,319	15.80	1,666	.104	.653	.49
1.1	5,227	-26,000	-1156	31.2	1.15	.140	36,196	18.73	1,932	.121	.777	.26
1.1	5,572	-16,000	- 571	25.3	1.37	.144	38,818	21.02	1,847	.115	.898	.10
1.3	5,853	- 9,000	- 316	25.3	1.37	.160	38,818	21.05	1,844	.115	.952	.03
1.3	5,979	- 1,000	- 35	25.3	1.37	.171	38,818	21.90	1,772	.111	.973	.01
1.3	5,793	+ 6,000	207	25.3	1.37	.173	38,818	22.33	1,738	.109	.969	.02
1.3	5,332	14,000	474	25.3	1.37	.173	38,818	23.58	1,646	.103	.937	.05
1.3	4,955	21,000	677	25.3	1.37	.162	38,818	25.33	1,532	.096	.873	.13
1.3	4,388	29,000	906	25.3	1.37	.152	38,818	27.22	1,426	.089	.811	.22
1.3	3,782	36,000	1091	25.3	1.37	.140	38,818	28.84	1,346	.084	.762	.30
1.3	2,905	44,000	1158	25.3	1.37	.117	38,818	37.58	1,033	.064	.654	.52
1.3	$R_3 \quad MS = \frac{2}{R_t + [R_t^2 + 4 (R_s)^2]^{\frac{1}{2}}} - 1$											

C

SUMMARY OF DATA

STATION x r	F _c	A	f _t	R ₁	M _{flap}	Z _{xx}	f _m (flap)	$\frac{D}{t}$ xx	$\frac{F_{rup}}{F_{tu}}$ xx	R ₂
in	lb	in ²	lb/in ²		in-lb	in ³	lb/in ²			
.9 495	24,000	6	4,000	.158	69,600	7.25	9,600	21.8	1.0	.379
.8 440	45,000	7.6	5,921	.234	85,200	8.5	10,024	18.8	1.0	.396
.7 385	65,000	8.4	7,738	.305	85,200	9.5	8,968	16	1.02	.347
.6 330	82,000	9.8	8,367	.330	86,400	11.0	7,854	14.9	1.06	.292
.55 302	90,000	10	9,000	.355	96,000	11.25	8,533	14.9	1.06	.318
.5 275	99,000	10.1	9,800	.387	98,400	11.5	8,556	14.5	1.075	.314
.45 248	105,500	10.3	10,243	.404	98,400	11.75	8,374	14.2	1.085	.305
.4 220	112,500	10.6	10,613	.419	98,400	12.25	8,033	13.6	1.105	.287
.35 192	119,000	11.2	10,625	.419	96,000	12.75	7,529	12.9	1.13	.263
.3 165	124,000	11.6	10,690	.422	96,000	13.5	7,111	12.2	1.16	.242
.25 138	129,000	12.2	10,574	.417	97,200	14.25	6,821	11.6	1.175	.229
.2 110	133,000	15.0	8,867	.350	105,600	16.5	6,400	9.49	1.25	.202

$$R_1 = \frac{f_t(1.5)}{F_{tu}}$$

$$R_2 = \frac{f_m(\text{flap})(1.5)}{(F_{rup})_{xx}}$$

$$R_3 = \frac{[f_m(\text{edge}) + (f_{te})]1.5}{(F_{rup})_{yy}}$$

$$R_s = \frac{f_{st}(1.5)}{F_{su}}$$

A

TABLE LI
SUMMARY OF LOADS, MOMENTS, AND STRESSES FOR CONDITION 5a

R_2	Z_{xx}	$f_m(\text{rlap})$	$\frac{D}{t}_{xx}$	$\frac{F_{rup}}{F_{tu}}_{xx}$	R_2	M_{edge}	Z_{yy}	$f_m(\text{edge})$	M_c	f_{te}	$\frac{D}{d}_{yy}$	$\frac{F_m}{F_{tu}}$
	in^3	lb/in^2				in-lb	in^3	lb/in^2	in-lb	lb/in^2		
379	7.25	9,600	21.8	1.0	.379	14,400	14.0	1,028	-55,000	-3,928	40.67	1.
396	8.5	10,024	18.8	1.0	.396	30,000	20.5	1,463	-40,000	-1,951	31.2	1.
347	9.5	8,968	16	1.02	.347	56,400	22.5	2,507	-35,000	-1,556	31.2	1.
292	11.0	7,854	14.9	1.06	.292	80,400	28.0	2,871	-23,000	- 821	25.3	1.
318	11.25	8,533	14.9	1.06	.318	87,600	28.5	3,074	-13,000	- 456	25.3	1.
314	11.5	8,556	14.5	1.075	.314	92,400	28.5	3,242	- 3,000	- 105	25.3	1.
305	11.75	8,374	14.2	1.085	.305	97,200	29.0	3,352	7,000	241	25.3	1.
287	12.25	8,033	13.6	1.105	.287	99,600	29.5	3,376	17,000	576	25.3	1.
263	12.75	7,529	12.9	1.13	.263	102,000	31.0	3,290	28,000	903	25.3	1.
242	13.5	7,111	12.2	1.16	.242	100,800	32.0	3,150	37,000	1,156	25.3	1.
229	14.25	6,821	11.6	1.175	.229	99,600	33.0	3,018	47,000	1,424	25.3	1.
202	16.5	6,400	9.49	1.25	.202	96,000	38.0	2,526	55,000	1,447	25.3	1.

$$\begin{aligned}
 &= \frac{[f_m(\text{edge}) + (f_{te})] 1.5}{(F_{rup})_{yy}} \quad R_s = \frac{f_{st}(1.5)}{F_{su}} \quad R_t = R_1 + R_2 + R_3 \quad MS = \frac{2}{R_t + [R_t^2 + 4(R_s)^2]^{\frac{1}{2}}} - 1
 \end{aligned}$$

13

FOR CONDITION 5a

c	f _{te}	$\frac{D}{d}$ yy	$\frac{F_{rup}}{F_{tu}}$ yy	n ₃	H _t	2A't	f _{st}	R _s	R _t	MS
-lb	lb/in ²				in-lb	in ³	lb/in ²			
,000	-3,928	40.67	1.0	-.114	16,000	13.175	1,214.	.076	.423	1.29
,000	-1,951	31.2	1.15	-.017	29,500	15.8	1,867	.117	.613	.58
,000	-1,556	31.2	1.15	.033	41,000	18.73	2,189	.137	.685	.40
,000	- 821	25.3	1.37	.059	50,000	21.02	2,379	.149	.681	.40
,000	- 456	25.3	1.37	.075	51,710	21.05	2,456	.153	.748	.28
,000	- 105	25.3	1.37	.090	51,710	21.9	2,361	.148	.791	.22
,000	241	25.3	1.37	.104	51,710	22.33	2,316	.145	.813	.19
,000	576	25.3	1.37	.114	51,710	23.58	2,193	.137	.820	.19
,000	903	25.3	1.37	.121	51,710	25.33	2,041	.128	.803	.22
,000	1,156	25.3	1.37	.124	51,710	27.22	1,900	.119	.788	.24
,000	1,424	25.3	1.37	.128	51,710	28.84	1,793	.112	.774	.26
,000	1,447	25.3	1.37	.114	51,710	37.58	1,376	.086	.666	.48

$$\frac{2}{+ [R_t^2 + 4 (R_s)^2]^{\frac{1}{2}}} - 1$$

C

Spar Fatigue Analysis

The BIM[®] system of continuous structural inspection makes possible the use of the blade for an indefinite period, with far greater reliability than can be obtained by retirement of the blade at a calculated "Safe Life". Replacement is thus required only "on condition", and arbitrary blade replacement life has no meaning.

Fatigue analysis of the spar was performed for each of the conditions in the flight spectrum. Spanwise station $r = 22.9$ ft. was the most highly stressed station of the spar for all conditions analyzed for fatigue. A sample calculation is shown in detail, and complete results are summarized in Table LII. The blade fatigue life calculated by FAA methods (Reference 33) is approximately 9000 flight hours. The magnitude of the calculated life, by an extremely conservative analysis, is interpreted as ample justification for "on-condition" replacement.

Steady-state flight conditions produce no fatigue damage, since the induced stresses are less than the endurance limit of the working curve. Thus, if the aircraft could be flown continuously in hovering and cruising flight, no finite life would exist. Various transient maneuver conditions induce higher stresses, however, so that the fatigue life is based entirely on maneuvering loads. The flight spectrum calculated for this aircraft (by the same method used in FAA certification of the S-64) indicates that 19 percent of the total flight time is spent in maneuvers. Of these, many are conditions that produce only moderate blade loadings. To simplify the analysis, it was conservatively assumed that all maneuvers are as severe as high speed pullouts. Power was assumed to be on during 83 percent of the time spent in maneuvers, while the remaining 17 percent of maneuver time was assumed to be spent in autorotative pullouts. Even though these are the most severe loading conditions that can be imposed upon the blades, the satisfactory results of the life calculation indicated that no refinement of the loading assumptions is necessary to prove the point. A more realistic survey of all maneuver conditions might well be expected to increase the calculated life by a factor of 100 or more, but would be of only academic interest.

The S-N curve used in the analysis is shown in Figure 189. It is based on full-sized test specimens of similar geometry, tested in the Sikorsky Fatigue Testing Laboratory. Specimens were tested with steady loads and combined flapwise and edgewise bending moments applied in proportion to actual flight values. The mean curve is then reduced to obtain a working curve.

TABLE LII
FATIGUE ANALYSIS OF SPAR

Condition	Mission	Time Percent	Vibratory Stress @ 8000 Pounds Per Square Inch	Steady Cycles	Allowable Hours	Damage
Warm-up and Takeoff	12 Ton	1.350	---	∞	∞	0
	20 Ton	1.225	---	∞	∞	0
Hover (Steady State)	12 Ton	3.300	---	∞	∞	0
	20 Ton	3.325	---	∞	∞	0
Cruise	12 Ton	56.850	4,781	∞	∞	0
	20 Ton	10.950	4,639	∞	∞	0
Maneuvers (Symmetrical Flight)	12 Ton	10.875	17,662	1.4×10^5	14.0	.0078
	20 Ton	5.000	16,978	1.6×10^5	16.0	.0030
Maneuvers (Autorotation)	12 Ton	2.625	12,250	6.5×10^5	65.0	.0004
	20 Ton	0.500	11,226	1.1×10^6	1100	0
		$\Sigma = 100.000$			$\Sigma = .0112$	

$$\text{Replacement Life} = \frac{100}{\text{Damage}} = \frac{100}{.0112} = 8928 \text{ hr}$$

* From Figure 189.

**Converted from cycles at 10,080 cycles/hour (N = 168 rpm). This assumption is conservative since some of the damage occurs at lower rotor speeds.

Outboard Spar Fatigue Data
(corrected to 8000 lb/in² steady stress)

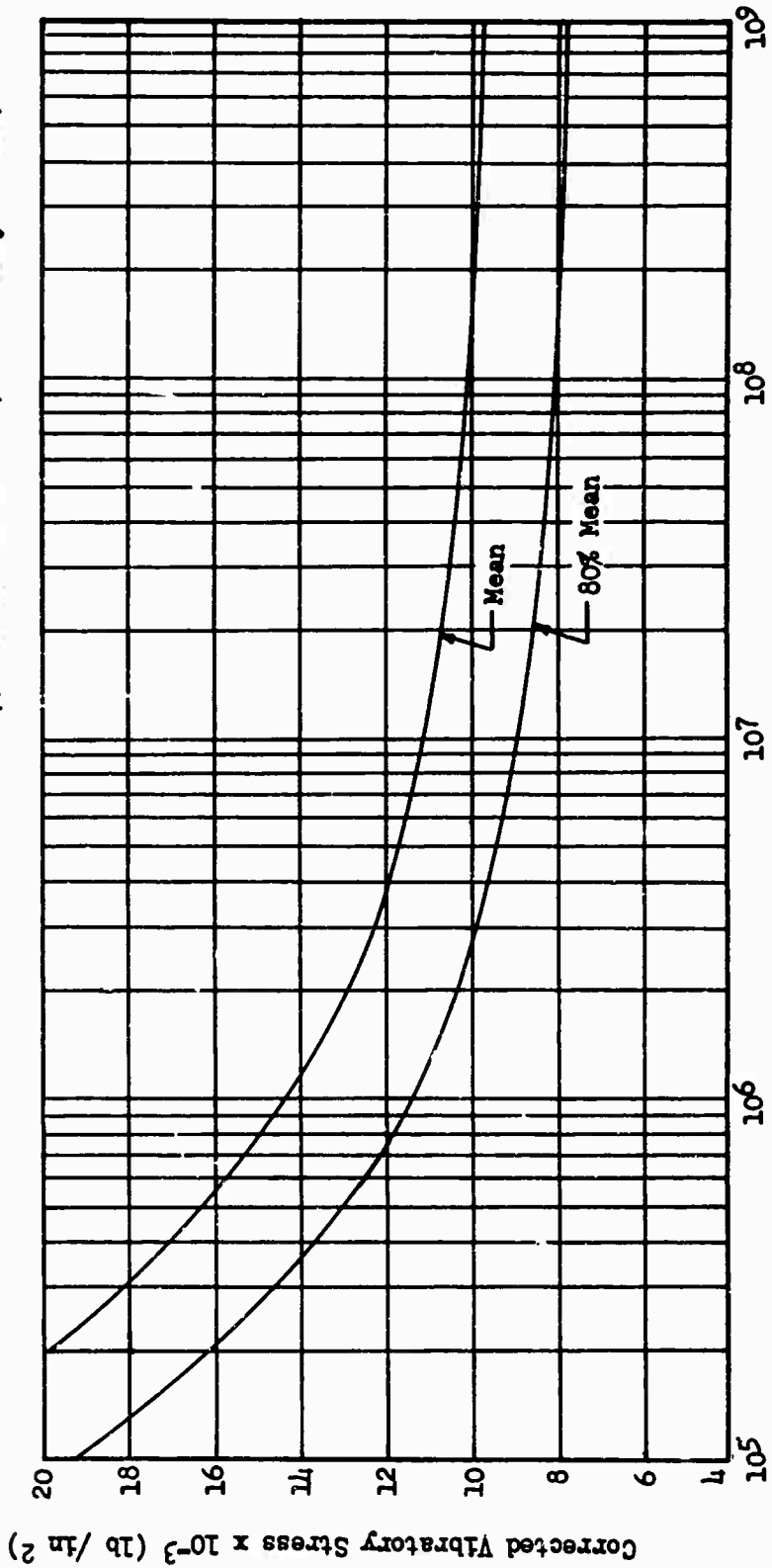


Figure 189 Maximum Vibratory, Back Corner Stress Versus Cycles to Crack Initiation

The cumulative damage to the blade is calculated by determining the allowable hours at each of the stress levels from the S-N curve. One hour is 8760 cycles at 146 revolutions per minute for normal operation, or 10,080 cycles at 168 revolutions per minute for the limit power-off condition.

For each condition, the damage is given by

$$\text{Damage} = \frac{\text{percent Time}}{\text{Allowable Hours}}$$

The total damage is obtained by summing the individual damage calculated for all conditions. A replacement time is then given by

$$\text{Replacement Time} = \frac{100}{\text{Total Damage}} \quad (\text{See Table LII})$$

Sample Calculations for Maximum Fatigue Condition

Cross-Sectional Properties @ $x = .5$:

$$A = 10.1 \text{ in}^2$$

$$Z_{x-x} = 11.5 \text{ in}^3$$

$$Z_{y-y} = 28.5 \text{ in}^3$$

Loads and Moments:

$$F_C = 74,000 \text{ lb}$$

$$\left. \begin{array}{l} M_{\text{flap}} = +156,000; -81,600 \text{ in-lb} \\ M_{\text{edge}} = +144,000; -182,400 \text{ in-lb} \end{array} \right\} \text{Condition 4b}$$

$$M_{\text{ecc}} = +1000 \text{ in-lb}$$

Stresses:

Centrifugal Stress

$$f_t = \frac{74,000}{10.1} = 7327 \text{ lb/in}^2$$

Flapwise Stress

$$M_{\text{flap(steady)}} = \frac{156,000 - 81,600}{2} = 37,200 \text{ in-lb}$$

$$M_{\text{flap(vibratory)}} = \frac{15,600 + 81,600}{2} = \pm 118,800 \text{ in-lb}$$

$$f_t = \frac{37,200}{11.5} \pm \frac{118,800}{11.5} = 3235 \pm 10,330 \text{ lb/in}^2$$

Edgewise Stress

$$M_{\text{edge(steady)}} = \frac{144,000 - 182,400}{2} = -19,200 \text{ in-lb}$$

$$M_{\text{edge(vibratory)}} = \frac{144,000 + 182,400}{2} = \pm 163,200 \text{ in-lb}$$

$$M_{\text{ecc(steady)}} = 1000 \text{ in-lb}$$

$$f_t = \frac{19,200 + 1000}{28.5} \pm \frac{163,200}{28.5} = -674 \pm 5726 \text{ lb/in}^2$$

$$f_{\text{tot}} = (f_t + f_{\text{flapsteady}} + f_{\text{edgesteady}}) \pm (f_{\text{flapvibratory}} + f_{\text{edgevibratory}})$$

$$f_{\text{tot}} = 11,201 \pm 16,056 \text{ lb/in}^2$$

To use the S-N curve, the vibratory stress must be converted to 8000-pounds-per-square-inch steady stress. The Goodman correction factor is

$$CF = \frac{42,000 - 8000}{42,000 - f_{\text{steady}}}$$

$$CF = \frac{34,000}{30,799} = 1.10$$

$$f_{\text{tot}} = 8000 \pm 17,662 \text{ lb/in}^2$$

Secondary Bending Analysis

Because of the large chordwise breadth of the spar, an analysis was performed to determine the amount of secondary bending of the spar section caused by flapwise bending of the blade. This action is similar to the flattening of a round tube into an elliptical section when bent, and is the reverse of the operating principle of the familiar Bourdon tube. The analysis relates the elastic curvature and flexural stress distribution in the spar to the loading which deforms the section. Deflections are then computed, and the resulting alteration in flapwise moment of inertia is calculated. Because it could then be determined by inspection that the secondary bending did not pose a problem, the analysis was carried no further. Used as an iterative procedure, however, this analysis can be used to define structural stability. If successively determined deflections of the section form a convergent sequence, the structure is stable, while a divergent sequence would indicate a failure by buckling.

The secondary bending is dependent on flexural loading and does not depend significantly on shear loading. The derivation therefore assumes a pure (or constant) bending moment imposed on the spar, as shown in Section A-A of Figure 190.

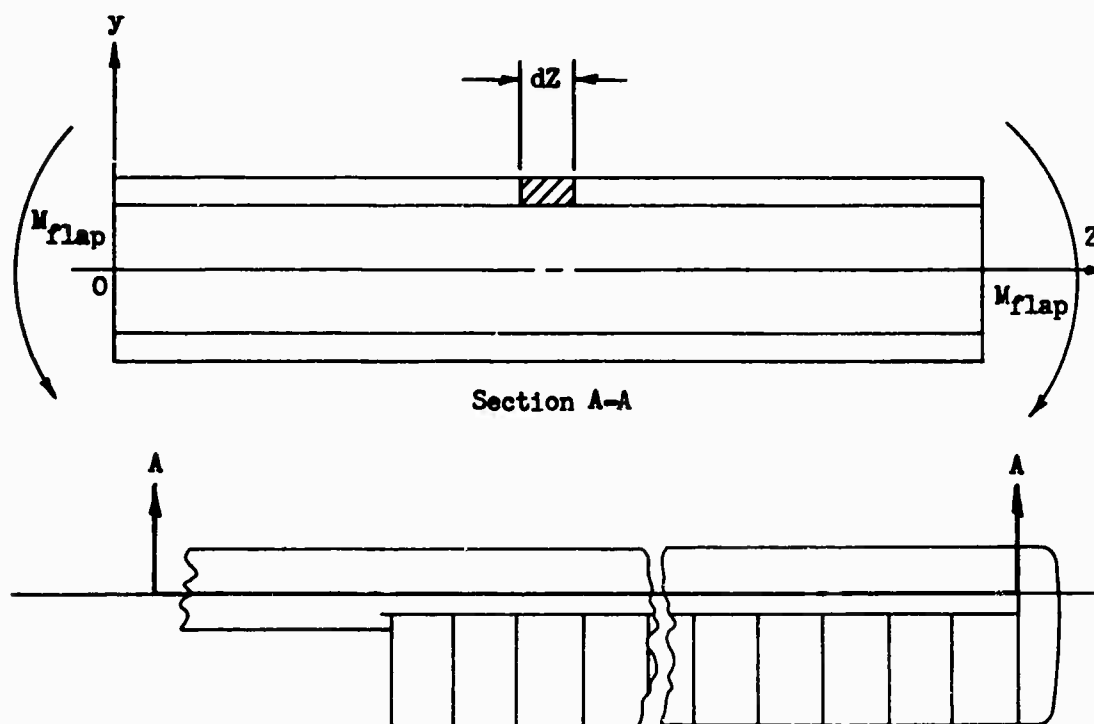


Figure 190 Blade Planform

The flapwise bending moment acting on the blade, as shown, causes the blade to deflect concave downward, producing tension in the upper sidewall and compression in the lower sidewall. Since the spar is symmetrical about the Z axis, only the upper surface will be considered. Taking an element of length dZ and thickness ds from the upper portion of the deflected blade,

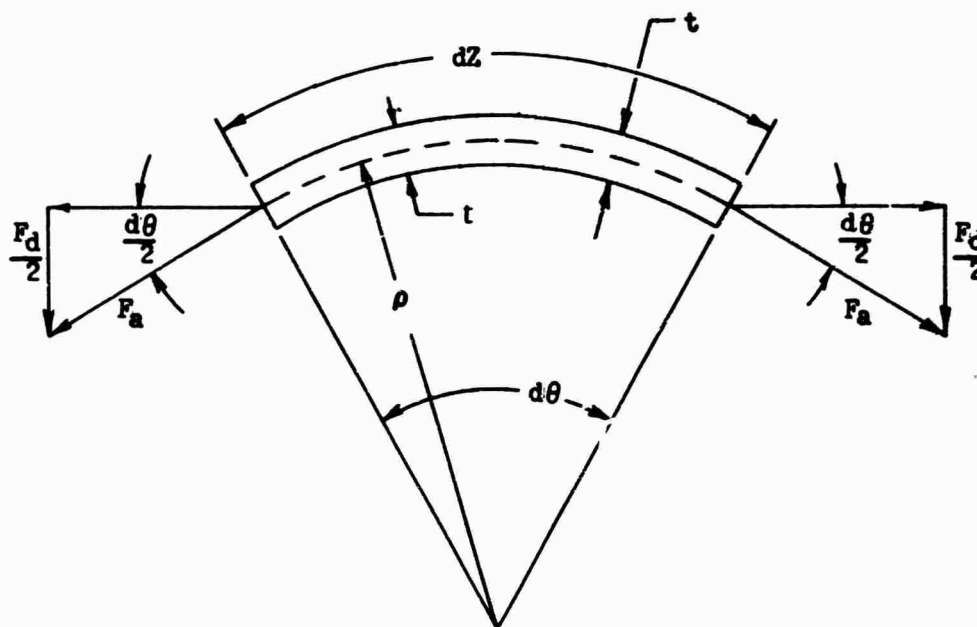


Figure 191 Spar Sidewall Element

we compute the force F_d as shown in Figure 191.

$$F_d = 2F_a \sin \frac{d\theta}{2} \quad (58)$$

Since for small angles, $\frac{d\theta}{2} = \sin \frac{d\theta}{2}$,

$$F_d = 2F_a \frac{d\theta}{2} \quad (59)$$

where F_a is the force on the spar due to M_{flap} . From simple beam theory, the stress is given by

$$S = \frac{F_a}{dA} = \frac{M_{\text{flap}} Y}{I_{xx}} \quad (60)$$

Therefore, $F_a = \frac{M_{\text{flap}} Y}{I_{xx}} dA$

Also, $dA = t ds$

From the geometry of the elastic curve,

$$dZ = \rho d\theta,$$

and since $\rho = \frac{EI}{M_{\text{flap}}}$,

$$\frac{d\theta}{2} = \frac{dZ M_{\text{flap}}}{2EI_{xx}} \quad (61)$$

Therefore,

$$F_d = 2F_a \frac{d\theta}{2} = \frac{2M_{\text{flap}}^2 Y t ds dZ}{2EI (I_{xx})^2} \quad (62)$$

for a unit length of spar ($dZ = 1$ in)

$$F_d = \frac{M_{\text{flap}}^2 Y t ds}{E (I_{xx})^2} \quad (63)$$

This equation is of interest, since it shows that the loading which tends to deform the section is proportional to the second power of applied bending moment. This is due to the influence of elastic curvature and flapwise bending stress, both of which depend on the applied moment. The second power relationship also shows why instability failures tend to be abrupt in their behavior.

Using this equation to calculate the chordwise loading, the moments and deflections are calculated for two stations along the spar.

The sections and loads used in this analysis were selected to approximate the maximum flapwise bending stress condition in cruise ($x = .860$) and in ground handling ($x = .244$). Because the analytical results were to be used as the basis of an early design decision, the loads and section locations are approximate and do not necessarily match exactly the loads and critical section locations determined in the final design analysis.

Blade Section at $r = 134$ in
 Airfoil = NACA 0012
 Chord = 2.58 ft
 Flapwise Bending Moment = 383,836 lb-in
 Nominal Sidewall Thickness = .350 in
 Nominal Backwall Thickness = .560 in

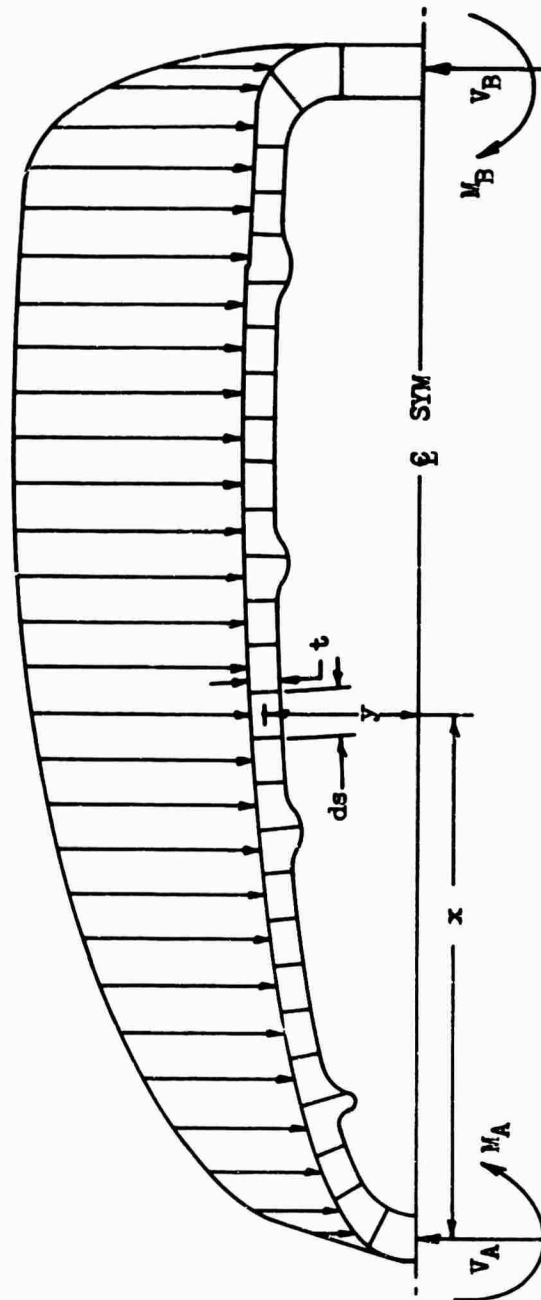


Figure 192 Chordwise Force Distribution, Secondary Bending Analysis, $x = .244$

Blade Section at $r = 473$ in
 Airfoil = NACA 0012
 Chord = 2.58 ft
 Flapwise Bending Moment = 82,080 lb-in
 Nominal Sidewall Thickness = .825 in
 Nominal Backwall Thickness = .160 in

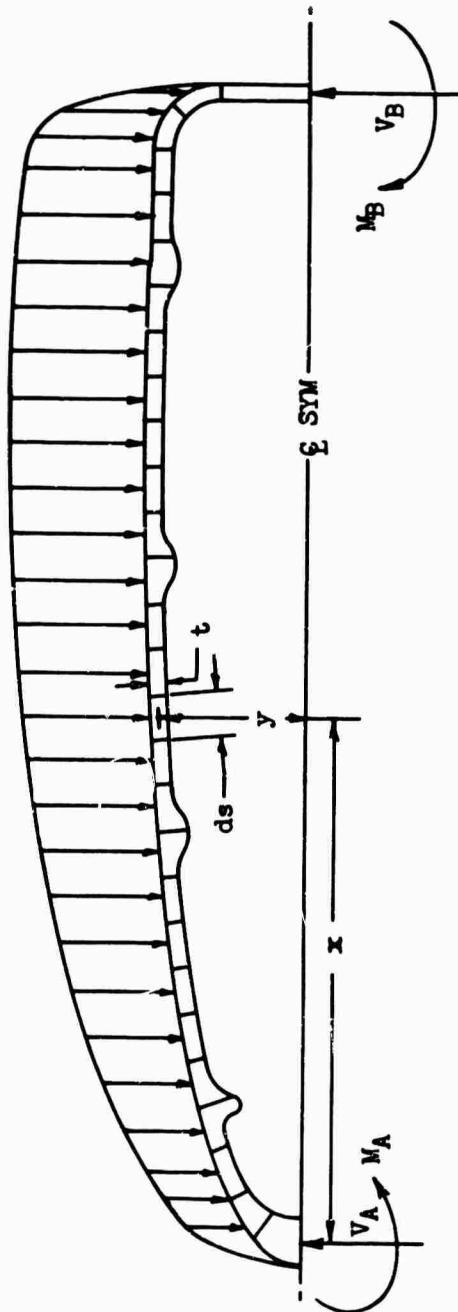


Figure 193 Chordwise Force Distribution, Secondary Bending Analysis, $x = .86$

Since F_d varies along the spar chord, the spar was divided into 56 elements and ΔF_d was calculated for each element. The results are summarized in Figures 192 and 193. They show the location of the spar stations and the chordwise loading for each of the elements.

The moments and deflections are found by considering the spar as an indeterminate structure (Reference 58, Page 143). See Figure 194.

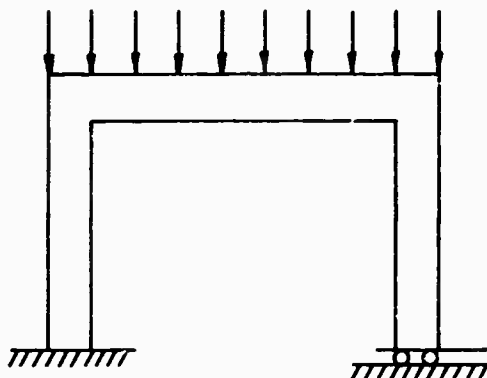


Figure 194 Chordwise Loading Analogy

The moments, slopes, and deflections have been plotted versus the mean line (NA) of the section and are shown in Figures 195 and 196.

Flapwise moments of inertia, recalculated for the deflected spar at each of the sections studied, were found to be reduced by less than 2 percent from those of the undeflected section. Since the maximum deflection of the sidewall was negligible (approximately .025 in both cases), no further analysis was considered to be necessary.

The effects of secondary bending deflections vary, depending on the loading conditions which cause them. Flight loads generally are caused by airloads and inertia forces and tend to bend the blade into a particular elastic curve at any given instant. Thus, any effect which reduces flexural stiffness tends to reduce the applied bending moment and thus actually reduces blade stresses. In steady ground loading conditions, caused by the weight of the blade or steady wind loads, severe secondary deflections could cause crippling of the structure. Under dynamic loads, however, caused by towing the aircraft across a bumpy field or by gusty winds, the effect of secondary bending would simply be to reduce the stiffness of the blade, allowing it to "give" with the load and thereby reduce stresses.

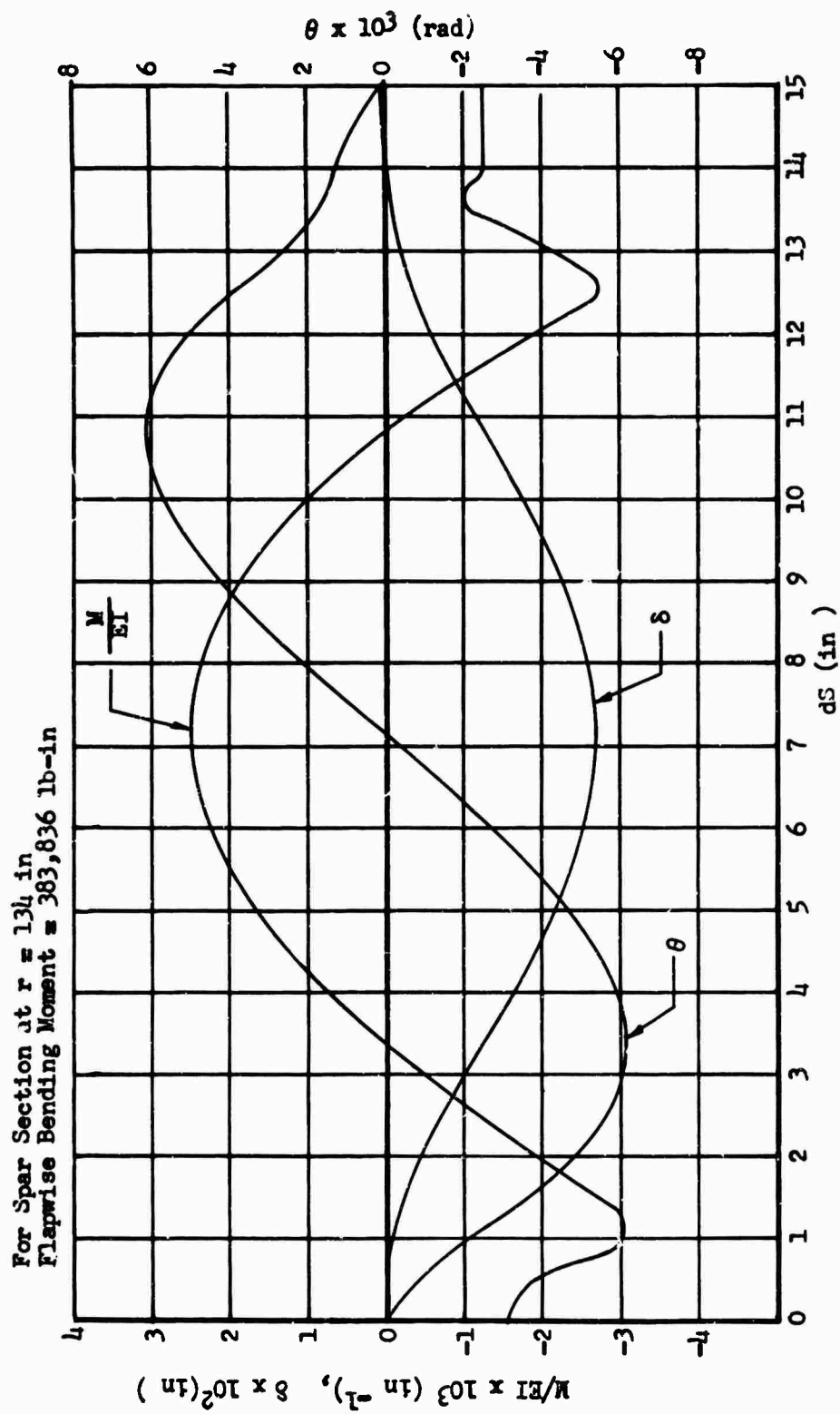


Figure 195 Moment, Slope, and Deflection Due to Secondary Spar Bending, $\alpha = .224$

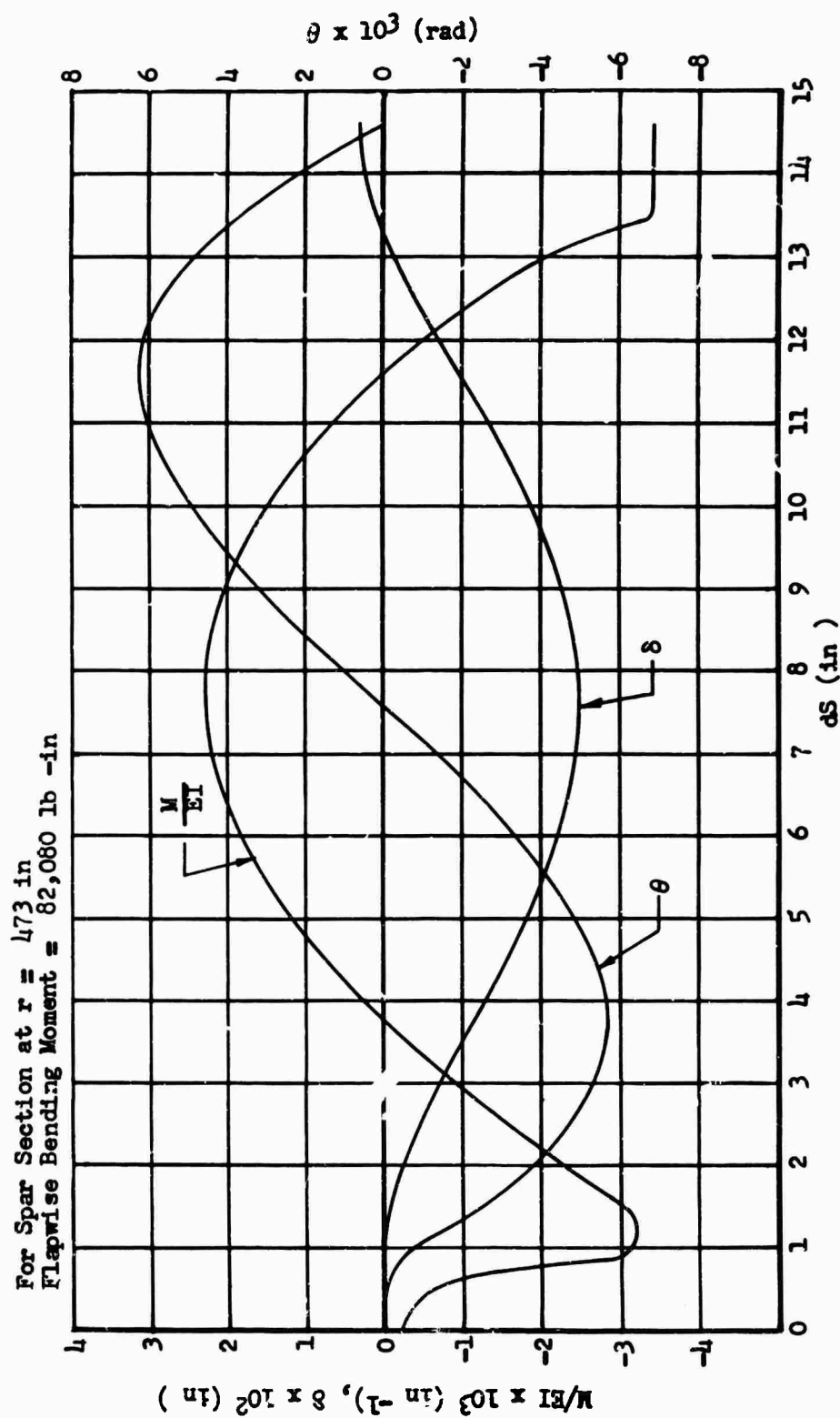


Figure 196 Moment, Slope, and Deflection Due to Secondary Spar Bending, $x = .86$

ROTOR HEAD STRUCTURAL ANALYSIS

Development of Design Loads

The design loads for the main rotor head and control system can be classified into three major categories:

1. Static structural design loads
2. Fatigue structural design loads
3. Bearing design loads

Static Structural Design Loads

All static loads presented are limit loads; i. e., the maximum anticipated load corresponding to a given condition. The two conditions considered in this analysis are the starting condition and rotor overspeed.

Fatigue Structural Design Loads

The selection of a design load for fatigue analysis is based on the application of Miner's cumulative damage concept (Reference 36) and the established curves of each structural material's stress versus cycle (S-N) curve to a given loading spectrum. This procedure is necessary in order to design for a minimum retirement time for structural components.

The standard shape of the S-N curve for a particular material is established by fitting the general equation (64) to large quantities of available test data on standard specimens. Such data were obtained from Reference 51, Alcoa test results, Sikorsky Aircraft test results, and other similar sources.

$$S = E' + \frac{\alpha}{N} \quad (64)$$

A typical S-N curve is illustrated in Figure 197. Note that the curve which lies approximately in the middle of the test data scatter and approaches an asymptote E'_m as the number of stress cycles N becomes infinite. This property E' of the material is called the endurance limit of the particular type of specimen tested. The subscript m indicates that this is the mean endurance limit, since it is the asymptote of the mean S-N curve.

If a standard specimen under fatigue loading is subjected to a slight rubbing or chafing due to metallic contact with another member, the stress-cycle relationship for the given metal changes quite markedly. Such a

chafing condition exists in bolted connections, lug-pin joints, interference fit surfaces, and, in general, wherever metallic surfaces in direct contact are exposed to relative movement or elastic deformation. Hence, for each material it is necessary to have a standard S-N curve shape for both the chafing and nonchafing condition.

In the process of establishing a design load for a component of given

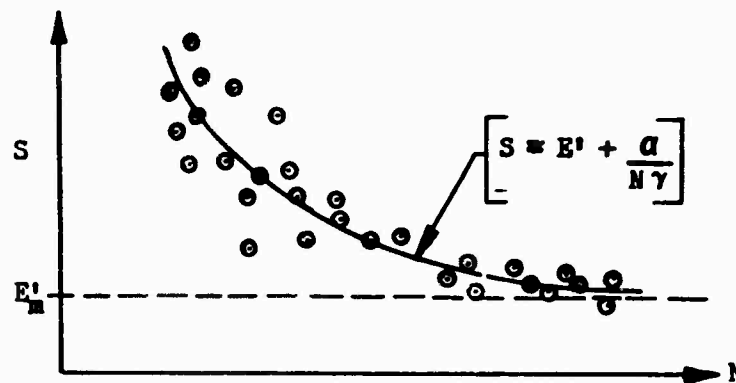


Figure 197 General Standard S-N Curve

material and chafing environment, it is convenient to work with a non-dimensional S-N curve (Figure 198). This curve is obtained directly from the standard S-N curve by dividing the shape equation (64) by the material's mean endurance limit E'_m .

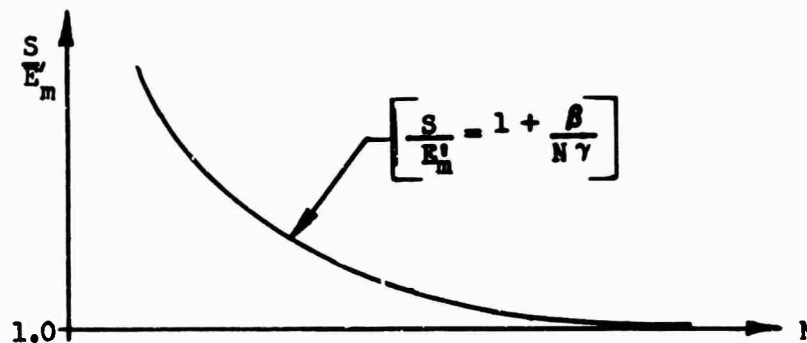


Figure 198 Nondimensionalized S-N Curve

Miner's cumulative damage theory provides a means by which the life of a structure of known endurance limit can be predicted for a given loading spectrum. For example, consider a specimen of known mean endurance limit E'_m loaded cyclically at some level S_1 above E'_m (see Figure 199).

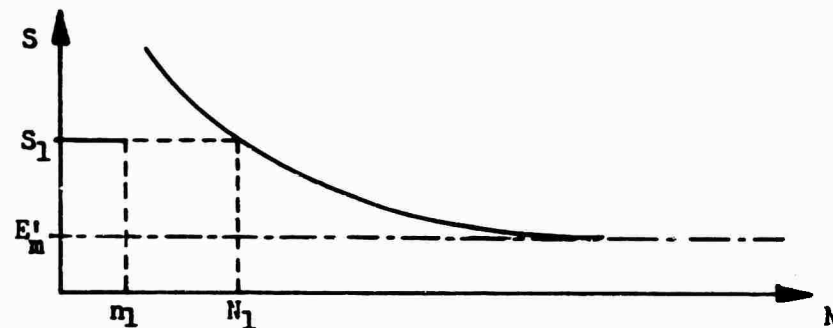


Figure 199 Typical Component S-N Curve

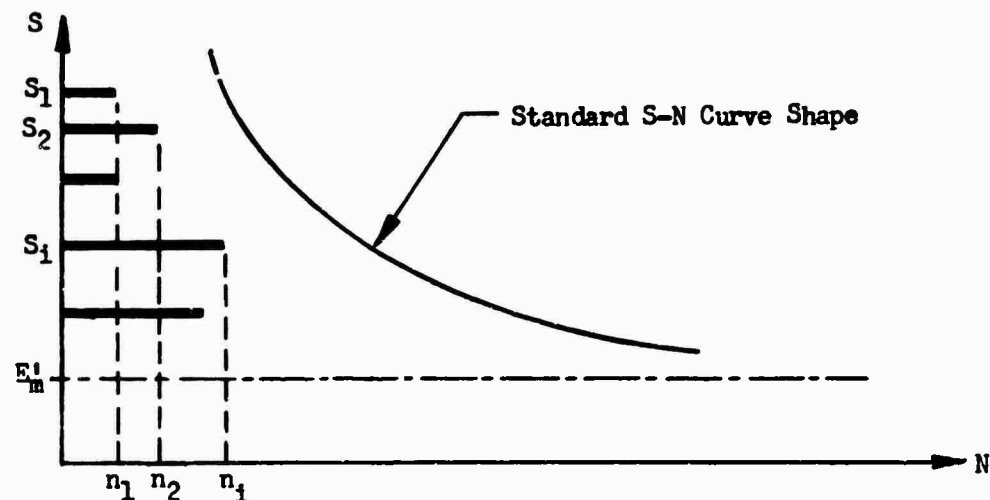


Figure 200 Standard S-N Curve Applied to Loading Spectrum

The S-N curve predicts that the mean life of the specimen at the S_1 load level will be N_1 cycles. Miner's theory claims that after n_1 cycles at load level S_1 , a portion of the virgin specimen life equal to (n_1/N_1) is consumed.

Consider the specimen to be subjected to a spectrum of loading; i. e., n_1 load cycles at load level S_1 , n_2 cycles at load S_2 , etc. This condition is graphically represented in Figure 200 and shown schematically in Figure 201.

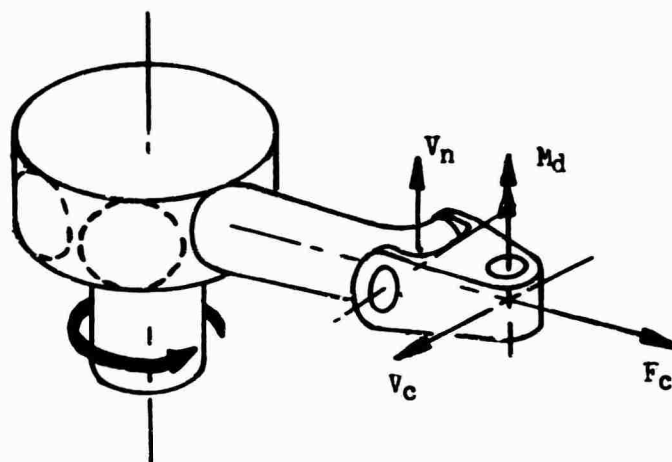


Figure 201 Rotor Head Fatigue Design Loads

Miner's theory applied to this type of fatigue loading spectrum would predict that the portion of the virgin specimen's life consumed is

$$\left(\frac{n_1}{N_1} + \frac{n_2}{N_2} + \cdots + \frac{n_i}{N_i} + \cdots \right) \quad (65)$$

Failure of the specimen will occur when this fraction equals unity.

The foregoing discussion should provide the necessary concepts for an understanding of how a design load is developed from a given loading spectrum. It is an iterative process in which a mean design endurance limit E'_m is initially assumed, and with the applicable standard nondimensional S-N curve, a life is computed corresponding to the given loading spectrum. If the computed life is greater than the required replacement time, then the assumed design endurance limit is reduced and the procedure is repeated. Conversely, if the computed life is less than that required, the assumed endurance limit is increased. This process is repeated until a life equal to the required replacement time is determined. The mean endurance limit corresponding to this life is the design load level to which the component is designed. Designing the component for infinite life at this load level is considered equivalent to designing for the required replacement time at the given loading spectrum.

The fatigue design loads are based primarily on the main rotor flapping and power spectra as given in Tables LIII and LIV. Basic mission requirements were used to develop the 12-ton and 20-ton mission profiles. Gross weight variation during a mission is based on full payload outbound

and no payload inbound for both the 12-ton and 20-ton missions. Additional changes in gross weight during a mission were made to reflect fuel usage.

The preliminary main rotor flapping spectra for the heavy lift helicopter are given in Table LIII for both the 12-ton transport mission and the 20-ton heavy lift mission. The longitudinal center-of-gravity range of +2.0 ft. at takeoff gross weights was used to establish flapping angles.

TABLE LIII
PRELIMINARY MAIN ROTOR FLAPPING SPECTRA

FLIGHT REGIME	12-TON TRANSPORT MISSION		20-TON HEAVY LIFT MISSION	
	% TIME	β_f (degrees)	% TIME	β_f (degrees)
Warm-up, takeoff and climb	1.8	2.8	4.9	3.2
Hover (steady state)	4.4	3.6	29.3	4.2
Hover (maneuvers)	1.6	4.2	10.5	4.9
	0.3	6.6	2.2	7.6
Cruise (steady state)	75.8	2.6	43.82	3.0
Cruise (maneuvers)	12.0	3.3	6.9	3.7
	3.5	5.0	2.02	5.8
	0.6	5.8	0.36	6.7
	100.0		100.0	

The heavy lift helicopter power spectra are likewise given in terms of the two missions in Table LIV.

It was assumed that the heavy lift helicopter would be utilized 75 percent of the time for the 12-ton transport mission and 25 percent of the time for the heavy lift mission. This assumption allows the combining of the transport and heavy lift spectra into a single design flapping spectrum and main rotor power spectrum. A comparison of the results shows great similarity of the HLH spectra to those computed for several other Sikorsky Aircraft models.

Bearing Design Loads

A bearing design load is obtained by a time prorated of the loading spectrum and the oscillation amplitude spectrum. The oscillatory frequency of all bearings in the main rotor head and control system is equal to the rotational speed of the main rotor.

TABLE LIV
PRELIMINARY MAIN ROTOR POWER SPECTRA

FLIGHT REGIME	12-TON			20-TON		
	TRANSPORT MISSION % TIME	GW	MRHP	HEAVY LIFT MISSION % TIME	GW	MRHP
Warm-up and takeoff	1.8	65,800	10,975	4.9	78,750	10,976
Hover @ origin	2.7	65,800	8,060	12.5	78,750	10,496
Cruise out @ 95 kn	-	-	-	31.0	77,788	5,245
Cruise out @ 110 kn	49.7	64,140	4,815	-	-	-
Hover @ destination	1.8	62,675	7,494	24.6	76,975	10,190
Cruise back @ 130 kn	42.2	37,435	3,869	22.1	36,292	3,804
Hover on return	1.8	36,200	3,560	4.9	35,897	3,520
	100.0			100.0		

METHODS OF STRUCTURAL DESIGN ANALYSIS

The preliminary design analysis included in this report serves as a general representation of the methods customarily used to substantiate structurally the main rotor head and control system components.

The stress analysis is divided into static and fatigue sections. The static analysis determines that no permanent distortion or fracture of components will result from application of maximum loads under infrequently experienced operating conditions. The fatigue analysis determines that components will operate with the desired structural reliability in the presence of repeated loadings.

Static Analysis

Static margins of safety have been written in accordance with Reference (51). Margins of safety have been computed against both yield and ultimate fracture.

$$MS \text{ (yield)} = \frac{\delta_{ty}}{1.15 \sqrt{(2\delta_s)^2 + (\delta_a + \delta_b)^2}} - 1 \quad (66)$$

$$MS \text{ (ultimate)} = \frac{1}{1.50 \sqrt{\left(\frac{\delta_a}{\delta_{tu}}\right)^2 + \left(\frac{\delta_b}{\delta_{bu}}\right)^2 - \left(\frac{\tau_s}{\tau_{su}}\right)^2}} - 1 \quad (67)$$

The material properties for the alloys considered in this study are given in Table I V (Reference 51).

TABLE LV
MATERIAL PROPERTIES

PROPERTY	MATERIAL		
	Aluminum 7075-T73	Steel SAE 4130, 4340 (150 KSI HT)	Titanium 6AL-4V (Annealed)
δ_{ty} (10^3 lb/in ²)	56	132	120
	52	132	120
δ_{tu} (10^3 lb/in ²)	66	150	130
	61	150	130
τ_{su} (10^3 lb/in ²)	42	95	76
E (10^6 lb/in ²)	10.3	29.0	16.0
G (10^6 lb/in ²)	3.9	11.0	6.2
w (lb/in ³)	0.101	0.283	0.160

Fatigue Analysis

It is the nature of metal structures that the application of a continuously varying load, generating stresses considerably below the yield stress of the material, may cause fracture of the metal after a finite number of stress cycles, depending on the magnitude of the applied stresses. The fatigue analysis is the method by which it is analytically demonstrated, to a desired probability, that the structural component will not fail within a

given number of cycles. Since the rotor system loads are at the same frequency as the rotational speed of the rotor shaft, the number of load cycles can be expressed in terms of hours of aircraft operation.

The working (allowable) endurance limit stress at some point in a critical cross section of the component is based on the mean material endurance limit stress, the size of effect factor, the probability factor, and the machining factor.

The mean endurance limit stress of a standard specimen of given material, size, and surface finish is experimentally known. For the steel and aluminum alloys used in the aircraft industry the endurance limits are given in Reference (51). The mean endurance limit for 6AL-4V titanium alloy is based on Sikorsky Aircraft's testing experience with this material, Table LVI summarizes the mean endurance limits used in the analysis of the HLH rotor head system.

TABLE LVI
MATERIAL MEAN ENDURANCE LIMIT STRESS

Material	Alloy	$(\delta_{en})_m$
Aluminum	7075-T73	22,000 lb/in ²
Steel	SAE 4130, 4340 (150 ksi HT)	60,000 lb/in ²
Titanium 6AL-4V	(Annealed Condition)	60,000 lb/in ²

In addition to the general material endurance limit stresses, the special case of cyclically loaded lugs in a chafing environment has been extensively studied (Reference 21). Testing was accomplished on standard size lugs, and a standard lug endurance limit nominal stress $(\sigma_{en})_s$ was determined. From this result, a mean endurance limit nominal stress for any lug (see Figure 202) can be determined by equation (68).

$$(\delta_{en})_m = \frac{2.8 (d + 0.1166D)}{D (1.0 + d)} (\delta_{en})_s \quad (68)$$

This relationship includes the effects of both lug size and stress concentration.

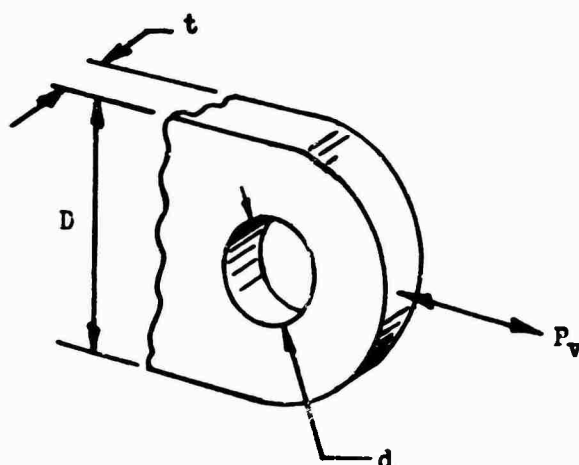


Figure 202 General Lug Configuration

The standard endurance limit stress for lugs with chafing is given in Table LVII.

TABLE LVII
STANDARD ENDURANCE LIMITS FOR LUGS WITH CHAFING

Material	Alloy	(δ en)s
Aluminum	7075-T73	1,880 lb/in ²
Steel	SAE 4130, 4340 (150 ksi HT)	7,400 lb/in ²
Titanium	6AL-4V (Annealed Condition)	11,400 lb/in ²

There are conflicting experimental data concerning the effect of specimen size on material endurance limit stress (Reference 19, Chapter VIII). The conservative approach of assuming a reduction in material endurance limit stress with increase in component size has been followed in this analysis. The ratio of the volume of highly stressed material in the component to the standard specimen volume is calculated and the size effect factor (SEF) is then obtained from a standard curve of SEF versus volume ratio (see Figure 203).

For machined surface finishes employed in rotor head structural components, a machining factor equal to 0.80 is used, and is based on various tests comparing machined specimens with standard polished specimens.

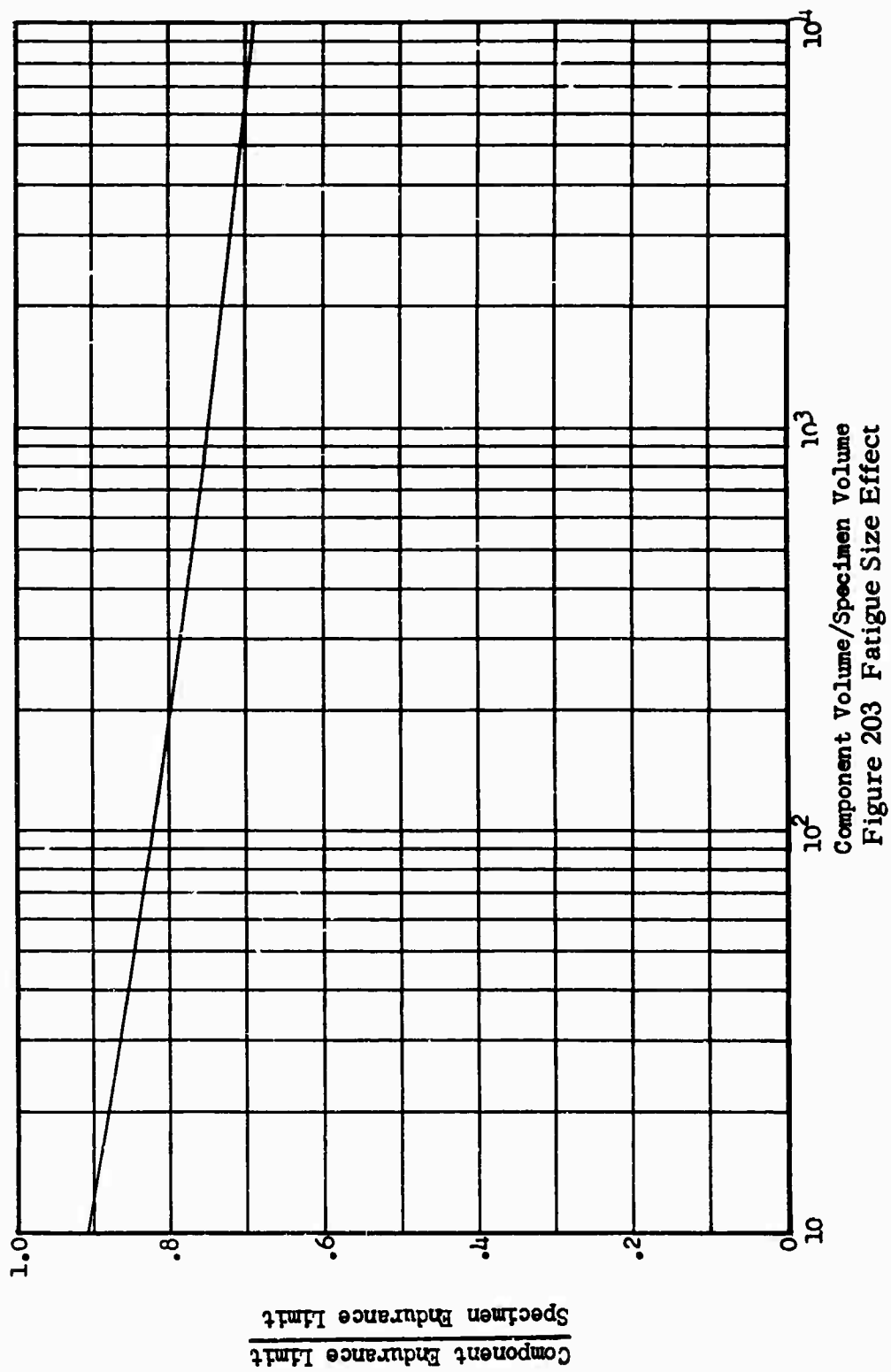


Figure 203 Fatigue Size Effect

If a component is to be designed to a given reliability, the scatter of test data with respect to the standard mean S-N curve must be taken into account. This is done by applying the normal distribution concept of statistics to the test data. A visual representation of this technique is shown in Figure 204.

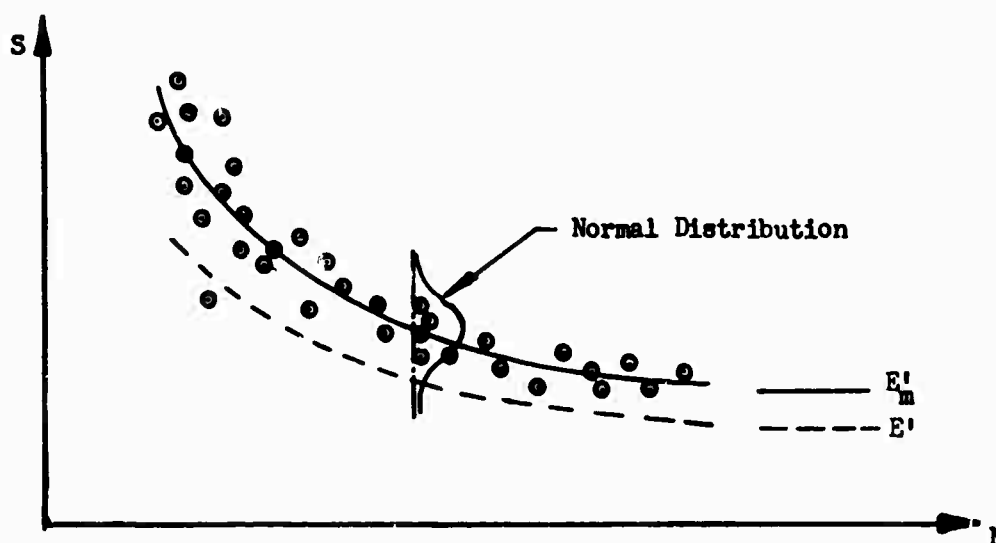


Figure 204 Allowable Endurance Limit

The allowable endurance limit (E') is obtained by reducing the mean endurance limit (E'_m) by multiplying it by a probability factor (PF) which accounts for both the given material and the desired degree of structural reliability.

The heavy lift helicopter rotor system will be designed for a reliability of 99.99 percent (a failure rate of 1 in 10,000 specimens). The factors for this reliability are given in Table LVIII

TABLE LVIII
PROBABILITY FACTORS FOR 99.99 PERCENT RELIABILITY

Material	Alloy	Probability Factor (PF)	
		Solid Sections	Hollow Shafts
Aluminum	7075-T73	0.519	0.519
Steel	SAE 4130, 4340 (150 ksi HT)	0.630	0.630
Titanium	6AL-4V (Annealed Condition)	0.630	0.482

In general, conservative idealizations of actual design geometries are made to enable use of the stress concentration data which are available in the literature (References 38 and 41). In areas where the theoretical stress concentration factor (SCF) is unity, an SCF equal to 1.2 is used. The reason for this practice is to account for accidental surface marring and future salvage operations on the component. This conservative approach permits component design to zero margins without compromising the in-service integrity of the aircraft. Stated otherwise, the margins can be considered to be representative of aircraft condition in the field.

The general solution for fatigue margin of safety is given by equation (69).

$$MS = \frac{1}{\frac{\delta_s}{\delta_{ty}} + \frac{(SCF)\delta_v}{E'}} - 1 \quad (69)$$

Sikorsky Aircraft's experience with the fatigue testing of 6AL-4V titanium alloy components has indicated that the steady stress in a region of stress concentration is not effectively reduced by local yielding, as would be implied by equation(70). The margin of safety for this titanium alloy is calculated with equation(70).

$$MS = \frac{1}{\frac{(SCF)\delta_s}{\delta_{ty}} + \frac{(SCF)\delta_v}{E'}} - 1 \quad (70)$$

These equations are based on the Soderberg relationship between steady stress and endurance limit stress (Reference 46). The Soderberg diagrams for the three primary structural metals considered in this study are given in Figure 205.

When the critical stress location of a cross section is on a shot-peened surface, an additional criterion must be satisfied. To prevent relief of the residual compressive stresses acquired from shot-peening, the maximum stress (i.e., the sum of steady and vibratory stress magnitudes) must be not greater than 60 percent of the minimum yield stress of the material.

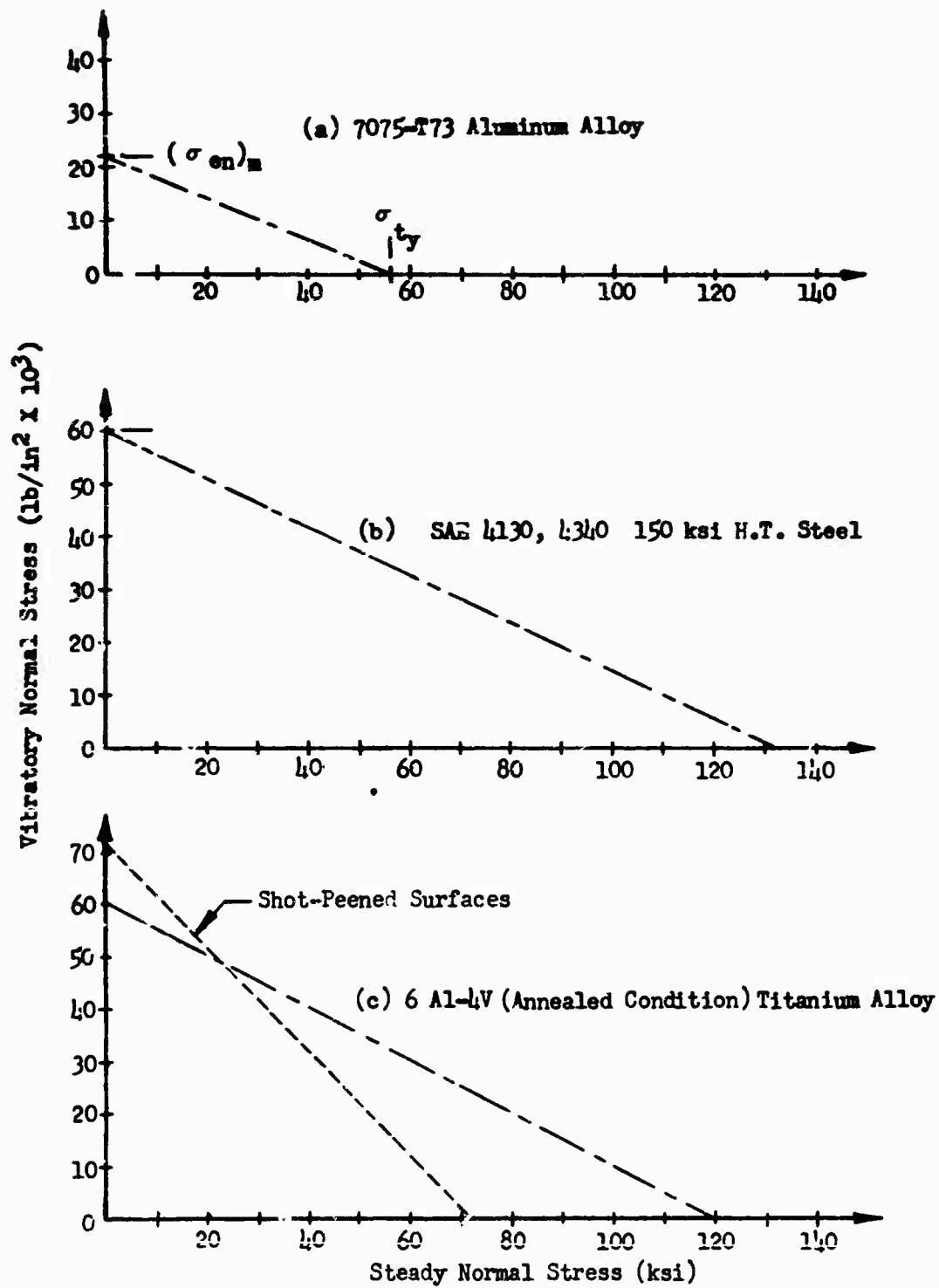


Figure 205 Soderberg Diagrams

CALCULATION OF DESIGN LOADS

Static Structural Design Loads

Starting Condition

The rotor is designed to be started and brought up to speed by either one or two engines. The maximum torque that can be applied by two engines at any rotor speed is 4,500,000 inch-pounds, based on the 5-second engine torque rating. Buildup of applied torque to this limiting value requires that a period of time on the order of several seconds must elapse. During this time the rotor would have accelerated sufficiently for the blades to move away from the lag stops under the influence of centrifugal force.

Critical rotor starting loads are generated, however, with the blades against their lag stops and with no centrifugal relief of in-plane moments. The rotor must therefore be stationary in the condition represented in the analysis. The starting torque for this condition is taken as 3,500,000 inch-pounds, which is estimated to be at least 50 percent greater than the maximum two-engine torque at zero speed. For the six-bladed rotor, the starting torque is assumed to be distributed to only four of the six blades.

It should be noted that although paragraph 3.3.1 of Reference 52 is not directly applicable, the above loading assumptions are in agreement with the spirit of that specification.

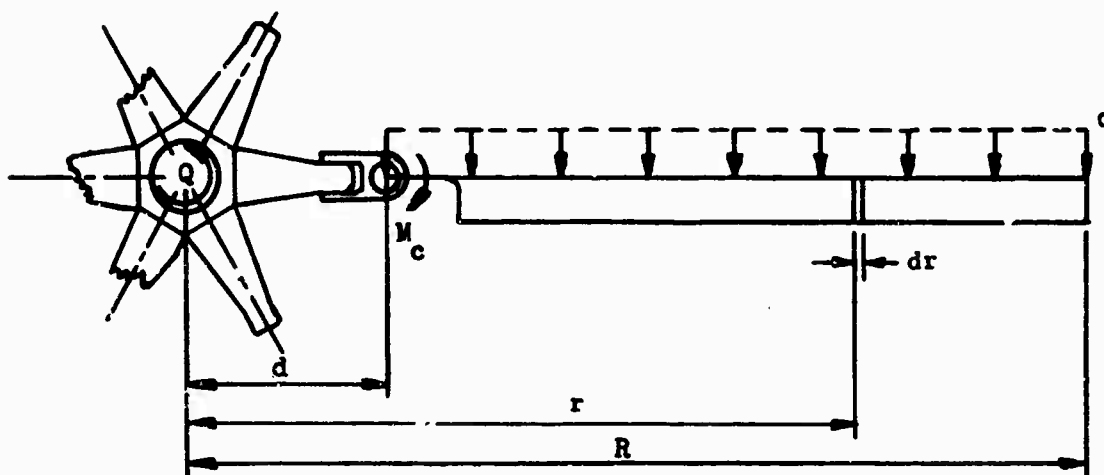


Figure 206 Blade Shear Distribution Under Starting Condition

The applied main rotor torque (Q) is conservatively assumed to be reacted solely by the inertial force distribution along the blades, the inertia of the rotor hub being neglected. The blade is against its lag stop and is there-

fore treated as a cantilever beam rigidly built in at the lead-lag pin.

The exact inertial load distribution along the blade radius (r) is quite complicated. It can be expressed as the discontinuous function

$$\begin{aligned} q(r) &= [\text{mass/unit length @ } r] [\text{tangential acceleration @ } r] \\ &= m(r) r \ddot{\alpha}_q \end{aligned}$$

The inboard portion of the blade is much heavier than the outboard portion. Not only does the spar taper, but there is a considerable concentration of mass at the extreme root end due to the flapping hinge, sleeve and spindle assembly, and blade cuff. Hence the mass per unit length term $m(r)$ decreases with increasing blade radius (r), while the tangential acceleration ($r\ddot{\alpha}_q$) increases linearly with increasing blade radius. The blade inertial loading, being the product of these terms, can most conveniently be approximated by a uniform load distribution $q(r) = q$ for analytical purposes (see Figure 206).

The reactions V and M_c of the blade at the lead-lag hinge are evaluated below.

$$V = \int_d^R q dr = q (R - d) \quad (71)$$

$$M = \int_d^R q r dr = \frac{1}{2} q (R - d)^2 \quad (72)$$

The torque applied to an individual blade, computed at the shaft centerline, is

$$\begin{aligned} 1/4Q &= Vd + M_c \\ &= q(R-d)d + 1/2 q (R-d)^2 \\ &= 1/2 q (R^2 - d^2) \end{aligned}$$

Solving for the blade distributed load (q),

$$q = \frac{Q}{2(R^2 - d^2)} \quad (73)$$

The load reactions at the lead-lag hinge for the critical torque are

$$q = \frac{3,500,000}{2[(550.0)^2 - (46.8)^2]} = 5.827 \text{ lb/in}$$

$$V = 5.827 (550.0 - 46.8) = 2930 \text{ lb}$$

$$M_c = 1/2 (5.827) (550.0 - 46.8)^2 = 737,200 \text{ in-lb}$$

The starting moment and shear at any radial distance (r) from the shaft centerline is given by equations(74) and(75).

$$V_r = q (R - r) \quad (74)$$

$$M_r = 1/2 q (R - r)^2 \quad (75)$$

Rotor Overspeed

The design maximum rotor speed occurs in the power-off autorotative condition (153 revolutions per minute). A design limit rotor speed equal to 1.10 times the design maximum speed (168 revolutions per minute) will be used for the static substantiation of the rotor system in the overspeed condition. Refer to Figure 119 for the centrifugal force at design limit rotor speed as a function of blade radius.

Fatigue Structural Design Loads

The fatigue structural design loads are developed herein. The fatigue loading of the heavy lift helicopter main rotor head and control system can be resolved into the following component loadings:

Centrifugal force (F_c)

Normal shear force (V_n)

Chordwise shear force (V_c)

Damping moment (M_d)

Pitching moment (M_p)

The fatigue design loads will be developed in detail for 6AL-4V titanium alloy without chafing, as described under "Development of Design Loads", to illustrate the approach used. Table LX at the end of this section lists the design loads for the materials and chafing conditions considered.

Centrifugal Force

With the main rotor blade in its radially outward position (i. e., perpendicular to the main rotor shaft) and the rotor shaft turning at normal power-on speed (146 revolutions per minute), the centrifugal force at the flapping pin is 115,000 pounds. However, since the blade is flapping with respect to the rotor hub (see Figure 207), the blade mass is continuously changing its radial position with respect to the main rotor shaft. Thus, the rotor head experiences a varying centrifugal force.

If the centrifugal force at the flapping pin $(F_C)_0$, the steady cone angle (β_s) , and the flapping angle (β_v) are all known, then the centrifugal force loading of the blade on the rotor hub can be determined.

If $\beta_v < \beta_s$, then

$$(F_C)_{\text{maximum}} = (F_C)_0 \cos (\beta_s - \beta_v) \quad (76)$$

$$(F_C)_{\text{minimum}} = (F_C)_0 \cos (\beta_s + \beta_v) \quad (77)$$

If $\beta_v > \beta_s$, then

$$(F_C)_{\text{maximum}} = (F_C)_0 \quad (78)$$

$$(F_C)_{\text{minimum}} = (F_C)_0 \cos (\beta_s + \beta_v) \quad (79)$$

Now let us determine the cone and flapping angles. Statistically, the cone angle (β_s) is given by the relationship

$$\tan \beta_s = \frac{1/b (\text{Aircraft GW}) - \text{blade weight}}{(F_C)_{\text{of blade at } \beta_s}} \quad (80)$$

Now, aircraft GW = 55,940 lb (prorated time)

Blade Weight \approx 1100 lb

b = number of blades = 6

$(F_C)_0$ = 115,000 lb

$$\text{Then, } \tan \beta_s = \frac{1/6(55940) - 1100}{(115,000) \cos \beta_s}$$

This relationship requires an iterative solution, since the unknown quantity (β_s) is given in terms of a variable $\cos \beta_s$ which itself is a function of the unknown.

$$\tan \beta_s = \frac{0.0715}{\cos \beta_s}$$

The iterative solution for the initial assumption of $\beta_s = 0.0^\circ$ is given in Table LIX.

Note that for the small coning angle involved here the convergence is essentially attained in one iteration.

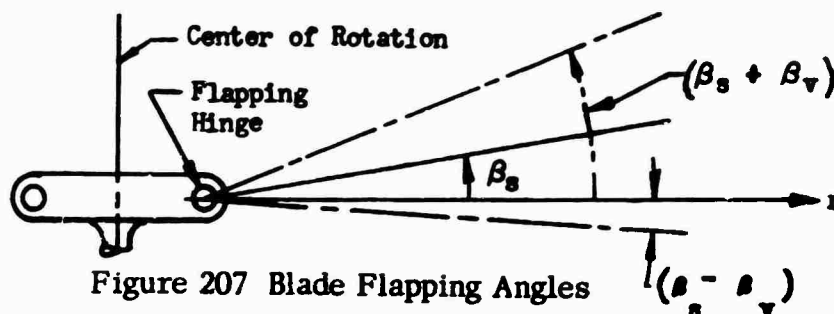


Figure 207 Blade Flapping Angles

TABLE LIX
BLADE CONING ANGLE ITERATION

β_s	$\cos \beta_s$	$x = \frac{0.0715}{\cos \beta_s}$	$\beta_s = \arctan x$
0.0°	1.000	0.07150	4° 5'
4° 5'	0.9975	0.07168	4° 6'
4° 6'	0.9974	0.07169	4° 6'

The design flapping angles are based on a component replacement time of 3,600 hours, the particular material being used, and their environmental surface condition. Figures 208 through 210 show plots of the design flapping angles versus replacement times for steel and titanium both with and without chafing. For example, the design flapping angle for 6AL-4V titanium alloy components, not subjected to a chafing environment, is determined by referring to Figure 208.

$$\beta_v = \pm 5.8 \text{ degrees}$$

In summary,

$$(F_c)_0 = 115,000 \text{ lb}$$

$$\beta_s = 4^\circ 6'$$

$$\beta_v = \pm 5^\circ 48'$$

Since $\beta_v > \beta_s$, the centrifugal force loading is

$$(F_c)_{\text{maximum}} = 115,000 \text{ lb}$$

$$\begin{aligned} (F_c)_{\text{minimum}} &= (115,000) \cos (4^\circ 6' + 5^\circ 48') \\ &= 113,200 \text{ lb} \end{aligned}$$

$$\text{Therefore, } F_c = (114,100 \pm 900) \text{ lb}$$

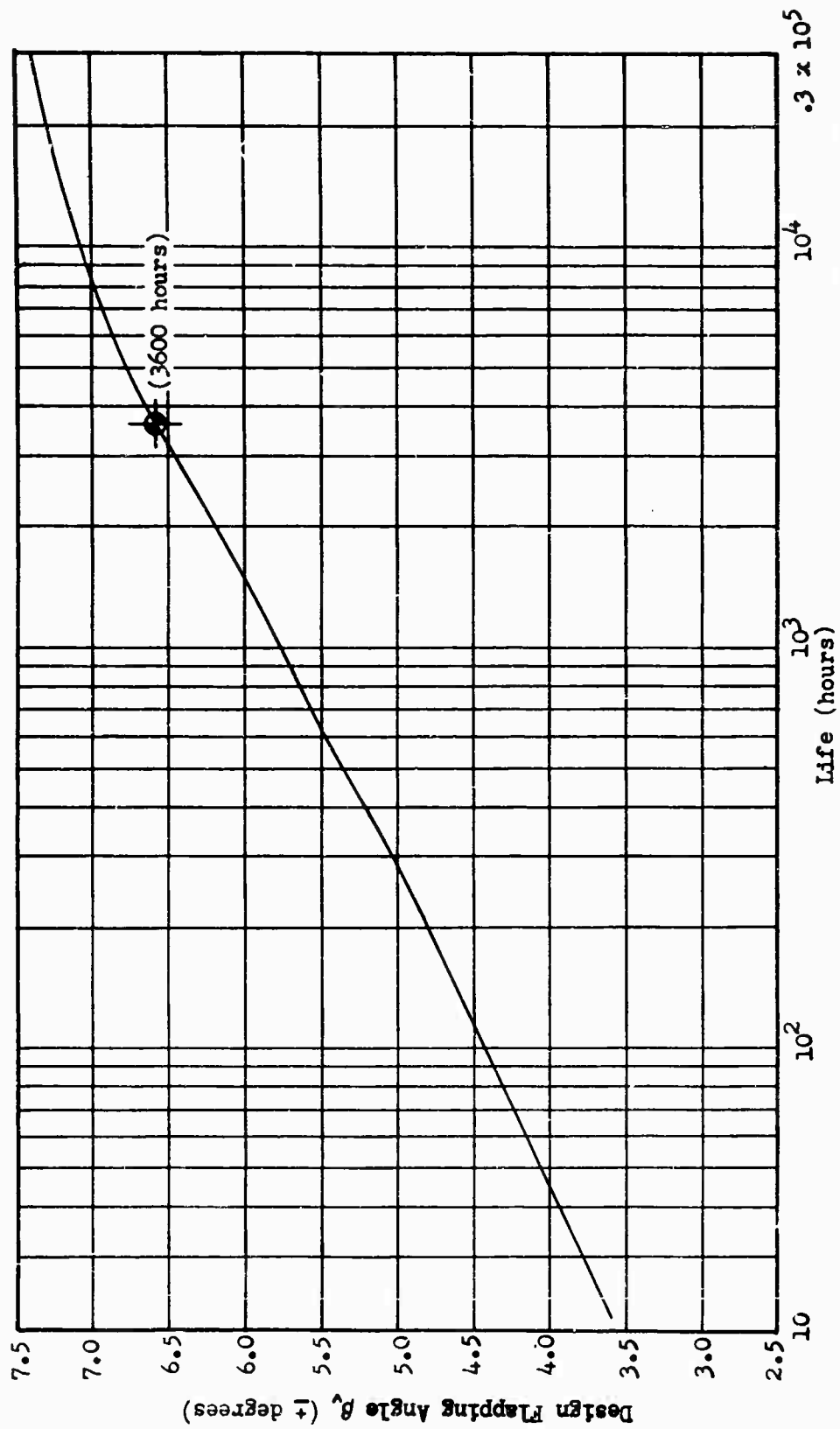


Figure 208 Flapping Angle Versus Structural Replacement Time, Titanium Without Chafing

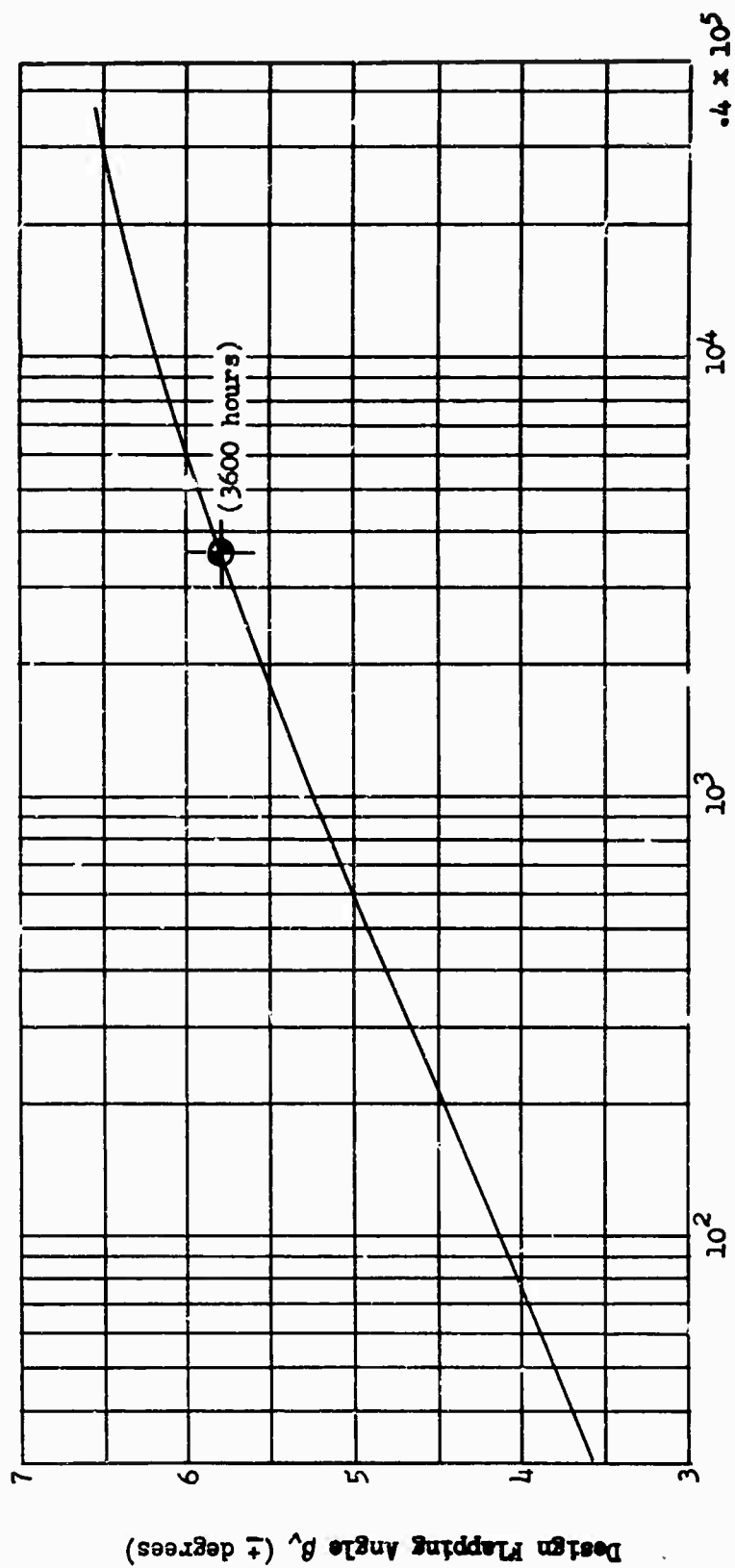


Figure 209 Flapping Angle Versus Structural Replacement Time, Steel without Chafing

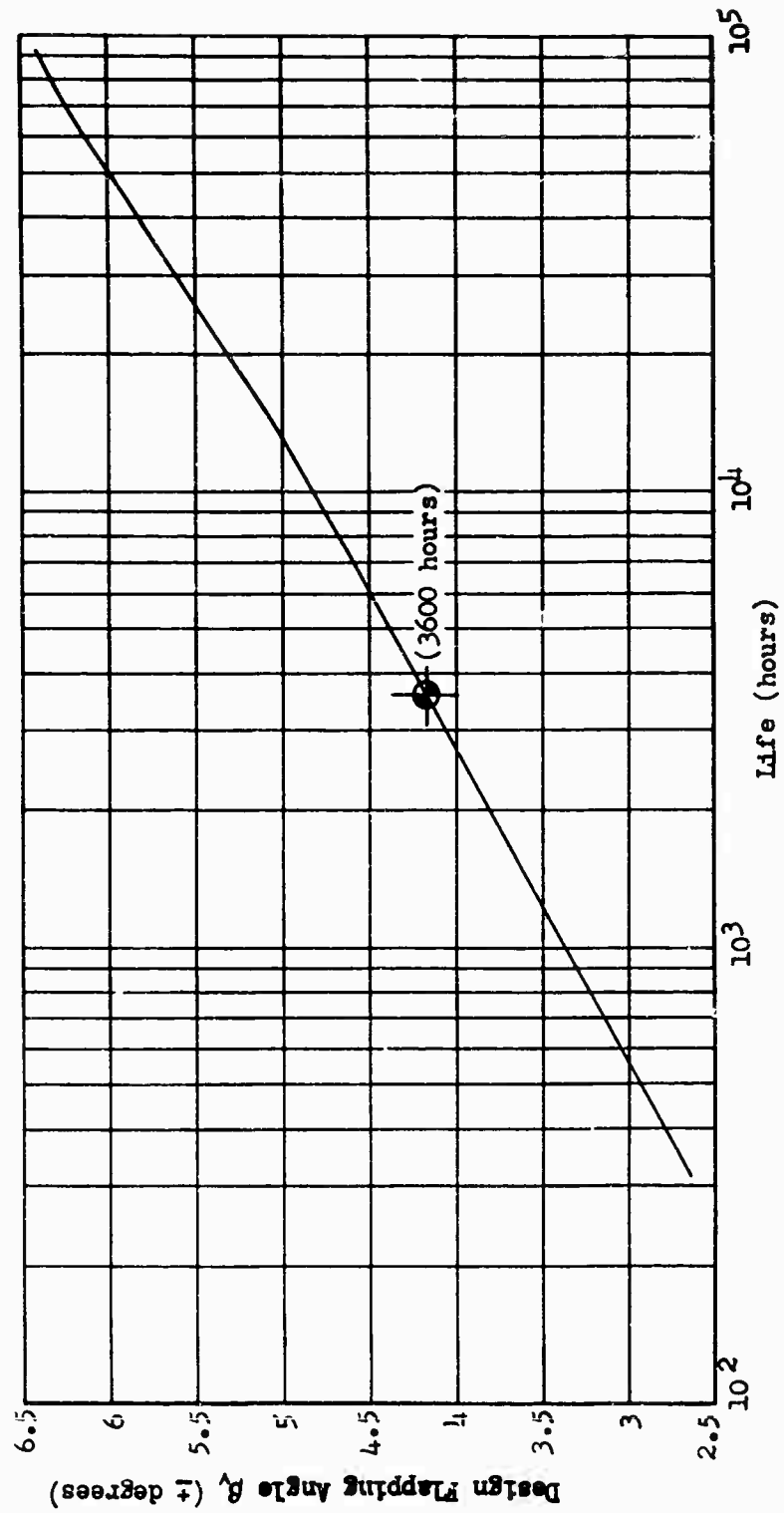


Figure 210 Flapping Angle Versus Structural Replacement Time, Steel and Titanium with Chafing

Normal Shear Force

The steady normal shear force $(V_n)_s$ is given simply by the static relationship below:

$$\begin{aligned}(V_n)_s &= \frac{1}{b} (\text{Aircraft GW}) - \text{blade weight} \\ &= \frac{1}{6} (55,940) - 1100 \\ &= 8220 \text{ lb}\end{aligned}\tag{81}$$

The vibratory normal shear is determined from the design flapping angle and the blade centrifugal force.

$$\begin{aligned}(V_n)_v &= F_c \tan \theta_v \\ &= (114,100) \tan (\pm 5^\circ 48') \\ &= \pm 11,590 \text{ lb}\end{aligned}\tag{82}$$

Chordwise Shear Force

The chordwise steady shear is based on the time prorated main rotor shaft horsepower. Assuming that all the blades react the shaft torque equally, the steady chordwise shear force is given by the formula

$$(V_c)_s = \frac{63,025 (\text{MRHP})}{e_d N b}\tag{83}$$

where e_d = hunting hinge offset = 46.8 in

N = 146 rpm

b = 6 blades

MRHP = 5230 horsepower (2 engines)

$$(V_c)_s = \frac{(63,025) (5230)}{(46.8) (146) (6)} = 8040 \text{ lb}$$

Hunting results from the Coriolis accelerations of the flapping blade. In normal forward flight, the advancing blade hunts forward, while the retreating blade hunts aft. The inflowing airstream and the damper moments oppose this motion, causing reduction of amplitude and modifying slightly the harmonic character of the motion. The amplitude is not strongly dependent on the amplitude of flapping motion. For blades of similar design, experience has consistently shown a 1:10 ratio of hunting to flapping amplitude over a wide range of blade sizes and aircraft characteristics. Thus, the design hunting amplitude is taken as $\pm 0.6^\circ$.

$$(V_C)_V = (F_C @ \text{hunting hinge}) \tan \delta_V \quad (84)$$

where $F_C @ \text{hunting hinge} = 112,500 \text{ lb}$

$$\delta_V = \pm 0.6 \text{ deg}$$

$$\begin{aligned} (V_C)_V &= (112,500) (\pm 0.01047) \\ &= \pm 1180 \text{ lb} \end{aligned}$$

Damping Moment

The damper must absorb energy from the dynamic system. For a wide variety of rotor systems designed by several manufacturers, the maximum value of damper moment has been shown to be directly related to blade rotational kinetic energy; for equal hunting amplitudes at one cycle per rotor revolution, this further implies absorption by the damper of a constant portion of the blade's hunting energy, which is a rotational basis for load prediction. The design value of damper moment for structural analysis is thus taken as

$$M_d = 0.002 I \Omega^2 \quad (85)$$

where M_d = design damping moment

I = blade mass moment of inertia about flapping hinge
(in-lb-sec²)

Ω = normal power-on rotor velocity (rad/sec)

For the heavy lift helicopter rotor system,

$$I = 127,900 \text{ in-lb-sec}^2$$

$$\Omega = 15.29 \text{ rad/sec}$$

The design damping moment is then

$$\begin{aligned} M_d &= (0.002) (127,900) (15.29)^2 \\ &= \pm 59,800 \text{ in-lb} \end{aligned}$$

Some degree of conservatism is indicated by the fact that the widespread landing gear of the heavy lift helicopter provides greater freedom from ground resonance than on most helicopters, which would in turn allow the use of lower damper settings.

Pitching Moment

Aeroelastic analysis of the blade yields pitching moments for steady-state conditions. For control system design, however, an empirical method is used to encompass both steady-state flight conditions and maneuver conditions for which the rotor may not be equilibrated. The pitching moment is determined on the basis of an empirical relationship among the basic rotor system parameters as determined from flight testing. The parameters of the rotor system required are

$$C_T = \text{Rotor Thrust Coefficient}$$

$$= \frac{(\text{Rotor Thrust})}{(\text{Tip Speed})^2 (\text{Disk Area}) (\text{Air Density})} = \frac{T}{(\Omega R)^2 \pi R^2 \rho} \quad (86)$$

$$\sigma = \text{Rotor Solidity} \quad (87)$$

$$= \frac{(\text{Number of Blades}) (\text{Blade Chord}) (\text{Blade Radius})}{(\text{Disk Area})} = \frac{bcR}{\pi R^2}$$

$$\mu = \text{Advance Ratio}$$

$$= \frac{(\text{Forward Speed})}{(\text{Tip Speed})} = \frac{V}{\Omega R} \quad (88)$$

The pitching moment coefficient (C_{mb}) is

$$C_{mb} = \frac{(M_p)_v}{c^2 R q} \quad (89)$$

where

$(M_p)_v$ = vibratory pitching moment, ft-lb

c = blade chord, ft

R = blade radius, ft

q = dynamic pressure = $\frac{1}{2} \rho \bar{V}^2$

\bar{V} = velocity at blade tip on retreating side

= $\Omega R - V$, ft/sec

V = forward velocity, ft/sec

ρ = air density = 0.0023 slugs/ft³

Flight test data from all models of Sikorsky Aircraft helicopters, when reduced to the quantities (C_{mb}/C_T) and μ , yield an exponential relation-

ship between them.

In order to determine a design pitching moment for the heavy lift helicopter, three conditions of flight were investigated:

- (1) 32,800 lb GW at 130 kn
- (2) 65,800 lb GW at 110 kn
- (3) 78,800 lb GW at 95 kn

It was found that condition (1) gave the highest pitching moment. The detailed development of the pitching moment for this condition of flight follows:

$$\frac{C_T}{\sigma} = \frac{T}{(\Omega R)^2 \rho R c b} \quad (90)$$

$$T = 32,800 \text{ lb}$$

$$\Omega = 15.29 \text{ rad/sec}$$

$$R = 550 \text{ in} = 45.8 \text{ ft}$$

$$\rho = 0.0023 \text{ slugs/ft}^3$$

$$c = 31 \text{ in} = 2.58 \text{ ft}$$

$$b = 6$$

Substitution into the above equation gives

$$\frac{C_T}{\sigma} = 0.0402$$

The advance ratio μ is

$$\mu = \frac{V}{\Omega R}$$

$$V = (130 \text{ kn}) (1.689 \frac{\text{ft/sec}}{\text{kn}}) = 219 \text{ ft/sec}$$

$$\Omega R = (15.29 \frac{\text{rad}}{\text{sec}}) (45.8 \text{ ft}) = 700 \text{ ft/sec}$$

$$\mu = 0.314$$

From the parametric curve relating $(C_{mh}/\frac{C_T}{\sigma})$ and μ , a value of 0.27 is obtained for $C_{mh}/\frac{C_T}{\sigma}$ for $\mu = 0.314$.

$$C_{mb} = 0.27 \frac{C_T}{\sigma} = (0.27) (0.0402) = 0.0108$$

$$\text{Now, } C_{mb} = \frac{(M_p)_v}{Rc^2q} = 0.0108 \quad (91)$$

$$q = \frac{1}{2} \rho \bar{v}^2 = \frac{1}{2} (0.0023) (700-219)^2$$

$$= 543 \text{ lb/ft}^2$$

$$\text{Then } (M_p)_v = (0.0108) (45.8) (2.58)^2 (543)$$

$$= \pm 1790 \text{ ft-lb} = 21,500 \text{ in-lb}$$

The steady pitching moment is conservatively taken as 60 percent of the vibratory pitching moment.

$$(M_p)_s = 0.60 (M_p)_v \quad (92)$$

$$= 12,900 \text{ in-lb}$$

In order to account for the effective moment arm of the control rod about the pitching axis, it is assumed that the true angle between the control rod axis and the horn offset at the maximum and minimum blade pitch angles is 65 degrees.

$$\text{Control rod load} = \frac{\text{Pitching Moment}}{\text{Effective Moment Arm}} \quad (93)$$

$$= \frac{(12,900 \pm 21,500)}{9.0 \sin 65^\circ}$$

$$= (1580 \pm 2640) \text{ lb}$$

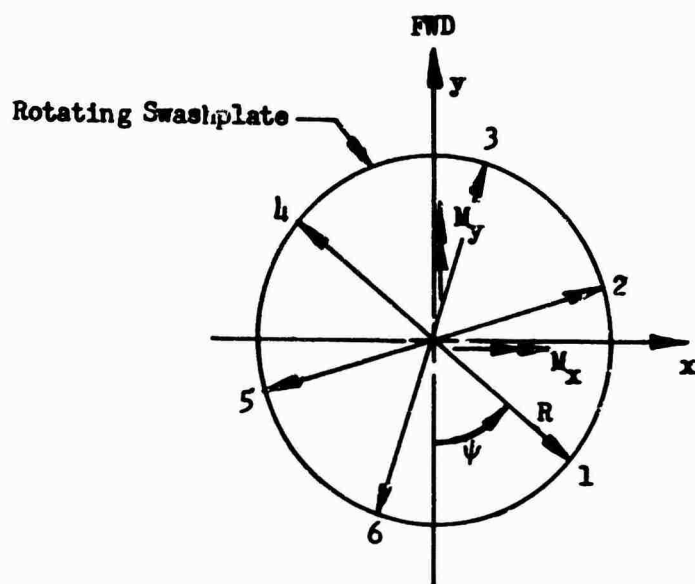


Figure 211 Swashplate Assembly Loading

The control rod vibratory load is considered to be a pure first harmonic.

If $P_1 = P_S + P_V \sin \psi$,

then $P_2 = P_S + P_V \sin (\psi + 60^\circ)$

$P_3 = P_S + P_V \sin (\psi + 120^\circ)$

$P_4 = P_S + P_V \sin (\psi + 180^\circ)$

$P_5 = P_S + P_V \sin (\psi + 240^\circ)$

$P_6 = P_S + P_V \sin (\psi + 300^\circ)$

NOTE: Points 1, 2, 3, 4, 5, and 6 correspond to loads P_1 , P_2 , P_3 , P_4 , P_5 , and P_6 perpendicular to the plane of the paper in Figure 211.

Now let us consider static equilibrium of the rotating swashplate (see Figure 211).

Sum of Vertical Forces (F_V)

$$F_V = \sum P_i$$

$$= 6P_S + P_V \left[\sin \psi + \sin (\psi + 60^\circ) + \sin (\psi + 120^\circ) + \sin (\psi + 180^\circ) + \sin (\psi + 240^\circ) + \sin (\psi + 300^\circ) \right]$$

$$F_V = 6P_S \quad (94)$$

Moments about x Axis (M_x)

$$\frac{M_x}{R} = P_1 \cos \psi + P_2 \cos (\psi + 60^\circ) + P_3 \cos (\psi + 120^\circ) + P_4 \cos (\psi + 180^\circ) + P_5 \cos (\psi + 240^\circ) + P_6 \cos (\psi + 300^\circ)$$

$$M_x = 0 \quad (95)$$

Moments about y Axis (M_y)

$$\frac{M_y}{R} = P_1 \sin \psi + P_2 \sin (\psi + 60^\circ) + P_3 \sin (\psi + 120^\circ) + P_4 \sin (\psi + 180^\circ) + P_5 \sin (\psi + 240^\circ) + P_6 \sin (\psi + 300^\circ)$$

$$M_y = 2P_v R \quad (96)$$

If our assumption of a pure first harmonic control rod force is accurate, then we should expect very small vibratory loads in the stationary control system.

For the heavy lift helicopter control system,

$$R = 22.2 \text{ in}$$

$$P_s = 1580 \text{ lb}$$

$$P_v = 2640 \text{ lb}$$

The stationary swashplate loads are

$$F_v = 6P_s = 9480 \text{ lb}$$

$$M_x = 0$$

$$M_y = 2P_v R_s = 117,200 \text{ in-lb}$$

The assumption of a pure first harmonic vibratory pitching moment in the rotating system of a six-bladed rotor has generated only steady loads (F_v and M_y) in the stationary system. In reality, the vibratory pitching moment contains higher harmonics, some of which will transfer into the stationary system as vibratory loads. For conservatism, the design stationary swashplate loads are therefore taken as

$$T \text{ (thrust)} = F_v \pm 0.50 F_v$$

$$M \text{ (moment)} = M_y \pm 0.50 M_y$$

or, $T = (9480 \pm 4740) \text{ lb}$

$$M = (117,200 \pm 58,600) \text{ in-lb}$$

The stationary swashplate, Figure 212, servo loads are maximum if the swashplate is oriented with respect to the y-axis, so that the single servo must resist the entire moment M_y .

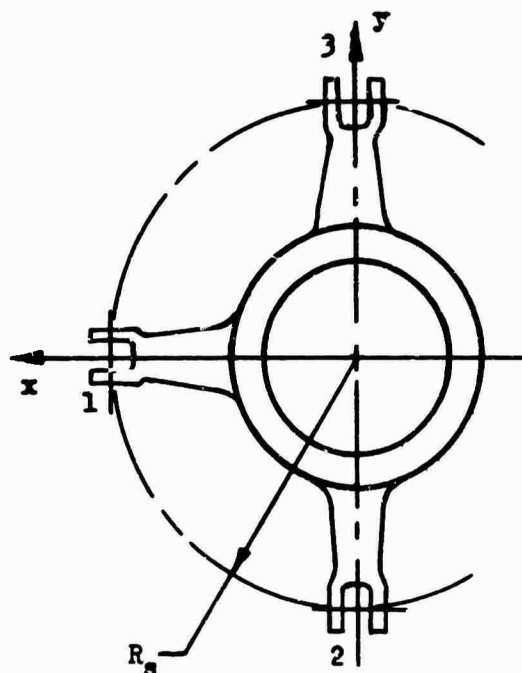


Figure 212 Stationary Swashplate Servo Loading

If P_1 , P_2 , P_3 are loads of servos 1, 2, and 3, respectively, then static equilibrium requires that

$$\left. \begin{aligned} P_1 + P_2 + P_3 &= T \\ P_2 &= P_3 \\ P_1 &= -M/R \end{aligned} \right\} \text{ NOTE: Points 1, 2, and 3 correspond to loads } P_1, P_2, \text{ and } P_3 \text{ perpendicular to the plane of the paper in Figure 212.}$$

Solving these equations for the applied loads F_v and M_y , the servo loads are

$$P_1 = (-4290 \pm 2150) \text{ lb}$$

$$P_2 = P_3 = (6890 \pm 3450) \text{ lb}$$

Table LX shows a summary of the design fatigue loads calculated for titanium without chafing. A comparison is shown with steel without chafing and steel/titanium with chafing.

STATIC STRESS ANALYSIS

Starting Condition

Section A-A of Figure 213 - Sleeve with Integral Control Arm

In order to determine the loads on this section, an assumption is made as to the transfer of load from sleeve to spindle. To be conservative, let 50 percent of the moment at this radial location be transferred through Section A-A.

Loads at Section A-A, $r = 56.8 \text{ in}$

$$\left. \begin{array}{l} V_r = 2873 \text{ lb} \\ M_r = 708,600 \text{ in-lb} \end{array} \right\} \begin{array}{l} \text{Refer to Equations} \\ 71 \text{ and } 72 \text{ Page } 360 \end{array}$$

For a sinusoidal distribution of moment at Section A-A, the maximum bearing force, per inch of circumference, between the shoulder and stack bearing is given by

$$q_{\max} = \frac{M}{\pi R^2} \quad (97)$$

For the inboard sleeve shoulder, see Detail E of Figure 213.

$$M = 0.50 M_r = 354,300 \text{ in-lb}$$

$$R = 4.37 \text{ in}$$

$$q_{\max} = \frac{354,300}{\pi(4.37)^2} = 5910 \text{ lb/in}$$

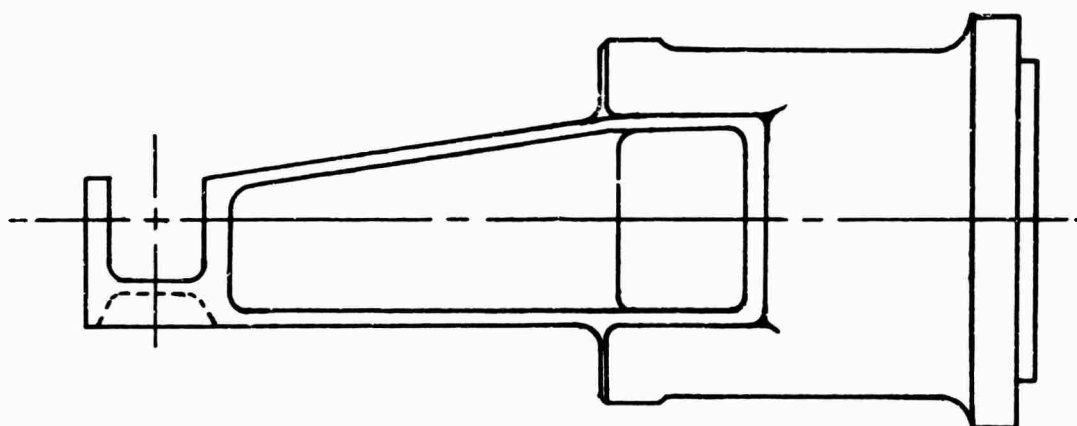
The corresponding moment distribution on Section A-A is

TABLE LX
DESIGN FATIGUE LOAD SUMMARY

DESIGN LOAD	MATERIAL & CHAFING ENVIRONMENT		
	STEEL WITHOUT CHAFING	TITANIUM WITHOUT CHAFING	STEEL & TITANIUM WITH CHAFING
Centrifugal Force @ Flapping Hinge (F_c)	(114,000 \pm 1000) lb	(114,100 \pm 900) lb	(114,400 \pm 600) lb
Normal Shear @ Flapping Hinge (V_n)	(8220 \pm 13,020) lb	(8220 \pm 11,590) lb	(8220 \pm 8400) lb
Chordwise Shear @ Hunting Hinge (V_c)	(8040 \pm 1310) lb	(8040 \pm 1180) lb	(8040 \pm 818) lb
Damping Moment (M_d)	\pm 59,800 in-lb	\pm 59,800 in-lb	\pm 59,800 in-lb
Pitching Moment (M_p)	(12,900 \pm 21,500) in-lb	(12,900 \pm 21,500) in-lb	(12,900 \pm 21,500) in-lb
MR Hub Moment (HM)	1,407,000 in-lb	1,252,000 in-lb	907,200 in-lb

STRESS ANALYSIS

STATIC ANALYSIS



Material: 6AL-4V Titanium Alloy (Annealed Condition)

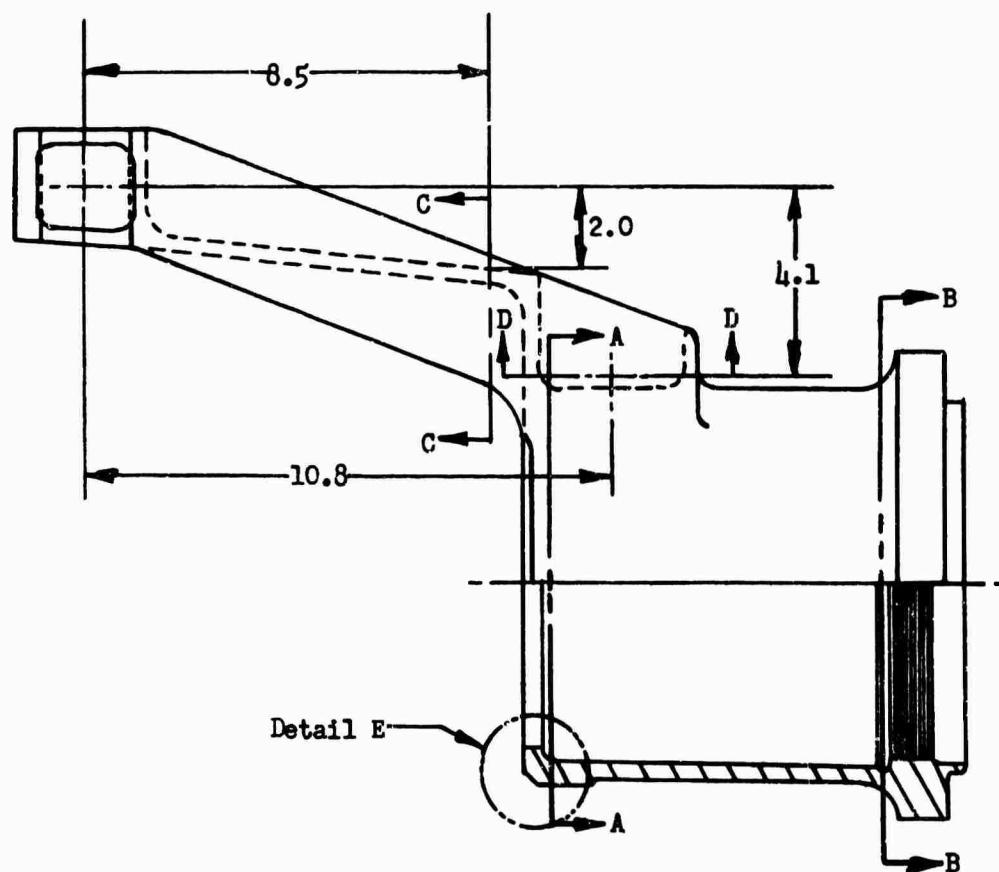
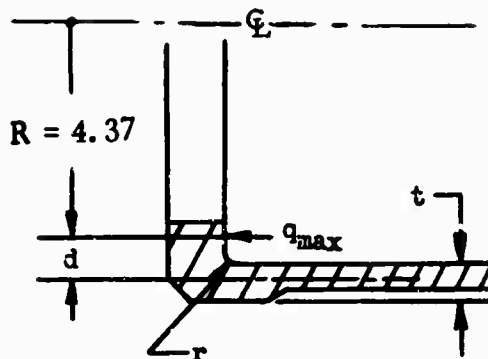


Figure 213 Sleeve with Integral Control Arm

$$\begin{aligned}
 M &= qd \\
 \text{Let } r &= 0.1 \text{ in} \\
 q &= q_{\max} = 5910 \text{ lb/in} \\
 d &= 0.42 \text{ in} \\
 t &= 0.46 \text{ in} \\
 M &= (5910)(.42) \\
 &= 2480 \text{ in-lb/in}
 \end{aligned}$$



Detail E of Figure 213

The maximum stress in the cylinder is calculated using the formula (case 11, Table XIII, Reference 44).

$$\delta_{\max} = \delta_a + \delta_b$$

$$\delta_a = \frac{q}{t} = \frac{5910}{(.46)} = 12,850 \text{ lb/in}^2$$

$$\delta_b = \frac{6M}{t^2} = \frac{6(2480)}{(.46)^2} = 70,320 \text{ lb/in}^2$$

$$\begin{aligned}
 \text{MS (yield)} &= \frac{\delta_{ty}}{1.15 (\delta_a + \delta_b)} - 1 \\
 &= \frac{120,000}{1.15(12,850 + 70,320)} - 1 \\
 &= +0.25
 \end{aligned}$$

$$\begin{aligned}
 \text{MS (ultimate)} &= \frac{1}{1.5 \left(\frac{\delta_a}{\delta_{tu}} + \frac{\delta_b}{\delta_{bu}} \right)} - 1 \\
 &= \frac{1}{1.5 \left(\frac{12,850}{130,000} + \frac{70,320}{190,000} \right)} - 1 \\
 &= +0.42
 \end{aligned}$$

Section B-B of Figure 213

Loads at Section B-B, $r = 63.8$ in

$$V_R = 2832 \text{ lb}$$

$$M_R = 688,600 \text{ in-lb}$$

Section Properties

$$\text{Area (A)} = 6.98 \text{ in}^2$$

$$I = 63.6 \text{ in}^4$$

Stress

$$\begin{aligned}\delta_b &= \frac{Mc}{I} = \frac{(688,600)(4.40)}{63.6} \\ &= 47,600 \text{ lb/in}^2\end{aligned}$$

$$\begin{aligned}\text{MS (yield)} &= \frac{\delta_{tu}}{1.15 \delta_b} - 1 \\ &= \frac{120,000}{1.15 (47,600)} - 1 \\ &= +1.19\end{aligned}$$

Rotor Overspeed

Section A-A of Figure 213

r at Section A-A = 56.8 in

$(F_c)_{cr}$ at A-A = 147,000 lb

$$q = \frac{(F_c)_{cr}}{2\pi R} = \frac{147,000}{2\pi (4.37)} = 5355 \text{ lb/in}$$

$$M = q r = (5355 \text{ lb/in})(0.42 \text{ in}) = 2249 \frac{\text{in-lb}}{\text{in}}$$

$$\text{Now } \delta_a = \frac{q}{t} = \frac{5355 \text{ lb/in}}{0.46 \text{ in}} = 11,600 \text{ lb/in}^2$$

$$\delta_b = \frac{oM}{t^2} = \frac{6 (2249 \frac{\text{in-lb}}{\text{in}})}{(.46 \text{ in})^2} = 63,800 \text{ lb/in}^2$$

$$\text{MS (yield)} = \frac{\delta_{ty}}{1.15 (\delta_a + \delta_b)}^{-1}$$

$$= \frac{120,000}{1.15 (11,600 + 63,800)}^{-1}$$

$$= +0.38$$

Section B-B of Figure 213

r at Section B-B = 63.8 in

$$(F_c)_{cr} = 144,000 \text{ lb}$$

$$\delta_a = \frac{(F_c)_{cr}}{A} = \frac{144,000 \text{ lb}}{6.98 \text{ in}^2}$$

$$= 20,700 \text{ lb/in}^2$$

$$\text{MS (ultimate)} = \frac{\delta_{tu}}{1.5 \delta_a}^{-1} = \frac{130,000}{1.5(20,700)}^{-1}$$

$$= +3.19$$

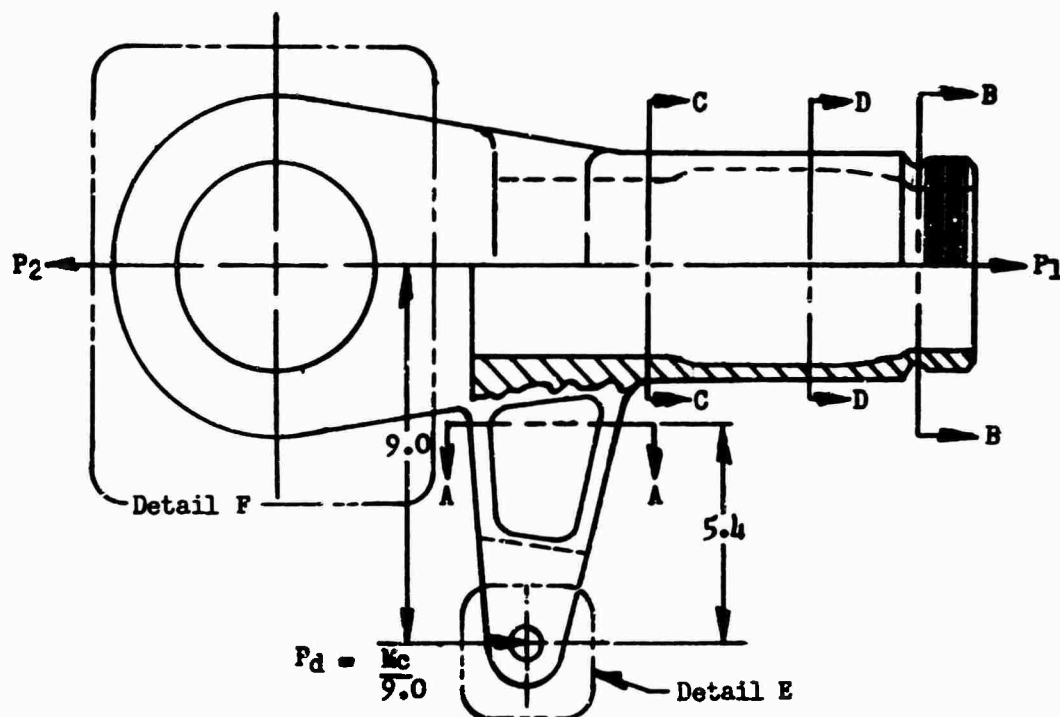
Starting Condition

Section A-A of Figure 214

The load in Section A-A is due to the moment (M_c) about the hunting hinge. The force (P_d) which must react this moment is in a direction approximately parallel to the longitudinal axis of the spindle.

$$P_d = \frac{M_c}{9.0} = \frac{737,200 \text{ in-lb}}{9.0 \text{ in}}$$

$$= 81,910 \text{ lb}$$



Material: 6Al-4V Titanium Alloy (Annealed Condition)

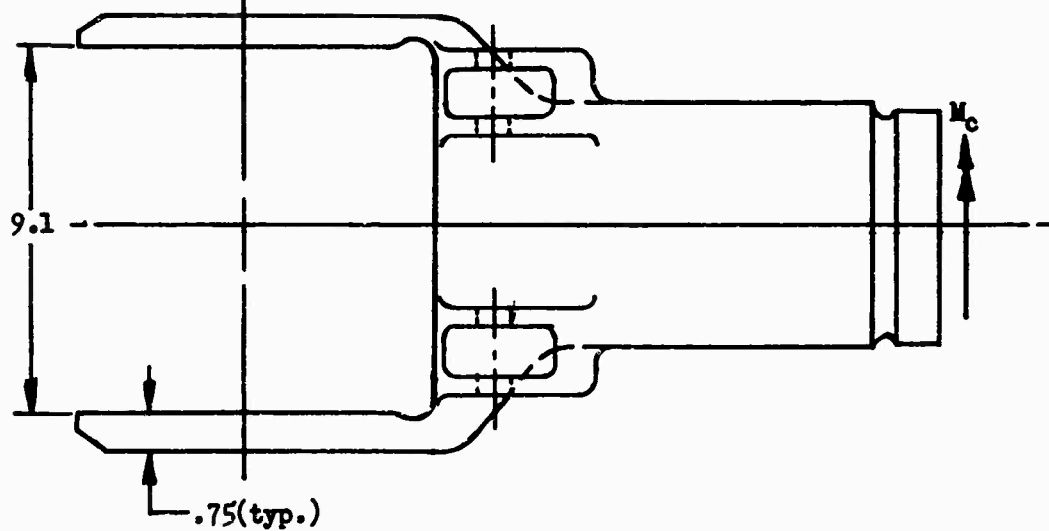
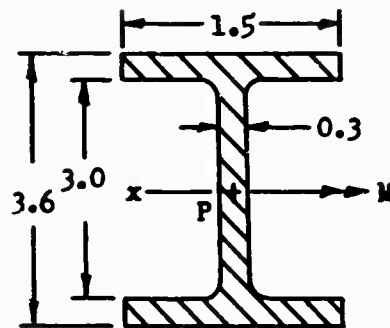


Figure 214 Spindle



Section A-A of Figure 214

The loads on Section A-A are

$$V = \frac{Pd}{2} = 40,960 \text{ lb}$$

$$M = 5.4 \frac{Pd}{2} = 221,220 \text{ in-lb}$$

The section properties are

$$A = 2.28 \text{ in}^2$$

$$c = 1.8 \text{ in}$$

$$I_x = \frac{1}{12} (1.8) (3.6)^3 - \frac{1}{12} (1.4) (3.0)^3 = 3.85 \text{ in}^4$$

$$\begin{aligned} \text{Stress } \delta_b &= \frac{Mc}{I} = \frac{(221,200 \text{ in-lb}) (1.8 \text{ in})}{3.85 \text{ in}^4} \\ &= 103,400 \text{ lb/in}^2 \end{aligned}$$

$$\begin{aligned}
 MS \text{ (yield)} &= \frac{s_{ty}}{1.15 s_b} - 1 \\
 &= \frac{120,000}{1.15(103,400)} - 1 \\
 &= + 0.01
 \end{aligned}$$

Section B-B of Figure 214

It is conservatively assumed that 30 percent of moment at this radial section is transferred through the spindle nut to Section B-B.

Loads: r at Section B-B = 63.3 in

$$V_r = 2835 \text{ lb}$$

$$M_r = 690,000 \text{ in-lb}$$

Section Properties

$$A = 4.33 \text{ in}^2$$

$$I = 11.5 \text{ in}^4$$

$$c = 2.45 \text{ in}$$

$$\begin{aligned}
 \text{Stress } s_b &= .3 \frac{M_r c}{I} = \frac{(.3)(690,000 \text{ in-lb})(2.45 \text{ in})}{11.5 \text{ in}^4}
 \end{aligned}$$

$$= 44,100 \text{ lb/in}^2$$

$$\begin{aligned}
 MS \text{ (yield)} &= \frac{s_{ty}}{1.15 s_b} - 1 \\
 &= \frac{120,000}{1.15(44,100)} - 1 \\
 &= +1.36
 \end{aligned}$$

Section C-C of Figure 214

Loads: r at Section C-C = 53.0 in

$$V_r = 2895 \text{ lb}$$

$$M_r = 719,500 \text{ in-lb}$$

Section Properties

$$A = 7.14 \text{ in}^2$$

$$I = 22.9 \text{ in}^4$$

$$c = 2.75 \text{ in}$$

$$\text{Stress: } \delta_b = \frac{M_r c}{I} = \frac{(719,500 \text{ in-lb})(2.75 \text{ in})}{22.9 \text{ in}^4}$$

$$= 86,400 \text{ lb/in}^2$$

$$\text{MS (yield)} = \frac{\delta_{ty}}{1.15 \delta_b} - 1$$

$$= \frac{120,000}{1.15 (86,400)} - 1$$

$$= +0.20$$

Damper Arm Lugs

The ultimate transverse load is given by the formula (page 167, Reference 22)

$$P'_{tru} = K_{tru} A_{br} F_{tu}$$

$$\text{Now } A_1 = (.80)(1.0) = 0.8 \text{ in}^2 \quad \text{See Detail E of Figure 214}$$

$$A_2 = (.50)(1.0) = 0.5 \text{ in}^2$$

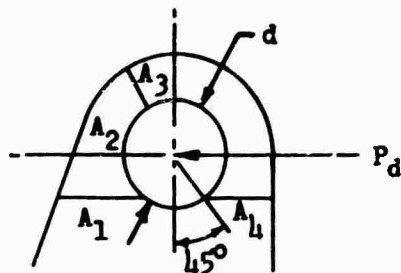
$$A_3 = (.50)(1.0) = 0.5 \text{ in}^2$$

$$A_4 = (.70)(1.0) = 0.7 \text{ in}^2$$

$$A_{av} = \frac{6}{\frac{3}{A_1} + \frac{1}{A_2} + \frac{1}{A_3} + \frac{1}{A_4}} = \frac{6}{9.18} = 0.65 \text{ in}^2 \quad (98)$$

$$A_{br} = (d)(t) = (1.0)(1.0) = 1.0 \text{ in}^2$$

$$\frac{A_{av}}{A_{br}} = \frac{0.65}{1.0} = 0.65$$



Detail E of Figure 214 (Damper Arm Lug)

Since at present no data exist on the static strength of transversely loaded titanium lugs, it is assumed that the efficiency factor for titanium lugs is the same as for steel lugs.

$$K_{tru} = 0.87 \text{ (Figure 17, page 168, Reference 22)}$$

$$\text{Therefore, } P'_{tru} = (0.87)(1.0)(130,000)$$

$$= 113,100 \text{ lb}$$

$$MS(\text{ultimate}) = \frac{P_{tru}}{1.5 P_{tr}} - 1$$

$$= \frac{113,100}{1.5 (53,440/2)} - 1$$

$$= +1.82$$

Rotor Overspeed

Section B-B of Figure 214

$$r \text{ at Section B-B} = 63.3 \text{ in}$$

$$(F_C)_{cr} = 144,500 \text{ lb}$$

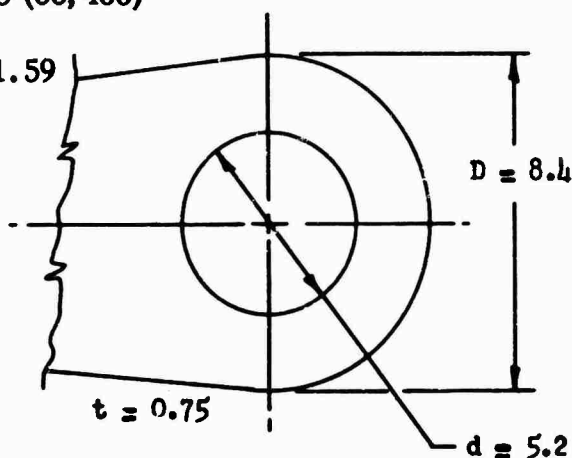
$$\text{Stress: } \sigma_a = \frac{(F_c)_{cr}}{A} = \frac{144,500}{4.33}$$

$$= 33,400 \text{ lb/in}^2$$

$$\text{MS (ultimate)} = \frac{\sigma_u}{1.5 \sigma_a} - 1$$

$$= \frac{130,000}{1.5 (33,400)} - 1$$

$$= +1.59$$



Detail F of Figure 214 (lug)

$(F_c)_{cr}$ at hinge axis = 152,000 lb

From Reference 21, the SCF for the lug, K_t , is (see Detail F of Figure 214)

$$K_t = \frac{1.666D}{d + 0.1166D} = \frac{1.666 (8.4)}{5.2 + (.1166) (8.4)}$$

$$= 2.26$$

$$\text{Stress: } \sigma = \frac{K_t P}{A}$$

$$P = \frac{(F_c)_{cr}}{2} = 76,000 \text{ lb}$$

$$A = (D-d)t = 2.4 \text{ in}^2$$

$$\begin{aligned}\delta_a &= \frac{(2.26)(76,000)}{2.4} = 71,600 \text{ lb/in}^2 \\ \text{MS (ultimate)} &= \frac{\delta_{tu}}{1.5 \delta_a} - 1 \\ &= \frac{130,000}{1.5 (71,600)} - 1 \\ &= +0.21\end{aligned}$$

Starting Condition

Outboard Lug, Figure 215

The load in the outboard lug is due to the damper reaction force P_d .

$$\begin{aligned}P_d &= \frac{M_c}{9.0} = \frac{737,200}{9.0} \\ &= 81,910 \text{ lb}\end{aligned}$$

The lug is analyzed such that only 70 percent of the lug width is considered to be effective due to the stress flow pattern from the inboard flapping lugs to the outboard lug.

Lug Stress Concentration Factor:

$$K_t = \frac{1.666D}{d + 0.1166D} = 1.59 \quad (99)$$

$$\begin{aligned}\text{Stress: } \delta &= \frac{K_t P_d}{A} = \frac{1.59 (81,910)}{0.70(8.4)(8.85-8.25)} \\ &= 36,900 \text{ lb/in}^2\end{aligned}$$

$$\begin{aligned}\text{MS (ultimate)} &= \frac{130,000}{1.5(36,900)} - 1 \\ &= +1.34\end{aligned}$$

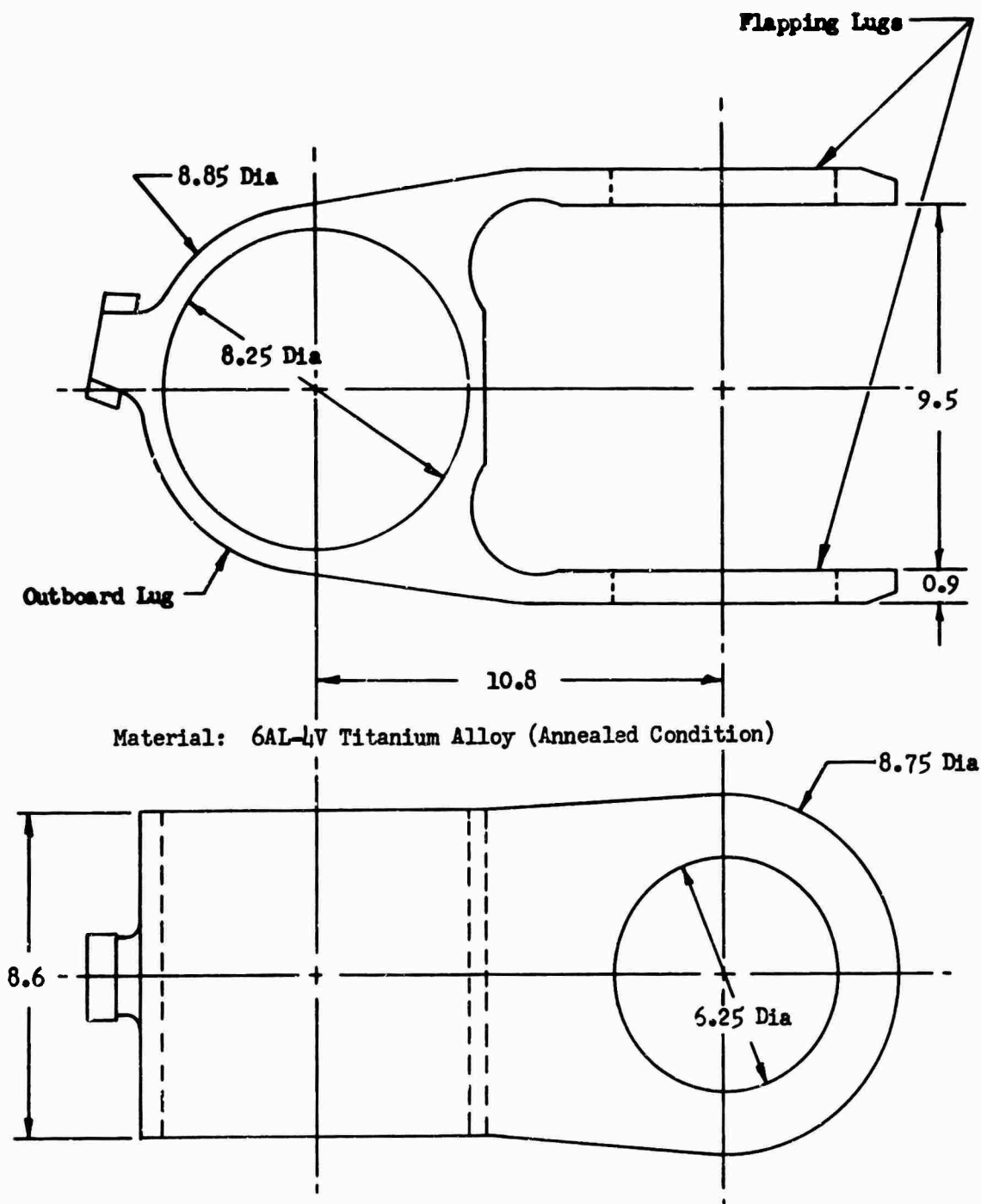


Figure 215 Flapping Hinge

Flapping Lug of Figure 215

The flapping lugs must react the moment about the flapping hinge offset.

Loads: r at flapping hinge offset = 36 in

$$V_R = 2994 \text{ lb}$$

$$M_R = 769,600 \text{ in-lb}$$

Lug Force:

$$P = \frac{M_R}{10.4} = \frac{769,600}{10.4} = 74,000 \text{ lb}$$

Lug Stress Concentration Factor:

$$K_t = \frac{1.666D}{d + 0.1166D} = 2.01$$

$$\text{Stress: } \delta = \frac{K_t P}{A} = \frac{(2.01)(74,000)}{(0.9)(8.75-6.25)}$$

$$= 66,100 \text{ lb/in}^2$$

$$\begin{aligned} \text{MS (ultimate)} &= \frac{\delta t_u}{1.5 \delta} - 1 \\ &= \frac{130,000}{1.5 (66,100)} - 1 \\ &= +0.31 \end{aligned}$$

Rotor Overspeed

Outboard Lug

$$r \text{ at Outboard lug} = 46.8 \text{ in}$$

$$(F_C)_{cr} = 152,000 \text{ lb}$$

Again, the lug is assumed to be 70 percent effective due to stress flow from the flapping lugs to the outboard lug.

$$\begin{aligned} \text{Stress: } \delta &= \frac{K_t P}{A} = \frac{1.59 (152,000)}{0.70 (8.4) (8.85-8.25)} \\ &= 68,500 \text{ lb/in}^2 \end{aligned}$$

$$\begin{aligned} \text{MS (ultimate)} &= \frac{\delta_{tu}}{1.5(\delta)} - 1 \\ &= \frac{130,000}{1.5 (68,500)} - 1 \\ &= +0.26 \end{aligned}$$

Flapping Lug

$$r \text{ at flapping lug} = 36.0 \text{ in}$$

$$(F_c)_{cr} = 159,000 \text{ lb}$$

Lug Force:

$$P = \frac{(F_c)_{cr}}{2} = 79,500 \text{ lb}$$

Stress:

$$\begin{aligned} \delta &= \frac{K_t P}{A} = \frac{(2.01) (79,500)}{(0.90) (8.75-6.25)} \\ &= 71,000 \text{ lb/in}^2 \end{aligned}$$

$$\begin{aligned} \text{MS (ultimate)} &= \frac{130,000}{1.5 (71,000)} - 1 \\ &= +0.22 \end{aligned}$$

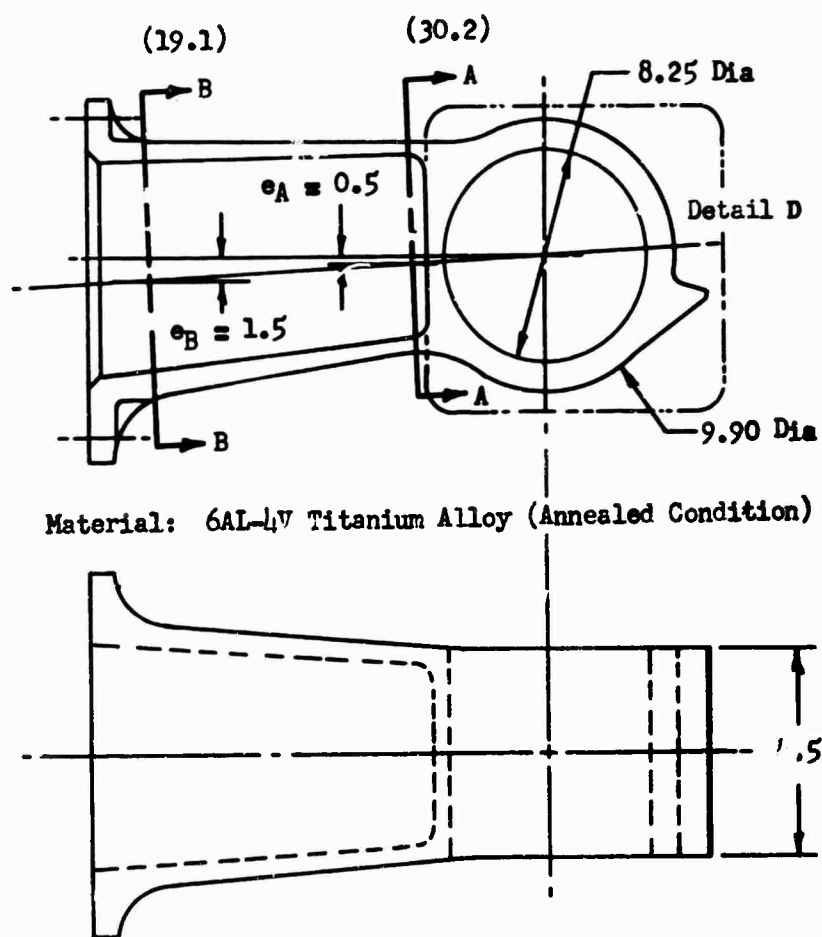


Figure 216 Hub Arm

Starting Condition

Hub Arm Lug, Figure 216

$$r \text{ at lug} = 36.0 \text{ in}$$

$$V_r = 2994 \text{ lb}$$

$$M_r = 769,600 \text{ in-lb}$$

The lug is assumed to be only 70 percent effective due to the stress flow from the flapping hinge lugs into the lug.

Lug Load: In order to analyze the lug using existing lug data, an effective lug force equivalent to the applied moment must be found. Figure 217 illustrates the definition of this effective lug force P .

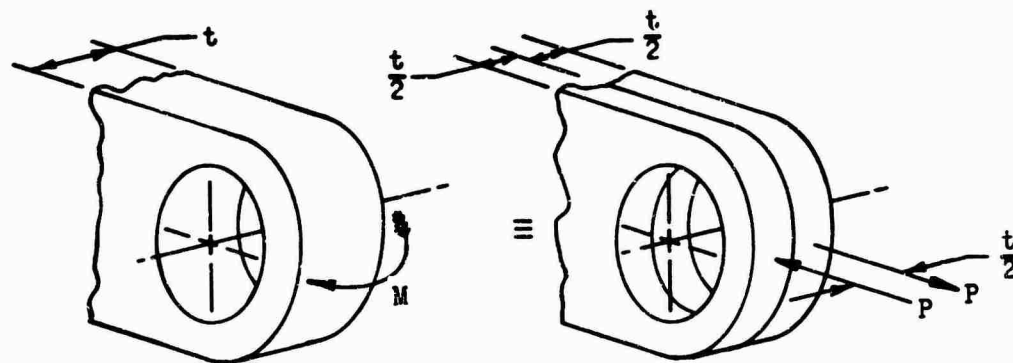


Figure 217 Effective Lug

If only η percent of the lug is considered to be effective, then the equivalent lug would be shown in Figure 218.

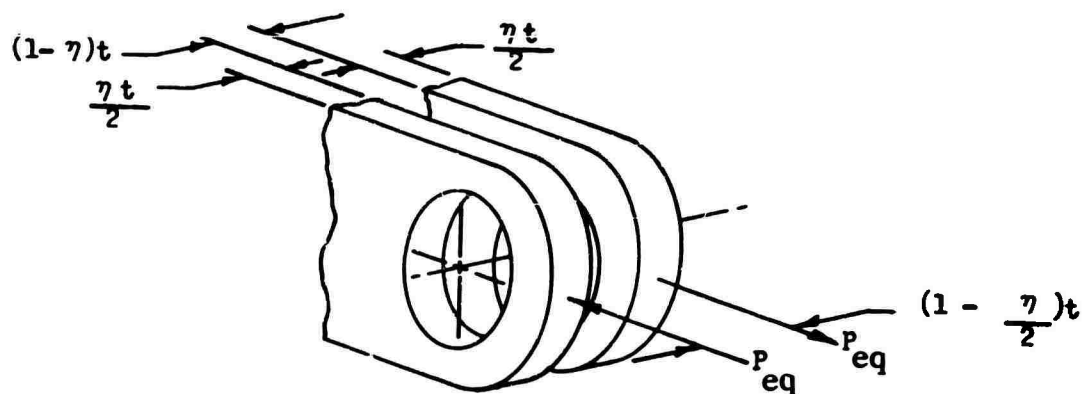


Figure 218 Effective Lug with Efficiency Factor

The equivalent lug load is

$$P_{eq} = \frac{L_i}{(1 - \eta/2)t} \quad (100)$$

$$P_{eq} = \frac{M}{\left(1 - \frac{\eta}{2}\right)t} = \frac{769,000}{\left(1 - \frac{70}{2}\right)(8.4)} = 141,200 \text{ lb}$$

Lug Stress Concentration Factor:

$$K_t = \frac{1.666D}{d + 0.1166D} = \frac{1.666(9.9)}{8.3 + 0.1166(9.9)} = 1.74$$

Stress:

$$\delta = \frac{K_t P_{eq.}}{A} = \frac{(1.74)(141,200)}{(0.35)(8.4)(1.70)} \\ = 49,140 \text{ lb/in}^2$$

$$MS(\text{ultimate}) = \frac{\delta_{tu}}{1.5(\delta)}^{-1} \\ = \frac{130,000}{1.5(49,140)}^{-1} \\ = +0.76$$

Section A-A of Figure 216

Loads:

$$r \text{ at Section A-A} = 30.2 \text{ in}$$

$$V_r = 2994 \text{ lb}$$

$$M_r = 787,000 \text{ in-lb}$$

Section Properties:

$$A = 9.4 \text{ in}^2 \quad OD = 8.9 \text{ in}$$

$$I = 86.1 \text{ in}^4 \quad ID = 8.2 \text{ in}$$

$$\text{Stress: } \delta = \frac{M_r c}{I} = \frac{(787,000)(4.45)}{86.1}$$

$$= 40,680 \text{ lb/in}^2$$

$$MS(\text{ultimate}) = \frac{130,000}{1.5(40,680)}^{-1}$$

$$= +1.13$$

Section B-B of Figure 216

Loads: r at Section B-B = 19.1 in

$$V_R = 2994 \text{ lb}$$

$$M_R = 820,200 \text{ in-lb}$$

Section Properties:

$$\text{OD} = 11.3 \text{ in}$$

$$\text{ID} = 10.3 \text{ in}$$

$$A = 17.0 \text{ in}^2$$

$$I = 248.0 \text{ in}^4$$

$$\text{Stress: } s = \frac{M_{rc}}{I} = \frac{(820,200)(5.65)}{248.0}$$

$$= 18,690 \text{ lb/in}^2$$

$$\text{MS(ultimate)} = \frac{s_{tu}^{-1}}{1.5s}$$

$$= \frac{130,000}{1.5(18,690)}^{-1}$$

$$= +3.74$$

Rotor Overspeed

Hub Arm Lug

$$(F_c)_{cr} = 159,000 \text{ lb}$$

The lug is assumed to be only 70 percent effective.

$$\text{Stress: } s = \frac{K_t P}{A} = \frac{1.76 (159,000)}{0.70 (8.4)(1.65)}$$

$$= 28,800 \text{ lb/in}^2$$

$$\begin{aligned}
 MS(\text{ultimate}) &= \frac{\delta_{tu}}{1.5\delta} - 1 \\
 &= \frac{130,000}{1.5(28,800)} - 1 \\
 &= + 2.00
 \end{aligned}$$

Section A-A of Figure 216

$$(F_c)_{cr} = 159,000 \text{ lb}$$

$$\begin{aligned}
 M_r &= (F_c)_{cr}(e) = (159,000)(0.5) \\
 &= 79,500 \text{ in-lb}
 \end{aligned}$$

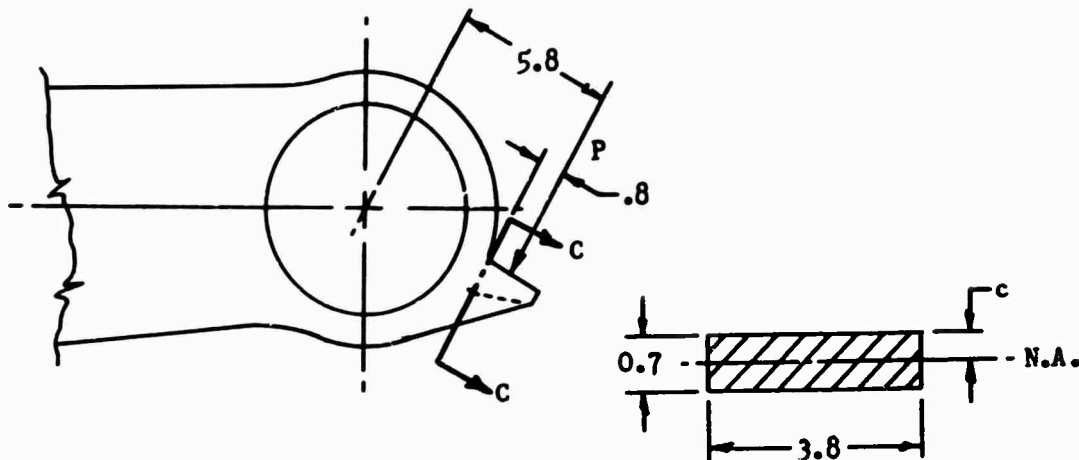
$$\delta_a = \frac{(F_c)_{cr}}{A} = \frac{159,000}{9.4} = 16,900 \text{ lb/in}^2$$

$$\delta_b = \frac{M_r c}{I} = \frac{(79,500)(4.45)}{86.1} = 4,110 \text{ lb/in}^2$$

The allowable bending modulus of rupture is taken as 190,000 lb/in²

$$\begin{aligned}
 MS(\text{ultimate}) &= \frac{1}{1.5\left(\frac{\delta_a}{\delta_{tu}} + \frac{\delta_b}{\delta_{bu}}\right)} - 1 \\
 &= \frac{1}{1.5\left(\frac{16,900}{130,000} + \frac{4,110}{190,000}\right)} - 1 \\
 &= + 3.37
 \end{aligned}$$

Droop Stop (Figure 216)



Detail D of Figure 216 (Droop Stop)

Section C-C

The droop stop must react the total weight moment of the blade.
The reaction force (P) on the droop stop surface is

$$\begin{aligned} P &= \frac{\text{Blade Weight Moment about Flapping Hinge}}{\text{Moment Arm}} \\ &= \frac{160,700 \text{ in-lb}}{5.8 \text{ in}} \\ &= 27,700 \text{ lb} \end{aligned}$$

Applying an inertia factor of 4.0 on this load,

$$P = 4.0 (27,700) = 110,800 \text{ lb}$$

Section C-C of Detail D of Figure 216

For purposes of analysis, the Section C-C is considered to be reduced in size so as to assure a conservative design analysis.

Section Properties:

$$A = 2.66 \text{ in}^2$$

$$I = 1.08 \text{ in}^4$$

$$c = 0.34 \text{ in}$$

Loads on Section C-C:

$$V_{\text{(shear)}} = 110,800 \text{ lb}$$

$$M = (0.8)V = 88,600 \text{ in-lb}$$

$$\text{Stress: } \sigma_b = \frac{Mc}{I} = \frac{(88,600)(0.35)}{1.08}$$

$$= 28,700 \text{ lb/in}^2$$

$$\begin{aligned} \text{MS(ultimate)} &= \frac{\sigma_{tu}^{-1}}{1.5\sigma} \\ &= \frac{130,000^{-1}}{1.5(28,700)} \\ &= +2.02 \end{aligned}$$

Fatigue Analysis

Sleeve with Integral Control Arm (Figure 213)

Lugs

Load: The pair of lugs on the control arm must react the full design control rod load.

Lug Dimensions: $D = 2.0 \text{ in}$

$$d = 0.875 \text{ in}$$

$$t = 0.3 \text{ in (single lug of pair)}$$

Lug Analysis: The Heywood lug (Reference 21) analysis is used, since a chafing condition can possibly exist between the lug and bushing.

The mean endurance limit $(\sigma_{en})_m$ (Equation 68, page 353) is

$$\begin{aligned} (\sigma_{en})_m &= \frac{2.8}{2.0} \frac{[0.875 + 0.1166(2.0)]}{(1.0 + 0.875)} (\pm 11,400) \\ &= \pm 9430 \text{ lb/in}^2 \end{aligned}$$

The working endurance limit is

$$\begin{aligned} s_{en} &= (PF) (s_{en})_m & (PF=\text{probability factor}) \\ &= (0.482) (\pm 9430) \\ &= \pm 4545 \text{ lb/in}^2 \end{aligned}$$

Nominal lug stress:

$$\begin{aligned} s &= \frac{\text{Control Rod Load}}{2 t (D-d)} = \frac{(1580 + 2640)}{2(0.3)(2.0-.88)} \\ &= (2350 \pm 3930) \text{ psi} \end{aligned}$$

$$\begin{aligned} MS &= \frac{1}{\frac{s_s}{s_{ty}} + \frac{s_v}{s_{en}}} - 1 \\ &= \frac{1}{\frac{2350}{120,000} + \frac{3930}{4545}} - 1 \\ &= +0.13 \end{aligned}$$

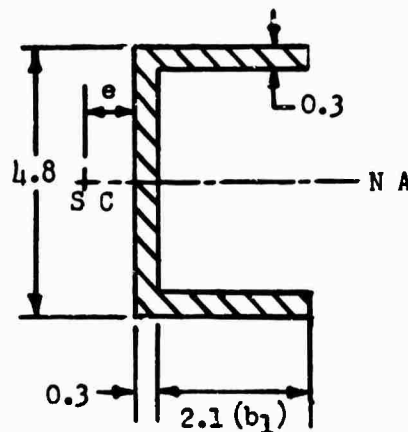
Section C-C (a) of Figure 213

The shear center (SC) of the channel section is found using the formula given below (page 104, Reference 47).

$$e = \frac{\frac{1}{2} b_1}{1 + \frac{1}{6} \frac{a_w}{a_f}} \quad (101)$$

where a_w = area of web

a_f = area of a flange



Section C-C (a) of Figure 213

$$a_w = 0.3(4.8) = 1.44 \text{ in}^2$$

$$a_f = 0.3(2.1) = 0.63 \text{ in}^2$$

$$e = \frac{\frac{1}{2}(1.8)}{1 + \frac{1}{6} \frac{1.44}{0.63}} = .065 \text{ in}$$

Loads on Section C-C:

$$V = \text{Control rod load} = (1580 \pm 2640) \text{ lb}$$

$$M = 8.5V = (13,430 \pm 22,440) \text{ in-lb}$$

$$T = (2.0 - e) V = (2130 \pm 3560) \text{ in-lb}$$

Section Properties:

$$A = (0.3)(9.0) = 2.7 \text{ in}^2$$

$$I = \frac{1}{12} [(2.4)(4.8)^3 - (2.1)(4.2)^3] = 9.15 \text{ in}^4$$

Computation of J (see Section C-C (b) of Figure 213)

(Reference 44, page 178, cases 19 and 20)

$$a = 2.4$$

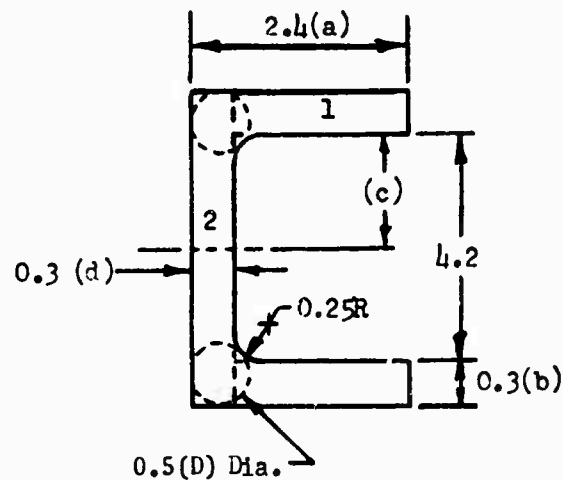
$$b = d = 0.3$$

$$c = 2.1$$

$$r = 0.25$$

$$D = 0.5$$

$$J = 2 (K_1 + K_2 + \alpha D^4)$$



Section C-C (b) of Figure 213

$$\begin{aligned}
\text{Now } K_1 &= ab^3 \left[\frac{1}{3} - 0.21 \left(\frac{b}{a} \right) \left(1 - \frac{b^4}{12a^4} \right) \right] \\
&= (2.4) (0.3)^3 \left[\frac{1}{3} - 0.21 \left(\frac{0.3}{2.4} \right) \left(1 - \frac{(0.3)^4}{12 (2.4)^4} \right) \right] \\
&= 0.6648 \left[\frac{1}{3} - 0.0263 \right] \\
&= 0.0199 \\
K_2 &= cd^3 \left[\frac{1}{3} - 0.105 \left(\frac{d}{c} \right) \left(1 - \frac{d^4}{192c^4} \right) \right] \\
&= (2.1)(0.3)^3 \left[\frac{1}{3} - 0.105 \left(\frac{0.3}{2.1} \right) \right] = 0.0180
\end{aligned}$$

$$\begin{aligned}
\alpha &= \frac{d}{b} \left(0.07 + 0.076 \frac{r}{b} \right) \\
&= \frac{0.3}{0.3} \left[0.07 + 0.076 \left(\frac{0.25}{0.3} \right) \right] = 0.133
\end{aligned}$$

$$\begin{aligned}
J &= 2 [0.020 + 0.018 + 0.133 (.5)^4] \\
&= 2 (0.046) \\
&= 0.092 \text{ in}
\end{aligned}$$

$$\text{Stress: } \tau = \frac{Tb}{J} = (6940 \pm 11,600) \text{ lb/in}^2$$

$$s = \frac{Mc}{I} = (3520 + 5890) \text{ lb/in}^2$$

Principal Stress: The formula for calculating the principal stress for an element under two-dimensional stress is given in most strength of materials books (page 57, Reference 47).

$$\epsilon_p(\text{principal stress}) = \frac{\epsilon_x + \epsilon_y}{2} \pm \sqrt{\frac{(\epsilon_y - \epsilon_x)^2}{4} + \tau_{xy}^2} \quad (102)$$

$$\epsilon_x = (3520 \pm 5890) \text{ lb/in}^2$$

$$\epsilon_y = 0$$

$$\tau_{xy} = (6940 \pm 11,600) \text{ lb/in}^2$$

A conservative approach is to compute the principal stress due to maximum and minimum component stresses separately and then assume that the principal stresses act on the same plane. In general, the maximum and minimum principal stress resultants do not act on the same plane. A vector representation of these stress resultants shows that the most critical stress condition exists if they act on the same plane.

$$(\epsilon_x)_{\max} = 3520 + 5890 = 9410 \text{ lb/in}^2$$

$$(\tau_{xy})_{\max} = 6940 + 11,600 = 18,540 \text{ lb/in}^2$$

$$\begin{aligned} \text{And, } (\epsilon_p)_{\max} &= \frac{9410}{2} + \sqrt{\frac{(9410)^2}{4} + (18,540)^2} \\ &= 23,800 \text{ lb/in}^2 \end{aligned}$$

$$(\epsilon_x)_{\min} = 3520 - 5890 = -2370 \text{ lb/in}^2$$

$$(\tau_{xy})_{\min} = 6940 - 11,600 = -4660 \text{ lb/in}^2$$

$$\begin{aligned} \text{And, } (\epsilon_p)_{\min} &= \frac{-2370}{2} - \sqrt{\frac{(-2370)^2}{4} + (-4660)^2} \\ &= -4810 \text{ lb/in}^2 \end{aligned}$$

The principal stress (ϵ_p) is therefore

$$\epsilon_p = (9500 \pm 14,300) \text{ lb/in}^2$$

Working Endurance Limit:

$$s_{en} = (SEF)(MF)(PF)(s_{en})_m \quad (103)$$

where SEF = size effect factor

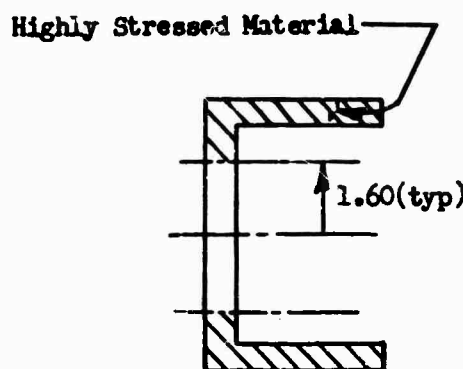
MF = machining factor

PF = probability factor

The control arm at Section C-C (c) of Figure 213 is treated as a cantilevered beam of length $L = 8.0$ inches, and constant cross section C-C over this length is assumed.

$$A (\text{highly stressed material}) = 1.72 \text{ in}^2$$

$$V = AL = 13.8 \text{ in}^3$$



The volume ratio is

Section C-C (c) of Figure 213

$$\frac{V (\text{component})}{V (\text{specimen})} = \frac{13.8}{0.009} = 1530$$

The SEF is now obtained from Figure 203, which is a plot of size effect factor versus volume ratio.

$$SEF = 0.74$$

The working endurance limit is now determined.

$$\begin{aligned} s_{en} &= (0.74)(0.80)(0.630)(\pm 60,000) \\ &= \pm 22,400 \text{ lb/in}^2 \end{aligned}$$

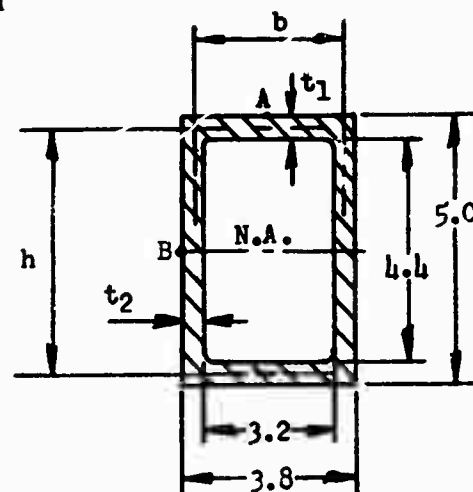
$$\begin{aligned}
 MS &= \frac{1}{\frac{(SCF)_{\delta_g}}{\delta_{ty}} + \frac{(SCF)_{\delta_v}}{\delta_{en}}} -1 \quad (104) \\
 &= \frac{1}{\frac{(1.2)(9,500)}{120,000} + \frac{(1.2)(14,300)}{22,400}} -1 \\
 &= +0.16
 \end{aligned}$$

Section D-D of Figure 213

The shear stress for a thin-walled rectangular closed box cross section under torsion is found using the formula given below (page 276, Reference 47).

$$\tau_A = T/(2bht_1)$$

$$\tau_B = T/(2bht_2)$$



Section D-D of Figure 213

Loads on Section D-D of Figure 213

$$V = \text{control rod load} = (1580 \pm 2640) \text{ lb}$$

$$M = 4.1 V = (6480 \pm 10,820) \text{ in-lb}$$

$$T = 10.8 V = (17,060 \pm 28,510) \text{ in-lb}$$

Section Properties: $A = (0.3)(16.4) = 4.92 \text{ in}^2$

$$I = \frac{1}{12} [(3.8)(5.0)^3 - (3.2)(4.4)^3] \\ = 16.9 \text{ in}^4$$

The critical stress condition occurs at point A.

$$\sigma_A = \frac{Mc}{I} = \frac{(6480 + 10,820)(2.5)}{16.9} \\ = (960 \pm 1600) \text{ lb/in}^2$$

$$\tau_A = \frac{T}{2bht_1} = \frac{(17,060 \pm 28,510)}{2(3.5)(4.7)(0.3)} \\ = (1730 \pm 2890) \text{ lb/in}^2$$

By inspection, it can be stated that the margin of safety at Section D-D is high (i. e., greater than +4.0). Such a high margin of safety is necessary since stiffness rather than strength is the design criteria in this region where the control arm mates with the sleeve cylinder.

Section B-B of Figure 213

Loads: The design loads for titanium without chafing apply.

$$P = F_c + V_c + V_n \\ = (115,350 \pm 1950) \text{ lb}$$

$$M = M_d = \pm 59,800 \text{ in-lb}$$

Section Properties :

$$A = 6.98 \text{ in}^2$$

$$I = 63.6 \text{ in}^4$$

$$c = 4.40 \text{ in}$$

Nominal stress:

$$\begin{aligned} s &= \frac{P}{A} + \frac{Mc}{I} \\ &= \frac{(115,350 \pm 1950)}{6.98} + \frac{(\pm 59,800)(4.40)}{63.6} \\ &= 16,530 \pm 4420 \text{ lb/in}^2 \end{aligned}$$

The working endurance limit stress is

$$\begin{aligned} s_{en} &= (SEF)(MF)(PF)(s_{en})_m \\ &= (0.80)(0.80)(0.482)(\pm 60,000) \\ &= \pm 18,510 \text{ lb/in}^2 \end{aligned}$$

An SCF equal to 2.5 is assumed at the thread relief groove.

$$\begin{aligned} MS &= \frac{1}{\frac{(SCF)s_s}{s_{ty}} + \frac{(SCF)s_v}{s_{en}}} - 1 \\ &= \frac{1}{\frac{(2.5)(16,530)}{120,000} + \frac{(2.5)(4420)}{18,510}} - 1 \\ &= +0.06 \end{aligned}$$

Lugs A of Bell Crank, Figure 219

Lug Dimensions: $D = 2.0 \text{ in}$

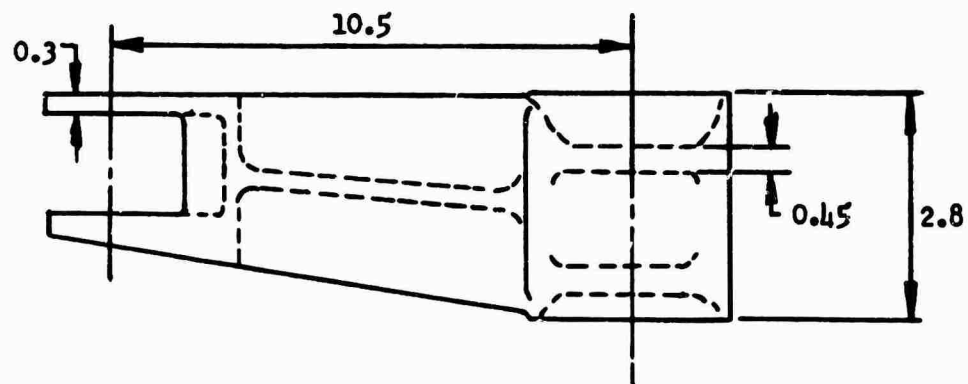
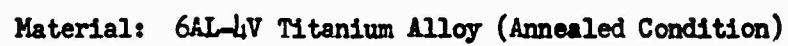
$d = 0.875 \text{ in}$

$t = 0.3 \text{ in (single lug of a pair)}$

Since these lugs are identical to the control arm lugs and the applied loading is the same, these lugs will have the same margin of safety.

$$MS = +0.13$$

$$P_3 = \sqrt{P_1^2 + P_2^2} = (3150 \pm 5250) \text{ lb}$$



407

Lugs, B of Figure 219

Lug Dimensions: $D = 2.2$ in

$$d = 0.88 \text{ in}$$

$$t = 0.45 \text{ (single lug of pair)}$$

Lug Analysis: The Heywood lug analysis is used, since a chafing condition exists between the lug and bushing.

The mean endurance limit $(s_{en})_m$ for the lug is

$$\begin{aligned}(s_{en})_m &= \frac{2.8 [0.88 + 0.1166(2.2)]}{2.2 (1. + 0.88)} (\pm 11,400) \\ &= \pm 8770 \text{ lb/in}^2\end{aligned}$$

The working endurance limit is

$$\begin{aligned}s_{en} &= (PF)(s_{en})_m = (0.482)(\pm 8770) \\ &= \pm 4230 \text{ lb/in}^2\end{aligned}$$

Nominal lug stress:

$$\begin{aligned}s &= \frac{P_2}{2t(D-d)} = \frac{(2720 \pm 4540)}{2(0.45)(2.2-0.88)} \\ &= (2290 \pm 3820) \text{ lb/in}^2 \\ MS &= \frac{1}{\frac{s_s}{s_{ty}} + \frac{s_v}{s_{en}}} \quad -1 \\ &= \frac{1}{\frac{2290}{120,000} + \frac{3820}{4170}} \quad -1 \\ &= +0.07\end{aligned}$$

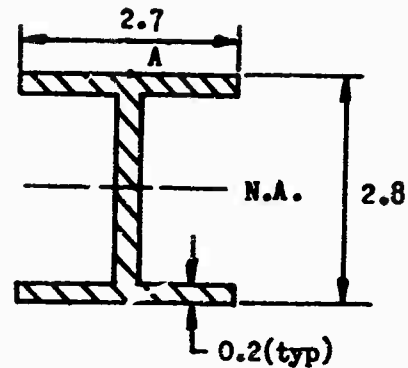
Section A-A of Figure 219

$$A = 1.56 \text{ in}^2$$

$$I = 2.06 \text{ in}^4$$

$$c = 1.40 \text{ in}$$

$$J = 0.021 \text{ in}^4$$



Section A-A of Figure 219

Loads on Section A-A:

$$V = P_1 = (1580 \pm 2640) \text{ lb}$$

$$M = 8.6 P_1 = (13,590 \pm 22,710) \text{ in-lb}$$

$$T = 0.2 P_1 = (316 \pm 528) \text{ in-lb}$$

Stress at point A of Section A-A of Figure 219:

$$\begin{aligned} s &= \frac{Mc}{I} = \frac{(13,590 \pm 22,710)(1.4)}{2.06} \\ &= (9240 \pm 15,400) \text{ lb/in}^2 \end{aligned}$$

$$\begin{aligned} \tau &= \frac{Th}{J} = \frac{(316 \pm 528)(0.2)}{0.021} \\ &= (3010 \pm 5030) \text{ lb/in}^2 \end{aligned}$$

Principal Stress:

$$s_p = \frac{s_x + s_y}{2} \pm \sqrt{\left(\frac{s_y - s_x}{2}\right)^2 + \tau_{xy}^2} \quad (105)$$

Now $s_x = (9240 \pm 15,400) \text{ lb/in}^2$

$$s_y = 0$$

$$\tau_{xy} = (3010 \pm 5030) \text{ lb/in}^2$$

$$\text{Then } (s_p)_{\max} = 27,000 \text{ lb/in}^2$$

$$(s_p)_{\min} = -6800 \text{ lb/in}^2$$

$$\text{or } s_p = (10,100 \pm 16,900) \text{ lb/in}^2$$

Working endurance limit:

$$s_{en} = (SEF)(MF)(PF)(s_{en})_m$$

$$\text{where } SEF = 0.74$$

$$MF = 0.80$$

$$PF = 0.63$$

$$\begin{aligned} s_{en} &= (0.74)(0.80)(0.63)(\pm 60,000) \\ &= \pm 22,400 \text{ lb/in}^2 \end{aligned}$$

$$\begin{aligned} MS &= \frac{1}{\frac{(SCF)s_s}{s_{ty}} + \frac{(SCF)s_v}{s_{en}}} - 1 \\ &= \frac{1}{\frac{(1.2)(10,000)}{120,000} + \frac{(1.2)(16,900)}{22,400}} - 1 \\ &= 0.0 \end{aligned}$$

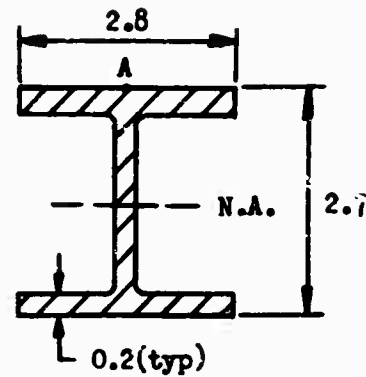
Section B-B of Figure 219

$$A = 1.58 \text{ in}^2$$

$$I = 2.16 \text{ in}^4$$

$$c = 1.35 \text{ in}$$

$$J = 0.021 \text{ in}^4$$



Section B-B of Figure 219

Loads on Section B-B of Figure 219:

$$V = P_2 = (2720 \pm 4540) \text{ lb}$$

$$M = 4.0 P_2 = (10,880 \pm 18,160) \text{ in-lb}$$

$$T = 0.2 P_2 = (544 \pm 908) \text{ in-lb}$$

Stress at point A of Section B-B:

$$\sigma = \frac{Mc}{I} = \frac{(10,880 \pm 18,160)(1.35)}{2.16}$$

$$= (6800 \pm 11,350) \text{ lb/in}^2$$

$$\tau = \frac{Th}{J} = \frac{(544 \pm 908)(0.2)}{0.021}$$

$$= (5180 \pm 8650) \text{ lb/in}^2$$

Principal Stress:

$$\sigma_p = \frac{\sigma_x - \sigma_y}{2} \pm \sqrt{\left(\frac{\sigma_y - \sigma_x}{2}\right)^2 + \tau_{xy}^2}$$

Now $\sigma_x = (6800 \pm 11,350) \text{ lb/in}^2$

$$\sigma_y = 0$$

$$\tau_{xy} = (5180 \pm 8650) \text{ lb/in}^2$$

Then $(s_p)_{\max} = 25,600 \text{ lb/in}^2$

$(s_p)_{\min} = -6400 \text{ lb/in}^2$

or, $s_p = (9600 \pm 16,000) \text{ lb/in}^2$

Working endurance limit:

$s_{en} = 22,400 \text{ lb/in}^2$

$$MS = \frac{1}{(1.2) \frac{9600}{120,000} + \frac{(1.2)(16,000)}{22,400}} - 1$$

$$= +0.05$$

Lug, Pivot of Figure 219

Lug Dimensions:

$D = 2.8 \text{ in}$

$d = 2.2 \text{ in}$

$t = 2.8 \text{ in}$

Lug Analysis: The Heywood lug analysis is used, since a chafing condition exists between the lug and bushing.

The mean endurance limit for the lug is

$$(s_{en})_m = \frac{2.8 [2.20 + 0.1166(2.8)] (\pm 11,400)}{2.8 (1. + 2.2)}$$

$$= \pm 9000 \text{ lb/in}^2$$

The working endurance limit is

$$s_{en} = (PF)(s_{en})_m = (.482)(\pm 9000)$$

$$= \pm 4340 \text{ lb/in}^2$$

Nominal lug stress:

$$= \frac{P_3}{t(D-d)} = \frac{(3150 \pm 5250)}{2.8(2.8-2.2)}$$

$$= (1870 \pm 3120) \text{ lb/in}^2$$

$$MS = \frac{1}{\frac{1870}{120,000} + \frac{3120}{4340}} - 1$$

$$= +0.36$$

Control Rod, Primary, Figure 220

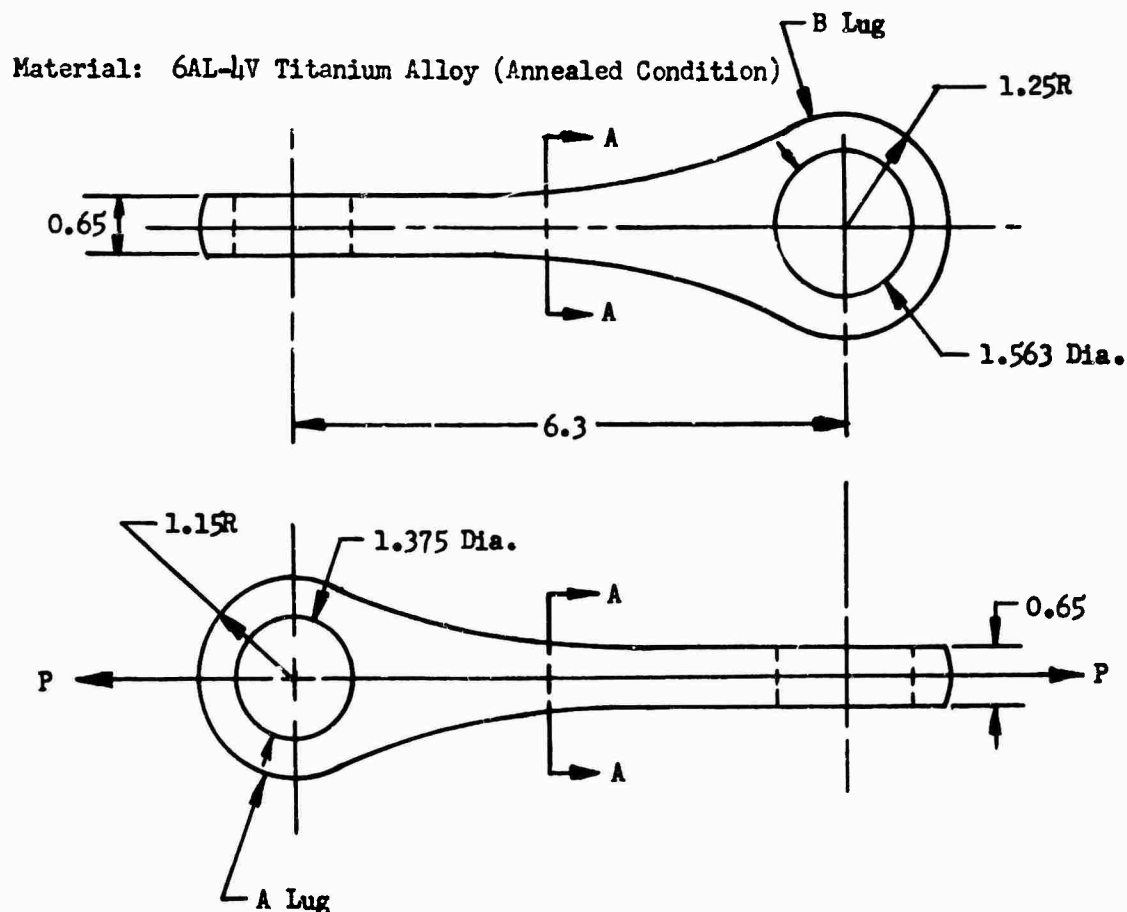


Figure 220 Primary Control Rod

Control Rod Load $P = 1580 \pm 2640$ lb

Lug A of Figure 220

Lug Dimensions:

$$D = 2.30 \text{ in}$$

$$d = 1.375 \text{ in}$$

$$t = 0.65 \text{ in}$$

Lug Analysis: The Heywood lug analysis is used, since a chafing condition exists between the lug and bushing.

The mean endurance limit $(s_{en})_m$ is

$$\begin{aligned}(s_{en})_m &= \frac{2.8 [1.375 + 0.1166 (2.3)]}{2.3 (1 + 1.375)} (\pm 11,400) \\ &= \pm 9600 \text{ lb/in}^2\end{aligned}$$

The working endurance limit is

$$\begin{aligned}s_{en} &= (PF)(s_{en})_m = (.482)(\pm 9600) \\ &= \pm 4630 \text{ lb/in}^2\end{aligned}$$

Nominal lug stress:

$$\begin{aligned}s &= \frac{P}{t(D-d)} = \frac{(1580 \pm 2640)}{0.65(2.3-1.375)} \\ &= (2630 \pm 4390) \text{ lb/in}^2\end{aligned}$$

$$\begin{aligned}MS &= \frac{1}{\frac{2630}{120,000} + \frac{4390}{4630}} - 1 \\ &= +0.03\end{aligned}$$

Lug B of Figure 220

Lug Dimensions:

$$D = 2.500 \text{ in}$$

$$d = 1.563 \text{ in}$$

$$t = 0.65 \text{ in}$$

Lug Analysis: The Heywood analysis is used, since a chafing condition exists.

The mean endurance limit is

$$\begin{aligned} (s_{en})_m &= \frac{2.8 [1.563 + 0.1166(2.5)]}{2.5 (1. + 1.563)} (\pm 11,400) \\ &= \pm 9240 \text{ lb/in}^2 \end{aligned}$$

The working endurance limit is

$$\begin{aligned} (s_{en}) &= (PF)(s_{en})_m = (0.482)(\pm 9240) \\ &= \pm 4450 \text{ lb/in}^2 \end{aligned}$$

Nominal lug stress:

$$\begin{aligned} s &= \frac{P}{t(D-d)} = \frac{(1580 \pm 2640)}{0.65 (2.50 - 1.563)} \\ &= (2590 \pm 4330) \text{ lb/in}^2 \end{aligned}$$

$$\begin{aligned} MS &= \frac{1}{\frac{2590}{120,000} + \frac{4330}{4450}} - 1 \\ &= +0.01 \end{aligned}$$

Section A-A of Figure 220

$$A = \frac{1}{4} \pi (0.5)^2 = 0.196 \text{ in}^2$$

$$\begin{aligned}\text{Stress: } \sigma &= \frac{P}{A} = \frac{(1580 \pm 2640)}{0.196} \\ &= (8060 \pm 13,470) \text{ lb/in}^2\end{aligned}$$

Working endurance limit:

$$\sigma_{en} = (\text{SEF})(\text{MF})(\text{PF})(\sigma_{en})_m$$

Size effect factor:

Since the control rod is under pure axial tension, the volume of highly stressed material is essentially equal to the total volume of the control rod. The volume ratio is

$$\frac{V(\text{control rod})}{V(\text{specimen})} = \frac{4.5}{0.009} = 500$$

The SEF is obtained from Figure 203:

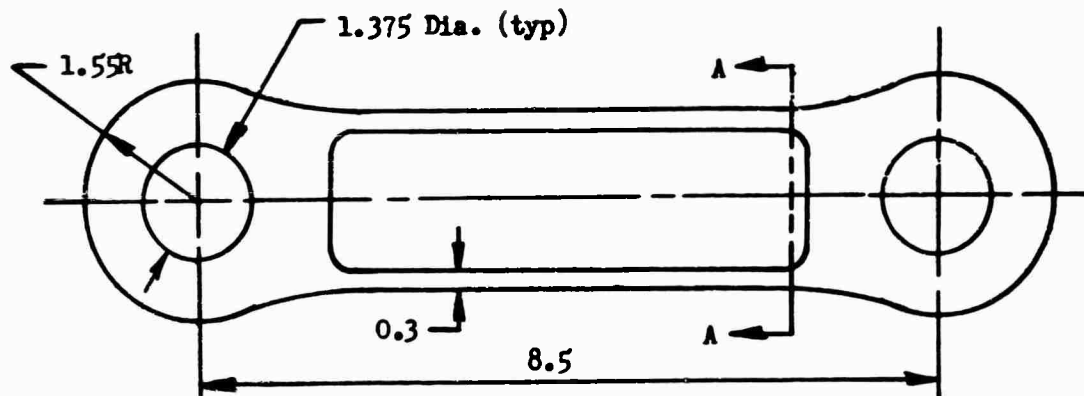
$$\text{SEF} = 0.77$$

The working endurance limit is

$$\begin{aligned}\sigma_{en} &= (0.77)(0.80)(0.630)(\pm 60,000) \\ &= \pm 23,300 \text{ lb/in}^2\end{aligned}$$

Stress Concentration Factor = 1.5

$$\begin{aligned}\text{MS} &= \frac{1}{\frac{(1.5)(8060)}{120,000} + \frac{(1.5)(13,470)}{23,300}} - 1 \\ &= +0.03\end{aligned}$$



Material: 6AL-4V Titanium Alloy (Annealed Condition)

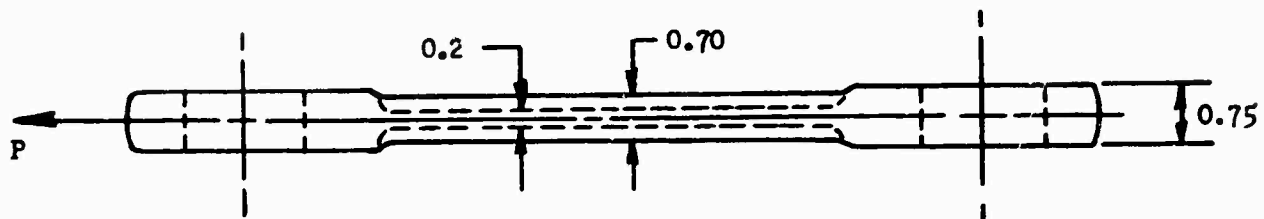


Figure 221 Transfer Link

Transfer Link, Figure 221

Lug

Lug Dimensions: $D = 3.1$ in

$d = 1.375$ in

$t = 0.75$ in

Lug Analysis: The Heywood lug analysis is used, since a chafing condition exists.

The mean endurance limit is

$$\begin{aligned} (\sigma_{en})_m &= \frac{2.8 [1.375 + 0.1166 (3.1)] (\pm 11,400)}{3.1 (1. + 1.375)} \\ &= \pm 7530 \text{ lb/in}^2 \end{aligned}$$

The working endurance limit is

$$\begin{aligned} \sigma_{en} &= (PF)(\sigma_{en})_m = (.482)(\pm 7530) \\ &= \pm 3630 \text{ lb/in}^2 \end{aligned}$$

Nominal lug stress:

$$\begin{aligned} \sigma &= \frac{P}{t(D-d)} = \frac{(2720 \pm 4540)}{0.75(3.1 - 1.375)} \\ &= (2100 \pm 3510) \text{ lb/in}^2 \end{aligned}$$

$$\begin{aligned} MS &= \frac{\frac{2100}{120,000} + \frac{3510}{3630}}{-1} \\ &= +0.01 \end{aligned}$$

Section A-A of Figure 221

Section Properties: $A = 0.70 \text{ in}^2$

$$I = 0.018 \text{ in}^4$$

The Euler buckling load for a column, both ends of which are pinned, is taken from basic Strength of Materials texts

$$\begin{aligned} P_{Cr} &= \frac{\pi^2 EI}{L^2} = \frac{\pi^2 (16.0 \times 10^6) (0.018)}{(5.5)^2} \\ &= 94,000 \text{ lb} \end{aligned}$$

The maximum design compressive force in the link is 7,260 lb. The nominal stress at section A-A is

$$\begin{aligned} s &= \frac{P}{A} = \frac{(2720 \pm 4540)}{0.7} \\ &= (3890 \pm 6490) \text{ lb/in}^2 \end{aligned}$$

The working endurance limit stress is

$$\begin{aligned} s_{en} &= (SEF)(MF)(PF)(s_{en})_m \\ &= (0.70)(0.80)(0.630)(\pm 60,000) \\ &= \pm 21,200 \text{ lb/in}^2 \end{aligned}$$

An SCF equal to 2.0 is assumed.

$$\begin{aligned} MS &= \frac{1}{\frac{2.0(3890)}{120,000} + \frac{2.0(6490)}{21,200}} - 1 \\ &= +0.47 \end{aligned}$$

The high margin of safety is necessary, since any eccentricity of loading will induce bending stresses in the link.

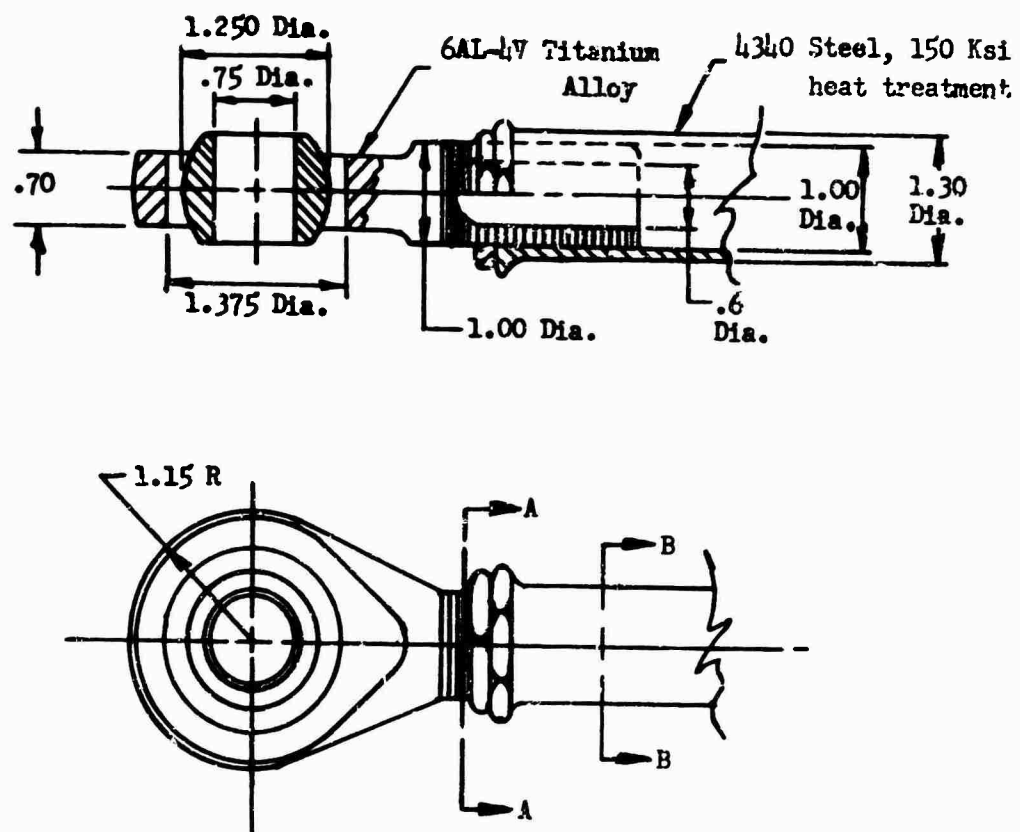


Figure 222 Adjustable Control Rod

Adjustable Control Rod, Figure 222

Lug, Spherical Rod End Bearing

Dimensions: $D = 2.30$ in

$d = 1.375$ in

$t = 0.70$ in

Lug Analysis: The Heywood lug analysis is used, since a chafing condition exists between the outer ring of the bearing and the lug.

The lug analysis is the same as the primary control rod lug analysis; therefore, MS of the lug is equal to +0.03.

Section A-A (Rod-End) of Figure 222

$$A = \frac{1}{4}\pi [(1.00)^2 - (0.60)^2]$$

$$= 0.50 \text{ in}^2$$

Nominal Stress:

$$s = \frac{P}{A} = \frac{(1580 \pm 2640)}{0.50}$$

$$= (3160 \pm 5280) \text{ lb/in}^2$$

Working endurance limit:

$$s_{en} = (SEF)(MF)(PF)(s_m)$$

$$= (0.82)(0.80)(0.482)(\pm 60,000)$$

$$= \pm 19,000 \text{ lb/in}^2$$

Stress Concentration Factor:

For a screw thread, an SCF of 3.0 is used.

$$MS = \frac{1}{\frac{(SCF)s_s}{s_{ty}} + \frac{(SCF)s_v}{s_{en}}} - 1$$

$$= \frac{1}{\frac{(3.0)(3160)}{120,000} + \frac{(3.0)(5280)}{19,000}} - 1$$

$$= +0.09$$

Section B-B (Barrel) of Figure 222

$$A = \frac{1}{4} \pi \left[(1.30)^2 - (1.10)^2 \right]$$
$$= 0.38 \text{ in}^2$$

Nominal Stress:

$$s = \frac{P}{A} = \frac{(1580 \pm 2640)}{0.38}$$
$$= (4160 \pm 6950) \text{ lb/in}^2$$

Working endurance limit:

$$s_{en} = (SEF)(MF)(PF)(s_{en})_m$$
$$= (0.82)(0.80)(0.630)(\pm 60,000)$$
$$= \pm 24,800 \text{ lb/in}^2$$

Stress Concentration Factor:

$$SCF = 3.0$$

$$MS = \frac{1}{\frac{s_s}{s_{ty}} + \frac{(SCF)s_v}{s_{en}}} - 1$$
$$= \frac{1}{\frac{4160}{132,000} + \frac{(3.0)(6950)}{24,800}} - 1$$
$$= +0.12$$

Rotating Swashplate, Figure 223

Rotating Swashplate Loading

i = an index referring to a given rotating star lug and control rod

P_i = load in i^{th} control rod

α_i = phase angle of i^{th} control rod

ψ = azimuth of reference blade

$$\text{then, } P_i = P_s + P_v \sin (\psi + \alpha_i)$$

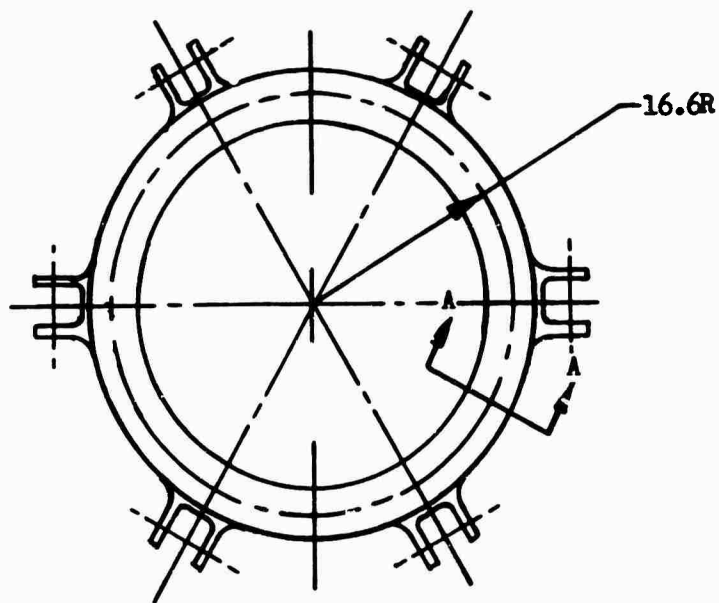
Lugs, Control Rod of Figure 223

Lug Dimensions:

$$D = 3.60 \text{ in}$$

$$d = 1.00 \text{ in}$$

$$t = 1.00 \text{ (single lug)}$$



Material: 7075-T73 Aluminum Alloy

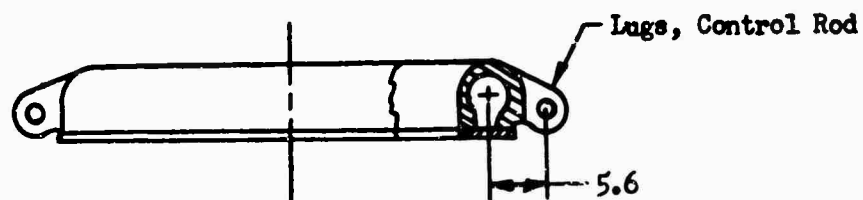


Figure 223 Rotating Swashplate

Lug Analysis: For this fatigue analysis, the transversely loaded lug is analyzed as an axially loaded lug. This is considered to be a conservative approach when the lug dimensions exceed specified limits.

The mean endurance limit stress for the lug is

$$\begin{aligned} (\sigma_{en})_m &= \frac{2.8 [1.00 + 0.1166(3.6)] (\pm 1800)}{3.6 (1. + 1.0)} \\ &= \pm 994 \text{ lb/in}^2 \end{aligned}$$

The working endurance limit is

$$\begin{aligned} \sigma_{en} &= (PF)(\sigma_{en})_m = (0.519)(\pm 994) \\ &= \pm 516 \text{ lb/in}^2 \end{aligned}$$

Nominal Lug Stress:

$$\begin{aligned} \sigma &= \frac{P}{2t(D-d)} = \frac{(1580 \pm 2640)}{2(1.0)(3.6-1.00)} \\ &= (304 \pm 508) \text{ lb/in}^2 \end{aligned}$$

$$\begin{aligned} MS &= \frac{1}{\frac{\sigma_s}{\sigma_{ty}} + \frac{\sigma_v}{\sigma_{en}}} - 1 \\ &= \frac{1}{\frac{304}{56,000} + \frac{508}{516}} - 1 \\ &= +0.01 \end{aligned}$$

Section A-A (Typical Ring Cross Section) of Figure 223

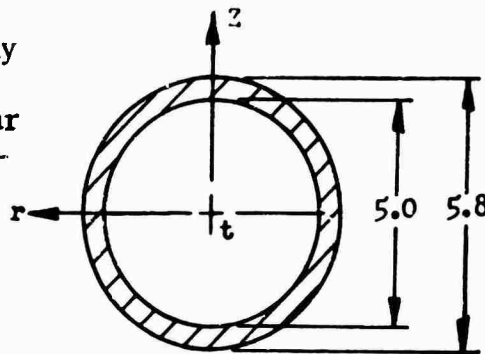
The cross section A-A is idealized as a tubular section.

$$A = 6.78 \text{ in}^2$$

$$I = 24.87 \text{ in}^4$$

$$J = 12.43 \text{ in}^4$$

The critical loading of a ring cross section is calculated using a Sikorsky computer program based on the inextensional theory for thin circular rings. The maximum loading determined from this computer program is shown graphically in Figures 225 and 226 and summarized as follows:



Section A-A of Figure 223
(Effective Ring Cross Section)

$$M_R = (-5330 \pm 5530) \text{ in-lb}$$

$$M_Z = (-2320 \pm 4120) \text{ in-lb}$$

$$M_T = (-4950 \pm 7050) \text{ in-lb}$$

$$V_Z = (790 \pm 1340) \text{ lb}$$

The critical stresses occur at point A (Figure 224).

$$s = \frac{(M_Z + M_R) c}{I} = \frac{(5813 \pm 6890) (2.9)}{24.87}$$

$$= (679 \pm 803) \text{ psi}$$

$$\tau_1 = \frac{M_T c}{J} = \frac{(4950 \pm 7050)(2.9)}{12.43}$$

$$= (1155 \pm 1645) \text{ lb/in}^2$$

The shearing stress (τ_2) at point A due to the vertical shear V_Z is given by the formula

$$\tau_2 = \frac{V_Z}{Ib} \bar{a}\bar{y}$$

$$\begin{aligned}\text{Now, } a &= \frac{A}{2} = 3.39 \text{ in}^2 \\ b &= (D-d) = 0.80 \text{ in} \\ \bar{y} &= \frac{2r_m}{\pi} = 3.44 \text{ in}\end{aligned}$$

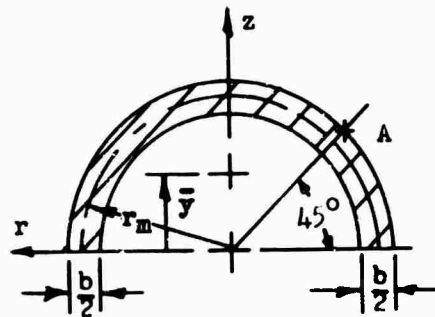


Figure 224 Vertical Shear Loading Geometry, Section A-A, Rotating Swashplate

$$\begin{aligned}\text{Therefore, } \tau_2 &= \frac{(790 \pm 1340)(3.39)(3.44)}{(24.87)(.80)} \\ &= (463 \pm 785) \text{ lb/in}^2\end{aligned}$$

Summarizing, the stresses are

$$\begin{aligned}\sigma &= (679 \pm 803) \text{ lb/in}^2 \\ \tau &= \tau_1 + \tau_2 = (1618 \pm 2430) \text{ lb/in}^2\end{aligned}$$

The principal stress is

$$\sigma_p = (1992 \pm 2910) \text{ lb/in}^2$$

The working endurance limit stress is

$$\begin{aligned}\sigma_{en} &= (SEF)(MF)(PF)(\sigma_{en})_m \\ &= (0.68)(0.80)(0.519)(\pm 22,000) \\ &= \pm 6210 \text{ lb/in}^2\end{aligned}$$

An SCF equal to 2.0 will be assumed:

$$MS = \frac{1}{\frac{\sigma_s}{\sigma_{ty}} + \frac{(SCF) \sigma_v}{\sigma_{en}}} - 1$$

$$= \frac{1}{\frac{1992}{56,000} + \frac{(2.0)(2910)}{6210}} - 1$$

$$= +0.028$$

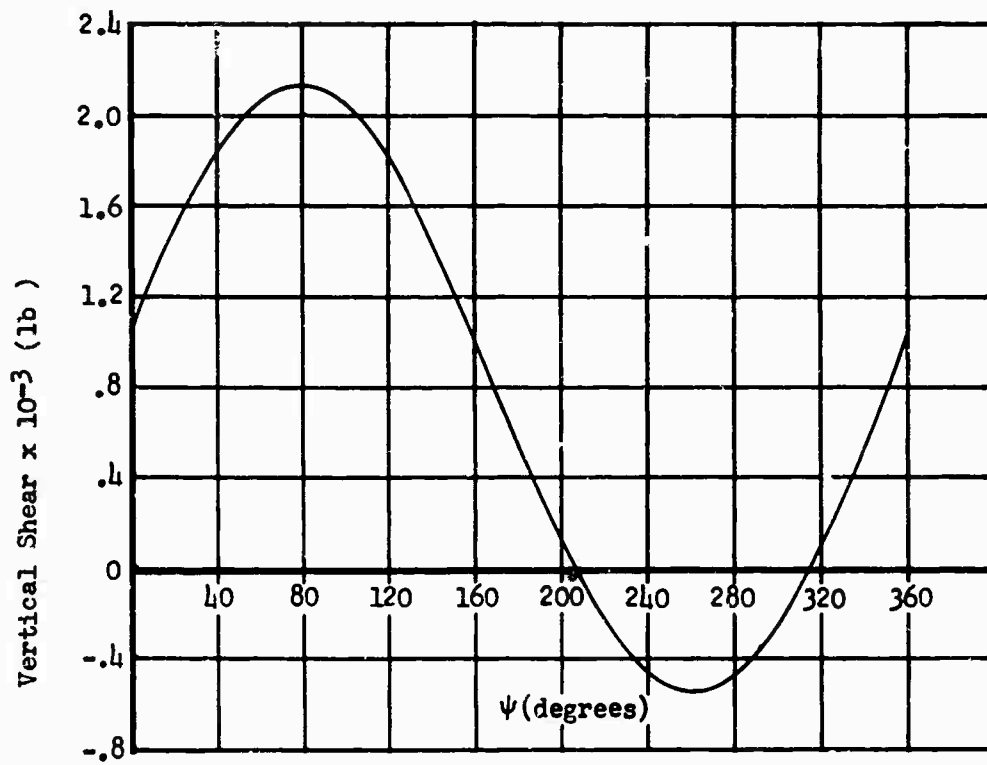


Figure 225 Shear on Critical Ring Cross Section,
Rotating Swashplate

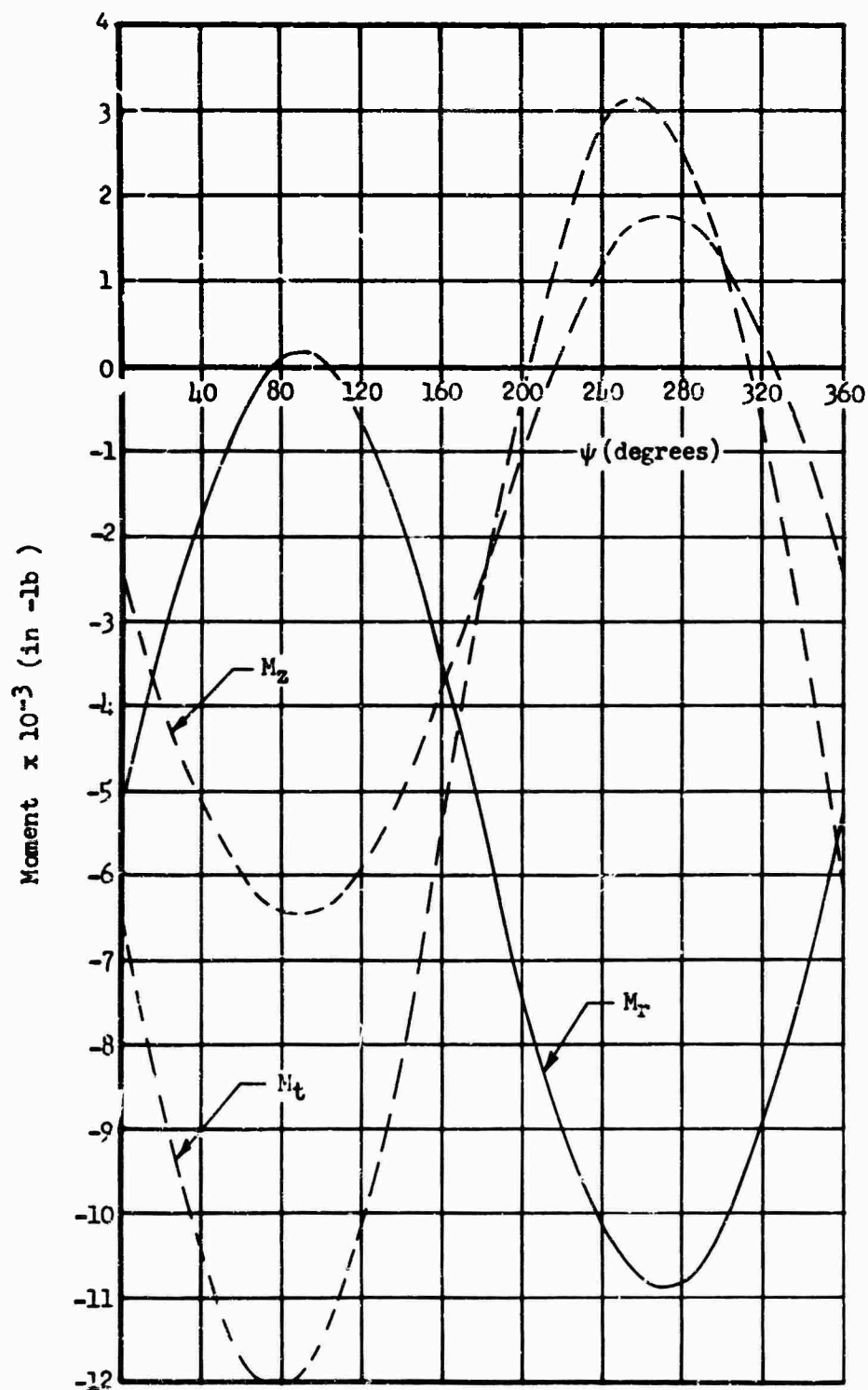


Figure 226 Bending Moments on Critical Ring Cross Section, Rotating Swashplate

Stationary Swashplate, Figure 227

Lugs, Servo

Lug Dimensions:

$$D = 4.0 \text{ in}$$

$$d = 1.0 \text{ in}$$

$$t = 1.25 \text{ in}$$

$$\text{Load: } P = (6890 \pm 3450) \text{ lb}$$

Lug Analysis: The lug is sized using the Heywood lug analysis, since a chafing condition exists between the lug and bushing.

The mean endurance limit stress for the lug is

$$\begin{aligned} (\sigma_{en})_m &= \frac{2.8 [1.0 + 0.1166 (4.0)]}{4.0 (1.0 + 1.0)} (\pm 1880) \\ &= \pm 965 \text{ lb/in}^2 \end{aligned}$$

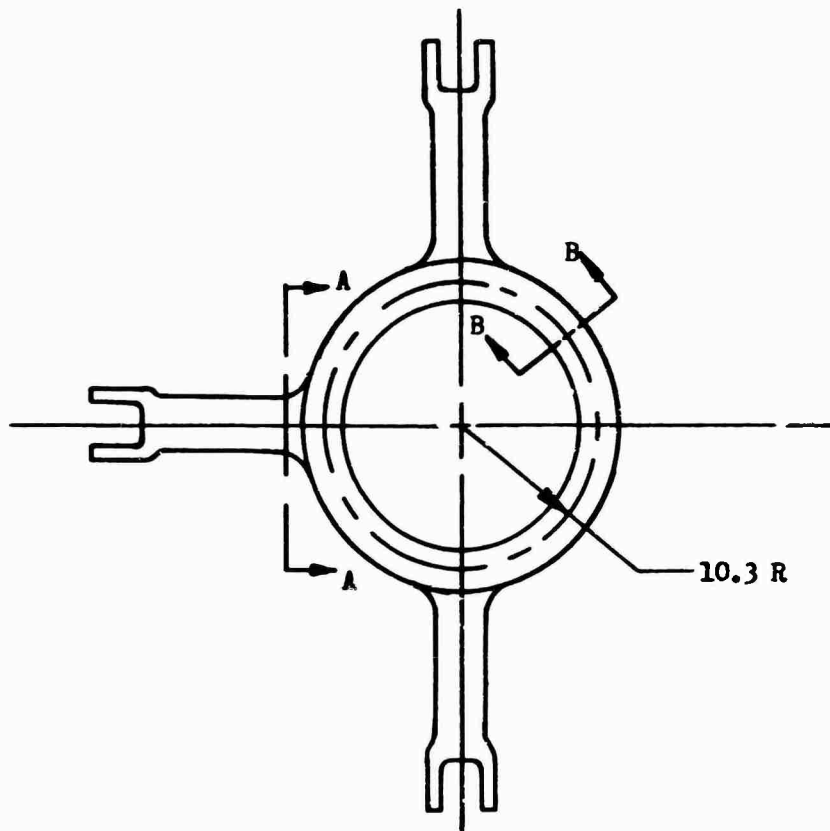
The working endurance limit stress is

$$\begin{aligned} \sigma_{en} &= (PF) (\sigma_{en})_m = (0.519)(\pm 965) \\ &= \pm 501 \text{ lb/in}^2 \end{aligned}$$

Nominal Lug Stress:

$$\begin{aligned} \sigma &= \frac{P}{2t(D-d)} = \frac{(6890 \pm 3450)}{2(1.25)(4.0-1.0)} \\ &= (955 \pm 494) \text{ lb/in}^2 \end{aligned}$$

$$MS = \frac{1}{\frac{\sigma}{\sigma_{ty}} + \frac{\sigma_v}{\sigma_{en}}} - 1$$



Material: 7075-T73 Aluminum Alloy

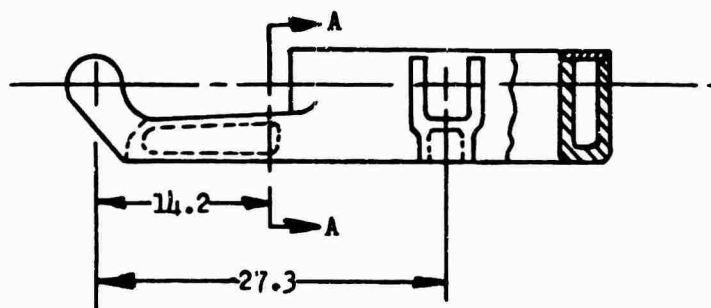


Figure 227 Stationary Swashplate

$$= \frac{1}{\frac{955}{56,000} + \frac{494}{501}} - 1$$

$$= 0.0$$

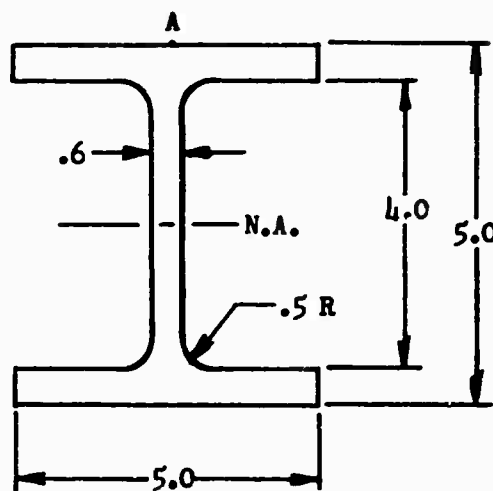
Section A-A of Figure 227

Section Properties:

$$A = 7.0 \text{ in}^2$$

$$I = 28.1 \text{ in}^4$$

$$c = 2.5 \text{ in}$$



Section A-A of Figure 227

Loads on Section A-A:

$$V = P = 6890 \pm 3450 \text{ lb}$$

$$M = 14.2 P$$

$$= 97,840 \pm 48,990 \text{ in-lb}$$

Nominal stress at point A:

$$s = \frac{Mc}{I} = \frac{(97,840 \pm 48,990)(2.5)}{28.1}$$

$$= (8700 \pm 4360) \text{ lb/in}^2$$

Working endurance limit stress is

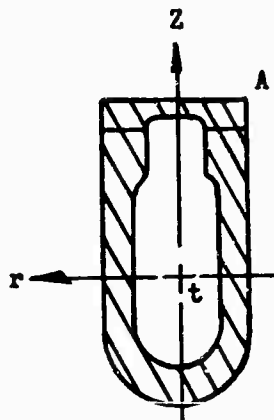
$$\begin{aligned} s_{en} &= (SEF)(MF)(PF)(s_{en})_m \\ &= (0.70)(0.80)(0.519)(\pm 22,000) \\ &= \pm 6390 \text{ lb/in}^2 \end{aligned}$$

$$\begin{aligned} MS &= \frac{1}{\frac{s}{s_{ty}} + \frac{(SCF) s_v}{s_{en}}} - 1 \\ &= \frac{1}{\frac{8700}{56,000} + \frac{(1.2)(4360)}{6390}} - 1 \\ &= +0.02 \end{aligned}$$

Section B-B of Figure 227

The internal loads at the critical ring section, of which section B-B is representative, are

$$\begin{aligned} V_z &= (2420 \pm 1350) \text{ lb} \\ M_r &= (93,660 \pm 49,230) \text{ in-lb} \\ M_t &= (-41,520 \pm 22,920) \text{ in-lb} \\ M_z &= (-25,080 \pm 13,440) \text{ in-lb} \end{aligned}$$



Section B-B of Figure 227

The cross section is conservatively idealized as a hollow rectangular section. The properties of the section are

$$A = 16.0 \text{ in}^2$$

$$I_r = 123.0 \text{ in}^2$$

$$c_r = 4.5 \text{ in}$$

$$I_z = 25.5 \text{ in}^4$$

$$c_z = 1.75 \text{ in}$$

$$J = 64.3 \text{ in}^4$$

The critical stresses occur at point A.

$$\begin{aligned} s &= \left(\frac{M_c}{I} \right)_r + \left(\frac{M_c}{I} \right)_z \\ &= \frac{(93,660 \pm 49,230)(4.5)}{123.0} + \frac{(25,080 \pm 13,440)(1.75)}{25.5} \\ &= (5150 \pm 2720) \text{ lb/in}^2 \end{aligned}$$

The working endurance limit stress is $\pm 6120 \text{ lb/in}^2$

An SCF equal to 2.0 will be assumed.

$$MS = \frac{1}{\frac{5150}{120,000} + \frac{(2.0)(2720)}{6210}} - 1 = +0.08$$

Flapping Hinge (Figure 228)

The known applied loads on the flapping hinge using the design loads for titanium without chafing are

$$\begin{aligned} P_r &= \left(F_c + \frac{Md}{9.0} \right) \rightarrow V_n = (114,900 \pm 8300) \text{ lb} \quad (106) \\ V_c &= (8040 \pm 1180) \text{ lb} \end{aligned}$$

The loads R_1 and R_2 are determined considering equilibrium of the bell-crank pin.

$$R_1 = (4030 \pm 6720) \text{ lb}$$

$$R_2 = (880 \pm 1470) \text{ lb}$$

The flapping lug forces P_1 and P_2 are determined considering equilibrium of the flapping hinge.

$$\Sigma F_h = P_1 + P_2 - R_1 \cos 31^\circ + R_2 \cos 31^\circ - P_r = 0$$

$$\Sigma M_o = 10.4 P_2 + 10.4 R_2 \cos 31^\circ - 5.2 P_r - 10.8 V_c = 0$$

Solving these equations for P_1 and P_2 gives

$$P_1 = (52,560 \pm 8680) \text{ lb}$$

$$P_2 = (65,040 \pm 4120) \text{ lb}$$

Outboard Lug of Figure 228

The outboard lug is assumed to be only 70 percent efficient.

Lug Dimensions: $D = 8.85 \text{ in}$

$$d = 8.25 \text{ in}$$

$$t = 8.4 \text{ in}$$

Lug Stress Concentration Factor:

$$SCF = \frac{1.666 D}{d + 0.1166 D} = 1.59$$

The Lug Load P is

$$P = P_r \rightarrow V_c = (115,200 \pm 8340) \text{ lb}$$

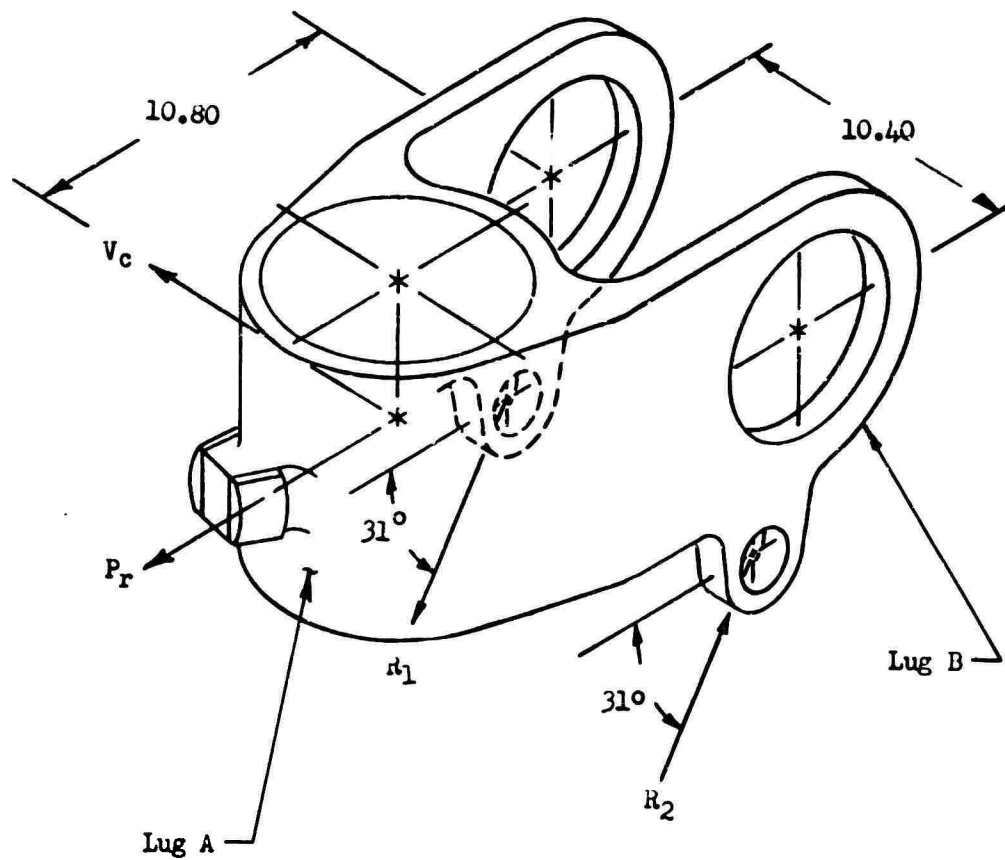


Figure 228 Flapping Hinge Fatigue Loading

Lug Nominal Stress

$$\begin{aligned} \delta &= \frac{P}{0.7t(D-d)} = \frac{(115,200 \pm 8340)}{0.7(0.4)(8.85-8.25)} \\ &= (32,650 \pm 2360) \text{ lb/in}^2 \end{aligned}$$

The working endurance limit stress is

$$\begin{aligned} \delta_{en} &= (SEF)(MF)(PF)(\delta_{en})_m \\ &= (0.75)(0.80)(0.482)(\pm 60,000) \\ &= \pm 17,350 \text{ lb/in}^2 \end{aligned}$$

$$\begin{aligned} MS &= \frac{1}{\frac{(SCF)\delta_s}{\delta_{en}} + \frac{(SCF)\delta_v}{\delta_{en}}} - 1 \\ &= \frac{1}{\frac{(1.59)(32,650)}{120,000} + \frac{(1.59)(2360)}{17,350}} - 1 \\ &= +0.54 \end{aligned}$$

Flapping Lug of Figure 228

Lug Dimensions: $D = 8.75 \text{ in}$

$d = 6.25 \text{ in}$

$t = 0.90 \text{ in}$

Lug Stress Concentration Factor:

$$SCF = \frac{1.666 D}{d + 0.1166 D} = 2.01$$

Lug Nominal Stress:

$$\delta = \frac{P_1}{t(D-d)} = \frac{(52,560 \pm 8680)}{(0.9)(8.75-6.25)}$$

$$= (23,360 \pm 3860) \text{ lb/in}^2$$

The working endurance limit stress $(s_{en})_m$ is $\pm 17,350 \text{ lb/in}^2$

$$MS = \frac{1}{\frac{2.01(23,360)}{120,000} + \frac{2.01(3860)}{17,350}} - 1$$

$$= +0.19$$

Spindle (refer to Figure 214)

The design loads for titanium without chafing apply.

$$\begin{aligned} P_1 &= F_c \rightarrow V_n \rightarrow V_c \\ &= (113,800 \pm 1100) \text{ lb} \end{aligned}$$

$$M_c = M_d = \pm 59,800 \text{ in-lb}$$

$$P_d = \frac{M_d}{9.0} = \frac{(\pm 59,800)}{9.0} = \pm 6640 \text{ lb}$$

$$P_2 = P_1 + P_d = (113,800 \pm 7740) \text{ lb}$$

Section A-A of Figure 214

The load on Section A-A is due to the damper force P_d . The loads on Section A-A are

$$V = \frac{P_d}{2} = \pm 3320 \text{ lb}$$

$$M = 5.4 \frac{P_d}{2} = \pm 17,930 \text{ in-lb}$$

Section Properties:

$$A = 2.28 \text{ in}^2$$

$$I = 3.85 \text{ in}^4$$

$$c = 1.8 \text{ in}$$

Nominal Stress:

$$s = \frac{Mc}{I} = \frac{(\pm 17,930)(1.8)}{3.85} = 8380 \text{ lb/in}^2$$

The working endurance limit stress is

$$\begin{aligned} s_{en} &= (SEF)(MF)(PF)(s_{en})_m \\ &= (0.75)(0.80)(0.630)(\pm 60,000) \\ &= \pm 22,680 \text{ lb/in}^2 \end{aligned}$$

$$\begin{aligned} MS &= \frac{s_{en}}{(SCF)s_v} - 1 \\ &= \frac{22,680}{(1.2)(8380)} - 1 \\ &= +1.25 \end{aligned}$$

Section B-B of Figure 214

It is conservatively assumed that 30 percent of the moment is transferred from the stack bearings through the spindle nut to Section B-B.

Loads: $P = P_1 = 113,800 \pm 1100 \text{ lb}$

$$M = 0.30 M_C = \pm 17,940 \text{ in-lb}$$

Section Properties:

$$A = 4.33 \text{ in}^2$$

$$c = 2.45 \text{ in}$$

$$I = 11.5 \text{ in}^4$$

Nominal Stress:

$$\begin{aligned} s &= \frac{P}{A} + \frac{M_C}{I} \\ &= \frac{(113,800 \pm 1100)}{4.33} + \frac{(17,940)(2.45)}{11.5} \\ &= (26,280 \pm 4070) \text{ lb/in}^2 \end{aligned}$$

The working endurance limit stress is

$$\begin{aligned} s_{en} &= (SEF)(MF)(PF)(s_{en})_m \\ &= (0.80)(0.80)(0.482)(\pm 60,000) \\ &= \pm 18,510 \text{ lb/in}^2 \end{aligned}$$

The SCF at the thread relief fillet is 2.0.

$$\begin{aligned} MS &= \frac{1}{\frac{(2.0)(26,280)}{120,000} + \frac{(2.0)(4070)}{18,510}} - 1 \\ &= +0.14 \end{aligned}$$

Section C-C of Figure 214

$$\text{Loads: } P = P_1 = (113,800 \pm 1100) \text{ lb}$$

$$M = M_d = \pm 59,800 \text{ in-lb}$$

Section Properties:

$$A = 7.14 \text{ in}^2$$

$$C = 2.75 \text{ in}$$

$$I = 22.9 \text{ in}^4$$

Nominal Stress:

$$s = \frac{P}{A} + \frac{M_C}{I}$$

$$= \frac{(113,800 \pm 1100)}{7.14} + \frac{(\pm 59,800)(2.75)}{22.9}$$

$$s = (15,940 \pm 7260) \text{ lb/in}^2$$

The working endurance limit stress is

$$s_{en} = (SEF)(MF)(PF)(s_{en})_m$$

$$= (0.75)(0.80)(0.482)(\pm 60,000)$$

$$= \pm 17,350 \text{ lb/in}^2$$

An SCF equal to 1.7 is assumed, since the load in the spindle must flow from the cylindrical shank into the extending damper arms.

$$MS = \frac{(1.7)(15,940)}{120,000} + \frac{(1.7)(7260)}{17,350} - 1$$

$$= +0.06$$

Damper Arm Lugs, (See Detail E of Figure 214)

Lug Dimensions: $D = 2.0 \text{ in}$

$$d = 1.0 \text{ in}$$

$$t = 0.7 \text{ in}$$

Lug Analysis: The Heywood lug analysis is used, since a chafing condition can possibly exist between the lug and bushing.

The mean endurance limit stress for the lug is

$$s_{en} = \frac{2.8 [1.0 + 0.1166 (2.0)]}{2.0 [1.0 + 1.0]} (\pm 11,400)$$

$$= \pm 9840 \text{ lb/in}^2$$

The working endurance limit stress is

$$(s_{en}) = (PF)(s_{en})_m = (0.482)(\pm 9840)$$

$$= \pm 4740 \text{ lb/in}^2$$

Nominal Lug Stress:

$$\begin{aligned} s &= \frac{P_d}{2t(D-d)} = \frac{\pm 6640}{2(0.7)(2.0-1.0)} \\ &= \pm 4740 \text{ lb/in}^2 \end{aligned}$$

$$\begin{aligned} MS &= \frac{s_{en}}{s} - 1 \\ &= \frac{4740}{4740} - 1 \\ &= 0.0 \end{aligned}$$

Lugs, (See Detail F of Figure 214)

$$\begin{aligned} \text{Load: } P &= \frac{P_2}{2} + \frac{M_c}{9.0} \\ &= \frac{(113,800 \pm 7740)}{2} + \frac{\pm 59,800}{9.0} \\ &= (56,900 \pm 10,510) \text{ lb} \end{aligned}$$

Lug Dimensions:

$$D = 8.4 \text{ in}$$

$$d = 5.2 \text{ in}$$

$$t = 0.75 \text{ in}$$

Chafing will be precluded from the spindle lugs by utilizing bonded washers and bushings.

Lug stress concentration factor is

$$\begin{aligned} K_c &= \frac{1.666 D}{d + 0.1166D} = \frac{1.666 (8.4)}{5.2 + (0.1166)(8.4)} \\ &= 2.26 \end{aligned}$$

Nominal Lug Stress:

$$\begin{aligned} s &= \frac{P}{t(D-d)} = \frac{(56,900 \pm 10,510)}{0.75(8.4-5.2)} \\ &= (23,700 \pm 4380) \text{ lb/in}^2 \end{aligned}$$

The working endurance limit stress is

$$\begin{aligned} s_{en} &= (SEF)(MF)(PF)(s_m) \\ &= (0.80)(0.80)(0.630)(\pm 60,000) \\ &= \pm 24,190 \text{ lb/in}^2 \end{aligned}$$

$$\begin{aligned} MS &= \frac{1}{\frac{K_C s}{s_{ty}} + \frac{K_C s_y}{s_{en}}} - 1 \\ &= \frac{1}{\frac{(2.26)(23,700)}{120,000} + \frac{(2.26)(4380)}{24,190}} - 1 = +0.16 \end{aligned}$$

Hub Arm, Figure 229

Steel Bolts (Flange Bolt Circle)

The design loads for steel without chafing apply.

$$F_C = (114,000 \pm 1000) \text{ lb}$$

$$V_n = (8220 \pm 13,020) \text{ lb}$$

$$V_C = (8040 \pm 1310) \text{ lb}$$

$$M_d = \pm 59,800 \text{ in-lb}$$

$$P_3 = (3150 \pm 5250) \text{ lb}$$

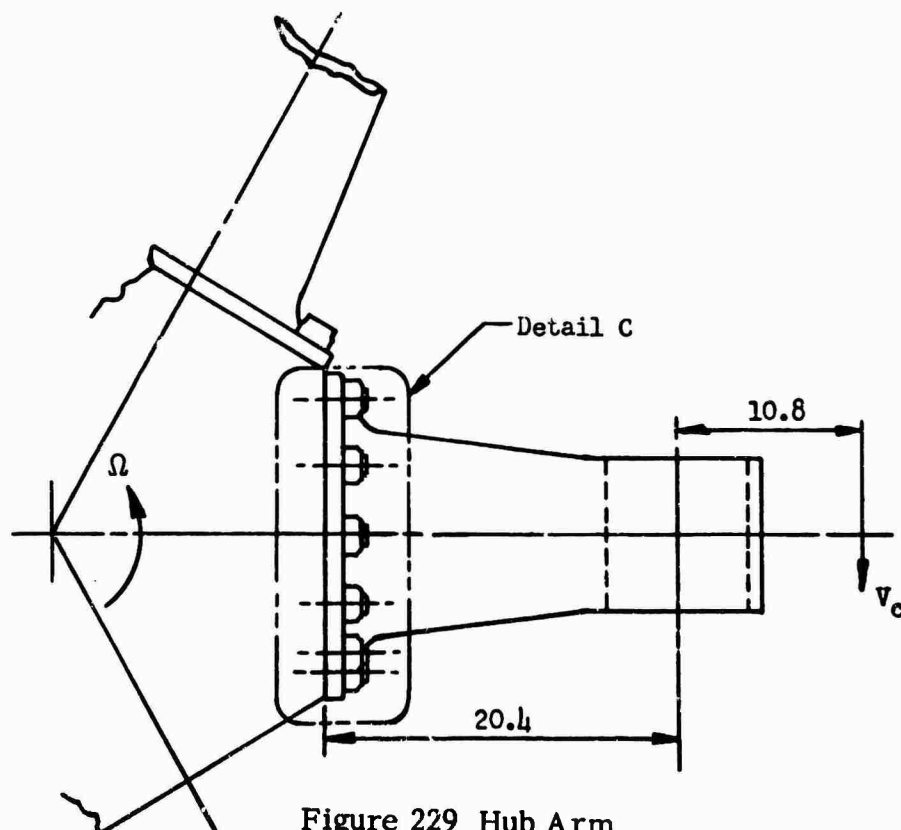
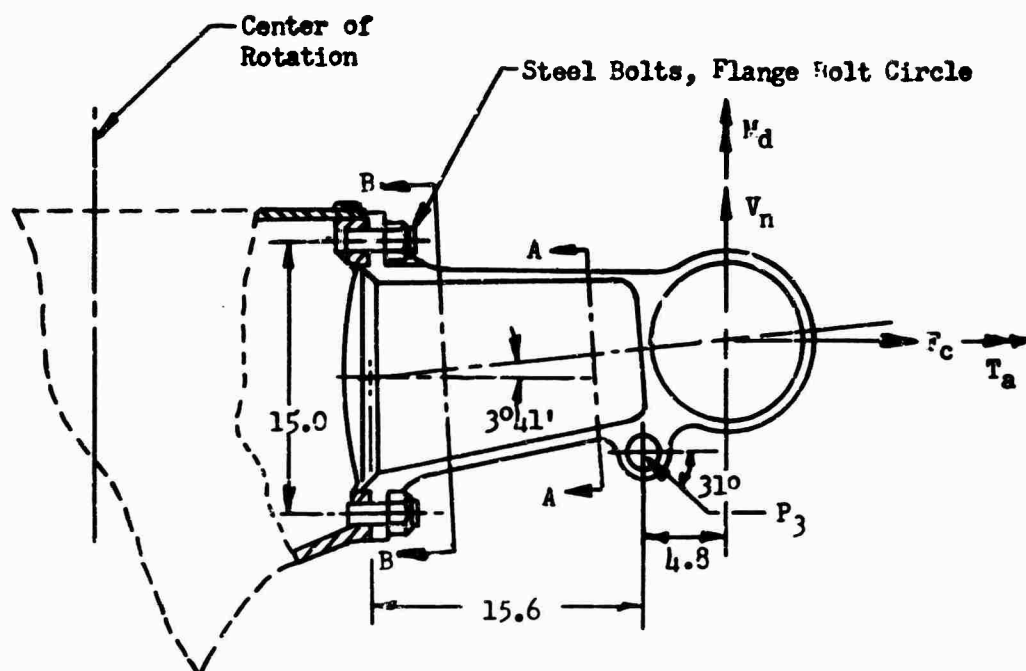


Figure 229 Hub Arm

The loads on the bolt circle are (See Detail C of Figure 229)

$$P = F_c - P_3 \cos 31^\circ = (111,300 \pm 5550) \text{ lb}$$

$$M_c = 31.2 V_c + M_d = (250,800 \pm 100,700) \text{ in-lb}$$

$$\begin{aligned} M_f &= 20.4 V_n + 15.6 (P_3 \sin 31^\circ) \\ &= (193,000 \pm 307,700) \text{ in-lb} \end{aligned}$$

In addition to the above loads there is a twisting moment (M_r) which is generated by the chordwise shear load (V_c). Consider the twisting moment at the flapping hinge (T_a).

$$\begin{aligned} (T_a)_{\max} &= (\text{Offset between hinges}) \sin (\beta_{\max}) (V_c)_{\max} \\ &= (10.8) \sin (4^\circ 6' + 5^\circ 48') (8040 + 1450) \\ &= 17,620 \text{ in-lb} \end{aligned}$$

$$\begin{aligned} (T_a)_{\min} &= (\text{Offset between hinges}) \sin (\beta_{\min}) (V_c)_{\min} \\ &= (10.8) \sin (4^\circ 6' - 5^\circ 48') (8040 - 1450) \\ &= -2110 \text{ in-lb} \end{aligned}$$

Therefore, $T_a = 9,870 \pm 11,980 \text{ in-lb}$

Note that the normal and chordwise shear loads are taken out on the tubular arm flange shoulder and hence are not resisted by the bolts.

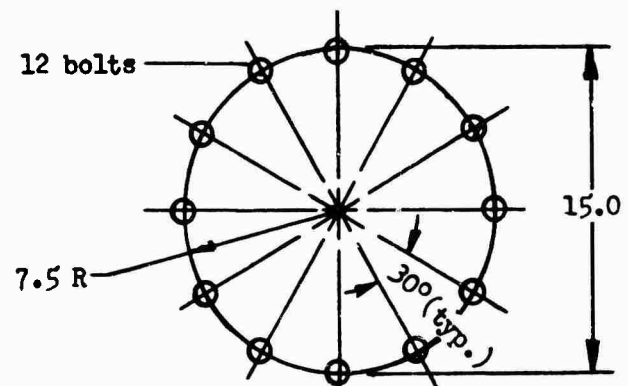
Bolt Circle Data:

n = number of bolts

= 12

r = bolt circle radius

= 7.5 in



Detail C of Figure 229 (Hub Arm Bolt Circle)

The bolt load is based on the assumption of a linear relationship between bolt load and its distance from the neutral bending axis.

$$P_b \text{ (axial bolt load)} = \frac{P}{n} + \frac{2M}{nr}$$

where $M = M_c \rightarrow M_f$

$$= (260,820 \pm 324,000) \text{ in-lb}$$

$$\begin{aligned} P_b &= \frac{(111,360 \pm 5550)}{12} + \frac{2(260,820 \pm 324,000)}{12(7.50)} \\ &= (15,080 \pm 7660) \text{ lb} \end{aligned}$$

For a 1.250-inch-diameter bolt, the nominal stress is

$$\begin{aligned} s &= \frac{P}{A} = \frac{15,080 \pm 7660}{1.227} \\ &= (12,290 \pm 6240) \text{ lb/in}^2 \end{aligned}$$

The working endurance limit stress is

$$s_{en} = (SEF)(MF)(PF)(s_{en})_m$$

$$SEF = 0.80$$

$$MF = 1.00$$

$$PF = 0.63$$

$$\begin{aligned} s_{en} &= (0.80)(1.00)(0.63)(\pm 60,000) \\ &= \pm 30,240 \text{ lb/in}^2 \end{aligned}$$

$$\begin{aligned} MS &= \frac{1}{\frac{s_s}{s_{ty}} + \frac{(SCF)s_v}{s_{en}}} - 1 \\ &= \frac{1}{\frac{12,290}{132,000} + \frac{(3.5)(6240)}{30,240}} - 1 \\ &= +0.22 \end{aligned}$$

Lug (flapping hinge)

The lug is assumed to be 70 percent effective. The formula for equivalent lug force is given by the equation

$$P_{eq} = \frac{P}{2} + \frac{M}{(1 - \eta/2) t}$$

where P = axial force on lug

M = applied moment on lug

t = width of barrel lug

η = assumed efficiency of lug

Note that the equivalent lug has a width equal to ($\eta t/z$). The use of a split journal sleeve bonded to the inner surface of the lug eliminates chafing of the lug. The loads for titanium without chafing apply.

$$F_C = (114,100 \pm 900) \text{ lb}$$

$$V_n = (8220 \pm 11,590) \text{ lb}$$

$$V_C = (8040 \pm 1180) \text{ lb}$$

$$M_d = \pm 59,800 \text{ in-lb}$$

The loads on the lugs are

$$P = F_C \rightarrow V_n = (114,950 \pm 1750) \text{ lb}$$

$$M = M_d + 10.8 V_C = (86,830 \pm 72,540) \text{ in-lb}$$

Lug Dimensions:

$$D = 10.0 \text{ in}$$

$$d = 8.3 \text{ in}$$

$$t = 8.4 \text{ in}$$

The equivalent lug force is

$$P_{eq} = \frac{(114,950 \pm 1750)}{2} + \frac{(86,830 \pm 72,540)}{(1 - 0.70/2)(8.4)}$$

$$= (73,380 \pm 14,160)$$

Lug stress concentration factor: SCF = 1.76

Equivalent lug dimensions:

$$D = 10.0 \text{ in}$$

$$d = 8.3 \text{ in}$$

$$t_{eq} = 2.94 \text{ in}$$

The working endurance limit stress is

$$(s_{en}) = (SEF)(MF)(PF)(s_{en})_m$$

$$= (0.70)(0.80)(0.482)(\pm 60,000)$$

$$= \pm 16,200 \text{ lb/in}^2$$

The nominal equivalent lug stress is

$$s = \frac{P_{eq}}{t_{eq}(D-d)} = \frac{(73,380 \pm 14,160)}{2.94(10.0-8.3)}$$

$$= (14,690 \pm 2830) \text{ lb/in}^2$$

$$MS = \frac{1}{\frac{1.76(14,690)}{120,000} + \frac{1.76(2830)}{16,200}} - 1$$

$$= +0.91$$

Section A-A of Figure 229

The design loads for titanium without chafing apply.

Loads: r at Section A-A = 30.2 in

$$P = (116,800 \pm 5550) \text{ lb}$$

$$\begin{aligned} M_c &= 16.6 V_c + M_d \\ &= (133,460 \pm 79,390) \text{ in-lb} \end{aligned}$$

$$\begin{aligned} M_f &= 5.8 V_n + 1.0 (P_3 \sin 31^\circ) \\ &= (49,300 \pm 69,920) \text{ in-lb} \end{aligned}$$

A resultant bending moment M_r is computed:

$$\begin{aligned} M_r &= M_c + M_f \\ &= (132,730 \pm 105,790) \text{ in-lb} \end{aligned}$$

Section Properties:

$$A = 9.4 \text{ in}^2$$

$$I = 86.1 \text{ in}^4$$

$$c = 4.45 \text{ in}$$

Nominal Stress:

$$\begin{aligned} s &= \frac{P}{A} + \frac{M_c}{I} \\ &= \frac{(116,800 \pm 5550)}{9.4} + \frac{(132,730 \pm 105,790)(4.45)}{86.1} \\ &= (19,500 \pm 6300) \text{ lb/in}^2 \end{aligned}$$

The working endurance limit stress is

$$\begin{aligned} s_{en} &= (SEF)(MF)(PF)(s_{en})_m \\ &= (0.70)(0.80)(0.482)(\pm 60,000) \\ &= \pm 16,200 \text{ lb/in}^2 \end{aligned}$$

An SCF equal to 1.8 will be assumed.

$$MS = \frac{1}{\frac{(1.8)(19,500)}{120,000} + \frac{(1.8)(6300)}{16,200}} - 1$$

$$= 0.0$$

Section B-B of Figure 229

The design loads for titanium without chafing apply.

Loads: r at Section B-B = 19.1 in

$$P = (116,800 \pm 5550) \text{ lb}$$

$$M_c = 27.7 V_c + M_d$$

$$= (222,700 \pm 92,490) \text{ in-lb}$$

$$M_f = 16.9 V_n + 12.1 (P_3 \sin 31^\circ)$$

$$= (158,500 \pm 228,500) \text{ in-lb}$$

A resultant bending moment M_r is computed.

$$M_r = M_c + M_f$$

$$= (230,490 \pm 246,500) \text{ in-lb}$$

Section Properties:

$$A = 17.0 \text{ in}^2$$

$$I = 248.0 \text{ in}^4$$

$$c = 5.65 \text{ in}$$

Nominal Stress:

$$s = \frac{P}{A} + \frac{M_c}{I}$$

$$= \frac{(116,800 \pm 5500)}{17.0} + \frac{(230,190 \pm 246,500)(5.6)}{248.0}$$

$$= 12,120 \pm 5940 \text{ lb/in}^2$$

An SCF equal to 2.0 will be assumed.

$$MS = \frac{1}{\frac{(2.0)(12,120)}{120,000} + \frac{(2.0)(5940)}{16,200}} - 1$$

$$= +0.07$$

Static and Fatigue Analyses of Hub, Structure, Alternate Design

Static Analysis

In the analysis of the central hub assembly, a conservative idealization of the structure is made in order to verify the strength of the design (see Figure 230).

The conical shell portion of the structure is replaced by a flat circular plate built in at the cylinder. The entire steady normal shear load $(V_N)_S$ is assumed to be carried by this plate. This is a conservative approximation, since a conical shell has considerably greater strength under normal shear loading than does a circular plate of equal thickness.

The upper and lower stiffening rings are assumed to react the entire centrifugal and hub moment load distributions in the radial direction.

Radial Load Distribution on Stiffening Rings

If the centrifugal load is assumed to be shared equally between the upper and lower stiffening rings, the distributed radial load is

$$q_1 = \frac{1}{2} \frac{(\text{total centrifugal load})}{2\pi R} \quad (107)$$

$$= \frac{6(F_C)}{4\pi R}$$

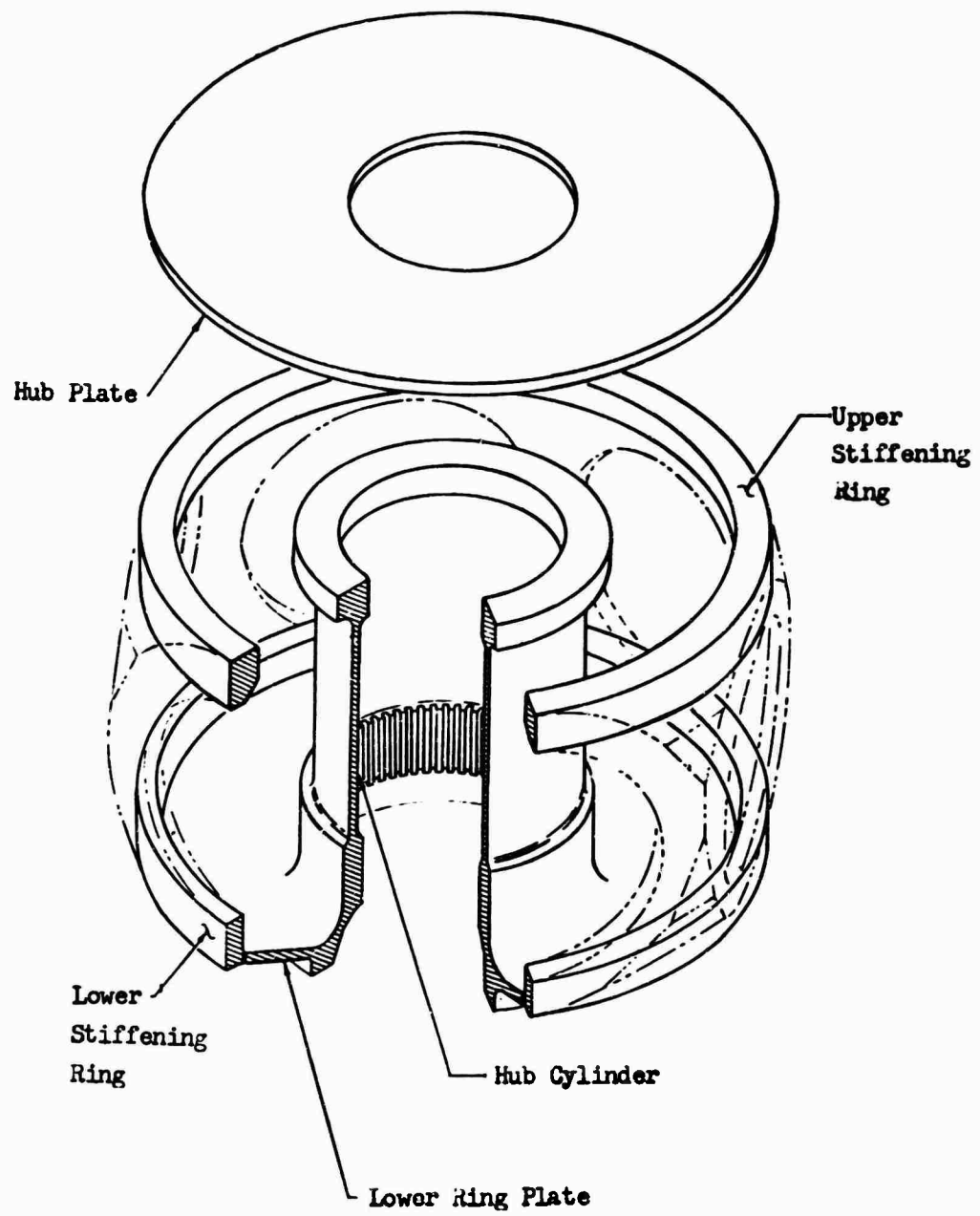


Figure 230 Alternate Hub Detail

The radial load distribution due to the hub moment (HM) is assumed to vary sinusoidally around the stiffening ring. If the rings are offset a distance (y), then the sinusoidally distributed load $q_2(\theta)$ is

$$y \int_0^{2\pi} q_2(\theta) \sin \theta R d\theta = HM \quad (108)$$

$$\text{where } q_2(\theta) = (q_2)_{\max} \sin \theta$$

$$(q_2)_{\max} y R \int_0^{2\pi} \sin^2 \theta d\theta = HM$$

$$(q_2)_{\max} y R \left[\frac{\theta}{2} - \frac{1}{4} \sin 2\theta \right]_0^{2\pi} = HM$$

$$\text{or finally, } (q_2)_{\max} = \frac{HM}{\pi y R} \quad (109)$$

The radial load distribution around the stiffening rings is (Figure 231)

$$\begin{aligned} q_r &= q_1 + q_2 \\ &= \frac{6F_c}{4\pi R} + \frac{HM}{\pi y R} \sin \theta \end{aligned} \quad (110)$$

The maximum radial load is

$$(q_r)_{\max} = 1.5 \frac{F_c}{\pi R} + \frac{HM}{\pi y R} \quad (111)$$

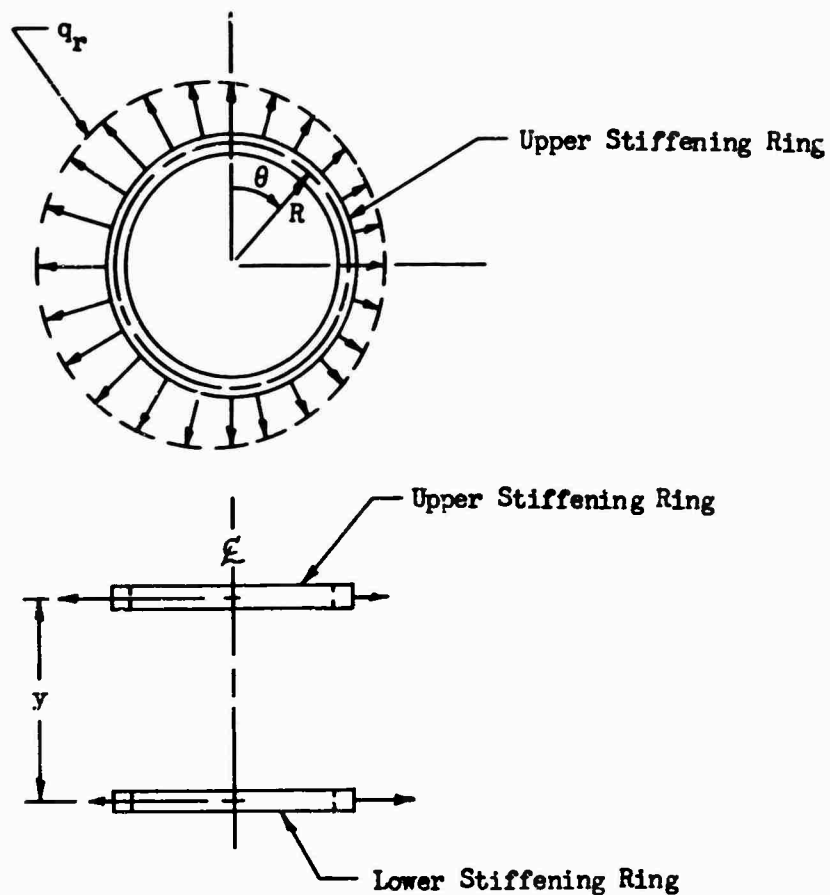


Figure 231 Radial Load Distribution in Stiffening Ring

The stiffening rings will be analyzed by assuming a uniform radial load equal in magnitude to $(q_r)_{\max}$.

Shear Load Distribution on Lower Ring Plate of Figure 232

The total normal shear load $6(V_n)_s$ is to be carried solely by the lower ring plate which is built in at the inner and outer edges.

$$q_n = \frac{6(V_n)_s}{2\pi a} \quad (112)$$

The in-plane shear load distribution in the plate on some radial section (r) is

$$q_s = \frac{T}{2\pi r^2} \quad (113)$$

Note that there is a net unbalanced in-plane load on the stiffening rings. These loads must be reacted by the upper hub plate and lower ring plate. If the stiffening rings are considered to be split from the plates, then this unbalanced force must be reacted solely by compression on one side of the plate (see Figure 233).

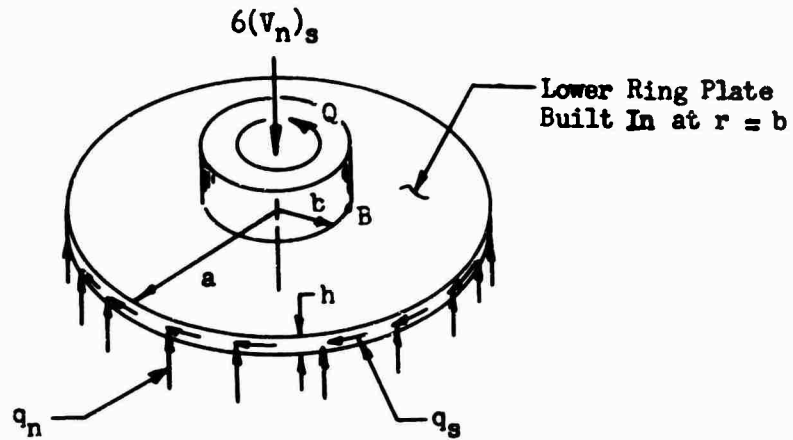


Figure 232 Shear Load Distribution on Lower Ring Plate

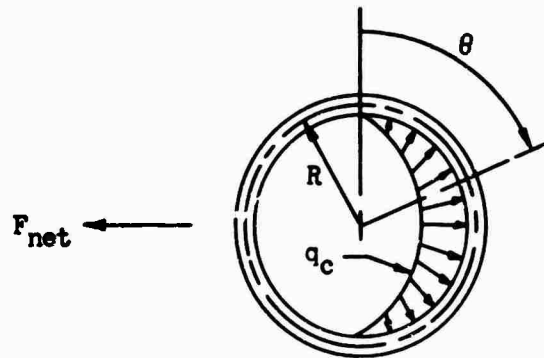


Figure 233 Compressive Load Distribution Between Stiffening Ring and Corresponding Ring Plate

Then, for equilibrium of the stiffening ring,

$$\int_0^{\pi} q_c(\theta) \sin \theta R d\theta = F_{\text{net}} = \frac{HM}{y}$$

$$q_c(\theta) = (q_c)_{\text{max}} \sin \theta, \text{ then}$$

$$\int_0^{\pi} (q_c)_{\text{max}} R \sin^2 \theta d\theta = F_{\text{net}}$$

$$\frac{(q_c)_{\text{max}} R \pi}{z} = F_{\text{net}}$$

$$(q_c)_{\max} = \frac{2F_{\text{net}}}{\pi R} = \frac{2(HM)}{\pi R y} \quad (114)$$

Starting Condition (Static)

Load: r at central hub assembly flange = 15.6 in

$$T = 3,500,000 \text{ in-lb}$$

$$F_c = 0$$

$$HM = 0$$

The components of the idealized central hub structure are now analyzed for the above loads.

Stiffening Rings

$$(q_r)_{\max} = 1.5 \frac{F_c}{\pi R} + \frac{HM}{\pi R y}$$

$$\text{but } F_c = 0$$

$$HM = 0$$

Therefore, the stiffening rings do not take any load in the starting condition.

Lower Ring Plate of Figure 230

The lower ring plate is assumed to carry the entire starting torque. The maximum shear load occurs at the section $r = b$ (see Figure 232).

$$\begin{aligned} (q_s)_{r=b} &= \frac{T}{2\pi b^2} \\ &= \frac{3,500,000}{2\pi(9.3)^2} \\ &= 6440 \text{ lb/in}^2 \end{aligned} \quad (115)$$

The shear stress is

$$\begin{aligned} \tau_s &= \frac{q_s}{h} = \frac{6440}{0.6} \\ &= 10,700 \text{ lb/in}^2 \end{aligned}$$

$$\begin{aligned}
 MS \text{ (ultimate)} &= \frac{r_{su}}{1.5 r_s} - 1 \\
 &= \frac{76,000}{1.5(10,700)} - 1 \\
 &= +3.73
 \end{aligned}$$

Rotor Overspeed (Static)

Load: r at central hub assembly = 15.6 in

$$F_C = 199,700 \text{ lb}$$

$$T = 2,258,000 \text{ in-lb}$$

$$HM = 0$$

Stiffening Ring, Lower, of Figures 230 and 232

The radial load distribution is

$$\begin{aligned}
 (q_r)_{\max} &= 1.5 \frac{(199,700)}{\pi (14.5)} \\
 &= 6580 \text{ lb/in}
 \end{aligned}$$

Splitting the ring along a diameter and imposing the condition of static equilibrium gives the relationship

$$\begin{aligned}
 2\delta A &= 2R (q_r)_{\max} & (116) \\
 \delta &= \frac{R (q_r)_{\max}}{A} \\
 &= \frac{(14.5)(6580)}{3.0} \\
 &= 31,800 \text{ lb/in}^2
 \end{aligned}$$

The tangential load distribution is

$$\begin{aligned} q_s &= \frac{T}{2 \pi R^2} \\ &= \frac{2,258,000}{2\pi(14.5)^2} \\ &= 1710 \text{ lb/in} \end{aligned}$$

The shear stress is

$$\begin{aligned} \tau &= \frac{q_s}{h} = \frac{1710}{0.6} \\ &= 2850 \text{ lb/in}^2 \end{aligned}$$

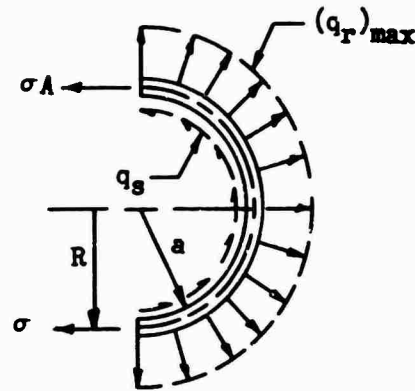


Figure 234 Stress in Stiffening Ring

The principal stress is

$$\begin{aligned} \sigma_p &= \frac{\sigma}{2} + \sqrt{\left(\frac{\sigma}{2}\right)^2 + \tau^2} \\ &= 32,100 \text{ psi} \end{aligned}$$

$$\begin{aligned} MS &= \frac{\sigma_{tu}}{1.5 \sigma_p} - 1 \\ &= \frac{130,000}{1.5 (32,100)} - 1 = +1.70 \end{aligned}$$

Alternate Design

Hub-Fatigue Analysis

The design loads for titanium without chafing apply.

r at central hub assembly = 15.6 in

$F_c = (119,000 \pm 900) \text{ lb}$

$$(V_n)_s = 8220 \text{ lb}$$

$$T = 2,258,000 \text{ in-lb}$$

$$M_h = 1,252,000 \text{ in-lb}$$

Stiffening Ring(s), See Figures 233 and 234

The radial load distribution is

$$\begin{aligned} (q_r)_{\max} &= 1.5 \frac{F_c}{\pi R} \pm \frac{M_h}{\pi R y} \\ &= \frac{1.5 (119,000 \pm 900)}{(14.5)} \pm \frac{1,252,000}{(14.5)(16.0)} \\ &= (3920 \pm 1750) \text{ lb/in} \end{aligned}$$

The axial hoop stress in the ring is

$$\begin{aligned} \sigma &= \frac{R (q_r)_{\max}}{A} \pm \frac{(14.5)(3920 \pm 1750)}{3.0} \\ &= (19,000 \pm 8500) \text{ lb/in}^2 \end{aligned}$$

The tangential load distribution is

$$\begin{aligned} q_s &= \frac{T}{2 \pi R^2} = \frac{2,252,000}{2 \pi (14.5)^2} \\ &= 1710 \text{ lb/in} \end{aligned}$$

The shear stress is

$$\begin{aligned} \tau &= \frac{q_s}{h} = \frac{1710}{0.6} \\ &= 2850 \text{ lb/in}^2 \end{aligned}$$

The principal stress is

$$\sigma_p = (19,500 \pm 8300) \text{ lb/in}^2$$

The working endurance limit stress is

$$\begin{aligned} s_{en} &= (SEF)(MF)(PF)(s_{en})_m \\ &= (0.80)(0.80)(0.630)(\pm 60,000) \\ &= \pm 24,200 \text{ lb/in}^2 \end{aligned}$$

The SCF is equal to 2.0

$$\begin{aligned} MS &= \frac{1}{\frac{2.0(19,500)}{120,000} + \frac{2.0(8300)}{24,200}} - 1 \\ &= 0.0 \end{aligned}$$

Lower Ring Plate of Figure 232

The normal shear load distribution is

$$\begin{aligned} q_n &= \frac{6(V_n)_s}{2\pi a} = \frac{6(8220)}{2\pi(14.5)} \\ &= 541 \text{ lb/in} \end{aligned}$$

The in-plane shear load distribution is

$$\begin{aligned} q_s &= \frac{T}{2\pi r^2} = \frac{2,258,000}{2\pi r^2} \\ &= \frac{359,400}{r^2} \text{ lb/in} \end{aligned}$$

The maximum stress condition in the lower circular plate structure occurs at the built-in inner boundary. The equation for the bending stress is given on page 113, case 6, Reference 56.

$$\text{For } \frac{a}{b} \cong 1.6, \quad s_b = \frac{0.24P}{h^2}$$

$$P = 2\pi a q_n = 2\pi(14.5)(541)$$

$$= 49,300 \text{ lb}$$

$$h = 0.5 \text{ in}$$

$$\sigma_b = \frac{0.24 (49,300)}{(0.6)^2} = 32,900 \text{ lb/in}^2$$

The in-plane shear stress is

$$\tau = \frac{q_s @ r = 9.3 \text{ in}}{h} = \frac{359,400}{(0.6)(9.3)^2}$$

$$= 6900 \text{ lb/in}^2$$

The principal stress is

$$\sigma_p = 34,300 \text{ lb/in}^2$$

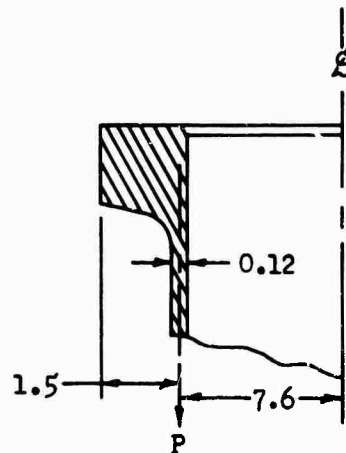
$$MS = \frac{130,000}{1.5 (34,300)} - 1$$

$$= +1.53$$

A high margin of safety is tolerated in this area because although the entire hub moment HM is assumed to be reacted by the stiffening rings with supporting structure, in actuality some of the moment would be carried by the built-in lower ring plate.

Hub Cylinder (See Detail A of Figure 230)

The cylinder structure must transmit the total rotor head lift to the main rotor shaft.



Detail A of Figure 230 (Hub Cylinder)

The axial cylinder load distribution (p) is

$$p = \frac{6 (V_n)_s}{2 \pi r} = \frac{6 (8220)}{2 \pi (7.6)}$$

$$= 103 \text{ lb/in}$$

The end moment distribution (M_o) is

$$M_o = 1.5 p = 155 \text{ in-lb/in}$$

The stress in the cylinder is

$$\delta = \frac{2 \pi r p}{A} + \frac{6 M_o}{t^2}$$

$$= \frac{2 \pi (7.6)(103)}{\pi 75} + \frac{6(155)}{(0.12)^2}$$

$$= 65,400 \text{ psi}$$

$$MS = \frac{130,000}{1.5 (65,400)} - 1$$

$$= +0.32$$

Hub Plate of Figure 230

The hub plate must react the compressive loading due to the hub moment. The radial compressive load distribution on the plate is

$$q_c = \frac{2 M_h}{\pi r y} = \frac{2 (1,252,000)}{\pi (8.0) (16.0)} \quad (117)$$

$$= 6230 \text{ lb/in}$$

The stress in the plate at $r = 8.0$ inches is

$$\delta_c = \frac{q_c}{t} + \frac{6 M_o}{t^2} = \frac{q_c}{t} + \frac{6 e q_c}{t^2}$$

$$= \frac{6230}{0.36} + \frac{6 (0.34) (6230)}{(0.36)^2}$$

$$= 115,400 \text{ lb/in}^2$$

$$MS = \frac{120,000}{115,400} - 1 = +0.04$$

AIRCRAFT AEROELASTIC AND FLUTTER ANALYSES AND DYNAMIC STABILITY

CONCLUSIONS

The aeroelastic analysis of the HLH blade indicates that the present design gives reasonable stress levels and stable responses for the envelope of flight conditions investigated. The HLH rotor blade, with its coincidence of the blade center of gravity and the aerodynamic center of pressure at the blade quarter chord, in conjunction with a high first torsional natural frequency, precludes the possibility of classical flutter of the advancing blade, even at velocities well in excess of those experienced in operation. A substantial margin of stability exists, indicating freedom from stall flutter in all operating conditions. This inherent stability results primarily from the high first torsional frequency of the HLH blade and the low disk loading of the HLH rotor system. The stability boundary of torsional divergence over the range of operating speeds shows that the operating conditions for the HLH blade are well removed from the unstable region, thus precluding the possibility of torsional divergence instability. The lag damper, designed to operate with a relief valve setting equivalent to 59,800 inch-pounds of moment, will provide damping rates far in excess of the value required to provide freedom from pitch-lag instability under all operating conditions. The fuselage landing gear configuration and geometry (designed with S-64 experience) and the reasonable range of acceptable stiffness parameters obtained from the ground resonance analysis show that the HLH design will be free from ground resonance for all operating conditions. The HLH rotor system possesses excellent inherent stability and control in the presence of a turbulent, unsteady flight environment.

The study of HLH stability and control, with an appropriately assumed fuselage, demonstrated the feasibility of such a design from a handling qualities viewpoint. Iteration of design parameters such as offset, shaft incidence, and tail incidence results in acceptable attitude and control positions throughout the flight regime. Investigation of control power and damping shows that the resulting design follows predicted trends for gross weight variation and compares favorably with existing criteria. The only areas noted which may require further investigation are the effects on the pilot response of vertical fuselage bounce and the relative position of the pilot with respect to the roll axis. A step-by-step comparison with MIL-H-8501-A shows that the HLH meets or exceeds the specifications in all major respects. Consideration of size effects and comparison with the CH-54A indicate that improvements in handling qualities can be expected, even without basic configuration changes, and that improve-

ments incorporated in the HLH, such as the 80-square-foot horizontal stabilizer, will further enhance these improvements. The use of root locus techniques provides an estimate of handling qualities improvement with an automatic flight control system. Finally, a comprehensive side-by-side comparison of all major aircraft characteristics with the operational CH-54A shows ample verification of analytical data by correlation with empirical data, indicating a firm basis for the conclusions reached.

HLH BLADE AEROELASTIC ANALYSIS

The aeroelastic response of the HLH blade to forward flight conditions was based on the fully coupled flatwise-edgewise-torsional analysis of helicopter rotor blades developed at Sikorsky Aircraft (References 18 and 59). A rapidly convergent iterative procedure, which takes into account blade stall, is used to put the rotor in trim. Elemental blade lifts and drags are computed using NACA 0012 wind tunnel airfoil data, which include Mach number effects. A relaxation method is used to initiate the coupled flatwise-edgewise-torsional response. Blade motions are coupled to the aerodynamic excitation. Rotor blade dynamics are determined using a set of complex equations based on an extension of Myklestad's analysis for rotating beams (Reference 37). The analysis takes into account 24 flatwise, edgewise, and torsional degrees of freedom with coupling due to blade twist. This analysis has been fully programmed for the IBM DCS-7040/7090 computer.

The general rotor system aeroelastic problem can be subdivided into three major categories: (1) air mass dynamics, (2) calculation of aerodynamic loads, and (3) rotor blade dynamics. The rotor disk is considered to be moving at the proper forward tilt to provide enough propulsive force to overcome the net drag of the aircraft. A sufficient lift force must be produced to support the aircraft, and there must be cyclic pitch to keep the rotor in equilibrium. Certain assumptions are made to initiate the analysis, such as an approximate coning angle, an estimate of the rotor drag, and an estimate of the radial position of the resultant thrust vector. These approximations do not affect the final accuracy, since they are corrected by an iteration technique.

For a high-speed flight condition, constant inflow through the rotor disk is taken. The blade is subdivided into 24 mass elements. For each azimuth interval of 10 degrees, the blade is considered set at two blade angles which bracket the expected blade pitch angles. Blade-element aerodynamic lifts and drags are then computed from which the moment of the thrust vector about the flapping hinge is calculated as a function of blade angle and azimuth position. Stall and reverse flow effects are taken into account by using two-dimensional airfoil data. The cyclic

pitch necessary to maintain the rotor system in equilibrium is then calculated by an iteration to enforce the condition that the first harmonic thrust moment about the flapping hinge is zero. Final determination of cyclic pitch yields angle-of-attack distribution, rotor drag, location of the resultant thrust vector, thrust moments, and resolved thrusts and drags on the 24 blade elements for each azimuth interval. A harmonic analysis is performed on this loading, and the steady plus the first 11 harmonics of blade loading, thrust and drag are obtained in complex form.

Harmonics of the airload distribution are now introduced into the blade dynamic analysis. These harmonics give rise to the vibratory responses of the blade. Analysis for the flexible blade dynamics is an extension of Myklestad's analysis for rotating beams and provides 24 flatwise, edgewise, and torsional degrees of freedom with coupling due to twist.

Equations are in a complex form to allow for aerodynamic damping and phasing of aerodynamic loads. Boundary conditions at the tip of the blade require that the shear and bending moments be zero. At the root of the blade, the boundary conditions require that the moment about the flapping hinge be zero, that the moment about the drag hinge be equal to the damper coefficient times the angular velocity, and that the angular twist at the root equal the product of the blade torsional moment and the control system flexibility. Total forced response of the blade is determined by superposition of separate harmonics of the blade dynamic response. This yields the azimuthal distribution of moments, torques, deflections, twist, and stresses at each of the 24 blade stations for the 10-degree azimuth intervals.

The natural frequency diagrams for the HLH blade are given in Figures 235 and 236. It can be seen that the first three flatwise and edgewise natural frequencies are well removed from the primary exciting frequencies of the rotor system. This placement of natural frequencies in the blade design is primarily responsible for the nonresonant characteristics of the HLH rotor system. The first five flatwise and edgewise normalized mode shapes are given in Figures 237 and 238. The radial flatwise moment distribution at azimuth locations (0 degrees, 90 degrees, 180 degrees, 270 degrees) is shown for the three standard flight conditions in Figures 239 through 241. The steady and vibratory components of the flatwise blade stress are given in Figures 242 and 243. Figure 244 shows the flatwise moment variation with azimuth at the 45-percent radius station. Figures 245 through 248 show plots of cyclic pitch, Mach number, angle of attack and flapping angle versus azimuth position.

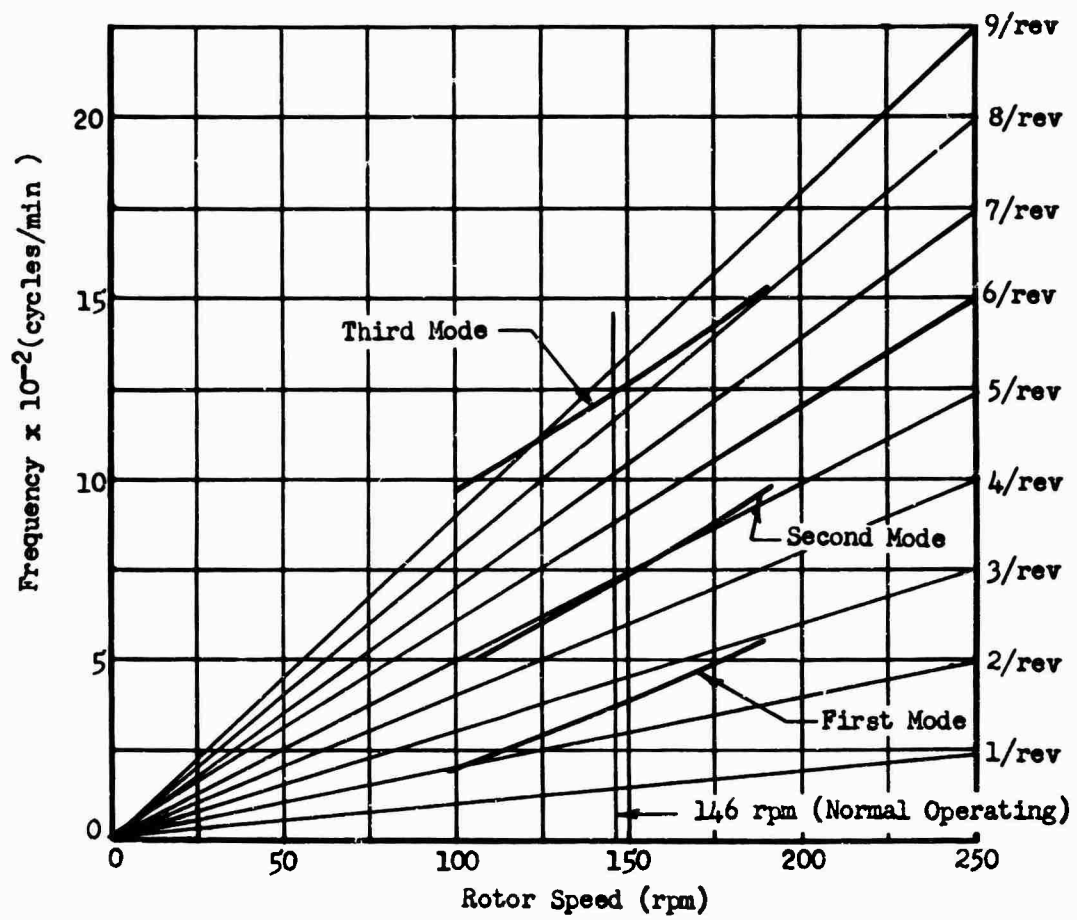


Figure 235 Natural Frequency, Flapwise Bending

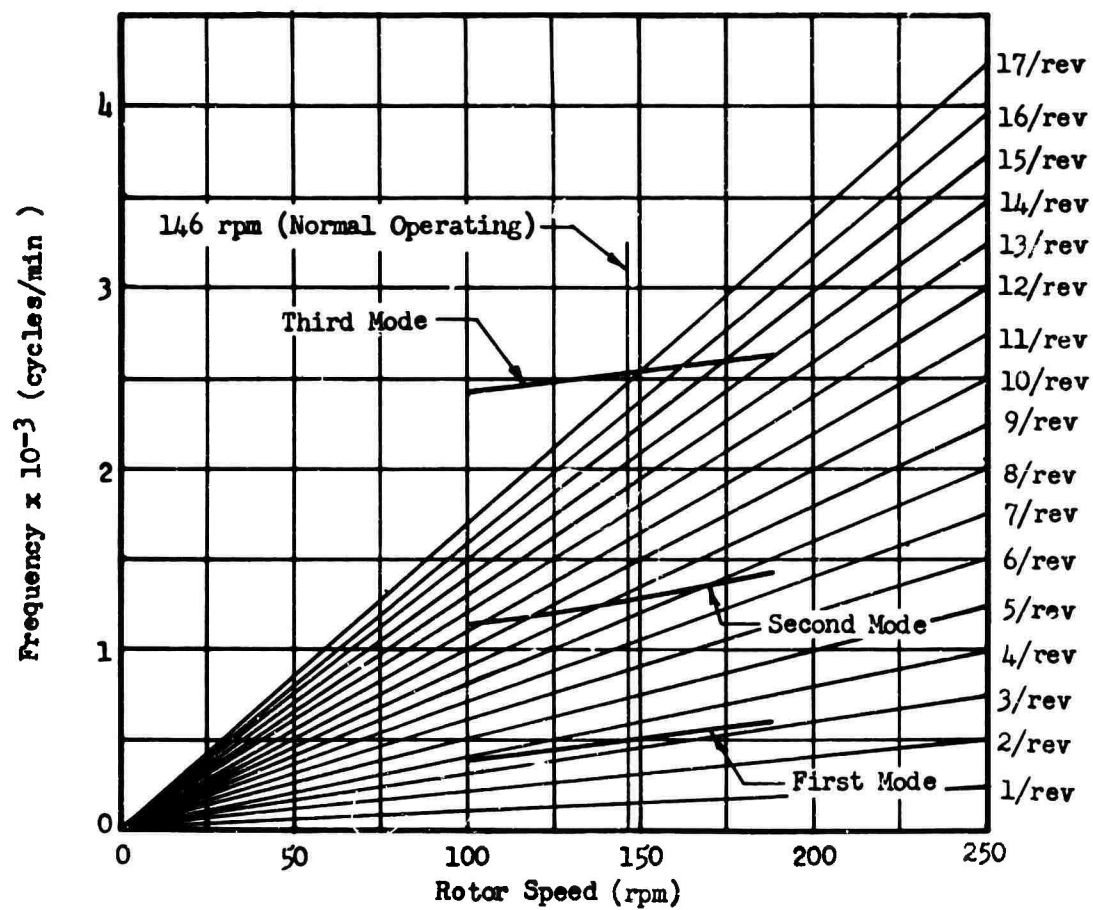


Figure 236 Natural Frequency, Edgewise Bending

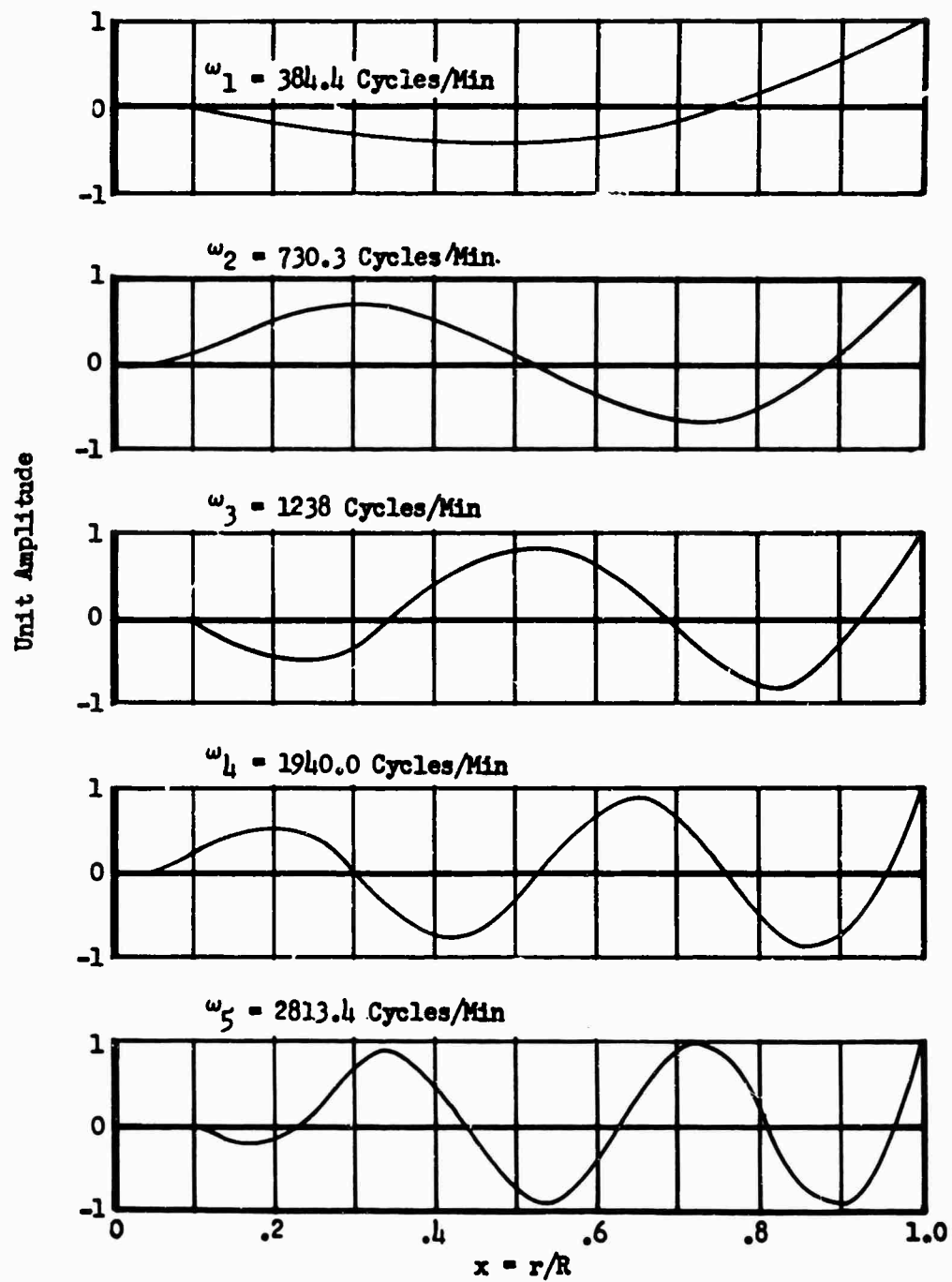


Figure 237 Flapwise Natural Frequencies and Mode Shapes

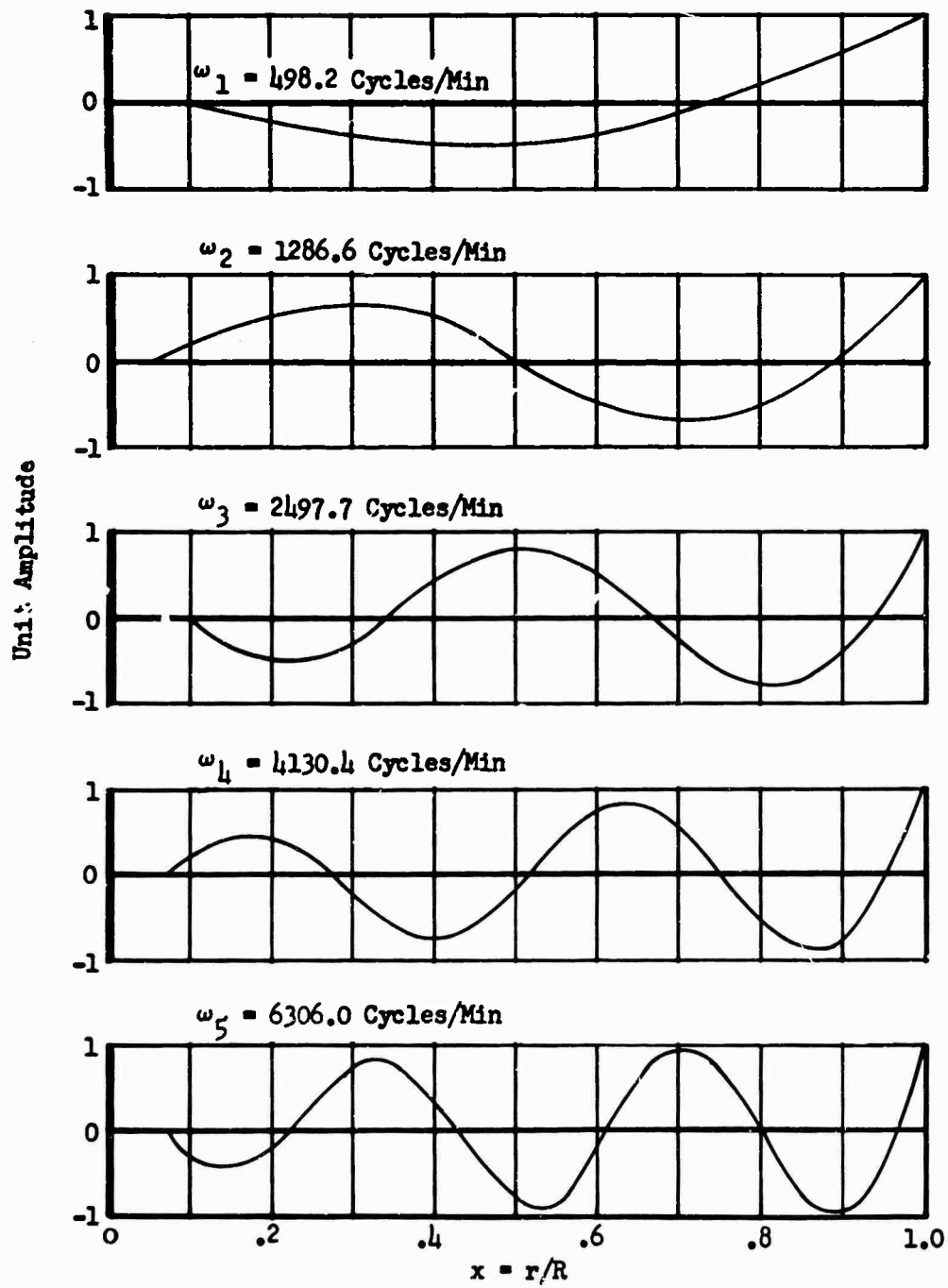


Figure 238 Edgewise Natural Frequencies and Mode Shapes

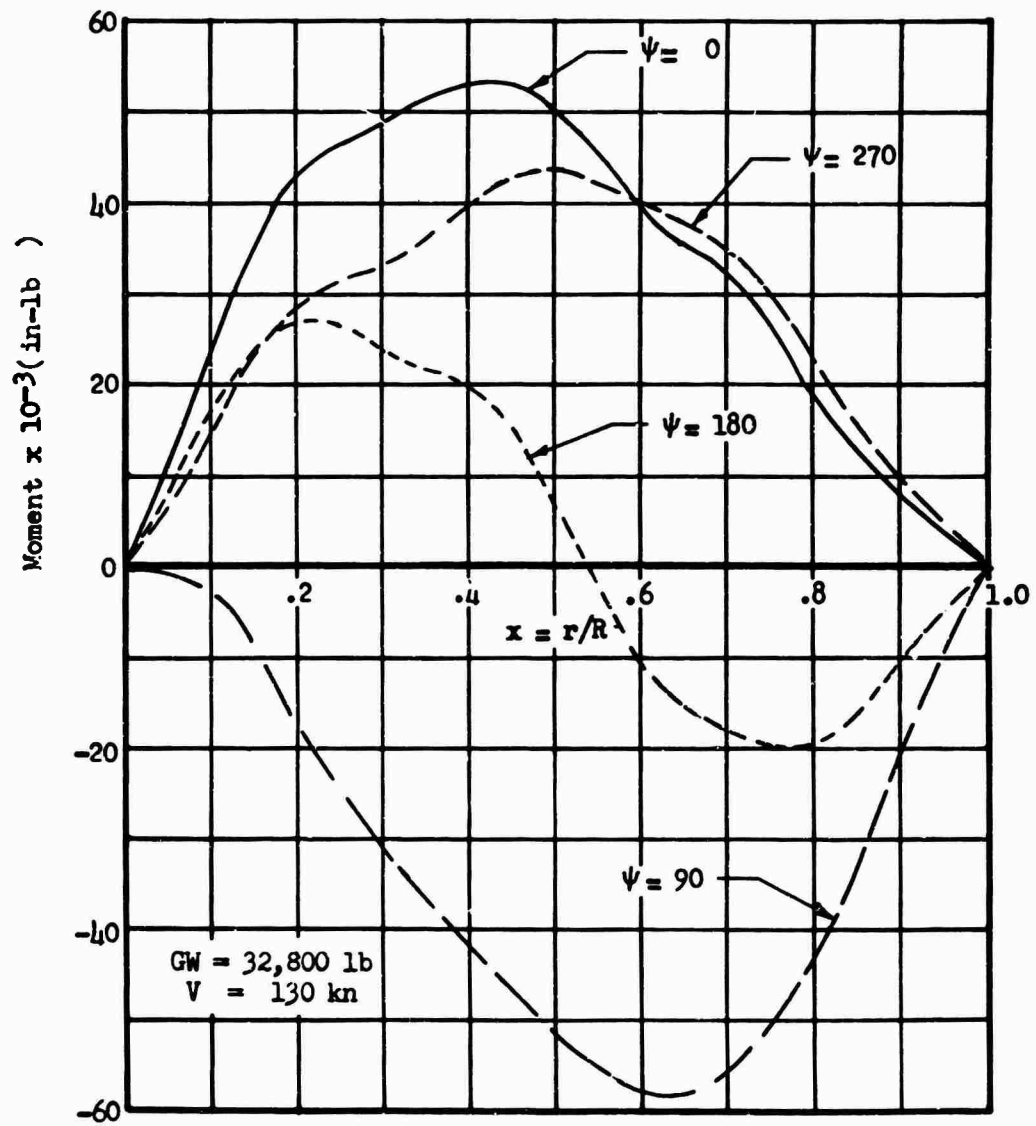


Figure 239 Flapwise Moment, Condition 3, Dynamic Analysis

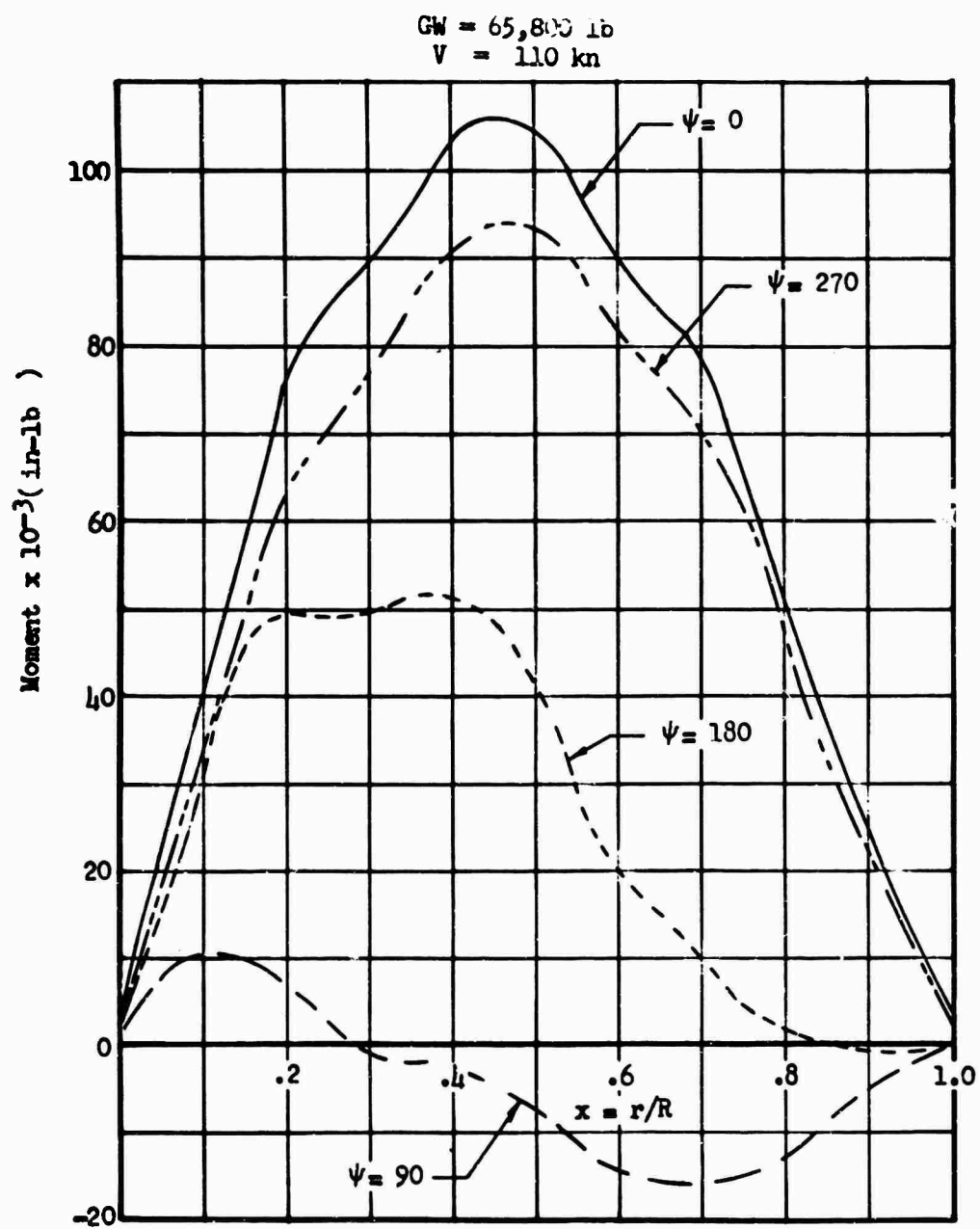


Figure 240 Flapwise Moment, Condition 2, Dynamic Analysis

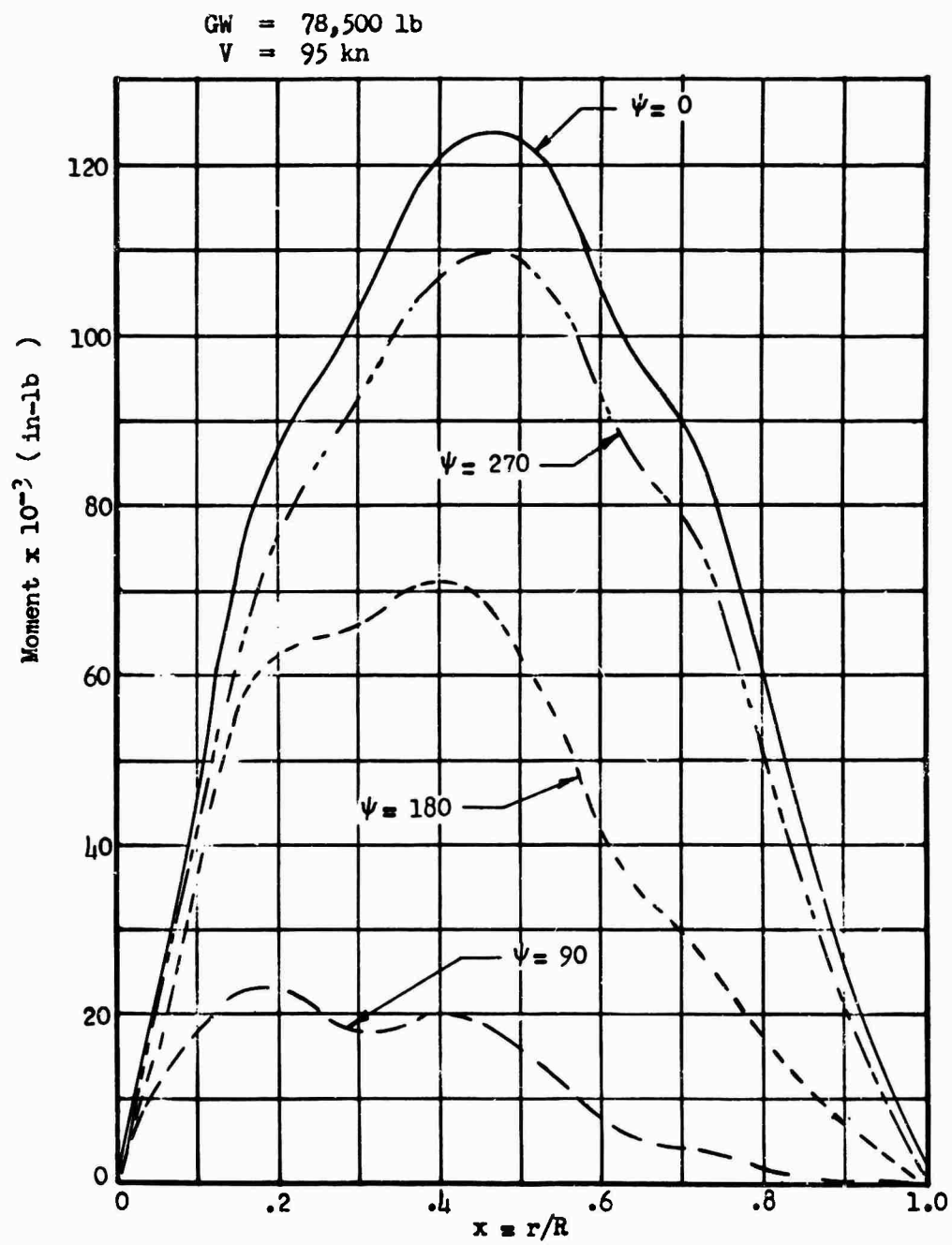


Figure 241 Flapwise Moment, Condition 1, Dynamic Analysis

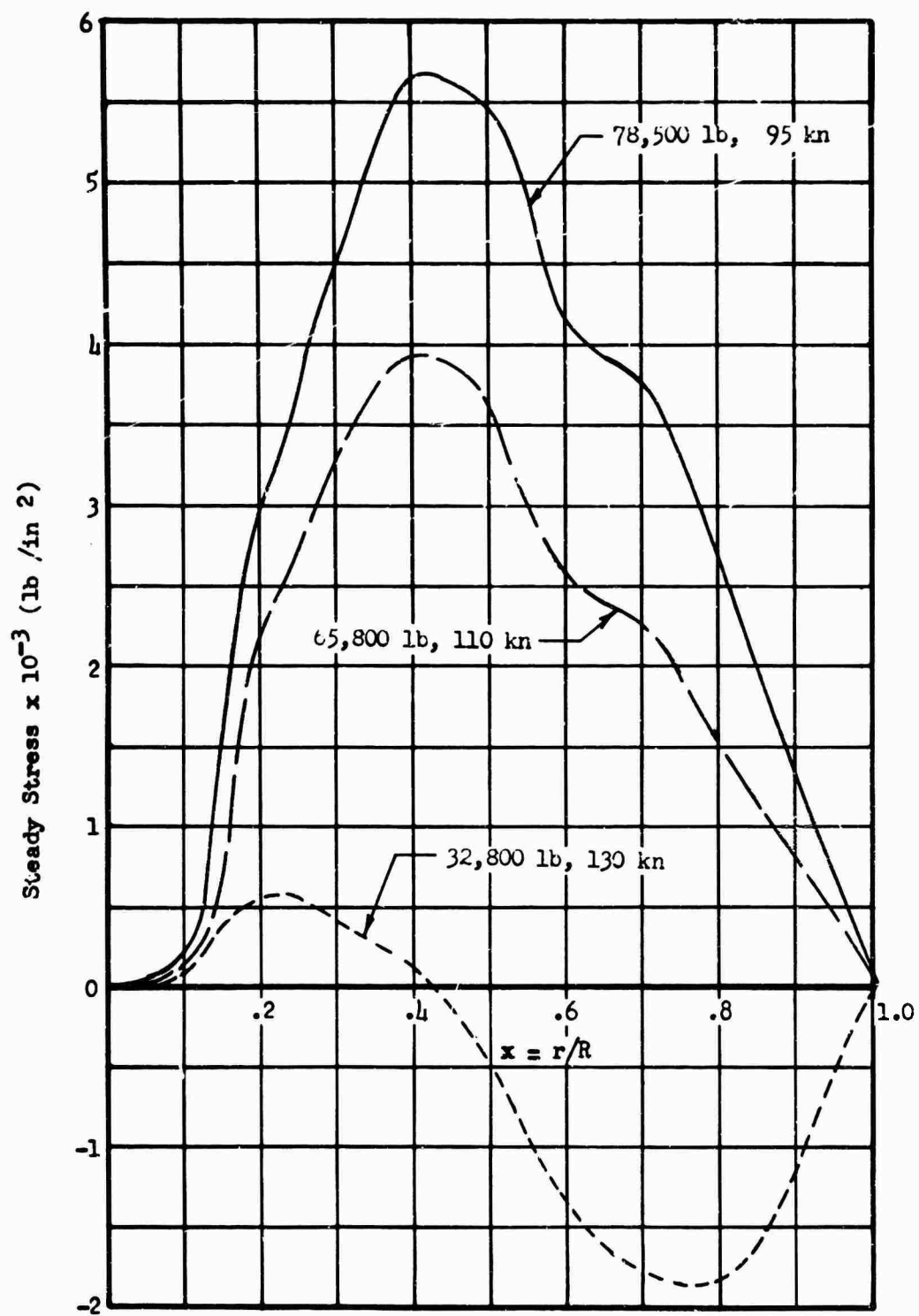


Figure 242 Maximum Flapwise Steady Stress, Dynamic Analysis

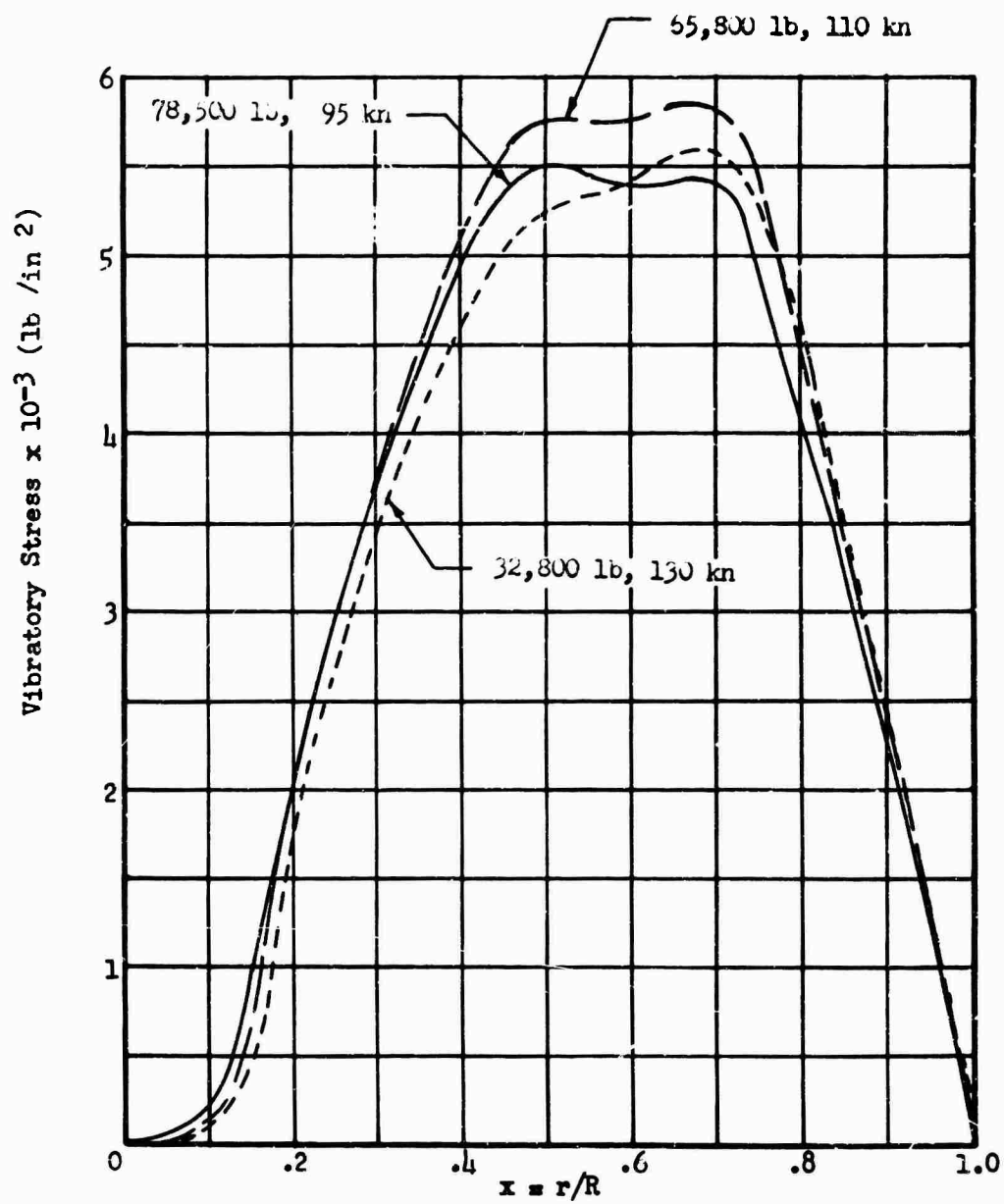


Figure 243 Maximum Flapwise Vibratory Stress, Dynamic Analysis

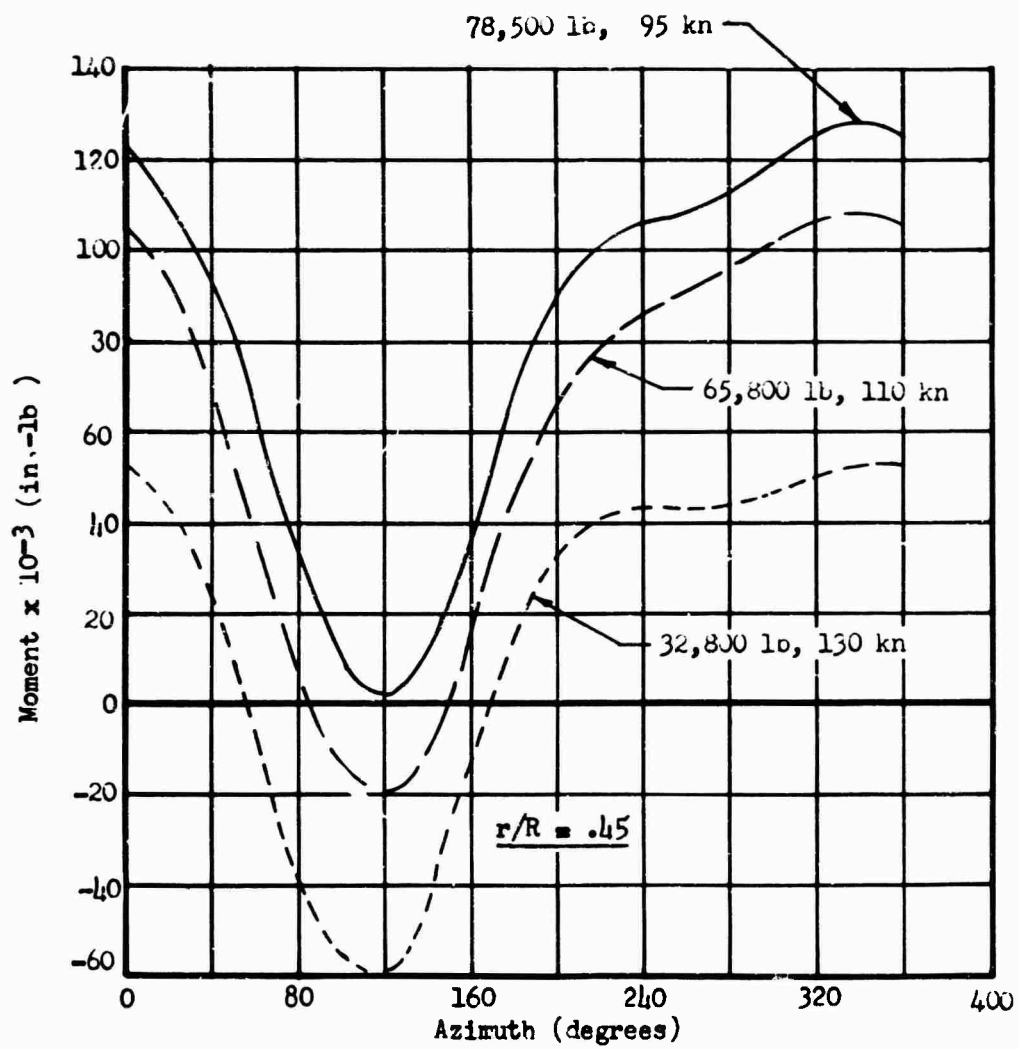


Figure 244 Flapwise Moment, Dynamic Analysis

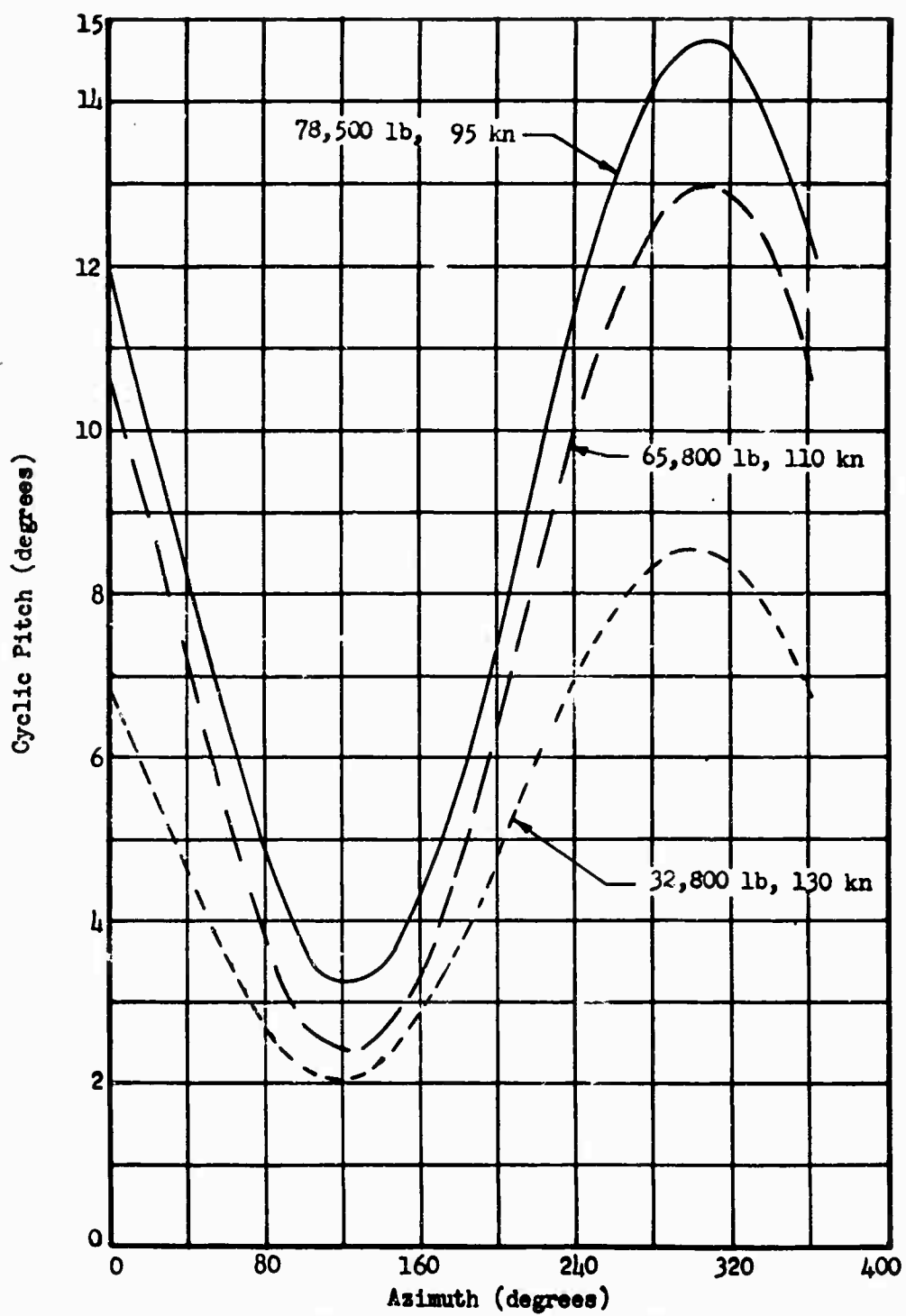


Figure 245 Cyclic Pitch Versus Azimuth Position, Dynamic Analysis

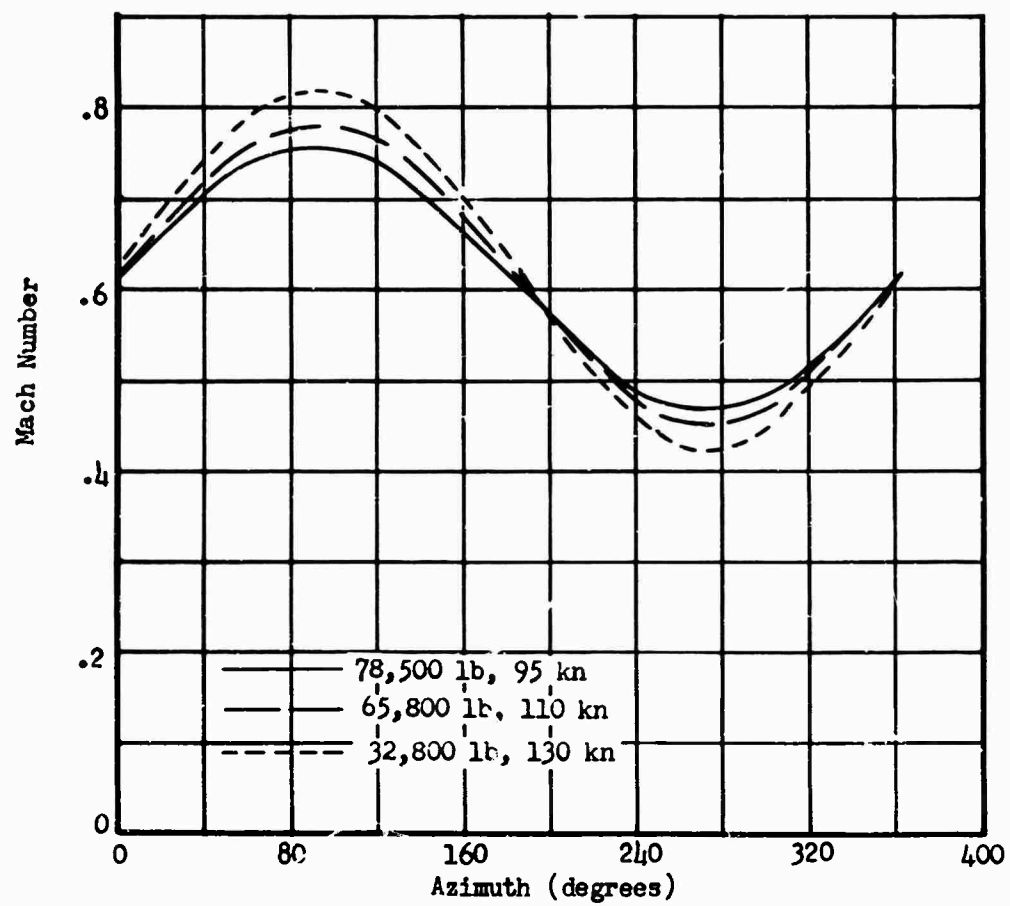


Figure 246 Mach Number Versus Azimuth Position, Dynamic Analysis

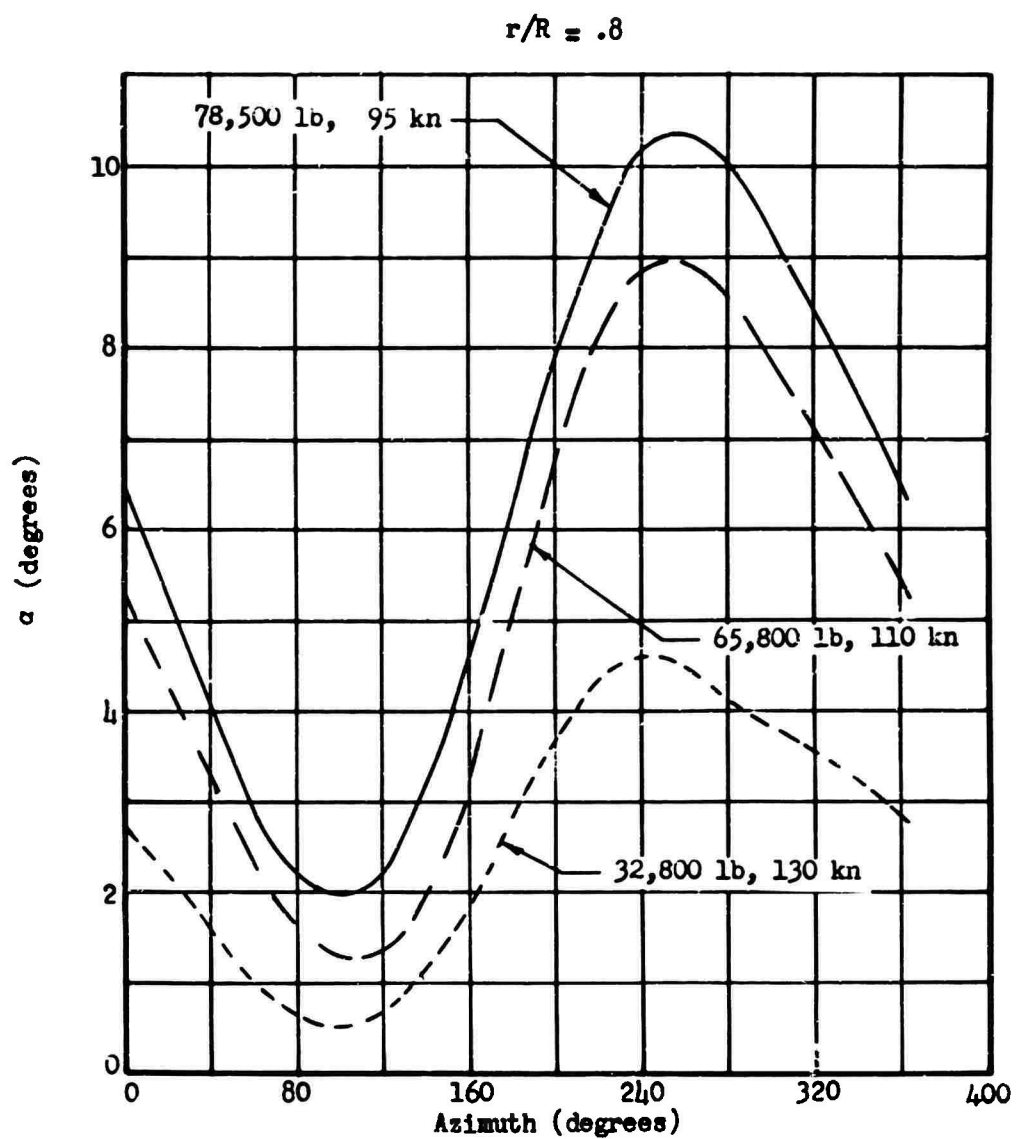


Figure 247 Angle of Attack Versus Azimuth Position, Dynamic Analysis

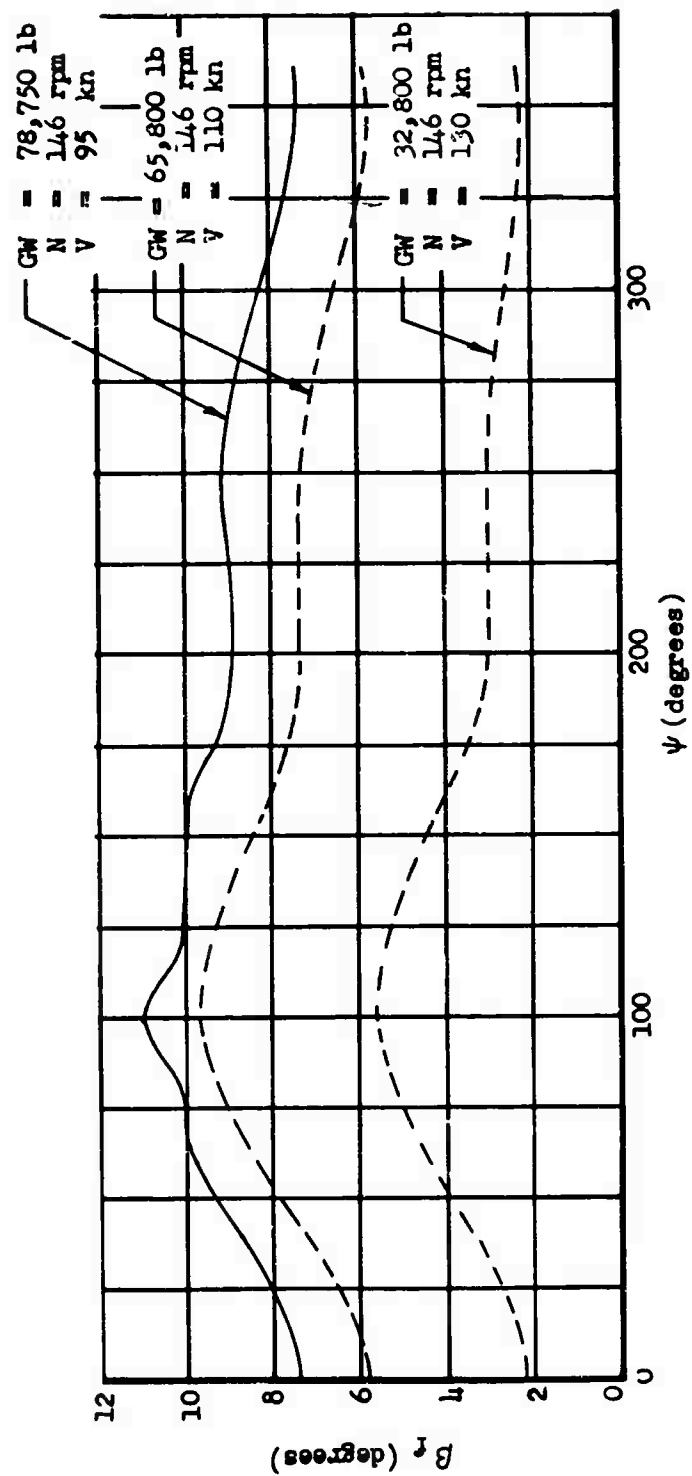


Figure 248 Flapping Angles Versus Azimuth Position, Dynamic Analysis

The aeroelastic analysis of the HLH blade indicates that the present design gives reasonable stress levels and stable responses for the envelope of flight conditions investigated.

CLASSICAL FLUTTER ANALYSIS

Classical flutter is a self-excited oscillation of a lifting surface initiated by the coupling of aerodynamic, elastic, and inertia properties of a rotating blade subjected to aerodynamic inflow. This phenomenon is characterized by an available energy supply and a zero or negatively damped elastic system and is manifested by a destabilizing coupling of aeroelastic modes which are normally uncoupled. Major terms which provide coupling are structural unbalance, inertia, and effective aerodynamic stiffness. Coupling may cause the uncoupled torsion and bending mode frequencies to approach each other. This proximity allows some modes to transfer energy into other modes, thus creating an unstable condition.

The flutter stability analysis of the HLH rotor blade was based on the superposition of normal blade vibration modes in Lagrange's equations of motion. The degrees of freedom considered were: (1) rigid body blade flapping (154 cycles per minute), (2) first flatwise bending mode (384 cycles per minute), and (3) first torsional mode (1210 cycles per minute). The flight conditions studied were 146-revolutions-per-minute rotor speed, sea level flight, blade located instantaneously at 90-degree azimuth angle, and forward velocities of 0, 100, 200, and 300 knots.

The generalized aerodynamic forces and moments are derived from thin airfoil, nonstationary, incompressible flow theory and are defined using Theodorsen's lift deficiency functions (Reference 54). Mach number effects are not considered, since compressibility tends to increase the flutter stability boundaries in the supersonic region where the center of pressure moves aft of the shear center. All damping present is assumed to be primarily aerodynamic in nature, but provision is made in the analysis for some small amount of mechanical and structural damping. The effect of preceding blade wakes is neglected in the main flutter analysis. However, for the hovering case, the influence of blade wake on aerodynamic flutter stability is analyzed using Loewy's (Reference 32) aerodynamic coefficients.

The analytic procedure used in the HLH classical flutter analysis is as follows. From an assumed value of flutter frequency, a velocity distribution consisting of forward flight and rotational speed defines the spanwise distribution of the reduced frequency parameter. Generalized aerodynamic, inertia, dissipation, and elastic matrices are calculated and coupled with the dynamic system. An exponential solution is chosen to

represent the oscillatory generalized airfoil motions, and a resulting characteristic flutter polynomial with real coefficients is obtained from which three complex conjugate roots are determined. These roots correspond to the flutter frequencies and damping associated with three degrees of freedom.

Freedom from classical flutter was established by the presence of positive aerodynamic damping for all modes at all velocities as shown in Figure 249. Reduction of the torsional natural frequency to a minimum value by changing the root spring constant showed some small decrease in the stability margin. The use of Loewy's aerodynamic coefficients, based on induced velocities from previous wakes, indicated an increase in stability for the least stable root.

The HLH rotor blade with its coincidence of the blade center of gravity and the aerodynamic center of pressure at the blade quarter chord, in conjunction with a high first torsional natural frequency, precludes the possibility of classical flutter of the advancing blade, even at velocities well in excess of those experienced in operation.

STALL FLUTTER ANALYSIS

Stall flutter is a self-excited oscillation which occurs on a lifting surface operating in a region of stalled flow. This instability depends on the appreciable reduction of blade aerodynamic torsional damping due to blade stalling. This loss of damping leads to transient pitch oscillations produced by the stall generated aerodynamic pitching moments. Although transient oscillations can become appreciable, they are not likely to lead to destructive instability, since these self-excited oscillations do not build up with time but periodically appear and disappear once per revolution. This can be attributed to the inherent aerodynamic damping in a helicopter rotor blade and the fact that it is not a fixed incidence device.

The HLH rotor blade was analyzed for stall flutter instability under the following operating conditions: (1) 78,750 pounds gross weight, 95 knots; (2) 65,800 pounds gross weight, 110 knots; (3) 32,800 pounds gross weight, 130 knots. Mach numbers and blade angles of attack were determined for the above flight conditions from an aeroelastic analysis of the HLH rotor system.

The flutter parameter was obtained from the blade Mach numbers at the 80-percent-radius station by the expression

$$\Phi^*(\Psi) = \left[A_0/b_s w_\alpha \right] MN(\Psi) \quad (118)$$

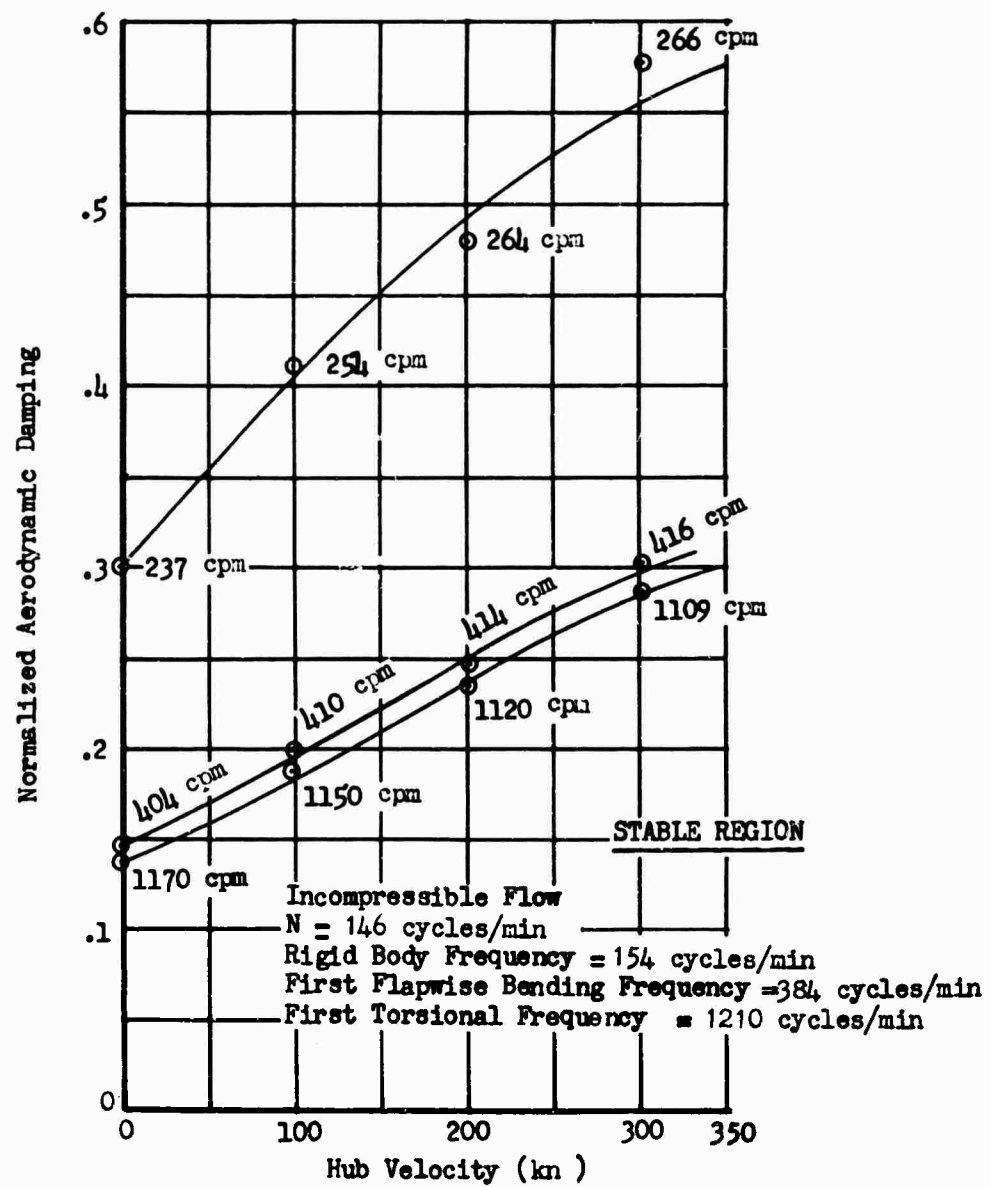


Figure 249 Classical Flutter, Dynamic Analysis

where

A_0 = velocity of sound

b_s = blade semi-chord

w_α = first blade torsional natural frequency

MN = Mach number

Figure 250 shows the stall flutter stability boundary and the region of HLH rotor operation as a function of blade pitch angle and flutter parameter. The stall flutter boundary was obtained from the experimental work of Norman D. Ham (Reference 20) on the stall flutter characteristics of model helicopter rotors and the study of the effect of mean incidence on flutter by A. Regier and G. Rainey (Reference 43). It can be observed that a substantial margin of stability exists, indicating freedom from stall flutter in all operating conditions. This inherent stability results primarily from the high first torsional frequency of the HLH blade and the low disk loading of the HLH rotor system.

TORSIONAL DIVERGENCE

Torsional divergence represents the state where the work done by the external aerodynamic forces in twisting the blade exceeds the associated change in elastic strain energy. This divergence is a result of the reverse flow over the retreating blades. The lift forces generated act at what is normally three-quarter chord, and the action of the lift force is destabilizing. The borderline case of neutral stability is defined by the requirement that the external work be equal to the change in strain energy during an arbitrary displacement.

Neglecting compressibility and local chordwise effects, an analysis for the torsional divergence characteristics of the HLH rotor blade was performed (Reference 5). The torsional divergence limit, $u = V/\Omega R$, may be found by using the following divergence criterion

$$\frac{2GJ_0}{A_0 \rho C_0 e_0 \Omega^2 R^4} - \frac{\sum_{n=1}^{\bar{n}} (x_n + u \sin \gamma)^2 r_\theta^2 \Delta x_n}{\sum_{n=1}^{\bar{n}} \left(\frac{dr_\theta}{d\theta_n} \right)^2 \Delta x_n} < 0 \quad (119)$$

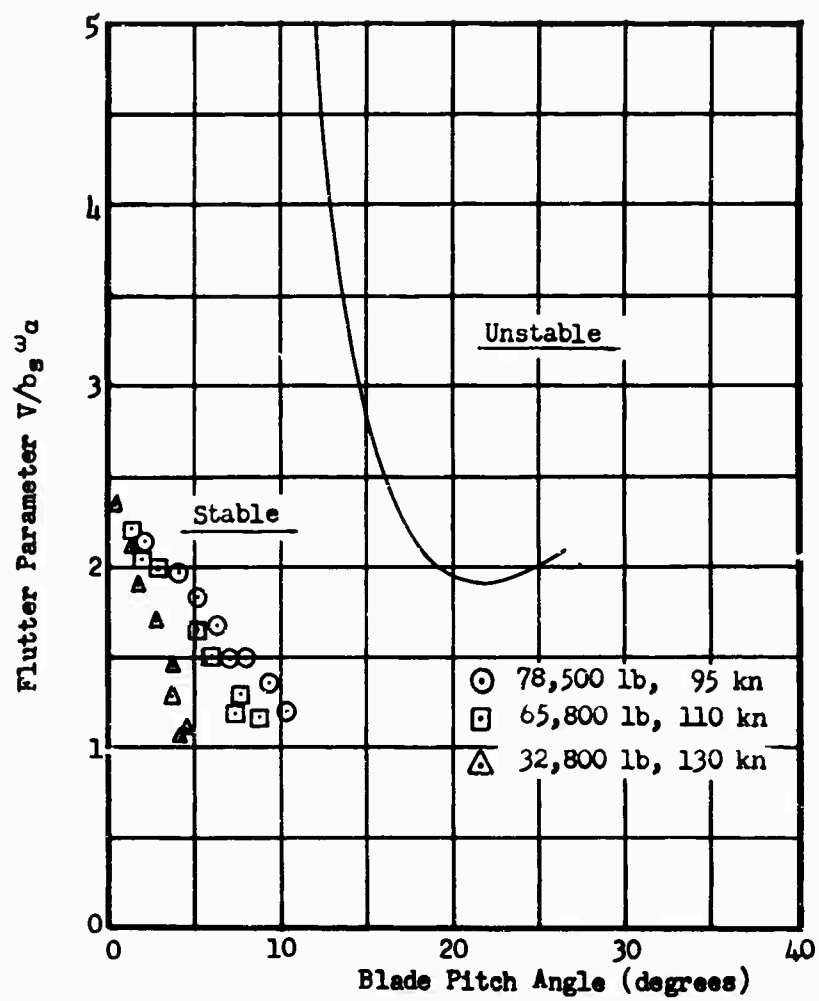


Figure 250 Stall Flutter, Dynamic Analysis

where

ρ = mass density of air

C_0 = reference value of blade chord

e_0 = reference elastic axis offset

GJ_0 = reference value of torsional stiffness

r_θ = first torsional mode shape

It was found that for forward velocities in excess of 500 knots, excessive torsional response of the blade was induced in the stall region. The stability boundary in Figure 251 shows that the operating conditions for the HLH blade are well removed from the unstable region, thus precluding the possibility of torsional divergence instability. The above results were obtained using the Torsional Divergence computer program developed at United Aircraft Research Laboratories.

PITCH-LAG INSTABILITY

The principal cause of this instability is negative pitch-lag coupling. The HLH blade was analyzed for the possibility of pitch-lag instability, and the values of damping required to stabilize the system were calculated. Based on the Pei Chi Chou stability criteria (Reference 10), the required damping is a function of the collective pitch angle, the steady coning angle, and the pitch-lag and pitch-flap coupling characteristics. The expression for the damping required for stability is given by

$$C_\zeta > \frac{-K_\zeta}{1 - \left(\frac{\beta_0}{\theta_0}\right) K_\beta} 2 \left(\frac{\beta_0}{\theta_0}\right)^2 I_M \Omega \quad (120)$$

where

θ_0 = steady-state pitch angle

β_0 = steady-state coning angle

K_β = pitch-flap coupling

K_ζ = pitch-lag coupling

I_M = mass moment of inertia about vertical hinge

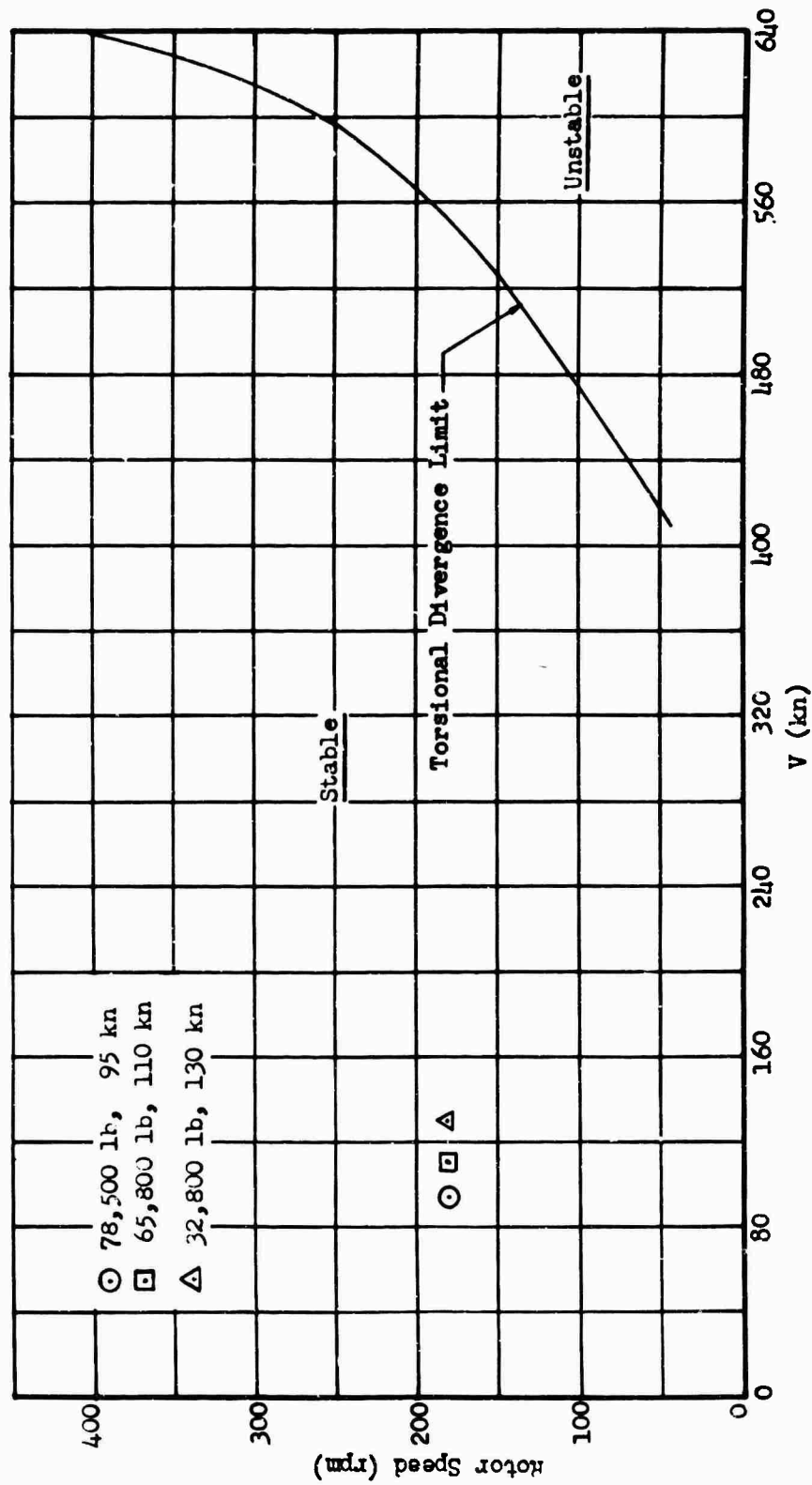


Figure 251 Torsional Divergence

For positive pitch-lag coupling, the above relation shows that the system is stable even for zero lag damping. For negative pitch-lag coupling, the positive lag damping required can be obtained from the above inequality.

Figure 252 shows the pitch-lag coupling characteristics of the HLH blade. It can be seen that positive pitch-lag coupling exists for values of lag angle up to 10 degrees. In this range no lag damping is required for stability. For lag angles greater than 10 degrees a small amount of negative pitch-lag coupling is present. The critical lag damping values associated with this condition for three flight conditions are given in Figure 253. This indicates that the lag damper, designed to provide a damping rate of 102,000 ft-lb-sec, will provide hydraulic damping far in excess of the value required to provide freedom from pitch-lag instability under all operating conditions.

GROUND RESONANCE

Ground resonance is an instability produced by a coupling between the pendular oscillations of the main rotor blades about their lag hinges and the rigid body oscillations of the fuselage resting on its landing gear. Coleman (Reference 11) established methods for determining the range of rotor speeds during which ground resonance would occur assuming no damping in the system. Deutsch (Reference 14) derived an expression for the product of blade and fuselage damping to eliminate the unstable band.

Basically, ground resonance occurs when there is a coincidence or near coincidence of a rigid body airframe mode with the frequency difference between rotor speed and the blade edgewise pendular mode. Thus, adequate separation of the airframe modes from this exciting frequency will provide freedom from ground resonance.

For the HLH rotor system, the normal operating speed is at 146 revolutions per minute, with the first edgewise pendular frequency at 49 cycles per minute. This results in a ground resonance exciting frequency of 97 cycles per minute, which must be avoided by airframe modes. To determine the ground resonance requirements for the HLH design, a preliminary investigation of the effects of landing gear stiffness on airframe modes for the proposed HLH airframe geometry was made. Predicted weight, mass moment of inertia, and dimensions for this configuration were used. Landing gear stiffness values were evolved from the CH-54A Skycrane design.

The coupled roll and lateral rigid body natural frequencies of the HLH fuselage are given by the following frequency equation:

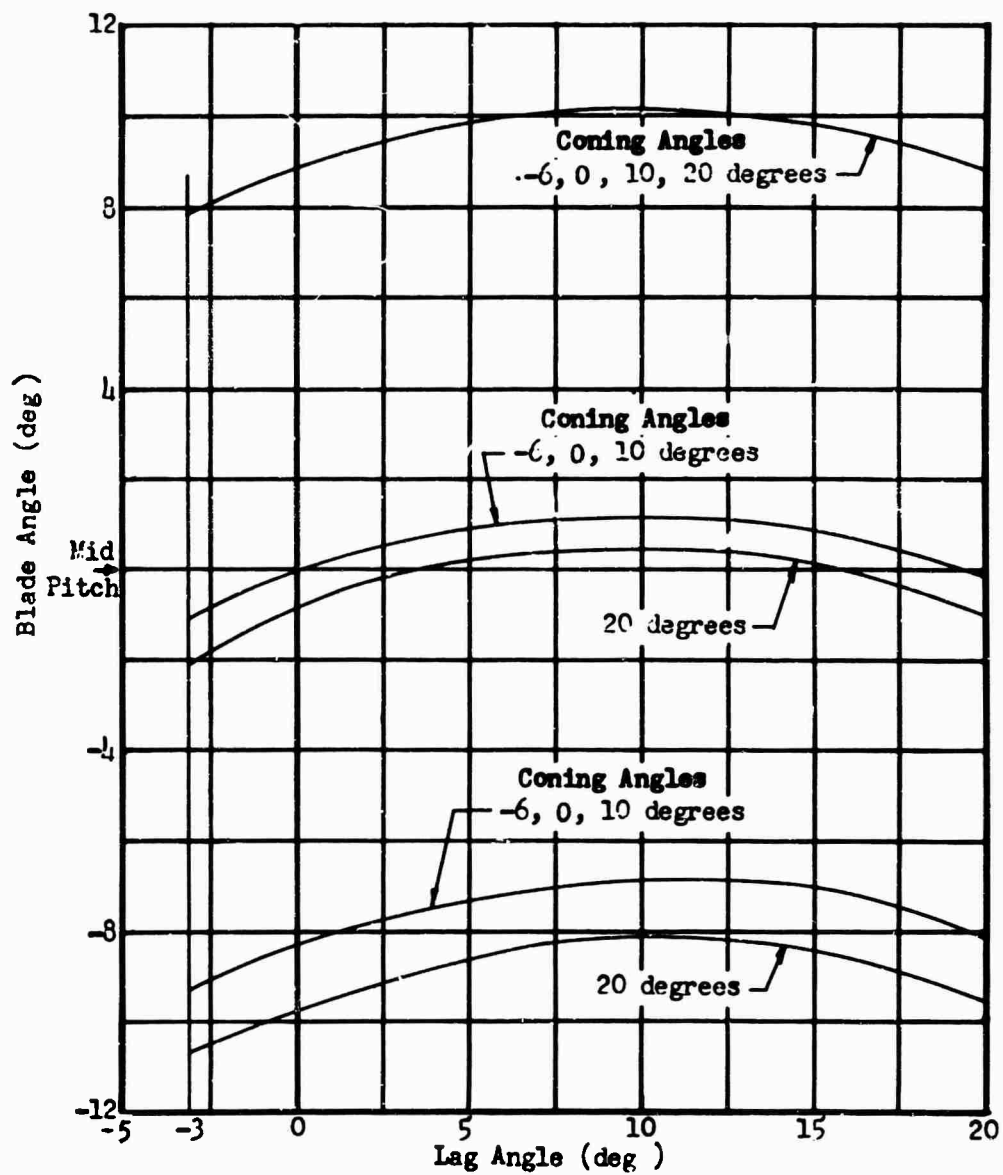


Figure 252 HLH Pitch Coupling, Blade Angle Versus Lag Angle for Various Cone Angles

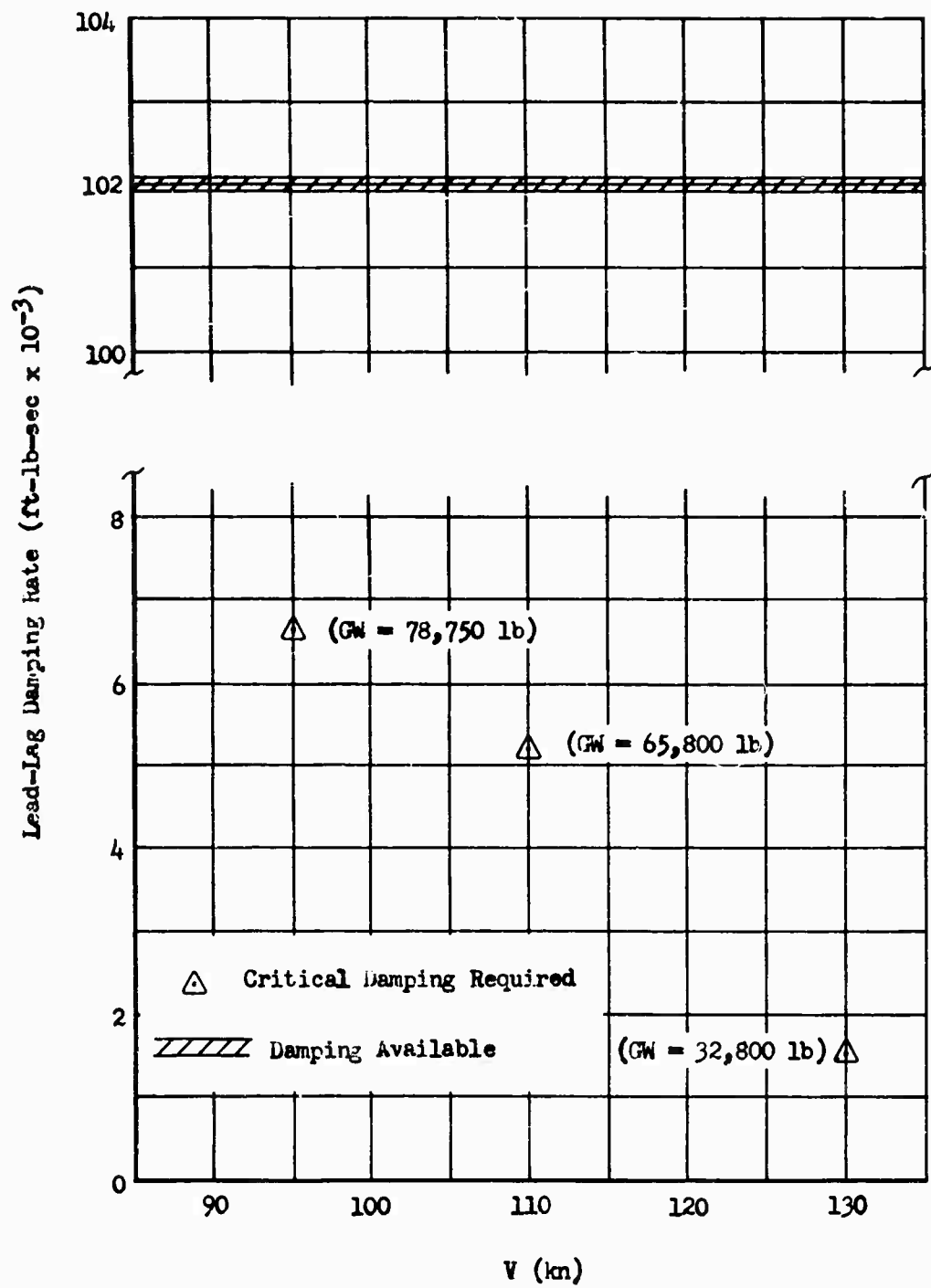


Figure 253 Pitch-Lag Instability

$$w_p^2 = \frac{1}{2} \left(\frac{K_h}{M} + \frac{K_\theta}{I_r} \right) \pm \frac{1}{2} \left[\left(\frac{K_h}{M} - \frac{K_\theta}{I_r} \right)^2 + \frac{4K_h^2 a^2}{I_r M} \right]^{\frac{1}{2}} \quad (121)$$

where

K_h = total lateral spring rate

K_θ = total roll spring rate

M = mass of aircraft

I_r = roll mass moment of inertia

a = vertical height of the center of gravity

A similar expression is applicable for determining the coupled pitch and fore-aft rigid body natural frequencies.

Figure 254 summarizes the effects of landing gear spring rate variations on the rigid body fuselage modes. It can be seen that using stiffness values of about 2.2 to 2.8 times the stiffness values for the CH-54A will give an adequate margin of stability from ground resonance.

The fuselage landing gear configuration and geometry for the HLH should pose no design difficulty based on the experience gained with the CH-54A Skycrane®. The range of acceptable stiffness parameters obtained from the ground resonance analysis is reasonable with respect to current design practices. Therefore, based on these results, the present HLH design will be free from ground resonance for all operating conditions.

HLH GUST RESPONSE

An analysis was conducted to evaluate the response character of the HLH rotor system subjected to a 30-foot-per-second gust during the forward flight of 95 knots.

The gust response analysis was conducted by utilizing a United Aircraft digital computer analysis which calculates rotor excitation and response at small azimuthal intervals as the blade rotates. Briefly, the method used to define the response of the system due to gusts consists of specifying a change in the rotor inflow over the entire disk from the steady-

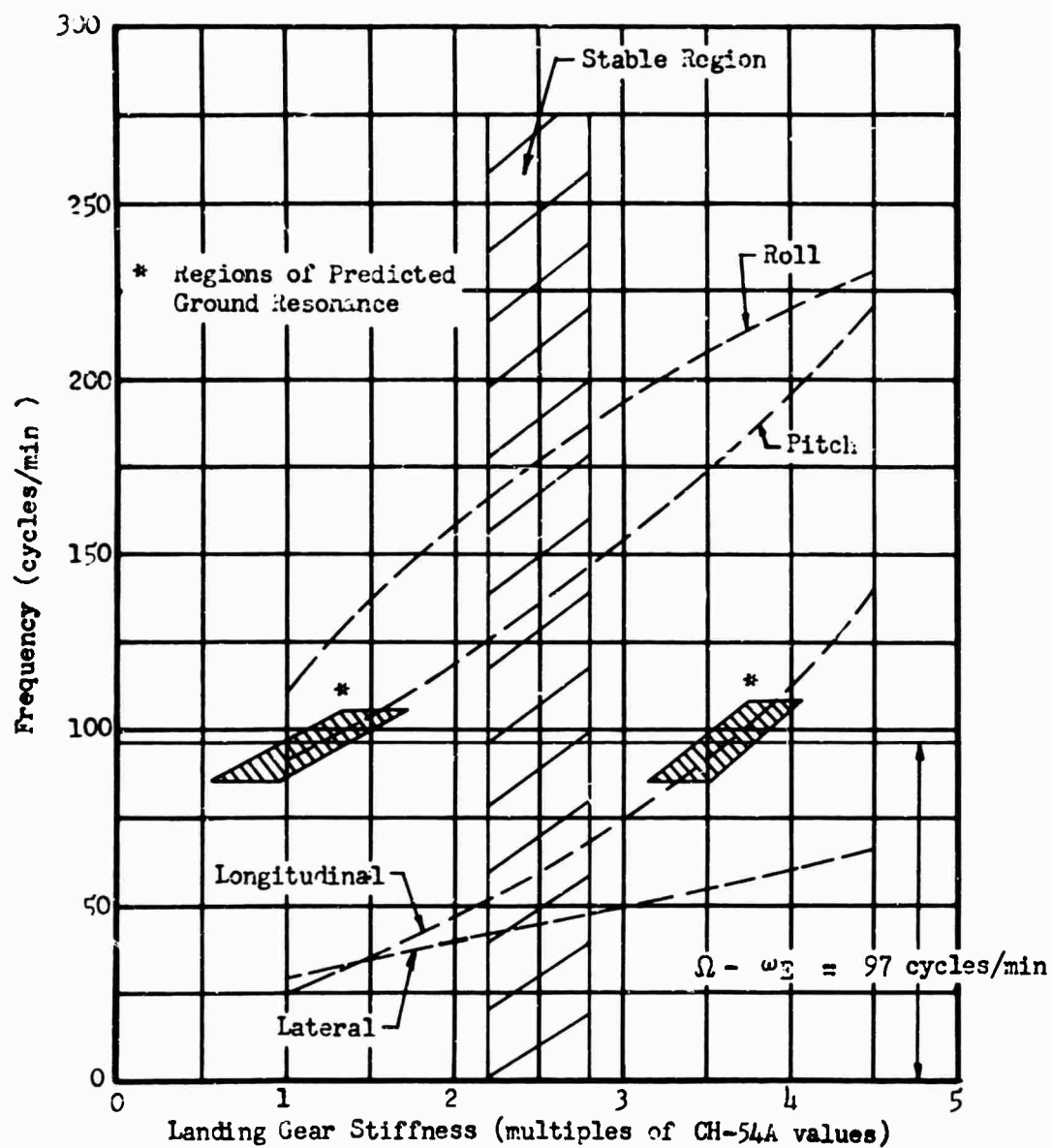


Figure 254 HLH Ground Resonance

state forward flight condition. The transient rotor response characteristics are then defined for a number of cycles following the gust application during which the rotor returns to a steady-state condition.

Figure 255 gives the first and second harmonic changes in the blade flapping angle as a result of applying a 30-foot-per-second gust loading for one rotor revolution. The rapid decrease in the flapping angle within a few cycles demonstrates the basic stability of the HLH rotor system. After ten rotor cycles or four seconds from the initial disturbance, rotor blade motions have returned to their previous steady-state values. Figure 256 shows the transient stress magnification resulting from the gust loading. Sixty-percent stress magnification is present over a small number of rotor revolutions, but these stresses diminish rapidly due to the damping inherent in the system and the pilot's response to readjustment of controlled collective and cyclic pitch. These transient stress levels are well within the elastic limit of the structural material of the blade, and a pure elastic deformation of the rotor due to the influence of a gust loading results.

These results indicate that the HLH rotor system possesses excellent inherent stability and control in the presence of a turbulent, unsteady flight environment.

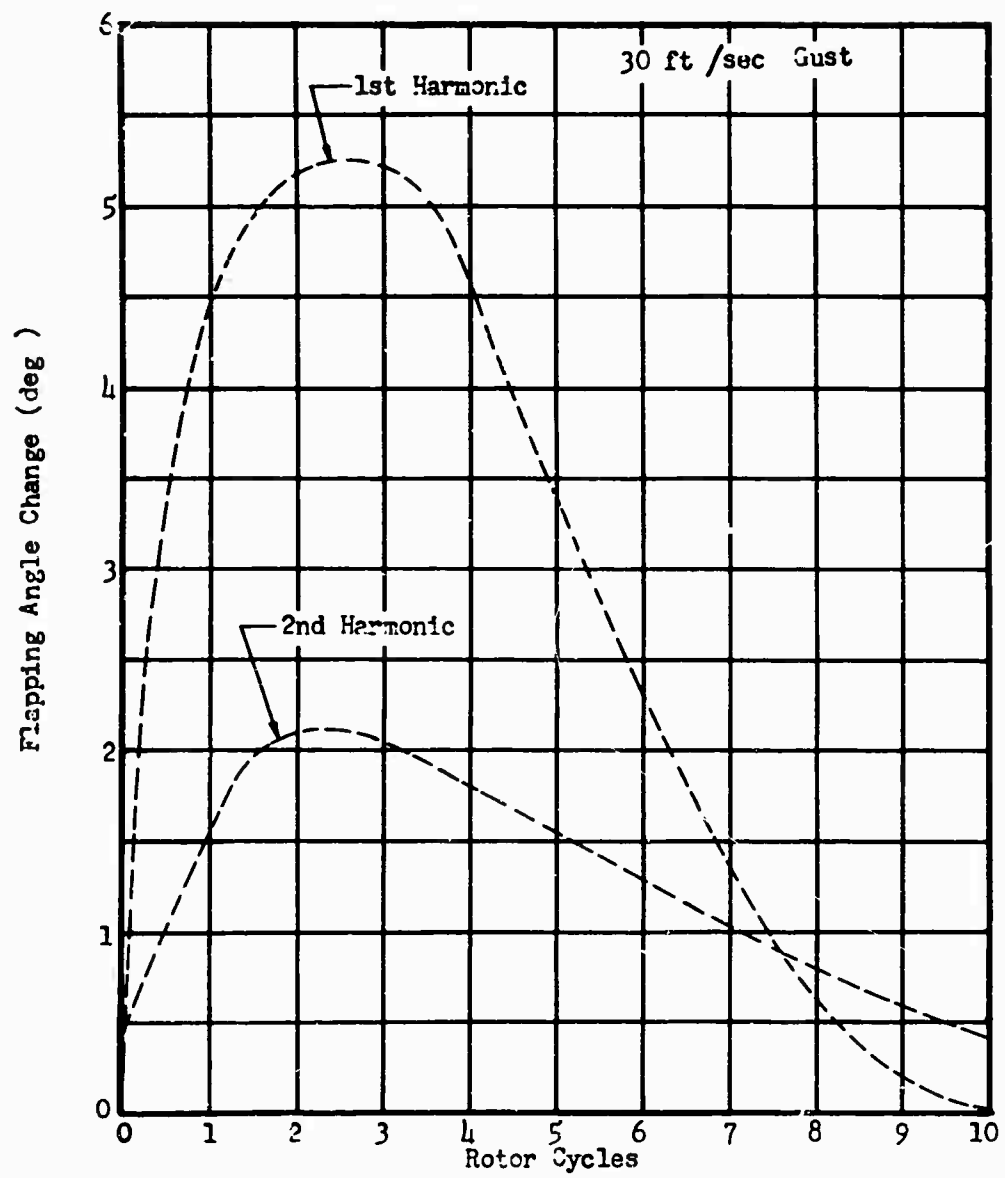


Figure 255 Gust Response Analysis - Flapping Angle

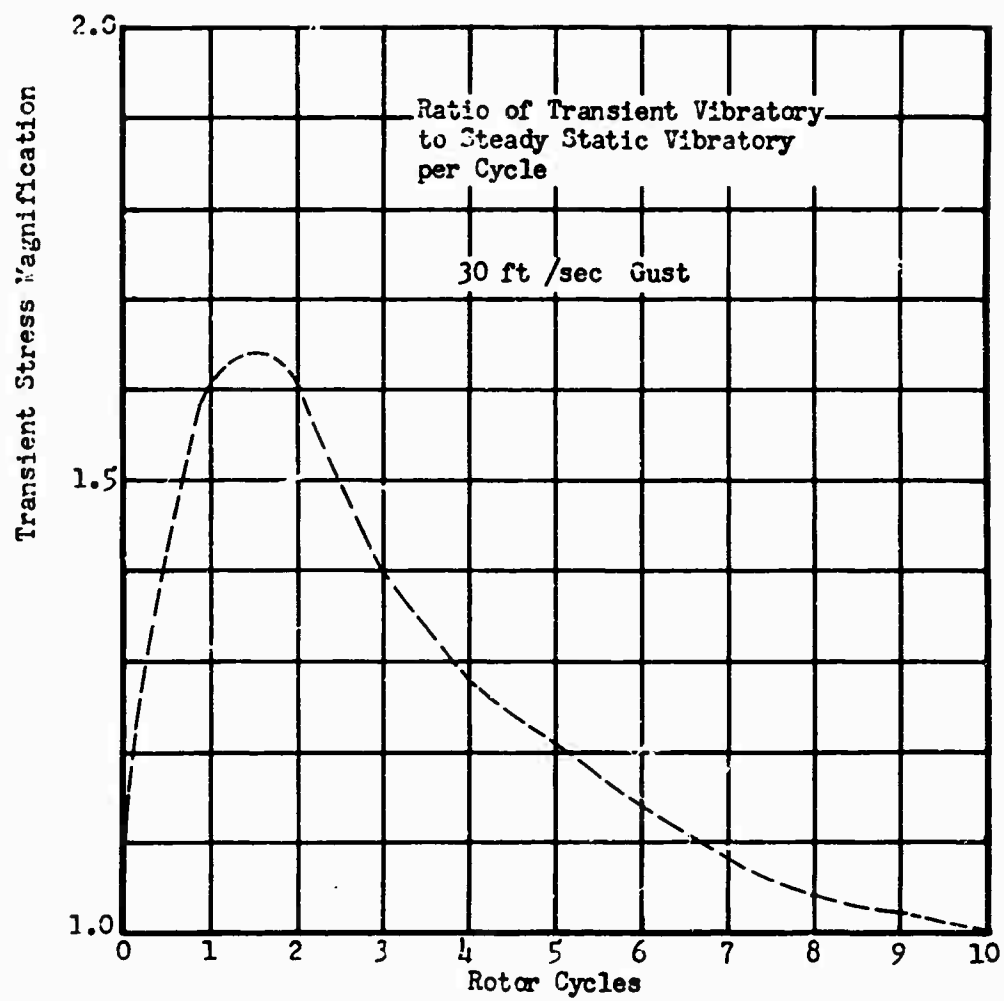


Figure 256 Gust Response Analysis - Transient Stress Magnification

AIRCRAFT AERODYNAMIC STABILITY AND CONTROL

For this analysis, the geometric solution for the HLH rotor system underwent further aerodynamic analysis in conjunction with an assumed fuselage. Fuselage properties were estimated from the general arrangement layout and from similarity to existing models. The major properties are listed in Table LXI with those of the CH-54A to show a comparison of the two machines and to provide a basis for comparative analysis of certain flying qualities.

TABLE LXI
COMPARISON OF HLH AND CH-54A MAJOR PROPERTIES

Main Rotor	HLH	CH-54A
Blade Radius, ft	45.8	36.0
Number of Blades	6	6
Blade Chord, ft	2.58	1.97
Solidity Ratio	.1076	.1046
Normal Tip Speed, ft/sec	700.0	696.0
Twist, Linear, deg	-8.0	-8.0
Airfoil Section	0012.	0012.
Offset, ft	3.0	2.0
Shaft Incidence in X-Z Plane, deg	2.0	3.0
Shaft Incidence in Y-Z Plane, deg	-3.0	-3.0
Blade Inertia About Flapping Hinge, 10,765. slug-ft ²		3546.
Blade Mass Moment, slug-ft	409.	160.6
Location	FS 550, WL 300	FS 336, WL 257.5
<u>Tail Rotor</u>		
Blade Radius, ft	11.4	7.5
Number of Blades	5	4
Blade Chord, ft	1.125	1.125
Solidity Ratio	.1571	.1910
Normal Tip Speed, ft/sec	700.0	656.0
Twist, Linear, deg	-8.0	-10.0
Airfoil Section	0012	0012
Delta Three Hinge Angle, deg	45	45
Location	FS 1246, WL 300	FS 864, WL 249

TABLE I.XI (cont'd)
COMPARISON OF HLH AND CH-54A MAJOR PROPERTIES

<u>Aerodynamic Surfaces</u>	<u>HLH</u>	<u>CH-54A</u>
Horizontal Tail Area, ft ²	80	26
Aero Center	FS 1246, WL 300	FS 843, WL 262
Incidence, deg	5	0
Vertical Tail Area, ft ²	84	29
Aero Center	FS 1186, WL 240	FS 814, WL 208
Incidence, deg	0	0

Weights and Inertias, HLH

<u>GW</u>	<u>I_x</u>	<u>I_y</u>	<u>I_z</u>	<u>FSCG</u>	<u>WLCG</u>
36000	34,400	140,000	117,500	526-574	233
65800	121,000	494,000	415,000	526-574	178
78750	155,900	635,000	533,000	526-574	154

Weights and Inertias, CH-54A

<u>GW</u>	<u>I_x</u>	<u>I_y</u>	<u>I_z</u>	<u>FSCG</u>	<u>WLCG</u>
38000	36,800	194,000	181,700	328-346	161

Control Kinematics, HLH

<u>Item</u>	<u>Stick Travel inches</u>	<u>Pitch Range @ .75R deg</u>	<u>Linkage deg/in</u>
Longitudinal Cyclic	13	-12 to +14	2.0
Lateral Cyclic	13	- 9 to + 7	1.23
Collective	11	- 2 to +14	1.454
Tail Rotor Pitch (Pedals)	5	- 5 to +25	6.0

Control Kinematics, CH-54A

<u>Item</u>	<u>Stick Travel inches</u>	<u>Pitch Range @ .75R deg</u>	<u>Linkage deg/in</u>
Longitudinal	12.6	-12 to +14	2.06
Lateral Cyclic	13.0	± 7.8	1.20
Collective	10.42	1.25 to 15.75	1.39
Tail Rotor Pitch (Pedals)	4.91	-6 to +20	5.29

DESIGN TECHNIQUES AND PHILOSOPHY

Wind tunnel data for the similarly configured CH-54A were used extensively in the estimation of HLH fuselage aerodynamics. Comparison of projected areas was used to yield both lift and side force curves. Drag curves were used directly with appropriate variation of the minimum drag point inserted in the trim program. The development of minimum drag is discussed in Reference 41, where it is shown that very little difference in absolute magnitude of the minimum drag point exists. Also, lift variation with angle of attack is small. Modification of pitching moment curves to reflect the relative increase in tail area was made linearly. The vertical tail also shows a relative increase in area. The ratio of vertical tail area to total projected side area for the CH-54A is .0874, while that for the HLH is .1014. Because of this, the yawing moment was estimated as improved to the point that the slope was made zero. This leaves variation of yawing moment with sideslip a pure function of tail rotor aerodynamics - a reasonable assumption at this stage of design. Figures 257 through 261 show the CH-54A data, and Figures 262 through 264 show the predicted data for the HLH. Because the digital computer trim program interpolates linearly between actual test data points, the CH-54A curves are shown as a number of straight line segments, exactly as the computer would use the data. One of the basic requirements in the selection of parameters for a crane-type helicopter is the ability to spend considerable time in hover. The HLH has been configured to carry pod-type loads as well as single-point winch loads. The fixed pod loads allow large variation in CG location, both laterally and longitudinally. Therefore, special consideration of CG variation was used in defining certain parameters.

In hover, nose-up attitude (θ_f) of 6.0 degrees is considered as a design boundary, based on a collection of pilot comments through the years. Roll attitude (ϕ) near zero is also desirable for a centrally slung load. Variation of flapping hinge offset (e) significantly affects the aircraft attitude for a given CG. In forward flight, variation of shaft incidence (i_s) and/or tail incidence (i_t) can be used to keep flapping (α_{ls}) equally distributed for fore and aft CG locations. It would then appear that there are four design parameters, e , i_s , i_t , and lateral shaft tilt (i_L), which can be varied to satisfy three design requirements, $\theta_{f(hov)}$, $\phi_{f(hov)}$, $\alpha_{ls(fwd flt)}$. However, the fourth design requirement is moderate tail lift. An effort must be made to keep C_{L_t} well below stall and preferably distributed plus and minus with CG variation. Figures 265 and 266 represent a composite of the major variables for the longitudinal solution. Since longitudinal CG variation is more common, this was used first to settle on e , i_s , and i_t .

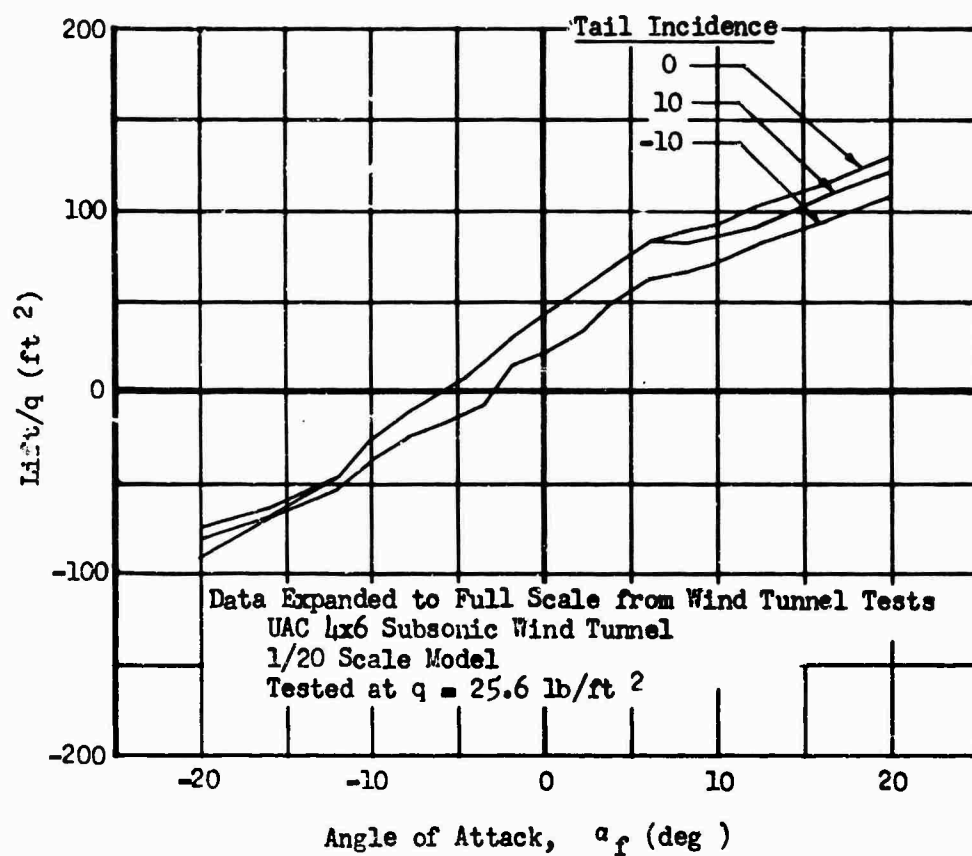


Figure 257 Lift/q Versus Angle of Attack, CH-54A

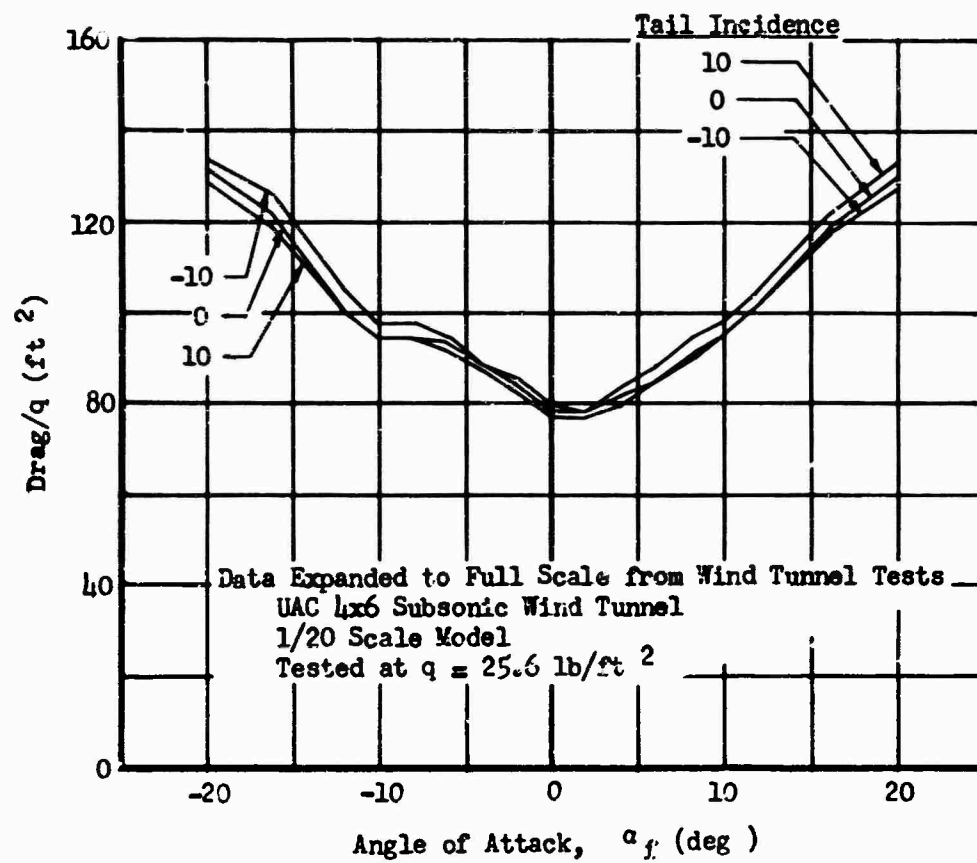


Figure 258 Drag/q Versus Angle of Attack, CH-54A

Data Expanded to Full Scale from Wind Tunnel Tests
 UAC 1x6 Subsonic Wind Tunnel
 1/20 Scale Model
 Tested at $q = 25.6 \text{ lb/ft}^2$

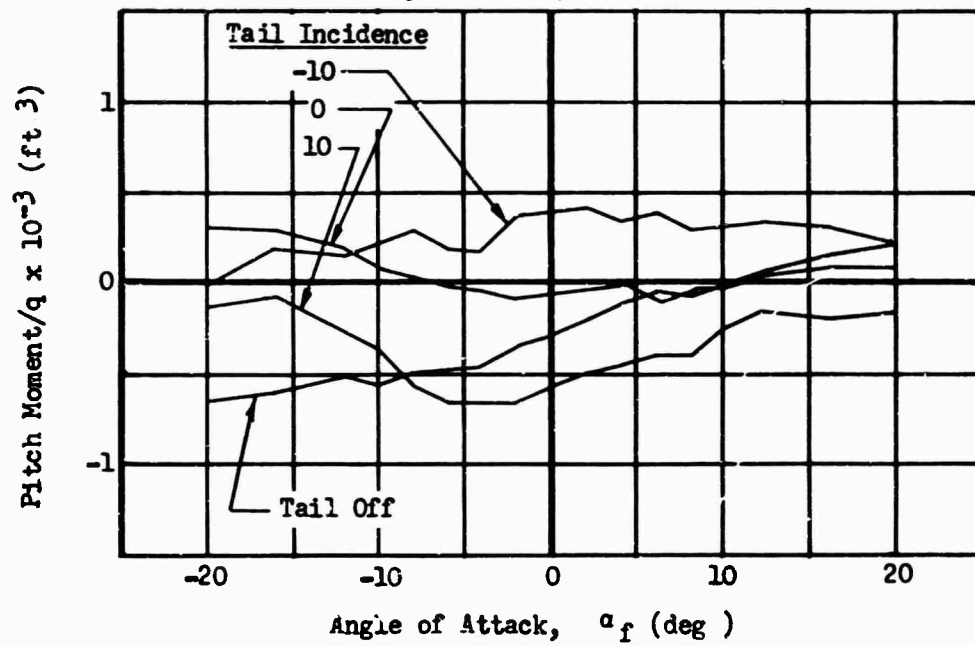


Figure 259 Pitch Moment/ q Versus Angle of Attack, CH-54A

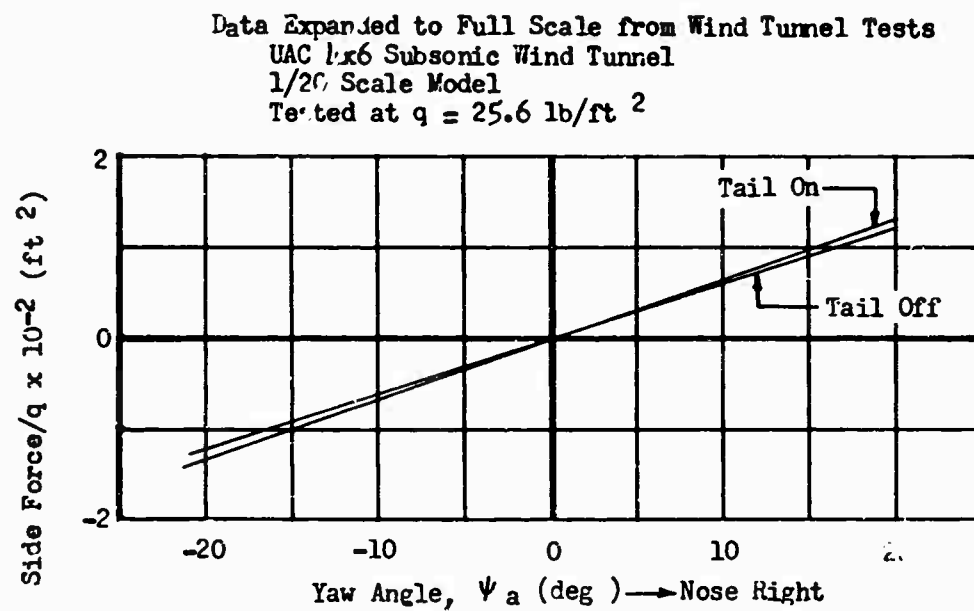


Figure 260 Side Force/ q Versus Yaw Angle, CH-54A

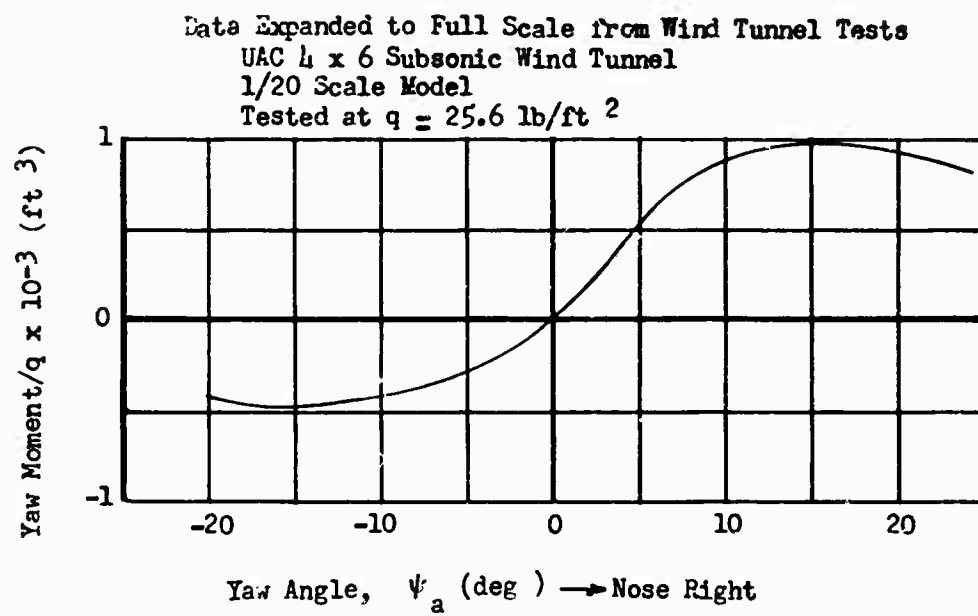


Figure 261 Yaw Moment/ q Versus Yaw Angle, CH-54A

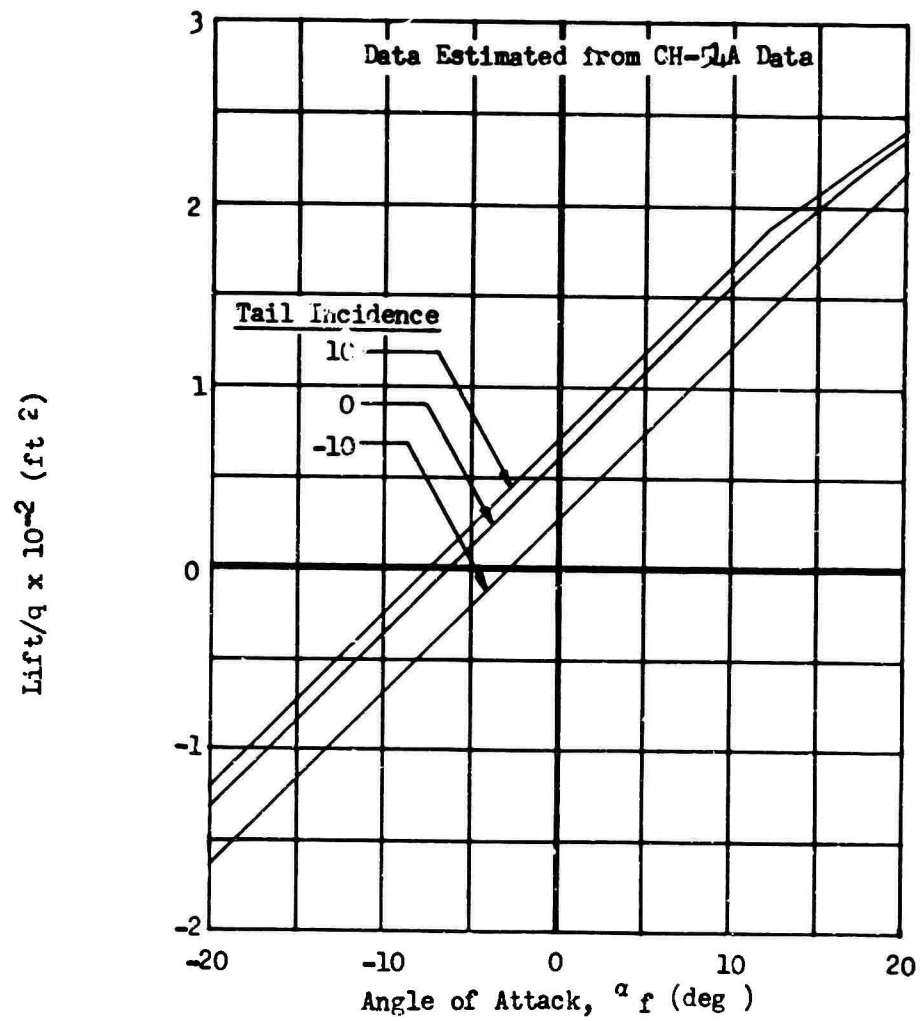


Figure 262 HLH Lift/q Versus Angle of Attack

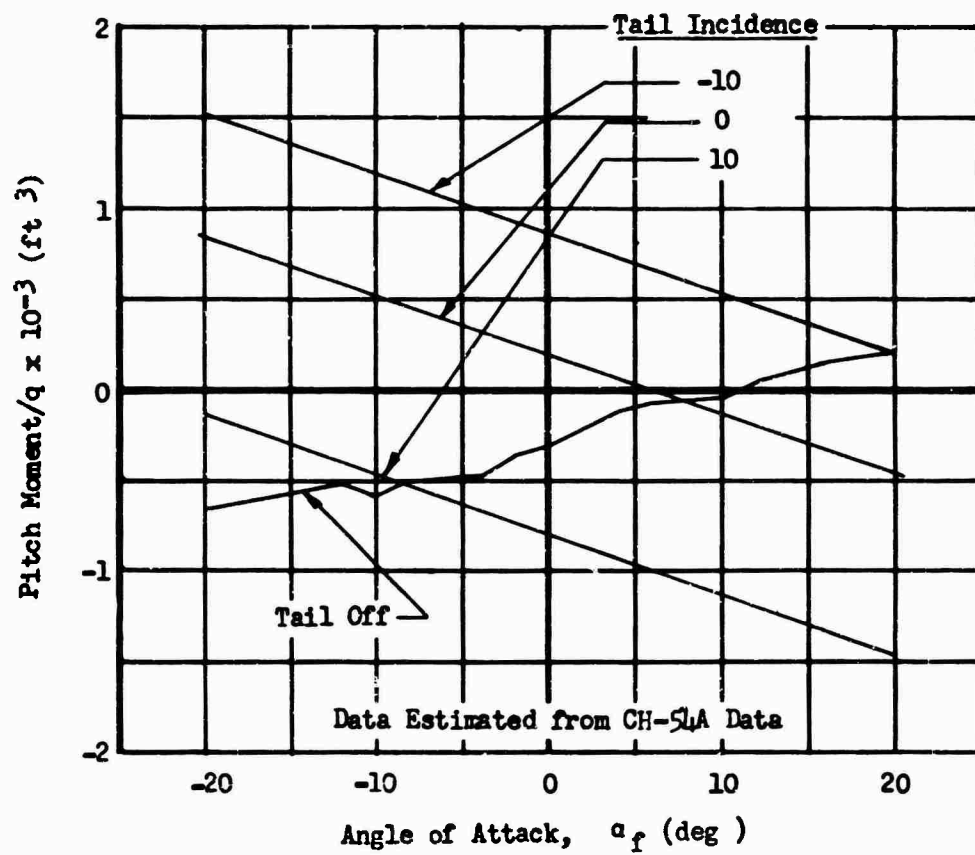


Figure 263 HLH Pitch Moment/ q Versus Angle of Attack

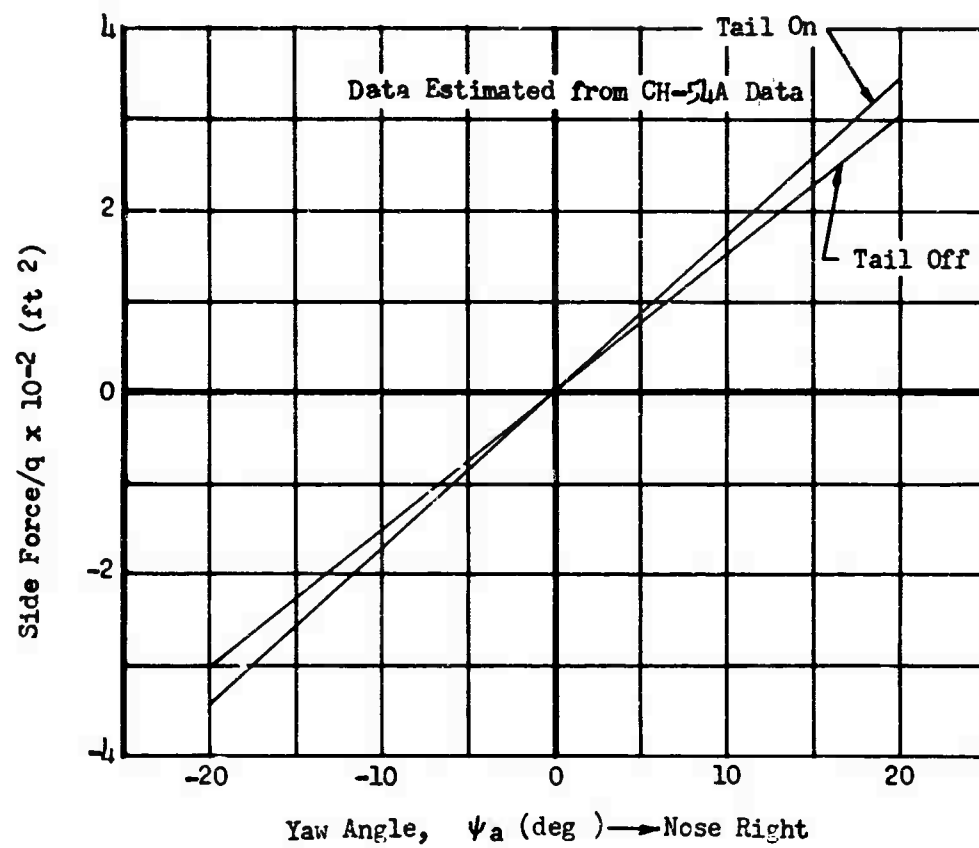


Figure 264 HLH Side Force/ q Versus Yaw Angle

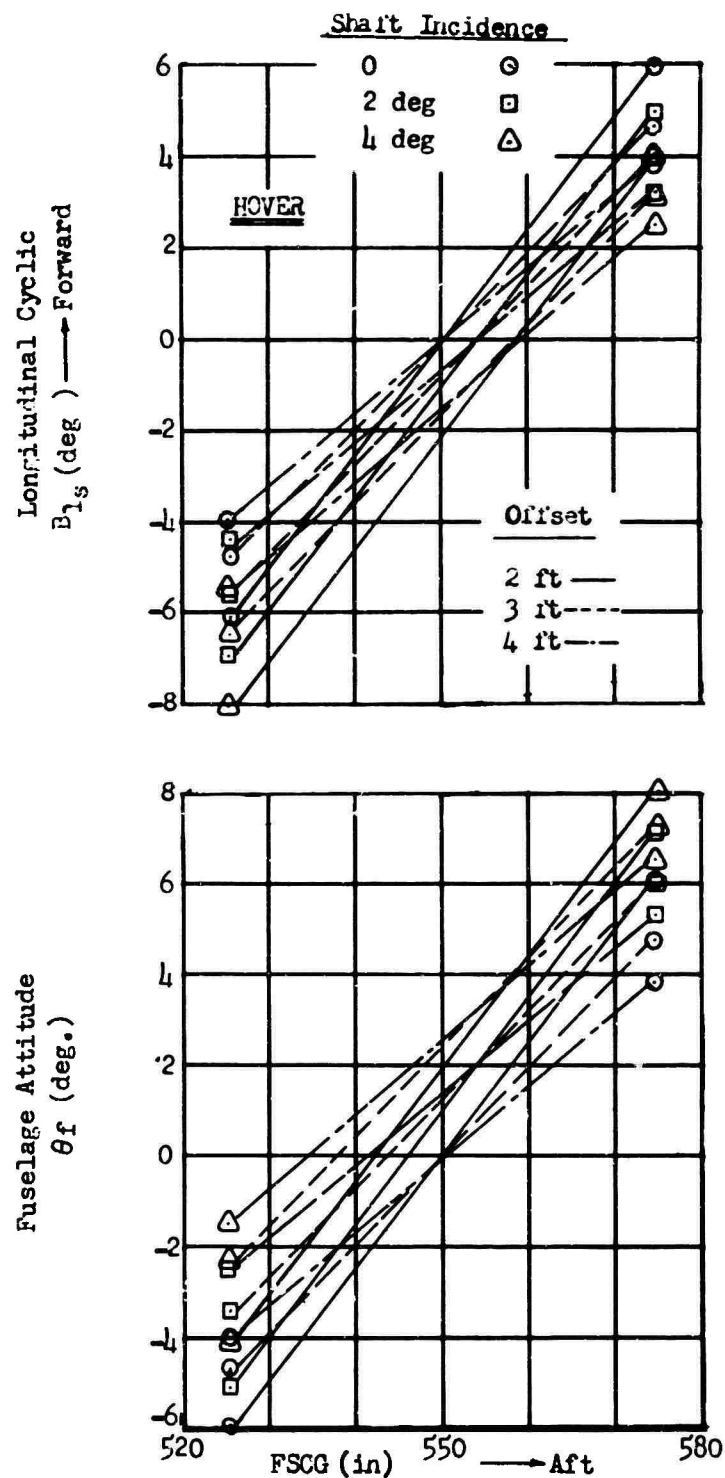


Figure 265 HLH Comparison of Pitch Attitude and Cyclic Required for Various Shaft Tilts, Offsets and CG Locations

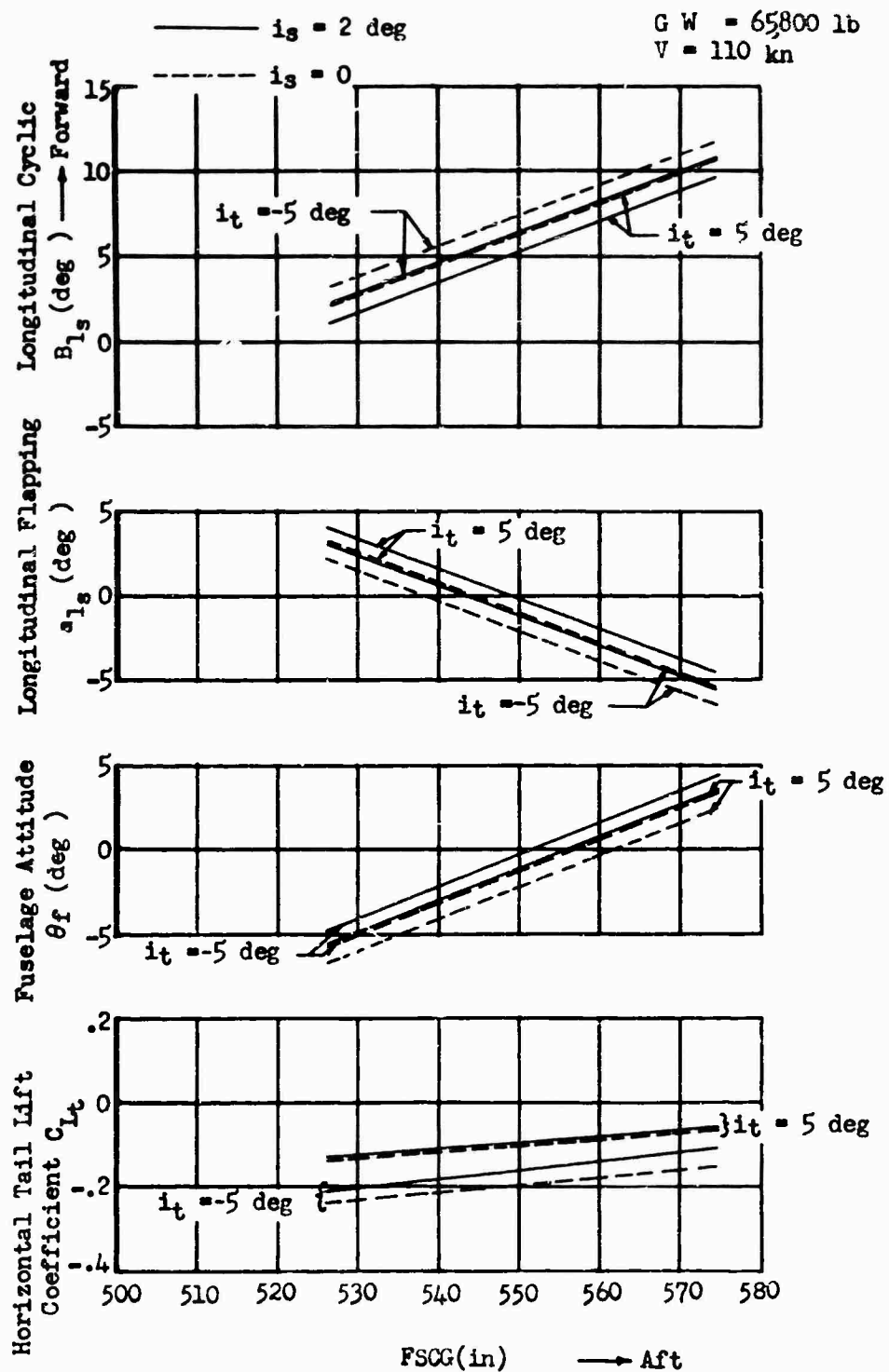


Figure 266 HLH Comparison of Longitudinal Trim Characteristics for Various Shaft and Tail Incidences Versus CG in Level Flight

An equal fore and aft CG displacement was assumed and pitch attitude was examined. Using the hover pitch attitude criterion, increased offset would allow increased CG variation (see Figure 265). The 3-foot offset was chosen to provide good longitudinal CG travel and to maintain good rotor characteristics, in terms of control sensitivity and gust response. In forward flight, either shaft incidence or tail incidence reduces flapping, but note that a change of 2 degrees in shaft incidence is almost equivalent to 10 degrees of tail incidence variation on the flapping plot (Figure 266) at 110 knots. Increased offset, while reducing the level of flapping in forward flight, yields equivalent net shaft moments for a given trim and CG condition. Calculations showed that for $i_s = 0$, a tail incidence of +18 degrees was necessary to yield equal \pm flapping distribution with equal \pm CG for both hover and 110 knots. This, however, would yield poor tail lift and pitch attitude in forward flight. A shaft incidence of +2° and tail incidence of +5° were finally chosen.

Next, variation of lateral CG was carried out to select i_L . Figure 267 shows lateral cyclic and roll angle vs lateral CG in hover at GW = 65800 pounds with a fixed load. Lateral shaft tilt of -3 degrees yielded the desired roll attitude. Figure 268 shows the effect of gross weight on these parameters, while Figure 269 is a similar plot for the CH-54A. Figures 276 through 278 show the trim values in forward flight, where additional benefits of lateral shaft tilt appear in terms of minimum slip-roll combinations about the origin.

Trim solutions for level flight, climb at 1500 ft/min and autorotation at constant tip speed of 700 ft/sec were calculated by using a comprehensive digital computer program on the IBM 7094 at the United Aircraft Research Laboratory, East Hartford, Connecticut. This program uses the Bailey "t" coefficient technique of Reference 6 in conjunction with wind tunnel data for a given configuration. The results of the trim calculations at the three "design" weights for fore and aft CG's are presented in Figures 270 through 278. Similar plots for the CH54A were generated at one gross weight with fore and aft CG for comparison (Figures 279 through 281.) Cross plots of cyclic, attitude, and rate of climb versus collective pitch were then made for the HLH, and the static stability plots (Figures 282 and 283) were taken at constant lines of collective.

The computer program cited above contains a derivative routine, useful for dynamic stability computations as well as the major trim iteration. Once the final configuration was chosen, this routine was used to generate a complete set of derivatives for the HLH. Reference 29 describes the equations for these derivatives. Next, solution of simultaneous linear differential equations, in groups of three, was performed and the roots of the characteristic equations were determined. The longitudinal solutions used the \dot{x} , \dot{z} , $\dot{\phi}$ degrees of freedom, while the lateral-

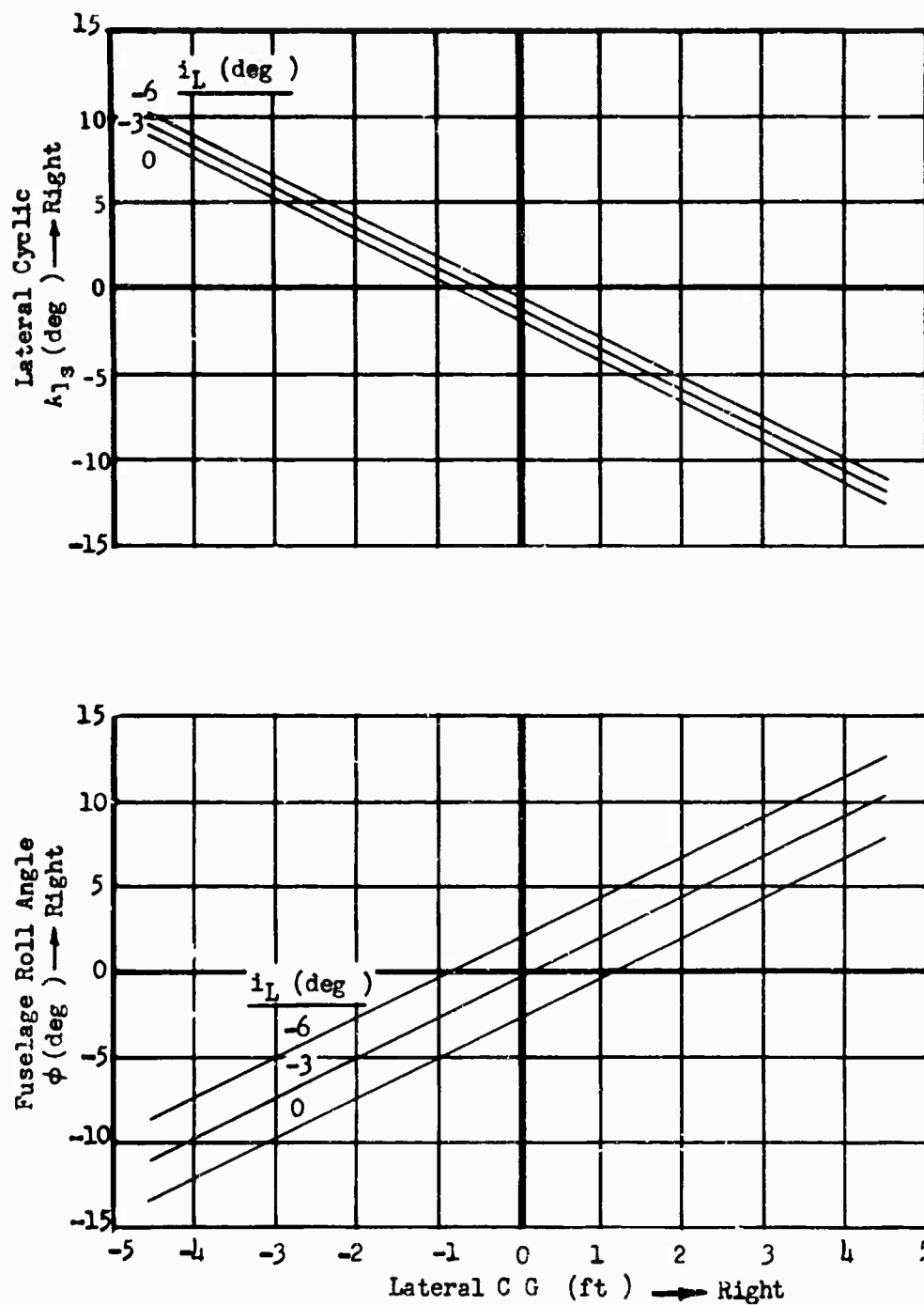


Figure 267 HLH Comparison of Roll Attitude and Cyclic Required for Various Lateral Shaft Tilts and CG Locations

$G_A = 36,000 \text{ lb}$ -----
 $G_W = 65,800 \text{ lb}$ -----
 $G_W = 78,750 \text{ lb}$ -----

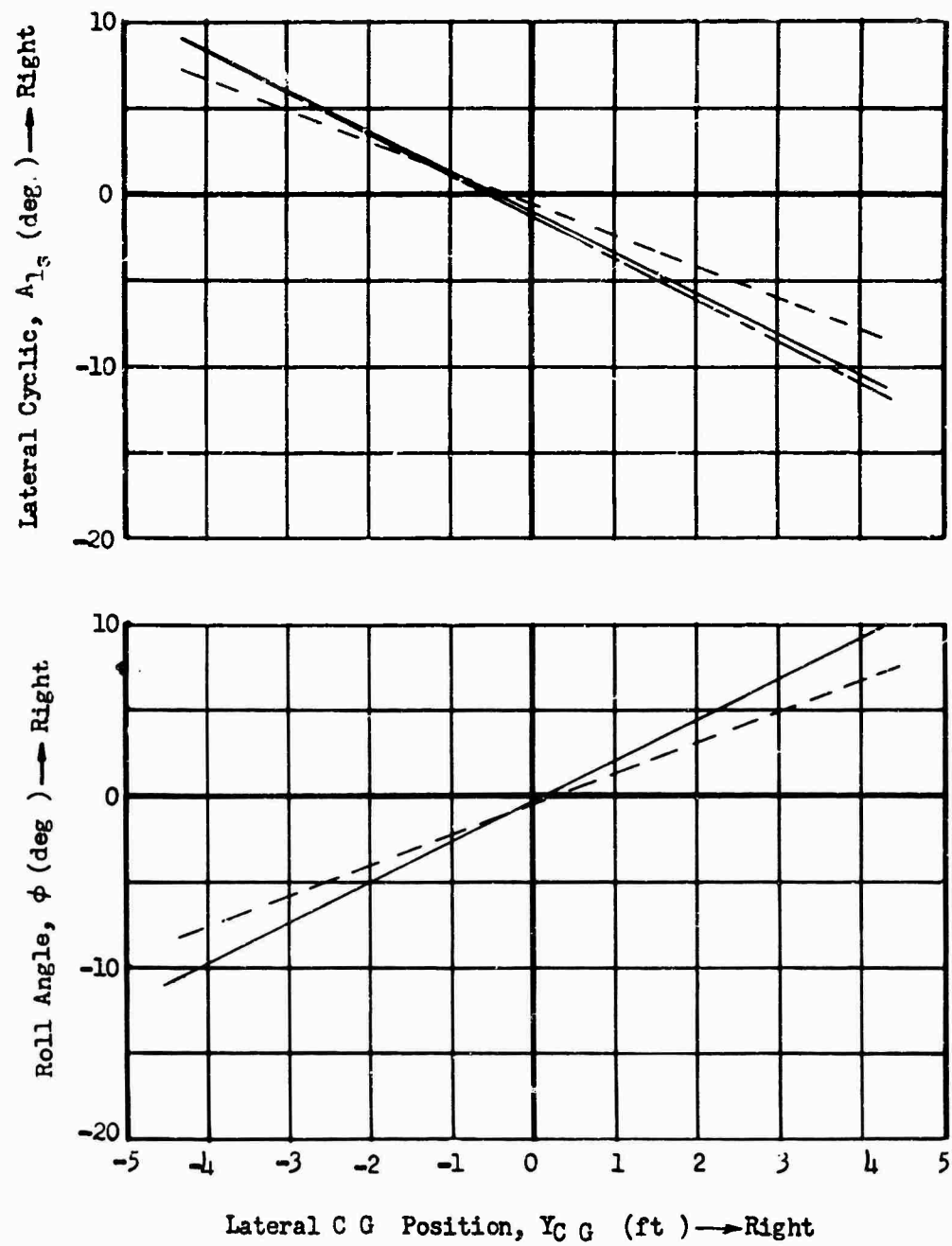


Figure 268 HLH Lateral Trim Versus Lateral CG Position in Ho or

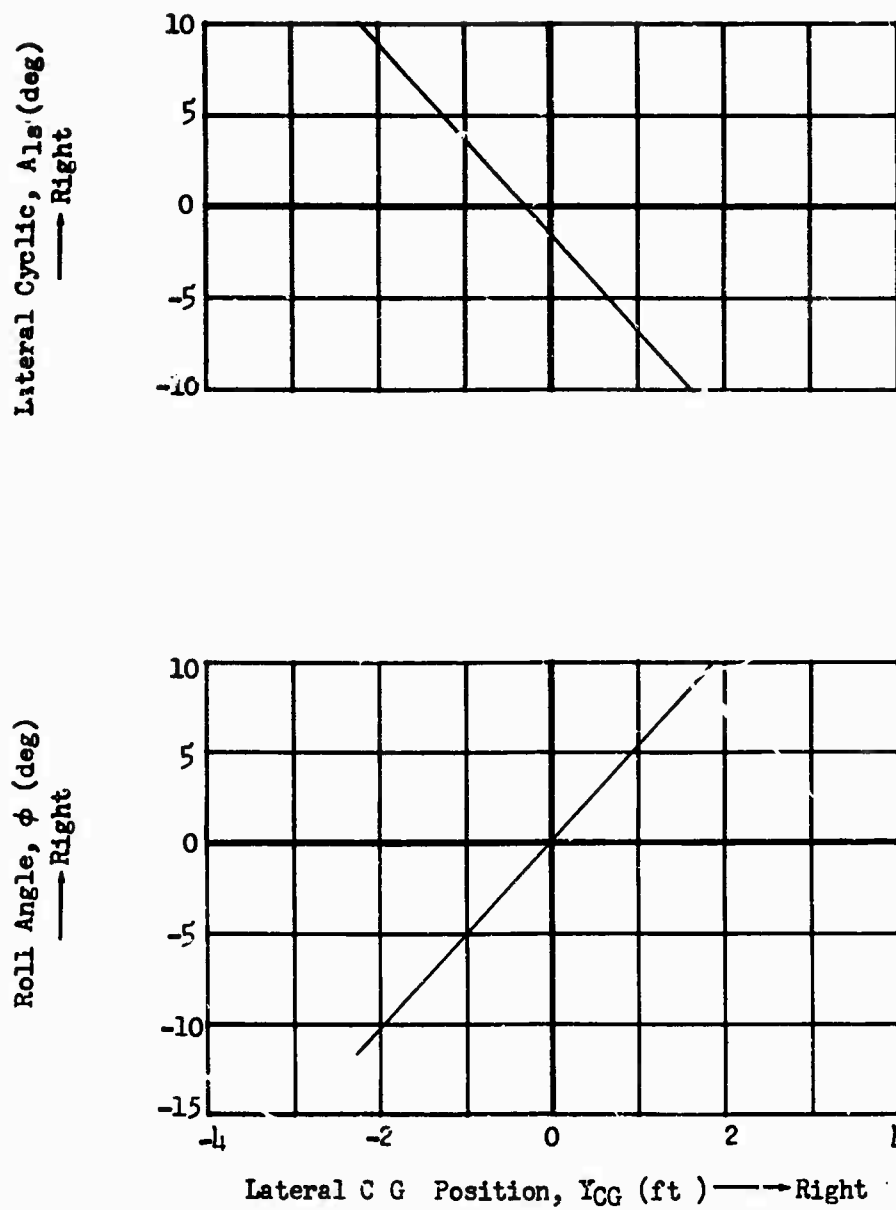


Figure 269 Lateral Trim Versus Lateral CG Position in Hover, CH-54A

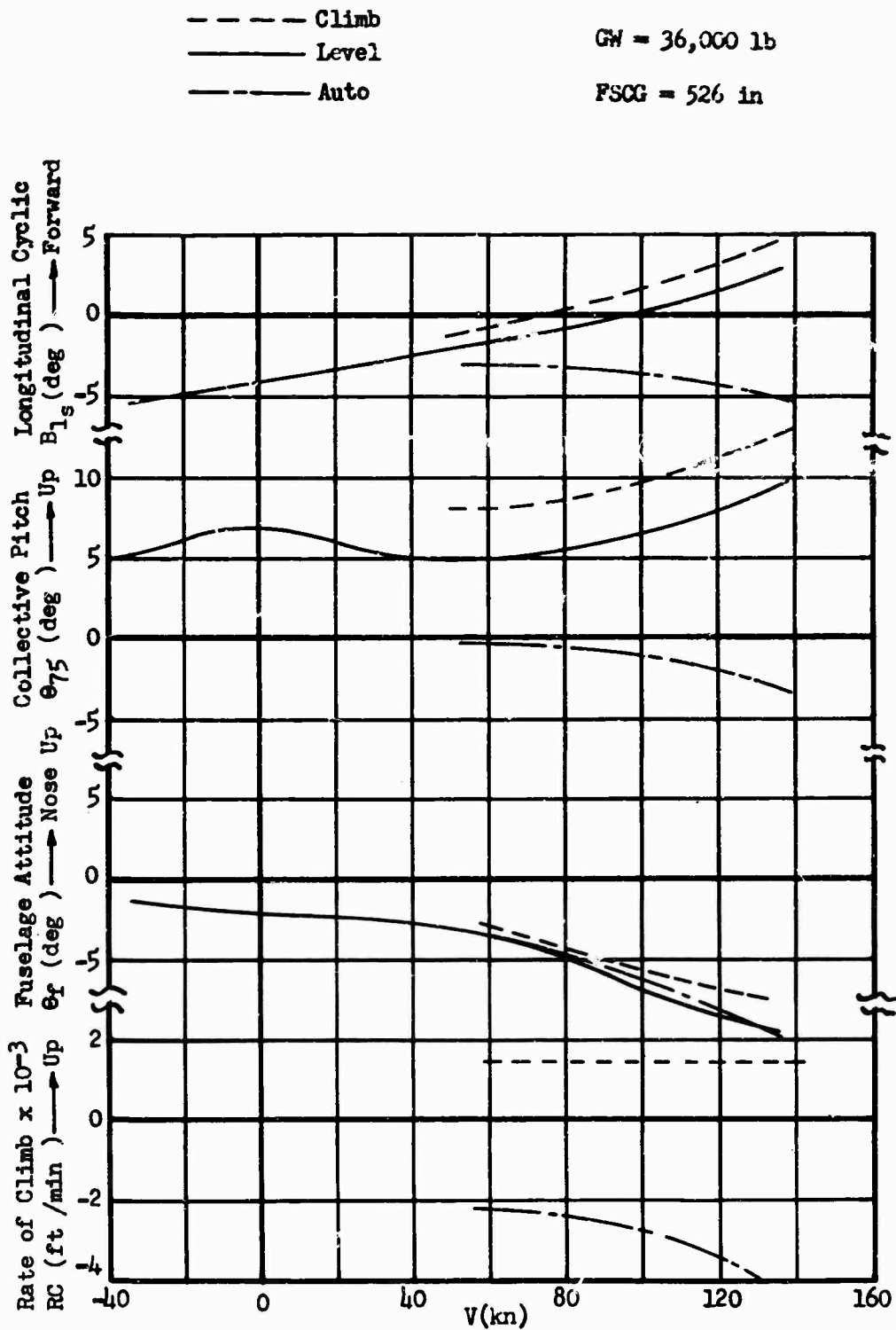


Figure 270 HLH Longitudinal Trim Characteristics

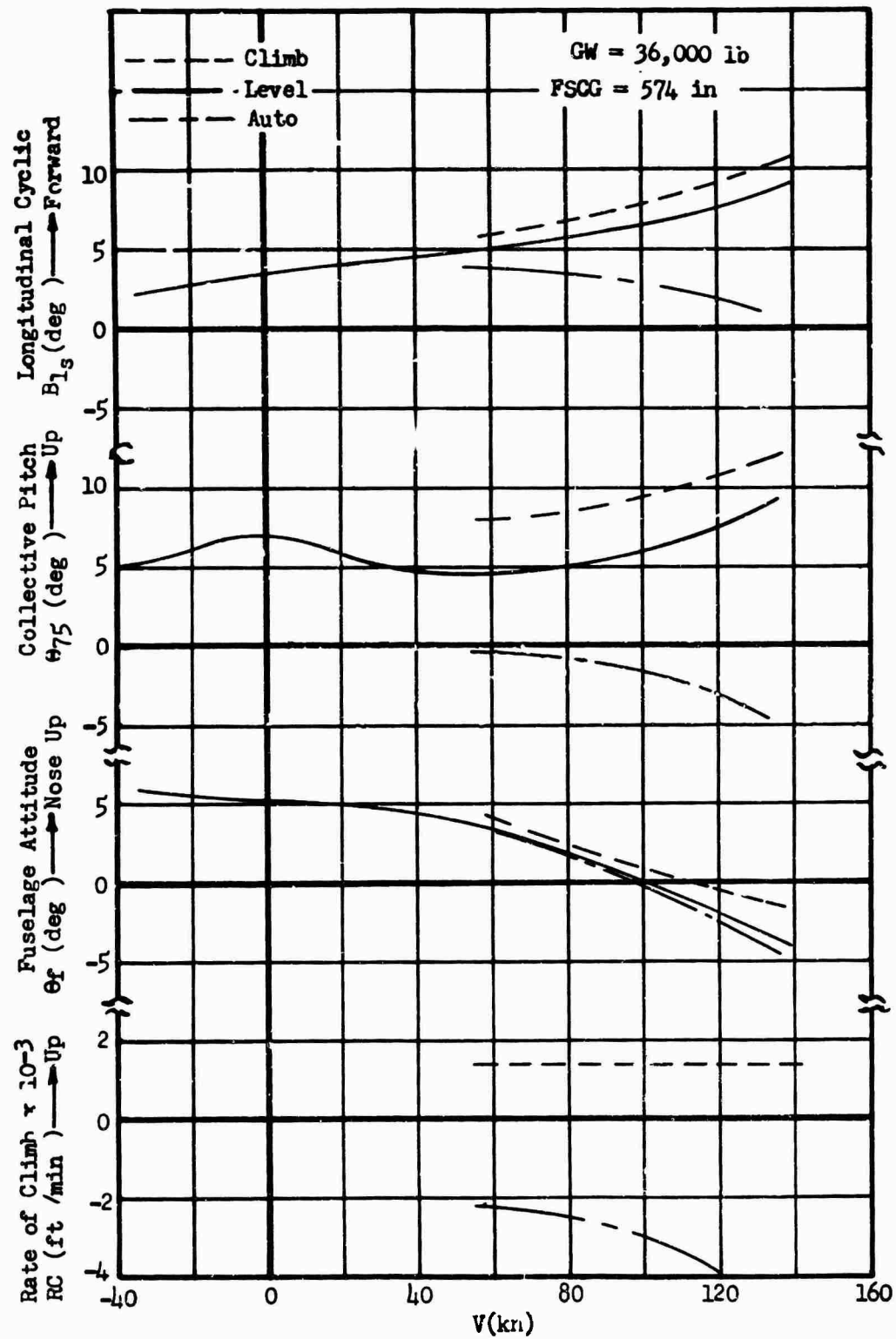


Figure 271 HLH Longitudinal Trim Characteristics

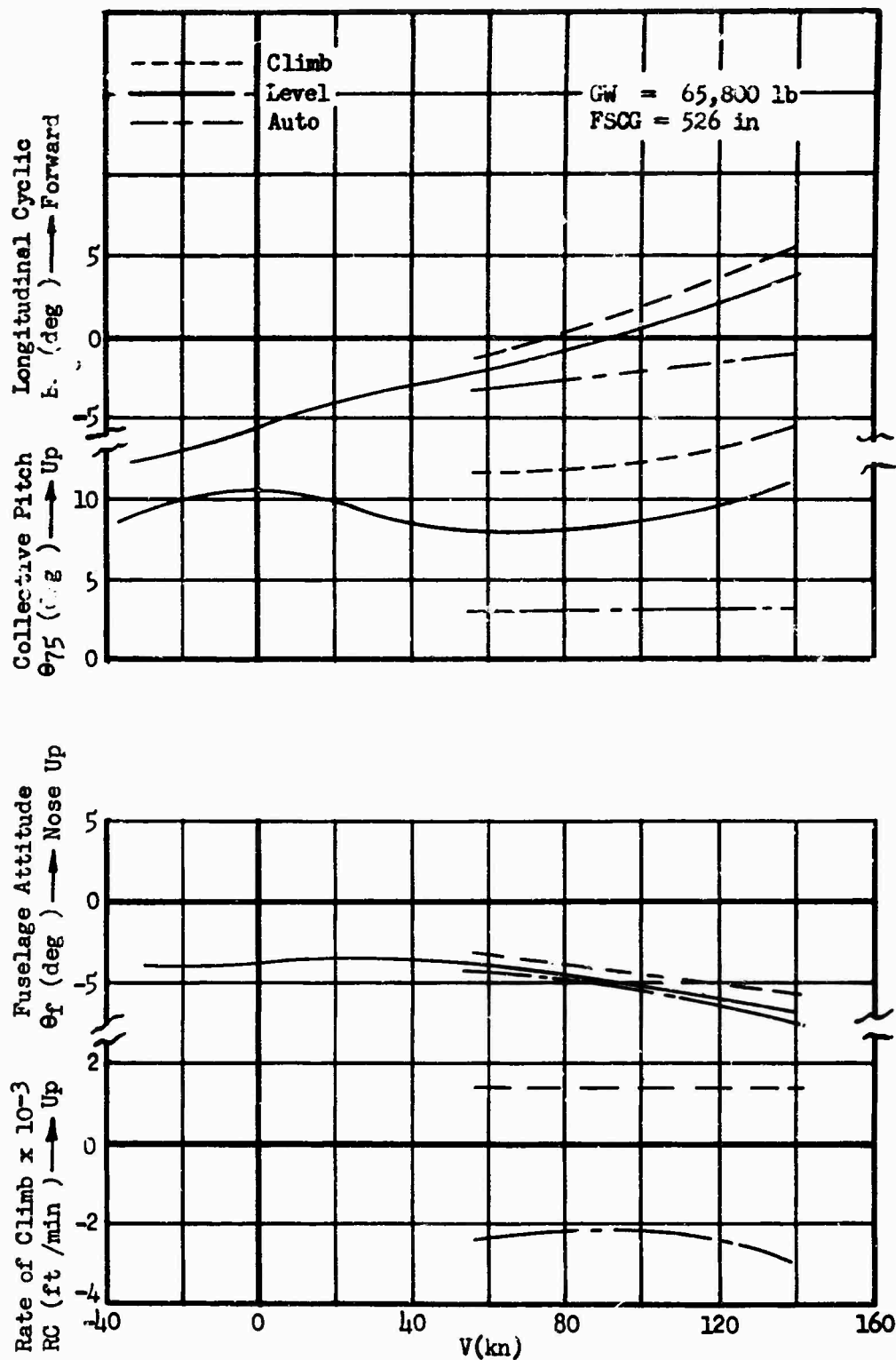


Figure 272 HLH Longitudinal Trim Characteristics

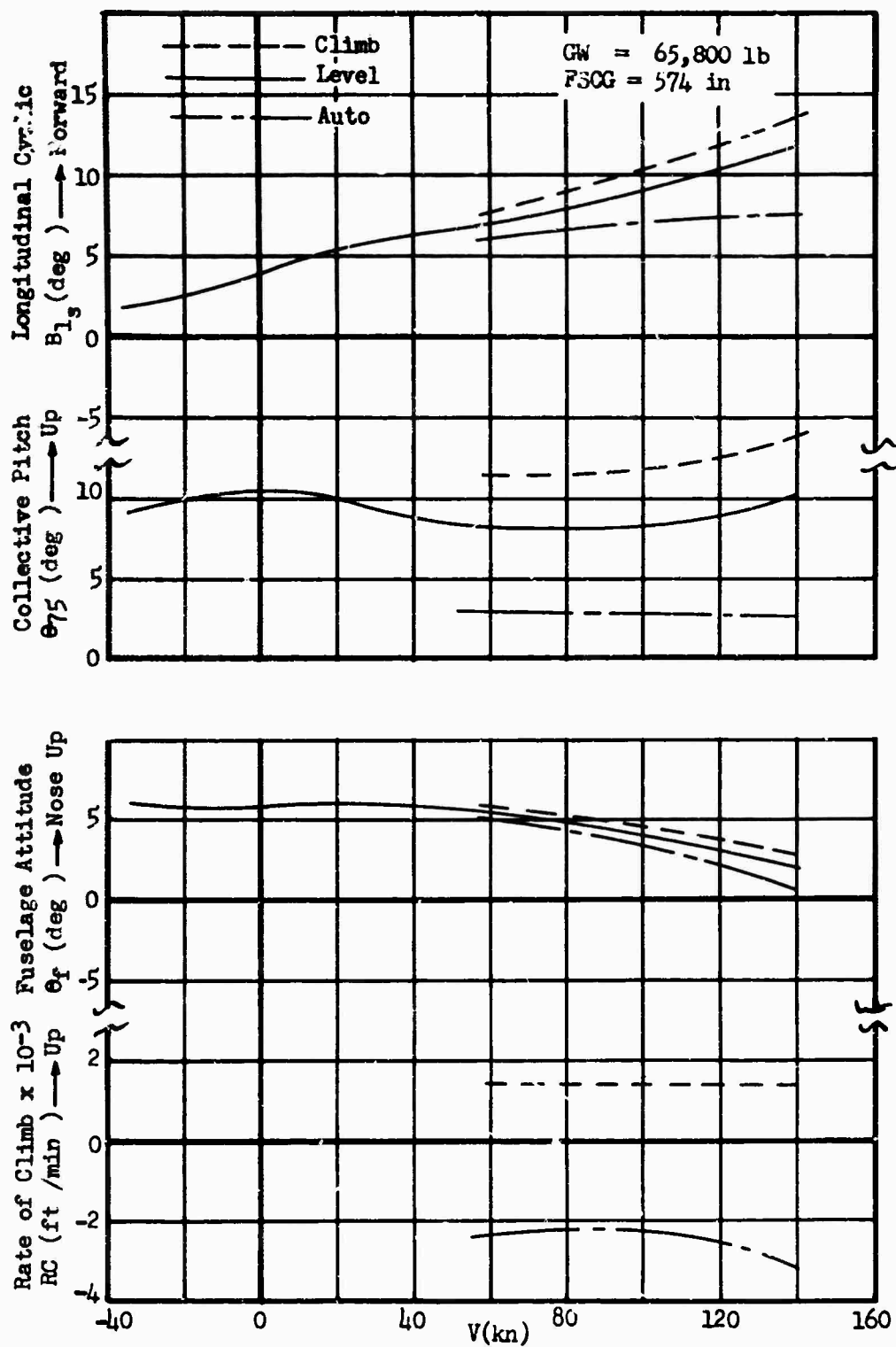


Figure 273 HLH Longitudinal Trim Characteristics

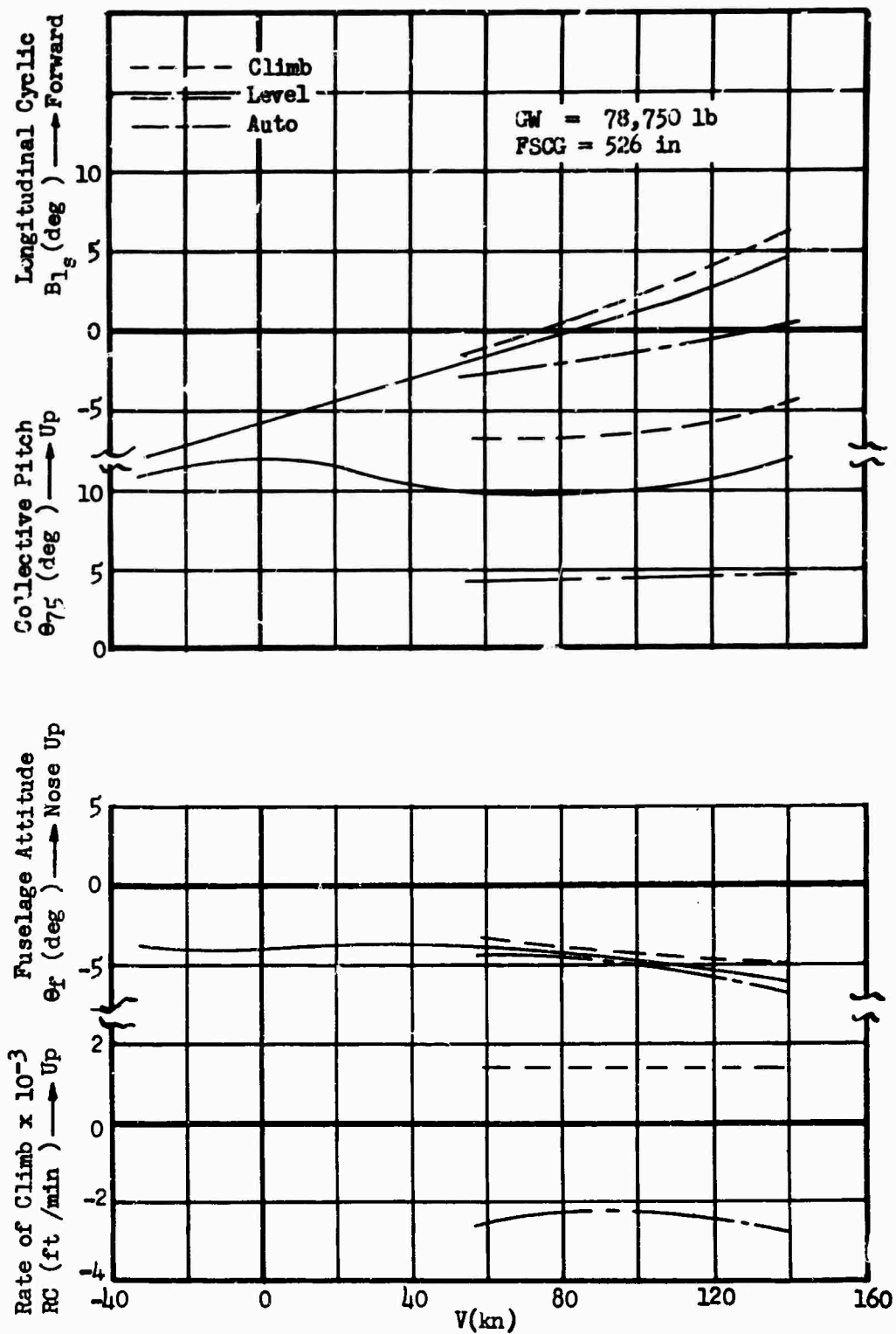


Figure 274 HLH Longitudinal Trim Characteristics

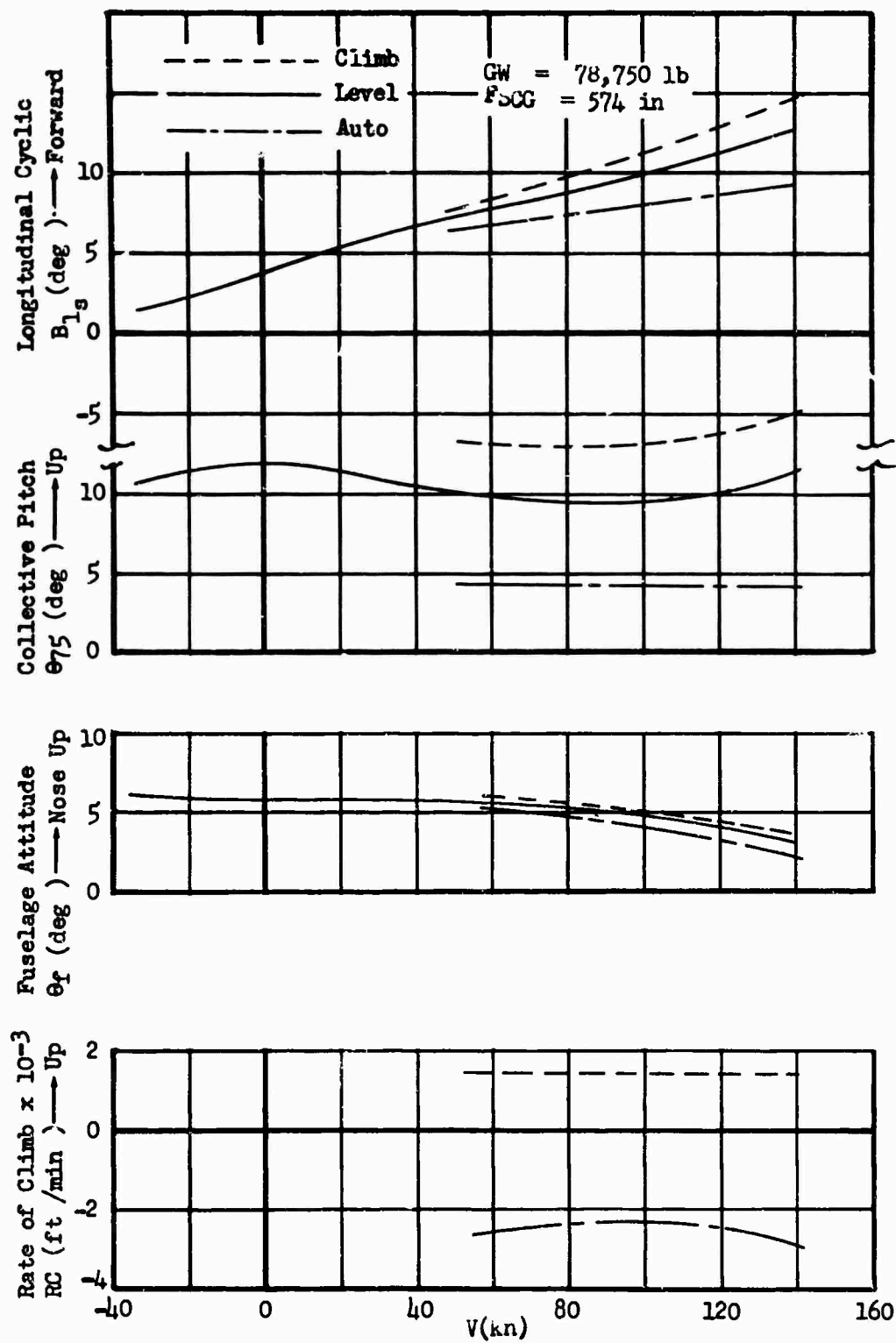


Figure 275 HLH Longitudinal Trim Characteristics

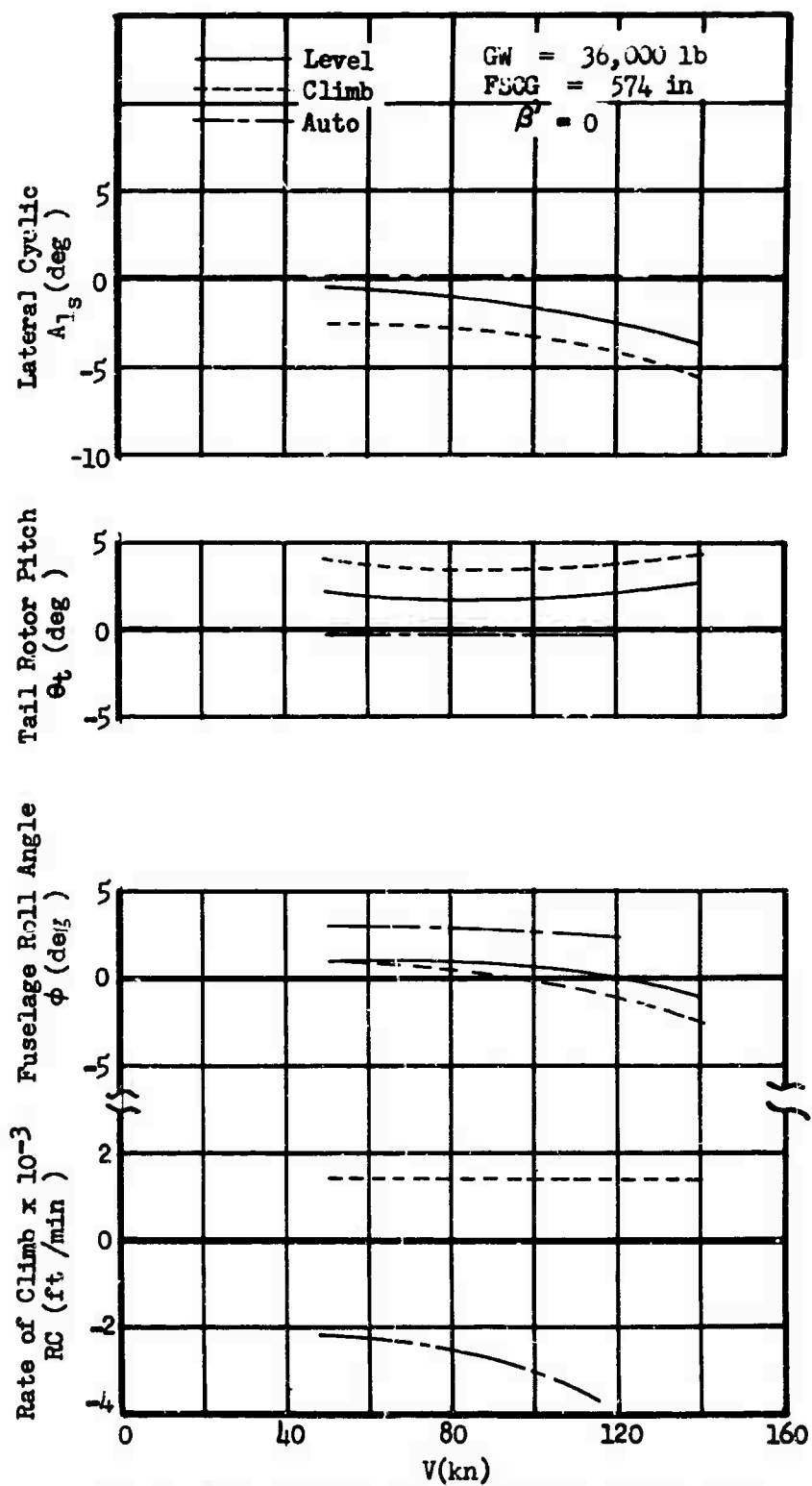


Figure 276 HLH Lateral Trim Characteristics

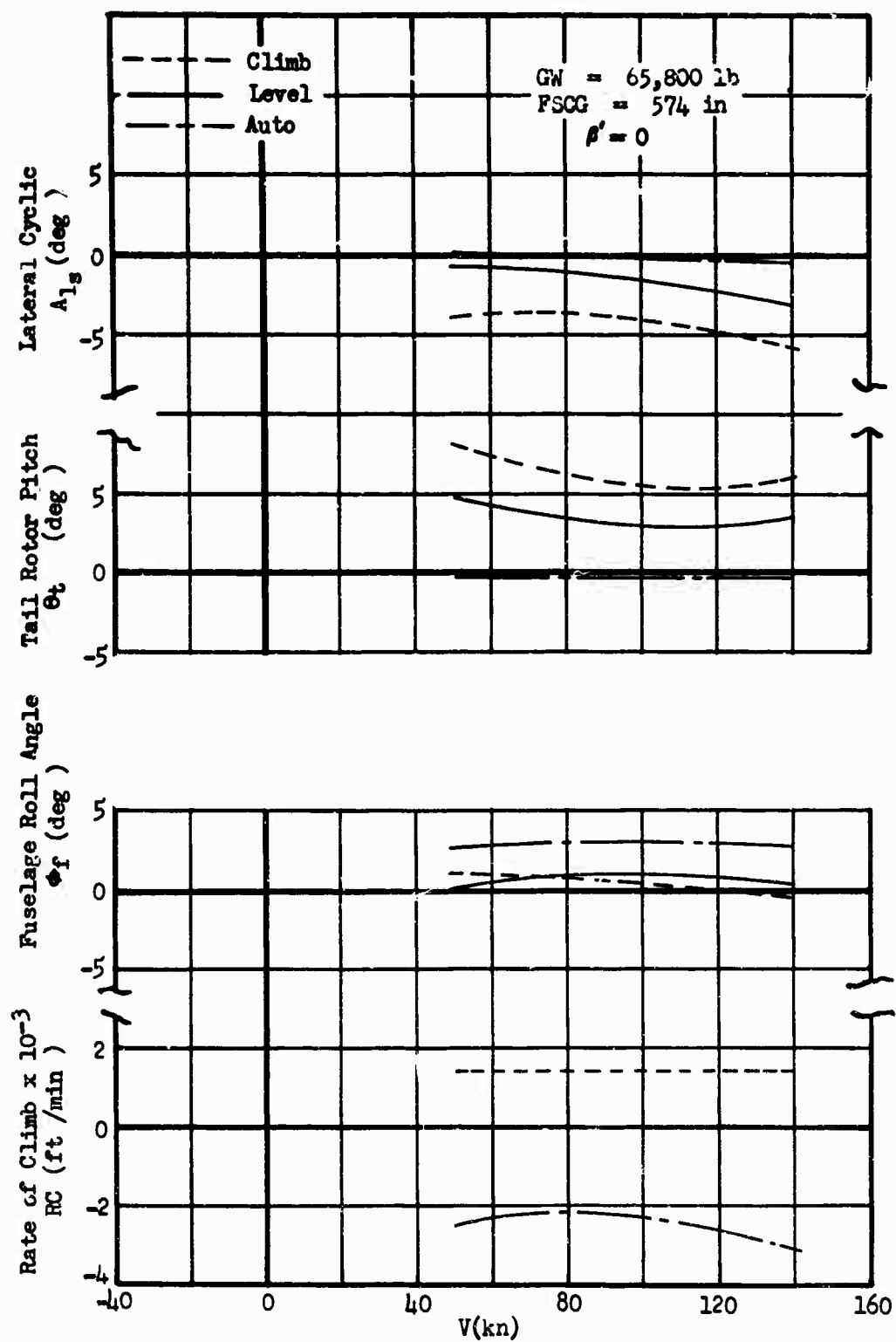


Figure 277 HLH Lateral Trim Characteristics

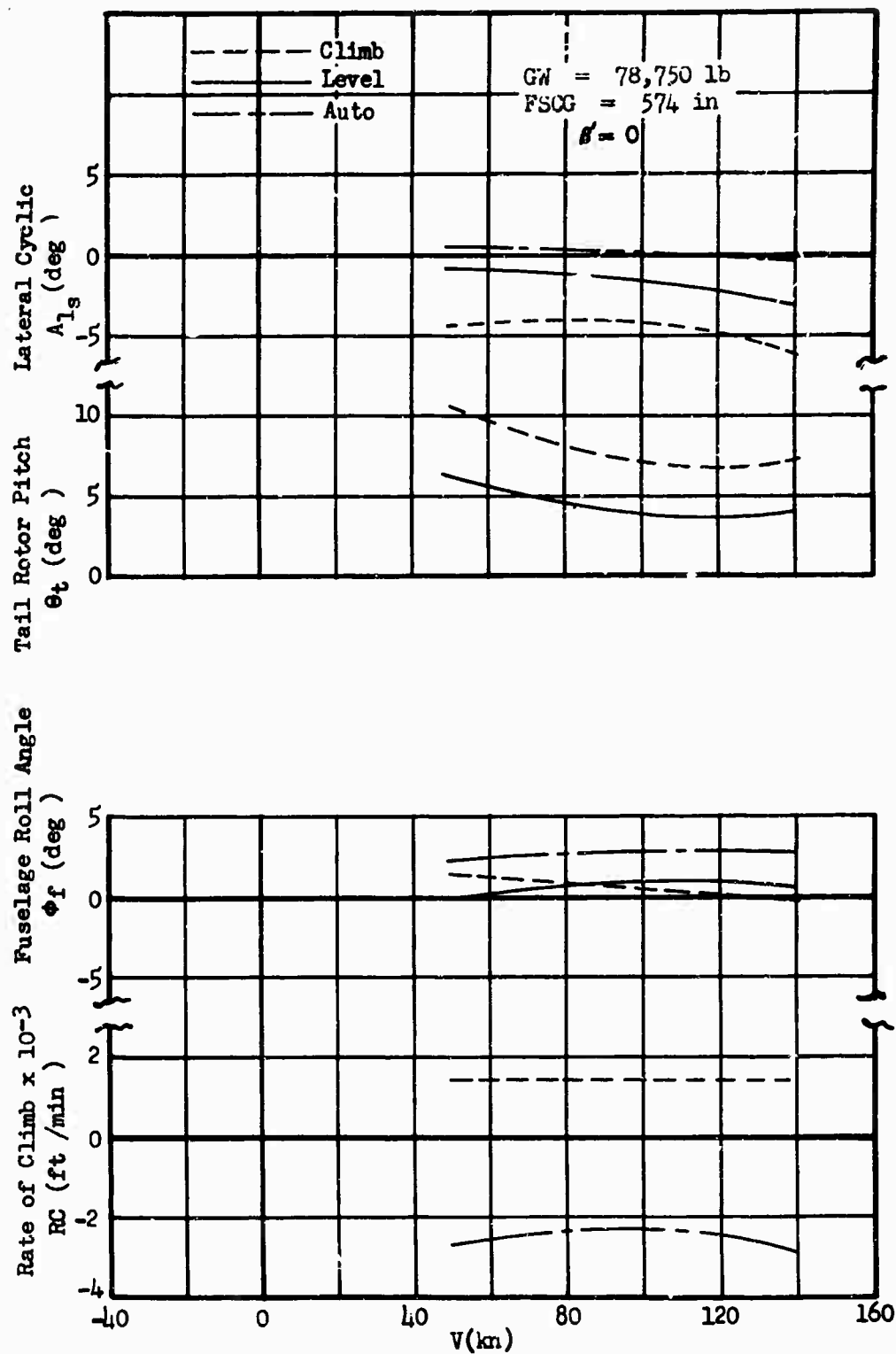


Figure 278 HLH Lateral Trim Characteristics

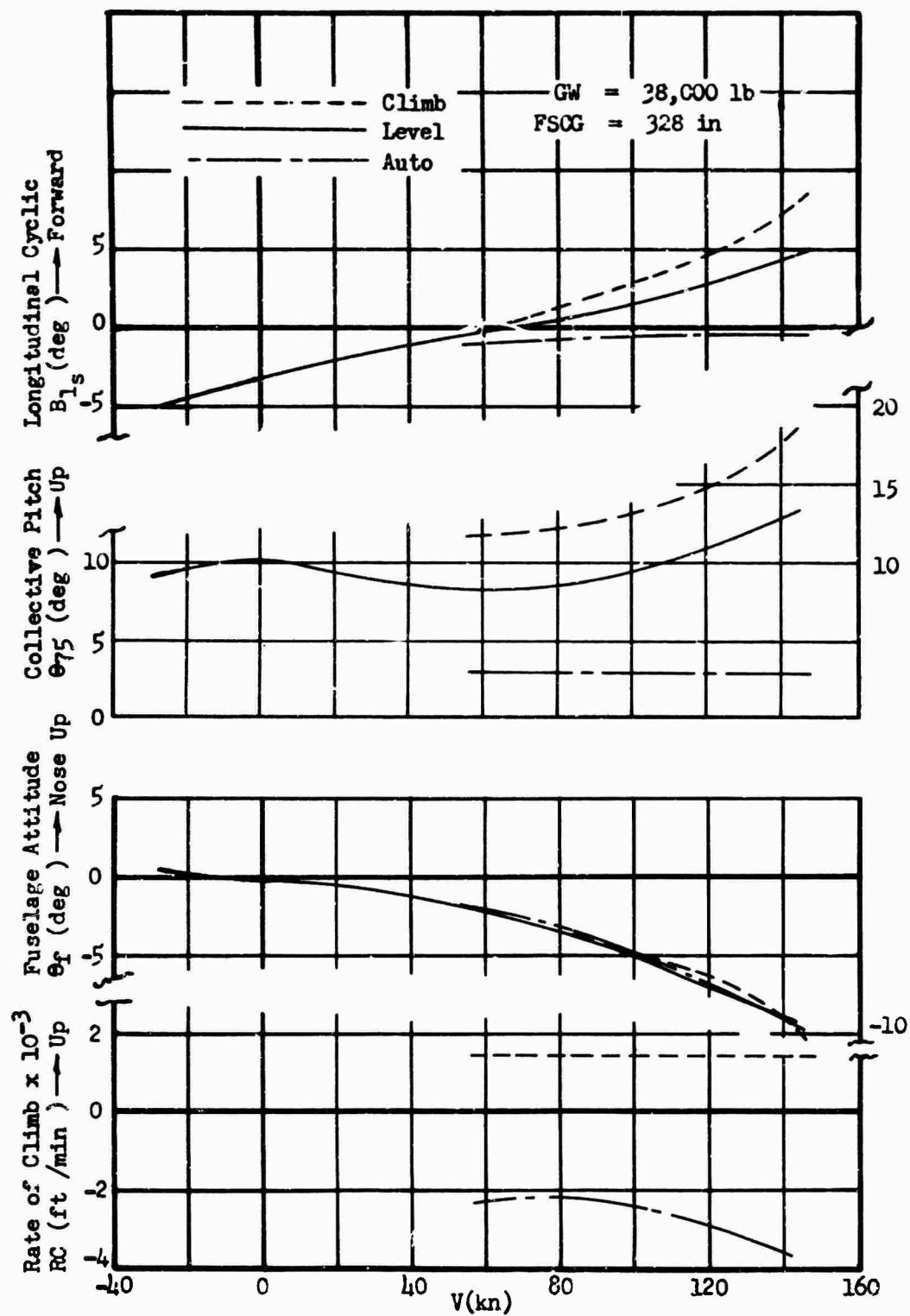


Figure 279 Longitudinal Trim Characteristics, CH-54A

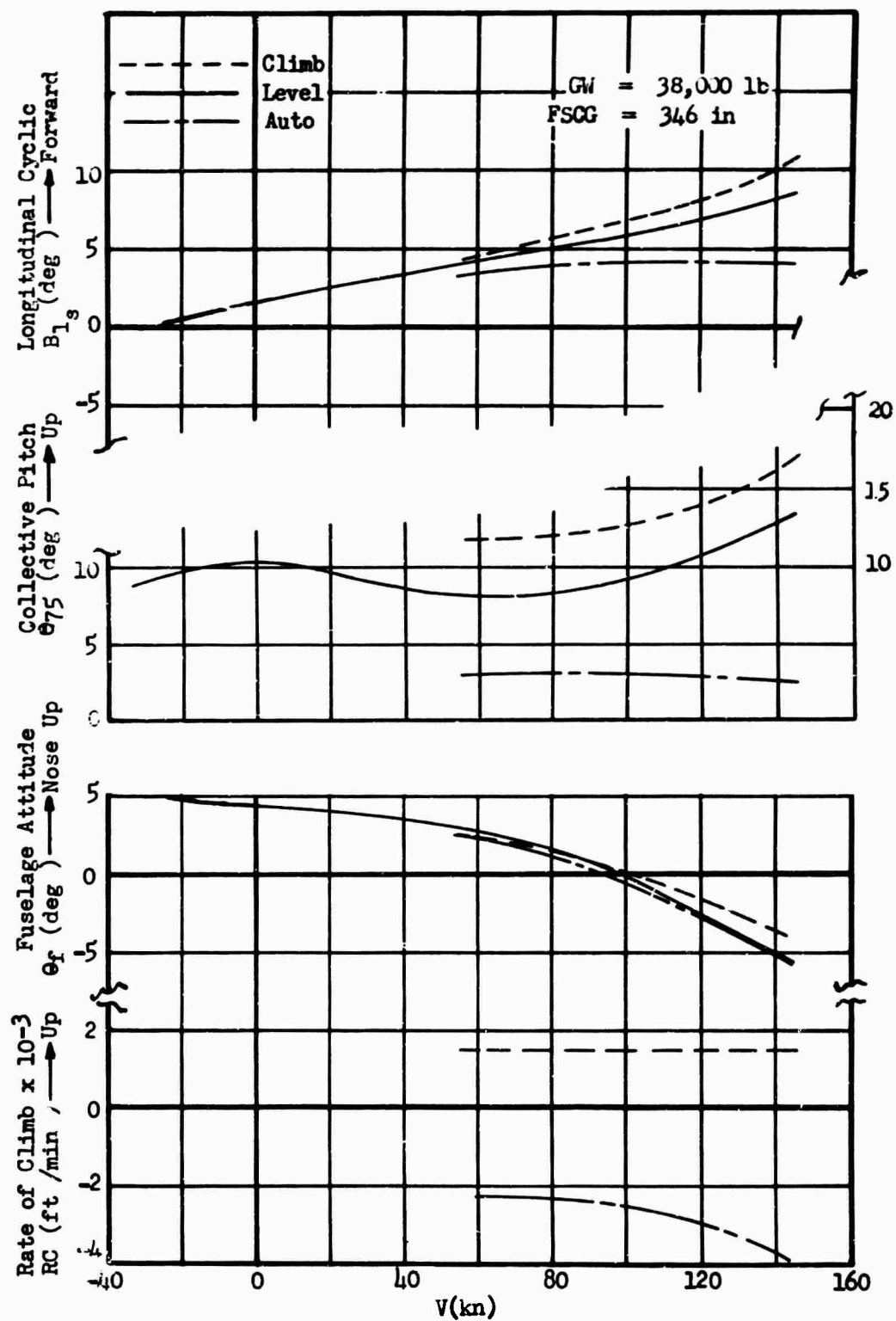


Figure 280 Longitudinal Trim Characteristics, CH-54A

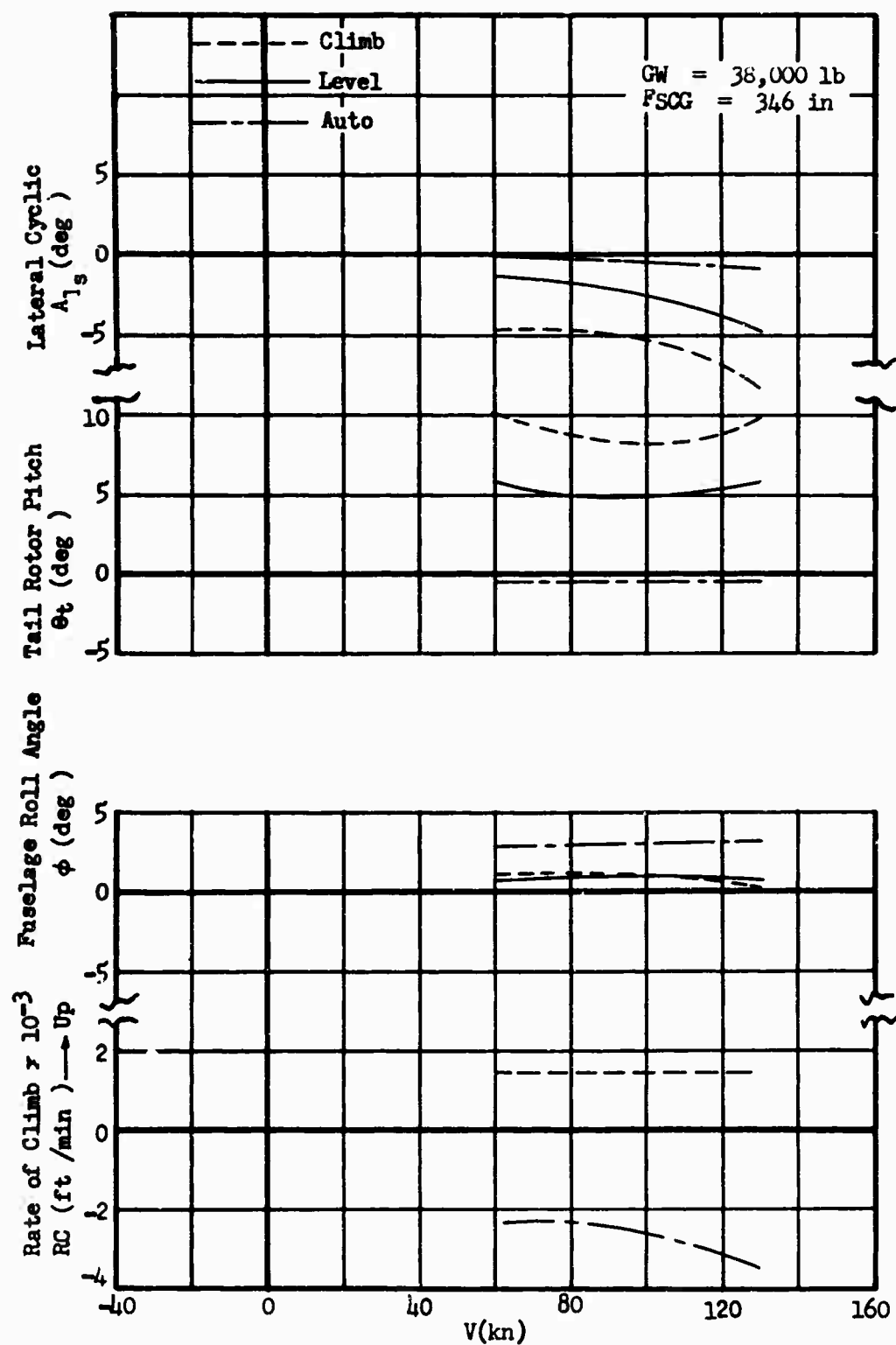


Figure 281 Lateral Trim Characteristics, Zero Sideslip, CH-54A

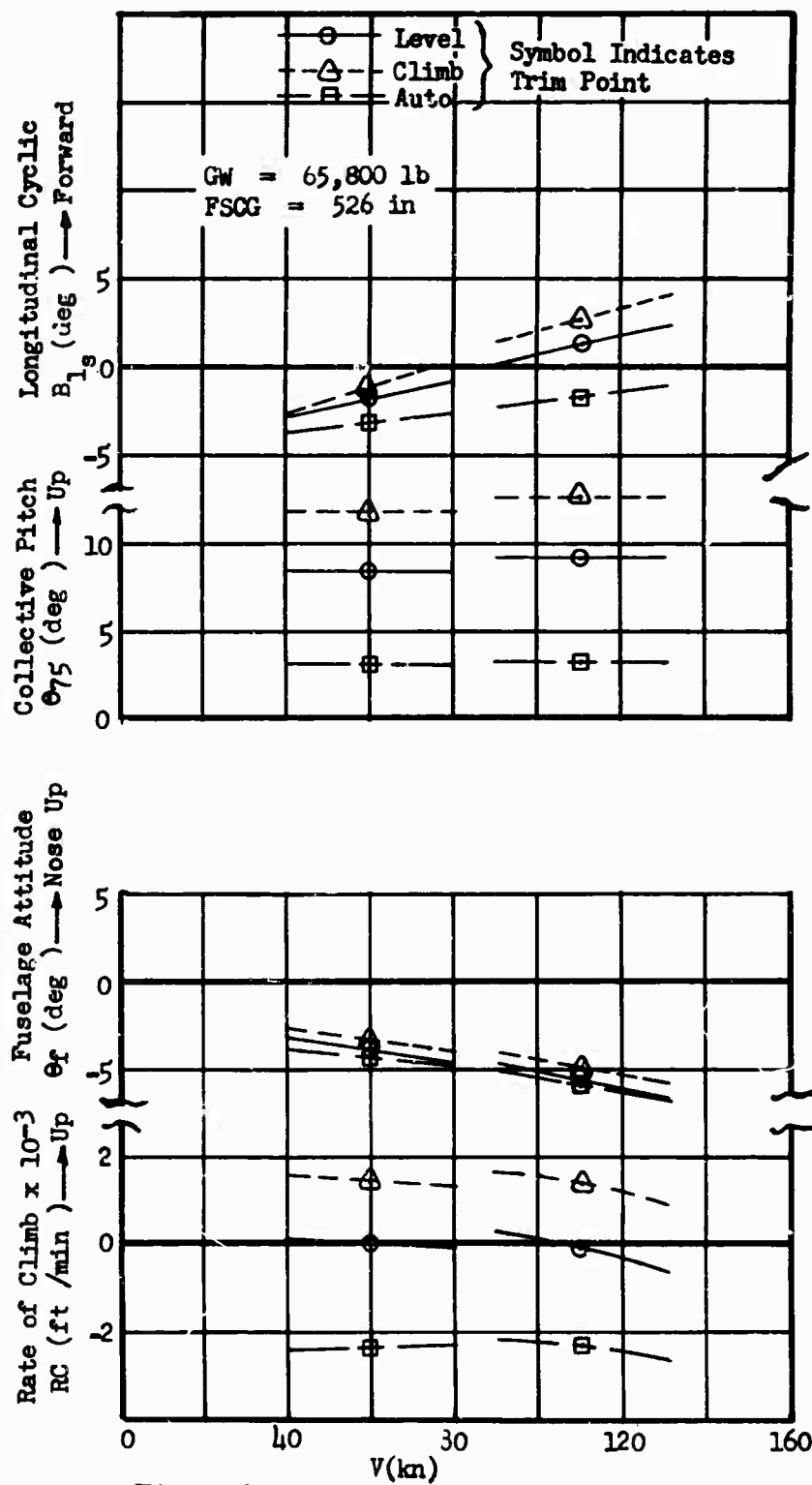


Figure 282 HLH Longitudinal Static Stability

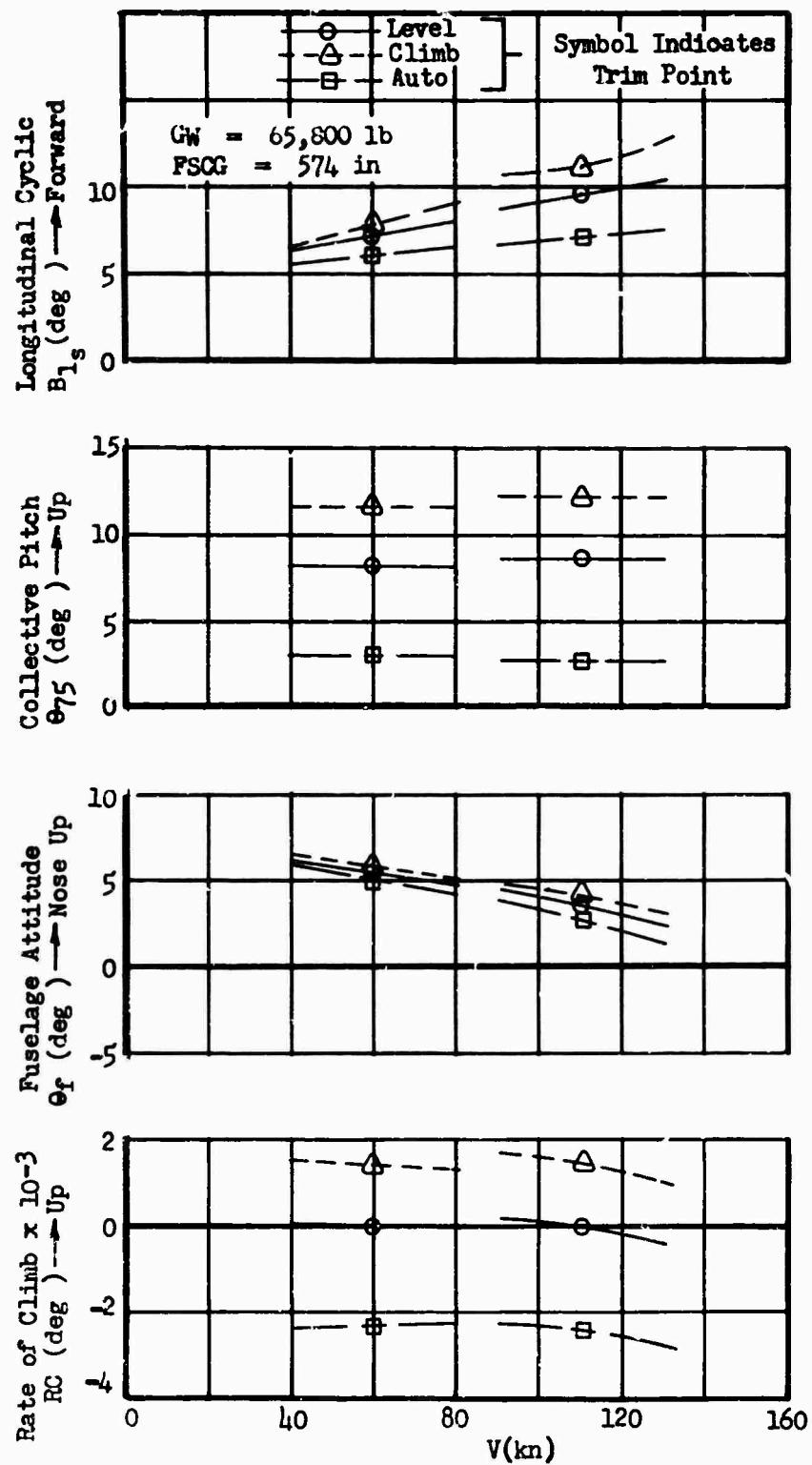


Figure 283 HLH Longitudinal Static Stability

directional used \dot{y}, ϕ, ψ . Addition of the CH-54A Automatic Flight Control System (AFCS) (see Figure 284) with gains modified by factors 0.5, 1.0, and 2.0 was investigated to give an indication of the pilot unburdening to be expected of a typical AFCS. Figures 285 through 287 are root locus plots (see Reference 16) which show these effects for the longitudinal cases. Note that the use of rate plus proportional feedback AFCS yields a desirable solution within the range of gains considered for every case. However, an alternate stabilization system is the type used in the Marine CH-53A. Since this system embodies many improvements over the CH-54A system, it has been selected as the basis for the HLH AFCS design. Since the lateral solution is stable without AFCS in all but the hover case, only a plot of basic roots for various velocities is shown in Figure 288. Similar plots for the CH-54A are shown in Figures 289 through 291. The final step in the dynamic analysis used selected transfer functions from the root locus study with factors of 1.0 for the CH-54A type AFCS in development of time histories. Figures 292 through 297 show pitch rate and load factor versus time for given inputs. The responses displayed are typical for either pilot inputs or gust inputs at the speeds cited.

Figures 298 and 299 show roll angle for given inputs and may be interpreted similarly. A review of the trim plots, plus attention to particular points not shown such as collective to hover at 6000 feet, 95°F, led to selection of control sensitivities and ranges similar to the CH-54A. Note, however, that the collective range was opened up somewhat. Experience with previous Sikorsky designs indicates that the high-speed, low-gross-weight autorotation case at constant tip speed is ignored in practice, and so a trade-off of revolutions per minute is made to keep control sensitivity within bounds. The predicted high collective pitch for hot day hover is 12.7 degrees at .75R, and an additional 10 percent was allowed at this point.

Reference to the plot of lateral cyclic versus CG, Figures 268 and 269, shows that offsetting the range 1 degree yields significant gain in right CG travel for both HLH and CH-54A. Figure 300 shows the effect of CG on longitudinal cyclic, and again offsetting the range is desirable. A margin of 20 percent on forward cyclic based on required velocities yielded 14 degrees forward cyclic. Note that 10 percent was allowed to satisfy Reference 4 and 10 percent was allowed for recovery from a positive pitch rate at high forward velocity. Experience shows that the combination of allowances is desirable here.

The growth of fixed-wing aircraft would indicate that the dimensions of the HLH do not present any size-effect problems. Predictions for structural deflections of the HLH rotor support this theory. Even the problems associated with the man-machine size ratio seem to be mastered for aircraft in forward flight. The area of particular interest,

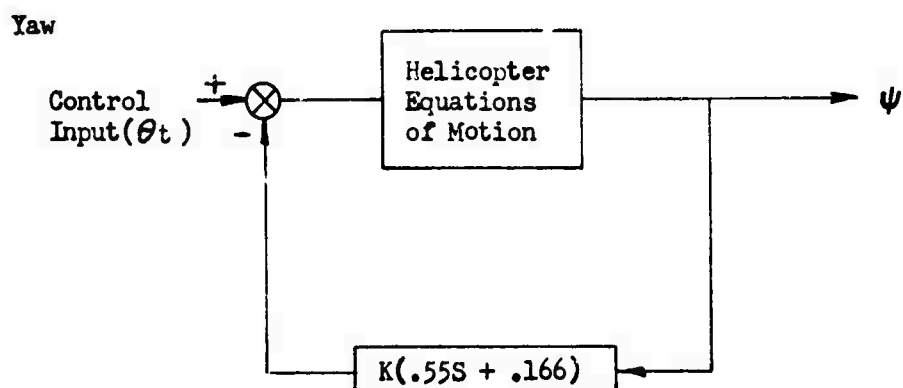
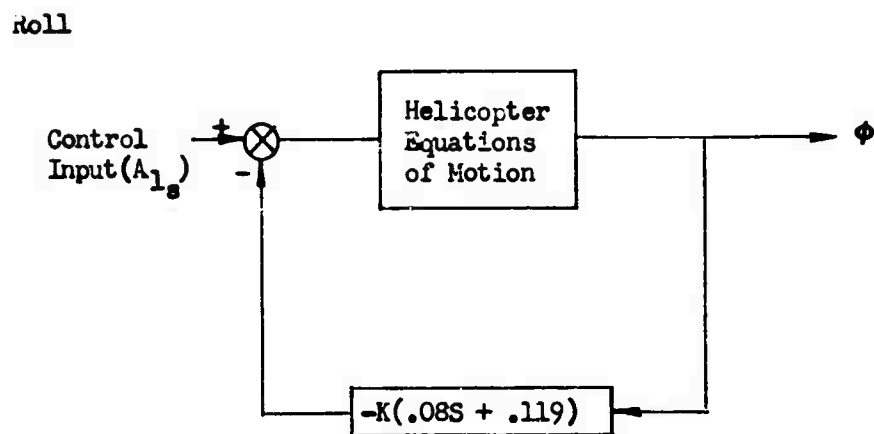
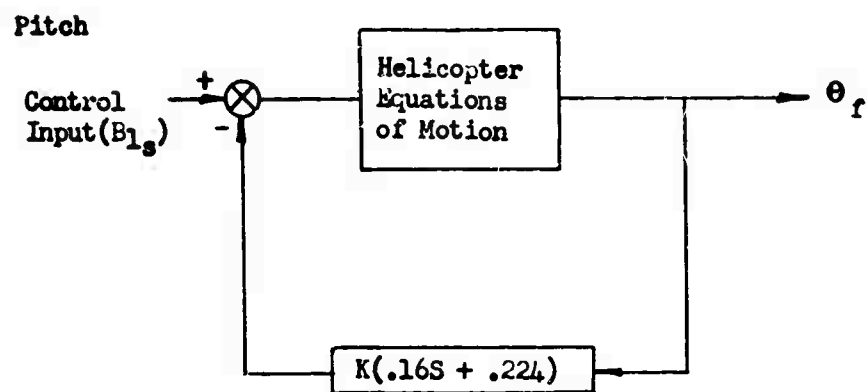


Figure 284 CH-54A AFCS Transfer Functions

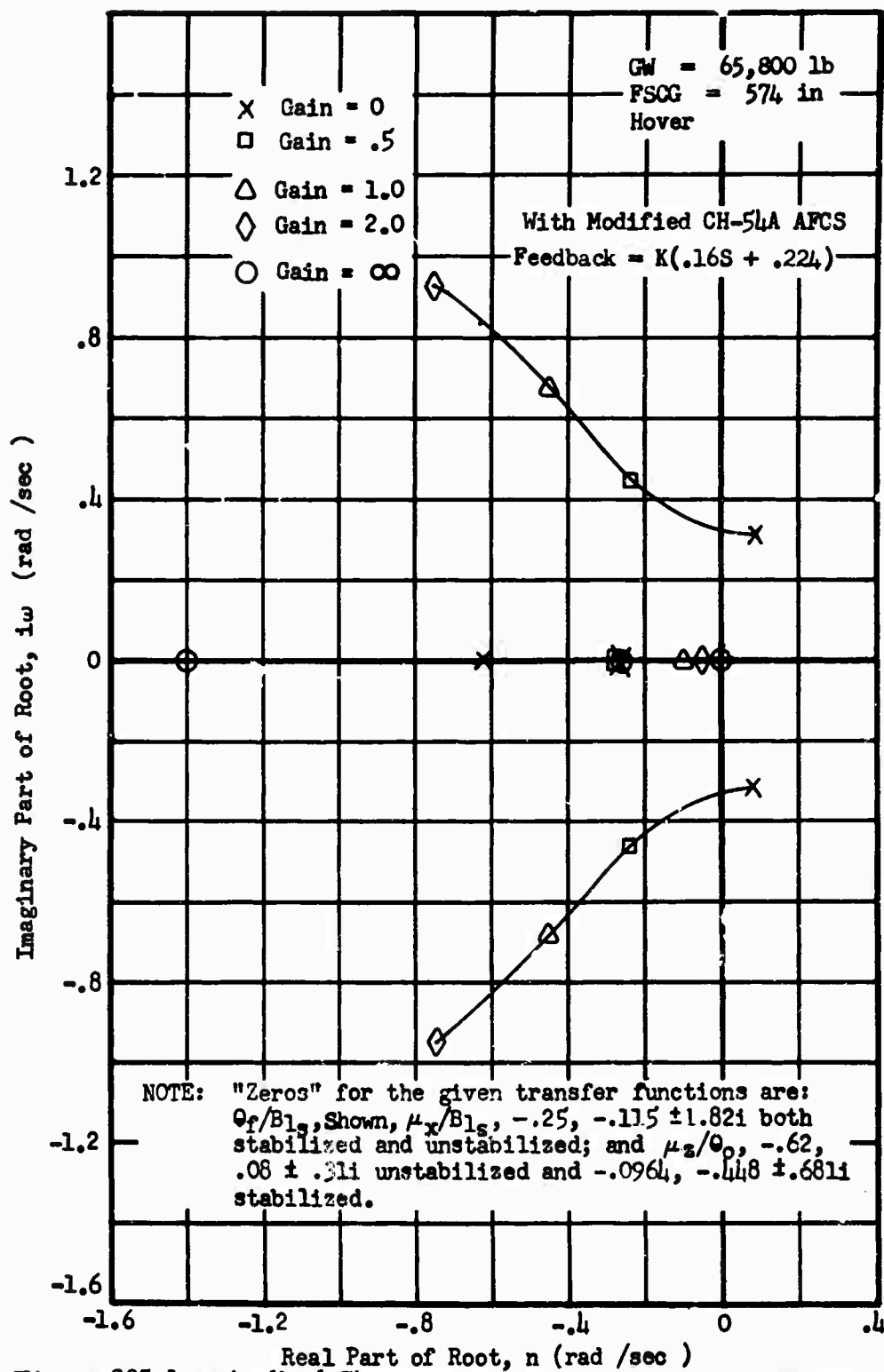


Figure 285 Longitudinal Characteristics, HLH Root Locus Survey, Hover

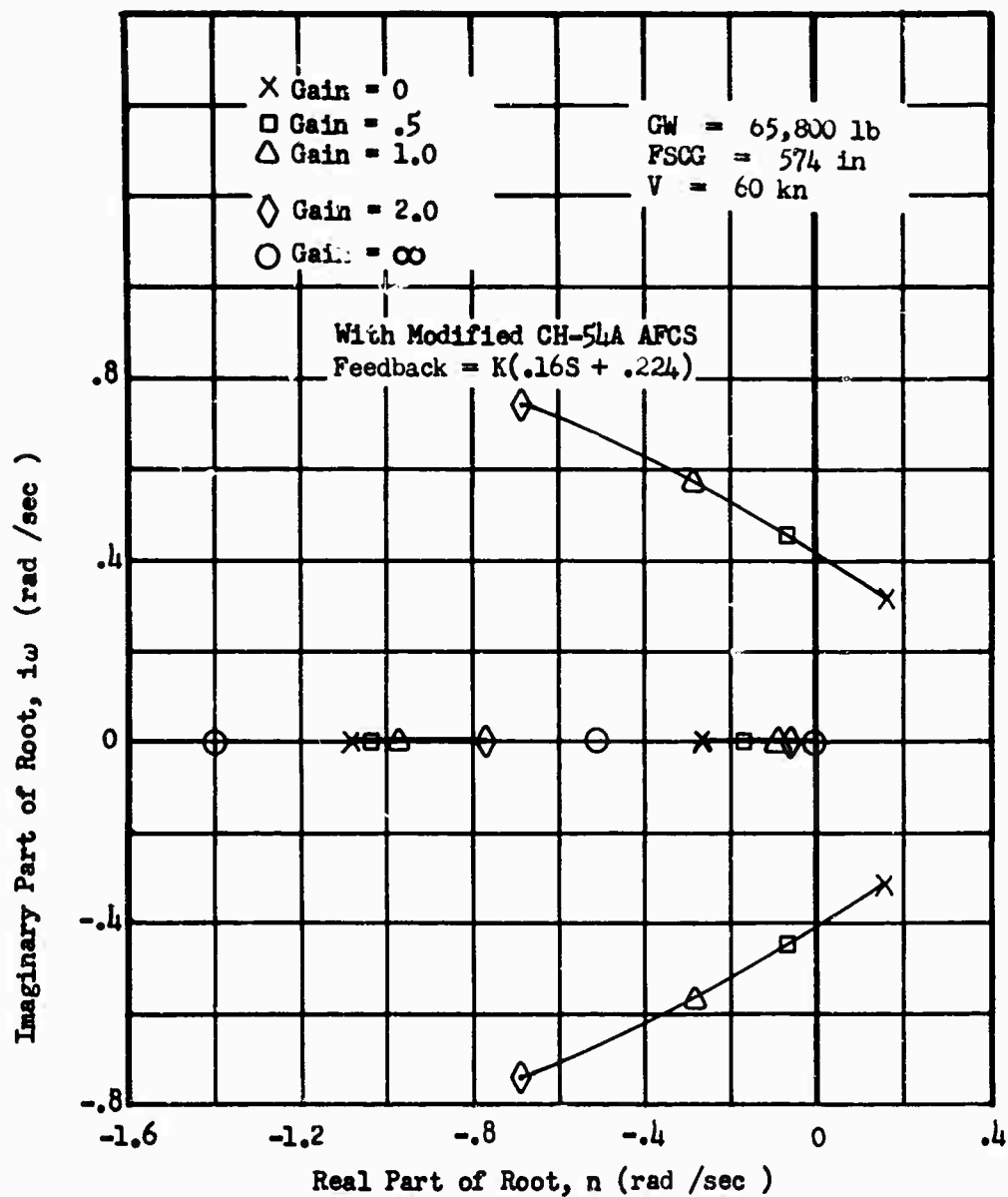


Figure 286
Longitudinal Characteristics, HLH Root Locus Survey, 60 Knots

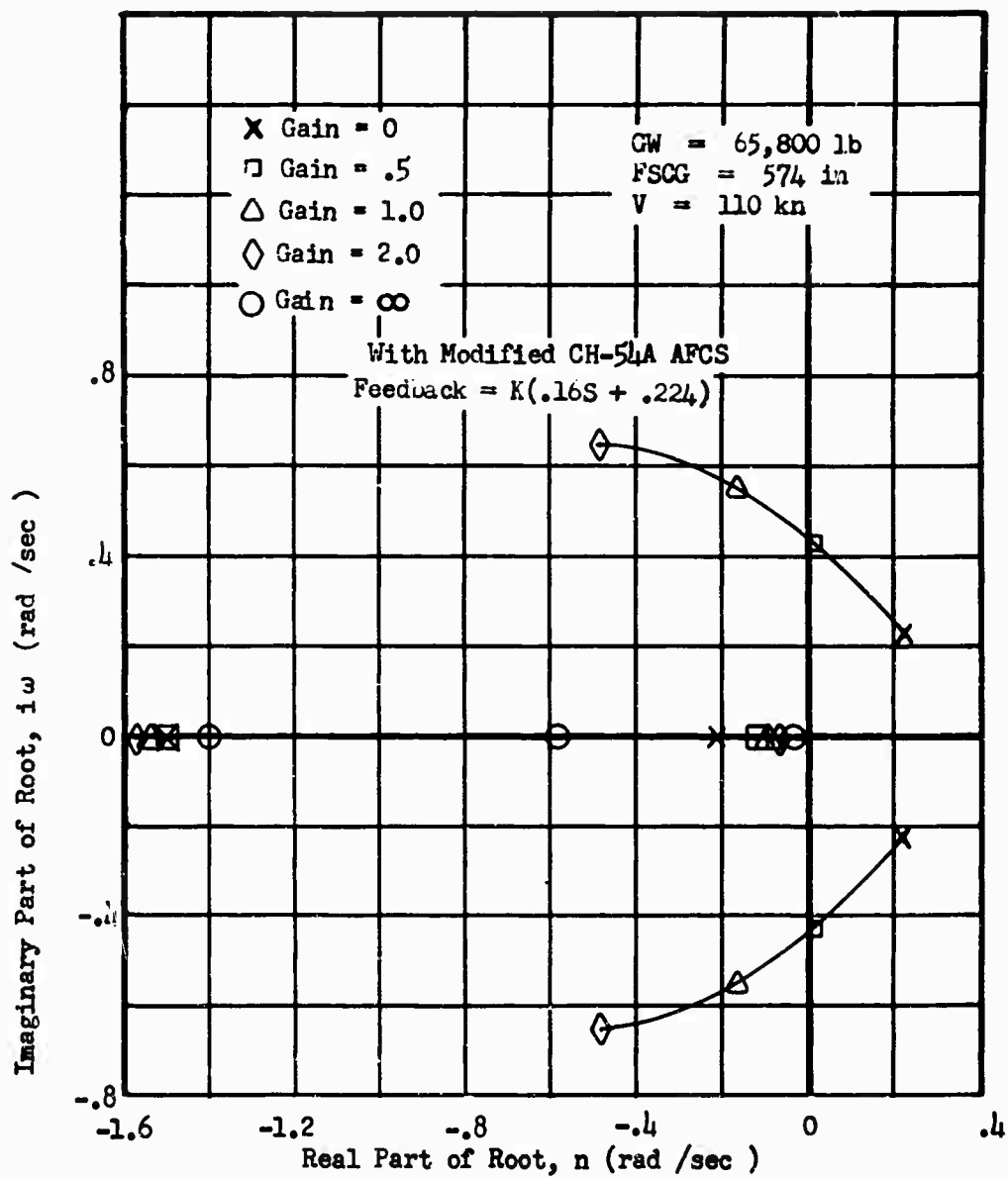


Figure 287
 Longitudinal Characteristics, HLH Root Locus Survey, 110 knots

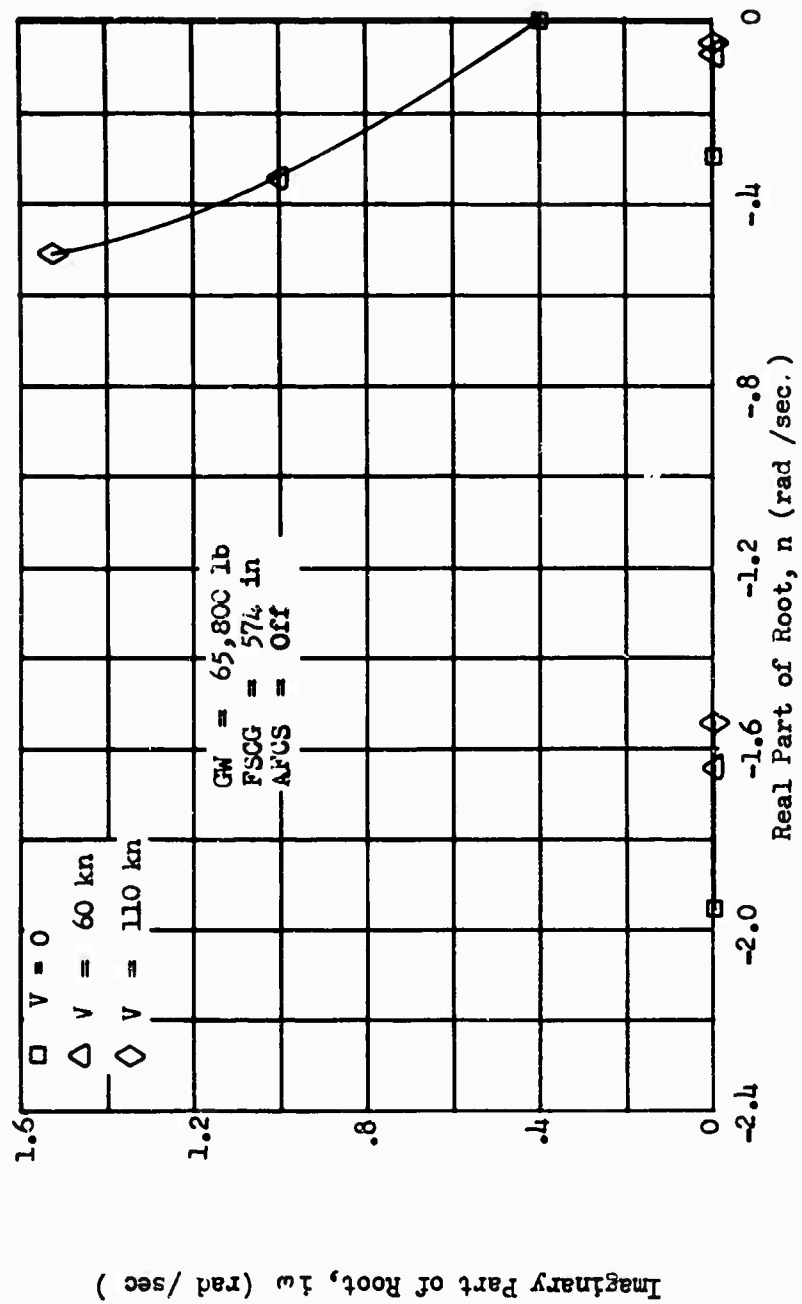


Figure 288 Lateral-Directional Characteristics, HLH Root Locus Survey

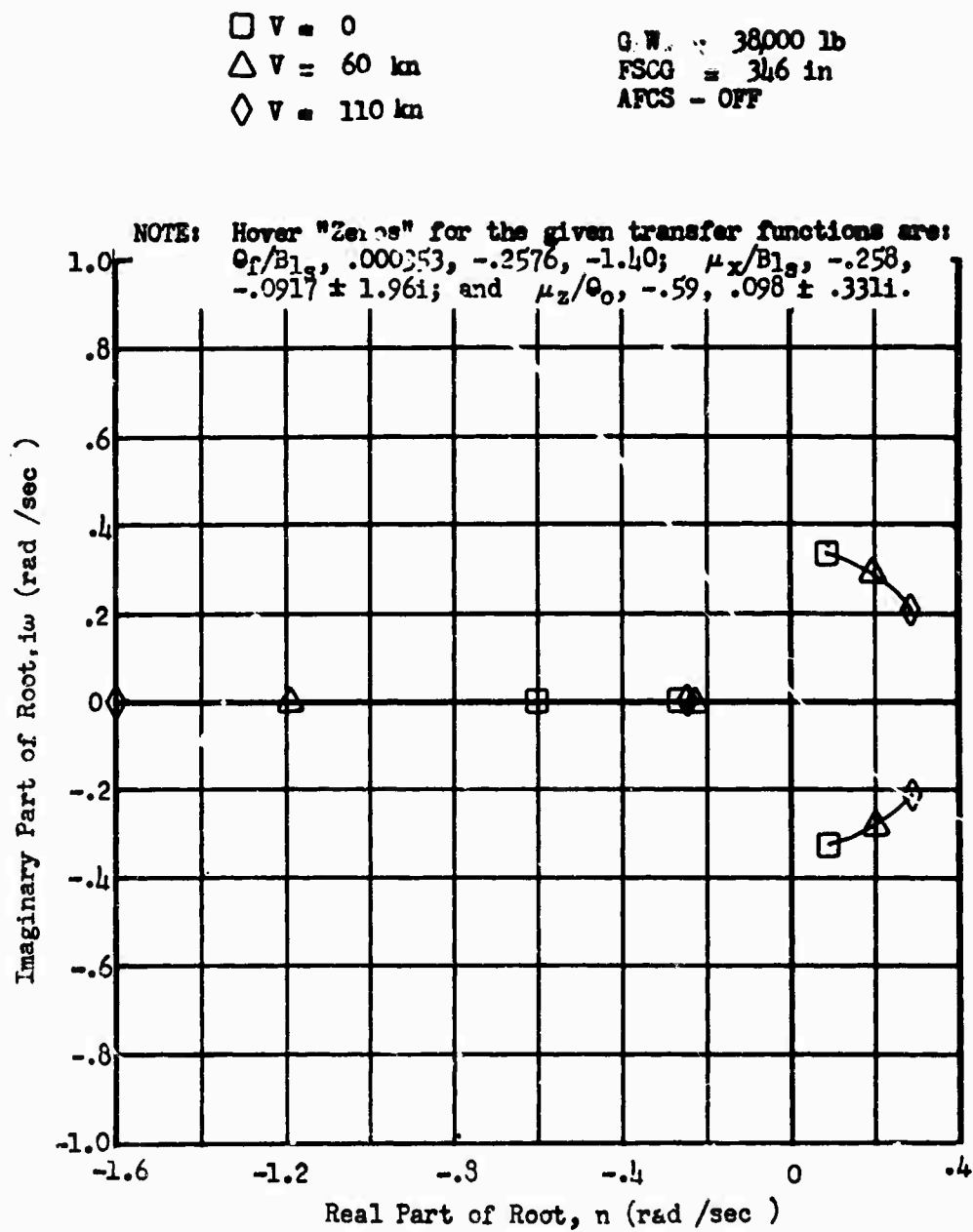


Figure 289 Longitudinal Characteristics, CH-54A Root Locus, AFCS Off

$\square V = 0$
 $\triangle V = 60 \text{ kn}$
 $\diamond V = 110 \text{ kn}$

$GW = 38,000 \text{ lb}$
 $FSCG = 346 \text{ in}$
 $AFCS = \text{On}$

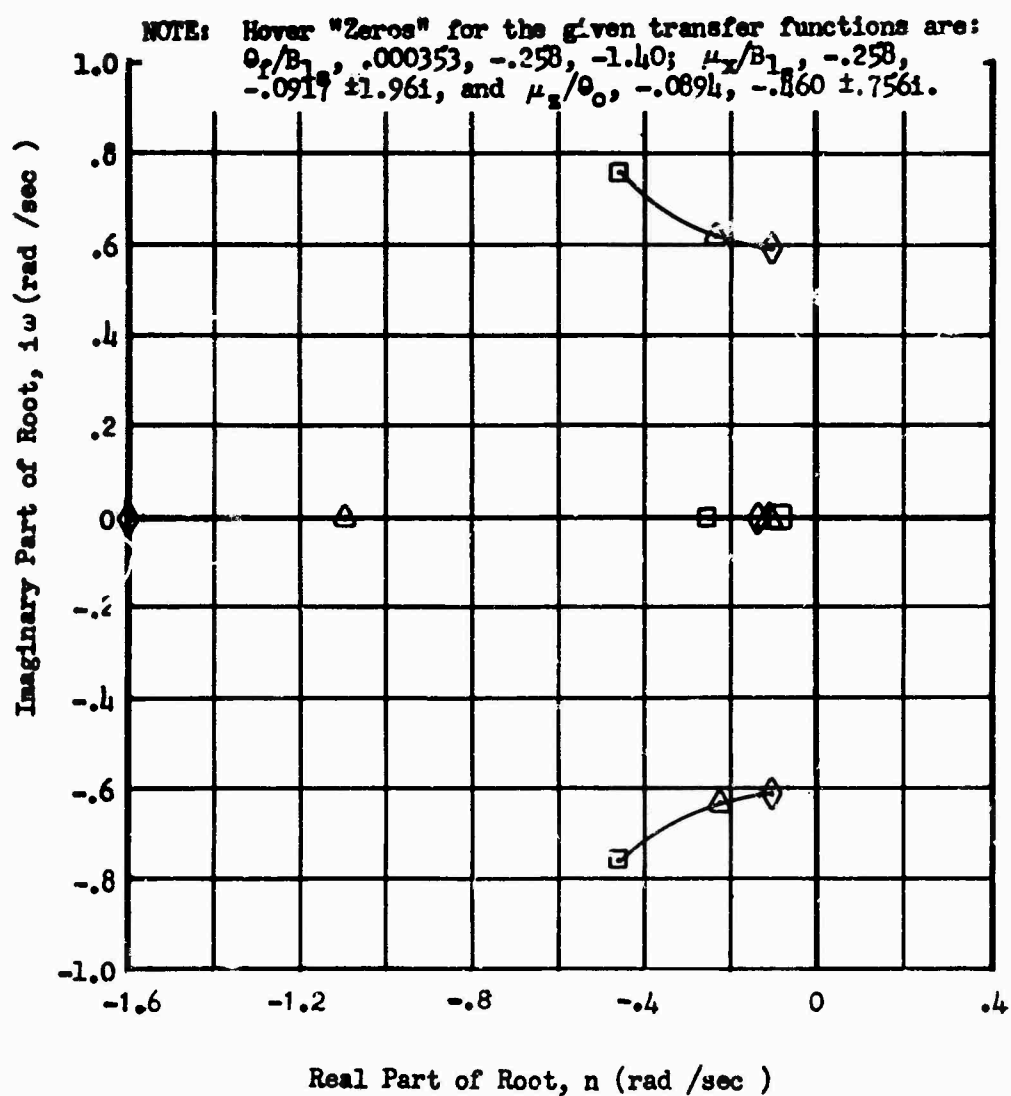


Figure 290 Longitudinal Characteristics, CH-54A Root Locus, AFCS on

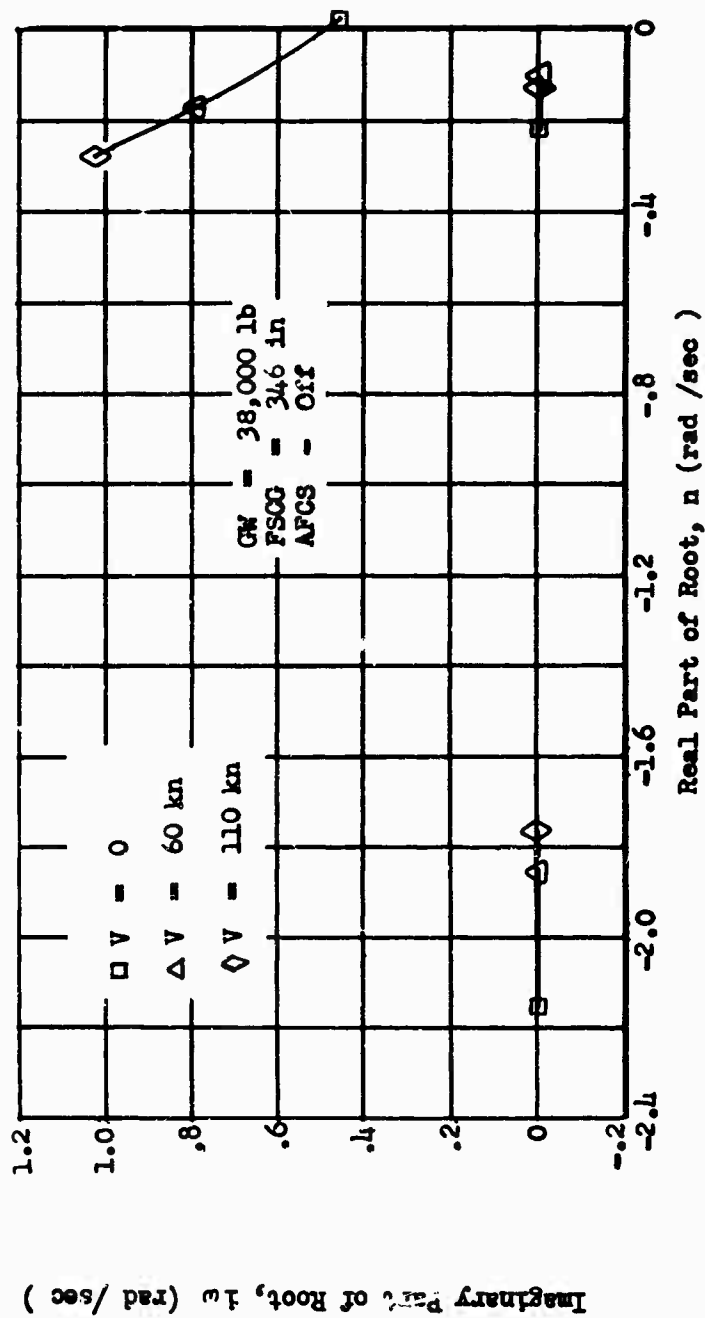
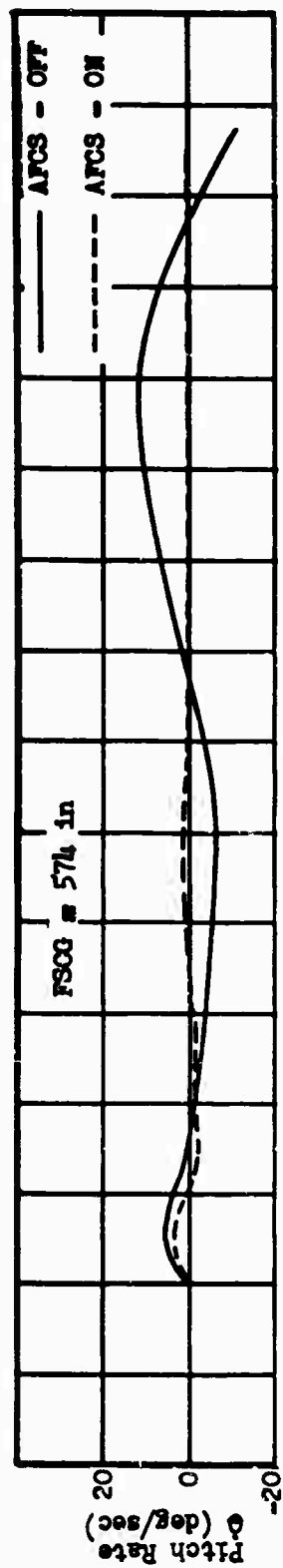


Figure 291 Lateral-Directional Characteristics, CH-54A Root Locus



534

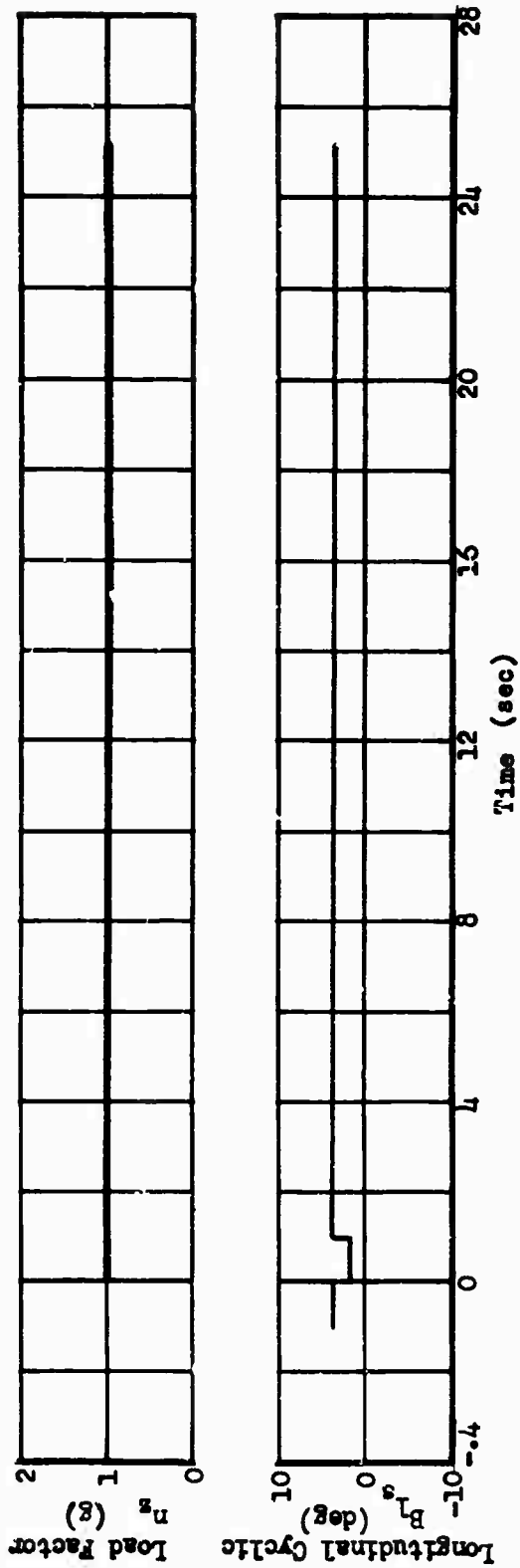


Figure 292 HLH Longitudinal Time History for Pull and Return in Hover

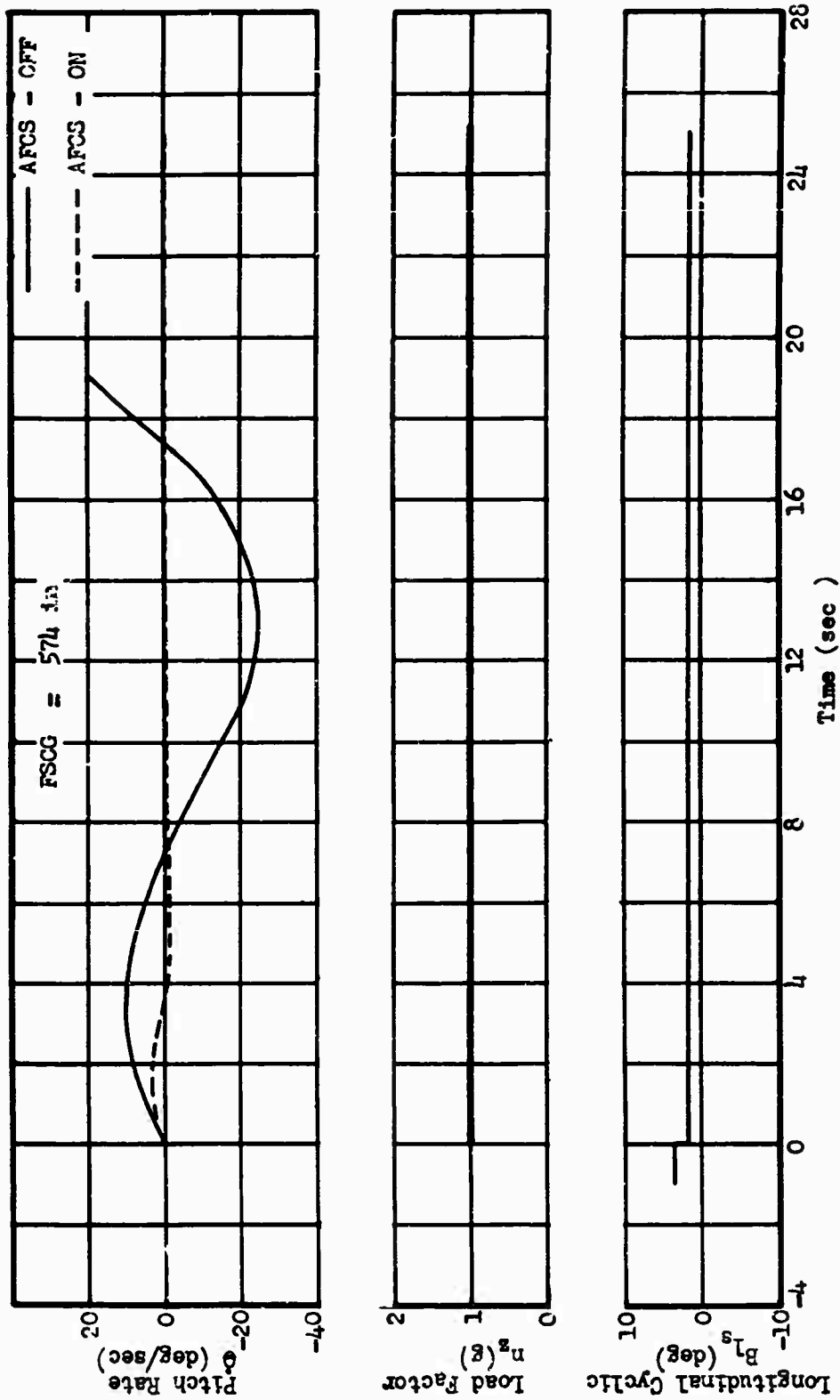


Figure 293 HLH Longitudinal Time History for Pull and Hold in Hover

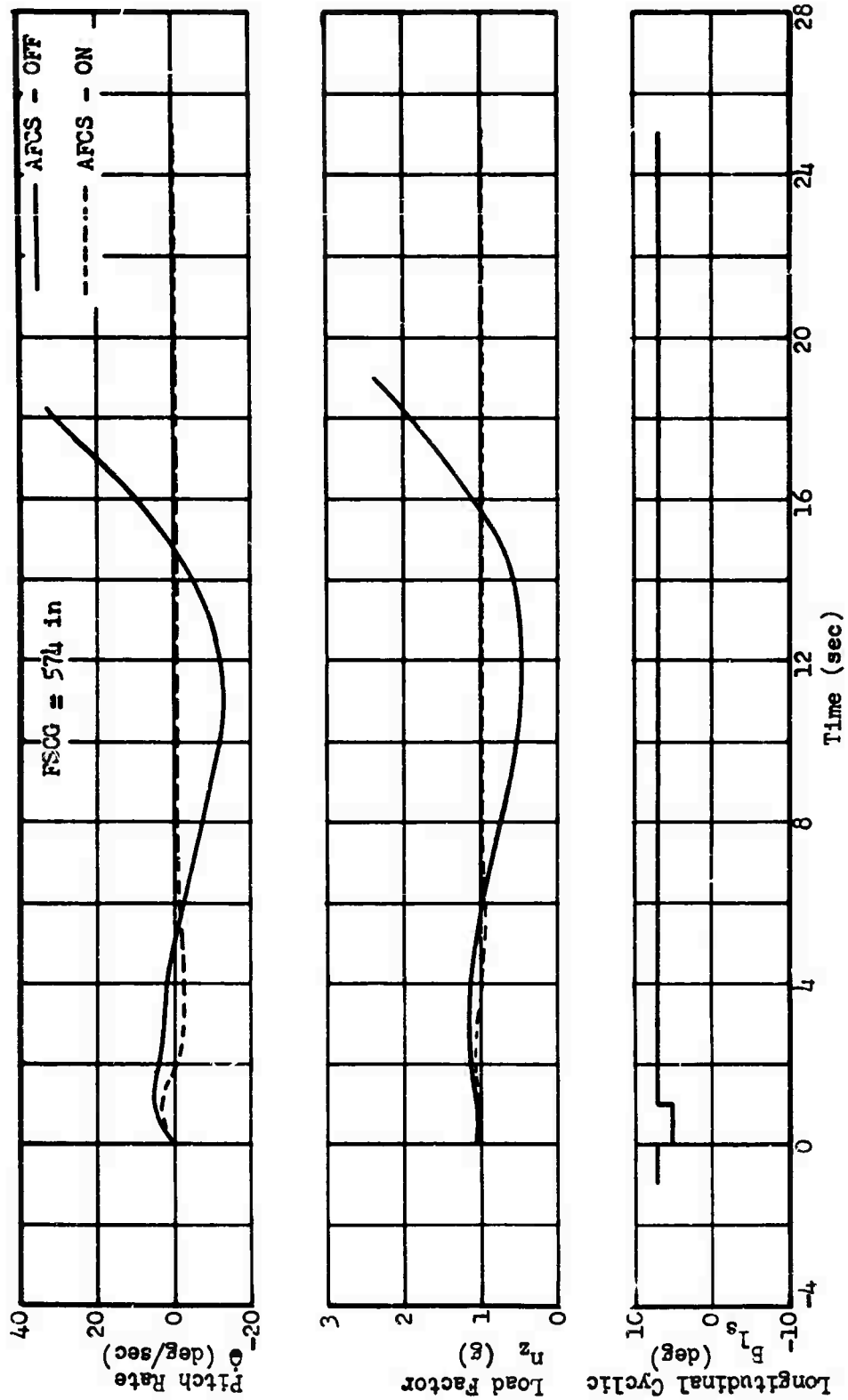


Figure 294 HLH Longitudinal Time History for Pull and Return at 60 Knots

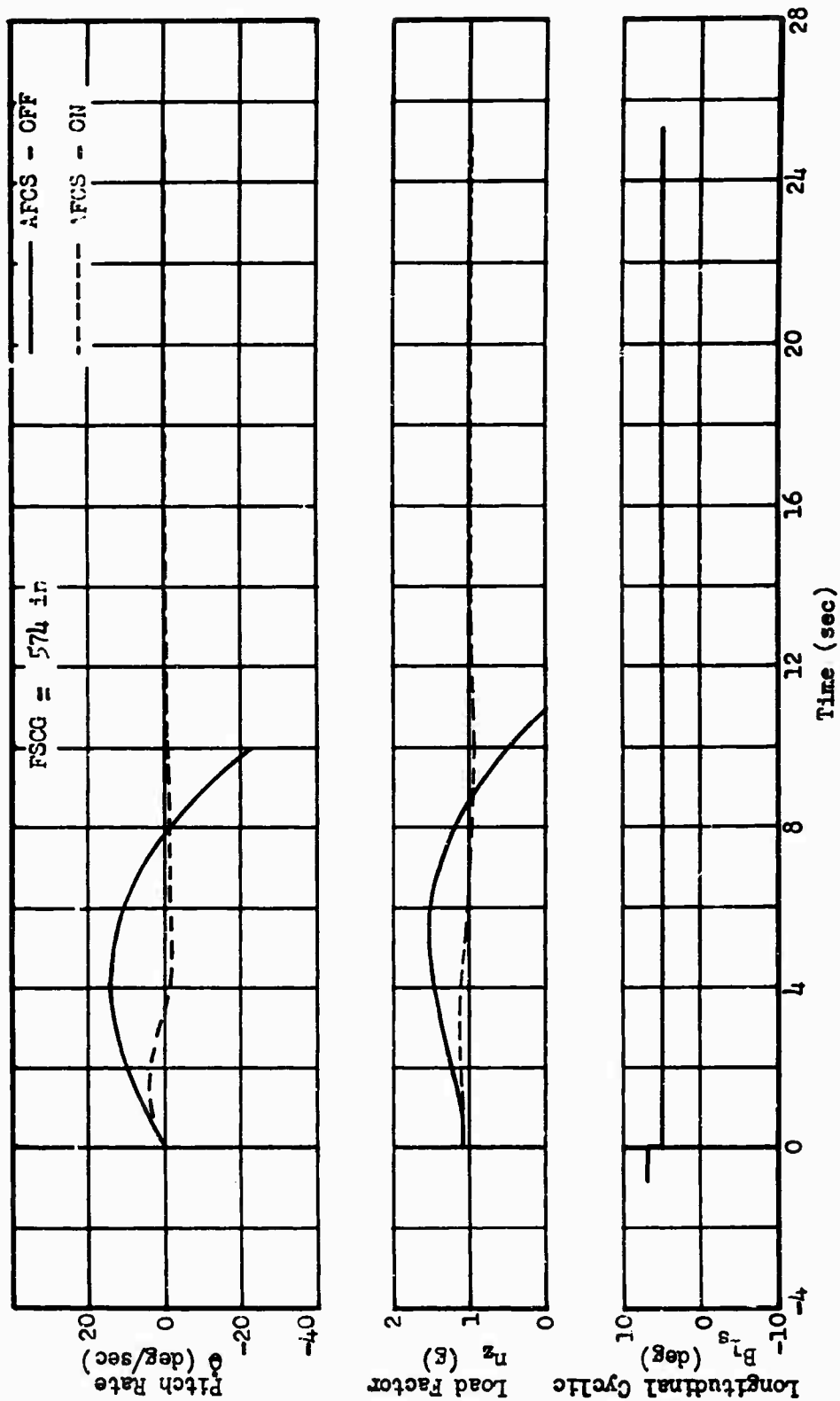


Figure 295 HLH Longitudinal Time History for Pull and Hold at 60 Knots

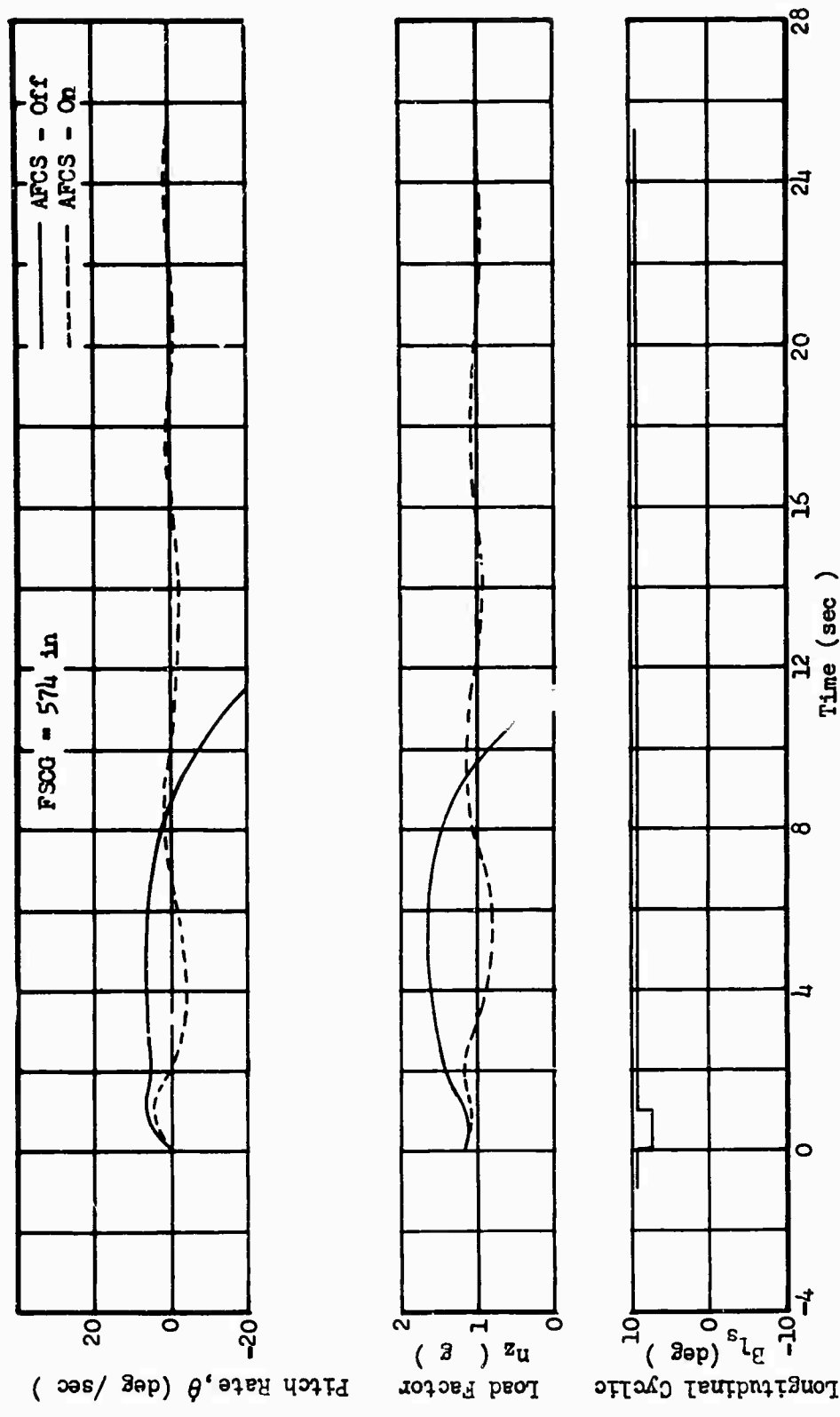


Figure 296 HLH Longitudinal Time History for Pull and Return at 110 Knots

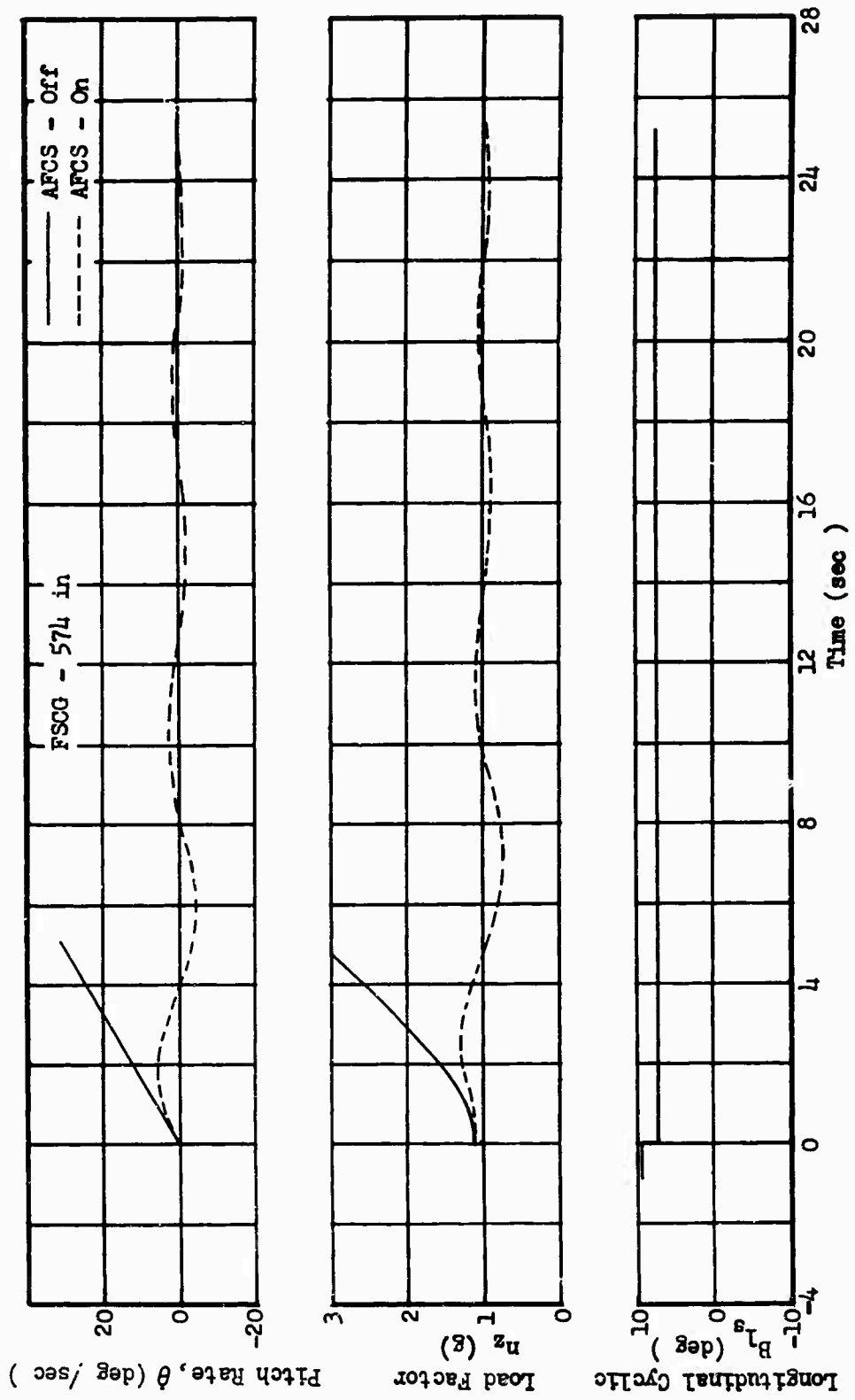


Figure 297 HLH Longitudinal Time History for Pull and Hold at 110 Knots

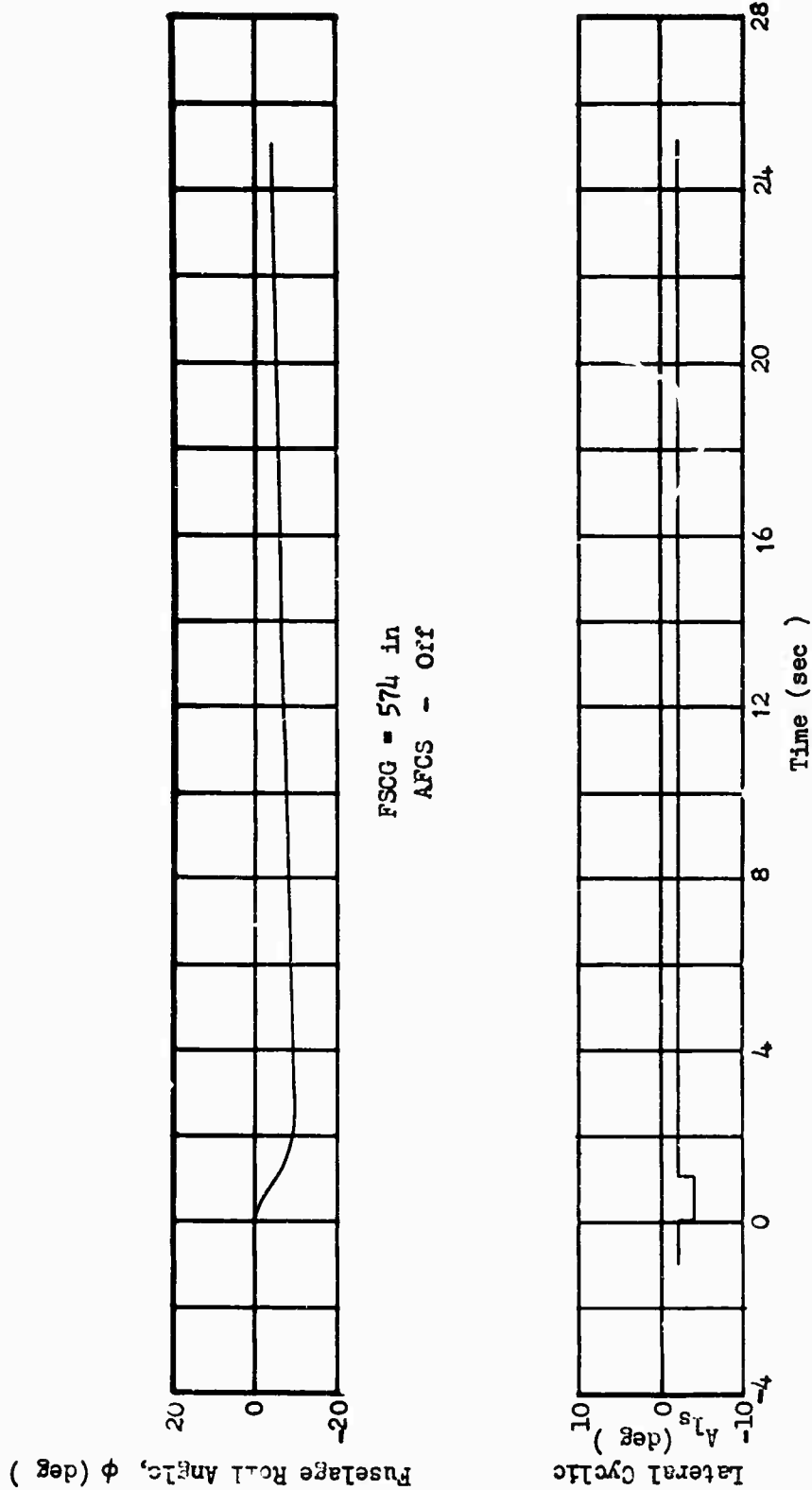


Figure 298 HLH Lateral Time History For Pull and Return at 110 Knots

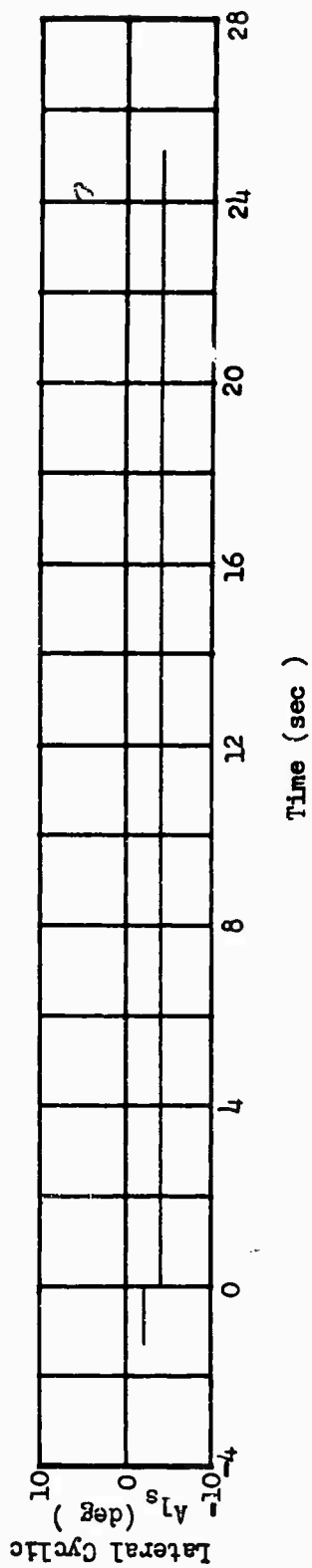
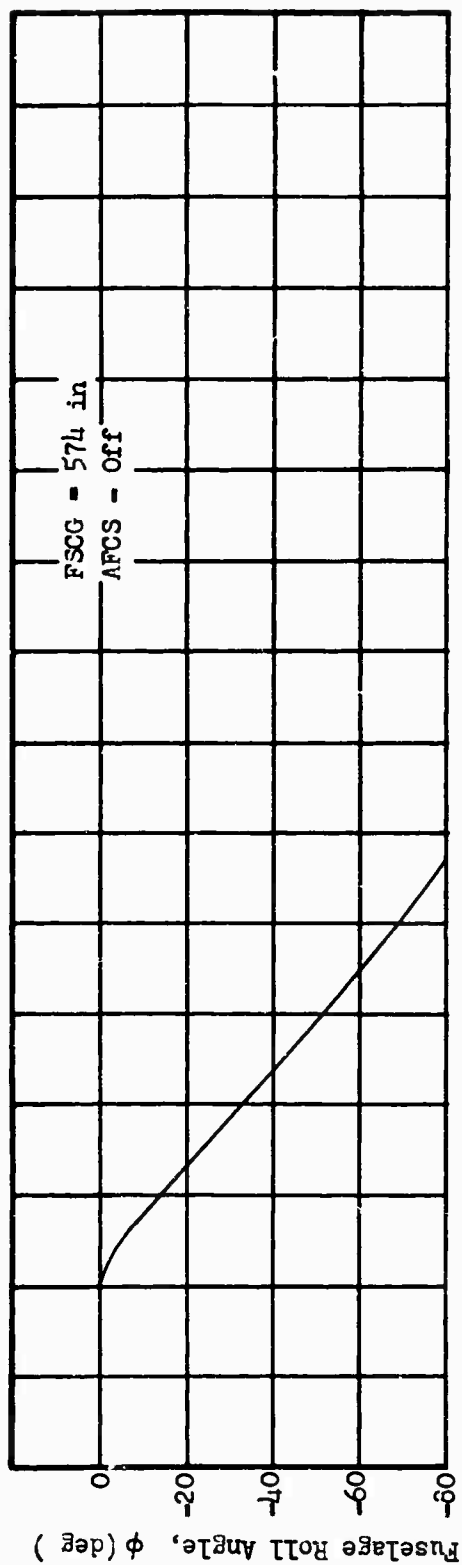


Figure 299 HLH Lateral Time History for Pull and Hold at 110 Knots

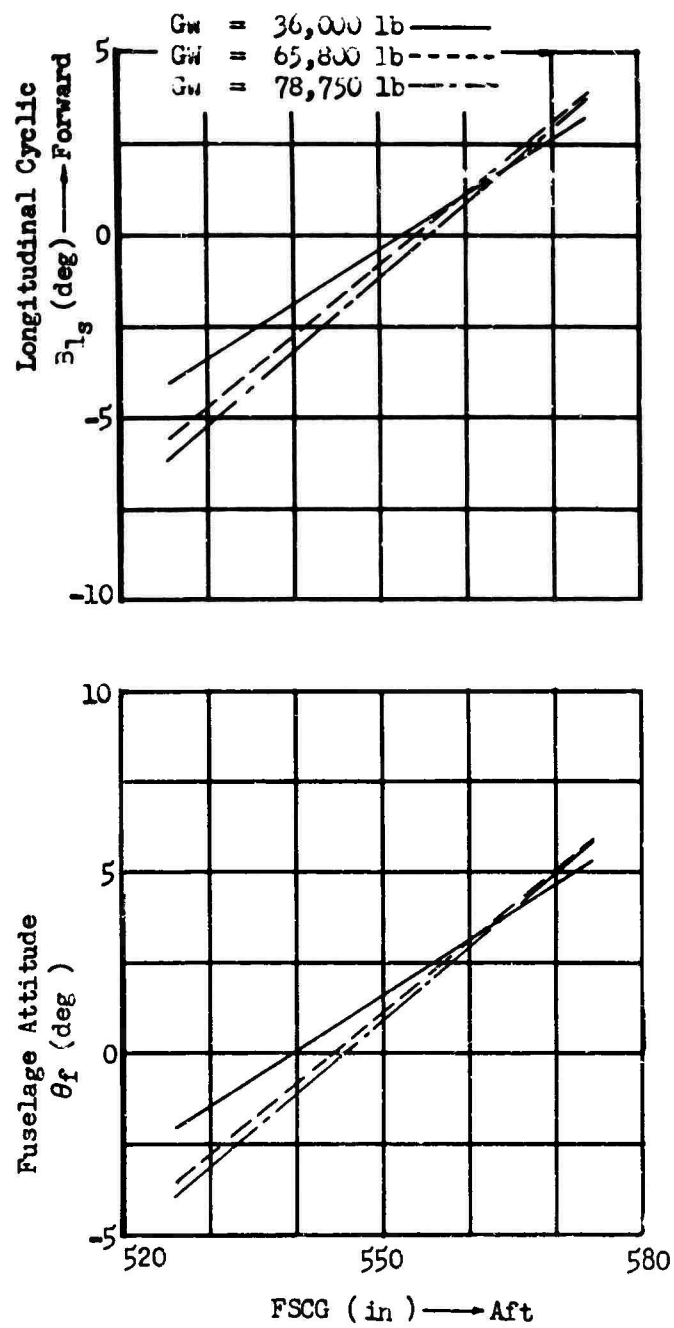


Figure 300 HLH Longitudinal Trim Versus CG Position in Hover

then, must be the effect of size in hovering.

A recent study for the U. S. Army (Reference 27) indicates that even this area will not present a problem. In fact, that report concludes that, assuming the growth factors described therein are followed, "The maximum angular error due to a disturbance decreases with (increasing) size." Slopes were calculated from Reference 27 and drawn through the calculated CH-54A points. Figures 301 and 302 show the "trend" lines of that report. Note that the actual HLH pitch and yaw damping are slightly better than trend lines, while the roll damping is right on the trend line.

Since the trend lines have been followed within reason, the conclusions of Reference 27 should also hold. That is, increases in vehicle inertia yield increases in the vehicle characteristic time, and this increase allows more time for a pilot to assess and correct deviations from the desired point. Maintenance of constant ratios of control power and damping to inertia are not necessary. In practice, Reference 27 indicates that the resulting angular displacement is the significant factor, being the quantity which the pilot must control. and this is essentially constant with size.

A recent paper on handling qualities of flying cranes (Reference 9) pointed out that the translational degrees of freedom are of significant interest in crane operation. Most hovering tasks for a crane require positioning of a load on a spot on the ground. Ideally, the crane should maneuver in the x and y directions without attitude changes. It is shown that cyclic pitch control allows this type of maneuver; and in the limit, a zero offset plus location of the CG at the rotor head would yield no attitude changes during hover translational maneuvers. The HLH configuration, like the CH-54A, uses low rotor offset and high hard points for loads, thus approaching the ideal case without losing the desirable attitude retention that offset affords with CG variation. Figure 303 is a plot of amplitude ratio versus frequency for longitudinal translation of the HLH, using the method of Reference 9. The conclusions reached therein, which point out the desirability of cyclic pitch for the hovering task, are again implied, and the total amplitude ratios for the HLH appear adequate in comparison with the curve for the CH-54A. At lower frequencies, the fuselage attitude contribution to translation is less for the HLH, a desirable feature in a crane. Note also that the frequency limitation due to blade degree of freedom in Reference 9 was shown at .52 times the CH-54A rotor frequency. Above this frequency, the analysis of that report would have had to include the blade degree of freedom. Using the same factor for the HLH, only a small reduction in upper frequency was imposed on the analysis. Assuming the 140-foot "maximum radius" rotor of Reference 27, the resulting amplitude ratio would apparently become very highly attitude - oriented within the analytical boundaries.

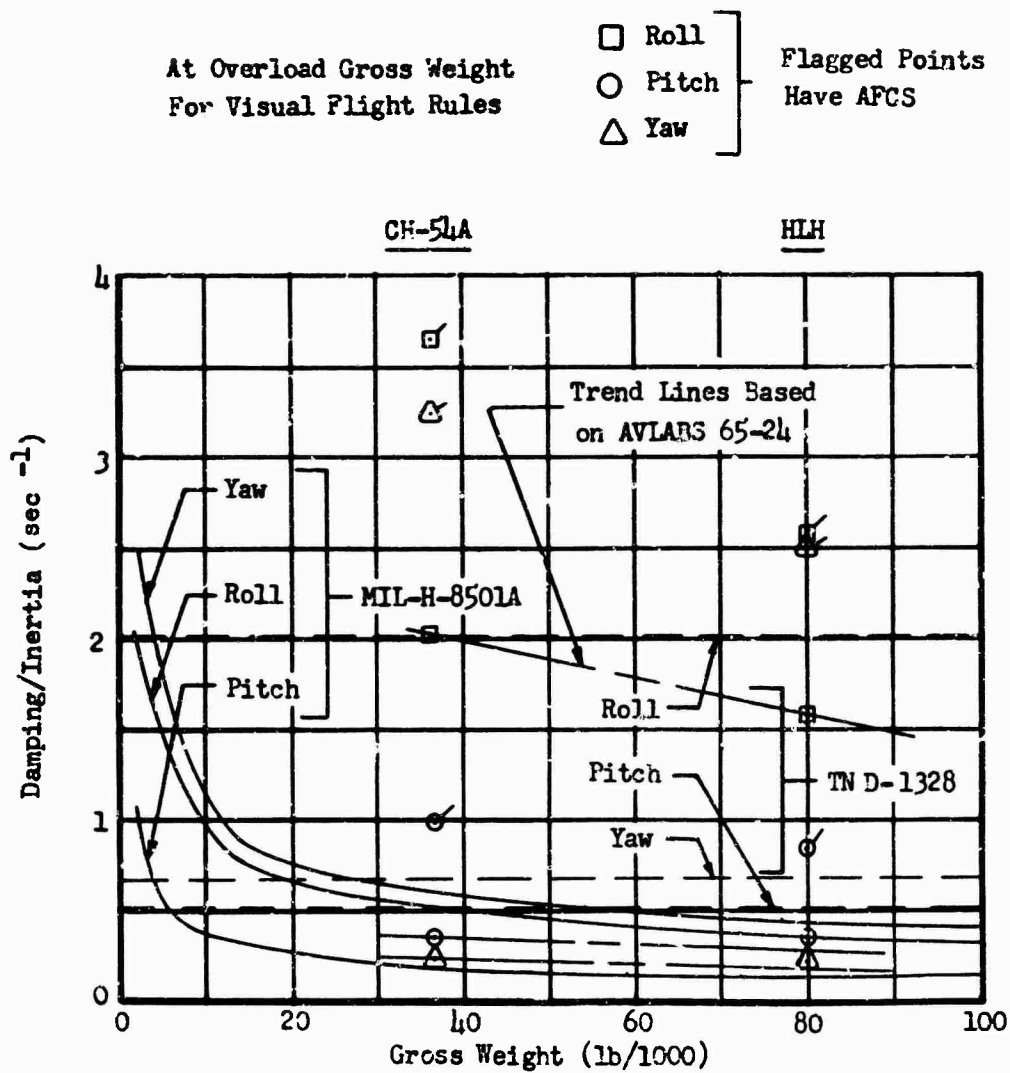


Figure 301 Comparison of Damping/Inertia

At Overload Gross Weight
For Visual Flight Rules

□ Roll
○ Pitch
△ Yaw

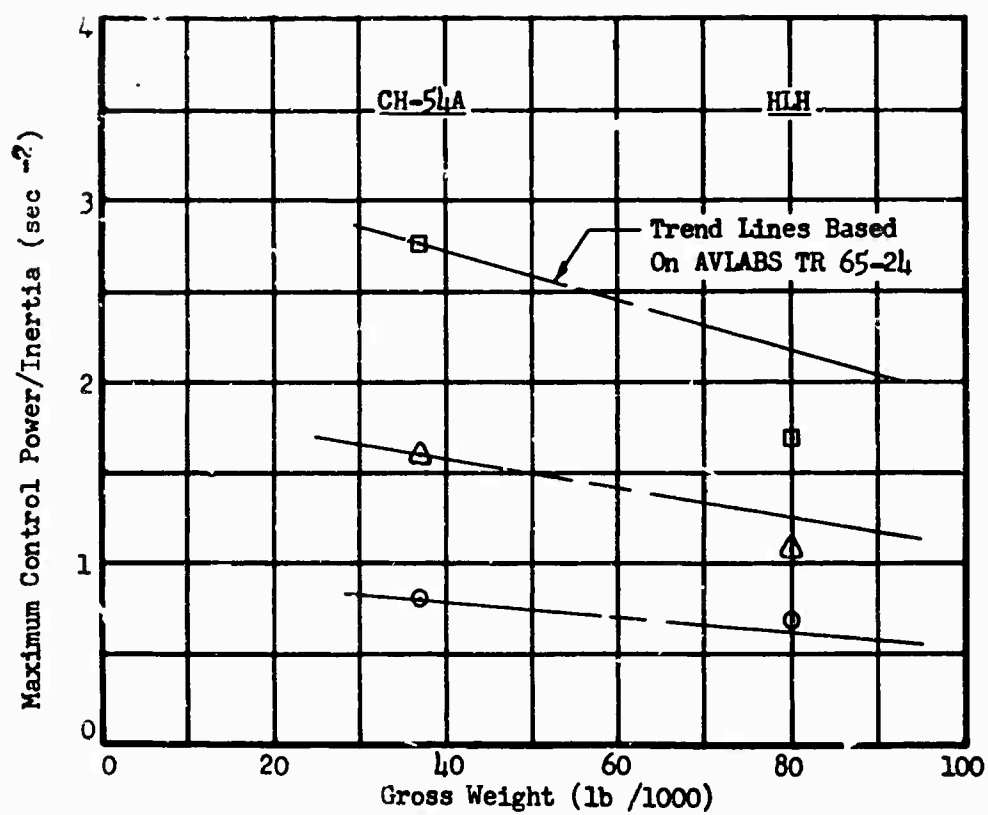


Figure 302 Comparison of Control Power/Inertia

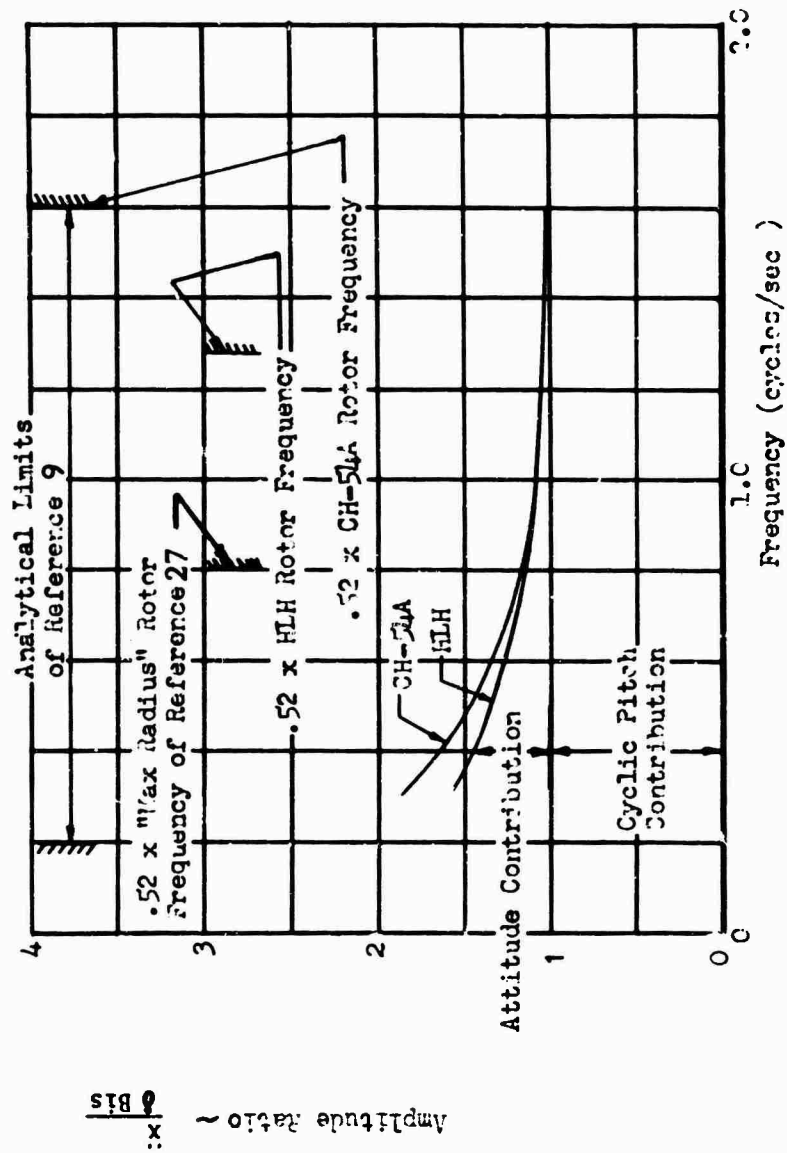


Figure 303 Comparison of Amplitude Ratio and Frequency for HLH and CH-54A in Fore and Aft Translation

Another interesting dynamic phenomenon associated with large aircraft involves linear accelerations at the pilot's seat. It is believed that among the cues which reach the pilot in attitude control is the effect of angular pitch acceleration on the vertical acceleration at his position. For the same angular acceleration, the HLH forward facing pilot will receive 1.82 times the vertical acceleration of the CH-54A pilot. Similarly, the aft-facing pilot will receive 1.65 times the vertical acceleration of his counterpart. The probable result of this added cue could be better attitude control plus a tendency to keep control inputs to a minimum. The roll situation is reversed, however, since the pilot in the aft-facing seat is below the principal axis of roll. This acceleration cue could conceivably cause control reversal. A comparison of flight experience of the experimental S-60 crane with the CH-54A (Reference 9) showed that the problem was less critical in the latter even though the relative position of the pilot should have been more critical. The conclusion reached therein is that visual reference was probably more important in roll control, a factor which had been greatly improved in the CH-54A. The improved visibility plus useful fuselage references, such as wide main landing gear, of the CH-54A have been carried over in the HLH.

AUTOMATIC FLIGHT CONTROL SYSTEM

As previously stated, the CH-54A automatic flight control system, or AFCS, has been shown to be suitable for the HLH. Improvements in the state of the art since the design of the CH-54A, including many of the features developed for the newer CH-53A system, will be incorporated into the AFCS for the HLH. While quantitative definition of the HLH system parameters has not been undertaken in this study, the system can be generally described with considerable accuracy.

The AFCS operates through a set of electro-hydraulic servos to provide stabilizing inputs to the aircraft flight control system. Attitude hold is provided by redundant pitch and roll channels while heading is maintained by a nonredundant yaw channel. Either of two modes of altitude retention, barometric or radar, may be selected at the pilot's discretion to supplement the pitch, roll and yaw stabilization.

All four channels have limited authority (inner loop) control, characterized by small AFCS servo outputs which provide stabilizing corrections without moving the pilot's flight controls. The roll, yaw, and altitude channels have, in addition, rate limited (outer loop) control characterized by stick or pedal motion for larger corrections. The outer loop, which operates through the stick trim amplifier in altitude and with an open loop spring in yaw, is responsible for the elimination of steady-state errors by virtue of the integral nature of its control. The roll outer loop

system, which also operates through the stick trim amplifier, provides for the extension of system control beyond the limited authority of the roll inner loop but in a proportional manner.

Engagement of the AFCS servos is effected by means of switches located on the AFCS control panel. Pitch and roll AFCS servos are engaged simultaneously, provision being made, however, for engaging either the number 1 or number 2 servos. The nonredundant yaw and altitude servos are also switched on and off simultaneously with a single switch on the control panel. Engagement of any combination of AFCS servos facilitates manual control of the aircraft (without AFCS) by the addition of hydraulic boost between the pilot's controls and the primary flight servos.

By engaging the appropriate pitch and roll AFCS and servo switches (see Figure 304), either number 1 or number 2 pitch and roll AFCS electronics can be channeled to its respective number 1 or number 2 pitch and roll servos. The aircraft is normally flown in the "ON-ON" configuration, i. e., all switches of Figure 304 are closed.

When engaged, the pitch channel uses the vertical gyro as a reference, deriving both proportional and rate signals from its output (see Figure 305). The one additional dynamic input to the pitch channel is the pitch stick position sensor, which establishes the reference point about which the AFCS operates. Dual CG trims are provided to allow compensation for aircraft loadings.

The roll channel (see Figure 306) derives its proportional signal from the vertical gyro, but due to aircraft roll response characteristics this channel utilizes a rate gyro for damping. The requirement for large bank angles predicates the use of a roll gyro synchronizer to null the gyro signal while a bank angle is being commanded if stick trim release or beeper trim is utilized. When the desired bank angle is established, deviations from that angle are passed through the synchronizer to the AFCS. Because the rate gyro output is not synchronized during bank angle commands, the aircraft responds as a rate damped system. That is, the stick returns to its original position after the establishment of a bank angle, while the aircraft displays well damped response characteristics. The outer loop system is employed here to extend the AFCS authority by repositioning the stick as a function of roll attitude and to allow banks initiated against the stick trim for automatic return to trim upon stick release by the pilot.

The yaw channel may be engaged with any selected mode of pitch and roll stabilization by engaging the yaw/altitude AFCS in addition to yaw/altitude servos (see Figure 307). Operation of the yaw channel includes the use

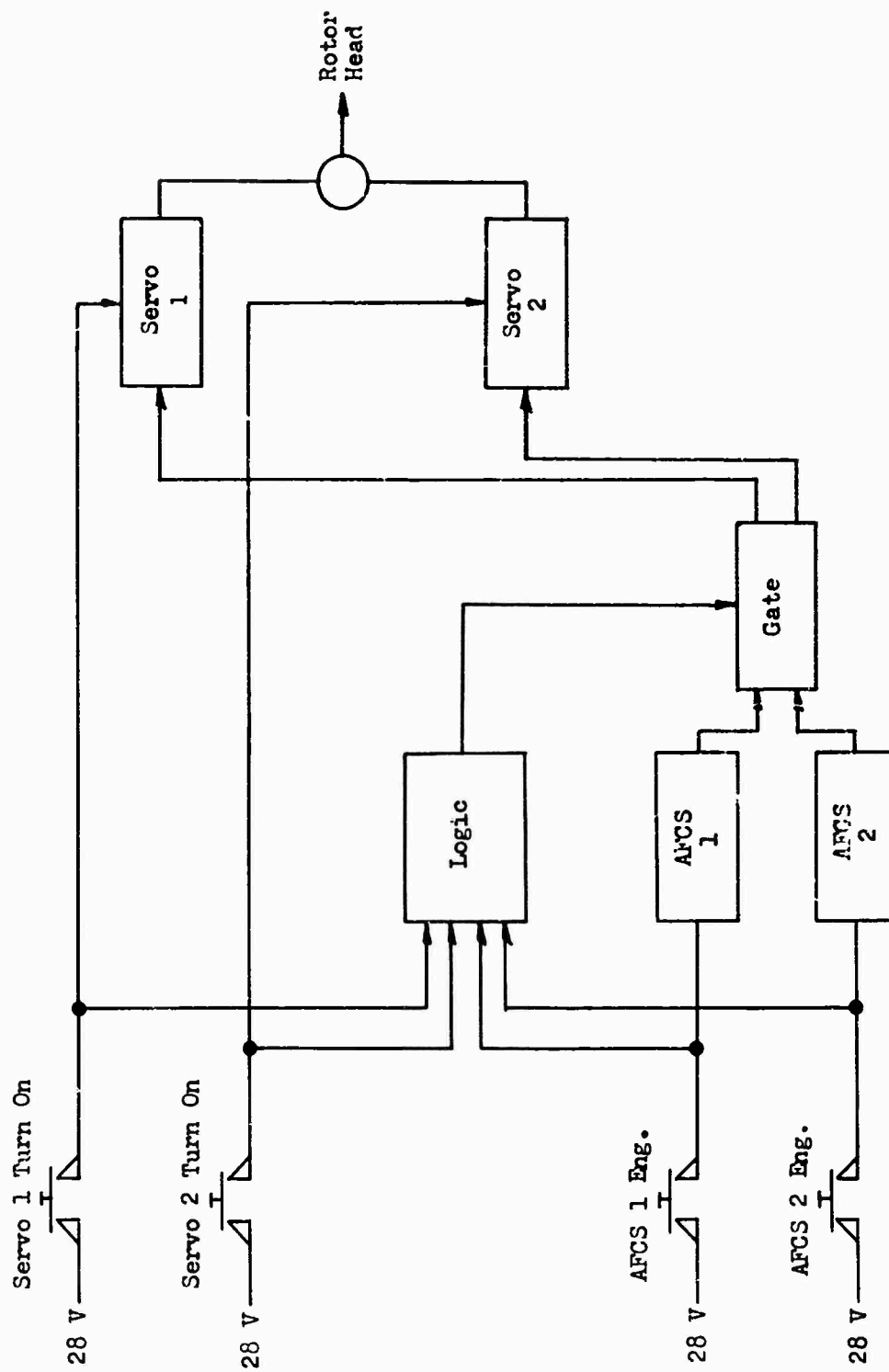


Figure 304 Pitch and Roll Switching

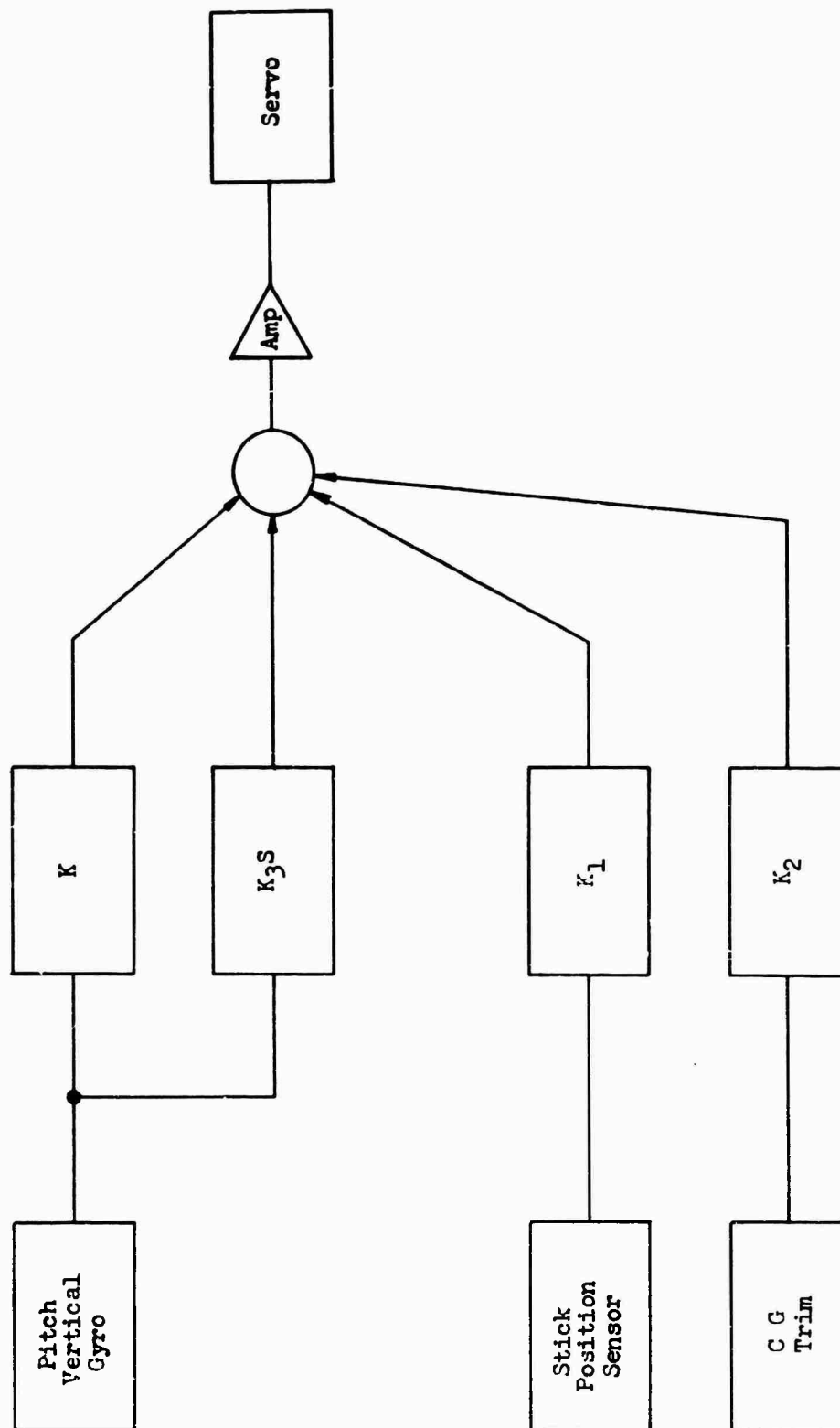


Figure 305 Pitch Channel Block Diagram

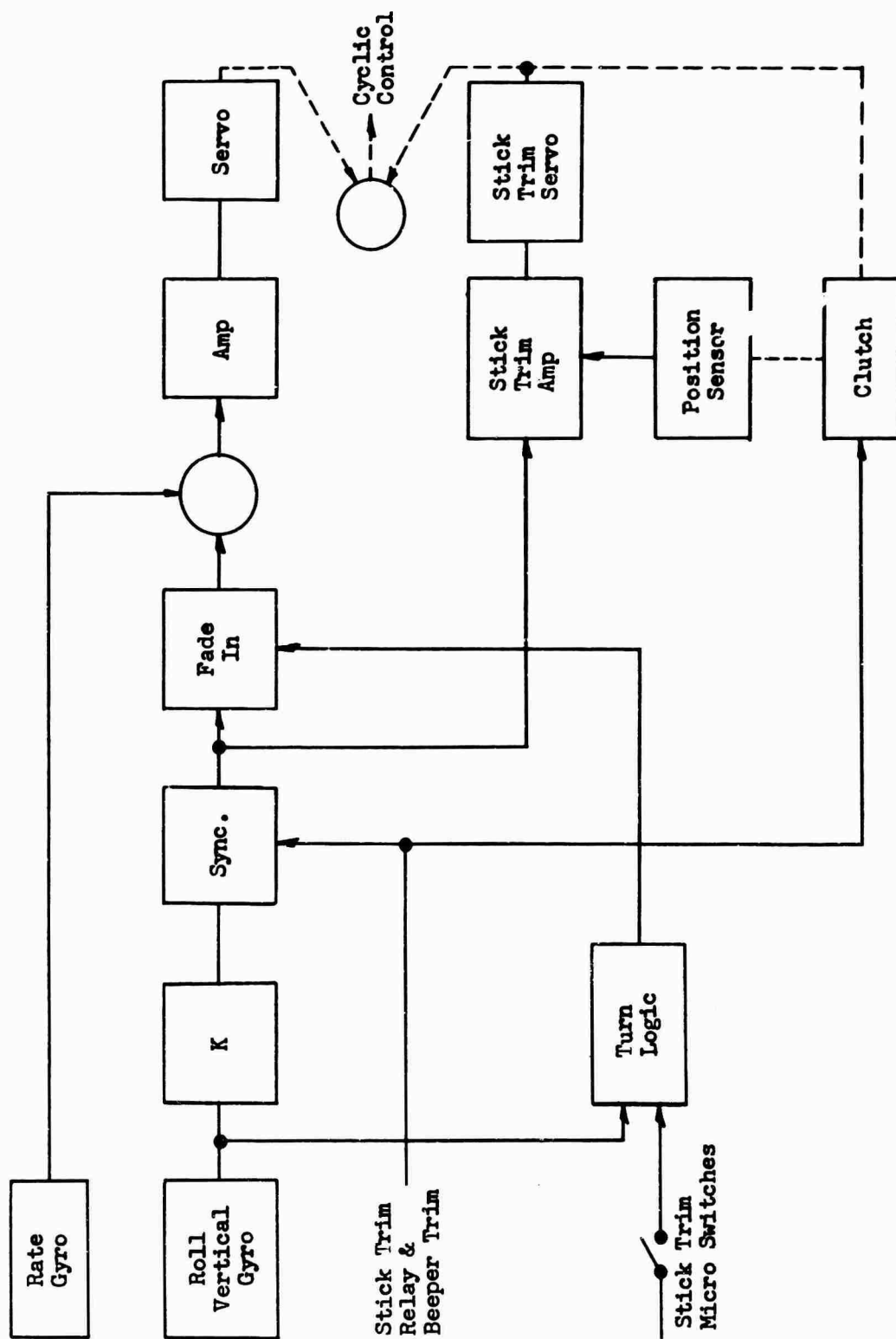


Figure 306 Roll Channel Block Diagram

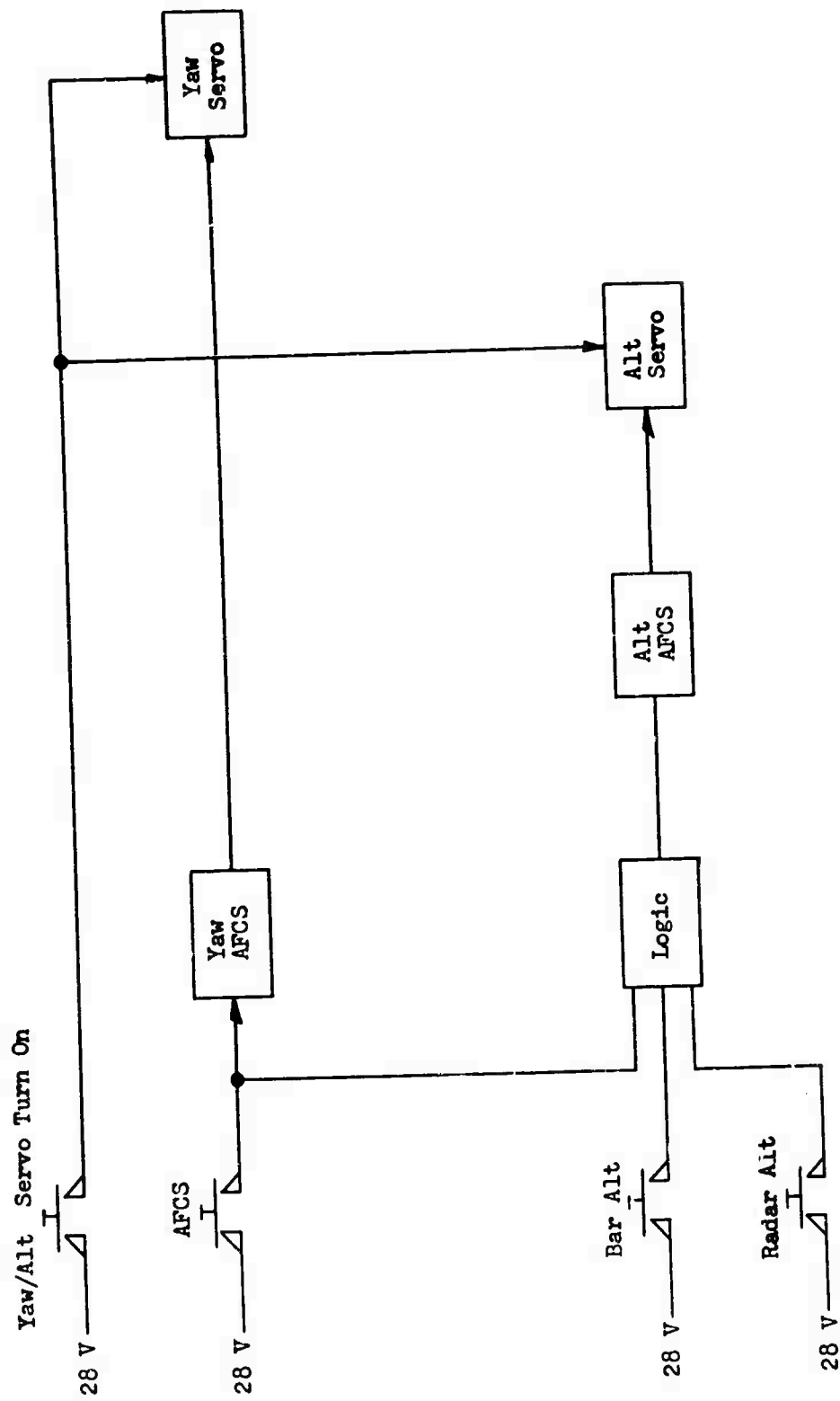


Figure 307 Yaw/Altitude Switching

of a pedal switch activated synchronizer to enable the pilot to change his heading reference merely by putting his feet on the pedals. The heading reference is provided by the compass system, while rate damping is provided by a rate gyro.

In addition to the normal pitch, roll, and yaw model of stabilization, an automatic coordinated turn mode is provided (refer to Figures 306 and 308). The coordinated turn circuitry utilizes an accelerometer and roll rate gyro to sense lateral acceleration and roll rate, both of which are necessary inputs to the yaw channel during the coordinated turn mode of operation. With an airspeed greater than 60 knots, initiation of an automatic coordinated turn by a commanded roll attitude and one or more energized pedal switches gates both roll rate gyro and lateral accelerometer signals to the yaw channel while synchronizing the directional gyro signal. A rate of turn is then commanded and increased until the lateral accelerometer output is zero, at which point the turn is coordinated.

The altitude retention capability of the aircraft provides two modes of altitude hold (see Figure 309), either of which may be energized when the yaw/altitude servo and electronics are engaged. Barometric altitude hold utilizes a barometric controller as an input to both inner and outer loops of control, the altitude reference being that at engagement. The barometric altitude hold may be disengaged, when desired, by energizing the collective trim release trigger on the collective stick or by depressing a button on the AFCS control panel.

The radar altitude mode permits the selection of an altitude reference by means of a dial on the AFCS control panel. The engagement of the radar mode automatically disengages the barometric altitude mode. Disengagement of the radar altitude mode may be effected by means of a radar altitude off button on the collective stick which, if energized, automatically reengages the entire collective channel as in the barometric altitude mode.

COMPLIANCE WITH MIL-H-8501-A

This section presents a comparison of the Sikorsky HLH to the MIL-H-8501-A (Reference 4) requirement. Paragraphs are numbered to correspond with the reference. The data presented are for hover and forward flight. Fuselage aerodynamic data were estimated using wind tunnel data for the CH-54A and reflected the expected improvement in pitching moment due to a greater tail volume coefficient. Figures 257 through 264 present the estimated data and comparable CH-54A data. Trim characteristics with various CG's and gross weights, plus root loci for the critical aft CG, are presented. Table LXI contains control system

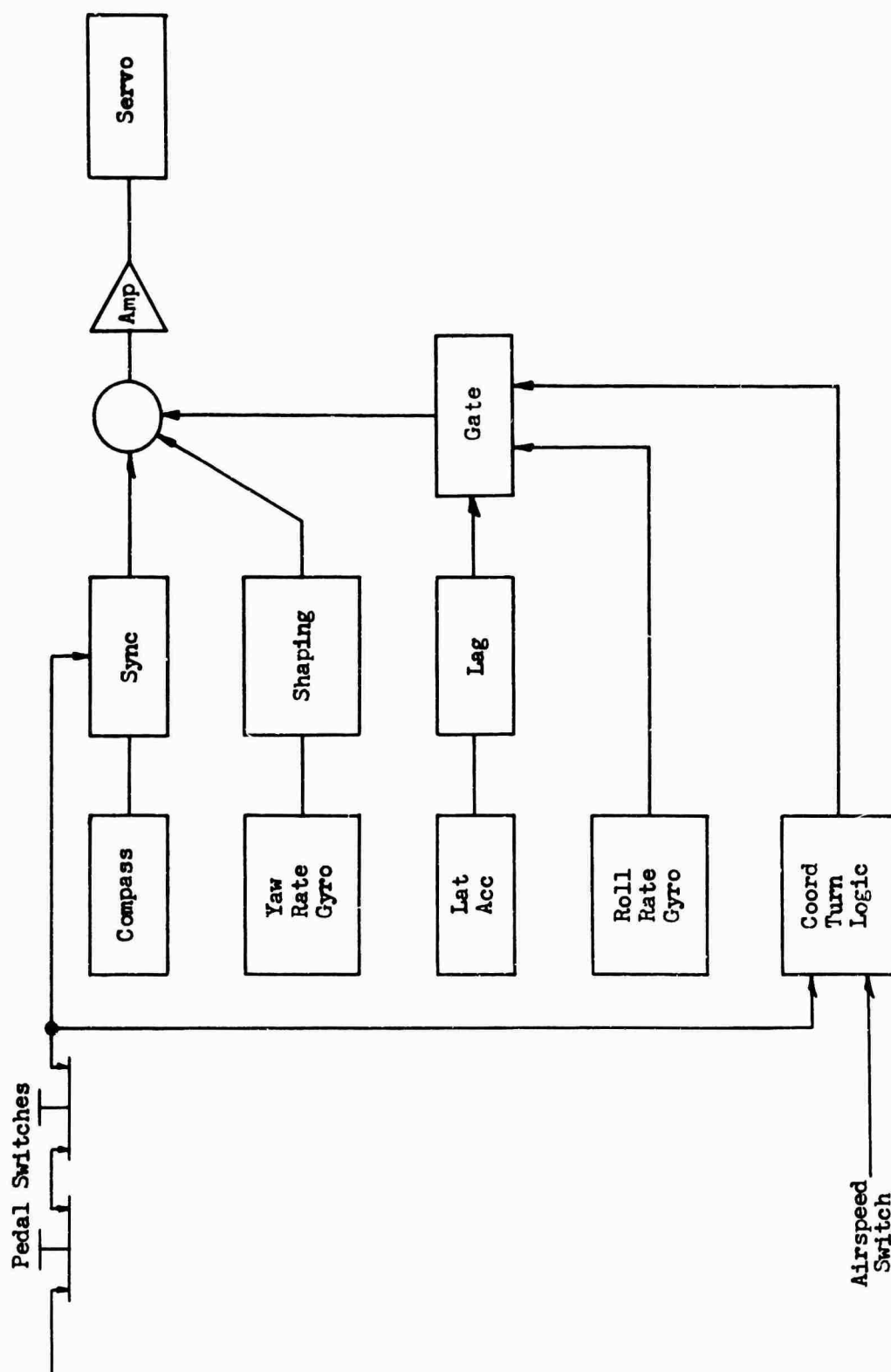


Figure 308 Yaw Channel Block Diagram

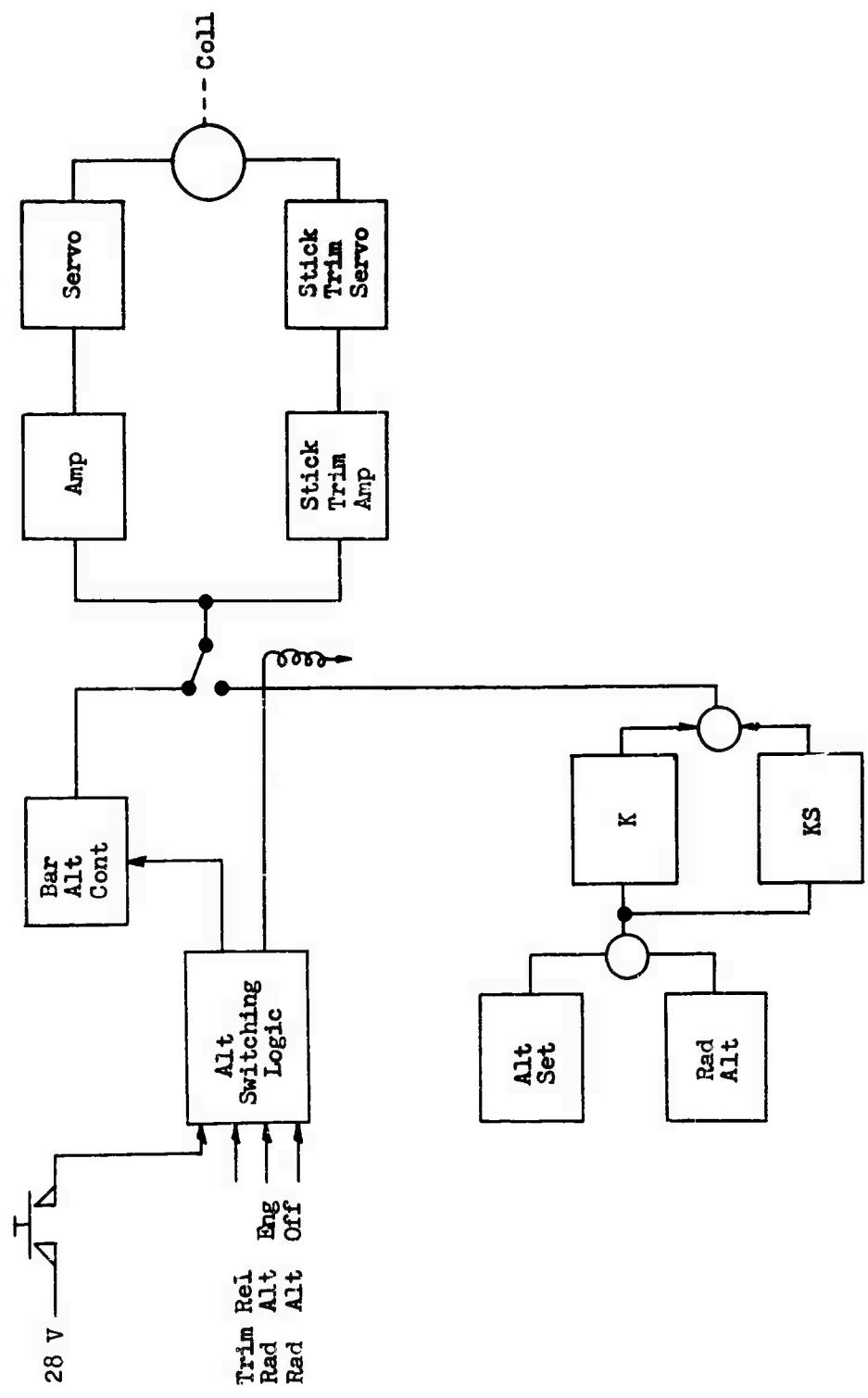


Figure 309 Altitude Block Diagram

travel and ranges. Discussion of the paragraphs of MIL-H-8501-A follows.

3.2 Longitudinal Characteristics

- 3.2.1 As indicated by the trim curves shown in Figures 270 through 275, the HLH is capable of obtaining steady, smooth flight over a speed range from -30 knots to +130 knots. Throughout this speed range the HLH exhibits a sufficient margin of control power to produce at least 10 percent of the maximum attainable pitching moment in hover to control the effects of longitudinal disturbances. The HLH control system is hydraulically and irreversibly powered and hence is free from objectionable shake, vibration, and roughness at all speeds.
- 3.2.2 Comparison of the HLH longitudinal dynamic stability in hover, Figure 285, with that of the CH-54A, Figures 289 and 290, shows dynamic similarity. These results, coupled with similar control sensitivities, indicate that the HLH, as well as the CH-54A, can be hovered with less than ± 1 inch of control deflection.
- 3.2.3 The controls of the HLH are powered. A control force trim system permits trimming the cyclic stick force gradients to any desired neutral position. This system consists of a spring loaded strut and an actuating cylinder such that the spring can be adjusted, or "beeped," by the pilot to a new zero force location. From the zero force position, a small breakout force is provided by a spring preload and a slight amount of system friction to prevent unattended stick motion following external disturbances. After the breakout force is overcome, force gradients are smooth and uniform. If the cyclic stick is moved to a new position and the stick trim button depressed, the stick will remain in this new setting when the button is released. The longitudinal control, therefore, is self-centering at the trim position. There can be no stick "jump" when the trim system is actuated, since the trim position coincides with the stick position on release of the "beeper" trim button.
- 3.2.4 The longitudinal stick force gradient meets the specification requirements with a gradient of .5 pound per inch for all the trim conditions and speeds specified in 3.2.1 (see part 3 of Table LXII). There are no undesirable discontinuities in the force gradient, and the gradient is positive in slope and essentially linear throughout. Figures 282 and 283 show the

gradients at forward and aft CG's at gross weight equal to 65,800 pounds. They were generated by cross plots of the trim curves and are typical of all weights. However, similar plots may be generated from Figures 270 through 275 for other gross weights if desired.

- 3.2.5 The similarity of the HLH design to that of all other Sikorsky designs insures the ability of this aircraft to perform safe accelerations and decelerations from hover to V_{max} and back.
- 3.2.6 As can be seen in Part 1 of Table LXII, the force and position gradients are such that the variation of the stick position through the speed range and maneuvers specified produces maximum forces within the range required by Table II of paragraph 3.2.6, Reference 4.
- 3.2.7 As shown in Part 2 of Table LXII, the breakout forces, including friction forces of the longitudinal control system, are within the range required by Table II of paragraph 3.2.6, Reference 4.
- 3.2.8 Since the flight controls are power operated, there are no control force coupling or objectionable transient forces in any direction following rapid cyclic or collective stick deflections.
- 3.2.9 The rotor follows the stick motion with a delay of less than one rotor revolution. The angular acceleration will be, in the desired sense, within 0.2 second following the initiation of a maneuver.
- 3.2.10 Figures 270 through 275 show static trim solutions for the HLH in level flight, climb at 1500 feet per minute, and autorotative descent. In general, all the requirements of this section may be demonstrated by reference to these figures. At low gross weight, longitudinal stick excursion for autorotative entry appears marginal, and stick slope tends to flatten at low velocity for certain loadings. However, comparison with the CH-54A, Figures 279 and 280, shows considerable similarity in trends. In particular, variation of attitude with velocity has been improved appreciably for the HLH. This is a direct result of the relative increase in horizontal tail area chosen for this design.
- 3.2.11 Figures 285 through 287 are root loci for the HLH longitudinal characteristics at normal gross weight and aft CG. In general, the aft CG is critical for dynamic stability. Note that the time

to double amplitude for the 110-knot case is smallest, at 3.3 seconds, but the period of oscillation is 29 seconds. Both the hover and 60-knot cases have 20-second periods. This meets the requirements of this paragraph without stability augmentation. Addition of the CH-54A AFCS with gains modified by factors of 0.5, 1.0, and 2.0 are shown to give an indication of the pilot unburdening to be expected of a typical AFCS.

- 3.2.11.1 Figures 293, 295, and 297 show time histories of the HLH for longitudinal pull and hold inputs. The normal acceleration and angular velocity time histories without AFCS are concave downward almost from the start of the maneuver at 60 knots but not at 110 knots. With AFCS, the time histories are satisfactory.
- 3.2.11.2 Figures 292, 294, and 296 show time histories of the HLH for longitudinal pull and return inputs. The normal acceleration without AFCS is again satisfactory at 60 knots but is marginal at 110 knots; with AFCS, the time histories are satisfactory.
- 3.2.12 As seen in Figures 292 through 297, the response of the helicopter's normal acceleration to the specified input will increase with time until the maximum acceleration is approached. Note that for a step input the first peak occurs at $t = 0$.
- 3.2.13, 3.2.14 TABLE LXIII demonstrates the ability of the HLH to meet the angular displacement requirements. Comparison of control power and damping of the HLH and the CH-54A with the required values is also shown.

3.3 Directional and Lateral Characteristics

- 3.3.1 The scope of this study is such that detailed aerodynamic design of a tail rotor was not undertaken. However, a representative tail rotor was chosen based on CH-54A experience. The blade size and the pitch range available are such that the HLH can taxi straight with a 35-knot wind from any direction. One-wheel pivot turns can also be accomplished.
- 3.3.2 The CH-54A meets this requirement; so, by the argument of 3.3.1 above, the HLH is also able to attain right- and left-side flight of 35 knots.

- 3.3.3 Comparison of the HLH lateral-directional stability in hover, Figure 288, with that of the CH-54A, Figure 291, shows dynamic similarity. These results, coupled with similar control sensitivities, indicate that the HLH, as well as the CH-54A, can be hovered with less than ± 1 inch of control deflection.
- 3.3.4 Figures 276 through 278 show lateral trim solutions for the HLH. Sufficient lateral trim range has been provided to allow wide variation of lateral CG within the 10-percent limitations of this requirement. In particular, Figure 268 shows lateral cyclic versus CG offset for the hover case at three gross weights. With 10-percent authority remaining, the CG can be 35 inches left or 32 inches right.
- 3.3.5 Table LXIII demonstrates the ability of the HLH to meet the yaw displacement requirements.
- 3.3.6 The requirements of this paragraph are met if .224 inch of HLH pedal remains while in the critical trim condition with the AFCS off or if .407 inch remains with the AFCS on. This condition is easily met by the CH-54A and by the applied design growth factors is also met by the HLH.
- 3.3.7 As indicated by the information of Table LXIII, yaw displacement in the first second, following a 1-inch pedal input, will not exceed 50 degrees.
- 3.3.8 Figures 276 through 278 show that sufficient tail rotor pitch and lateral cyclic are available to make coordinated turns in each direction while in autorotation.
- 3.3.9 Figure 310 shows that the lateral-directional trim characteristics of the HLH meet these requirements. Figure 311 is a similar plot for the CH-54A.
- 3.3.9.1 It is possible to make complete turns in each direction with pedals fixed using only the cyclic control stick at all speeds above 50 knots. Figure 299 shows a typical lateral cyclic input, and the resulting roll rates are in compliance with this requirement.
- 3.3.9.2 During pedal fixed rolling maneuvers, the CH-54A presents no objectionable adverse yaw. Since the lateral wind tunnel data estimated for the HLH are linear, no adverse effects are predicted for this aircraft.

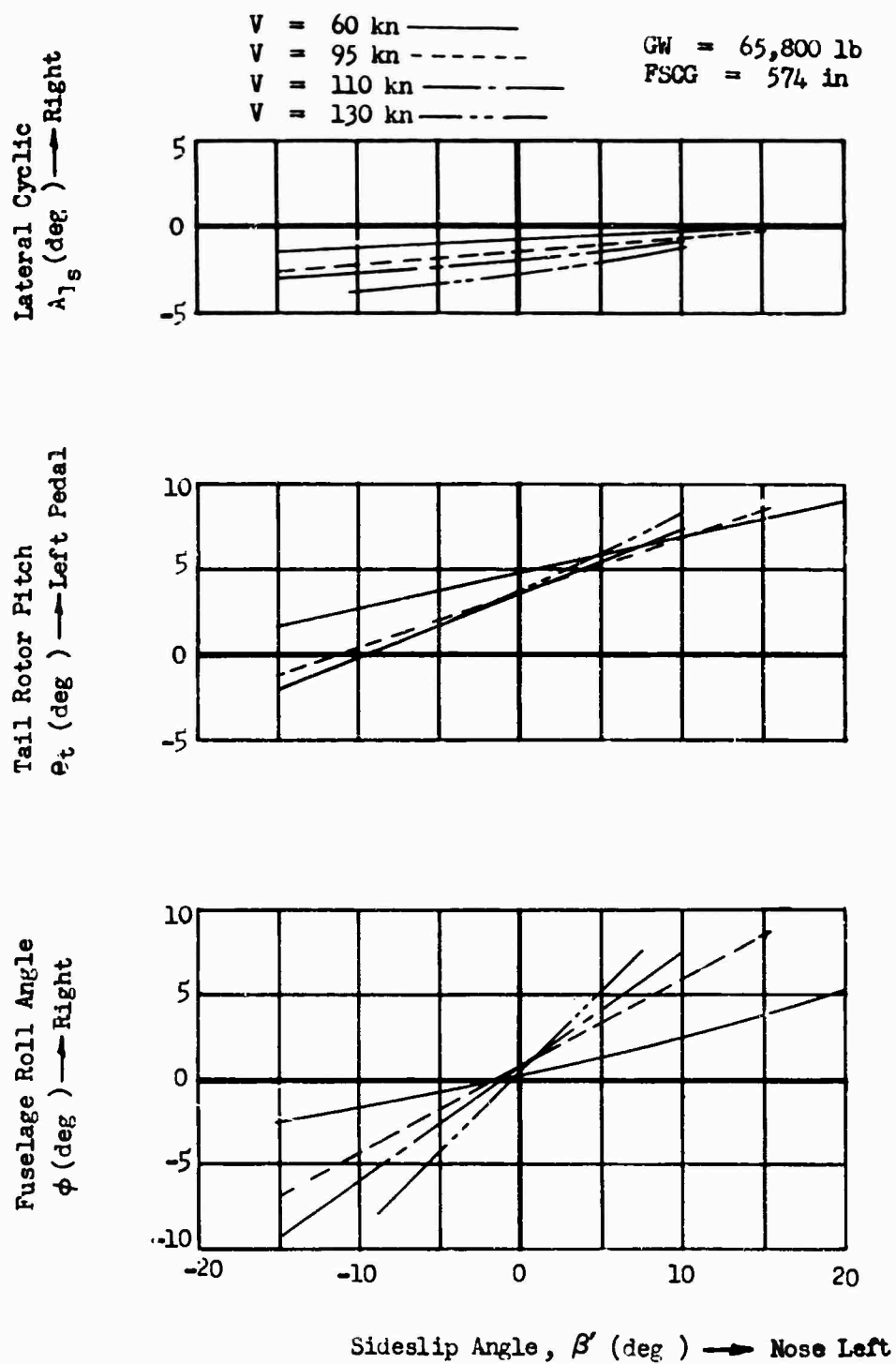


Figure 310 HLH Lateral Trim Characteristics Versus Sideslip

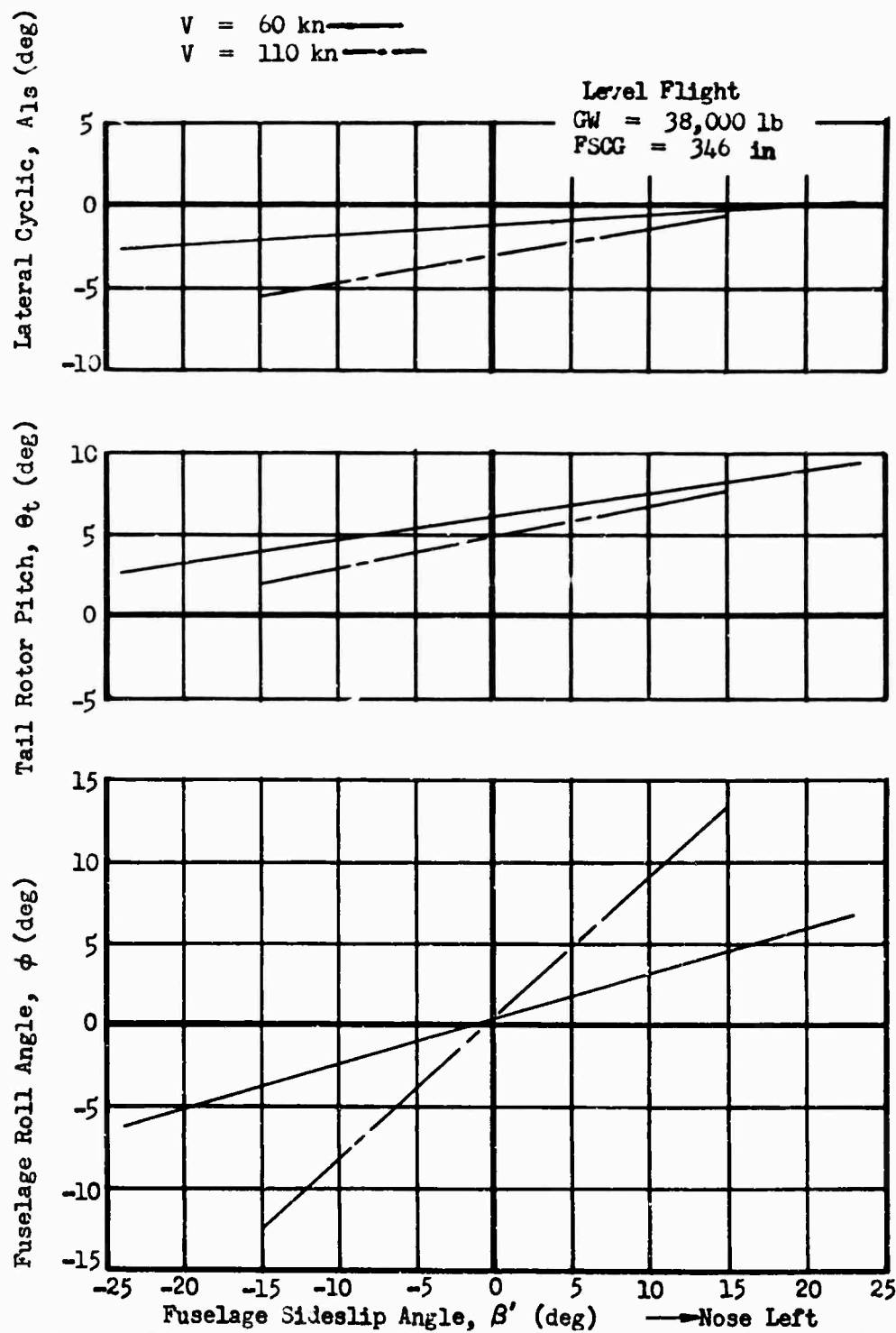


Figure 311 Lateral Trim Characteristics Versus Sideslip, CH-54A

- 3.3.10 The lateral control forces are generated in the same manner as the longitudinal control forces (see paragraph 3.2.3). The hydraulically powered control system reacts the flight loads, and the beeper trim system provides force centering with breakout and gradient forces.
- 3.3.11 The lateral cyclic stick trim is designed to meet the force gradient requirement and to be always positive and approximately linear. The directional system uses a spring and damper in series. This provides a pseudo gradient with automatic retrimming, a desirable feature for cross wind hovering.
- 3.3.12 The maximum force in the lateral system is within the requirements (see parts 1 and 3 of Table LXII), such that the specified maneuvers cannot require forces in excess of these requirements.
- 3.3.13 As shown in Part 2 of Table LXII, the breakout forces in the directional and lateral systems meet this requirement.
- 3.3.14 The controls of the HLH are free from objectionable transient forces in any direction following rapid lateral stick or pedal deflections. Since power operated controls are used throughout, no cross coupling of forces is present.
- 3.3.15 The response of the helicopter to a lateral control input will not cause the pilot to overcontrol unintentionally. The greatest rate of roll for this helicopter is below the limit of 20 degrees per second per inch of stick input. Figure 299 shows the result of a 1-inch step at 110 knots.
- 3.3.16 The lateral and directional responses following control displacement are in the proper direction within 0.2 second, and the comments of paragraph 3.2.9 apply.
- 3.3.17 The lateral trim curves, Figures 276 to 278, indicate that no excessive lateral trim changes accompany collective and/or power changes throughout the flight envelope. Figure 281 gives comparable and acceptable curves for the CH-54A.
- 3.3.18 Table LXIII indicates that the lateral control power of the HLH is sufficient to meet these requirements.
- 3.3.19 Table LXIII indicates that the roll damping of the HLH meets this requirement with AFCS on and off. This table also indicates that the yaw damping meets the requirement with

AFCS on but not with it off.

3.4 Vertical Characteristics

- 3.4.1 The so-called "zeros" of the vertical transfer functions for both the CH-54A and HLH are shown on the root locus plots, Figures 285 and 289. The predicted characteristics are similar, and the altitude hold requirements should be acceptable.
- 3.4.2 The collective stick of the HLH has a pilot operated friction lock which prevents "creeping" at any time. Since all controls are irreversibly power operated, no cross coupling of cyclic or pedals to collective stick occurs even with the lock disengaged. The control and breakout forces are presented in parts 1 and 2 of Table LXII and, as can be seen, comply with those required.
- 3.4.3 The power operated controls are irreversible and, hence, have no control force coupling.

3.5 Autorotation, Rotor Characteristics, Miscellaneous Requirements

- 3.5.1 While direct analytical substantiation of this requirement was not performed during this study, past experience indicates that while on the ground, the HLH can start and stop the rotor blades in winds up to 45 knots or more. The CH-54A and other models have repeatedly demonstrated this ability.
- 3.5.2 Cyclic pitch control allows the HLH, without the use of wheel chocks, to maintain a fixed position on a level paved surface with takeoff rotor speed while power is being increased to takeoff power in wind, as specified in paragraph 3.5.4.1.
- 3.5.3 The HLH can perform all required maneuvers, including taxiing and pivoting, without damage to the rotor head and without contact between the blades and any part of the aircraft's structure.
- 3.5.4, 3.5.4.1 Based on the experience gained with the CH-54A and other single, low offset, cyclically controlled rotor configurations, the HLH is capable of making safe vertical take-offs and landings in steady winds up to 45 knots and winds with 45-knot gusts.
- 3.5.4.2, 3.5.4.3 Structural design of the landing gear for the HLH

was outside the scope of this study. However, assuming standard design practices, the HLH is capable of safe running takeoff at ground speeds from zero to over 35 knots. Safe landings with power on or power off at ground speeds to 35 knots is also possible.

3.5.4.4 Through the application of rearward cyclic pitch and brakes, the requirement to reduce speeds from 35 knots to zero within 200 feet on a level paved surface is complied with.

3.5.4.5 Emergency Flotation - Not applicable.

3.5.5 Sikorsky helicopters have repeatedly demonstrated adequate controllability following complete multi-engine power loss or power application at any speed. Time delays of up to 2 seconds for manual collective control motion have been demonstrated on H-3 type aircraft. At the request of the Bureau of Naval Weapons, Sikorsky Aircraft conducted un-alerted system failure studies to determine the general alertness of pilots and specific delay time involved. It was found that, depending on the type of input and associated cues, the pilot reaction times ranged from 0.25 to 0.85 second (Reference 39). Based on these findings, Sikorsky can demonstrate safe transition from full power loss using standard pilot reaction times for cyclic control inputs and the required 2-second delay in collective inputs.

3.5.6 The control forces during the transition to autorotative flight under the conditions of paragraph 3.5.5 will never exceed the values specified. The hydraulic pumps for the control system are geared to the rotor, not the engines, so control forces remain within the maximum values cited in Table LXII.

3.5.7 Minimum autorotational touchdown speed is a function of pilot technique; the "Relative Autorotative Index" (Reference 29) gives a qualitative criterion for autorotation ability.

The formula
$$RAI = \frac{I_R/GW}{GW/DA} \quad (122)$$

was evaluated for both the HLH and the CH-54A, and a marked improvement in the HLH rotor is apparent. For the CH-54A, $RAI \times 10^3 = 4.6$; while for the HLH, $RAI \times 10^3 = 6.8$. Based on these results, the HLH should demonstrate excellent autorotative characteristics, and touchdown speeds less than 15 knots will easily be achieved.

3.5.8 This paragraph of Reference 4 specifies the requirements to be met by the control system in the event of primary control system failure. Since cyclic and collective controls are arranged with independent auxiliary and primary servos, each section of this paragraph can be met with ease. Both the primary and the auxiliary servo are capable of reacting the control forces independently. Hydraulic pumps are geared to the main rotor at the main gearbox, and thus will not be affected by engine or electrical failure. On the ground, an auxiliary power unit supplies hydraulic pressure for the servo system.

3.5.9 A comprehensive study of automatic flight control systems (AFCS) was beyond the scope of this report. However, to show the expected trends, the AFCS of the CH-54A was applied to the HLH with gains modified by multiples of 0.5, 1.0, and 2.0. Root locus plots for these cases are presented as Figures 285 through 288. In addition, Figure 290 is a comparable plot for the CH-54A. It can be noted that similar results are possible; and with similar equipment, the requirements of this section can be met. The projected AFCS for the HLH is discussed further under a separate heading in this section.

3.5.10 For all operating conditions, the dead spots in any of the control systems will not exceed ± 0.2 inch of motion of cockpit control without corresponding motion of the rotor blades, since this criterion is used in the mechanical design of the control linkage.

3.5.11 For all operating conditions, mechanical coupling between controls does not introduce adverse response of the helicopter. These couplings would be very similar in direction and magnitude to those of the CH-54A, an acceptable solution.

3.5.11.1 Inclusion of sufficient overtravel on control position allows mechanical coupling without adverse limitations in control power and range.

3.6 Instrument Flight - Not Applicable

3.7 Vibration Characteristics

3.7.1 Vibration characteristics are an inherent part of detailed airframe design, and as such, are beyond the scope of this study. However, assuming standard design practices, the

HLH is free of objectionable shake, vibration, and roughness, and the intent of this paragraph is satisfied.

- 3.7.2 Since the control system is fully powered, the magnitude of the vibratory force at the controls in any direction during rapid longitudinal or lateral stick deflections is practically zero.
- 3.7.3 The comments of paragraph 3.7.1 apply here also. However, assuming standard design practices, the HLH is free of mechanical instability including ground resonance. It is also free from rotor weaving and flutter that influence helicopter handling qualities during all operating conditions, such as landing, takeoff, and forward flight.

3.8 Multi-Engine Characteristics

The hydraulic system of the HLH is driven from the main gearbox. Therefore, with one engine inoperative, the control force gradients are not affected by the number of engines operating.

TABLE LXII
CONTROL FORCES AND GRADIENTS

Control System	MIL-H-8501-A			
	Min	Max	Sikorsky HLH	CH-54A
1. <u>Limit Control Forces (lb)</u>				
Longitudinal Cyclic	-	8.0	6.5	4.58
Lateral Cyclic	-	7.0	6.5	4.45
Collective	-	7.0	-	-
Directional	-	15.0	-	-
2. <u>Breakout Forces (lb)</u>				
Longitudinal Cyclic	0.5	1.5	1.5	1.5
Lateral Cyclic	0.5	1.5	1.5	1.5
Collective	1.0	3.0	1.0	1.0
Directional	3.0	7.0	5.0	5.0
3. <u>Force Gradients (lb/in)</u>				
Longitudinal Cyclic	0.5	2.0	0.5	0.363*
Lateral Cyclic	0.5	2.0	0.5	0.342*
Collective	-	-	-	-
Directional	-	-	-	-

* These gradients were the result of collected pilot opinion during early flight tests of the CH-54A and are considered optimum for this aircraft.

TABLE LXIII
COMPARISON OF HLH AND CH-54A HOVER CHARACTERISTICS

HLH - 80,000 POUNDS - GROSS WEIGHT					
		Required		Available	
		VFR	IFR	Basic	AFCs*
Pitch (1 sec)					
CP/I		---	---	.105	.105
D/I		.144	.271	.381	.862
Disp. (1 inch input), deg		1.040	1.687	2.660	3.060
Disp. (max control input), deg		4.160	6.750	17.300	19.900
Pitch Rate @ 1 sec (1 inch), $\frac{\text{deg}}{\text{sec}}$		---	---	5.010	5.040
Roll (0.5 sec)					
CP/I		---	---	.263	.263
D/I		.496	.688	1.611	2.590
Disp. (1 inch input), deg		.624	.740	1.466	1.477
Disp. (max control input), deg		1.872	2.220	9.530	9.600
Roll Rate @ .5 sec (1 inch), $\frac{\text{deg}}{\text{sec}}$		< 20	< 20	5.170	5.130
Yaw (1 sec)					
CP/I		---	---	.431	.431
D/I		.513	.513	.256	2.520
Disp. (1 inch input), deg		2.54 $\leq \psi \leq 50$	2.54 $\leq \psi \leq 50$	11.370	6.230
Disp. (max control input), deg		7.620	7.620	28.400	15.580
Yaw Rate @ 1 sec (1 inch), $\frac{\text{deg}}{\text{sec}}$		---	---	21.800	9.020

REFERENCES

1. Abbott, Ira H., Von Doenhoff, Albert E., and Stivers, Louis S., Jr., Summary of Airfoil Data, NACA Report No. 824, United States Government Printing Office, Washington 25, D.C., 1949.
2. "Aluminum Alloy Forgings, Heat Treated", MIL-A-22771, Revision B, September 1964.
3. "A Method for Determining the Fully Coupled Aeroelastic Response of Helicopter Rotor Blades", Proceeding of American Helicopter Society, May 1963.
4. Anon., "Helicopter Flying and Ground Handling Qualities; General Requirements for", U.S. Military Specification MIL-H-8501-A, September 7, 1961.
5. Arcidiacono, P. J., "Analytical and Experimental Investigations of the Aeroelastic Characteristics of Helicopter Rotors Operating at High Advance Ratios", Report B-1100-2-1, UAC Research Laboratories, East Hartford, Connecticut, March 1963.
6. Bailey, F. J., Jr., Simplified Theoretical Method of Determining the Characteristics of a Lifting Rotor in Forward Flight, NACA Technical Report No. 716, United States Government Printing Office, Washington 25, D.C., March 17, 1941.
7. Bruhn, E. F., Analysis and Design of Aircraft Structures, Tri-State Offset Co., Cincinnati, Ohio, 1958.
8. Burroughs, L. R., Power Transmission Studies for Shaft-Driven Heavy Lift Helicopter, Sikorsky Engineering Report-50401, (Draft Report) Stratford, Connecticut, February 1956.
9. Carter, E. S., Decker, R. S., and Cooper, D. E., "Handling Qualities Considerations of Large Crane Helicopters", Annals of the New York Academy of Sciences, Volume 107, Article 1, March 25, 1963.
10. Chou, P. C., "Pitch-Lag Instability of Helicopter Rotors", Journal of the American Helicopter Society, Volume 3, Number 3, July 1958.

11. Coleman, R. P. and Feingold, A. M., Theory of Self-Excited Mechanical Oscillations of Helicopter Rotors with Hinged Blades, NACA Report 1351, United States Government Printing Office, Washington 25, D. C., 1959.
12. Critzos, C., Heyson, H., and Boswinkle, R., Aerodynamic Characteristics of NACA 0012 Airfoil Section at Angles of Attack from 0° to 180°, NACA TN 3361, United States Government Printing Office, Washington 25, D. C., 1955.
13. Den Hartog, J. P., Mechanical Vibration, McGraw-Hill Book Co., Inc., New York, 1956.
14. Deutsch M. L., "Ground Vibrations of Helicopters", Journal of the Aeronautical Sciences, Volume 13, May 1946.
15. DuWaldt, F. A., Gates, C. A., Piziali, R. A., "Investigation of the Flutter of a Model Helicopter Rotor Blade in Forward Flight", WADD TR 60-479, Cornell Aeronautical Laboratory Inc., Buffalo, New York, July 1960.
16. Evans, W. R., Control System Dynamics, McGraw-Hill Book Co., Inc., New York, New York, 1954.
17. Gerdes, W. H., and Tanner, W. H., Generalized Rotor Performance Method, Sikorsky Engineering Report-50355, Stratford, Connecticut, November 1964.
18. Gerstenberger, W., and Wood, E. R., "Analysis of Helicopter Aeroelastic Characteristics in High-Speed Flight", AIAA Journal, Volume 1, Number 10, October 1963.
19. Grover, H. J., Gordon, S. A., and Jackson, L. R., Fatigue of Metals and Structures, NAVWEPS 00-25-534, Washington, D. C., 1954, Revised June 1, 1960.
20. Ham, Norman D., "An Experimental Investigation of Stall Flutter on a Model Helicopter Rotor in Forward Flight", Journal of the American Helicopter Society, Volume 7, January 1962.
21. Heywood, R. B., Designing Against Fatigue of Metals, First Edition, Reinhold Publishing Corporation, New York, New York, 1962.

22. Hoblit, F. M., and Melcon, M. A., "Developments in the Analysis of Lugs and Shear Pins", Product Engineering, McGraw-Hill Book Co., Inc., New York, June 1953.
23. Hoerner, S. F., Fluid-Dynamic Drag, S. F. Hoerner, 148 Busted Drive, Midland Park, New Jersey, 1958.
24. In-Flight Measurements of Helicopter Rotor Shaft Loads Under Control Cyclic Trim Variation, ASD Technical Report 61-523, 1961.
25. Jensen, H. T., "The Application of Reliability Concept to Fatigue Loaded Helicopter Structures", 18th Annual Forum, American Helicopter Society, May 1962.
26. Jepson, D., Leoni, R., Magri, J., and Sibbick, L., U. S. Army Crane Helicopter Parametric Study 12 to 20-Ton Payload, Sikorsky Engineering Report-50273, Stratford, Connecticut, June 1966.
27. Johnston, J. F., Culver, L. H., and Friend, C. F., Study of Size Effects on VTOL Handling Qualities Criteria, USAAVLABS Technical Report 65-24, U. S. Army Aviation Materiel Laboratories, Fort Eustis, Virginia, September 1965.
28. Kaplita, T. T., Equations for Determining the Dynamic Stability Characteristics of a Single Rotor Helicopter in Steady Forward Flight and Hover, Sikorsky Engineering Report No. 5086, Stratford, Connecticut, January 15, 1957.
29. Katzenberger, E. F., and Rich, M. J., "An Investigation of Helicopter Descent and Landing Characteristics Following Power Failure", Journal of the Aeronautical Sciences, April 1966.
30. Labriola, R., Flight Tests of a 3-Bladed S-61 to Verify Characteristics at High Lift Coefficients, Sikorsky Engineering Report - 611043, Stratford, Connecticut, November 1964.
31. Leone, P. F., "Mechanical Stability of a Two-Bladed Cantilever Helicopter Rotor", Journal of Aeronautical Sciences, Volume 23, Number 7, July 1956.

32. Loewy, R. G., "A Two-Dimensional Approximation to the Unsteady Aerodynamics of Rotary Wings", Journal of the Aeronautical Sciences, Volume 24, Number 2, February 1957.
33. "Main Rotor Service Life Determination", CAM 6, Appendix A, Revision, January 1963.
34. "Military Specifications, Structural Design Requirements, Helicopters", MIL-S-8698, July 1954.
35. Miller, R. H. and Ellis, C. W., "Blade Vibration and Flutter", Journal of the American Helicopter Society, July 1956.
36. Miner, M. A., "Cumulative Damage in Fatigue", Journal of Applied Mechanics, Trans., A. S. M. E., Volume 67, 1945.
37. Myklestad, N. O., Vibration Analysis, McGraw-Hill Book Co., Inc., New York, 1956.
38. Neuber, H., Theory of Notch Stresses - Principles for Exact Stress Calculation, J. W. Edwards Co., Ann Arbor, Michigan, 1946.
39. O'Leary, E. B., 100 Hour Flight Endurance Test Program, Sikorsky Engineering Report No. 61528, Stratford, Connecticut, October 27, 1961.
40. Olson, J. R., Parametric Analysis and Preliminary Design of a Shaft Driven Rotor System for a Heavy Lift Helicopter, Sikorsky Engineering Report No. 50406, Stratford, Connecticut, April 14, 1965.
41. Peterson, R. E., Stress Concentration Design Factors, First Edition, John Wiley & Sons, Inc., New York, New York, 1953.
42. "Power Transmission Studies for Shaft-Driven Heavy-Lift Helicopters", USAAVLABS Technical Report 65-40, U. S. Army Aviation Materiel Laboratories, Fort Eustis, Virginia, October 1965.
43. Regier, A. A., and Rainey, A. G., Effect of Mean Incidence on Flutter, Langley Research Center, Hampton, Virginia, 1958.
44. Roark, R. J., Formulas for Stress and Strain, Third Edition, McGraw-Hill Book Co., Inc., New York, New York, 1954.

45. Scalon, R. H., and Rosenbaum, Introduction to the Study of Aircraft Vibration and Flutter, MacMillan and Company, New York, 1951.
46. Sederoerg, C. R., "Factor of Safety and Working Stress", Trans. A. S. M. E., 1930.
47. Seely, F. B., and Smith, J. O., Advanced Mechanics of Materials, Second Edition, John Wiley & Sons, Inc., New York, New York, 1952.
48. Sepulveda, B. B., and Williams, P., Crane Helicopter Parametric Study, Sikorsky Engineering Report-50025, Stratford, Connecticut, Revision, November 1957.
49. Shulman, Y., "Stability of a Flexible Helicopter Rotor Blade in Forward Flight", Journal of the Aeronautical Sciences, July 1956.
50. Stepniewski, W. Z., Introduction to Helicopter Aerodynamics, Rotary Aircraft Series, Revised Edition, Rotorcraft Publishing Committee, Morton, Pa., 1955.
51. "Strength of Metal Aircraft Elements", MIL-HDBK-5, United States Government Printing Office, Washington 25, D. C., August 1962.
52. "Structural Design Requirements of Helicopters", MIL-S-8698(ASG), Amendment 1, February 1958.
53. Tanner, W. T., Charts for Estimating Rotary Wing Performance in Hover and High Forward Speeds, NASA CR-114, (Sikorsky Engineering Report-50379), October 1964.
54. Theodorsen, Theodore, General Theory of Aerodynamic Instability and the Mechanism of Flutter, NACA Number 496, 1935.
55. Timoshenko, S., Strength of Materials-Part I, Second Edition, D. Van Nostrand Company, Inc., New York, New York, 1941.
56. Timoshenko, S., Strength of Materials-Part II, Third Edition, D. Van Nostrand Company, Inc., Princeton, New Jersey, 1956.
57. Von Hardenberg, P. and Paul, W., CH-3C Helicopter Vibration Analysis and Test Report, Sikorsky Engineering Report-61856, Stratford, Connecticut, 1964.
58. Williams, C. D., Analysis of Statically Indeterminate Structures, International Textbook Company, Scranton, Pa., 1950.

59. Wood, E. R., and Hilzinger, K. D., "A Method of Determining the Fully Coupled Aeroelastic Response of Helicopter Rotor Blades", Proceedings of the American Helicopter Society, May 1963.

APPENDIX

MAIN ROTOR BLADE DESIGN STUDY RESULTS

The design study which was conducted as a part of the establishment of criteria for parametric analysis produced data of value in establishing weight trends (Figure 4 in Reference 40 shows the correlation achieved) but which did not fall into any of the categories discussed in the report. For this reason, the results of the design study are presented here for information and background.

The blade designed was for a six-bladed rotor of 95-foot diameter. Blade aspect ratio was 16.1; chord was 2.95 feet. A typical outboard section is shown in Figure 312. It will be noted that the spar is a D-shaped machined extrusion with a nonstructural trailing edge attached by adhesive bonding and a nonstructural leading edge counterweight supported in an elastomer within the nose of the spar. The inner spar cavity is of constant contour over the entire length of the blade, while the outer top and bottom surfaces are tapered, and the backwall has three steps.

Various spar section contours showing the variation of wall thickness are shown in Figures 313 and 314. Actual thickness variation selected for 680-foot-per-second tip speed resulted in the spar section property distributions shown in Figures 315 through 317, the trend being similar for all of the spar designs studied. The weight distribution for the 680-foot-per-second blade is shown in Figure 318, representing the weight of the spar, and estimated contributions of nonstructural components, tip balance weight installation, BIM® seals, and various items of hardware. The blade cuff and its associated attaching hardware are not included in this plot. Figure 319 summarizes the weights of several blades designed for various tip speeds and shows the 700-foot-per-second point finally selected, with a blade weight of 840 pounds.

The resonant frequencies determined for this blade are shown in Reference 40, Figures 42* and 43*; the frequency plot was found to be nearly identical to those for several main rotor blades of present production models. An indication of blade stress distribution can be obtained from the bending moment envelope plot of Figure 320 for one of the flight conditions checked during the design study.

*These curves are repeated as Figures 50 and 51 of this report.

Airfoil = NACA 0012
Chord = 2.95 feet

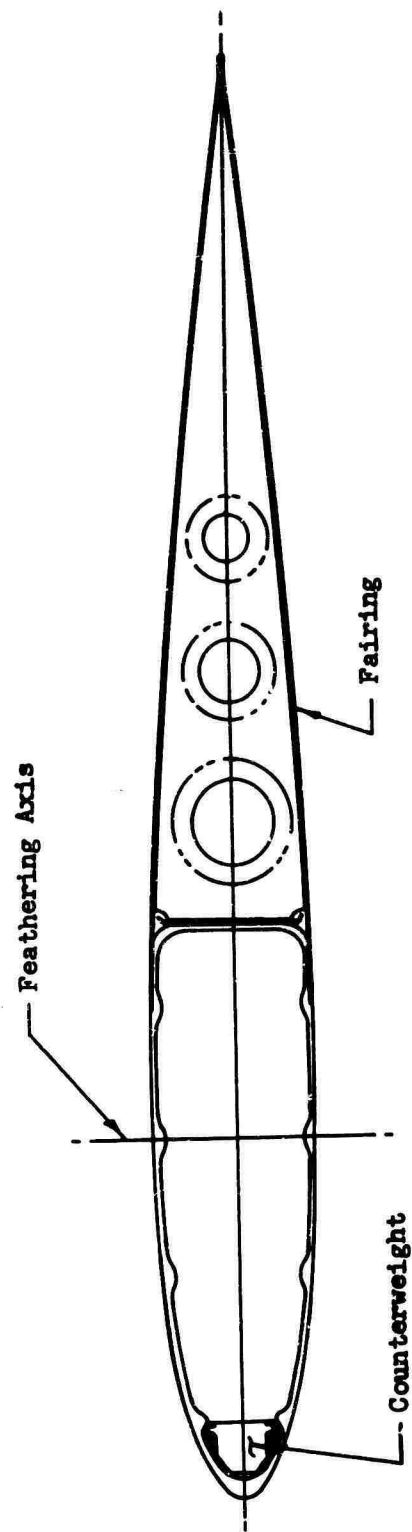


Figure 312 HLH Outboard Blade Section

Airfoil = NACA 0012
 Chord = 2.95 feet
 Spar Width (h) = 40% Chord at Tip End

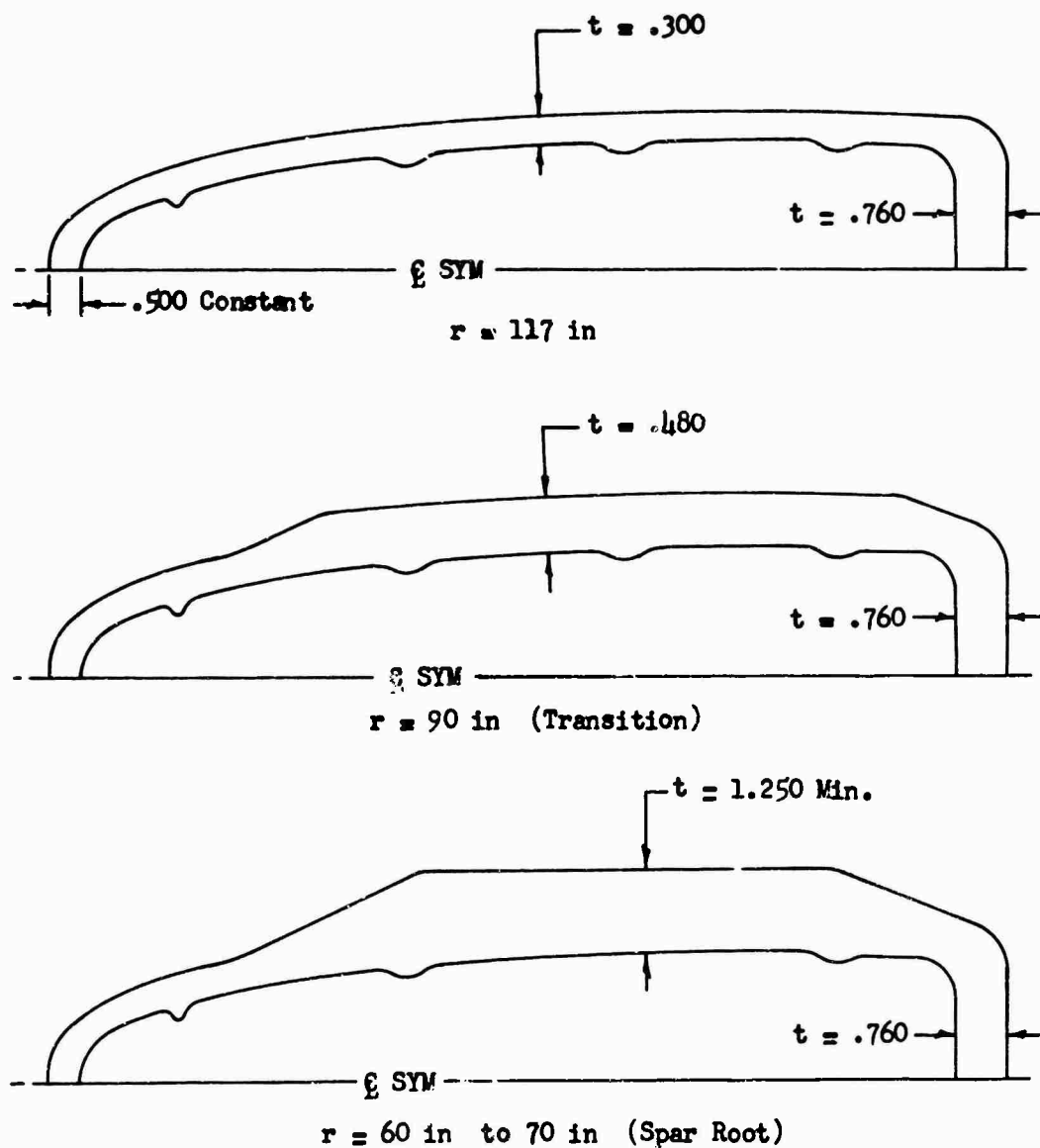


Figure 313 HLH Spar Half-Sections

Airfoil = NACA 0012
 Chord = 2.95 feet
 Spar Width (h) = 40% Chord at Tip End

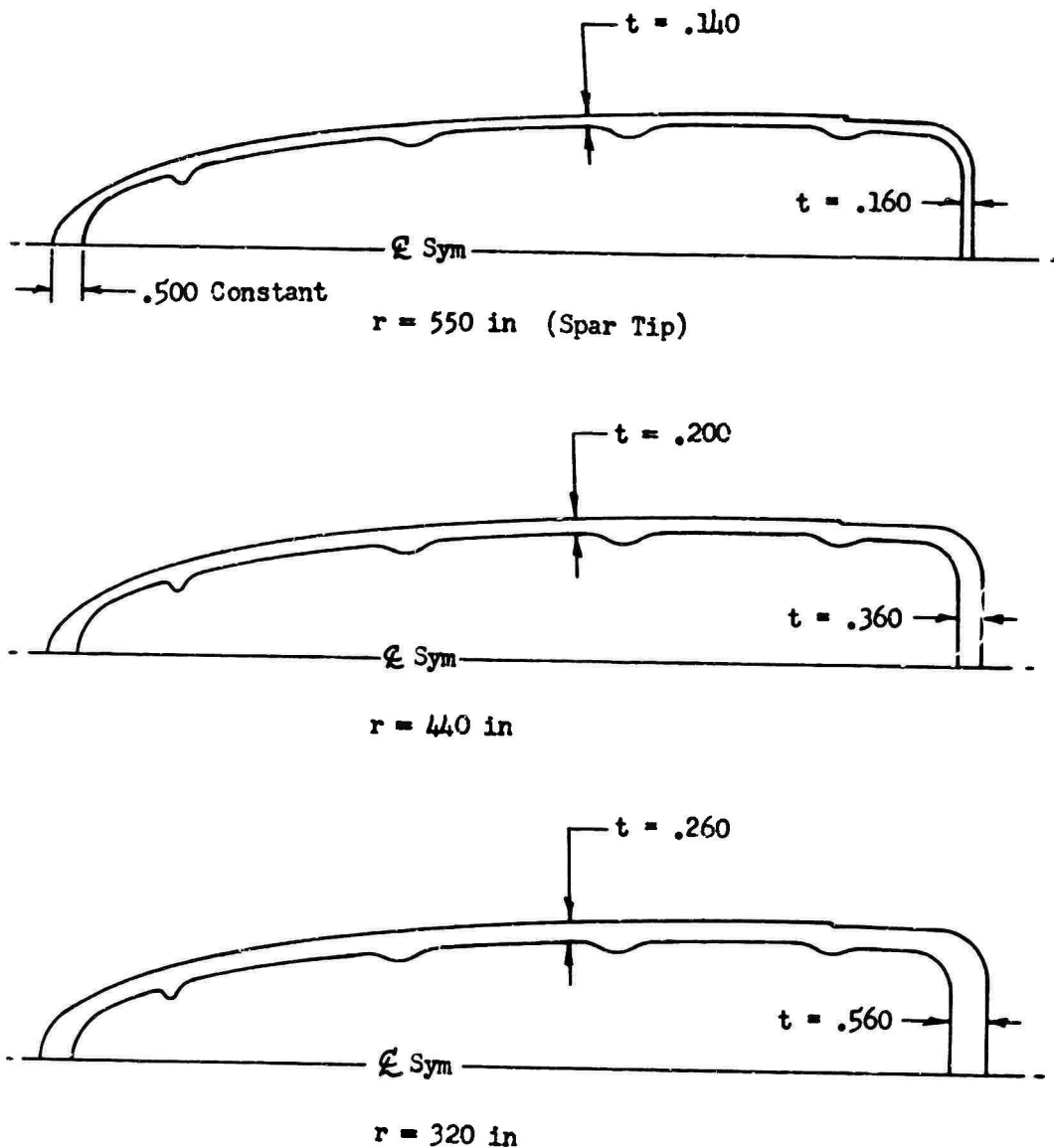


Figure 314 HLH Spar Half-Sections

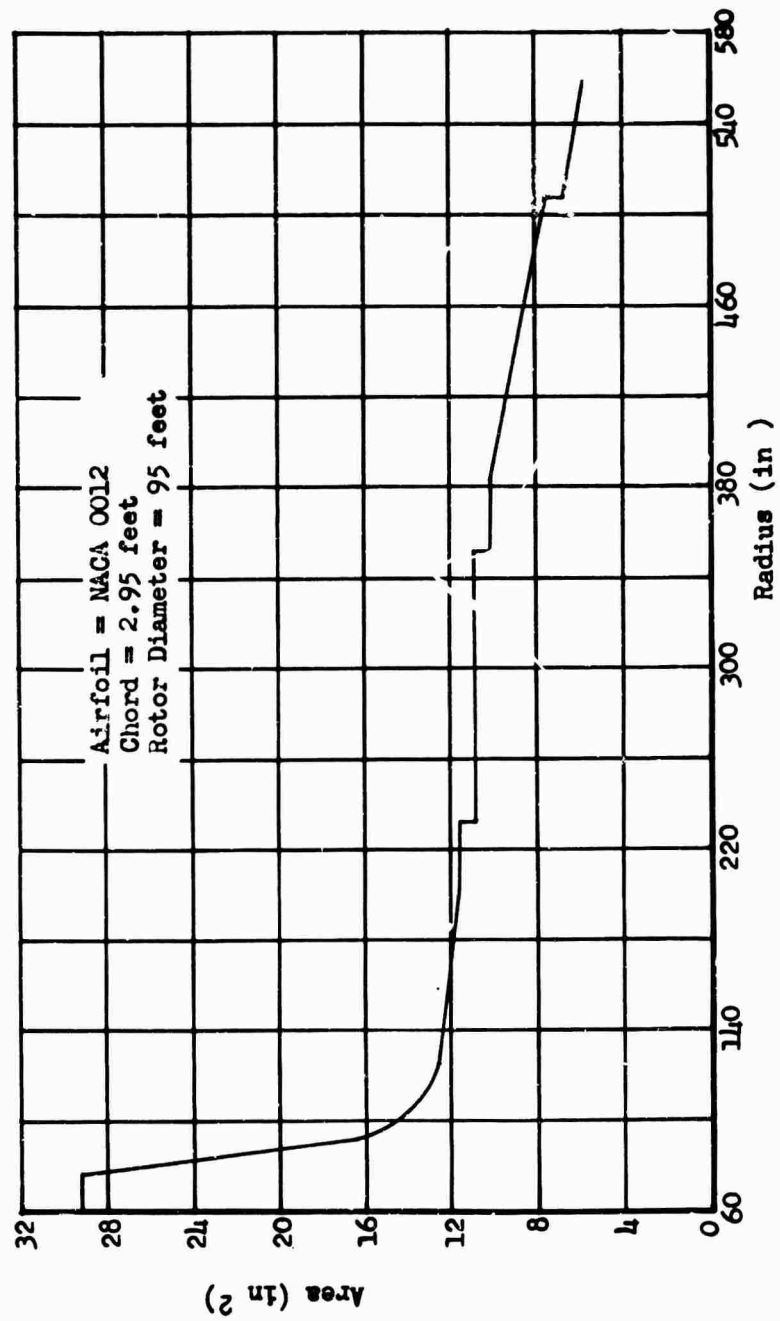


Figure 315 Main Rotor Blade Spar Area

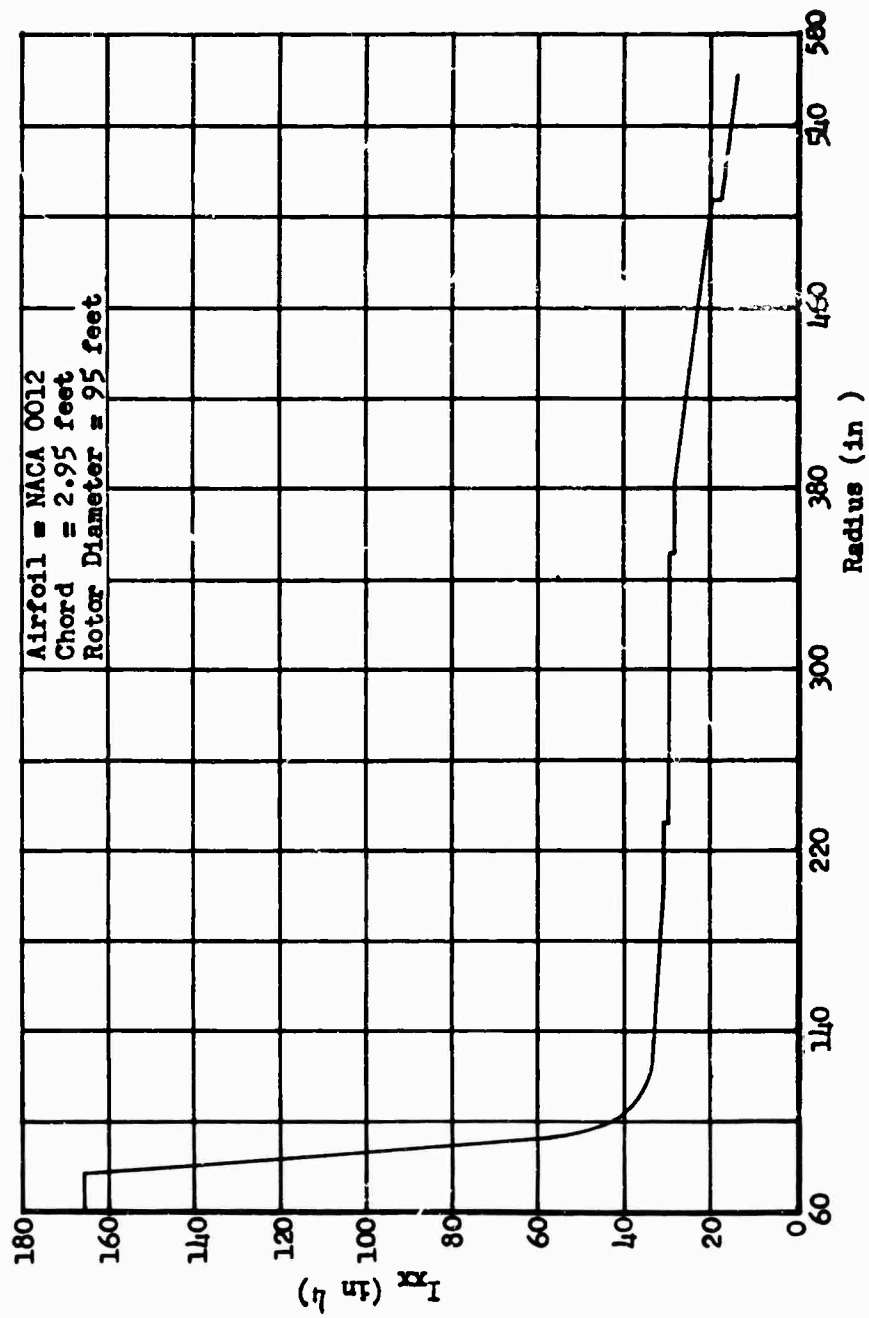


Figure 316 Main Rotor Blade Flapwise Moment of Inertia

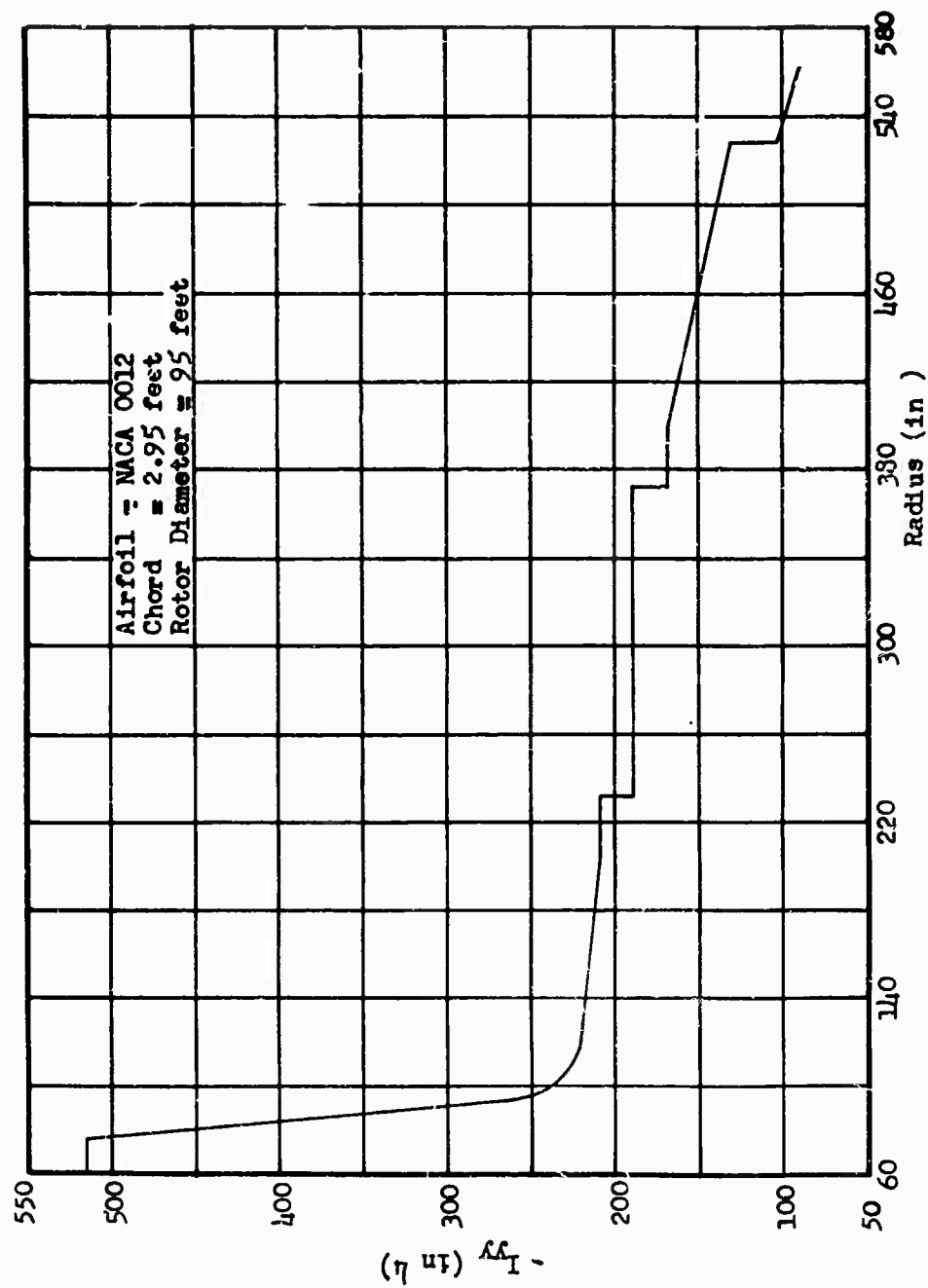


Figure 317 Main Rotor Blade Edgewise Moment of Inertia

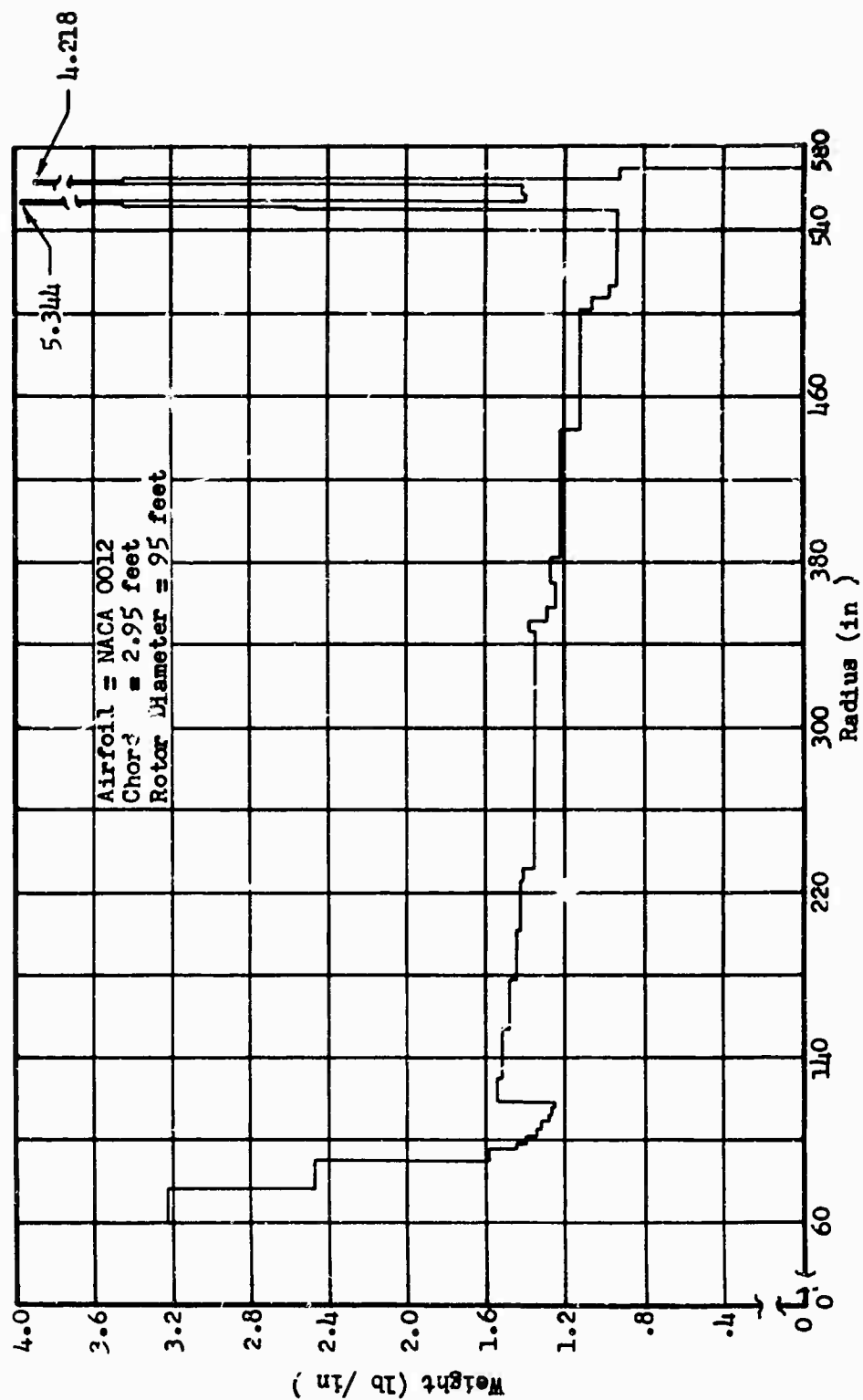


Figure 318 Main Rotor Blade Weight Distribution

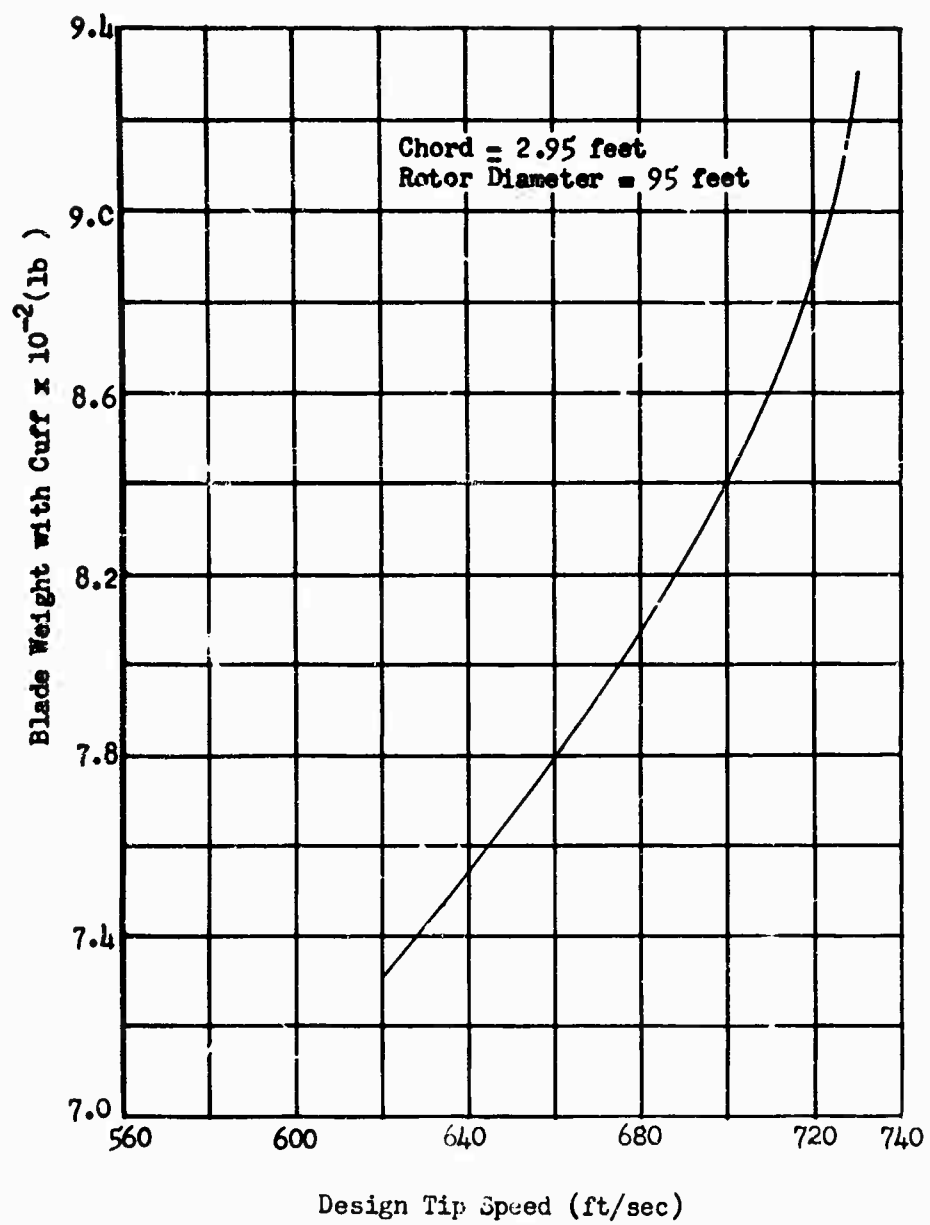


Figure 319 Blade Weight Versus Design Tip Speed

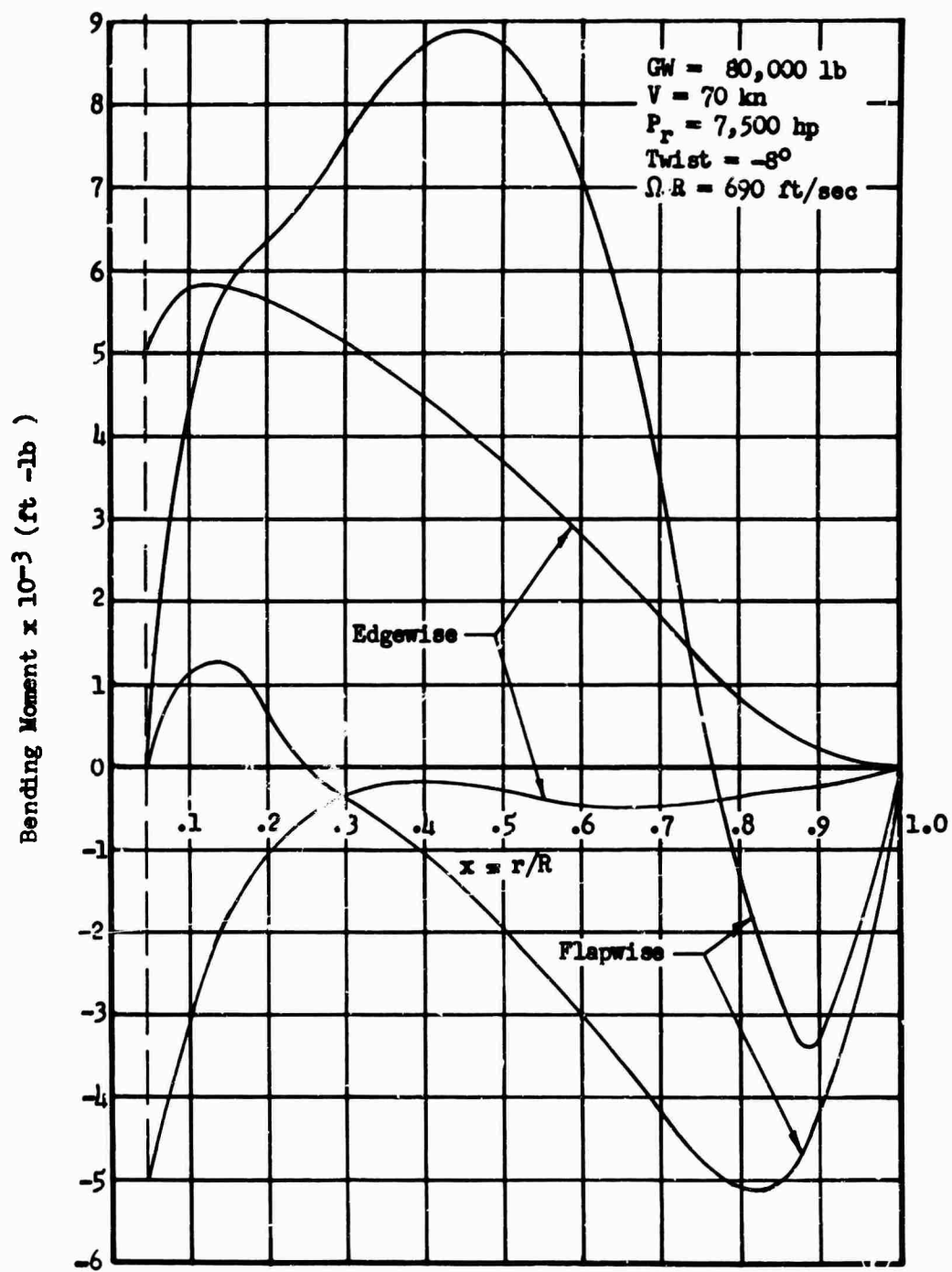


Figure 320 Main Rotor Blade Moment Envelope

ROTOR LOADS FOR DYNAMIC ANALYSIS

Presented are the estimated rotor loads used for the dynamic analysis. The loads are considered adequate for a comparative evaluation of the single and tandem rotor configuration.

One-Cycle-Per-Revolution Rotor Load

Blade out-of-track conditions are the primary causes of one-cycle-per-revolution excitation. The out-of-track condition results in one-cycle-per-revolution hub moments and shear. The shear component was neglected, resulting in a conservative estimate of one-cycle-per-revolution loads. The estimated one-cycle-per-revolution loads are as follows:

Tandem	83,000 in-lb/in, blade out-of-track
Single	54,000 in-lb/in, blade out-of-track

The tandem load is higher because of greater blade mass (771 lb/blade versus 658 lb/blade) and because of the higher tandem rotor rpm (189 revolutions per minute versus 146 revolutions per minute). Two tandem one-per-revolution load phasings were considered, representing both in phase and out of phase between the two rotors.

N-Cycles-Per-Revolution Rotor Loads

Forces transmitted to the fuselage from blade root shear have been measured for the H-21 and SH-3A helicopters. These forces were scaled to the HLH configuration by using a $C_{1/2}$ scaling factor and are tabulated below for 100 knots indicated airspeed.

Single Rotor

Force - vertical, 6 per revolution	-	1925 lb
Force - longitudinal, 6 per revolution (fixed system)	-	1290 lb

Tandem Rotor

Fwd Rotor

Force - vertical, 3 per revolution	-	1500 lb
Force - longitudinal, 3 per revolution (fixed system)	-	3000 lb

Aft Rotor

Force - vertical, 3 per revolution	-	3600 lb
Force - longitudinal, 3 per revolution (fixed system)	-	2100 lb

For the HLH, the phasing of the forces is unknown. Hence, all possible (real) phase additions were analyzed. Results presented in the dynamic analysis section considered both the poorest and best vector additions of loads.

Unclassified

Security Classification

DOCUMENT CONTROL DATA - R&D		
(Security classification of title, body of abstract and indexing annotation must be entered when the overall report is classified)		
1. ORIGINATING ACTIVITY (Corporate author) Sikorsky Aircraft Division of United Aircraft Corporation Stratford, Connecticut 06497		2a. REPORT SECURITY CLASSIFICATION Unclassified
		2b. GROUP N/A
3. REPORT TITLE PARAMETRIC ANALYSIS AND PRELIMINARY DESIGN OF A SHAFT-DRIVEN ROTOR SYSTEM FOR A HEAVY LIFT HELICOPTER		
4. DESCRIPTIVE NOTES (Type of report and inclusive dates) Final Report 15 October 1965 to 15 October 1966		
5. AUTHOR(S) (Last name, first name, initial) Dutton, Walter J.		
6. REPORT DATE February 1967	7a. TOTAL NO. OF PAGES 627	7b. NO. OF REFS 59
8a. CONTRACT OR GRANT NO. DA 44-177-AMC-275(T)	9a. ORIGINATOR'S REPORT NUMBER(S) USAAVLABS Technical Report 66-56	
b. PROJECT NO. Task 1D131001D157	9b. OTHER REPORT NO(S) (Any other numbers that may be assigned this report) Sikorsky Engineering Report 50444	
c.		
d.		
10. AVAILABILITY/LIMITATION NOTICES Distribution of this document is unlimited.		
11. SUPPLEMENTARY NOTES		12. SPONSORING MILITARY ACTIVITY U. S. Army Aviation Materiel Laboratories Fort Eustis, Virginia 23604
13. ABSTRACT The primary objective of this program was to select and design a shaft-driven lifting rotor system for a heavy lift helicopter. The selection included a complete parametric analysis of the aircraft, based on three defined missions: lifting a 20-ton payload 20 nautical miles, lifting a 12-ton payload 100 nautical miles, and ferrying. Several aircraft configurations were studied, and a single rotor crane arrangement was selected. Included in the study were selection of engines and parametric sizing of all major aircraft component systems. The aircraft defined in this study has a takeoff gross weight for the 20-ton mission of approximately 79,000 pounds and uses a single lifting rotor 91.6 feet in diameter. Ferry range exceeds 2400 nautical miles. While differing in detail from any existing hardware, the rotor system design follows directly from present practice. Methods of analysis and allowable stresses used in this study are the same as those used in existing models. Analyses of aircraft stability and control characteristics and rotor system stability for the selected configuration have been performed, and the methods and results reported herein. For all of the properties studied, both the aircraft and the rotor system have been shown to meet or exceed the requirements of applicable specifications and/or accepted practice.		

DD FORM 1 JAN 64 1473

Unclassified

Security Classification

Unclassified

Security Classification

KEY WORDS	LINK A		LINK B		LINK C	
	ROLE	WT	ROLE	WT	ROLE	WT
Helicopter - Heavy Lift Crane - 12 to 20 ton Rotor System - Shaft Driven Rotor System - Preliminary Design Rotor System - Parametric Analysis						

INSTRUCTIONS

1. ORIGINATING ACTIVITY: Enter the name and address of the contractor, subcontractor, grantee, Department of Defense activity or other organization (*corporate author*) issuing the report.

2a. REPORT SECURITY CLASSIFICATION: Enter the overall security classification of the report. Indicate whether "Restricted Data" is included. Marking is to be in accordance with appropriate security regulations.

2b. GROUP: Automatic downgrading is specified in DoD Directive 5200.10 and Armed Forces Industrial Manual. Enter the group number. Also, when applicable, show that optional markings have been used for Group 3 and Group 4 as authorized.

3. REPORT TITLE: Enter the complete report title in all capital letters. Titles in all cases should be unclassified. If a meaningful title cannot be selected without classification, show title classification in all capitals in parenthesis immediately following the title.

4. DESCRIPTIVE NOTES: If appropriate, enter the type of report, e.g., interim, progress, summary, annual, or final. Give the inclusive dates when a specific reporting period is covered.

5. AUTHOR(S): Enter the name(s) of author(s) as shown on or in the report. Enter last name, first name, middle initial. If military, show rank and branch of service. The name of the principal author is an absolute minimum requirement.

6. REPORT DATE: Enter the date of the report as day, month, year, or month, year. If more than one date appears on the report, use date of publication.

7a. TOTAL NUMBER OF PAGES: The total page count should follow normal pagination procedures, i.e., enter the number of pages containing information.

7b. NUMBER OF REFERENCES: Enter the total number of references cited in the report.

8a. CONTRACT OR GRANT NUMBER: If appropriate, enter the applicable number of the contract or grant under which the report was written.

8b, 8c, & 8d. PROJECT NUMBER: Enter the appropriate military department identification, such as project number, subproject number, system numbers, task number, etc.

9a. ORIGINATOR'S REPORT NUMBER(S): Enter the official report number by which the document will be identified and controlled by the originating activity. This number must be unique to this report.

9b. OTHER REPORT NUMBER(S): If the report has been assigned any other report numbers (either by the originator or by the sponsor), also enter this number(s).

10. AVAILABILITY/LIMITATION NOTICES: Enter any limitations on further dissemination of the report, other than those imposed by security classification, using standard statements such as:

- (1) "Qualified requesters may obtain copies of this report from DDC."
- (2) "Foreign announcement and dissemination of this report by DDC is not authorized."
- (3) "U. S. Government agencies may obtain copies of this report directly from DDC. Other qualified DDC users shall request through _____."
- (4) "U. S. military agencies may obtain copies of this report directly from DDC. Other qualified users shall request through _____."
- (5) "All distribution of this report is controlled. Qualified DDC users shall request through _____."

If the report has been furnished to the Office of Technical Services, Department of Commerce, for sale to the public, indicate this fact and enter the price, if known.

11. SUPPLEMENTARY NOTES: Use for additional explanatory notes.

12. SPONSORING MILITARY ACTIVITY: Enter the name of the departmental project office or laboratory sponsoring (paying for) the research and development. Include address.

13. ABSTRACT: Enter an abstract giving a brief and factual summary of the document indicative of the report, even though it may also appear elsewhere in the body of the technical report. If additional space is required, a continuation sheet shall be attached.

It is highly desirable that the abstract of classified reports be unclassified. Each paragraph of the abstract shall end with an indication of the military security classification of the information in the paragraph, represented as (TS), (S), (C), or (U).

There is no limitation on the length of the abstract. However, the suggested length is from 150 to 225 words.

14. KEY WORDS: Key words are technically meaningful terms or short phrases that characterize a report and may be used as index entries for cataloging the report. Key words must be selected so that no security classification is required. Identifiers, such as equipment model designation, trade name, military project code name, geographic location, may be used as key words but will be followed by an indication of technical context. The assignment of links, rules, and weights is optional.

Unclassified

Security Classification

AD-651416

New pages

Spar Fatigue Analysis

A complete fatigue analysis of the spar was performed for each of the conditions in the flight spectrum. Spanwise station $r = 22.9$ feet was the most highly stressed station of the spar for all conditions analyzed for fatigue. A sample calculation is shown in detail, and the complete results are summarized in Table L11.

Evaluation of the spar shows a service life of almost 9000 hours, greatly exceeding the design requirements of the work statement. However, its replacement is on an "on-condition" basis. The blade BLM system provides a fail-safe spar design, by visually indicating the structural integrity of the spar. The service time combined with the BLM system eliminates the need for any arbitrary replacement time. (Replacement is "on condition" as determined by BLM indications.)

The method used to predict the effect of repeated loads on the blade spar uses the hypothesis by M. A. Miner (Reference 36) on the concept of cumulative damage. If N is the number of applied stress cycles at a specified stress level and M is the number of cycles required to initiate a fatigue crack at that stress level, Miner's hypothesis states that a fatigue crack will be initiated when the summation of the increments of fatigue damage equals unity, or

$$\sum_{i=1}^N \frac{N_i}{M_i} = 1$$

The reliability of the damage calculation is the same as the reliability associated with the S-N curve used to determine the various values of M .

An S-N curve is shown in Figure 189. It is based on full-sized test specimens of similar geometry tested in the Sikorsky Fatigue Testing Laboratory. The specimens were tested with steady loads and combined flapwise and edgewise bending moments applied in proportion to actual flight values. The mean curve is then reduced to obtain a working curve.

RECEIVED

OCT 13 1967

TABLE LII
FATIGUE ANALYSIS OF SPAR

CFSTI

Condition	Mission	Time %	Vibratory Stress at 8000 lb/in ² Steady	Allowable Cycles Figure 189	Allowable Time hr	Damage
Warm-up and Takeoff	12 Ton	1.350	-	∞	∞	0
	20 Ton	1.225	-	∞	∞	0
Hover	12 Ton	14.100	-	∞	∞	0
(Steady State)	20 Ton	7.325	-	∞	∞	0
Hover	12 Ton	1.425	-	∞	∞	0
(Turns and Reversals)	20 Ton	3.175	-	∞	∞	0
Cruise	12 Ton	53.125	-	∞	∞	0
(Steady State)	20 Ton	11.275	-	∞	∞	0
Maneuvers and Gusts	12 Ton					
L. F. =1.13	12 Ton	3.504	5,750	∞	∞	0
L. F. =1.38	12 Ton	.950	8,000	1.0 X 10 ⁸	11,410	.00008
L. F. =1.63	12 Ton	.300	10,000	2.5 X 10 ⁶	285	.00105
L. F. =1.88	12 Ton	.100	12,250	7.0 X 10 ⁵	80	.00125
L. F. =2.13	12 Ton	.079	14,250	3.4 X 10 ⁵	39	.00202
L. F. =2.50*	12 Ton	.007	12,250	7.0 X 10 ⁵	69	.00010
L. F. =2.50	12 Ton	.060	17,662	1.4 X 10 ⁵	16	.00375
		<u>5.000</u>				
Maneuvers and Gusts	20 Ton					
L. F. =1.13	20 Ton	1.500	5,500	∞	∞	0
L. F. =1.38	20 Ton	.270	7,000	∞	∞	0
L. F. =1.63	20 Ton	.124	9,500	4.5 X 10 ⁶	514	.00024
L. F. =1.88	20 Ton	.062	11,800	8.0 X 10 ⁵	91	.00068
L. F. =2.50*	20 Ton	.007	11,226	1.1 X 10 ⁶	109	.00006
L. F. =2.50	20 Ton	.037	16,978	1.65 X 10 ⁵	19	.00197
		<u>2.000</u>				

Σ =100.000

Total Damage = .01120

Replacement Life = $\frac{100}{\text{Damage}} = \frac{100}{.01120} = 8928 \text{ hr.}$

Note: All conditions are at 8,760 cycles/hour except as noted by asterisk.

* Power Off at 10,080 cycles/hr.